Universidade de
Aveiro

2022

Bohdan Kulyk

Grafeno em papel para dispositivos flexíveis: sensores e OLEDs

Graphene on paper for flexible devices: sensors and OLEDs

Universidade de Aveiro

2022

Bohdan Kulyk

Grafeno em papel para dispositivos flexíveis: sensores e OLEDs

Graphene on paper for flexible devices: sensors and OLEDs

Tese apresentada à Universidade de Aveiro para cumprimento dos requisitos necessários à obtenção do grau de Doutor em Nanociências e Nanotecnologias, realizada sob a orientação científica da Prof. Doutora Florinda Mendes da Costa, Professora Associada com Agregação do Departamento de Física da Universidade de Aveiro, do Prof. Doutor Luiz Fernando Ribeiro Pereira, Professor Auxiliar do Departamento de Física da Universidade de Aveiro, e do Prof. Doutor Luís Miguel Nunes Pereira, Professor Associado Convidado do Departamento de Ciência dos Materiais da NOVA School of Science and Technology | FCT NOVA.

Apoio financeiro da FCT através da bolsa de doutoramento SFRH/BD/141525/2018 e do Laboratório Associado i3N (LA/P/0037/2020, UIDB/50025/2020 e UIDP/50025/2020), financiado através da FCT, do MCTES e do FSE.

Dedicado à minha mãe e à minha irmã, bem como a todos os ucranianos que têm ensinado a mim e ao mundo o verdadeiro significado de coragem, resiliência e determinação.

o júri

presidente

Prof. Doutor Victor Miguel Carneiro de Sousa Ferreira
professor catedrático da Universidade de Aveiro

vogais

Prof. Doutora Maria Goreti Ferreira Sales
professora catedrática da Universidade de Coimbra

Prof. Doutor Henrique Leonel Gomes
professor associado com agregação da Universidade de Coimbra

Prof. Doutora Florinda Mendes da Costa
professora associada com agregação da Universidade de Aveiro

Prof. Doutor Pedro Miguel Cândido Barquinha
professor associado da Universidade Nova de Lisboa

Prof. Doutor Vítor João Gomes da Silva Sencadas
professor auxiliar em regime laboral da Universidade de Aveiro

acknowledgements

I would like to begin by expressing my gratitude to my supervisors, Professor Florinda Costa, Professor Luiz Pereira and Professor Luís Pereira, for guiding my work while still giving me all the freedom I could ask for to grow and develop in my own way. I am also grateful to my former co-supervisor, Professor Elvira Fortunato, particularly for welcoming me at her laboratories at NOVA School of Science and Technology.

A very special thank you to Professor Florinda and to António José Fernandes, not just for creating a great working environment, but also for being there for me as friends and mentors, with full support and dedication to helping me in so many ways. Also, a big thank you to Alexandre Carvalho, for contributing to this great working environment and being always available to help. I truly feel lucky to be a part of this group.

I would also like to thank José Germino for all his work, dedication and shared knowledge concerning the development of OLEDs, as well as for not giving up even when it seemed like nothing would work and there was barely any time left. Big thanks to Beatriz Silva as well, for helping me take the first (and most important) steps in the synthesis and applications of paper-LIG, spending countless of hours on fickle lasers and helping me to make sense of it all. I am also grateful to Diana Gaspar, for being always available to help with the cellulose substrates.

To Professor Caroline Murawski and everyone at her group (Rabiul, Ilenia, Jens and Giuseppe), as well as to everyone at KSI Meinsberg, I am thankful for welcoming me at their institute, and for making my stay in Waldheim as comfortable and as productive as possible.

I also thank Nuno Santos, Sónia Oliveira, Jorge Moura, Júlia Zanoni, Ana Luís Moreira, Joana Rodrigues and everyone who works or worked alongside me in the working space where I spent so many hours. Thanks as well to everyone who contributed to the works that comprise this thesis, as well as to everyone at the Department of Physics who has helped me along the way.

To conclude, I am extremely grateful to my friends Vedrana Radović, Ioana Șerban, Rita Sardão, Rita Almeida, Joana Sabino, Filipe Martinho, Pedro Ouro and João Lucas Gomes, all of whom, in one way or another, have been important throughout this journey. And, of course, thank you to my family.

palavras-chave

grafeno, papel, OLEDs, sensores físicos, sensores eletroquímicos, celulose, deposição química em fase vapor, grafeno induzido por laser, paper-LIG, eletrónica flexível.

resumo

O interesse na eletrónica flexível tem crescido consideravelmente devido ao desenvolvimento de produtos e dispositivos com novas funcionalidades e maior conforto na utilização dos mesmos. O grafeno, com uma combinação única de propriedades, surge como um candidato natural para este tipo de aplicações. Simultaneamente, a eletrónica em papel tem-se revelado como uma vertente potencialmente significativa na área da eletrónica flexível. Assim, torna-se particularmente interessante investigar a combinação destes dois materiais para o desenvolvimento de novas e disruptivas aplicações.

Este trabalho explora o desenvolvimento de dois tipos de dispositivos flexíveis à base de grafeno em papel: sensores físicos e eletroquímicos e díodos orgânicos emissores de luz (OLEDs).

No contexto dos sensores é abordada uma das mais recentes adições à família dos materiais à base de grafeno: o grafeno induzido por laser obtido a partir do papel (*paper-LIG*), uma espuma de grafeno sintetizada por um processo rápido e de baixo custo. É demonstrada pela primeira vez a sensibilidade do *paper-LIG* a estímulos mecânicos (distensão e flexão), bem como à humidade e temperatura (neste último caso também para o grafeno induzido por laser obtido a partir de xilana, um biopolímero semelhante à celulose). O desenvolvimento destes dispositivos é acompanhado por um estudo da influência dos parâmetros de síntese no material obtido, constituindo uma contribuição significativa para a descrição deste material e das suas aplicações na literatura. É ainda apresentado um transdutor não-enzimático de *paper-LIG*, para a deteção e quantificação eletroquímica de ácido úrico, demonstrando a sua capacidade de resposta em amostras reais de urina humana, com uma sensibilidade de 0.363 $\mu A\ cm^{-2}\ \mu M^{-1}$ e uma gama linear que abrange o intervalo de concentrações clinicamente relevante para este parâmetro fisiológico.

No âmbito dos OLEDs, é apresentado um processo otimizado de síntese de grafeno monocamada por deposição química em fase vapor, com vista à sua utilização como elétrodo transparente. A questão da elevada rugosidade tipicamente associada ao papel é colmatada pelo uso de membranas de celulose nanocristalina e de mortalhas transparentes como substratos flexíveis e biodegradáveis, acompanhado pelo desenvolvimento de técnicas modificadas de transferência e empilhamento de múltiplas camadas de grafeno. As propriedades deste material são melhoradas pela evaporação térmica de MoO_3, permitindo a construção de OLEDs com 0.34% de eficiência quântica externa.

O desenvolvimento destes dispositivos não só contribui para reafirmar o vasto potencial do grafeno em conjugação com o papel, como serve também para introduzir novas abordagens no contexto de dispositivos flexíveis de baixo custo e biodegradáveis.

keywords

graphene, paper, OLEDs, physical sensors, electrochemical sensors, cellulose, chemical vapour deposition, laser-induced graphene, paper-LIG, flexible electronics.

abstract

The interest in flexible electronics has been growing considerably due to the possibility of products and devices with novel functionalities and improved comfort in their utilization. Graphene, with a combination of properties, is a natural candidate for these applications. Simultaneously, paper electronics is proving itself as a potentially significant branch of flexible electronics. Thus, it is particularly interesting to investigate the combination of these two materials for the development of novel and disruptive applications.

This work covers the development of two types of flexible devices based on graphene and paper: physical and electrochemical sensors and organic light emitting diodes (OLEDs).

In the context of sensors, one of the most recent additions to the family of graphene-based materials is explored: laser-induced graphene obtained from paper (paper-LIG), a graphene foam synthesized by a fast and low-cost process. The sensibility of paper-LIG to mechanical stimuli (strain and bending), as well as to humidity and temperature (in the latter case also shown for laser-induced graphene obtained from xylan, a biopolymer similar to cellulose) is demonstrated. The development of these devices is accompanied by a study of the influence of the synthesis parameters on the obtained material, comprising a sizeable contribution to the description of this material and its applications in the literature. Additionally, a non-enzymatic paper-LIG transductor for the electrochemical detection and quantification of uric acid is presented, demonstrating its response capability in real human urine samples, with a sensitivity of 0.363 $\mu A\ cm^{-2}\ \mu M^{-1}$ and a linear range that covers the clinically relevant concentration range for this physiological parameter.

In the scope of OLEDs, an optimized graphene synthesis process by chemical vapour deposition is presented, with the goal of using this single-layer graphene as a transparent electrode. The issue of high surface roughness typical of paper is addressed by the use of cellulose nanocrystal membranes and transparent rolling papers as flexible, biodegradable substrates, accompanied by the development of modified graphene film transfer and stacking approaches. The properties of this material are improved by thermal evaporation of MoO_3, allowing the construction of OLEDs with 0.34% external quantum efficiency.

The development of these devices not only contributes to reaffirm the vast potential of graphene, but also serves to introduce novel approaches in the context of low-cost and biodegradable flexible devices.

Contents

Abbreviations

μPAD – microfluidic paper-based assay device (or microfluidic paper-based analytical device)
AFM – atomic force microscopy
CE – current efficiency
CNTs – carbon nanotubes
CVD – chemical vapour deposition
DPV – differential pulse voltammetry
EIL – electron injection layer
ELISA – enzyme-linked immunosorbent assay
EML – emissive layer
EQE – external quantum efficiency
ETL – electron transport layer
FET – field effect transistor
GFET – graphene field effect transistor
GMR – giant magnetoresistance
GO – graphene oxide
HIL – hole injection layer
HOMO – highest occupied molecular orbital
HTL – hole transport layer
ISC – intersystem crossing
ITO – indium tin oxide
LIG – laser-induced graphene
LOD – limit of detection
LUMO – lowest unoccupied molecular orbital
NP – nanoparticle
OLED – organic light emitting diode
PAD – paper-based assay device (or paper-based analytical device)
Paper-LIG – laser-induced graphene obtained from paper
PDMS – polydimethylsiloxane
PEDOT:PSS – poly(3,4-ethylenedioxythiophene):poly(styrenesulphonate)
PET – polyethylene terephthalate
PI – polyimide
PMMA - poly(methyl methacrylate)
rGO – reduced graphene oxide
RH – relative humidity
SEM – scanning electron microscopy
SPP – surface plasmon polariton
SPR – surface plasmon resonance
TADF – thermally activated delayed fluorescent
TCM – transparent conductive material
TEM – transmission electron spectroscopy
TTA – triplet-triplet annihilation
UPS – ultraviolet photoelectron spectroscopy
XPS – X-ray photoelectron spectroscopy

Organic compounds commonly used in OLEDs:

Alq_3 – tris-(8-hydroxyquinolate)-aluminium
FIrpic – iridium(III) bis[(4,6-difluorophenyl)-pyridinato-N,C2'] picolinate
$Ir(ppy)_2(acac)$ – bis[2-(2-pyridinyl-N)phenyl-C](2,4-pentanedionato-O^2,O^4)iridium(III)
NPB – N,N-bis-(1-naphthyl)-N,N'-diphenyl-1,1'-biphenyl-4,4'-diamin
TAPC – 1,1-Bis[(di-4-tolylamino)phenyl]cyclohexane
TCTA – 4,4',4''-tri(N-carbazolyl)triphenylamine
TPBi – 1,3,5-tris(2-N-phenylbenzimidazolyl) benzene
TPD – N,N'-Bis(3-methylphenyl)-N,N'-diphenylbenzidine

Preface

Thesis motivation and structure

The aim of this preface is to give the reader a general understanding of the motivation behind this thesis, along with a brief description of its structure.

Graphene is a two-dimensional carbon allotrope that has been attracting a large amount of interest since it was isolated, in 2004, by Andre Geim and Konstantin Novoselov [1]. This interest is based on the unique properties of this material, the combination of which has opened the door not only to interesting new science, but also to the possibility of a wide range of technological applications.

A particularly exciting field where graphene is attracting a lot of attention is the field of flexible electronics [2]. Graphene's excellent mechanical properties, such as large Young's modulus and intrinsic tensile strength [3], allied to the outstanding electron mobility of this material [4], make it a very good candidate for the role of a flexible conductor. Such properties are very important for novel devices where flexibility will provide new functionality and increased comfort for their users.

Low-cost sensors are one group of such flexible devices. Here, flexibility allows them to be used as wearables for continuous monitoring of physiological parameters. In fact, graphene has shown great potential as a biosensing platform [5–7]. This is due to the large specific surface area of graphene, which makes graphene highly sensitive to different chemical species on its surface. Additionally, this characteristic helps in the efforts towards the miniaturization of biosensors, important for the integration of different types of sensors on the same platform (enabling multisensing systems), as well as to decrease the amount of sample and biological reagents required for their operation.

Another type of devices that can benefit from flexible conductors are Organic Light Emitting Diodes (OLEDs) [8]. Having a prominent role in consumer electronics, such as smartphone and TV displays, OLEDs may be important in the development of the flexible counterparts of these products. Graphene is particularly appealing for the use in flexible OLEDs as it is also an optically transparent material [9].

Also gaining prominence in the context of flexible electronics is the use of paper [10]. It can be employed as a substrate or even as an active component of devices such as paper-based transistors [11]. The main selling points of this material for flexible electronics are its low cost, biodegradability and widespread availability. Moreover, the capillarity properties of paper may be important for flexible sensors [12,13], allowing the development of microfluidic systems. As for OLEDs, devices based on paper and cellulose materials are largely underexplored [14–19], due to considerable challenges that such substrates present in terms of surface roughness and affinity to water.

With this in mind, the goal of this thesis is to **explore the opportunities and challenges in combining graphene and paper as components of flexible electronic devices**, in particular paper-based sensors and OLEDs. This is motivated by the desire to expand the range of graphene applications, hoping to introduce new ones capable of taking full advantage of its unique combination of properties. Specifically in the case of paper-based sensors, this work aims to explore some novel approaches relying on the most recent developments in the field of graphene-based materials, such as the synthesis of laser-induced graphene (LIG). As for OLEDs, the objective is to take on the challenge of using paper as a viable substrate, despite its seeming incompatibility with this type of device, and to demonstrate the first cellulose-supported OLED with a graphene as a transparent electrode.

***

This thesis is structured in a way that allows the reader to get a general understanding of the most relevant concepts in each of the fields covered in this work, before diving into the new experimental results stemming from it, most of which have been published in peer-reviewed journals.

Chapter 1 introduces graphene as a versatile material with outstanding properties (**Section 1.1**), as well as the field of paper electronics (**Section 1.2**). This is followed by **Section 1.3** and **Section 1.4** providing a literature review of the use of paper and graphene in sensing and the most relevant trends in the field of OLEDs, respectively.

Chapter 2 presents detailed accounts of four works undertaken in the context of this PhD. The first one (**Section 2.1**), concerning the synthesis and application of laser-induced graphene derived from paper (paper-LIG) in strain and bending sensors has been published in the journal "ACS Applied Materials & Interfaces", under the reference "Laser-Induced Graphene from Paper for Mechanical Sensing," *ACS Appl. Mater. Interfaces*, 13(8), 10210-10221, 2021 (https://doi.org/10.1021/acsami.0c20270). The second one (**Section 2.2**), describing the formation of paper-LIG using an ultraviolet (UV) laser and its functioning as a sensor of humidity and temperature, has been published in "Advanced Materials Technologies" under the reference "Laser-Induced Graphene from Paper by Ultraviolet Irradiation: Humidity and Temperature Sensors," *Adv. Mater. Technol.*, 7, 2101311, 2022 (https://doi.org/10.1002/admt.202101311). The third work (**Section 2.3**), concerning, among other topics, the synthesis of LIG from xylan and its application in temperature sensing, has been published in "Diamond and Related Materials", under the reference "Conversion of paper and xylan into laser-induced graphene for environmentally friendly sensors," *Diam. Relat. Mater.*, 123, 108855, 2022 (https://doi.org/10.1016/j.diamond.2022.108855). Lastly, **Section 2.4** presents results regarding the application of paper-LIG in non-enzymatic electrochemical biosensors for the detection and quantification of uric acid, published in "Carbon" under the reference "Laser-induced graphene from paper for non-enzymatic uric acid electrochemical sensing in urine," *Carbon*, 197, 253-263, 2022 (https://doi.org/10.1016/j.carbon.2022.06.013).

Chapter 3 is devoted to two works concerning the development of graphene transparent electrodes and OLEDs. **Section 3.1** begins by introducing a novel graphene synthesis approach, aimed at reducing the nucleation density and the amount of adlayers to improve the electronic properties and uniformity of the resulting graphene. This work was published in "Carbon" under the reference "Millimetre sized graphene domains through in situ oxidation/reduction treatment of the copper substrate," *Carbon*, 169, 403-415, 2020 (https://doi.org/10.1016/j.carbon.2020.08.002). **Section 3.2** describes the development of OLEDs using the high-quality graphene films obtained in the previously described work, reporting a flexible OLED using a graphene anode on a cellulose substrate (a manuscript in preparation for submission).

Finally, **Chapter 4** draws the main conclusions from all the work developed in this thesis, highlighting its contributions to the fields of flexible devices, paper electronics and graphene. Opportunities for future work are also discussed, and the main outputs of the thesis are listed.

References

[1] K.S. Novoselov, A.K. Geim, S. V. Morozov, D. Jiang, Y. Zhang, S. V. Dubonos, I. V. Grigorieva, A.A. Firsov, "Electric field effect in atomically thin carbon films," *Science*, 306, 666–669, **2004**. https://doi.org/10.1126/science.1102896.

[2] A.C. Ferrari, F. Bonaccorso, V.I. Fal'ko, K.S. Novoselov, S. Roche, P. Bøggild, S. Borini, F.H.L. Koppens, V. Palermo, N.M. Pugno, J.A. Garrido, R. Sordan, A. Bianco, L. Ballerini, M. Prato, E. Lidorikis, J. Kivioja, C. Marinelli, T. Ryhänen, A.F. Morpurgo, J.N. Coleman, V. Nicolosi, L. Colombo, A. Fert, M. Garcia-Hernandez, A. Bachtold, G.F. Schneider, F. Guinea, C. Dekker, M. Barbone, Z.Z. Sun, C. Galiotis, A.N. Grigorenko, G. Konstantatos, A. Kis, M.I. Katsnelson, L.M.K. Vandersypen, A. Loiseau, V. Morandi, D. Neumaier, E. Treossi, V. Pellegrini, M. Polini, A. Tredicucci, G.M. Williams, B. Hee Hong, J.-H. Ahn, J. Min Kim, H. Zirath, B.J. van Wees, H. van der Zant, L. Occhipinti, A. Di Matteo, I.A. Kinloch, T. Seyller, E. Quesnel, X.L. Feng, K.B.K. Teo, N.L. Rupesinghe, P.J. Hakonen, S.R.T. Neil, Q. Tannock, T. Löfwander, J.M. Kinaret, "Science and technology roadmap for graphene, related two-dimensional crystals, and hybrid systems," *Nanoscale*, 7, 4598–4810, **2015**. https://doi.org/10.1039/C4NR01600A.

[3] C. Lee, X. Wei, J.W. Kysar, J. Hone, "Measurement of the elastic properties and intrinsic strength of monolayer graphene," *Science*, 321, 385–388, **2008**. https://doi.org/10.1126/science.1157996.

[4] A.H. Castro Neto, F. Guinea, N.M.R. Peres, K.S. Novoselov, A.K. Geim, "The electronic properties of graphene," *Rev. Mod. Phys.*, 81, 109–162, **2009**. https://doi.org/10.1103/RevModPhys.81.109.

[5] C.I.L. Justino, A.R. Gomes, A.C. Freitas, A.C. Duarte, T.A.P. Rocha-Santos, "Graphene based sensors and biosensors," *TrAC - Trends Anal. Chem.*, 91, 53–66, **2017**. https://doi.org/10.1016/j.trac.2017.04.003.

[6] S. Kochmann, T. Hirsch, O.S. Wolfbeis, "Graphenes in chemical sensors and biosensors," *TrAC - Trends Anal. Chem.*, 39, 87–113, **2012**. https://doi.org/10.1016/j.trac.2012.06.004.

[7] T. Kuila, S. Bose, P. Khanra, A.K. Mishra, N.H. Kim, J.H. Lee, "Recent advances in graphene-based biosensors," *Biosens. Bioelectron.*, 26, 4637–4648, **2011**. https://doi.org/10.1016/j.bios.2011.05.039.

[8] T.-H. Han, H. Kim, S.-J. Kwon, T.-W. Lee, "Graphene-based flexible electronic devices," *Mater. Sci. Eng. R Reports.*, 118, 1–43, **2017**. https://doi.org/https://doi.org/10.1016/j.mser.2017.05.001.

[9] R.R. Nair, P. Blake, A.N. Grigorenko, K.S. Novoselov, T.J. Booth, T. Stauber, N.M.R. Peres, A.K. Geim, "Fine Structure Constant Defines Visual Transparency of Graphene," *Science*, 320, 1308–1308, **2008**. https://doi.org/10.1126/science.1156965.

[10] D. Tobjörk, R. Österbacka, "Paper Electronics," *Adv. Mater.*, 23, 1935–1961, **2011**. https://doi.org/10.1002/adma.201004692.

[11] E. Fortunato, N. Correia, P. Barquinha, L. Pereira, G. Goncalves, R. Martins, "High-

performance flexible hybrid field-effect transistors based on cellulose fiber paper," *IEEE Electron Device Lett.*, 29, 988–990, **2008**. https://doi.org/10.1109/LED.2008.2001549.

[12] A.M. López-Marzo, A. Merkoçi, "Paper-based sensors and assays: a success of the engineering design and the convergence of knowledge areas," *Lab Chip*., 16, 3150–3176, **2016**. https://doi.org/10.1039/C6LC00737F.

[13] D.D. Liana, B. Raguse, J. Justin Gooding, E. Chow, "Recent advances in paper-based sensors," *Sensors (Switzerland)*, 12, 11505–11526, **2012**. https://doi.org/10.3390/s120911505.

[14] E.F. Gomez, A.J. Steckl, "Improved performance of OLEDs on cellulose/epoxy substrate using adenine as a hole injection layer," *ACS Photonics*, 2, 439–445, **2015**. https://doi.org/10.1021/ph500481c.

[15] S. Purandare, E.F. Gomez, A.J. Steckl, "High brightness phosphorescent organic light emitting diodes on transparent and flexible cellulose films," *Nanotechnology*, 25, **2014**. https://doi.org/10.1088/0957-4484/25/9/094012.

[16] E. Najafabadi, Y.H. Zhou, K.A. Knauer, C. Fuentes-Hernandez, B. Kippelen, "Efficient organic light-emitting diodes fabricated on cellulose nanocrystal substrates," *Appl. Phys. Lett.*, 105, **2014**. https://doi.org/10.1063/1.4891046.

[17] H. Zhu, Z. Xiao, D. Liu, Y. Li, N.J. Weadock, Z. Fang, J. Huang, L. Hu, "Biodegradable transparent substrates for flexible organic-light-emitting diodes," *Energy Environ. Sci.*, 6, 2105, **2013**. https://doi.org/10.1039/c3ee40492g.

[18] S.H. Min, C.K. Kim, H.N. Lee, D.G. Moon, "An OLED using cellulose paper as a flexible substrate," *Mol. Cryst. Liq. Cryst.*, 563, 159–165, **2012**. https://doi.org/10.1080/15421406.2012.689153.

[19] S. Ummartyotin, J. Juntaro, M. Sain, H. Manuspiya, "Development of transparent bacterial cellulose nanocomposite film as substrate for flexible organic light emitting diode (OLED) display," *Ind. Crops Prod.*, 35, 92–97, **2012**. https://doi.org/10.1016/j.indcrop.2011.06.025.

Chapter 1

Graphene, paper and OLEDs: fundamentals and state of the art

This chapter provides an overview of the different fields relevant to this thesis, both in terms of the basic concepts which underly them and some of the research directions that have been explored in the literature.

Section 1.1 *begins by introducing the most relevant concepts about graphene, focusing on its main properties. This is followed by a brief overview of the different production methods of graphene, highlighting the differences between the resulting materials. Parts of this section reproduce portions of a review article published in the journal* Critical Reviews in Solid State and Materials Sciences *(https://doi.org/10.1080/10408436.2021.1886046). Finally, some of the most relevant characterization approaches are covered, providing an important basis for the discussion of both the reviewed literature and the novel experimental results presented in the following chapters.*

Section 1.2 *presents the field of paper electronics, giving a short rundown of the merits of paper and its modification and processing approaches.*

Section 1.3 *covers paper-based sensors, with particular focus on the field of biosensing, as this is where this material has seen the most success. Some of the most prominent and most recent reports published in the literature are discussed, giving an overview of the most active research avenues and pointing towards potential new ones. When appropriate, relevant examples of the use of graphene in these sensors (particularly paper-based ones) are given.*

Section 1.4 *provides an overview of the different components of OLEDs, covering the basics of the underlying physics as well as the commonly used materials. Particular attention is given to the potential of graphene as a flexible transparent electrode, discussing also the main challenges faced by its adoption in OLEDs. Efforts to address these challenges are then reviewed, with particular emphasis on graphene doping and transfer, along with the most prominent examples of successful development of graphene-based OLEDs.*

1.1 Graphene

1.1.1 General description of graphene and its properties

Graphene is an atomically thin sheet of sp^2-bonded carbon atoms, arranged in a honeycomb pattern, which is either freely suspended or adhered to a substrate [1]. The stacking of individual graphene sheets results in materials known as bilayer, trilayer, few-layer and multilayer graphene, depending on the number of sheets.

The two-dimensional (2D) lattice of monolayer graphene is formed by two interpenetrating planar triangular lattices, with a relative shift corresponding to the distance between two neighbouring carbon atoms, a=142 pm (**Figure 1.1.1**) [2]. This results in inequivalent carbon atoms, depending on whether each of them belongs to the lattice site A or B. Consequently, the properties of electron transport, to which the delocalized π electrons are subject (due to the sp^2 hybridization of the bonds), are such that two conically-shaped energy bands appear, intersecting at a single point at each 1st Brillouin zone corner [3]. These are the so-called Dirac cones, and it can be seen that at low energies they correspond to a linear dispersion relation, such that $E=\hbar k v_F$ (where $\hbar$ is the reduced Planck's constant, k is the electron wavenumber, and v_F is the Fermi velocity) [4]. This, in turn, describes the fact that, in graphene, electrons behave as massless Dirac fermions, moving through the material ballistically. In fact, electron mobilities as high as 350 000 $cm^2 V^{-1} s^{-1}$ have been experimentally achieved in single-layer graphene [5]. Another interesting consequence of this peculiar dispersion relation is the ambipolar electric field-effect [6]. This consists of the tunability of charge carrier density, from hole to electrons and vice-versa, by the application of an electric field perpendicular to the plane defined by the graphene film.

Other unique properties of graphene include very high thermal conductivity (K=5.30×10³ W $m^{-1} K^{-1}$) [7], large Young's modulus and intrinsic tensile strength (E_{Young}=1.0 TPa and σ_{int}=130 GPa) [8], and optical transparency of 97.7% across the entire visible spectrum [9].

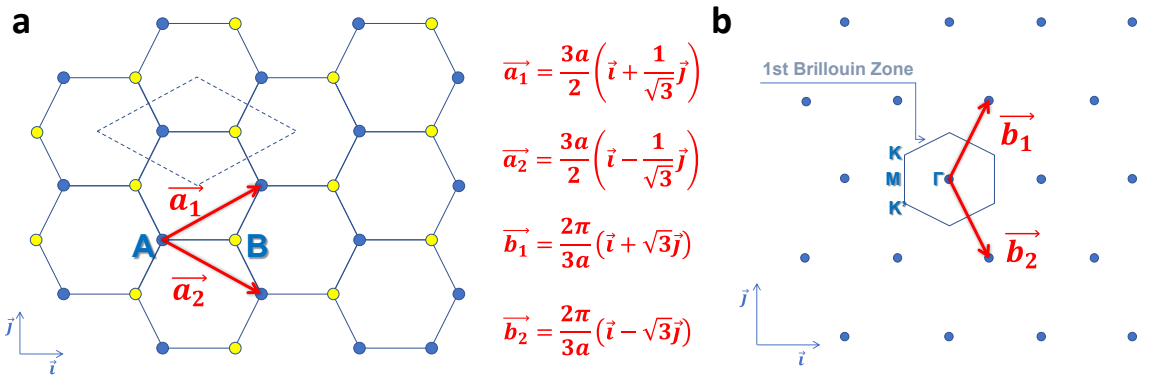

Figure 1.1.1. Graphene's atomic structure in **(a)** real and **(b)** reciprocal space, along with the respective unit vectors, where a is the distance between two neighbouring carbon atoms. $\vec{a_1}$ and $\vec{a_2}$ are the real lattice unit vectors; $\vec{b_1}$ and $\vec{b_2}$ are the reciprocal lattice unit vectors.

1.1.2 Production methods of graphene and graphene-based materials

Graphene's properties are closely linked to the way it is obtained. The first successful method to isolate graphene was through mechanical exfoliation of graphite by successive peelings using scotch tape [6]. This method produces high-quality, single crystal, one atom thick graphene flakes. However, its throughput is very low, and its upscaling is unreasonable.

One of the earliest alternative synthesis methods that emerged was that of epitaxial graphene obtained by graphitization of silicon carbide (SiC) [10]. By heating up single-crystal SiC in ultrahigh vacuum conditions (or even at atmospheric pressure), the Si atoms are sublimated, with the remaining C atoms undergoing graphitization [11]. This process can occur on both the Si-terminated face and on the C-terminated one. In the former case, a C-rich buffer layer covalently bonded to the substrate is present underneath the formed graphene, while in the latter case the interaction with the substrate is much weaker [12]. With the emergence of this synthesis approach, it was quickly established that the obtained graphene is of high quality, with charge carrier mobilities up to 27 000 $cm^2\ V^{-1}\ s^{-1}$ reported as early as 2006, for graphene obtained on the C-terminated face [10]. However, the main disadvantage of graphene synthesis from SiC remains the high price of the substrates [13], as well as the associated limitations in terms of size and difficulties in micromachining of the obtained material [14].

Alternatively, chemical vapor deposition (CVD) has been one of the most prominent graphene synthesis techniques since the early reports showing surface segregation of carbon atoms into graphene domains and continuous layers from transition metals [15–17]. Yu et al. were able to form high-quality graphene layers by exposing a Ni foil to a mixture of CH_4, H_2, and Ar at 1000 °C (at atmospheric pressure). The process was explained on the basis of hydrocarbon gas decomposition, followed by carbon atom diffusion into the metal foil. A controlled cooling of the substrate then leads to carbon segregation, forming graphene at the surface. Moreover, the authors showed that it can be transferred onto insulating substrates using a support layer (silicone rubber) applied to the grown film, followed by the etching of the metal and the application of the graphene/support stack onto the desired substrate.

Shortly after, copper came forth as the preferred growth substrate, thanks to its low carbon solubility and catalytic effect on the hydrocarbon precursor breakdown, allowing to grow continuous SLG films [18]. Typical CVD graphene synthesis on copper is conducted at temperatures close to the latter's melting point. However, low-temperature (300-400 °C) growth has also been demonstrated, using microwave plasma to assist in the decomposition of the hydrocarbon precursors [19]. Currently, the CVD method allows to obtain arbitrarily large single-crystal films [20], as well as graphene with charge carrier mobilities as high as 350 000 $cm^2\ V^{-1}\ s^{-1}$ at room temperature [5] and up to $3\times10^6\ cm^2\ V^{-1}\ s^{-1}$ at 1.8 K [21], with growth at both low and atmospheric pressures possible [22].

It should be pointed out that, while direct growth on insulating substrates is being actively explored [23,24], graphene grown epitaxially or using a catalyst must be, in many cases, transferred onto a different substrate, where it can be processed or incorporated directly for the desired application. An example of this is the transfer of graphene onto insulating substrates for lithographic fabrication of electronic devices, or onto transparent substrates for optical applications. In the case of CVD graphene grown on copper, the metal can be etched away [25,26], or the graphene can be separated from it. The latter can be done electrochemically, by forming hydrogen gas bubbles, through hydrolysis, between graphene and copper, detaching the

former from the latter [27]. Alternatively, water molecules can be intercalated between the graphene and the substrate, weakening their interaction and allowing to pick up the sample using a stamp [21]. Either way, in most cases, a supporting material must be used in order to avoid the tearing or any other damage to the graphene film after its separation from the copper. The most commonly used supporting material is poly(methyl methacrylate) (PMMA), which is usually spin coated on the as-grown graphene at the beginning of the transfer process. However, the removal of the PMMA support layer at the end of the transfer, which is typically done by placing the transferred sample in acetone, leaves behind PMMA residues which are known to be difficult to eliminate completely [28,29]. These residues influence graphene's properties, mainly by giving rise to a p-type doping. Some solutions to this problem have been reported in the literature, namely by means of high-temperature annealings [29] or plasma treatments [30]. Other approaches seek to avoid PMMA altogether by exploring other supporting materials that can be removed without leaving any residues [31–34].

Looking towards mass production of graphene, other processes have emerged, stemming from the basic principle of top-down separation of graphite into individual layers which underlies the original mechanical exfoliation technique. One of the earliest has been through the oxidation of graphite, as in the Hummers method [35]. The resulting material, known as graphene oxide (GO) and most often presented as microscopic flakes, is a form of graphene with a high content of oxygen-containing functional groups. Because of these functionalities, the network of sp^2 bonds characteristic of pristine graphene is disrupted, leading to a poor performance in terms of charge transport. This can be partially recovered, by chemical [36] or thermal [37] reduction of GO, restoring electrical conductivity in what is referred to as reduced graphene oxide (rGO). Both GO and rGO have been explored extensively by the scientific community, benefitting from simplicity of production, good dispersibility in aqueous media [38] and ease of functionalization.

The idea of large-scale mechanical exfoliation has also been explored in ball milling. This is achieved in containers with milling balls which roll against the container's walls, transferring their energy, through direct impact and shear stresses, to the precursor (typically graphite powder) [39]. Usually, a significant aspect of this and other large-scale mechanical exfoliation methods is the solvent used, important to help in the exfoliation process and to stabilize the separated flakes (although dry ball milling is also common). These solvents are typically organic, as their properties usually show a better compatibility with graphene, which improves the exfoliation process [40,41]. However, as this often requires additional purification steps to remove the solvent [42], which can be particularly difficult with high-boiling point ones, inorganic solvents have been explored [43]. Overall, while ball milling is a scalable process only limited by the size of the milling vessel, there is a high degree of structural defects, including oxidation, as well as the inherent functionalization which, in many cases, restricts the spectrum of application of these graphene products. The bare impact of the balls fragments the graphene flakes into smaller ones and induces severe structural defects to the graphene lattice, especially in the basal planes [44–46]. This can be minimized by slowing the rotation speed at the expense of the process time, which can extend to more than one day [47,48]. Ball milling is, thus, time consuming and many thick flakes are present in the final product.

An alternative approach relies on sonication. Here, ultrasonic waves produce localized compressions and rarefactions in the liquid medium, forming vacuum cavities which then collapse, generating high pressure jets. These jets are capable of peeling off graphene layers from graphite, as well as weakening the Van der Waals interaction between the layers. This facilitates the

intercalation of solvent molecules between graphitic planes, allowing for further exfoliation and consequent stabilization of the dispersion. As with other graphite exfoliation approaches, attention must be paid to the choice of the dispersing solvent. Some which have been explored in the literature include N-methyl-2-pyrrolidone (NMP), a wide range of aromatic molecules [49–51] and aqueous surfactants [52,53]. The main drawbacks of sonication exfoliation are the relatively low yields and the long processing times with continuous energy input.

Enhanced exfoliation rates at reduced processing times (down to a few hours or less) can be achieved with methods taking advantage of fluid dynamics effects. Examples of this include exfoliation in tubes rotating at high speeds, where shear forces become strong enough to overcome Van der Waals interactions [54], as well as exfoliation by passing pressurized fluids containing graphite precursors through narrow constriction channels and openings [55]. Besides shear forces, collisions, cavitation and pressure release can also play an important role, with the latter two mechanisms exerting normal forces aiding exfoliation. Other common and efficient approaches using fluid dynamics rely on rotor-stator setups [46,56–58] or rotating blades [59,60] immersed in a fluid containing the graphite precursor and suitable surfactants, while Taylor-Couette flow has also been exploited in arrangements consisting of two concentric cylinders that are able two rotate independently with a graphite dispersion in an appropriate fluid in between them. Importantly, for similar exfoliation energy density, the exfoliation yield of shear stress using fluid dynamics can be about one order of magnitude larger when compared to purely sonication routes [42,46,54,56]. Still, similarly to other exfoliation approaches, the graphene products by shear exfoliation generally suffer from size and thickness polydispersity [61], and there is still a need for more studies with non-toxic and low-cost solvents [57].

Finally, and still in the context of these liquid-phase exfoliation techniques, electrochemical exfoliation is a very attractive prospect, where electric potential is applied to a graphite electrode to promote intercalation of ionic species present in the electrolyte between its layers, leading to physical deformation and an increase in the interlayer distance, and thus weakening the Van der Walls forces to separate the graphene layers [62–64]. The applied potential can be positive or negative, and either constant or varying. Several solutions and ionic liquids are also available for the role of the electrolyte. Despite the recent progress, further studies are needed in order to establish electrochemical exfoliation as a definite alternative for scalable graphene production, preferentially without the aid of post-sonication or other co-assisting routes. Such should be accomplished using cheap, environmental-friendly, and widely available chemicals, which remains a challenge.

An entirely different type of graphene-based material became available when, in 2014, the group of James Tour, from the University of Rice, reported the direct conversion of flexible commercial polymers into porous graphene films using laser radiation (**Figure 1.1.2**) [65]. The resulting material, dubbed laser-induced graphene (LIG), exhibits high electrical conductivity, and benefits from a fast production process using cheap equipment, with the possibility of being patterned by controlling the laser beam path along the substrate. Moreover, this direct conversion mechanism is applicable to a wide range of carbon containing substrates, including naturally derived ones such as wood [66], cork [67] and paper [68]. These characteristics continue to attract a lot of interest from the scientific community, particularly in terms of proposed applications. These include supercapacitors [69], energy harvesting devices [70], flexible heaters [71], antibacterial coatings [72] and, particularly, sensors [73], where wearable components and low-cost biosensors constitute the main research avenues.

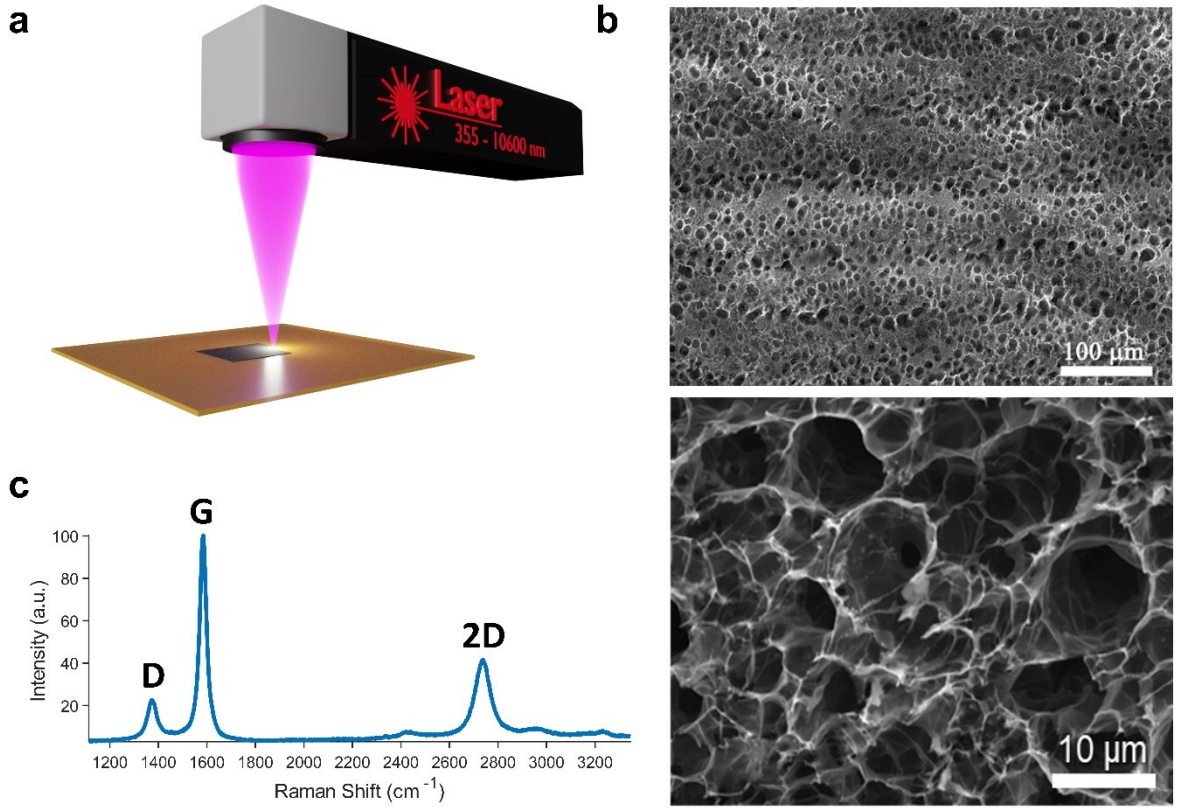

Figure 1.1.2. (a) Schematic illustration of the direct laser writing process for the synthesis of laser-induced graphene (LIG). **(b)** Secondary electron SEM images of LIG. **(c)** Typical Raman spectrum of LIG. Adapted from ref. [74].

Lastly, as an example of the continued efforts in the search for high-volume production of graphene materials, a technique similar to flash sintering has been recently used to produce graphene powder from organic waste in a fast and inexpensive way, with outstanding yields of 1 g per batch [75].

This remarkable variety of types of graphene, each with different properties resulting from the respective production method, gives rise to an even wider range of possible applications for this material. At the same time, it requires careful consideration of the desired characteristics for the choice of how graphene should be obtained.

1.1.3 Characterization of graphene

When talking about the characterization of graphene, perhaps the most relevant technique is Raman spectroscopy. Traditionally being a simple and non-destructive technique, Raman spectroscopy assumes particular importance in the identification of different types of graphene materials, as well as in providing valuable information about their quality and characteristics. For the 514 nm excitation wavelength, the typical Raman spectrum of pristine single-layer graphene shows sharp peaks at ~1580 cm^{-1} and ~2700 cm^{-1} [76]. The former, known as the G peak, is due to the stretching of the sp^2-hybridized bonds, while the latter, referred to as the 2D peak, is originated by the scattering of photo-excited electrons by two phonons, by means of a double resonance mechanism [77]. This mechanism is particularly interesting, as it gives information about the dispersion relation of the graphene material. In the case of pristine SLG, the dispersion relation is linear, and so the resulting 2D peak is narrow and symmetrical. But for a larger number of layers with Bernal stacking, the band structure is different, resulting in a splitting of the 2D peak into several components, with a consequent loss of symmetry, lower

intensity and broadening. This allows to distinguish single-layer graphene, where the intensity ratio of 2D and G peaks is $I_{2D}/I_G \approx 4$, from bi-, tri- and multi-layer graphene [76]. This does not apply to turbostratic multi-layer graphene (where the graphene layers are oriented randomly with respect to each other), as in this case the misorientation helps to preserve the band structure of each layer. As a result, in this case the 2D peak maintains its symmetry, but becomes broader and less intense as the number of layers is increased [78]. The same double resonance mechanism behind the 2D peak is also responsible, when involving scattering by a single phonon, for the D peak at ~1350 cm^{-1}. This peak serves as an indication of the presence of structural defects, which are required to satisfy the fundamental Raman selection rule to allow the appearance of this peak [77]. As such, the I_D/I_G intensity ratio is often used as a measure of how defective the graphene sample is. Also interesting to note is that both the D and 2D peaks are dispersive with excitation energy, with a linear upshift with a slope of 50 cm^{-1} eV^{-1} for the D peak [79] and 100 cm^{-1} eV^{-1} for the 2D peak [80]. Finally, other characteristic Raman peaks of graphene include D' (~1620 cm^{-1}), 2D' (~3240 cm^{-1}), D+D'' (~2450 cm^{-1}), D+D' (~2970 cm^{-1}) and 2D+G (~4260 cm^{-1}) [81,82].

As for other characterization techniques that have been successfully used to provide important information about graphene, one can briefly mention optical microscopy and scanning electron microscopy (SEM), which can, for example, provide great contrast for the identification of graphene flakes and films with different numbers of layers [83,84]. Transmission electron microscopy (TEM) is also a well-known technique capable of atomic resolution imaging of graphene and its defects [85], while atomic force microscopy (AFM) is commonly employed in the measurements of the thickness of this material [86]. Different types of photoelectron spectroscopies, such as X-ray photoelectron spectroscopy (XPS) and ultraviolet photoelectron spectroscopy (UPS) have also been used to great effect in the study of surface chemistry and work function of graphene [87].

---------- // ----------

Graphene possesses some truly outstanding properties, and the unique combination of these properties paves the way for a wide range of potential applications. These applications, in turn, are enabled by the rapid developments in the techniques of production of graphene-based materials, expanding even further its possibilities thanks to the variety of the resulting types of graphene. In this context, chemical vapour deposition stands out as the main candidate for large scale production of high-quality single-layer graphene, while approaches like laser-induction and flash synthesis are emerging as particularly well-suited for low-cost applications.

1.1.4 References

[1] A. Bianco, H.M. Cheng, T. Enoki, Y. Gogotsi, R.H. Hurt, N. Koratkar, T. Kyotani, M. Monthioux, C.R. Park, J.M.D. Tascon, J. Zhang, "All in the graphene family - A recommended nomenclature for two-dimensional carbon materials," *Carbon*, 65, 1–6, **2013**. https://doi.org/10.1016/j.carbon.2013.08.038.

[2] P.K. Misra, Physics of Condensed Matter, Academic Press, **2012**.

[3] K.S. Novoselov, S. V. Morozov, T.M.G. Mohinddin, L.A. Ponomarenko, D.C. Elias, R. Yang, I.I. Barbolina, P. Blake, T.J. Booth, D. Jiang, J. Giesbers, E.W. Hill, a. K. Geim, "Electronic properties of graphene," *Phys. Status Solidi*, 244, 4106–4111, **2007**. https://doi.org/10.1002/pssb.200776208.

[4] K.S. Novoselov, a K. Geim, S. V Morozov, D. Jiang, M.I. Katsnelson, I. V Grigorieva, S. V Dubonos, a a Firsov, "Two-dimensional gas of massless Dirac fermions in graphene.," *Nature*, 438, 197–200, **2005**. https://doi.org/10.1038/nature04233.

[5] C. Stampfer, F. Haupt, T. Taniguchi, M. Schmitz, L. Banszerus, K. Watanabe, M. Oellers, J. Dauber, S. Engels, B. Beschoten, "Ultrahigh-mobility graphene devices from chemical vapor deposition on reusable copper," *Sci. Adv.*, 1, e1500222, **2015**. https://doi.org/10.1126/sciadv.1500222.

[6] K.S. Novoselov, A.K. Geim, S. V. Morozov, D. Jiang, Y. Zhang, S. V. Dubonos, I. V. Grigorieva, A.A. Firsov, "Electric field effect in atomically thin carbon films," *Science*, 306, 666–669, **2004**. https://doi.org/10.1126/science.1102896.

[7] A.A. Balandin, S. Ghosh, W. Bao, I. Calizo, D. Teweldebrhan, F. Miao, C.N. Lau, "Superior thermal conductivity of single-layer graphene," *Nano Lett.*, 8, 902–907, **2008**. https://doi.org/10.1021/nl0731872.

[8] C. Lee, X. Wei, J.W. Kysar, J. Hone, "Measurement of the Elastic Properties and Intrinsic Strength of Monolayer Graphene," *Science*, 321, 385–388, **2008**. https://doi.org/10.1126/science.1157996.

[9] R.R. Nair, P. Blake, A.N. Grigorenko, K.S. Novoselov, T.J. Booth, T. Stauber, N.M.R. Peres, A.K. Geim, "Fine Structure Constant Defines Visual Transparency of Graphene," *Science*, 320, 1308–1308, **2008**. https://doi.org/10.1126/science.1156965.

[10] C. Berger, Z. Song, X. Li, X. Wu, N. Brown, C. Naud, D. Mayou, T. Li, J. Hass, A.N. Marchenkov, E.H. Conrad, P.N. First, W.A. de Heer, "Electronic confinement and coherence in patterned epitaxial graphene," *Science*, 312, 1191, **2006**. http://dx.doi.org/10.1126/science.1125925.

[11] K. V. Emtsev, A. Bostwick, K. Horn, J. Jobst, G.L. Kellogg, L. Ley, J.L. McChesney, T. Ohta, S.A. Reshanov, J. Röhrl, E. Rotenberg, A.K. Schmid, D. Waldmann, H.B. Weber, T. Seyller, "Towards wafer-size graphene layers by atmospheric pressure graphitization of silicon carbide," *Nat. Mater.*, 8, 203–207, **2009**. https://doi.org/10.1038/nmat2382.

[12] K. V. Emtsev, F. Speck, T. Seyller, L. Ley, J.D. Riley, "Interaction, growth, and ordering of epitaxial graphene on SiC{0001} surfaces: A comparative photoelectron spectroscopy study," *Phys. Rev. B - Condens. Matter Mater. Phys.*, 77, 1–10, **2008**. https://doi.org/10.1103/PhysRevB.77.155303.

[13] A.C. Ferrari, F. Bonaccorso, V.I. Fal'ko, K.S. Novoselov, S. Roche, P. Bøggild, S. Borini, F.H.L. Koppens, V. Palermo, N.M. Pugno, J.A. Garrido, R. Sordan, A. Bianco, L. Ballerini, M. Prato, E. Lidorikis, J. Kivioja, C. Marinelli, T. Ryhänen, A.F. Morpurgo, J.N. Coleman, V. Nicolosi, L. Colombo, A. Fert, M. Garcia-Hernandez, A. Bachtold, G.F. Schneider, F. Guinea, C. Dekker, M. Barbone, Z.Z. Sun, C. Galiotis, A.N. Grigorenko, G. Konstantatos, A. Kis, M.I. Katsnelson, L.M.K. Vandersypen, A. Loiseau, V. Morandi, D. Neumaier, E. Treossi, V. Pellegrini, M. Polini, A. Tredicucci, G.M. Williams, B. Hee Hong, J.-H. Ahn, J. Min Kim, H. Zirath, B.J. van Wees, H. van der Zant, L. Occhipinti, A. Di Matteo, I.A. Kinloch, T. Seyller, E. Quesnel, X.L. Feng, K.B.K. Teo, N.L. Rupesinghe, P.J. Hakonen, S.R.T. Neil, Q. Tannock, T. Löfwander, J.M. Kinaret, "Science and technology roadmap for graphene, related two-dimensional crystals, and hybrid systems," *Nanoscale*, 7, 4598–4810, **2015**. https://doi.org/10.1039/C4NR01600A.

[14] N. Mishra, J. Boeckl, N. Motta, F. Iacopi, "Graphene growth on silicon carbide: A review," *Phys. Status Solidi Appl. Mater. Sci.*, 213, 2277–2289, **2016**. https://doi.org/10.1002/pssa.201600091.

[15] P.W. Sutter, J.I. Flege, E.A. Sutter, "Epitaxial graphene on ruthenium," *Nat. Mater.*, 7, 406–411, **2008**. https://doi.org/10.1038/nmat2166.

[16] Q. Yu, J. Lian, S. Siriponglert, H. Li, Y.P. Chen, S.S. Pei, "Graphene segregated on Ni surfaces and transferred to insulators," *Appl. Phys. Lett.*, 93, 1–4, **2008**. https://doi.org/10.1063/1.2982585.

[17] J. Coraux, A.T. N'Diaye, C. Busse, T. Michely, "Structural coherency of graphene on Ir(111)," *Nano Lett.*, 8, 565–570, **2008**. https://doi.org/10.1021/nl0728874.

[18] X. Li, W. Cai, J. An, S. Kim, J. Nah, D. Yang, R. Piner, A. Velamakanni, I. Jung, E. Tutuc, S.K. Banerjee, L. Colombo, R.S. Ruoff, "Large area synthesis of high quality and uniform graphene films on copper foils," *Science*, 324, 1312–1314, **2009**. https://doi.org/10.1126/science.1171245.

[19] J. Kim, M. Ishihara, Y. Koga, K. Tsugawa, M. Hasegawa, S. Iijima, "Low-temperature synthesis of large-area graphene-based transparent conductive films using surface wave plasma chemical vapor deposition," *Appl. Phys. Lett.*, 98, 2011–2014, **2011**. https://doi.org/10.1063/1.3561747.

[20] X. Xu, Z. Zhang, J. Dong, D. Yi, J. Niu, M. Wu, L. Lin, R. Yin, M. Li, J. Zhou, S. Wang, J. Sun, X. Duan, P. Gao, Y. Jiang, X. Wu, H. Peng, R.S. Ruoff, Z. Liu, D. Yu, E. Wang, F. Ding, K. Liu, "Ultrafast epitaxial growth of metre-sized single-crystal graphene on industrial Cu foil," *Sci. Bull.*, 62, 1074–1080, **2017**. https://doi.org/https://doi.org/10.1016/j.scib.2017.07.005.

[21] L. Banszerus, M. Schmitz, S. Engels, M. Goldsche, K. Watanabe, T. Taniguchi, B. Beschoten, C. Stampfer, "Ballistic Transport Exceeding 28 μm in CVD Grown Graphene," *Nano Lett.*, 16, 1387–1391, **2016**. https://doi.org/10.1021/acs.nanolett.5b04840.

[22] R. Muñoz, C. Gómez-Aleixandre, "Review of CVD synthesis of graphene," *Chem. Vap. Depos.*, 19, 297–322, **2013**. https://doi.org/10.1002/cvde.201300051.

[23] Y. Dong, S. Guo, H. Mao, C. Xu, Y. Xie, J. Deng, L. Wang, Z. Du, F. Xiong, J. Sun, "In Situ Growth of CVD Graphene Directly on Dielectric Surface toward Application," *ACS Appl. Electron. Mater.*, 2, 238–246, **2020**. https://doi.org/10.1021/acsaelm.9b00719.

[24] J. Li, M. Chen, A. Samad, H. Dong, A. Ray, J. Zhang, X. Jiang, U. Schwingenschlögl, J. Domke, C. Chen, Y. Han, T. Fritz, R.S. Ruoff, B. Tian, X. Zhang, "Wafer-scale single-crystal monolayer graphene grown on sapphire substrate," *Nat. Mater.*, **2022**. https://doi.org/10.1038/s41563-021-01174-1.

[25] J.W. Suk, A. Kitt, C.W. Magnuson, Y. Hao, S. Ahmed, J. An, A.K. Swan, B.B. Goldberg, R.S. Ruoff, "Transfer of CVD-grown monolayer graphene onto arbitrary substrates," *ACS Nano*, 5, 6916–6924, **2011**. https://doi.org/10.1021/nn201207c.

[26] X. Li, Y. Zhu, W. Cai, M. Borysiak, B. Han, D. Chen, R.D. Piner, L. Colombo, R.S. Ruoff, "Transfer of large-area graphene films for high-performance transparent conductive electrodes.," *Nano Lett.*, 9, 4359–63, **2009**. https://doi.org/10.1021/nl902623y.

[27] Y. Wang, Y. Zheng, X. Xu, E. Dubuisson, Q. Bao, J. Lu, K.P. Loh, "Electrochemical Delamination of CVD Grown Graphene Film: Toward the Recyclable Use of Copper Catalyst SI," *ACS Nano*, 1–10, **2011**. http://pubs.acs.org/doi/abs/10.1021/nn203700w?mi=tkj5eh&af=R&pageSize=20&title=graphene.

[28] A. Pirkle, J. Chan, A. Venugopal, D. Hinojos, C.W. Magnuson, S. McDonnell, L. Colombo, E.M. Vogel, R.S. Ruoff, R.M. Wallace, "The effect of chemical residues on the physical and electrical properties of chemical vapor deposited graphene transferred to SiO 2," *Appl. Phys. Lett.*, 99, 122108, **2011**. https://doi.org/10.1063/1.3643444.

[29] J. Chan, A. Venugopal, A. Pirkle, S. McDonnell, D. Hinojos, C.W. Magnuson, R.S. Ruoff, L. Colombo, R.M. Wallace, E.M. Vogel, "Reducing extrinsic performance-limiting factors in graphene grown by chemical vapor deposition," *ACS Nano*, 6, 3224–3229, **2012**. https://doi.org/10.1021/nn300107f.

[30] N. Peltekis, S. Kumar, N. McEvoy, K. Lee, A. Weidlich, G.S. Duesberg, "The effect of downstream plasma treatments on graphene surfaces," *Carbon*, 50, 395–403, **2012**. https://doi.org/10.1016/j.carbon.2011.08.052.

[31] Z. Zhang, J. Du, D. Zhang, H. Sun, L. Yin, L. Ma, J. Chen, D. Ma, H.-M. Cheng, W. Ren, "Rosin-enabled ultraclean and damage-free transfer of graphene for large-area flexible organic light-emitting diodes," *Nat. Commun.*, 8, 14560, **2017**. https://doi.org/10.1038/ncomms14560.

[32] D. Luo, X. You, B.-W. Li, X. Chen, H.J. Park, M. Jung, T.Y. Ko, K. Wong, M. Yousaf, X. Chen, M. Huang, S.H. Lee, Z. Lee, H.-J. Shin, S. Ryu, S.K. Kwak, N. Park, R.R. Bacsa, W. Bacsa, R.S. Ruoff, "Role of Graphene in Water-Assisted Oxidation of Copper in Relation to Dry Transfer of Graphene," *Chem. Mater.*, 29, 4546–4556, **2017**. https://doi.org/10.1021/acs.chemmater.7b01276.

[33] J.-Y. Hong, Y.C. Shin, A. Zubair, Y. Mao, T. Palacios, M.S. Dresselhaus, S.H. Kim, J. Kong, "A Rational Strategy for Graphene Transfer on Substrates with Rough Features," *Adv. Mater.*, 28, 2382–2392, **2016**. https://doi.org/10.1002/adma.201505527.

[34] A.F. Carvalho, A.J.S. Fernandes, M. Ben Hassine, P. Ferreira, E. Fortunato, F.M. Costa, "Millimeter-sized few-layer suspended graphene membranes," *Appl. Mater. Today*, 21, 100879, **2020**. https://doi.org/10.1016/j.apmt.2020.100879.

[35] W.S. Hummers, R.E. Offeman, "Preparation of Graphitic Oxide," *J. Am. Chem. Soc.*, 80, 1339–1339, **1958**. https://doi.org/10.1021/ja01539a017.

[36] M.C. Kim, G.S. Hwang, R.S. Ruoff, "Epoxide reduction with hydrazine on graphene: A first principles study," *J. Chem. Phys.*, 131, 064704, **2009**. https://doi.org/10.1063/1.3197007.

[37] D. Yang, A. Velamakanni, G. Bozoklu, S. Park, M. Stoller, R.D. Piner, S. Stankovich, I. Jung, D.A. Field, C.A. Ventrice, R.S. Ruoff, "Chemical analysis of graphene oxide films after heat and chemical treatments by X-ray photoelectron and Micro-Raman spectroscopy," *Carbon*, 47, 145–152, **2009**. https://doi.org/10.1016/j.carbon.2008.09.045.

[38] G. Wang, B. Wang, J. Park, J. Yang, X. Shen, J. Yao, "Synthesis of enhanced hydrophilic and hydrophobic graphene oxide nanosheets by a solvothermal method," *Carbon*, 47, 68–72,

2009. https://doi.org/10.1016/j.carbon.2008.09.002.

[39] C. Knieke, A. Berger, M. Voigt, R.N. Klupp Taylor, J. Röhrl, W. Peukert, "Scalable production of graphene sheets by mechanical delamination," *Carbon*, 48, 3196–3204, **2010**. https://doi.org/10.1016/j.carbon.2010.05.003.

[40] W. Zhao, F. Wu, H. Wu, G. Chen, "Preparation of colloidal dispersions of graphene sheets in organic solvents by using ball milling," *J. Nanomater.*, 2010, **2010**. https://doi.org/10.1155/2010/528235.

[41] Y. Hernandez, M. Lotya, D. Rickard, S.D. Bergin, J.N. Coleman, "Measurement of multicomponent solubility parameters for graphene facilitates solvent discovery," *Langmuir*, 26, 3208–3213, **2010**. https://doi.org/10.1021/la903188a.

[42] M.I. Kairi, S. Dayou, N.I. Kairi, S.A. Bakar, B. Vigolo, A.R. Mohamed, "Toward high production of graphene flakes-a review on recent developments in their synthesis methods and scalability," *J. Mater. Chem. A*, 6, 15010–15026, **2018**. https://doi.org/10.1039/c8ta04255a.

[43] L. Liu, Z. Xiong, D. Hu, G. Wu, P. Chen, "Production of high quality single- or few-layered graphene by solid exfoliation of graphite in the presence of ammonia borane," *Chem. Commun.*, 49, 7890–7892, **2013**. https://doi.org/10.1039/c3cc43670e.

[44] A.E. Del Rio-Castillo, C. Merino, E. Díez-Barra, E. Vázquez, "Selective suspension of single layer graphene mechanochemically exfoliated from carbon nanofibres," *Nano Res.*, 7, 963–972, **2014**. https://doi.org/10.1007/s12274-014-0457-4.

[45] I.Y. Jeon, H.J. Choi, S.M. Jung, J.M. Seo, M.J. Kim, L. Dai, J.B. Baek, "Large-scale production of edge-selectively functionalized graphene nanoplatelets via ball milling and their use as metal-free electrocatalysts for oxygen reduction reaction," *J. Am. Chem. Soc.*, 135, 1386–1393, **2013**. https://doi.org/10.1021/ja3091643.

[46] M. Yi, Z. Shen, "A review on mechanical exfoliation for the scalable production of graphene," *J. Mater. Chem. A*, 3, 11700–11715, **2015**. https://doi.org/10.1039/c5ta00252d.

[47] A.S. Al-Sherbini, M. Bakr, I. Ghoneim, M. Saad, "Exfoliation of graphene sheets via high energy wet milling of graphite in 2-ethylhexanol and kerosene," *J. Adv. Res.*, 8, 209–215, **2017**. https://doi.org/10.1016/j.jare.2017.01.004.

[48] W. Zhao, M. Fang, F. Wu, H. Wu, L. Wang, G. Chen, "Preparation of graphene by exfoliation of graphite using wet ball milling," *J. Mater. Chem.*, 20, 5817–5819, **2010**. https://doi.org/10.1039/c0jm01354d.

[49] A.B. Bourlinos, V. Georgakilas, R. Zboril, T.A. Sterioti, A.K. Stubos, "Liquid-Phase Exfoliation of Graphite Towards Solubilized Graphenes," *Small*, 5, 1841–1845, **2009**. https://doi.org/10.1002/smll.200900242.

[50] M. Zhang, R.R. Parajuli, D. Mastrogiovanni, B. Dai, P. Lo, W. Cheung, R. Brukh, P.L. Chiu, T. Zhou, Z. Liu, E. Garfunkel, H. He, "Production of graphene sheets by direct dispersion with aromatic healing agents," *Small*, 6, 1100–1107, **2010**. https://doi.org/10.1002/smll.200901978.

[51] X. An, T. Simmons, R. Shah, C. Wolfe, K.M. Lewis, M. Washington, S.K. Nayak, S. Talapatra, S. Kar, "Stable aqueous dispersions of noncovalently functionalized graphene from graphite and their multifunctional high-performance applications," *Nano Lett.*, 10, 4295–4301, **2010**. https://doi.org/10.1021/nl903557p.

[52] M. Lotya, Y. Hernandez, P.J. King, R.J. Smith, V. Nicolosi, L.S. Karlsson, F.M. Blighe, S. De, Z. Wang, I.T. McGovern, G.S. Duesberg, J.N. Coleman, "Liquid Phase Production of Graphene by Exfoliation of Graphite in Surfactant/Water Solutions," *J. Am. Chem. Soc.*, 131, 3611–3620, **2009**. https://doi.org/10.1021/ja807449u.

[53] L. Guardia, M.J. Fernández-Merino, J.I. Paredes, P. Solís-Fernández, S. Villar-Rodil, A. Martínez-Alonso, J.M.D. Tascón, "High-throughput production of pristine graphene in an aqueous dispersion assisted by non-ionic surfactants," *Carbon*, 49, 1653–1662, **2011**. https://doi.org/10.1016/j.carbon.2010.12.049.

[54] X. Chen, J.F. Dobson, C.L. Raston, "Vortex fluidic exfoliation of graphite and boron nitride," *Chem. Commun.*, 48, 3703–3705, **2012**. https://doi.org/10.1039/c2cc17611d.

[55] K. Zhang, J. Tang, J. Yuan, J. Li, Y. Sun, Y. Matsuba, D.-M. Zhu, L.-C. Qin, "Production of Few-Layer Graphene via Enhanced High-Pressure Shear Exfoliation in Liquid for Supercapacitor Applications," *ACS Appl. Nano Mater.*, 1, 2877–2884, **2018**. https://doi.org/10.1021/acsanm.8b00515.

[56] K.R. Paton, E. Varrla, C. Backes, R.J. Smith, U. Khan, A. O'Neill, C. Boland, M. Lotya, O.M. Istrate, P. King, T. Higgins, S. Barwich, P. May, P. Puczkarski, I. Ahmed, M. Moebius, H. Pettersson, E. Long, J. Coelho, S.E. O'Brien, E.K. McGuire, B.M. Sanchez, G.S. Duesberg, N. McEvoy, T.J. Pennycook, C. Downing, A. Crossley, V. Nicolosi, J.N. Coleman, "Scalable production of large quantities of defect-free few-layer graphene by shear exfoliation in liquids," *Nat. Mater.*, 13, 624–630, **2014**. https://doi.org/10.1038/nmat3944.

[57] Y. Xu, H. Cao, Y. Xue, B. Li, W. Cai, "Liquid-Phase Exfoliation of Graphene: An Overview on Exfoliation Media, Techniques, and Challenges," *Nanomaterials*, 8, 942, **2018**. https://doi.org/10.3390/nano8110942.

[58] J. Tian, L. Guo, X. Yin, W. Wu, "The liquid-phase preparation of graphene by shear exfoliation with graphite oxide as a dispersant," *Mater. Chem. Phys.*, 223, 1–8, **2019**. https://doi.org/10.1016/j.matchemphys.2018.10.039.

[59] M. Yi, Z. Shen, "Kitchen blender for producing high-quality few-layer graphene," *Carbon*, 78, 622–626, **2014**. https://doi.org/10.1016/j.carbon.2014.07.035.

[60] E. Varrla, K.R. Paton, C. Backes, A. Harvey, R.J. Smith, J. McCauley, J.N. Coleman, "Turbulence-assisted shear exfoliation of graphene using household detergent and a kitchen blender," *Nanoscale*, 6, 11810–11819, **2014**. https://doi.org/10.1039/c4nr03560g.

[61] J. Phiri, P. Gane, T.C. Maloney, "High-concentration shear-exfoliated colloidal dispersion of surfactant–polymer-stabilized few-layer graphene sheets," *J. Mater. Sci.*, 52, 8321–8337, **2017**. https://doi.org/10.1007/s10853-017-1049-y.

[62] L. Li, M. Wang, J. Guo, M. Cao, H. Qiu, L. Dai, Z. Yang, "Regulation of radicals from electrochemical exfoliation of a double-graphite electrode to fabricate high-quality graphene," *J. Mater. Chem. C*, 6, 6257–6263, **2018**.

https://doi.org/10.1039/c8tc01565a.

[63] S. Yang, A.G. Ricciardulli, S. Liu, R. Dong, M.R. Lohe, A. Becker, M.A. Squillaci, P. Samorì, K. Müllen, X. Feng, "Ultrafast Delamination of Graphite into High-Quality Graphene Using Alternating Currents," *Angew. Chemie - Int. Ed.*, 56, 6669–6675, **2017**. https://doi.org/10.1002/anie.201702076.

[64] T.C. Achee, W. Sun, J.T. Hope, S.G. Quitzau, C.B. Sweeney, S.A. Shah, T. Habib, M.J. Green, "High-yield scalable graphene nanosheet production from compressed graphite using electrochemical exfoliation," *Sci. Rep.*, 8, 1–8, **2018**. https://doi.org/10.1038/s41598-018-32741-3.

[65] J. Lin, Z. Peng, Y. Liu, F. Ruiz-Zepeda, R. Ye, E.L.G.G. Samuel, M.J. Yacaman, B.I. Yakobson, J.M. Tour, "Laser-induced porous graphene films from commercial polymers," *Nat. Commun.*, 5, 1–8, **2014**. https://doi.org/10.1038/ncomms6714.

[66] R. Ye, Y. Chyan, J. Zhang, Y. Li, X. Han, C. Kittrell, J.M. Tour, "Laser-Induced Graphene Formation on Wood," *Adv. Mater.*, 29, 1–7, **2017**. https://doi.org/10.1002/adma.201702211.

[67] A.F. Carvalho, A.J.S. Fernandes, R. Martins, E. Fortunato, F.M. Costa, "Laser-Induced Graphene Piezoresistive Sensors Synthesized Directly on Cork Insoles for Gait Analysis," *Adv. Mater. Technol.*, 5, 2000630, **2020**. https://doi.org/10.1002/admt.202000630.

[68] Y. Chyan, R. Ye, Y. Li, S.P. Singh, C.J. Arnusch, J.M. Tour, "Laser-Induced Graphene by Multiple Lasing: Toward Electronics on Cloth, Paper, and Food," *ACS Nano*, 12, 2176–2183, **2018**. https://doi.org/10.1021/acsnano.7b08539.

[69] Z. Peng, J. Lin, R. Ye, E.L.G. Samuel, J.M. Tour, "Flexible and stackable laser-induced graphene supercapacitors," *ACS Appl. Mater. Interfaces*, 7, 3414–3419, **2015**. https://doi.org/10.1021/am509065d.

[70] M.G. Stanford, J.T. Li, Y. Chyan, Z. Wang, W. Wang, J.M. Tour, "Laser-Induced Graphene Triboelectric Nanogenerators," *ACS Nano*, 13, 7166–7174, **2019**. https://doi.org/10.1021/acsnano.9b02596.

[71] J. Chen, Y. Wang, F. Liu, S. Luo, "Laser-Induced Graphene Paper Heaters with Multimodally Patternable Electrothermal Performance for Low-Energy Manufacturing of Composites," *ACS Appl. Mater. Interfaces*, 12, 23284–23297, **2020**. https://doi.org/10.1021/acsami.0c02188.

[72] S.P. Singh, Y. Li, A. Be'er, Y. Oren, J.M. Tour, C.J. Arnusch, "Laser-Induced Graphene Layers and Electrodes Prevents Microbial Fouling and Exerts Antimicrobial Action," *ACS Appl. Mater. Interfaces*, 9, 18238–18247, **2017**. https://doi.org/10.1021/acsami.7b04863.

[73] A.F. Carvalho, B. Kulyk, A.J.S. Fernandes, E. Fortunato, F.M. Costa, "A Review on the Applications of Graphene in Mechanical Transduction," *Adv. Mater.*, 2101326, **2021**. https://doi.org/10.1002/adma.202101326.

[74] B. Kulyk, M.A. Freitas, N.F. Santos, F. Mohseni, A.F. Carvalho, K. Yasakau, A.J.S. Fernandes, A. Bernardes, B. Figueiredo, R. Silva, J. Tedim, F.M. Costa, "A critical review on the production and application of graphene and graphene-based materials in anti-corrosion coatings," *Crit. Rev. Solid State Mater. Sci.*, 0, 1–48, **2021**.

https://doi.org/10.1080/10408436.2021.1886046.

[75] D.X. Luong, K. V. Bets, W.A. Algozeeb, M.G. Stanford, C. Kittrell, W. Chen, R. V. Salvatierra, M. Ren, E.A. McHugh, P.A. Advincula, Z. Wang, M. Bhatt, H. Guo, V. Mancevski, R. Shahsavari, B.I. Yakobson, J.M. Tour, "Gram-scale bottom-up flash graphene synthesis," *Nature*, 577, 647–651, **2020**. https://doi.org/10.1038/s41586-020-1938-0.

[76] A.C. Ferrari, "Raman spectroscopy of graphene and graphite: Disorder, electron-phonon coupling, doping and nonadiabatic effects," *Solid State Commun.*, 143, 47–57, **2007**. https://doi.org/10.1016/j.ssc.2007.03.052.

[77] A.C. Ferrari, J.C. Meyer, V. Scardaci, C. Casiraghi, M. Lazzeri, F. Mauri, S. Piscanec, D. Jiang, K.S. Novoselov, S. Roth, A.K. Geim, "Raman spectrum of graphene and graphene layers," *Phys. Rev. Lett.*, 97, 1–4, **2006**. https://doi.org/10.1103/PhysRevLett.97.187401.

[78] D.R. Lenski, M.S. Fuhrer, "Raman and optical characterization of multilayer turbostratic graphene grown via chemical vapor deposition," *J. Appl. Phys.*, 110, 013720, **2014**. https://doi.org/10.1063/1.3605545.

[79] S. Piscanec, M. Lazzeri, F. Mauri, A.C. Ferrari, J. Robertson, "Kohn anomalies and electron-phonon interactions in graphite," *Phys. Rev. Lett.*, 93, 1–4, **2004**. https://doi.org/10.1103/PhysRevLett.93.185503.

[80] M. Hulman, Raman spectroscopy of graphene, in: A. Skakalova, V; Kaiser (Ed.), Graphene Prop. Prep. Characterisation Devices, Woodhead Publishing Limited, London, **2014**: pp. 156–183. https://doi.org/10.1533/9780857099334.2.156.

[81] A.C. Ferrari, D.M. Basko, "Raman spectroscopy as a versatile tool for studying the properties of graphene," *Nat. Publ. Gr.*, 8, 235–246, **2013**. https://doi.org/10.1038/nnano.2013.46.

[82] D. Li, D. Zhan, J. Yan, C. Sun, Z. Li, Z. Ni, L. Liu, Z. Shen, "Thickness and stacking geometry effects on high frequency overtone and combination Raman modes of graphene," *J. Raman Spectrosc.*, 44, 86–91, **2013**. https://doi.org/10.1002/jrs.4156.

[83] P. Blake, E.W. Hill, a. H. Castro Neto, K.S. Novoselov, D. Jiang, R. Yang, T.J. Booth, A.K. Geim, "Making graphene visible," *Appl. Phys. Lett.*, 91, 063124, **2007**. https://doi.org/10.1063/1.2768624.

[84] H. Hiura, H. Miyazaki, K. Tsukagoshi, "Determination of the number of graphene layers: Discrete distribution of the secondary electron intensity stemming from individual graphene layers," *Appl. Phys. Express*, 3, **2010**. https://doi.org/10.1143/APEX.3.095101.

[85] A.W. Robertson, J.H. Warner, "Atomic resolution imaging of graphene by transmission electron microscopy," *Nanoscale*, 5, 4079, **2013**. https://doi.org/10.1039/c3nr00934c.

[86] P. Nemes-Incze, Z. Osváth, K. Kamarás, L.P. Biró, "Anomalies in thickness measurements of graphene and few layer graphite crystals by tapping mode atomic force microscopy," *Carbon*, 46, 1435–1442, **2008**. https://doi.org/10.1016/j.carbon.2008.06.022.

[87] A. Siokou, F. Ravani, S. Karakalos, O. Frank, M. Kalbac, C. Galiotis, "Surface refinement and electronic properties of graphene layers grown on copper substrate: An XPS, UPS

and EELS study," *Appl. Surf. Sci.*, 257, 9785–9790, **2011**. https://doi.org/10.1016/j.apsusc.2011.06.017.

1.2 Paper electronics and flexible electronic devices

The importance of paper in people's everyday lives has been clear and undisputed for centuries. Yet, remarkably, this material continues to assert itself in a range of new fields and potential applications [1–3]. This shows that, despite having an age of more than two millennia [4], thanks to a unique set of properties and characteristics paper is finding ways of being even more relevant from a technological point of view.

One of the main appeals of paper comes from its versatility. Paper is a flexible, lightweight, porous and naturally abundant material. Another feature of note is its unique structure. Its building block is cellulose – a biopolymer which forms fibres and complex three-dimensional architectures in paper [5]. This gives paper unique properties, such as capillarity, due to the hydrophilic character of cellulose and the voids between the fibres. The latter are particularly useful to accommodate other materials, endowing paper with novel functionalities to extend and adapt its intrinsic properties [6]. Here, techniques such as inkjet printing, screen printing, spray or spin coating, blending, pen writing, and vacuum filtration are some of the paper-compatible techniques commonly used to enhance its properties or provide it with new functionalities.

Moreover, the structure of paper is heterogeneous, and parameters such as the width and length of the fibres, or the relative orientation and spacing between them can vary greatly between different papers. The longer fibres, for example, contribute to the material's strength, while the shorter ones reduce the pore size. For example, M. Nogi et al. were able to achieve very dense fibre packing, thus impeding light scattering inside the paper and, consequently, making it transparent [7]. This possibility of manipulating the fibres' size, packing, orientation and other properties leads to a very wide range of paper types with different characteristics, showing, once again, how versatile this material is.

Paper is also biocompatible, as cellulose is a natural polymer, typically derived from wood [8] or cotton (although cellulose can also be produced by bacteria [9]). It is also biodegradable, which is promising for the current efforts to reduce waste, for example in electronics, where the materials and components commonly used, in general, do not possess this characteristic [10]. Note that, despite cellulose being a natural material, paper itself may contain synthetic additives and coatings, such as pigments and binders, which may hinder its biodegradability, for example [11].

Paper also benefits greatly from being a low-cost material, especially when compared to other materials in fields such as electronics. Considering its role as a substrate, for example, paper is more than two orders of magnitude cheaper than polyethylene terephthalate (PET) or polyimide (PI), which are the most commonly used flexible substrates in flexible electronics and optoelectronics [12]. This opens the door to a wide range of low-cost and disposable devices, which, in turn, will be particularly important for the widespread implementation of the Internet of Things concept, for example, in addition to helping provide access of lower-income populations to technology.

The flexibility of paper is another particularly attractive property [6]. Devices that are already well established in the industry, such as silicon-based electronics for example, can, if successfully adapted, benefit greatly from the flexibility that paper provides, allowing new types of

form-factors to satisfy the end-users' needs and requirements. Moreover, the flexibility aspect can open the door to a range of entirely new devices and technologies, such as wearables.

Paper's electrical properties can also be of interest. In fact, it being an insulating material has allowed it to be implemented in high-voltage, high-power applications, such as power transformers [13]. The electrical resistivity of this material is known to vary greatly with humidity. For relative humidity (RH) in the range of 20–40%, the volume resistivity is typically in the range of 10^{10}–10^{14} Ω cm, while the surface resistivity is of about 10^{11}–10^{15} Ω sq^{-1} [5]. However, by increasing RH to 99%, the volume resistivity value decreases to as low as 10^{4} Ω cm. Still, one should note that reliable measurements of this parameter can be complicated to carry out [5]. As for the dielectric constant, for example, its typical value is in the range of 1.2–4 (at 1 MHz) [14], being increased, for power applications, by filling the paper's voids with materials with higher dielectric constants, such as oils, resins, and electrolytes, among others [5,15]. It is also interesting to be aware that the charge transport mechanism in paper isn't fully understood, but several reports point towards hopping of ions between hydroxyl groups [16,17].

This combination of qualities and unique properties have allowed paper to attract attention in a number of fields. Devices such as transistors [12,18,19], supercapacitors [20–23], light-emitting devices [24–26], and nanogenerators [27–30], among many others [5,6], have been reported, with paper as an important constituent. For example, a transistor developed by Fortunato et al. employed paper as both the substrate and the gate dielectric, and is one of the best examples of the concept of "paper electronics" [19]. Paper has also been used as a substrate for light-harvesting devices [31]. In the field of energy harvesting, paper has been recognized as a promising substrate thanks to its good thermal stability, unlike many commonly employed flexible substrates which present a large mismatch of the coefficient of thermal expansion relative to the active materials of the harvesting devices [27]. Such a wide spectrum of practical applications of paper (too many to cover here) requires a complete exploitation of paper modifying techniques, with, in some cases, novel ones having to be developed. Some of these are discussed in the following subsection.

1.2.1 Modification methods of the properties of paper

In order to adapt paper to the different applications, it is often necessary to process it for a better fit to the requirements of each specific function or purpose. Several tools and techniques have been developed throughout the years to this end, often inspired by our daily interactions with this material in more mundane contexts.

Printing is one of the most common actions involving paper, and as such has been one of the most used techniques in the development of paper-based devices [5]. Inkjet printing is a popular deposition technique, consisting in the ejection through a nozzle of a fixed quantity of material or materials dispersed in a solvent [32]. Here, the printed shape and resolution are important factors, depending on the viscosity of the ink (the dispersion being printed), and there are several process parameters to adjust. For example, inkjet printing using graphene-based inks requires an appropriate solvent which prevents the aggregation of graphene flakes while ensuring that the dispersion possesses appropriate viscosity and surface tension. This can be achieved, for example, by exfoliating graphite in dimethylformamide (DMF) and then exchanging this solvent, through distillation, by terpineol, which has a higher viscosity and is environmentally friendly [33]. The surface of paper itself can be modified to improve the resolution and stability of the printed patterns, as demonstrated by J. Lessing et al., who treated paper with organosilanes in order to improve its hydrophobicity, which in turn led to better lateral

resolution of the printed patterns [34]. The versatility and accessibility of the inkjet printing technique has made it attractive for the development of novel devices, such as, for example, the vapour sensor based on inkjet-printed rGO reported by V. Dua and colleagues [35]. Some of the disadvantages of inkjet printing are its limited printing speed and a higher degree of occurrence of the coffee stain effect (relative to other printing methods) [5]. The latter is due to the pinning of the printed structure's edge, where the evaporation is faster and has to be compensated by an outward flow which carries material towards the edge [36], an effect that is attenuated on paper due to liquid absorption [5].

Screen printing is another popular approach to the transfer of printing materials onto paper in well-defined patterns. The ink is applied to the substrate by spreading it with a blade or a squeegee across a mesh, with specific regions blocked by a stencil, often defined lithographically [37]. Here, the resolution of the printed pattern is governed by the lithography resolution of the blocking layer, the mesh dimensions, and the viscosity of the ink. The screen printing of graphene-based electrodes on flexible substrates, for example, was reported in a work where a stencil mask made of a thinned silicon wafer was used, along with an optimization of the ink itself, to improve the resolution of the printed patterns up to ~4 μm [38]. Screen-printing can also be relevant for sensing application, as exemplified by an amperometric glutathione sensor using screen-printed graphene electrodes [39], or by the screen-printing of conductive inks on paper for temperature and humidity sensors [40].

Another method to apply materials to paper (or other) substrates is spray coating. Here, the ink's particles are directed onto the substrate with the help of a compressed gas, such as air [6]. This technique has been successfully used to deposit, onto paper, the different layers of a flexible light-emitting electrochemical cell, with the authors noting the importance of the control of the different process parameters such as solute concentration of the ink, solvent vapour pressure, substrate temperature, gas velocity, and nozzle-substrate distance and deposition motion [41]. Spray coating of graphene oxide onto a copper substrate, with subsequent partial reduction to rGO by a thermal annealing, was performed for the deposition of a graphene-based corrosion-protection layer, for example [42].

Spin coating can also be used to spread material onto different substrates. This technique consists in applying a drop of the coating onto the substrate, followed by the fast spinning of the latter to thin the material by centrifugal force [6]. Spin coating can also be used for the deposition of graphene-based materials, as seen, for example, in the work of Z. Li et al., who spin coated a quartz plate with a graphene oxide film, followed by the dipping of the latter in a mixture containing $KMnO_4$, for the formation of MnO_2 nanoparticles by a hydrothermal process [43]. The material thus formed was then used in a flexible supercapacitor. Coating techniques, compared to conventional printing approaches, tend to result in more homogeneous structures and are compatible with a wider range of coating materials, with techniques like slot-die available for large area continuous deposition [5].

Other techniques for physical modification of paper's surface properties that are worth mentioning are vacuum filtration [44,45] and pen-writing [46,47]. As for bulk properties, blending is an attractive approach, as demonstrated, for instance, by the addition of 1-butyl-3-methylimidazolium bis(trifluoromethylsulfonyl)imide (BMITFSI) to the cellulose matrix, which resulted in an improvement of the electromechanical properties of a BMITFSI-cellulose actuator device [48].

The properties of paper can also be extended chemically, particularly by the in situ formation on functional materials [49]. For instance, cellulose paper has been modified with amino groups using a silane coupling technique, for catalysis purposes [50]. Metal nanoparticles can be grown in situ on paper, by submerging it in aqueous solutions of $AgNO_3$, $Pd(NO_3)_2$, $AuCl_3$, and $PtCl_4$, followed by a reduction in $NaBH_4$, with potential applications in the manufacturing of nanocomposites, antimicrobial materials, and catalysts [51]. More complex structures, such as zeolitic imidazolate framework-8 (ZIF-8) nanocrystals can also be synthesized on paper to improve the gas adsorption capacity of air filters [52]. For sensing applications, a hybrid nanomaterial composed of glucose oxidase-containing phosphate solution and manganese sulphate ($MnSO_4$) was grown on cellulose paper, by drop-casting each solution onto the latter [53]. The functionality of the resulting sensing device was shown by the specific detection of glucose in complex biological samples, leading to a change in colour of the chromogenic substrate 3,3,5,5-tetramethylbenzidine (TMB), also deposited in the sensing area, with the inorganic framework $Mn_3(PO_4)_2{\cdot}3H_2O$ providing peroxidase-like activity.

Modification of paper's characteristics with polymers is also possible. For example, polypyrrole (PPy) can be coated onto paper by soaking the latter in pyrrole monomer, followed by dipping into a ferric chloride solution with hydrochloric acid [54]. This results in an electrically conductive paper-based composite for supercapacitor applications. A very similar approach was used by C. Wan et al., who, after in situ pyrrole polymerization, coated the hybrid material with graphene oxide, with the subsequent reduction of the latter [55]. Polyaniline (PANi) is another polymer commonly used to modify paper, which can be deposited in situ electrochemically [56,57]. PANi-coated cellulose has a disadvantage of high conductivity loss when soaked in alkaline aqueous solution, which can be prevented by in situ polymerization of both aniline and metanilic acid, resulting in a self-doped polyaniline/paper hybrid [58].

Several examples of the use of lasers for paper patterning and modification have been reported, such as the work of G. Chitnis et al., who were able to define hydrophilic channels on papers with hydrophobic coatings by subjecting them to a CO_2 laser [59]. A CO_2 laser can also be used to etch and cut nitrocellulose substrates [60]. The width of the laser-patterned features on paper directly correlates with the size of the cellulose fibres [61]. But, perhaps more interestingly, Y. Chyan et al. were able to directly convert paper treated with a commercial phosphate fire retardant into graphene (laser-induced graphene or LIG), using a CO_2 laser beam, without damaging or ablating the underlying substrate [62]. Such a technique allows to define electrically conductive paths in a fast manner and without requiring a controlled atmosphere.

---------- // ----------

As can be seen in this brief overview, paper is a fascinating material. Its properties make it extremely versatile, while still being cheap, naturally abundant, biodegradable, and easily processable. The latter aspect is particularly important, with many different printing, coating, and writing techniques, further complemented by chemical modification approaches, being capable of enhancing paper's characteristics, as well as endowing it with new functionalities. All of this makes it very attractive for a wide range of practical applications, spanning a vast and diverse spectrum of fields.

1.2.2 References

[1] R. Martins, I. Ferreira, E. Fortunato, "Electronics with and on paper," *Phys. Status Solidi - Rapid Res. Lett.*, 5, 332–335, **2011**. https://doi.org/10.1002/pssr.201105247.

[2] Y. Yang, E. Noviana, M.P. Nguyen, B.J. Geiss, D.S. Dandy, C.S. Henry, "Paper-Based Microfluidic Devices: Emerging Themes and Applications," *Anal. Chem.*, 89, 71–91, **2017**. https://doi.org/10.1021/acs.analchem.6b04581.

[3] R.-P. Xu, Y.-Q. Li, J.-X. Tang, "Recent advances in flexible organic light-emitting diodes," *J. Mater. Chem. C*, 4, 9116–9142, **2016**. https://doi.org/10.1039/C6TC03230C.

[4] C.J. Biermann, Handbook of pulping and papermaking, Second, Elsevier Science, **1996**.

[5] D. Tobjörk, R. Österbacka, "Paper Electronics," *Adv. Mater.*, 23, 1935–1961, **2011**. https://doi.org/10.1002/adma.201004692.

[6] Y. Zhang, L. Zhang, K. Cui, S. Ge, X. Cheng, M. Yan, J. Yu, H. Liu, "Flexible Electronics Based on Micro/Nanostructured Paper," *Adv. Mater.*, 30, 1801588, **2018**. https://doi.org/10.1002/adma.201801588.

[7] M. Nogi, S. Iwamoto, A.N. Nakagaito, H. Yano, "Optically Transparent Nanofiber Paper," *Adv. Mater.*, 21, 1595–1598, **2009**. https://doi.org/10.1002/adma.200803174.

[8] J. Credou, T. Berthelot, "Cellulose: From biocompatible to bioactive material," *J. Mater. Chem. B*, 2, 4767–4788, **2014**. https://doi.org/10.1039/c4tb00431k.

[9] F.M. Gama, P. Gatenholm, D. Klemm, Bacterial nanocellulose: A sophisticated multifunctional material, **2016**.

[10] M.J. Tan, C. Owh, P.L. Chee, A.K.K. Kyaw, D. Kai, X.J. Loh, "Biodegradable electronics: Cornerstone for sustainable electronics and transient applications," *J. Mater. Chem. C*, 4, 5531–5558, **2016**. https://doi.org/10.1039/c6tc00678g.

[11] M. Irimia-Vladu, "'Green' electronics: Biodegradable and biocompatible materials and devices for sustainable future," *Chem. Soc. Rev.*, 43, 588–610, **2014**. https://doi.org/10.1039/c3cs60235d.

[12] R. Martins, D. Gaspar, M.J. Mendes, L. Pereira, J. Martins, P. Bahubalindruni, P. Barquinha, E. Fortunato, "Papertronics: Multigate paper transistor for multifunction applications," *Appl. Mater. Today*, 12, 402–414, **2018**. https://doi.org/10.1016/j.apmt.2018.07.002.

[13] D. Linhjell, L. Lundgaard, U. Gäfvert, "Dielectric response of mineral oil impregnated cellulose and the impact of aging," *IEEE Trans. Dielectr. Electr. Insul.*, 14, 156–169, **2007**. https://doi.org/10.1109/TDEI.2007.302884.

[14] G.T. Kohman, "Cellulose as an Insulating Material," *Ind. Eng. Chem.*, 31, 807–817, **1939**. https://doi.org/10.1021/ie50355a005.

[15] T.Y.A. Fahmy, F. Mobarak, M.G. El-Meligy, "Introducing undeinked old newsprint as a new resource of electrical purposes paper," *Wood Sci. Technol.*, 42, 691–698, **2008**. https://doi.org/10.1007/s00226-008-0180-y.

[16] J.H. Christie, S.H. Krenek, I.M. Woodhead, "The electrical properties of hygroscopic solids," *Biosyst. Eng.*, 102, 143–152, **2009**. https://doi.org/10.1016/j.biosystemseng.2008.09.023.

[17] C.S. Boland, U. Khan, C. Backes, A. O'Neill, J. McCauley, S. Duane, R. Shanker, Y. Liu, I. Jurewicz, A.B. Dalton, J.N. Coleman, "Sensitive, high-strain, high-rate bodily motion

sensors based on graphene-rubber composites," *ACS Nano*, 8, 8819–8830, **2014**. https://doi.org/10.1021/nn503454h.

[18] D. Gaspar, S.N. Fernandes, A.G. De Oliveira, J.G. Fernandes, P. Grey, R. V. Pontes, L. Pereira, R. Martins, M.H. Godinho, E. Fortunato, "Nanocrystalline cellulose applied simultaneously as the gate dielectric and the substrate in flexible field effect transistors," *Nanotechnology*, 25, **2014**. https://doi.org/10.1088/0957-4484/25/9/094008.

[19] E. Fortunato, N. Correia, P. Barquinha, L. Pereira, G. Goncalves, R. Martins, "High-performance flexible hybrid field-effect transistors based on cellulose fiber paper," *IEEE Electron Device Lett.*, 29, 988–990, **2008**. https://doi.org/10.1109/LED.2008.2001549.

[20] M.M. Pérez-Madrigal, M.G. Edo, C. Alemán, "Powering the future: Application of cellulose-based materials for supercapacitors," *Green Chem.*, 18, 5930–5956, **2016**. https://doi.org/10.1039/c6gc02086k.

[21] M.P. Down, C.W. Foster, X. Ji, C.E. Banks, "Pencil drawn paper based supercapacitors," *RSC Adv.*, 6, 81130–81141, **2016**. https://doi.org/10.1039/c6ra18499e.

[22] M. Sevilla, G.A. Ferrero, A.B. Fuertes, "Graphene-cellulose tissue composites for high power supercapacitors," *Energy Storage Mater.*, 5, 33–42, **2016**. https://doi.org/10.1016/j.ensm.2016.05.008.

[23] J. Edberg, O. Inganäs, I. Engquist, M. Berggren, "Boosting the capacity of all-organic paper supercapacitors using wood derivatives," *J. Mater. Chem. A*, 6, 145–152, **2017**. https://doi.org/10.1039/c7ta06810g.

[24] Y. Zhang, L. Ge, M. Li, M. Yan, S. Ge, J. Yu, X. Song, B. Cao, "Flexible paper-based ZnO nanorod light-emitting diodes induced multiplexed photoelectrochemical immunoassay," *Chem. Commun.*, 50, 1417–1419, **2014**. https://doi.org/10.1039/c3cc48421a.

[25] P. Andersson, D. Nilsson, P.O. Svensson, M. Chen, A. Malmström, T. Remonen, T. Kugler, M. Berggren, "Active matrix displays based on all-organic electrochemical smart pixels printed on paper," *Adv. Mater.*, 14, 1460–1464, **2002**. https://doi.org/10.1002/1521-4095(20021016)14:20<1460::AID-ADMA1460>3.0.CO;2-S.

[26] C. Legnani, C. Vilani, V.L. Calil, H.S. Barud, W.G. Quirino, C.A. Achete, S.J.L. Ribeiro, M. Cremona, "Bacterial cellulose membrane as flexible substrate for organic light emitting devices," *Thin Solid Films*, 517, 1016–1020, **2008**. https://doi.org/10.1016/j.tsf.2008.06.011.

[27] K.H. Kim, K.Y. Lee, J.S. Seo, B. Kumar, S.W. Kim, "Paper-based piezoelectric nanogenerators with high thermal stability," *Small*, 7, 2577–2580, **2011**. https://doi.org/10.1002/smll.201100819.

[28] Q. Zhong, J. Zhong, B. Hu, Q. Hu, J. Zhou, Z.L. Wang, "A paper-based nanogenerator as a power source and active sensor," *Energy Environ. Sci.*, 6, 1779–1784, **2013**. https://doi.org/10.1039/c3ee40592c.

[29] X. He, Y. Zi, H. Yu, S.L. Zhang, J. Wang, W. Ding, H. Zou, W. Zhang, C. Lu, Z.L. Wang, "An ultrathin paper-based self-powered system for portable electronics and wireless

human-machine interaction," *Nano Energy*, 39, 328–336, **2017**. https://doi.org/10.1016/j.nanoen.2017.06.046.

[30] J.P. Rojas, D. Conchouso, A. Arevalo, D. Singh, I.G. Foulds, M.M. Hussain, "Paper-based origami flexible and foldable thermoelectric nanogenerator," *Nano Energy*, 31, 296–301, **2017**. https://doi.org/10.1016/j.nanoen.2016.11.012.

[31] A.T. Vicente, A. Araújo, M.J. Mendes, D. Nunes, M.J. Oliveira, O. Sanchez-Sobrado, M.P. Ferreira, H. Águas, E. Fortunato, R. Martins, "Multifunctional cellulose-paper for light harvesting and smart sensing applications," *J. Mater. Chem. C*, 6, 3143–3181, **2018**. https://doi.org/10.1039/c7tc05271e.

[32] M. Singh, H.M. Haverinen, P. Dhagat, G.E. Jabbour, "Inkjet printing-process and its applications," *Adv. Mater.*, 22, 673–685, **2010**. https://doi.org/10.1002/adma.200901141.

[33] J. Li, F. Ye, S. Vaziri, M. Muhammed, M.C. Lemme, M. Östling, "Efficient inkjet printing of graphene," *Adv. Mater.*, 25, 3985–3992, **2013**. https://doi.org/10.1002/adma.201300361.

[34] J. Lessing, A.C. Glavan, S.B. Walker, C. Keplinger, J.A. Lewis, G.M. Whitesides, "Inkjet printing of conductive inks with high lateral resolution on omniphobic 'rF paper' for paper-based electronics and MEMS," *Adv. Mater.*, 26, 4677–4682, **2014**. https://doi.org/10.1002/adma.201401053.

[35] V. Dua, S.P. Surwade, S. Ammu, S.R. Agnihotra, S. Jain, K.E. Roberts, S. Park, R.S. Ruoff, S.K. Manohar, "All-organic vapor sensor using inkjet-printed reduced graphene oxide," *Angew. Chemie - Int. Ed.*, 49, 2154–2157, **2010**. https://doi.org/10.1002/anie.200905089.

[36] R.D. Deegan, O. Bakajin, T.F. Dupont, G. Huber, S.R. Nagel, T.A. Witten, "Capillary flow as the cause of ring stains from dried liquid drops," *Nature*, 389, 827–829, **1997**. https://doi.org/10.1038/39827.

[37] H.D. Goldberg, R.B. Brown, D.P. Liu, M.E. Meyerhoff, "Screen printing: a technology for the batch fabrication of integrated chemical-sensor arrays," *Sensors Actuators B. Chem.*, 21, 171–183, **1994**. https://doi.org/10.1016/0925-4005(94)01249-0.

[38] W.J. Hyun, E.B. Secor, M.C. Hersam, C.D. Frisbie, L.F. Francis, "High-resolution patterning of graphene by screen printing with a silicon stencil for highly flexible printed electronics," *Adv. Mater.*, 27, 109–115, **2015**. https://doi.org/10.1002/adma.201404133.

[39] C. Karuwan, A. Wisitsoraat, P. Chaisuwan, D. Nacapricha, A. Tuantranont, "Screen-printed graphene-based electrochemical sensors for a microfluidic device," *Anal. Methods*, 9, 3689–3695, **2017**. https://doi.org/10.1039/c7ay00379j.

[40] R. Barras, I. Cunha, D. Gaspar, E. Fortunato, R. Martins, L. Pereira, "Printable cellulose-based electroconductive composites for sensing elements in paper electronics," *Flex. Print. Electron.*, 2, 014006, **2017**. https://doi.org/10.1088/2058-8585/aa5ef9.

[41] A. Asadpoordarvish, A. Sandström, C. Larsen, R. Bollström, M. Toivakka, R. Österbacka, L. Edman, "Light-emitting paper," *Adv. Funct. Mater.*, 25, 3238–3245, **2015**.

https://doi.org/10.1002/adfm.201500528.

[42] G.-C. Son, D.-K. Hwang, J. Jang, S.-S. Chee, K. Cho, J.-M. Myoung, M.-H. Ham, "Solution-processed highly adhesive graphene coatings for corrosion inhibition of metals," *Nano Res.*, 12, 19–23, **2019**. https://doi.org/10.1007/s12274-018-2056-2.

[43] Z. Li, Y. An, Z. Hu, N. An, Y. Zhang, B. Guo, Z. Zhang, Y. Yang, H. Wu, "Preparation of a two-dimensional flexible MnO2/graphene thin film and its application in a supercapacitor," *J. Mater. Chem. A*, 4, 10618–10626, **2016**. https://doi.org/10.1039/c6ta03358j.

[44] J.W. Han, B. Kim, J. Li, M. Meyyappan, "A carbon nanotube based ammonia sensor on cellulose paper," *RSC Adv.*, 4, 549–553, **2014**. https://doi.org/10.1039/c3ra46347h.

[45] S. Leijonmarck, A. Cornell, G. Lindbergh, L. Wågberg, "Single-paper flexible Li-ion battery cells through a paper-making process based on nano-fibrillated cellulose," *J. Mater. Chem. A*, 1, 4671–4677, **2013**. https://doi.org/10.1039/c3ta01532g.

[46] H. Zhao, T. Zhang, R. Qi, J. Dai, S. Liu, T. Fei, "Drawn on Paper: A Reproducible Humidity Sensitive Device by Handwriting," *ACS Appl. Mater. Interfaces*, 9, 28002–28009, **2017**. https://doi.org/10.1021/acsami.7b05181.

[47] H. Yang, Q. Kong, S. Wang, J. Xu, Z. Bian, X. Zheng, C. Ma, S. Ge, J. Yu, "Hand-drawn&written pen-on-paper electrochemiluminescence immunodevice powered by rechargeable battery for low-cost point-of-care testing," *Biosens. Bioelectron.*, 61, 21–27, **2014**. https://doi.org/10.1016/j.bios.2014.04.051.

[48] S.K. Mahadeva, C. Yi, J. Kim, "Electrical and electromechanical properties of 1-butyl-3-methylimidazolium bis(trifluoromethylsulfonyl)imide-blended cellulose," *Ionics (Kiel).*, 17, 41–47, **2011**. https://doi.org/10.1007/s11581-010-0478-2.

[49] S. Ge, L. Zhang, Y. Zhang, F. Lan, M. Yan, J. Yu, "Nanomaterials-modified cellulose paper as a platform for biosensing applications," *Nanoscale*, 9, 4366–4382, **2017**. https://doi.org/10.1039/c6nr08846e.

[50] H. Koga, T. Kitaoka, A. Isogai, "In situ modification of cellulose paper with amino groups for catalytic applications," *J. Mater. Chem.*, 21, 9356–9361, **2011**. https://doi.org/10.1039/c1jm10543d.

[51] J. He, T. Kunitake, A. Nakao, "Facile In Situ Synthesis of Noble Metal Nanoparticles in Porous Cellulose Fibers," *Chem. Mater.*, 15, 4401–4406, **2003**. https://doi.org/10.1021/cm034720r.

[52] Z. Su, M. Zhang, Z. Lu, S. Song, Y. Zhao, Y. Hao, "Functionalization of cellulose fiber by in situ growth of zeolitic imidazolate framework-8 (ZIF-8) nanocrystals for preparing a cellulose-based air filter with gas adsorption ability," *Cellulose*, 25, 1997–2008, **2018**. https://doi.org/10.1007/s10570-018-1696-4.

[53] W.Y. Li, S.Y. Lu, S.J. Bao, Z.Z. Shi, Z. Lu, C.M. Li, L. Yu, "Efficient in situ growth of enzyme-inorganic hybrids on paper strips for the visual detection of glucose," *Biosens. Bioelectron.*, 99, 603–611, **2018**. https://doi.org/10.1016/j.bios.2017.08.015.

[54] L. Yuan, B. Yao, B. Hu, K. Huo, W. Chen, J. Zhou, "Polypyrrole-coated paper for flexible solid-state energy storage," *Energy Environ. Sci.*, 6, 470–476, **2013**.

https://doi.org/10.1039/c2ee23977a.

[55] C. Wan, Y. Jiao, J. Li, "Flexible, highly conductive, and free-standing reduced graphene oxide/polypyrrole/cellulose hybrid papers for supercapacitor electrodes," *J. Mater. Chem. A*, 5, 3819–3831, **2017**. https://doi.org/10.1039/c6ta04844g.

[56] B. Yao, L. Yuan, X. Xiao, J. Zhang, Y. Qi, J. Zhou, J. Zhou, B. Hu, W. Chen, "Paper-based solid-state supercapacitors with pencil-drawing graphite/polyaniline networks hybrid electrodes," *Nano Energy*, 2, 1071–1078, **2013**. https://doi.org/10.1016/j.nanoen.2013.09.002.

[57] H.P. Cong, X.C. Ren, P. Wang, S.H. Yu, "Flexible graphene-polyaniline composite paper for high-performance supercapacitor," *Energy Environ. Sci.*, 6, 1185–1191, **2013**. https://doi.org/10.1039/c2ee24203f.

[58] H. Mao, X. Liu, X. Qian, X. An, "Preparation and dedoping-resistant effect of self-doped polyaniline/cellulose fibers (SPANI/CF) hybrid," *Cellulose*, 22, 2641–2650, **2015**. https://doi.org/10.1007/s10570-015-0689-9.

[59] G. Chitnis, Z. Ding, C.L. Chang, C.A. Savran, B. Ziaie, "Laser-treated hydrophobic paper: An inexpensive microfluidic platform," *Lab Chip*, 11, 1161–1165, **2011**. https://doi.org/10.1039/c0lc00512f.

[60] P. Spicar-Mihalic, B. Toley, J. Houghtaling, T. Liang, P. Yager, E. Fu, "CO 2 laser cutting and ablative etching for the fabrication of paper-based devices," *J. Micromechanics Microengineering*, 23, **2013**. https://doi.org/10.1088/0960-1317/23/6/067003.

[61] M.A. Mahmud, E.J.M. Blondeel, M. Kaddoura, B.D. MacDonald, "Features in microfluidic paper-based devices made by laser cutting: How small can they be?," *Micromachines*, 9, 1–12, **2018**. https://doi.org/10.3390/mi9050220.

[62] Y. Chyan, R. Ye, Y. Li, S.P. Singh, C.J. Arnusch, J.M. Tour, "Laser-Induced Graphene by Multiple Lasing: Toward Electronics on Cloth, Paper, and Food," *ACS Nano*, 12, 2176–2183, **2018**. https://doi.org/10.1021/acsnano.7b08539.

1.3 Sensors and paper-based detection

The interest in the use of paper in sensing devices can be traced back to the emergence of paper chromatography and its use in the semi-quantitative detection of glucose in urine, reported by J. P. Comer, in 1956 [1]. The idea behind such paper-based detection evolved into lateral flow or dipstick tests, exemplified by the pregnancy test kits [2]. These are immunoassays where a sample is introduced onto a paper strip and, by capillary forces, is moved towards a region with an antibody (or antigen) conjugate to the analyte. The antibody/antigen pair is then captured in another region, leading to a positive signal, typically expressed, in a qualitative manner, by coloured latex microspheres. Such detection is attractive due to the simplicity and low cost of these tests [3].

The basic principles behind the passive transport of fluids, thanks to paper's capillarity, have been developed for more precise and more complex flow control, resulting in more advanced systems, best exemplified by microfluidics on paper [4]. The field of microfluidics, enabling high sensitivity detection using very small amounts of sample, emerged thanks to the influence of molecular analysis, which uses techniques such as chromatography and capillary electrophoresis, as well as microelectronics, where micropatterning techniques were developed [5]. Not only does microfluidics render the sensors more sensitive, but it also enables multiplex analysis of several analytes in the same sample, as shown by A. W. Martinez et al., who patterned a chromatography paper with a photoresist, in order to define hydrophilic channels bound by hydrophobic polymer (**Figure 1.3.1**) [6]. These channels lead the sample to different test wells for simultaneous detection of glucose and protein (with the respective wells spotted with appropriate reagents prior to contact with the sample). Not only did the authors show that such a microfluidic paper-based assay device (μPAD) responds to different concentrations of the analytes (by changing the colour of the test wells, with colour intensities roughly corresponding to the concentration of each analyte, as seen in **Figure 1.3.1c**), taking around 10-11 min to do so, but they also displayed the ability of such an assay to be performed on samples contaminated with particulates, such as dirt, plant pollen, and graphite.

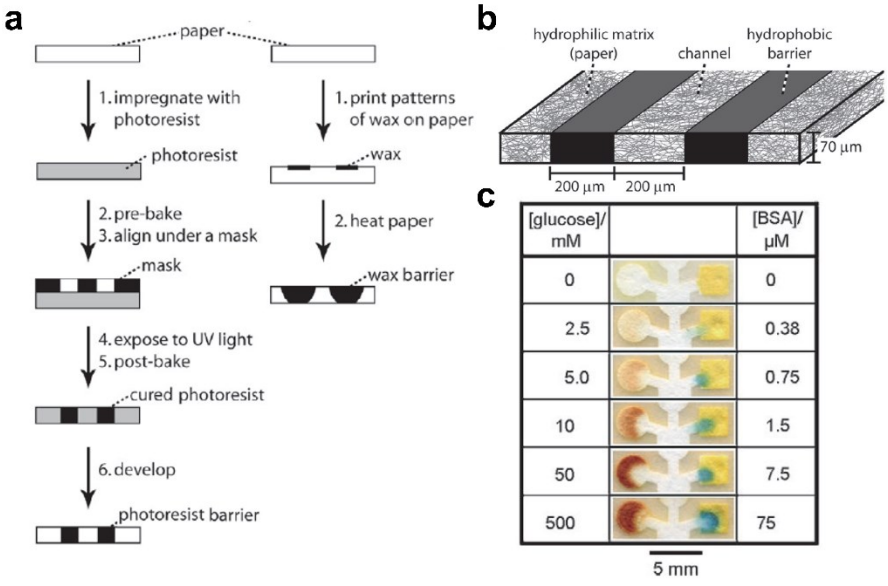

Figure 1.3.1. (a) Two approaches to define hydrophilic microfluidic channels in paper. **(b)** Cross-section view of a microfluidic channel in paper defined by hydrophobic barriers, with an example of possible dimension. Both images adapted from ref. [4]. **(c)** A μPAD in action. Adapted from ref. [6].

The work of Martinez and co-workers showed that the use of microfluidics lends itself nicely to the development of paper-based biosensors [6]. Biosensors transform a biochemical stimulus into an analytically useful signal through a biochemical recognition mechanism [7,8]. Currently, such devices are very prominent in a wide range of fields, particularly in the medical one, with glucose biosensors accounting for approximately 85% of biosensors' world market [9]. A typical biosensor is comprised of (1) a recognition element, which establishes a specific link or relationship with the analyte (in certain cases, the recognition element can be omitted if selectivity can be ensured by distinct signatures of the signals coming from the different interacting analytes and interferents), (2) a transducer, which gives rise to a measurable signal in response to the analyte, and (3) a processing module which converts the generated signal into easily accessible information. Different implementations of these components result in different categories of biosensors. Based on the recognition element, two classes of biosensors can be identified [8]:

- **Biocatalytic recognition** – a component incorporated into the biosensor catalyses a chemical reaction, the parameters of which are then monitored. The most common example of such devices is the glucose biosensor, where glucose oxidase (GOx) immobilized on the biosensor catalyses the oxidation of β-D-glucose [10]. The reaction produces gluconic acid and hydrogen peroxide (H_2O_2), with oxygen consumption, hydrogen peroxide production and electron transfer from GOx to an electrode being the parameters that can be monitored to give information on glucose concentration.
- **Biocomplexing or bioaffinity recognition** – a receptor is integrated into the recognition element, interacting directly with the analyte (through binding, for example). Specific antibodies can be used to bind to an antigen analyte, or an aptamer ligand, which can bind to specific nucleic acid sequences. Usually, in this type of sensors equilibrium is reached once the binding is completed, and regeneration (forced dissociation of the bonds) is required to reuse the device. If regeneration is impossible, the biosensor must be discarded. To avoid non-specific binding (the binding of molecules other than the analyte), the surface of the biosensor can be passivated with a blocking agent, such as bovine serum albumin (BSA) or salmon sperm DNA [11].

Biosensors can also be separated into different categories according to their transduction mechanism:

- **Magnetic biosensors** – interaction with the analyte leads to a measurable signal through effects such as giant magnetoresistance (GMR) [12], Hall effect [13], or superconducting quantum interference [14]. The use of magnetic nanoparticles is quite common in such biosensors, either through their direct integration in the device or by dispersing them in the sample, the latter allowing multi-analyte detection [15,16].
- **Optical biosensors** – the analyte is identified/quantified in terms of the response of the recognition element to changes in the optical signal. Among the phenomena exploited in this type of transducers are surface plasmon resonance, evanescent wave fluorescence, luminescence and surface-enhanced Raman scattering [17].
- **Piezoelectric biosensors** – typically built in the form of what is known as a piezoelectric quartz microbalance, a piezoelectric crystal coated with a selective biocomponent that binds to the analyte is placed between two electrodes to which an AC voltage is applied. This voltage forces the crystal to vibrate at a specific resonance frequency, which is altered by the binding of the analyte to the crystal's surface in response to the change in the device's mass [18].

- **Thermometric (or calorimetric) biosensors** – the detection/quantification is based on the measurement of the temperature variations in response to the heat produced or absorbed by a chemical reaction involving the analyte [19].
- **Electrochemical biosensors** – an electrode, which is typically chemically modified, is used as a transducer, directly translating an interaction with the analyte (be it a reaction or a binding event) into an electrical signal [8]. This is by far the most common type of transducing mechanism, thanks to its widespread use in glucose biosensors [20].

One should also note that, despite paper-based sensing having been largely influenced by the ideas behind biosensing, this material can also be employed in other types of detection and monitoring systems. Pressure sensors are one of such systems, with paper's porous structure and good elasticity being advantageous [21].

In the following sections a brief overview of the main developments in different types of paper-based sensing, according to the transduction mechanism, is given. Some examples of the use of graphene, even if without paper, are also provided for reference.

1.3.1 Colorimetric sensors

Colorimetry relies on a change in colour (or its intensity) in response to the analyte [3], as exemplified by the previously discussed work of Martinez et al. [6]. Building on their initial multiplex assay concept, the authors reported, in 2008, a simple colorimetric sensing device on paper capable of quantifying the concentration of several analytes (in this case, glucose and protein) [22]. The change in colour could be scanned by a cell phone or a smartphone camera and read remotely by an expert (**Figure 1.3.2a**). By digitally analysing the transmitted images, the mean pixel value of each test zone can be measured. These values correlate to the concentration of the analytes, meaning that calibration curves can be traced and used to analyse unknown samples. The same group also showed that microfluidic colorimetric assays based on paper can also have a 3D configuration, by stacking multiple patterned (using hydrophobic polymer walls) sheets of paper separated by tape with holes in appropriate positions, filled with cellulose powder to provide microfluidic paths between the different paper sheets [23]. This allows to distribute a single sample equally by a large number of test zones, using overlapping paths that can cross without mixing. Different analytes can be measured in the different test zones, according to the reagent in that test zone. A further development of this concept was realized forgoing the filling of tape holes with cellulose powder, which results in a gap between the different paper layers [24]. This gap can be eliminated by applying a modest compressive force perpendicular to the interfaces between the layers (**Figure 1.3.2b**). As such, the microfluidic paper-based device becomes programmable, in the sense that the user can select where to direct the flow of the sample.

Modified silver nanoparticles (AgNPs) can also be employed in colorimetric paper-based sensing [25]. Through self-assembly of aminothiol on AgNPs' surface, the latter were functionalized with homocysteine (Hcy) and dithiothreitol (DTT). By spotting the test zone of a μPAD with a solution of the modified nanoparticles, followed by dropping of a solution of Cu^{2+} into the loading zone, the modified nanoparticles aggregated in the presence of Cu^{2+}, which in turn gave rise to a decrease in the surface plasmon resonance (SPR) absorption peak of AgNPs at 404 nm and to a formation of a new absorption at 502 nm, resulting in a colour change visible by the naked eye. These sensors were also shown to be selective towards Cu^{2+} (after comparing with other metal ions), due to higher stability constant between DTT and Cu^{+} relative to other metals. A

potential application of these μPADs is in the monitoring of Cu^{2+} concentration in drinking water. The same group later used silver nanoplatelets (AgNPls) functionalized with hex-adecyltrimethylammonium bromide for the same analyte [26]. The modified AgNPls were etched in the presence of $S_2O_3^{2-}$, resulting in a slight colour change of the solution, with the etching accelerating after contact with Cu^{2+}. The latter rendered the solution colourless, and such detection was applied in paper-based sensors similar to the ones reported previously. Gold nanoparticles (AuNPs) have also been used in μPADs for tuberculosis diagnosis [27]. In the presence of healthy DNA, unmodified single-stranded deoxyribonucleic acid (ssDNA) sequences protected the AuNPs from aggregation, in a sodium chloride solution. However, the interaction with DNA containing a specific sequence indicative of tuberculosis led to hybridization with ssDNA, which in turn allowed the aggregation of AuNPs. This aggregation results in a shift of the optical absorbance due to SPR, causing a visible change in colour from red to blue in the presence of the tuberculosis-indicative analyte. The paper's role was to wick the AuNP-ssDNA-analyte DNA solution, confining it to a specific region using wax barriers, for further colorimetric analysis of the solution by means of a camera and image processing. More recently, metal nanoparticles, namely Au@Ag core-shell NPs, were employed for colorimetric detection of explosive nitroaromatics such as TNT (trinitrotoluene), due to electron transfer from amine groups, introduced on the NPs' surface by β-cysteamine functionalization, to electron deficient TNT groups (**Figure 1.3.2c**) [28]. The functionalized NPs were immobilized on a piece of filter paper by immersing it in the solution of the former, followed by the addition of the sample to be analysed. The colour change, from pale-yellow to dark-brown, modulates the optical properties of the modified nanoparticles, resulting in an appearance of an absorption peak at 510 nm, the intensity of which increased in response to increased concentration of TNT.

Detection of phenolic compounds, which can pose toxic risks to human health and environment due to bioaccumulation, have been detected in a semi-quantitative manner using colorimetric paper-based sensor [29]. Layer-by-layer assembly of alginate and chitosan on paper's surface, with the tyrosinase enzyme intercalated between these layers, allowed a reaction of the latter with different phenolic compounds, followed by a colour change of chitosan due to this reaction's products.

Three distinct colorimetric approaches were also reported by M. Costa et al., who were able to perform sensing, on paper, through enzymatic reactions, immunoassays, and nucleic acid sequence identification, for the detection of glucose, anti-*Leishmania* antibodies, and *Mycobacterium tuberculosis* complexes [30].

An example of the use of graphene in paper-based colorimetric sensing can be seen in the work of K. V. Ragavan and co-workers [31]. A reduced graphene oxide-palladium (rGO-Pd) nanocomposite was used as a biomimetic enzyme for the oxidation of glutamate and H_2O_2, the latter reacting, through the nanocomposite's peroxidase activity, with 3,3',5,5'-tetramethylbenzidin (TMB), forming coloured complexes in proportion to the amount of glutamate. By spotting a piece of paper with a solution of rGO-Pd and glutamate, the intensity of the resulting colour could be evaluated. The presence of rGO was important due to its large surface area, which helps to better disperse the Pd nanoparticles.

In an interesting recent development, a glucose and uric acid μPAD was developed on nitrocellulose not by defining hydrophobic walls to guide the sample flow, but rather by treating the zones where the sample should be spatially confined with chitosan oligosaccharide lactate (COL) [32]. In this way, the flow rate difference between the treated and the untreated regions,

caused by the blocking of cellulose pores by the chitosan derivative, led to a colour focusing effect in the treated regions (**Figure 1.3.2d**).

In summary, colorimetric paper-based sensing is an active avenue of research. Its appeal relies in the simplicity of signal readout, making it appropriate for point-of-care diagnostics and remote monitoring.

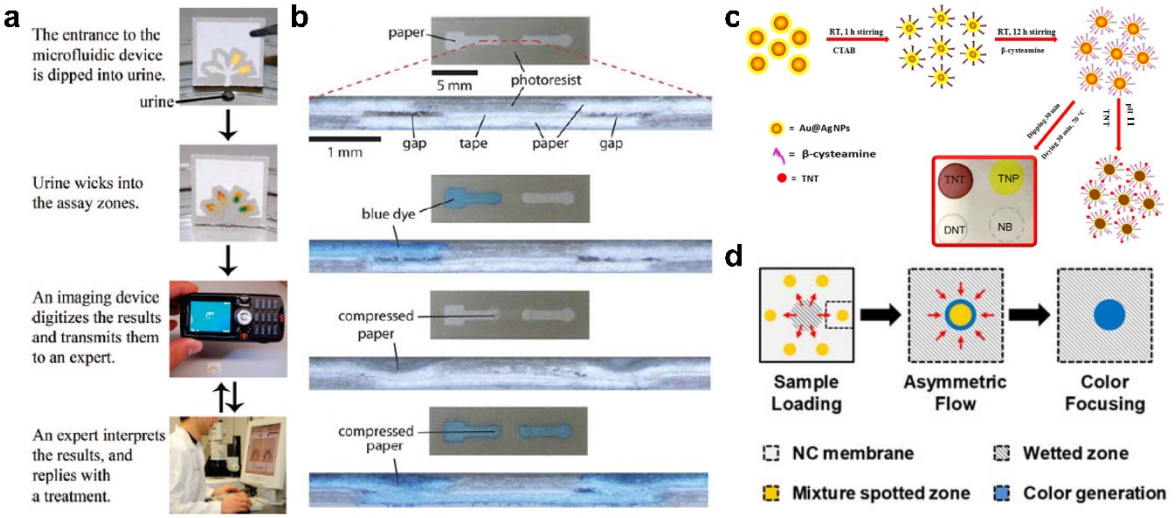

Figure 1.3.2. (a) An example of quantitative colorimetric μPAD. Adapted from ref. [22]. **(b)** Cross-section view of "programmable" microfluidic channels using stacked sheets of paper. Adapted from ref. [24]. **(c)** Example of the use of metal nanoparticles in μPADs. Adapted from ref. [28]. **(d)** Colour focusing effect by localized change in flow rate. Adapted from ref. [32].

1.3.2 Electrochemical sensors

Electrochemical sensors can have different configurations depending on the type of electrical signal that is measured.

In amperometric electrochemical sensors, the measured signal is that of a current that originates in response to an interaction with the analyte. Typically, three electrodes separated by an electrolyte are used: a working-electrode, where the sensing occurs, a reference-electrode, held at a known constant potential, and a counter-electrode, which completes the circuit in a setup known as the electrochemical cell [7].

Alternatively, potentiometric electrochemical sensors measure the potential build-up at the surface of the working electrode which occurs due to the accumulation of ionic charge, without any current flowing through this electrode. Typically, ion-selective electrodes (ISE) are used in such sensors, so that only a specific ion can be allowed to build-up at the interface. One example of a potentiometric biosensor is the one reported by Shishkanova et al. [33], where a PVC membrane in an ISE has single-stranded oligonucleotides as the active components. The hybridisation of these components causes a redistribution of the ion concentration at the membrane's surface, which in turn induces a measurable potential difference across the membrane, as described above.

One can also measure changes in resistivity between two electrodes placed in a solution of interest. This is the working principle of conductometric electrochemical biosensors. Such devices are typically associated with enzyme-based biosensors, where a catalysed reaction leads to a change in the ion strength of the solution in which the reaction occurs [7,8,34].

Alternatively, the change in resistivity might be due to the decrease in the conductivity across the electrode's surface, such as in the biosensor reported by Yagiuda et al. [35]. Here, due to the immunoreaction of the immobilized layer of the methamphetamine antibody with the methamphetamine itself, the conductivity across this layer decreases.

Instead of measuring the resistivity, as in conductometric devices, it is possible to measure the impedance, Z, of the entire electrochemical system in response to a sinusoidally oscillating potential. Impedimetric electrochemical biosensors evaluate both the resistance, Z', and the reactance, Z'', which are, respectively, the real and the imaginary parts of the complex impedance [7]. Note that, in these devices, the entire system is evaluated, which includes the solution in which the measurement is conducted, as well as the interfaces between the electrodes and the solution, and the electrodes themselves. The frequency, f, at which the potential oscillates can be swept across a wide range of values. This technique is known as electrochemical impedance spectroscopy (EIS) and gives information on the change in the charge dynamics both in the bulk and at the electrodes in response to an analyte [36].

The first example of a paper-based electrochemical sensor was reported by W. Dungchai and colleagues [37]. The authors defined microfluidic channels on filter paper, using photolithography, and electrodes, using screen-printing. The latter were modified with appropriate enzymes for the detection of glucose, lactate, and uric acid, by direct current chronoamperometry (**Figure 1.3.3a**). The performance of this device was characterized in terms of limit of detection (LOD) and limit of quantification (LOQ), which were shown to be below the range of normal levels of the analytes in urine, for example, showing the potential of this technology. In a similar approach, Whitesides' group built μPADs for electrochemical sensing of glucose and heavy metal ions [38]. Paper-based electrochemical sensors can also be designed to be compatible with commercial electrochemical readers, such as glucometers, for instance [39].

Exploiting the idea of paper chromatography, R. F. Carvalhal et al. developed a paper-based sensor capable of separating a mixture of ascorbic and uric acids, and detecting the respective concentrations by chronoamperometry [40]. The separation was achieved using paper as a chromatographic column, with a mobile phase such that, due to its pH value, the ascorbic acid becomes ionized and thus much more soluble in the solvent, while the uric acid remains easily retained by the cellulose fibres. With the paper in close contact with the gold electrodes patterned onto a polyester film, chronoamperometry could be performed, with different current peaks corresponding to the different analytes, allowing quantification by the intensity of said peaks. In a similar work, separation and electrochemical detection of paracetamol and 4-aminophenol on paper was achieved [41].

Electrochemical sensing on paper was also used for the measurement of four cancer markers on a single flexible and low-cost device (**Figure 1.3.3b**) [42]. The testing zones on paper were modified with multi-walled carbon nanotubes (MWCNTs), due to their high surface area and good electronic conductivity. The MWCNTs were coated with chitosan, the amino-groups of which, after glutaraldehyde cross-linking, acted as anchoring points for the different cancer marker antibodies. The working electrodes were screen-printed using carbon ink, while a second paper sheet, with counter and reference electrodes (the latter having been printed using Ag/AgCl ink), was placed on top of the first one. Performing a sandwich-type immunoassay using horseradish peroxidase-labelled immunocomplexes, followed by differential pulse voltammetry (DPV) measurements, the concentration of the cancer markers could be determined.

Several electrochemical paper-based sensors employing graphene-based materials have also been reported. Following in the footsteps of the previously described work of D. Zang et al. [42], Y. Wu and colleagues coated the working regions, defined on cellulose, with GO and chitosan, followed by the electroreduction of the former [43]. After glutaraldehyde cross-linking, four cancer marker antibodies were immobilized on chitosan. The immunoassay was completed, after application of samples with different cancer markers, by SiO_2 particles coated with the respective antibodies and horseradish peroxidase. The detection was done by differential pulse voltammetry. The presence of rGO was shown to improve the signal, due to faster electron transfer compared to a device with chitosan immobilized directly on cellulose. Composites of rGO and cellulose microfibres have also been used in various types of electrochemical sensors for the detection of analytes such as fenitrothion organophosphorus pesticide [44] and H_2O_2 [45], the latter achieved through haemoglobin immobilization on the composite electrode, reaching a limit of detection of 0.01 μM. An rGO/AgNPs/poly(pyronin Y) composite has also been reported for amperometric nitrite detection [46]. Still in the context of graphene-based composites, a screen-printed carbon electrode was functionalized with rGO, polyaniline, Au nanoparticles, and glucose oxidase for the detection of glucose in blood (**Figure 1.3.3c**) [47]. A paper disk spotted with a whole blood sample could then be brought in contact with the modified electrode. A subsequent reaction between glucose and glucose oxidase resulted in a current decrease of flavin adenine dinucleotide, a decrease proportional to the concentration of glucose and which can be measured by differential pulse voltammetry. P. Labroo et al. used a two-electrode system, by printing, on paper, a pad with graphene-based ink, connected to two silver paste terminals [48]. The graphene-coated regions were functionalized with enzymes corresponding to the different analytes (glucose, lactate, xanthine, and cholesterol). The flow of the analyte was guided to the different graphene sensing pads by microfluidic channels defined on paper. The detection was performed by measuring the current across the graphene pads as a function of time, reaching a limit of detection of 0.3 μM for all the analytes. In another report, J. Jaewjaroenwattana et al. screen-printed graphene ink electrodes on Whatman filter paper [49]. The working electrode was then modified with the SARS-COV-2 monoclonal antibody CR3022, for the detection of the spike protein of this virus which is responsible for the COVID-19 pandemic. Here, the binding of the spike protein to the monoclonal antibody resulted in a decrease in the intensity of the current response in the DPV scans. These biosensors were tested using 14 clinical nasopharyngeal and throat swab samples and were shown to reproduce the ones obtained by the standard reverse transcription polymerase chain reaction (RT-PCR) test.

As for CVD graphene, its use in flexible electrochemical sensors is unfavourable due to slow electron transfer kinetics, similarly to what is observed for the basal plane of graphite [50]. Nonetheless, CVD graphene transferred onto paper has been employed in the detection of NO_2 gas, by monitoring the resistance of the film between two electrodes [51]. As covered in the previous section, the binding of an analyte to the sensing surface can be identified by the changes in the EIS spectra of the biosensor. S. Eissa et al. [52], for example, developed an impedimetric biosensor by covalently functionalising CVD graphene with 4-carboxyphenyl diazonium salt, for further immobilisation of the anti-ovalbumin monoclonal antibody. By fitting the faradaic EIS spectra corresponding to different concentrations of ovalbumin, a relationship between the percent change of the charge-transfer resistance of the chosen equivalent circuit and the logarithm of ovalbumin concentration was established. The reported LOD was of 0.9 pg mL^{-1}. A. H. Loo et al. [53], on the other hand, achieved detection of the rabbit IgG protein using CVD-grown graphene as a platform for the physical adsorption of the anti-rabbit IgG

antibody (**Figure 1.3.3d**). A resistance value, which the authors attributed to the charge-transfer process, was extracted from the EIS spectra and the relative changes of this parameter were used as the concentration dependant signal. The selectivity of the sensors was verified by exposure to proteins other than the rabbit IgG. The reported linear range was 0.1–100 μg mL^{-1}, with an estimated limit of detection of 0.134 μg mL^{-1}.

One should note that the use of printed electrodes is common not only in electrochemical sensing, but also in strictly electrical sensors. In an example of the use of glossy paper (cellulose with SiO_2 filler) for sensing applications, an ethanol sensor was developed, employing a composite of indium tin oxide (ITO) nanopowder and poly-diallyldimethylammonium chloride (PDDAC) as the sensing element, with carbon nanotube-based electrodes [54]. The use of glossy paper is important because Si-O groups establish bonds with PDDAC, improving the adhesion of the sensing film. The concentration of ethanol, in the gas phase, is measured by tracing current vs potential between interdigitated carbon nanotube electrodes, followed by a linear fit and slope determination of said fit, which correlates with the concentration of the analyte.

Electrochemical sensing can also be combined with other detection methods, such as colorimetry. This was demonstrated by A. Apilux et al., who complemented their electrochemical μPAD for Au(III) sensing with a colorimetric test for the presence of Fe(III), a common interferent in Au(III) sensing [55]. The gold ion concentration was determined by square wave voltammetry, while the interferent detection was achieved by spotting the test zone with a phenanthroline solution and ascorbic acid.

Laser-induced graphene (LIG) has also been successfully employed in flexible electrochemical sensing, by directly writing the electrodes on polyimide and other substrates. In one example (**Figure 1.3.3e**), the working electrode was modified by bulk electropolymerization of Eriochrome black T (EBT), using the analyte, chloramphenicol, as a template [56]. Using EIS for the assays, a limit of detection of 0.62 nM was achieved. Santos et al. compared LIG obtained by infrared and ultraviolet laser irradiation in terms of their electrochemical performance in the detection of dopamine, achieving sensitivities as high as 93 and 58 μA μM^{-1} cm^{-2} for infrared and ultraviolet LIGs, respectively [57]. Also worth mentioning is the use of LIG in the context of the COVID-19 pandemic. T. Beduk et al. reported on gold-modified LIG electrodes functionalized with the SARS-CoV-2 spike protein antibody [58]. These sensors, relying on DPV measurements, achieved a LOD of 2.9 ng mL^{-1} for this protein.

Several examples of electrochemical sensing using laser-induced graphene obtained from cellulose-based materials also exist. A molybdenum carbide-graphene composite, formed by spraying gelatine inks containing Mo^{5+} onto paper and then irradiating it with a CO_2 laser, was used as an electrochemical ion detector and gas sensor (among other applications) [59]. LIG has also been obtained from cardboard without any preceding treatment, taking advantage of its high grammage and consequent ability to withstand laser irradiation [60]. This was then used for electrochemical detection of ascorbic, caffeic and picric acid, with relevance for the alimentary and forensic fields. More recently, Pinheiro et al. fabricated enzymatic glucose sensors using LIG obtained by direct irradiation of chromatographic and office papers [61]. Lignocellulosic biomass converted into LIG has also been used for electrochemical detection of dopamine, with a sensitivity of 2080 μA mM^{-1} cm^{-2} [62].

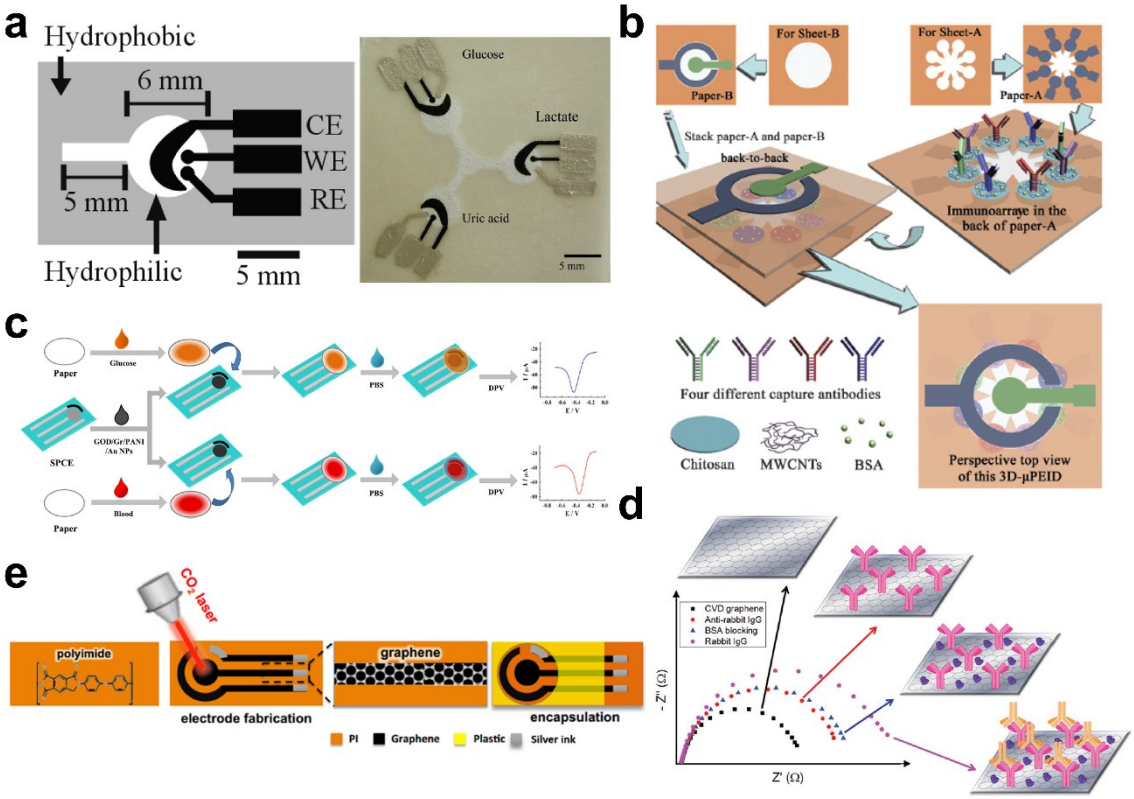

Figure 1.3.3. (a) An example of an electrochemical μPAD for simultaneous detection of glucose, lactose and uric acid. Adapted from ref. [37]. **(b)** Electrochemical immunoassay on a μPAD. Adapted from ref. [42]. **(c)** Example of the use of rGO in an electrochemical μPADs for glucose sensing in whole blood samples. Adapted from ref. [47]. **(d)** Monitoring of functionalization and detection of an analyte, by EIS, on a CVD graphene electrode. Adapted from ref. [53]. **(e)** Fabrication of a LIG-based electrochemical sensor. Adapted from ref. [56].

In summary, electrochemical detection on paper, aided by microfluidics, is a powerful tool. A wide range of approaches has been developed for different types of analytes. Graphene has an important role to play in this field, particularly in the form of printable inks and composites, while the potential of electrochemical sensing using laser-induced graphene has been demonstrated on flexible substrates. The latter, allied with its ability to be directly produced on paper [63], can become an important player in electrochemical sensing on these substrates.

1.3.3 Field effect transistor (FET) sensors

Field effect transistor (FET) sensors are based on the same principle as regular FET devices in electronics. In such devices, a change in potential induced by the gate electrode results in an electric field which changes the charge carrier concentration in the conducting channel, which connects the drain and source electrodes. In sensing, and particularly in biosensing, many molecules and bioprocesses carry charges or involve electric potential shifts [64]. This, along with the fact that the FET technology is compatible with miniaturization, parallel sensing, and easy integration with electronic circuits and systems, makes it very attractive for sensing applications [65]. A wide range of choices of the target analytes, immobilization elements, and conducting channels is possible, resulting in many different FET sensor configurations.

The case of graphene FET (GFET) sensors is particularly interesting. Here, this material excels thanks to its high carrier density and mobility, as well as its low intrinsic noise. More importantly, graphene's electronic properties (and, consequently, its conductivity) can be

modulated by minute external influences such as those of an analyte. In particular, graphene's Fermi level is sensitive to external electric fields, which can be induced by a charged molecule [66]. A shift in the Fermi level results in a change of the carrier density, and, due to graphene's zero band gap, can result in a change of the charge carrier responsible for the electrical conductivity (from holes to electrons and vice-versa). Other sensing mechanisms rely on direct charge-transfer between an analyte and graphene, the introduction (or attenuation) of charge carrier scattering and the change of the local dielectric environment [67].

The variation of graphene's conductivity can be monitored by plotting the current across the graphene channel (I_{DS}) vs the gate voltage (V_G), with the latter being applied either by an electrode under the conducting channel, in a configuration called backgated FET, or by an electrode immersed in an electrolyte which, in turn, comes in contact with graphene. The latter configuration is known as liquid gate and operates thanks to the electrical double-layer formed at the graphene/electrolyte interface, which acts as the gate dielectric [68]. The I_{DS} vs V_G plots, also designated by transfer curves, are V-shaped for single-layer graphene, reflecting its ambipolarity and linear dispersion relation. The minimum of such a transfer curve is the voltage for which the Fermi level lies at the Dirac point (the charge neutrality point). When a charged analyte, such as an antigen, approaches graphene's surface, the electric field caused by the analyte gets imposed on the field created by the gate electrode, shifting the Fermi level and, accordingly, the minimum of the transfer curve. By monitoring this shift (either by tracing the entire transfer curve for each analyte concentration, or by fixing a gate potential and by measuring the corresponding I_{DS}), the analyte's concentration can be quantified (**Figure 1.3.4**). Alternatively, if the analyte induces a change in the mobility of graphene's charge carriers, the slope of the transfer curve will change in accordance. Here, by fixing the gate potential at an appropriate value and by monitoring the change in I_{DS} for that potential, one can relate this change to the concentration of the analyte.

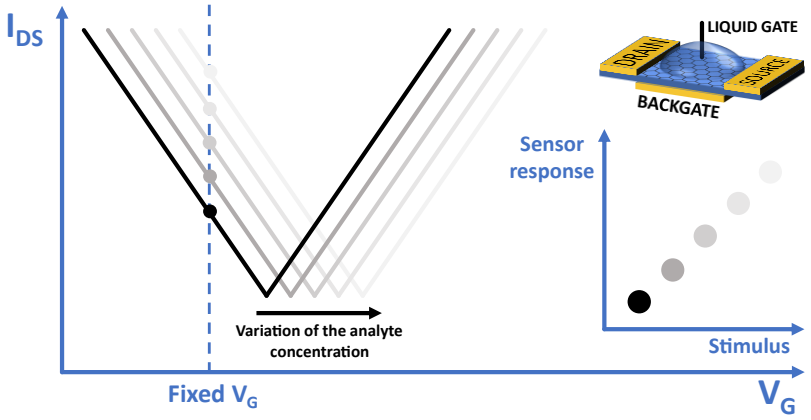

Figure 1.3.4. The measurement mechanism of a GFET sensor. The analyte solution is placed on top of the graphene conducting channel, leading to the shift of graphene's Fermi level and, consequently, its transfer curve. The sensor response in this case is the drain-source current (I_{DS}) change at a fixed gate potential (V_G), with the latter being applied wither by a back or a liquid gate.

Several examples of GFET-based biosensors have been reported in the literature. Y. Ohno et al. [68] demonstrated the potential of GFETs as a biosensing platform by measuring the concentration of bovine serum albumin attached onto graphene's surface in a phosphate buffer saline solution, with the latter acting as the electrolyte of a liquid gate. In a follow-up work, the authors immobilized Immunoglobulin E (IgE) aptamers on single-layer graphene [69]. After the

introduction of IgE onto the graphene channel, a reduction in drain current, for a constant gate voltage, was observed, due to the neutralization of the aptamers' negative charges by the analytes' positive ones.

G. Xu et al. [70] developed an array of GFET biosensors functionalised with biotinylated single-stranded DNA (immobilized on CVD graphene with biotinylated BSA and streptavidin molecules), capable of sensing 100 fM of target DNA. Each graphene channel also acted as an electrophoretic electrode, helping with the immobilization of the target DNA. In another work, it was shown that DNA sensing on a CVD graphene GFET is possible due to electron transfer, rather than due to electrostatic gating [71]. Moreover, by decorating the graphene surface with Au nanoparticles, the upper limit of detection was extended. Bacteria detection with GFET biosensors has also been shown by Y. Huang et al. [72]. Here, CVD grown graphene was non-covalently modified with 1-pyrenebutanoic acid succinimidyl ester, in order to immobilize anti-*E*. *coli* antibodies. By monitoring the change in the conductivity of the graphene channel at a fixed gate voltage in response to different concentrations of *E. coli* bacteria, a LOD of 10 cfu mL^{-1} was achieved. Recently, T. Rodrigues et al. reported GFETs employing CVD graphene for the detection and quantification of cardiac troponin I, a biomarker used for the diagnosis of acute myocardial infarction [73]. The graphene film, transferred onto interdigitated microelectrodes, was modified with single stranded nucleic acid cTnI azide-aptamer with a TTT-TCA loop and a CCCTC portion and with polyethylene glycol. The sensing was performed by monitoring the shift of the transfer curves of the GFETs in serum, and was also demonstrated in clinical samples, performing remarkably well when compared with an enzyme-linked immunosorbent assay (ELISA) and allowing to differentiate healthy patients from patients with myocardial ischemia in less than 10 min.

FETs based on reduced graphene oxide have also been reported. For instance, the detection of a prostate cancer biomarker, prostate specific antigen/α1-antichymotrypsin (PSA-ACT) complex, was demonstrated, by immobilizing PSA monoclonal antibodies on the rGO channel [74]. The same group was able to detect and quantify protective antigen, an anthrax toxin, by immobilizing single-stranded DNA (ssDNA) aptamer probes on an rGO channel and by monitoring the shift of the minimum of the transfer curve of the FET in response to the analyte [75].

GFETs can also benefit from microfluidics. P. K. Ang et al. have demonstrated a GFET device capable of sensing red blood cells infected with malaria [76]. The sample containing the analyte is introduced in a microfluidic channel lined with an array of GFETs, the latter being functionalized with CD36 receptor proteins which can interact with the positively charged membrane knobs formed on the infected red blood cells. This positive charge induces a change in graphene's conductance. The advantage of having an array of GFETs is that it allows to monitor the speed with which each cell crosses each graphene channel, which in turn can be related to the cell's stiffness, which increases as the infection progresses.

Attention has been also given, by several authors, to the transfer process of CVD graphene for the fabrication of GFETs. J. H. Jung and co-workers showed that by using a thermally evaporated layer of gold as a supporting material, instead of the commonly employed poly(methyl methacrylate) (PMMA), polymer residues on graphene were avoided, which in turn resulted in higher sensitivity, enhanced limit of detection, and larger dynamic range in the GFET sensing of a pancreatic cancer biomarker (carbohydrate antigen 19-9) [77]. Alternatively, C. Zheng et al. reported an approach by which a pre-cut graphene film can be transferred onto a substrate with an appropriate layout of electrodes, thus avoiding the patterning of graphene [78].

In what concerns flexible GFETs, CVD graphene was transferred onto polyethylene naphthalate (PEN), for further functionalization with carboxylated polypyrrole (CPPy) nanoparticles and HIV-2 gp36 antigen [79]. Thus, detection and quantification of HIV-2 gp36 antibody was possible. The device was complemented by the use of microfluidics, allowing a baseline flow of phosphate buffered saline buffer solution across an array of GFETs before the introduction of the analyte solution. More recently, a layer of rGO coated onto flexible PMMA substrate was modified with anti-CA125 ssDNA immobilized onto multi-wall carbon nanotubes, for the detection of CA125 ovarian cancer biomarker [80]. The functionalized rGO layer acted as a conducting channel between source and drain electrodes, with the detection being performed by monitoring the charge carrier mobility in the channel.

In another recent report, L. Zhou et al. [81] reported a CVD GFET biosensor for carcinoembryonic antigen, using 1-pyrenebutanoic acid succinimidyl ester as a linker for the antibody. The GFET was operated at −0.3 V gate voltage, on account of a more significant change in the transfer curves for different concentrations of the analyte at this potential. A LOD of 100 pg mL^{-1} was achieved for real-time measurements.

The GFET sensing technology is a very promising area of research. It is capable of addressing a broad spectrum of detection and quantification challenges, and possesses a wide range of advantages, while also benefiting from being compatible with microfluidics and flexible sensors. As such, the implementation of GFET sensors on paper may be of great interest.

1.3.4 Luminescence sensors

In sensors based on the concept of luminescence, the signal is measured in terms of the light emitted (or changes in said emission) in response to an analyte, either directly or indirectly caused by the latter [82].

In an early example of luminescence-based sensors on a cellulose substrate, S. Choi et al. labelled human serum albumin (HSA) with a fluorescent dye, integrating the labelled protein into the buffer carrying the sample [83]. By immobilising HSA antibodies onto the test strip of the sensor, the labelled protein, after flowing by capillary action across this strip, has to compete with the sample for the binding with the antibody (**Figure 1.3.5a**). The higher the concentration of HSA in the sample, the fewer labelled proteins bind to the antibody, resulting in a lower fluorescence signal as detected by a laser FL scanner. As such, the authors were able to quantify HSA in whole blood samples, which can give valuable information about metabolic diseases.

Quantum-dots (QDs) are also highly attractive for fluorescent sensing, due to their emission spectra allowing simultaneous excitation of different sizes of QDs, resulting in emission at varying wavelengths, which in turn allows the detection of multiple analytes simultaneously [84]. L. Zhaohui and co-workers developed a nitrated ceruloplasmin (a biomarker for cardiovascular disease, lung cancer, and stress response to smoking) fluorescent sensor on nitrocellulose membranes, using QD-conjugated antinitrotyrosine [85]. By applying the sample onto the sample pad, the analyte binds to the QD-antinitrotyrosine conjugate, followed by migration, by capillary action, towards a test line where the analyte, now carrying the fluorescent conjugate, is captured by the immobilized anticeruloplasmin antobody (**Figure 1.3.5b**). Fluorescent emission is then measured at the test line.

An interesting approach is that of fluorescence quenching by Förster resonance energy transfer (FRET), as seen in the work of E. Petryayeva, for example [86]. There, three CdSeS/ZnS

quantum dots (a red, a blue and a green one) were conjugated with dye-labelled peptides containing recognition sites hydrolysed by one of three proteases (trypsin, chymotrypsin, or enterokinase). In the absence of protease activity, the dye remains close to the respective QD, quenching (making less intense) the fluorescence of the latter by resonant energy transfer. However, after the breakdown of the peptide, the dye is released and the QD luminescence is restored. Moreover, it is shown that the fluorescence intensity at each colour can be measured with a smartphone camera for easily accessible diagnostics. The authors used a very similar approach to develop a paper-based analytic device (**Figure 1.3.5c**) [87]. The quenching of QD fluorescence by gold nanorods has also been exploited in a ochratoxin A paper-based sensor, for instance [88].

Recently, fluorescent chelating agents were employed in a microfluidic paper-based device for simultaneous detection and quantification of electrolytes in human tear fluid [89]. The fluorescence intensity of the chelating agents used in this work changed upon interaction with metal ions, having been measured by a smartphone camera. A μPAD for fluorescence-based detection of adrafinil, a performance-enhancing drug, has also been reported, using two distinct approaches (**Figure 1.3.5d**) [90]. The first one, using a Cu(II) complex, relied on the displacement of a fluorescent indicator (Coumarin 343) by the analyte, turning on its fluorescence. The second, employing the same ligand but complexed with Zn(II), rather than Cu(II), relied on the ligand's intrinsic fluorescence which would then become quenched by the attachment of the analyte. By integrating both sensing methods on the same microfluidic paper strip (one at each tip, with a central sampling zone), the quantification of adrafinil in urine, along with its discrimination from other compounds, was possible.

The incorporation of graphene in fluorescence-based sensors has also been reported in several works. By using rGO as a fluorescence quencher of a fluorescein amidite dye, a thrombin sensor was developed (**Figure 1.3.5e**) [91]. Aptamers labelled with the dye were immobilized onto rGO, leading to fluorescence quenching due to proximity. However, the presence of thrombin causes a change in the geometry of the aptamer, by forming a complex that has much less affinity with rGO. This, in turn, moves the dye away from rGO, restoring the fluorescence. The distance-dependant quenching effect was also shown for CVD graphene, where it was concluded to be due to nonradiative decay of the fluorophore rather than due to charge transfer [92]. More recently, graphene oxide quantum dots were introduced into a nitrocellulose paper structure, inside wax defined test zones [93]. The luminescence of these quantum dots is then quenched by the analyte itself, namely 4-nitrophenol and paraoxon pollutants. Demonstrating a combination of photoluminescent and electrochemical transduction mechanisms, J. Zanoni et al. prepared ZnO/laser-induced graphene composites by mixing ZnO tetrapods with scraped LIG [94]. These composites were used for H_2O_2 detection, by measuring changes in the intensity of the luminescence bands and of the anodic peak related to H_2O_2 oxidation in the cyclic voltammograms. Importantly, the two transduction mechanisms covered different concentration ranges, extending the detection domain of the sensor.

A large body of work has also been developed regarding chemiluminescent sensors, where a chemical reaction results in light emission. One of the earliest examples of this sensing approach on μPADs was one in which a sample containing uric acid, after being introduced onto a paper strip sandwiched between two adhesive tapes, moved up the strip, by capillary action, across a bioactive channel containing urate oxidase [95]. After interacting with the latter, H_2O_2 was produced, which in turn migrated towards a chemiluminescence detection area where it reacted with a rhodamine derivative, emitting light with intensity proportional to the analyte's

concentration. The limits of detection and quantification achieved were 1.9 mM L^{-1} and 2.6 mM L^{-1}, respectively, with the normal levels of uric acid in urine being 1.5–4.4 mM L^{-1}. The same principle was later extended to simultaneous detection of glucose and uric acid [96].

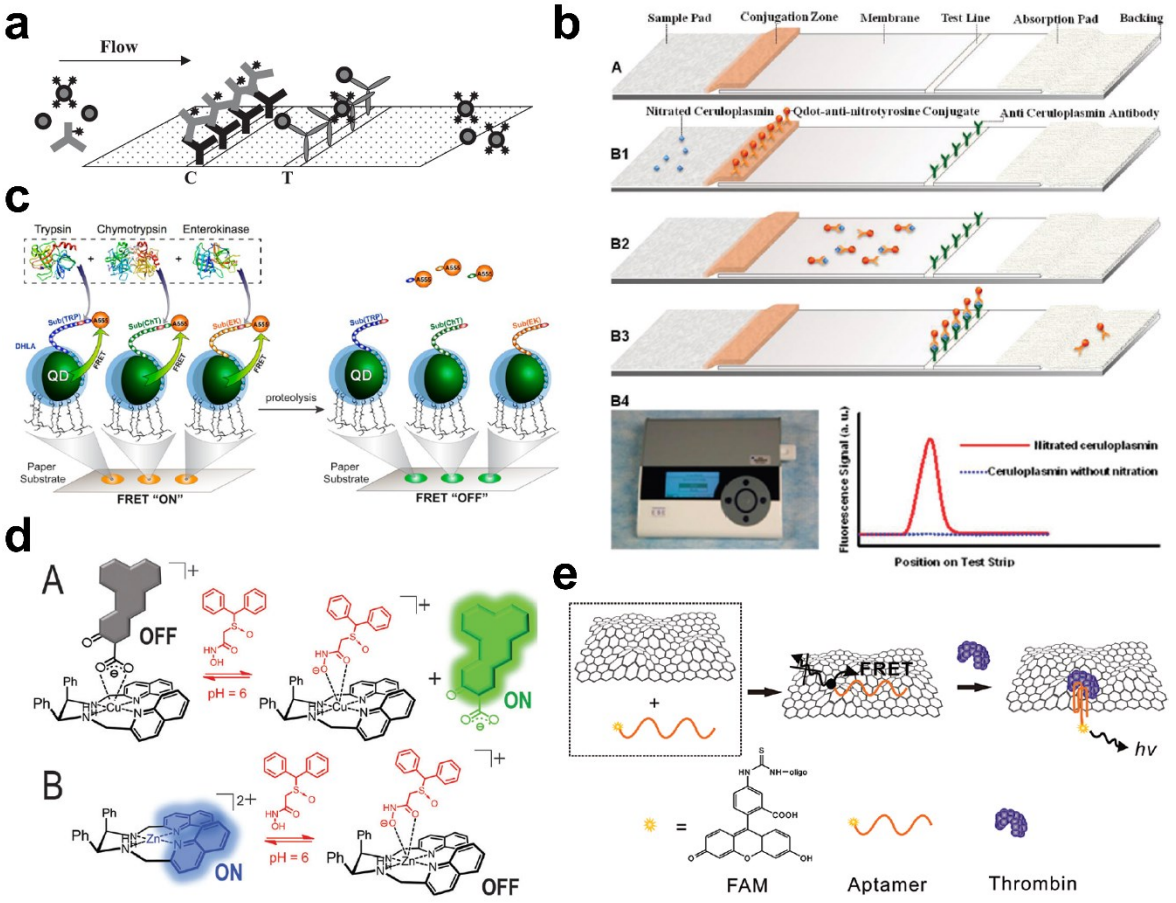

Figure 1.3.5. (a) Example of the use of a fluorescent dye for labelling in a paper-based sensor. Adapted from ref. [83]. **(b)** A labelled antibody is captured by the sample and carried towards a test line where the fluorescence can be measured. Adapted from ref. [85]. **(c)** Example of the use of fluorescence quenching by quantum dots for sensing. Adapted from ref. [87]. **(d)** Fluorescent sensor based on two different transition metal complexes. Adapted from ref. [90]. **(e)** Fluorescence quenching by graphene. Adapted from ref. [91].

Some chemical reactions lead to light emission only when subjected to an electric field, as in the case of species that undergo, at the surface of an electrode, electron-transfer reactions that lead to photon emission, in a process called electrochemiluminescence [97]. One of such species that is commonly used in electrochemiluminescent sensors is tris-(bipyridine)-ruthenium (II) ($Ru(bpy)_3^{2+}$), as exemplified by G. Lei et al., who were able to measure four different cancer markers on a single μPAD, using a sandwich immunoassay with an antibody labelled with the ruthenium complex [98].

In another example, a paper-based electrochemiluminescent sensor for genotoxic compounds was developed [99]. First, the toxins were activated electrochemically, in the presence of oxygenated reagents flowing across the paper strip under capillary action, to damage the DNA immobilized on the device's paper strip. Then, the exposed guanines of the DNA reacted, at +1.25 V, with a ruthenium metallopolymer, giving origin to light emission by the latter, at 610 nm.

Metal nanostructures can also be integrated into electrochemiluminescent paper-based sensors, as demonstrated, for instance, by C. Gao and colleagues [100]. The authors realized a sandwich immunoassay for carcinoembryonic antigen using $Ru(bpy)_3^{2+}$-labelled antibodies on Au nanocages for electrochemical signal amplification. The working electrode of this device was modified with AgNPs, in order to increase its surface area.

Graphene-based materials have also found use in electrochemiluminescent sensors on paper. L. Li et al. were able to monitor H_2S gas emission from living tumour cells [101]. Reduced graphene oxide quantum dots were immobilized on a paper substrate modified with Au@Pt core-shell nanoparticles, which acted as the working electrode. Aptamers were then used to immobilize tumour cells on this electrode. By adding Cu^{2+} ions to the sensors, the electrochemiluminescence of rGO QDs is quenched. However, the H_2S emitted by the cells, as well as S^{2-}, can bind competitively to Cu^{2+}, thus restoring the electrochemiluminescence intensity.

In summary, luminescence is a powerful tool in sensing. More interestingly, it has been shown to be compatible with paper-based detection and quantification, particularly in terms of low-cost approaches. As such, attention should be given to this avenue of research, focusing on the development of novel sensing protocols for yet to be addressed analytes.

1.3.5 Physical parameter sensors

The sensing of physical parameters such as strain, pressure, temperature and humidity is of great interest for fields such as healthcare monitoring and consumer electronic devices [102]. In particular, the development of flexible sensing platforms for these parameters opens the door towards a large spectrum of wearable devices with different purposes.

The use of paper in such sensors is best exemplified by the work of S. Gong et al. [103]. The authors impregnated tissue paper with gold nanowires (AuNWs). After sandwiching the paper between two polydimethylsiloxane (PDMS) sheets, with interdigitated electrodes patterned onto one of them, the sensor could detect pressure changes, such as those caused by arterial pulse at the wrist or by a speaker, with a sensitivity of 1.14 kPa^{-1}. The mechanism behind this sensor response was the force-dependent contact between AuNWs and the electrodes (**Figure 1.3.6a**), benefiting from paper's porosity and softness. Strain sensors based on paper have also been developed, as in the case of a device where tissue paper was converted into carbon paper by high temperature pyrolysis in N_2 atmosphere, followed by encapsulation by PDMS [104]. The device could be operated by monitoring the change in the resistance of the encapsulated carbon paper in response to different strains. More recently, G.-W. Huang et al. developed a touch sensor on a single sheet of paper [105]. Silver nanowire (AgNW) electrodes were laser printed on both sides of the sheet. Next, a silicon wafer with microneedles was used to perforate the paper in order to form 50 μm-wide microchannels, which were then filled with AgNWs to form probe arrays connected to the back electrodes. By touching this sensor with the fingers, the user closes the circuit between the microprobe arrays and the front electrode, resulting in a change in resistance (**Figure 1.3.6b**). This signal is dependent on pressure, as it influences the number of microprobes in contact with the finger, allowing to distinguish different types of user inputs.

Graphene-based materials have also been used in a number of physical sensing devices and prototypes taking advantage of this materials' conductivity and flexibility, and even though most such devices do not include paper, it is worth mentioning a few examples, as paper-based ones often rely on the same mechanisms. H. Tian reported a strain sensor made of graphene

oxide reduced by a DVD burner laser on a flexible PET film (**Figure 1.3.6c**) [106]. The use of a laser for localized GO reduction allowed to form strain sensors with different layouts. The measured signal was the resistance across the rGO conductive channels, which changes with variations in the overlap between different flakes that compose the conductive channel. The authors then took advantage of the foam-like structure of the rGO formed by the localized reduction approach discussed above to build a flexible, graphene-based pressure sensor [107]. This was achieved by putting in contact, face to face, two rGO films, so that, when under pressure, a small compressive deformation of the foam-like graphene structures results in more electrical pathways between the films (**Figure 1.3.6d**). The achieved sensitivity was as high as 0.96 kPa^{-1}, in a wide range of pressures (0–50 kPa).

Also worth mentioning is a graphene-rubber composite obtained by expanding, through swelling in toluene, natural rubber-based elastic bands, followed by immersion in a graphene-flake suspension [108]. The graphene flakes impregnated the rubber, lowering its resistivity (from 4 MΩ to as low as 57 kΩ). This parameter then varied in response to varying strain, increasing exponentially due to the decrease in interparticle tunnelling caused by the divergence of adjacent nanosheets of graphene. The performance of this strain sensor was demonstrated in a number of applications, from finger movement sensing to the monitoring of pulse and breathing patterns. A transparent graphene-based strain sensor using lithographically patterned CVD graphene has also been reported [109].

Laser-induced graphene (LIG) has been widely employed in strain and bending sensors, as exemplified by the work of A. F. Carvalho et al., who synthesized porous conductive paths directly on polyimide substrates using an ultraviolet laser (**Figure 1.3.6e**) [110]. The advantage of the UV laser irradiation consisted in shallower penetration depth, allowing to pattern these sensors on thinner substrates, as well as better patterning resolution. The sensing mechanism is explained by the change in the contact between the walls of the pores of LIG as it is deformed, a deformation which is easier to achieve with thinner substrates. Arterial waveform detection and monitoring based on this material was demonstrated by the authors. An optimization of the piezoresistive mechanism was undertaken by F. Liu et al. [111]. The authors employed extrusion printing to deposit polyamic acid which was then imidized and converted into LIG by a CO_2 laser. The piezoresistive performance of the resulting material, characterized by the gauge factor of the fabricated strain sensors, was then optimized by employing multiple lasing steps and a pre-deformation, as well as a hierarchical circular array pattern. Ultimately, a gauge factor of 648.8 was obtained. A term that appears several times in the literature regarding LIG devices is laser-induced graphene paper [112]. This, however, does not refer to any cellulosic material, but instead describes LIG obtained from intertwined polyimide fibres which form a continuous sheet. The advantage is that this material does not deform under laser irradiation like regular polyimide films and allows folding into arbitrary shapes. Several devices based on this LIG paper have been demonstrated, including piezoresistive motion sensors [112].

For temperature sensing, graphene nanowalls grown by plasma-enhanced CVD on copper have been used [113]. Placed between two electrodes on a flexible PDMS substrate, this material shows a variation in resistance due to cracks developed by thermal expansion. The crack formation is reversible, and the sensor is shown to be stable. Reduced graphene oxide has also been employed for temperature sensing on a flexible PET substrate, by measuring the resistance change of the rGO film [114]. Interestingly, the authors found that the resistance decreased with temperature, explaining this behaviour by the semiconducting nature of rGO.

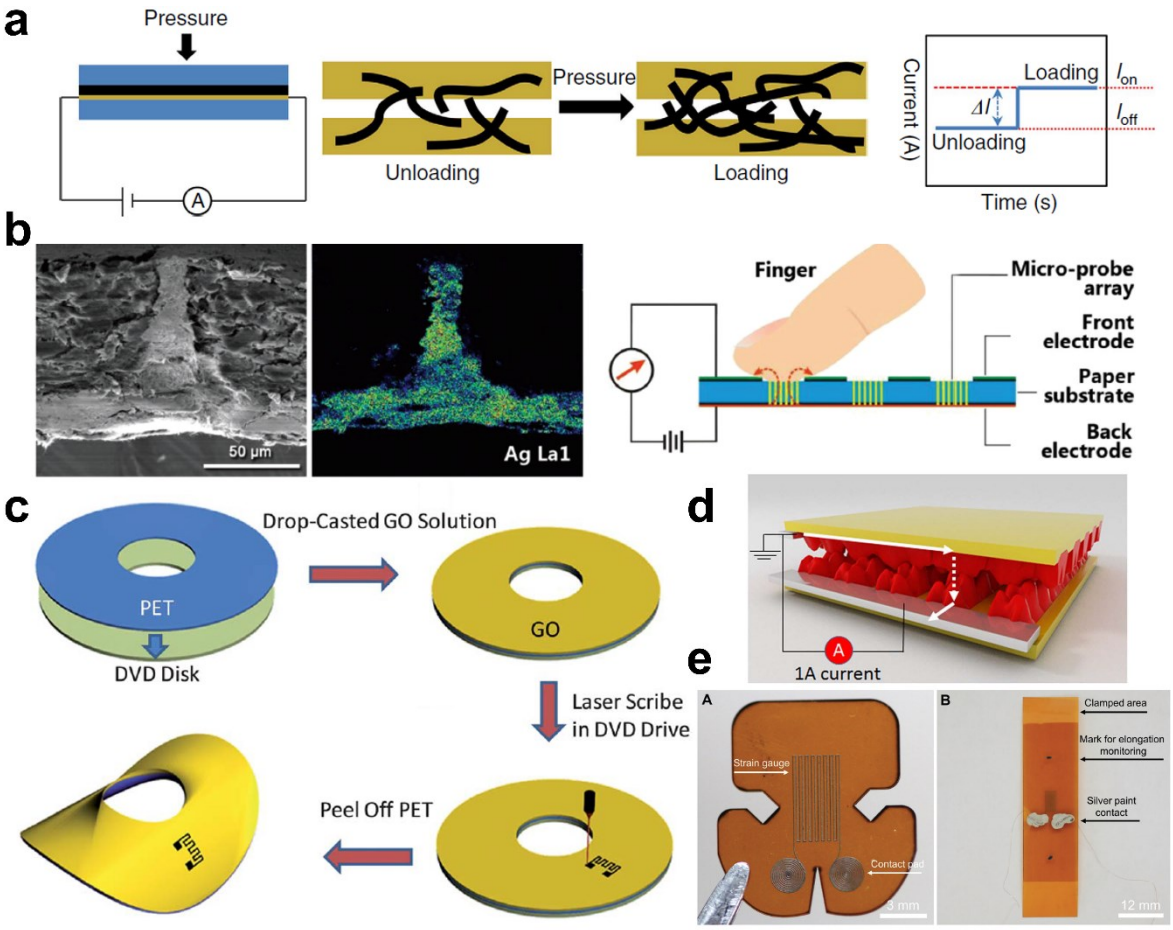

Figure 1.3.6. (a) Working mechanism behind a AuNW/paper-based pressure sensor. When pressure is applied, more AuNWs come into contact, increasing the current flowing between the two electrodes. Adapted from ref. [103]. **(b)** On the left, cross-section view, by scanning electron microscopy (SEM) and elemental imaging, of a AgNW microprobe in paper. On the right, the working principle of a touch sensor using such microprobes. Adapted from ref. [105]. **(c)** Fabrication process of a flexible, graphene-based strain sensor by localized laser-induced reduction of GO. Adapted from ref. [106]. **(d)** Working principle of a pressure sensor obtained by the same process as in (c). Adapted from ref. [107]. **(e)** A flexible, UV laser-induced graphene strain sensor fabricated directly on a polyimide substrate. Adapted from ref. [110].

Several reports of the combined use of graphene and cellulose-based materials are also available. C. Yan et al. developed a stretchable strain sensor by forming a composite of crumpled rGO and nanocellulose [115]. After impregnating this material with PDMS to confer it stretchability, resistance changes in the composite could be correlated with the applied strain, due to variations in the overlap between the rGO flakes. A cellulose paper coated by graphene-based flakes, followed by seeded in situ growth of MoS_2, was also reported [116]. This material was then used as a conductive channel in a FET device with another paper sheet as the dielectric and a graphite pencil-defined gate electrode. Similarly to other reports, the sensor responded to applied strain by varying its resistance, due to the changes in the overlap between the flakes of the conducting channel. The response of the sensor was shown to increase by applying a positive gate voltage.

Laser-induced graphene obtained from cellulose-based materials has been used in the field of sensing of physical parameters. One such example consists of LIG obtained by irradiation, with a CO_2 laser, of cellulose kraft paper treated with $NH_4H_2PO_4$, which was then used to fabricate

force and displacement sensors [117]. The authors show that $NH_4H_2PO_4$ helps to initiate the dehydration/crosslinking/char formation in the paper under the laser beam. Molybdenum carbide-graphene composites formed by laser scribing of printing paper coated with gelatine Mo^{5+} ink have been employed as strain and bending sensors for monitoring of human body motions, as well as in acoustic sensors [118]. S. Yang converted kraft lignin into LIG and then transferred this material onto an elastomeric substrate, by spin coating the elastomer onto the LIG, curing it and then immersing into water to separate the LIG from the lignin substrate [119]. The elastomer with embedded LIG was then used as a strain sensor for the detection of human speaking, breath, seismocardiography (SCG) and pulse and eye movements, achieving a gauge factor of 960.

Humidity sensors using graphene-based materials also constitute an interesting category of applications. CVD graphene, for example, has been utilized in resistive humidity sensors, where the resistance of a bilayer graphene film changes in response to varying relative humidity (RH) [120]. By monitoring the relative change in the current passing through the graphene with a constant potential difference applied across it, an approximately linear dependence on RH can be established. Using laser-induced graphene, M. Stanford et al. demonstrated a humidity sensor capable of human breath detection, by patterning two electrodes on polyimide with a 7 μm gap between them [121]. Variations in the current passing through this gap were correlated with changes in relative humidity caused by repeated breathing onto the sensor. The sensor readout can also be capacitive, with the capacitance of the sensing material changing in response to varying RH, as in the LIG sensor reported by J.-U. Lee et al. [122]. Concerning the use of paper and cellulosic materials, M Khalifa et al. coated cellulose paper with graphene nanoplatelets, and showed that the resistance of the deposited conductive film increased with RH (the same report also describes a piezoresistive force sensor) [123]. It should be noted that the response mechanisms of these humidity sensors are still somewhat unclear, with conflicting explanations given in the literature.

---------- // ----------

To conclude, the rich field of sensing, thanks in particular to the recent developments in microfluidics and biosensing, is well-suited to take full advantage of the benefits of paper in terms of its ubiquity, low cost and biodegradability. With plenty of noteworthy examples of the use of graphene-based materials in this field, there are still many opportunities in terms of sensing devices which combine paper with graphene. Among these, laser-induced graphene obtained by direct conversion of paper (paper-LIG) stands out as a particularly promising research avenue, due to its ease of fabrication, low-cost and novelty.

1.3.6 References

[1] J.P. Comer, "Semiquantitative Specific Test Paper for Glucose in Urine," *Anal. Chem.*, 28, 1748–1750, **1956**. https://doi.org/10.1021/ac60119a030.

[2] P. Von Lode, "Point-of-care immunotesting: Approaching the analytical performance of central laboratory methods," *Clin. Biochem.*, 38, 591–606, **2005**. https://doi.org/10.1016/j.clinbiochem.2005.03.008.

[3] D.D. Liana, B. Raguse, J. Justin Gooding, E. Chow, "Recent advances in paper-based sensors," *Sensors (Switzerland)*, 12, 11505–11526, **2012**. https://doi.org/10.3390/s120911505.

[4] E. Carrilho, A.W. Martinez, S.T. Phillips, G.M. Whitesides, "Diagnostics for the Developing World: Microfluidic Paper-Based Analytical Devices," *Anal. Chem.*, 82, 3–10, **2010**. https://doi.org/10.1021/ac9013989.

[5] G.M. Whitesides, "The origins and the future of microfluidics," *Nature*, 442, 368–373, **2006**. https://doi.org/10.1038/nature05058.

[6] A.W. Martinez, S.T. Phillips, M.J. Butte, G.M. Whitesides, "Patterned paper as a platform for inexpensive, low-volume, portable bioassays," *Angew. Chemie - Int. Ed.*, 46, 1318–1320, **2007**. https://doi.org/10.1002/anie.200603817.

[7] D. Grieshaber, R. MacKenzie, J. Vörös, E. Reimhult, "Electrochemical Biosensors -Sensor Principles and Architectures," *Sensors*, 8, 1400–1458, **2008**. https://doi.org/10.3390/s8031400.

[8] D.R. Thevenot, K. Toth, R.A. Durst, G.S. Wilson, Electrochemical biosensors: recommended definitions and classification, **2001**.

[9] J.D. Newman, An.P.F. Turner, "Home blood glucose biosensors: a commercial perspective," *Biosens. Bioelectron.*, 20, 2435–2453, **2005**.

[10] E.-H. Yoo, S.-Y. Lee, "Glucose Biosensors: An Overview of Use in Clinical Practice," *Sensors*, 10, 4558–4576, **2010**. https://doi.org/10.3390/s100504558.

[11] J.S. Danielsa, N. Pourmand, "Label-Free Impedance Biosensors: Opportunities and Challenges," *Electroanalysis*, 19, 1239–1257, **2007**.

[12] B. Srinivasan, Y. Li, Y. Jing, C. Xing, J. Slaton, "A Three-Layer Competition-Based Giant Magnetoresistive," 2996–3002, **2011**.

[13] D. Issadore, H.J. Chung, J. Chung, G. Budin, R. Weissleder, H. Lee, "μ Hall Chip for Sensitive Detection of Bacteria," 1224–1228, **2013**. https://doi.org/10.1002/adhm.201200380.

[14] H.J. Hathaway, K.S. Butler, N.L. Adolphi, D.M. Lovato, R. Belfon, D. Fegan, T.C. Monson, J.E. Trujillo, T.E. Tessier, H.C. Bryant, D.L. Huber, R.S. Larson, E.R. Flynn, "Detection of breast cancer cells using targeted magnetic nanoparticles and ultra-sensitive magnetic field sensors," 1–13, **2011**.

[15] D. Issadore, J. Chung, H. Shao, M. Liong, A.A. Ghazani, C.M. Castro, R. Weissleder, H. Lee, "Ultrasensitive Clinical Enumeration of Rare Cells ex Vivo Using a Micro-Hall Detector," *Sci. Transl. Med.*, 4, 141ra92, **2012**. https://doi.org/10.1126/scitranslmed.3003747.

[16] T.A.P. Rocha-Santos, "Sensors and biosensors based on magnetic nanoparticles," *Trends Anal. Chem.*, 62, 28–36, **2014**. https://doi.org/10.1016/j.trac.2014.06.016.

[17] P. Damborsky, J. Svitel, J. Katrlik, "Optical biosensors," *Essays Biochem.*, 60, 91–100, **2016**. https://doi.org/10.1042/EBC20150010.

[18] P. Skládal, "Piezoelectric biosensors," *TrAC - Trends Anal. Chem.*, 79, 127–133, **2016**. https://doi.org/10.1016/j.trac.2015.12.009.

[19] K. Ramanathan, B. Danielsson, "Principles and applications of thermal biosensors," *Biosens. Bioelectron.*, 16, 417–423, **2001**. https://doi.org/10.1016/S0956-5663(01)00124-5.

[20] J.L. Hammond, N. Formisano, P. Estrela, S. Carrara, J. Tkac, "Electrochemical biosensors and nanobiosensors.," *Essays Biochem.*, 60, 69–80, **2016**. https://doi.org/10.1042/EBC20150008.

[21] Y. Zhang, L. Zhang, K. Cui, S. Ge, X. Cheng, M. Yan, J. Yu, H. Liu, "Flexible Electronics Based on Micro/Nanostructured Paper," *Adv. Mater.*, 30, 1801588, **2018**. https://doi.org/10.1002/adma.201801588.

[22] A.W. Martinez, E. Carrilho, S.W. Thomas, S.T. Phillips, G.M. Whitesides, H. Sindi, "Simple Telemedicine for Developing Regions: Camera Phones and Paper-Based Microfluidic Devices for Real-Time, Off-Site Diagnosis," *Anal. Chem.*, 80, 3699–3707, **2008**. https://doi.org/10.1021/ac800112r.

[23] A.W. Martinez, S.T. Phillips, G.M. Whitesides, "Three-dimensional microfluidic devices fabricated in layered paper and tape," *Proc. Natl. Acad. Sci.*, 105, 19606 LP – 19611, **2008**. https://doi.org/10.1073/pnas.0810903105.

[24] A.W. Martinez, S.T. Phillips, Z. Nie, C.M. Cheng, E. Carrilho, B.J. Wiley, G.M. Whitesides, "Programmable diagnostic devices made from paper and tape," *Lab Chip*, 10, 2499–2504, **2010**. https://doi.org/10.1039/c0lc00021c.

[25] N. Ratnarathorn, O. Chailapakul, C.S. Henry, W. Dungchai, "Simple silver nanoparticle colorimetric sensing for copper by paper-based devices," *Talanta*, 99, 552–557, **2012**. https://doi.org/10.1016/j.talanta.2012.06.033.

[26] S. Chaiyo, W. Siangproh, A. Apilux, O. Chailapakul, "Highly selective and sensitive paper-based colorimetric sensor using thiosulfate catalytic etching of silver nanoplates for trace determination of copper ions," *Anal. Chim. Acta*, 866, 75–83, **2015**. https://doi.org/10.1016/j.aca.2015.01.042.

[27] T.T. Tsai, S.W. Shen, C.M. Cheng, C.F. Chen, "Paper-based tuberculosis diagnostic devices with colorimetric gold nanoparticles," *Sci. Technol. Adv. Mater.*, 14, **2013**. https://doi.org/10.1088/1468-6996/14/4/044404.

[28] A. Arshad, H. Wang, X. Bai, R. Jiang, S. Xu, L. Wang, "Colorimetric paper sensor for sensitive detection of explosive nitroaromatics based on Au@Ag nanoparticles," *Spectrochim. Acta - Part A Mol. Biomol. Spectrosc.*, 206, 16–22, **2019**. https://doi.org/10.1016/j.saa.2018.07.095.

[29] R.S.J. Alkasir, M. Ornatska, S. Andreescu, "Colorimetric paper bioassay for the detection of phenolic compounds," *Anal. Chem.*, 84, 9729–9737, **2012**. https://doi.org/10.1021/ac301110d.

[30] M.N. Costa, B. Veigas, J.M. Jacob, D.S. Santos, J. Gomes, P. V. Baptista, R. Martins, J. Inácio, E. Fortunato, "A low cost, safe, disposable, rapid and self-sustainable paper-based platform for diagnostic testing: lab-on-paper," *Nanotechnology*, 25, **2014**. https://doi.org/10.1088/0957-4484/25/9/094006.

[31] K. V. Ragavan, P. Egan, S. Neethirajan, "Multi mimetic Graphene Palladium nanocomposite based colorimetric paper sensor for the detection of neurotransmitters," *Sensors Actuators, B Chem.*, 273, 1385–1394, **2018**. https://doi.org/10.1016/j.snb.2018.07.048.

[32] H. Jang, J.H. Park, J. Oh, K. Kim, M.G. Kim, "Advanced Colorimetric Paper Sensors Using Color Focusing Effect Based on Asymmetric Flow of Fluid," *ACS Sensors*, 4, 1103–1108, **2019**. https://doi.org/10.1021/acssensors.9b00390.

[33] T. V. Shishkanova, R. Volf, M. Krondak, V. Král, "Functionalization of PVC membrane with ss oligonucleotides for a potentiometric biosensor," *Biosens. Bioelectron.*, 22, 2712–2717, **2007**. https://doi.org/10.1016/j.bios.2006.11.014.

[34] N. Jaffrezic-Renault, S. V. Dzyadevych, "Conductometric microbiosensors for environmental monitoring," *Sensors*, 8, 2569–2588, **2008**. https://doi.org/10.3390/s8042569.

[35] K. Yagiuda, A. Hemmi, S. Ito, Y. Asano, Y. Fushinuki, C.Y. Chen, I. Karube, "Development of a conductivity-based immunosensor for sensitive detection of methamphetamine (stimulant drug) in human urine," *Biosens. Bioelectron.*, 11, 703–707, **1996**. https://doi.org/10.1016/0956-5663(96)85920-3.

[36] J.K. Macdonald, E. Barsoukov, Impedance Spectroscopy, **2005**. https://doi.org/10.1002/0471716243.

[37] W. Dungchai, O. Chailapakul, C.S. Henry, "Electrochemical Detection for Paper-Based Microfluidics," *Anal. Chem.*, 81, 5821–5826, **2009**. https://doi.org/10.1021/ac9007573.

[38] Z. Nie, C.A. Nijhuis, J. Gong, X. Chen, A. Kumachev, A.W. Martinez, M. Narovlyansky, G.M. Whitesides, "Electrochemical sensing in paper-based microfluidic devices," *Lab Chip*, 10, 477–483, **2010**. https://doi.org/10.1039/b917150a.

[39] Z. Nie, F. Deiss, X. Liu, O. Akbulut, G.M. Whitesides, "Integration of paper-based microfluidic devices with commercial electrochemical readers," *Lab Chip*, 10, 3163–3169, **2010**. https://doi.org/10.1039/c0lc00237b.

[40] R.F. Carvalhal, M.S. Kfouri, M.H.O. De Piazetta, A.L. Gobbi, L.T. Kubota, "Electrochemical detection in a paper-based separation device," *Anal. Chem.*, 82, 1162–1165, **2010**. https://doi.org/10.1021/ac902647r.

[41] L.Y. Shiroma, M. Santhiago, A.L. Gobbi, L.T. Kubota, "Separation and electrochemical detection of paracetamol and 4-aminophenol in a paper-based microfluidic device," *Anal. Chim. Acta*, 725, 44–50, **2012**. https://doi.org/10.1016/j.aca.2012.03.011.

[42] D. Zang, L. Ge, M. Yan, X. Song, J. Yu, "Electrochemical immunoassay on a 3D microfluidic paper-based device," *Chem. Commun.*, 48, 4683–4685, **2012**. https://doi.org/10.1039/c2cc16958d.

[43] Y. Wu, P. Xue, Y. Kang, K.M. Hui, "Paper-based microfluidic electrochemical immunodevice integrated with nanobioprobes onto graphene film for ultrasensitive multiplexed detection of cancer biomarkers," *Anal. Chem.*, 85, 8661–8668, **2013**. https://doi.org/10.1021/ac401445a.

[44] V. Velusamy, S. Palanisamy, S.W. Chen, S. Balu, T.C.K. Yang, C.E. Banks, "Novel electrochemical synthesis of cellulose microfiber entrapped reduced graphene oxide: A sensitive electrochemical assay for detection of fenitrothion organophosphorus pesticide," *Talanta*, 192, 471–477, **2019**. https://doi.org/10.1016/j.talanta.2018.09.055.

[45] V. Velusamy, S. Palanisamy, S.M. Chen, T.W. Chen, S. Selvam, S.K. Ramaraj, B.S. Lou, "Graphene dispersed cellulose microfibers composite for efficient immobilization of hemoglobin and selective biosensor for detection of hydrogen peroxide," *Sensors Actuators, B Chem.*, 252, 175–182, **2017**. https://doi.org/10.1016/j.snb.2017.05.041.

[46] K. Dağcı, M. Alanyalıoğlu, "Preparation of Free-Standing and Flexible Graphene/Ag Nanoparticles/Poly(pyronin Y) Hybrid Paper Electrode for Amperometric Determination of Nitrite," *ACS Appl. Mater. Interfaces*, 8, 2713–2722, **2016**. https://doi.org/10.1021/acsami.5b10973.

[47] F.Y. Kong, S.X. Gu, W.W. Li, T.T. Chen, Q. Xu, W. Wang, "A paper disk equipped with graphene/polyaniline/Au nanoparticles/glucose oxidase biocomposite modified screen-printed electrode: Toward whole blood glucose determination," *Biosens. Bioelectron.*, 56, 77–82, **2014**. https://doi.org/10.1016/j.bios.2013.12.067.

[48] P. Labroo, Y. Cui, "Graphene nano-ink biosensor arrays on a microfluidic paper for multiplexed detection of metabolites," *Anal. Chim. Acta*, 813, 90–96, **2014**. https://doi.org/10.1016/j.aca.2014.01.024.

[49] J. Jaewjaroenwattana, W. Phoolcharoen, E. Pasomsub, P. Teengam, O. Chailapakul, "Electrochemical paper-based antigen sensing platform using plant-derived monoclonal antibody for detecting SARS-CoV-2," *Talanta*, 251, 123783, **2023**. https://doi.org/10.1016/j.talanta.2022.123783.

[50] A. Ambrosi, M. Pumera, "Electrochemistry at CVD grown multilayer graphene transferred onto flexible substrates," *J. Phys. Chem. C*, 117, 2053–2058, **2013**. https://doi.org/10.1021/jp311739n.

[51] G. Yang, C. Lee, J. Kim, F. Ren, S.J. Pearton, "Flexible graphene-based chemical sensors on paper substrates," *Phys. Chem. Chem. Phys.*, 15, 1798–1801, **2013**. https://doi.org/10.1039/c2cp43717a.

[52] S. Eissa, G.C. Jimenez, F. Mahvash, A. Guermoune, C. Tlili, T. Szkopek, M. Zourob, M. Siaj, "Functionalized CVD monolayer graphene for label-free impedimetric biosensing," *Nano Res.*, 8, 1698–1709, **2015**. https://doi.org/10.1007/s12274-014-0671-0.

[53] A.H. Loo, A. Ambrosi, A. Bonanni, M. Pumera, "CVD graphene based immunosensor," *RSC Adv.*, 4, 23952–23956, **2014**. https://doi.org/10.1039/c4ra03506b.

[54] A. Arena, N. Donato, G. Saitta, A. Bonavita, G. Rizzo, G. Neri, "Flexible ethanol sensors on glossy paper substrates operating at room temperature," *Sensors Actuators, B Chem.*, 145, 488–494, **2010**. https://doi.org/10.1016/j.snb.2009.12.053.

[55] A. Apilux, W. Dungchai, W. Siangproh, N. Praphairaksit, C.S. Henry, O. Chailapakul, "Lab-on-Paper with Dual Electrochemical/Colorimetric Detection for Simultaneous Determination of Gold and Iron," *Anal. Chem.*, 82, 1727–1732, **2010**. https://doi.org/10.1021/ac9022555.

[56] A.R. Cardoso, A.C. Marques, L. Santos, A.F. Carvalho, F.M. Costa, R. Martins, M.G.F. Sales, E. Fortunato, "Molecularly-imprinted chloramphenicol sensor with laser-induced graphene electrodes," *Biosens. Bioelectron.*, 124–125, 167–175, **2019**. https://doi.org/10.1016/j.bios.2018.10.015.

[57] N.F. Santos, S.O. Pereira, A. Moreira, A. V Girão, A.F. Carvalho, A.J.S. Fernandes, F.M. Costa, "IR and UV Laser-Induced Graphene: Application as Dopamine Electrochemical Sensors," *Adv. Mater. Technol.*, 6, 2100007, **2021**. https://doi.org/10.1002/admt.202100007.

[58] T. Beduk, D. Beduk, J.I. de Oliveira Filho, F. Zihnioglu, C. Cicek, R. Sertoz, B. Arda, T. Goksel, K. Turhan, K.N. Salama, S. Timur, "Rapid Point-of-Care COVID-19 Diagnosis with a Gold-Nanoarchitecture-Assisted Laser-Scribed Graphene Biosensor," *Anal. Chem.*, 93, 8585–8594, **2021**. https://doi.org/10.1021/acs.analchem.1c01444.

[59] X. Zang, C. Shen, Y. Chu, B. Li, M. Wei, J. Zhong, M. Sanghadasa, L. Lin, "Laser-Induced Molybdenum Carbide-Graphene Composites for 3D Foldable Paper Electronics," *Adv. Mater.*, 30, 1800062, **2018**. https://doi.org/10.1002/adma.201800062.

[60] W.R. de Araujo, C.M.R. Frasson, W.A. Ameku, J.R. Silva, L. Angnes, T.R.L.C. Paixão, "Single-Step Reagentless Laser Scribing Fabrication of Electrochemical Paper-Based Analytical Devices," *Angew. Chemie - Int. Ed.*, 56, 15113–15117, **2017**. https://doi.org/10.1002/anie.201708527.

[61] T. Pinheiro, S. Silvestre, J. Coelho, A.C. Marques, R. Martins, M.G.F. Sales, E. Fortunato, "Laser-Induced Graphene on Paper toward Efficient Fabrication of Flexible, Planar Electrodes for Electrochemical Sensing," *Adv. Mater. Interfaces*, 2101502, 2101502, **2021**. https://doi.org/10.1002/admi.202101502.

[62] H. Zhang, Y. Sun, Q. Li, C. Wan, "Upgrading Lignocellulose to Porous Graphene Enabled by Deep Eutectic Solvent Pretreatment: Insights into the Role of Lignin and Pseudo-lignin," *ACS Sustain. Chem. Eng.*, 10, 11501–11511, **2022**. https://doi.org/10.1021/acssuschemeng.2c02586.

[63] Y. Chyan, R. Ye, Y. Li, S.P. Singh, C.J. Arnusch, J.M. Tour, "Laser-Induced Graphene by Multiple Lasing: Toward Electronics on Cloth, Paper, and Food," *ACS Nano*, 12, 2176–2183, **2018**. https://doi.org/10.1021/acsnano.7b08539.

[64] Y.-C. Syu, W.-E. Hsu, C.-T. Lin, "Review—Field-Effect Transistor Biosensing: Devices and Clinical Applications," *ECS J. Solid State Sci. Technol.*, 7, Q3196–Q3207, **2018**. https://doi.org/10.1149/2.0291807jss.

[65] M. Kaisti, "Detection principles of biological and chemical FET sensors," *Biosens. Bioelectron.*, 98, 437–448, **2017**. https://doi.org/10.1016/j.bios.2017.07.010.

[66] R. Forsyth, A. Devadoss, O.J. Guy, "Graphene Field Effect Transistors for Biomedical Applications: Current Status and Future Prospects," *Diagnostics*, 7, 45, **2017**. https://doi.org/10.3390/diagnostics7030045.

[67] Y. Liu, X. Dong, P. Chen, "Biological and chemical sensors based on graphene materials," *Chem. Soc. Rev.*, 41, 2283–2307, **2012**. https://doi.org/10.1039/c1cs15270j.

[68] Y. Ohno, K. Maehashi, Y. Yamashiro, K. Matsumoto, "Electrolyte-Gated Graphene Field-Effect Transistors for Detecting pH and Protein Adsorption," *Nano Lett.*, 9, 3318–3322, **2009**.

[69] Y. Ohno, K. Maehashi, K. Matsumoto, "Label-free biosensors based on aptamer-modified graphene field-effect transistors," *J. Am. Chem. Soc.*, 132, 18012–18013, **2010**.

https://doi.org/10.1021/ja108127r.

[70] G. Xu, J. Abbott, L. Qin, K.Y.M. Yeung, Y. Song, H. Yoon, J. Kong, D. Ham, "Electrophoretic and field-effect graphene for all-electrical DNA array technology," *Nat. Commun.*, 5, 4866, **2014**. https://doi.org/10.1038/ncomms5866.

[71] X. Dong, Y. Shi, W. Huang, P. Chen, L.J. Li, "Electrical detection of DNA hybridization with single-base specificity using transistors based on CVD-grown graphene sheets," *Adv. Mater.*, 22, 1649–1653, **2010**. https://doi.org/10.1002/adma.200903645.

[72] Y. Huang, X. Dong, Y. Liu, L.-J. Li, P. Chen, "Graphene-based biosensors for detection of bacteria and their metabolic activities," *J. Mater. Chem.*, 21, 12358, **2011**. https://doi.org/10.1039/c1jm11436k.

[73] T. Rodrigues, V. Mishyn, Y.R. Leroux, L. Butruille, E. Woitrain, A. Barras, P. Aspermair, H. Happy, C. Kleber, R. Boukherroub, D. Montaigne, W. Knoll, S. Szunerits, "Highly performing graphene-based field effect transistor for the differentiation between mild-moderate-severe myocardial injury," *Nano Today*, 43, 101391, **2022**. https://doi.org/10.1016/j.nantod.2022.101391.

[74] D.J. Kim, I.Y. Sohn, J.H. Jung, O.J. Yoon, N.E. Lee, J.S. Park, "Reduced graphene oxide field-effect transistor for label-free femtomolar protein detection," *Biosens. Bioelectron.*, 41, 621–626, **2013**. https://doi.org/10.1016/j.bios.2012.09.040.

[75] D.J. Kim, H.C. Park, I.Y. Sohn, J.H. Jung, O.J. Yoon, J.S. Park, M.Y. Yoon, N.E. Lee, "Electrical graphene aptasensor for ultra-sensitive detection of anthrax toxin with amplified signal transduction," *Small*, 9, 3352–3360, **2013**. https://doi.org/10.1002/smll.201203245.

[76] P.K. Ang, A. Li, M. Jaiswal, Y. Wang, H.W. Hou, J.T.L. Thong, C.T. Lim, K.P. Loh, "Flow Sensing of Single Cell by Graphene Transistor in a Microfluidic Channel," *Nano Lett.*, 11, 5240–5246, **2011**. https://doi.org/10.1021/nl202579k.

[77] J.H. Jung, I.Y. Sohn, D.J. Kim, B.Y. Kim, M. Jang, N.E. Lee, "Enhancement of protein detection performance in field-effect transistors with polymer residue-free graphene channel," *Carbon*, 62, 312–321, **2013**. https://doi.org/10.1016/j.carbon.2013.05.069.

[78] C. Zheng, L. Huang, H. Zhang, Z. Sun, Z. Zhang, G.J. Zhang, "Fabrication of Ultrasensitive Field-Effect Transistor DNA Biosensors by a Directional Transfer Technique Based on CVD-Grown Graphene," *ACS Appl. Mater. Interfaces*, 7, 16953–16959, **2015**. https://doi.org/10.1021/acsami.5b03941.

[79] O.S. Kwon, S.H. Lee, S.J. Park, J.H. An, H.S. Song, T. Kim, J.H. Oh, J. Bae, H. Yoon, T.H. Park, J. Jang, "Large-scale graphene micropattern nano-biohybrids: High-performance transducers for FET-type flexible fluidic HIV immunoassays," *Adv. Mater.*, 25, 4177–4185, **2013**. https://doi.org/10.1002/adma.201301523.

[80] S. Mansouri Majd, A. Salimi, "Ultrasensitive flexible FET-type aptasensor for CA 125 cancer marker detection based on carboxylated multiwalled carbon nanotubes immobilized onto reduced graphene oxide film," *Anal. Chim. Acta*, 1000, 273–282, **2018**. https://doi.org/10.1016/j.aca.2017.11.008.

[81] L. Zhou, H. Mao, C. Wu, L. Tang, Z. Wu, H. Sun, H. Zhang, Hongbo Zhou, C. Jia, Q. Jin, X. Chen, J. Zhao, "Label-free graphene biosensor targeting cancer molecules based on non-

covalent modification," *Biosens. Bioelectron.*, 87, 701–707, **2017**. https://doi.org/10.1016/J.BIOS.2016.09.025.

[82] A.T. Singh, D. Lantigua, A. Meka, S. Taing, M. Pandher, G. Camci-Unal, "Paper-based sensors: Emerging themes and applications," *Sensors (Switzerland)*, 18, 1–22, **2018**. https://doi.org/10.3390/s18092838.

[83] S. Choi, E.Y. Choi, D.J. Kim, J.H. Kim, T.S. Kim, S.W. Oh, "A rapid, simple measurement of human albumin in whole blood using a fluorescence immunoassay (I)," *Clin. Chim. Acta*, 339, 147–156, **2004**. https://doi.org/10.1016/j.cccn.2003.10.002.

[84] E.R. Goldman, G.P. Anderson, J.M. Mauro, I.L. Medintz, A.R. Clapp, H.T. Uyeda, H. Mattoussi, "Multiplexed Toxin Analysis Using Four Colors of Quantum Dot Fluororeagents," *Anal. Chem.*, 76, 684–688, **2004**. https://doi.org/10.1021/ac035083r.

[85] Z. Li, Y. Wang, J. Wang, Z. Tang, J.G. Pounds, Y. Lin, "Rapid and Sensitive Detection of Protein Biomarker Using a Portable Fluorescence Biosensor Based on Quantum Dots and a Lateral Flow Test Strip," *Anal. Chem.*, 82, 7008–7014, **2010**. https://doi.org/10.1021/ac101405a.

[86] E. Petryayeva, W.R. Algar, "Multiplexed homogeneous assays of proteolytic activity using a smartphone and quantum dots," *Anal. Chem.*, 86, 3195–3202, **2014**. https://doi.org/10.1021/ac500131r.

[87] E. Petryayeva, W.R. Algar, "Proteolytic assays on quantum-dot-modified paper substrates using simple optical readout platforms," *Anal. Chem.*, 85, 8817–8825, **2013**. https://doi.org/10.1021/ac4020066.

[88] R. Velu, N. Frost, M.C. DeRosa, "Linkage inversion assembled nano-aptasensors (LIANAs) for turn-on fluorescence detection," *Chem. Commun.*, 51, 14346–14349, **2015**. https://doi.org/10.1039/c5cc06013c.

[89] A.K. Yetisen, N. Jiang, A. Tamayol, G.U. Ruiz-Esparza, Y.S. Zhang, S. Medina-Pando, A. Gupta, J.S. Wolffsohn, H. Butt, A. Khademhosseini, S.H. Yun, "Paper-based microfluidic system for tear electrolyte analysis," *Lab Chip*, 17, 1137–1148, **2017**. https://doi.org/10.1039/c6lc01450j.

[90] M.G. Caglayan, S. Sheykhi, L. Mosca, P. Anzenbacher, "Fluorescent zinc and copper complexes for detection of adrafinil in paper-based microfluidic devices," *Chem. Commun.*, 52, 8279–8282, **2016**. https://doi.org/10.1039/c6cc03640f.

[91] J. Jiang, J. Li, H. Chang, L. Tang, Y. Wang, "Graphene fluorescence resonance energy transfer aptasensor for the thrombin detection," *Anal. Chem.*, 82, 2341–2346, **2010**. https://doi.org/10.1021/ac9025384.

[92] A. Kasry, A.A. Ardakani, G.S. Tulevski, B. Menges, M. Copel, L. Vyklicky, "Highly efficient fluorescence quenching with graphene," *J. Phys. Chem. C*, 116, 2858–2862, **2012**. https://doi.org/10.1021/jp207972f.

[93] R. Álvarez-Diduk, J. Orozco, A. Merkoçi, "Paper strip-embedded graphene quantum dots: A screening device with a smartphone readout," *Sci. Rep.*, 7, 1–9, **2017**. https://doi.org/10.1038/s41598-017-01134-3.

[94] J. Zanoni, J.P. Moura, N.F. Santos, A.F. Carvalho, A.J.S. Fernandes, T. Monteiro, F.M. Costa, S.O. Pereira, J. Rodrigues, "Dual Transduction of H2O2 Detection Using ZnO/Laser-Induced Graphene Composites," *Chemosensors*, 9, 102, **2021**. https://doi.org/10.3390/chemosensors9050102.

[95] J. Yu, S. Wang, L. Ge, S. Ge, "A novel chemiluminescence paper microfluidic biosensor based on enzymatic reaction for uric acid determination," *Biosens. Bioelectron.*, 26, 3284–3289, **2011**. https://doi.org/10.1016/j.bios.2010.12.044.

[96] J. Yu, L. Ge, J. Huang, S. Wang, S. Ge, "Microfluidic paper-based chemiluminescence biosensor for simultaneous determination of glucose and uric acid," *Lab Chip*, 11, 1286–1291, **2011**. https://doi.org/10.1039/c0lc00524j.

[97] M.M. Richter, "Electrochemiluminescence," *Opt. Biosens.*, 317–384, **2008**. https://doi.org/10.1016/B978-044453125-4.50009-7.

[98] L. Ge, J. Yan, X. Song, M. Yan, S. Ge, J. Yu, "Three-dimensional paper-based electrochemiluminescence immunodevice for multiplexed measurement of biomarkers and point-of-care testing," *Biomaterials*, 33, 1024–1031, **2012**. https://doi.org/10.1016/j.biomaterials.2011.10.065.

[99] V. Mani, K. Kadimisetty, S. Malla, A.A. Joshi, J.F. Rusling, "Paper-based electrochemiluminescent screening for genotoxic activity in the environment," *Environ. Sci. Technol.*, 47, 1937–1944, **2013**. https://doi.org/10.1021/es304426j.

[100] C. Gao, M. Su, Y. Wang, S. Ge, J. Yu, "A disposable paper-based electrochemiluminescence device for ultrasensitive monitoring of CEA based on Ru(bpy)32+@Au nanocages," *RSC Adv.*, 5, 28324–28331, **2015**. https://doi.org/10.1039/C5RA00393H.

[101] L. Li, Y. Zhang, F. Liu, M. Su, L. Liang, S. Ge, J. Yu, "Real-time visual determination of the flux of hydrogen sulphide using a hollow-channel paper electrode," *Chem. Commun.*, 51, 14030–14033, **2015**. https://doi.org/10.1039/c5cc05710h.

[102] Kenry, J.C. Yeo, C.T. Lim, "Emerging flexible and wearable physical sensing platforms for healthcare and biomedical applications," *Microsystems Nanoeng.*, 2, **2016**. https://doi.org/10.1038/micronano.2016.43.

[103] S. Gong, W. Schwalb, Y. Wang, Y. Chen, Y. Tang, J. Si, B. Shirinzadeh, W. Cheng, "A wearable and highly sensitive pressure sensor with ultrathin gold nanowires," *Nat. Commun.*, 5, 1–8, **2014**. https://doi.org/10.1038/ncomms4132.

[104] Y. Li, Y.A. Samad, T. Taha, G. Cai, S.Y. Fu, K. Liao, "Highly Flexible Strain Sensor from Tissue Paper for Wearable Electronics," *ACS Sustain. Chem. Eng.*, 4, 4288–4295, **2016**. https://doi.org/10.1021/acssuschemeng.6b00783.

[105] G.W. Huang, N. Li, H.M. Xiao, Q.P. Feng, S.Y. Fu, "A paper-based touch sensor with an embedded micro-probe array fabricated by double-sided laser printing," *Nanoscale*, 9, 9598–9605, **2017**. https://doi.org/10.1039/c7nr02469j.

[106] H. Tian, Y. Shu, Y.L. Cui, W.T. Mi, Y. Yang, D. Xie, T.L. Ren, "Scalable fabrication of high-performance and flexible graphene strain sensors," *Nanoscale*, 6, 699–705, **2014**. https://doi.org/10.1039/c3nr04521h.

[107] H. Tian, Y. Shu, X.F. Wang, M.A. Mohammad, Z. Bie, Q.Y. Xie, C. Li, W.T. Mi, Y. Yang, T.L. Ren, "A graphene-based resistive pressure sensor with record-high sensitivity in a wide pressure range," *Sci. Rep.*, 5, 1–6, **2015**. https://doi.org/10.1038/srep08603.

[108] C.S. Boland, U. Khan, C. Backes, A. O'Neill, J. McCauley, S. Duane, R. Shanker, Y. Liu, I. Jurewicz, A.B. Dalton, J.N. Coleman, "Sensitive, high-strain, high-rate bodily motion sensors based on graphene-rubber composites," *ACS Nano*, 8, 8819–8830, **2014**. https://doi.org/10.1021/nn503454h.

[109] S.H. Bae, Y. Lee, B.K. Sharma, H.J. Lee, J.H. Kim, J.H. Ahn, "Graphene-based transparent strain sensor," *Carbon*, 51, 236–242, **2013**. https://doi.org/10.1016/j.carbon.2012.08.048.

[110] A.F. Carvalho, A.J.S. Fernandes, C. Leitão, J. Deuermeier, A.C. Marques, R. Martins, E. Fortunato, F.M. Costa, "Laser-Induced Graphene Strain Sensors Produced by Ultraviolet Irradiation of Polyimide," *Adv. Funct. Mater.*, 28, 1–8, **2018**. https://doi.org/10.1002/adfm.201805271.

[111] F. Liu, L. Li, G. Wang, D. Wang, X. Ding, S. Luo, "Combined extrusion-printed and laser-induced graphene enabled self-sensing composites with a strategic roadmap toward optimization of piezoresistivity," *Compos. Part A Appl. Sci. Manuf.*, 149, 106553, **2021**. https://doi.org/10.1016/j.compositesa.2021.106553.

[112] Y. Wang, Y. Wang, P. Zhang, F. Liu, S. Luo, "Laser-Induced Freestanding Graphene Papers: A New Route of Scalable Fabrication with Tunable Morphologies and Properties for Multifunctional Devices and Structures," *Small*, 14, 1–9, **2018**. https://doi.org/10.1002/smll.201802350.

[113] J. Yang, D. Wei, L. Tang, X. Song, W. Luo, J. Chu, T. Gao, H. Shi, C. Du, "Wearable temperature sensor based on graphene nanowalls," *RSC Adv.*, 5, 25609–25615, **2015**. https://doi.org/10.1039/c5ra00871a.

[114] G. Liu, Q. Tan, H. Kou, L. Zhang, J. Wang, W. Lv, H. Dong, J. Xiong, "A flexible temperature sensor based on reduced graphene oxide for robot skin used in internet of things," *Sensors (Switzerland)*, 18, **2018**. https://doi.org/10.3390/s18051400.

[115] C. Yan, J. Wang, W. Kang, M. Cui, X. Wang, C.Y. Foo, K.J. Chee, P.S. Lee, "Highly stretchable piezoresistive graphene-nanocellulose nanopaper for strain sensors," *Adv. Mater.*, 26, 2022–2027, **2014**. https://doi.org/10.1002/adma.201304742.

[116] P. Sahatiya, S. Badhulika, "Wireless, Smart, Human Motion Monitoring Using Solution Processed Fabrication of Graphene–MoS2 Transistors on Paper," *Adv. Electron. Mater.*, 4, 1–9, **2018**. https://doi.org/10.1002/aelm.201700388.

[117] Y. Yao, X. Duan, M. Niu, J. Luo, R. Wang, T. Liu, "One-step process for direct laser writing carbonization of NH4H2PO4 treated cellulose paper and its use for facile fabrication of multifunctional force sensors with corrugated structures," *Cellulose*, 26, 7423–7435, **2019**. https://doi.org/10.1007/s10570-019-02617-4.

[118] Y. Long, P. He, R. Xu, T. Hayasaka, Z. Shao, J. Zhong, L. Lin, "Molybdenum-carbide-graphene composites for paper-based strain and acoustic pressure sensors," *Carbon*, 157, 594–601, **2020**. https://doi.org/10.1016/j.carbon.2019.10.083.

[119] S. Yang, Y. Ling, Q. Wu, H. Zhang, Z. Yan, G. Huang, J. Lin, C. Wan, "Lignin-derived porous graphene for wearable and ultrasensitive strain sensors," *J. Mater. Chem. C*, 10, 11730–11738, **2022**. https://doi.org/10.1039/D2TC00953F.

[120] M. Chen, C. Hsu, T. Hsueh, "Fabrication of Humidity Sensor Based on Bilayer Graphene," *IEEE Electron Device Lett.*, 35, 590–592, **2014**. https://doi.org/10.1109/LED.2014.2310741.

[121] M.G. Stanford, C. Zhang, J.D. Fowlkes, A. Hoffman, I.N. Ivanov, P.D. Rack, J.M. Tour, "High-Resolution Laser-Induced Graphene. Flexible Electronics beyond the Visible Limit," *ACS Appl. Mater. Interfaces*, 12, 10902–10907, **2020**. https://doi.org/10.1021/acsami.0c01377.

[122] J.-U. Lee, Y.-W. Ma, S.-Y. Jeong, B.-S. Shin, "Direct Fabrication of Ultra-Sensitive Humidity Sensor Based on Hair-Like Laser-Induced Graphene Patterns," *Micromachines*, 11, 476, **2020**. https://doi.org/10.3390/mi11050476.

[123] M. Khalifa, G. Wuzella, H. Lammer, A.R. Mahendran, "Smart paper from graphene coated cellulose for high-performance humidity and piezoresistive force sensor," *Synth. Met.*, 266, 116420, **2020**. https://doi.org/10.1016/j.synthmet.2020.116420.

1.4 Organic Light Emitting Diodes

1.4.1 General description of the structure and working principle of OLEDs

The basic working principle of an OLED is radiative recombination in an organic layer (called the emissive layer, EML) of electrons and holes injected from a cathode and an anode, respectively [1]. As such, the simplest structure of an OLED would be an organic layer sandwiched between two electrodes. This was the structure adopted by P. Vincett et al., who demonstrated electroluminescence of a thin anthracene film (around 0.6 μm in thickness) sandwiched between two electrodes [2]. Such configuration, however, has several shortcomings.

The design of an efficient OLED should take into account every stage of the electroluminescence process, from the starting point of charge carriers at the electrodes to the extraction of light from the device (**Figure 1.4.1a**). The first stage consists of the injection of holes and electrons in response to an applied potential. This requires overcoming energy barriers at the interfaces of the different layers [3]. Next, the charge carriers must reach the EML in a balanced way, so each electron has a hole to recombine with and vice-versa [1]. The charge carriers should also be confined to the EML, so that they cannot simply traverse the entire device and exit at the opposite electrode. The same confinement should be verified for the excitons (which can be seen as pairs of interacting holes and electrons before recombination), to make sure that the recombination occurs only in the EML [4]. Moreover, recombinations near electrodes are the main reason for electroluminescence quenching, leading to an efficiency loss. Different types of excitons are possible, which should also be taken in account, as not all of them recombine radiatively [1]. Lastly, the produced light should be properly extracted from the devices [4].

In 1987, Tang and VanSlyke addressed some of the shortcomings of Vincett's work with the addition of another organic layer, a p-type one, while also using a cathode with a low work function for better electron injection [5]. Simultaneously, the authors showed the first OLED working at low applied voltages. Still, there was room for improvement on their design.

Currently, OLEDs contain an even larger number of layers. Among these are, for example, the hole transport layer (HTL) and the electron transport layer (ETL), which help with the charge balance and with carrier and exciton confinement through a proper alignment of their molecular orbitals, namely the highest occupied molecular orbital (HOMO) and the lowest unoccupied molecular orbital (LUMO), and thanks to appropriate charge mobilities. Additional layers often employed are designed to facilitate the charge injection from the electrodes, resulting in rather complex devices (**Figure 1.4.1b**).

The following subsections will address the different elements of OLEDs, their requirements and the commonly used materials, following the different stages from initial charge carrier injection to the light emission from the device. This is important to better understand the state of the art in flexible OLEDs with potential for paper and graphene integration.

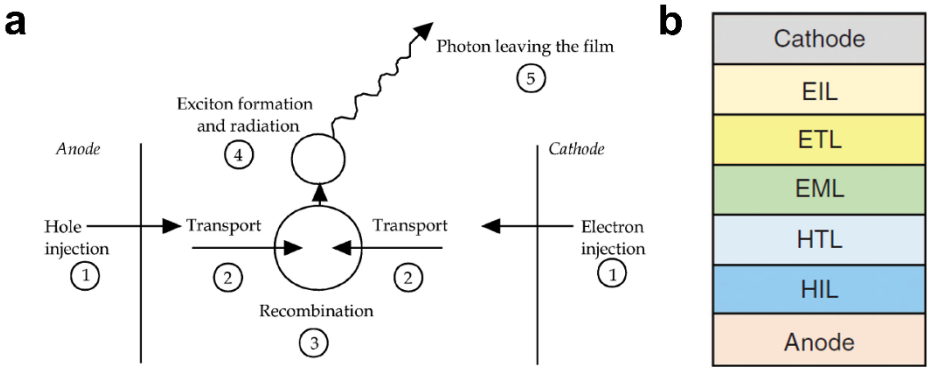

Figure 1.4.1. (a) The different stages of the electroluminescence process in an OLED. Adapted from [6]. **(b)** The generic structure of a modern OLED. Adapted from [7]. HTL – hole transport layer; ETL – electron transport layer; EML – emissive layer; EIL – electron injection layer; HIL – hole injection layer.

1.4.1.1 Electrodes

For the electrodes, one of the most basic requirements is that one of them is transparent, in order to allow the generated light to get out from the device. Several transparent conductive materials (TCMs) can be used. Independent of the material used, the desired properties are low resistivity and high optical transparency with low surface roughness, in order to avoid short-circuits between the anode and the cathode, as, on average, the total thickness of all OLED organic layers is in order of 100–200 nm. [1].

Transparent conductive oxides (TCOs) such as indium tin oxide (ITO, In_2O_3-SnO_2) and indium zinc oxide (IZO, amorphous In_2O_3-ZnO) possess high optical transparency in the visible range (≥80%) and resistivities as low as 10^{-5} Ω cm (which at thicknesses of 100-150 nm corresponds to sheet resistances of ~1 Ω sq^{-1}) [8]. This, along with their (relatively) high work functions, makes these materials the most commonly used ones as TCMs (as anodes) [3]. One of the associated disadvantages, however, is the fact that indium is a rare material, which has been leading to a considerable increase of its price (as much as $678/kg in the period from 2002 to 2011) [1]. Moreover, ITO is chemically unstable. During device operation, In atoms diffuse into the organic layers, reducing the performance of OLEDs [9]. Doped ZnO has been attracting attention as an alternative TCO, with aluminium- and gallium-doped ZnO showing a lot of promise [8]. TCOs are most commonly deposited using magnetron sputtering [8].

Another approach resides in the use of metals. On their own, metals aren't suitable as TCMs due to high reflectivity in the visible spectrum [1]. This, however, can be overcome by the use of sandwiched structures of semiconductor-metal-semiconductor. Here, silver is the most commonly used metal, sandwiched between materials such as ZnO, ZnS or ITO. The low roughness values achievable, as well as the low deposition temperatures for such structures are some of their main advantages [1].

When one considers the possibility of fabricating flexible OLEDs, the use of bendable TCMs becomes a necessity. In fact, another big disadvantage of ITO is its brittleness [10]. Here, metals are once again a viable TCM candidate, namely in the form of grids or meshes. These allow to control the optical transparency by modifying the line widths of the metal, which is possible due to the fact that these structures are typically deposited by thermal evaporation (with the use of shadow masks), lithographic patterning or printing, reaching optical transparencies of 80% and sheet resistances of ~10 Ω sq^{-1} [11]. This concept can be further developed by considering nanowire networks (such as silver nanowires, AuNWs), which can be processed in

liquid form for simpler deposition [1]. The main drawback of such structures is the roughness of the electrode. Poor adhesion to the substrate's surface can also be an issue [11]. These disadvantages can be mitigated by embedding the metal grids or nanomeshes into the substrates themselves, typically by the use of polymer buffer layers like polyethylene terephthalate (PET) or poly(3,4-ethylenedioxythiophene):poly(styrenesulphonate) (PEDOT:PSS). One should note that particularly the latter can be considered as a flexible TCM on its own, reaching sheet resistances of ~45 Ω sq^{-1} with a transmittance of 90% at 550 nm [12]. One of the main disadvantages of PEDOT:PSS as a TCM is its sensitivity to moisture [11,13].

An alternative strategy in terms of nanowire networks is the use of carbon nanotubes (CNT). These structures present a wide range of processing and deposition techniques, such as drop casting, Langmuir-Blodgett deposition and vacuum filtration [1]. However, despite reaching relatively low sheet resistances (60 Ω sq^{-1}) at high optical transmittances (90.9%) [14], several challenges remain. Namely, the purity of the CNT films has a large effect on their resistivity, due to the presence of contaminants and the mixture between semiconducting and metallic CNTs [11].

It is here that graphene presents itself as another option, showing high, broad-band optical transmittance and excellent charge carrier mobility, making it a very promising candidate for TCM applications. However, before graphene can fully take on this role, some challenges have to be overcome. Graphene often requires to be doped in order to reduce its sheet resistance [15]. Moreover, graphene's work function has also to be tailored, typically, as it is rather low (between 4.2 and 4.8 eV), which may result in larger charge-injection barriers than for ITO anodes [16].

As a general remark regarding TCMs for OLED anode applications, these should have sufficiently high work functions [1], in order to reduce the potential barrier to the HOMO orbitals of the organic layers (usually at high level, >5.5 eV). For the materials briefly discussed above, these have values of ~5 eV [1]. As for the cathode, the material of choice should have a low work function, with aluminium being the most common one [3]. Despite its high work function (~4.2 eV), it is a chemically stable metal which is cheap and easy to evaporate. The potential gap between Al and the organic layer LUMO orbitals can be reduced by using calcium between the organic and Al, or a very thin layer (5Å) of a dielectric material (e.g. lithium fluoride), allowing carrier tunnelling between Al and the organic. Note that the cathode doesn't have to be transparent, depending on the configuration of the device. In fact, it being highly reflective can be advantageous as it acts as a back reflector for the produced light.

1.4.1.2 Charge injection layers

With such a large number of requirements for TCMs, the alignment between their Fermi level and the appropriate energy levels of the organic molecules is often established with the help of charge injection layers (**Figure 1.4.2**).

A proper energy alignment depends, on one hand, on the work function of the electrode. This represents the energy required to remove an electron from the electrode and is defined as the difference between the Fermi level and the absolute vacuum level [1]. Note that the latter is different from the local vacuum level, due to the surface dipole present when an electron is removed to just outside the electrode's surface. In fact, this difference can cause a shift of the organic molecule's energy levels when it is brought in contact with the electrode [1].

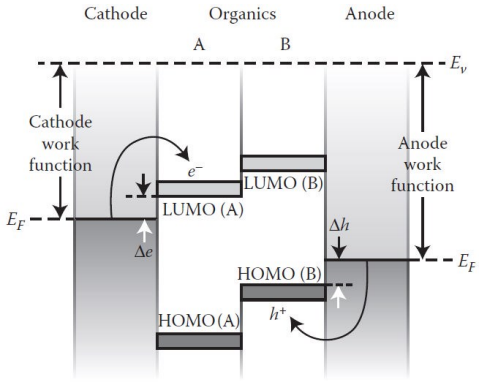

Figure 1.4.2. The role of the charge injection layers in the improvement of the charge carrier injection, through alignment of the appropriate energy levels. Adapted from [1]. LUMO and HOMO are lowest and highest unoccupied molecular orbital, respectively.

Focusing a bit more on the electrode-organic interface, several scenarios in terms of energy level alignment are possible depending on the strength of interaction between the molecules and the electrode.

For weakly interacting interfaces, the general trend is that when the Fermi level of the electrode is located between the HOMO and LUMO of the organic layer, the energy barrier for the injection of charge carriers varies linearly [1]. A higher anode work function results in a lower hole injection barrier Conversely, a higher cathode work function will increase the electron injection barrier. However, as the electrode work function increases beyond the organic layer's ionisation energy (IE, the difference between the HOMO and the vacuum level), the HOMO level becomes pinned to the Fermi level, following it as it shifts even further toward lower energies [17]. The same happens if the Fermi level lies above the LUMO, with the latter also getting pinned to the former. As such, in these regimes the charge carrier barrier remains constant, independently of the electrode's work function. This has been explained on account of charge-transfer between the two components of the interface, leaving ionised molecules at the interface, which in turn leads to an electrostatic field that shifts the organic layer's energy levels [1].

In the case of moderately interacting interfaces, the variation of the potential barrier isn't linear with the Fermi level of the electrode (when it is between HOMO and LUMO). The reason for that is the creation of a continuous density of states at the interface due to the (moderate) overlap between electron wavefunctions of the two layers [18]. These states get filled up to a certain charge neutrality level that will lie in the gap between HOMO and LUMO. The interfacial region will have its own Fermi level that will be closer to the charge neutrality level than the electrode's Fermi level, thus acting as a buffer and affecting the energy alignment.

Lastly, for strong interactions between the electrode and the organic layer, there's an overlap of wavefunctions such that new electronic states are formed [1]. Such situations have to be considered individually by numerical calculations of these states.

In any case, it is important to be able to measure the different energy levels relevant to this discussion. This is most typically done using photoelectron spectroscopy [1]. In this type of techniques, a beam of photons is focused on the sample where they can cause the emission of electrons by the photoelectric effect. The kinetic energy of these electrons is given by the photon's energy minus the binding energy of the electron. By using X-rays, for example, one can probe the core energy levels of the atoms that compose the sample. Additionally, and especially in the case of metals, the electrons from the valence band can be photoemitted by ultraviolet

photons, as done in the UPS technique, which typically uses photons from the He Iα emission line of a helium plasma discharge lamp, with an energy of 21.22 eV. The relevance of this technique comes from its ability to measure the Fermi level of metals as well as the HOMO of organic compounds.

In practical terms, some hole injecting layers (HILs) that are commonly used to reduce the potential barrier are copper phthalocyanine (CuPc), triphenyldiamine, naphthyl-phenyl-aminobiphenyl (α-NPD), tricarbizoletriamine, and 4,4',4''-tris(3-methyl-phenylphenylamino) triphenylamine (m-MTDATA) [1]. Considering, for example, an OLED with an ITO anode (work function of ~4.7 eV) and tris-(8-hydroxyquinolate)-aluminium (Alq_3, with the HOMO level at 5.8 eV) as the EML, the hole injection barrier would be of 1.1 eV. However, the introduction of a HIL of m-MTDATA, which has the HOMO level at 5.1 eV, reduces the initial injection barrier to 0.4 eV and the barrier at the interface with Alq_3 becomes 0.7 eV, allowing a step-by-step injection of holes with lower potential barriers [3]. Polymers, such as PEDOT:PSS, with work functions in the range of ~5.2-5.6 eV, as well as metal oxides like MoO_3, with a work function of ~6.9 eV, can also be used as HILs [1].

On the cathode side, LiF, Cs_2CO_3, NaF, ZnO, and even Alq_3 itself can be used as electron injection layers (EILs).

1.4.1.3 Charge transport layers

As mentioned previously, another big concern in terms of efficient light emission resides in providing a balanced supply of charge carriers to the EML (at as low a driving voltage as possible), while, at the same time, keeping them confined there. Additionally, the potential barriers for the majority carriers at the interfaces should continue being minimized.

The charge carrier supply depends on the mobility of the carriers. Charge transport in organic structures is different from the inorganic case. In most organic molecules, it relies on the delocalization of charge carriers due to π orbital conjugation [3]. Different degrees of delocalization are possible, depending on the extent of conjugation, which in turn depends on the strength of the bonds and the overlap between molecules [1]. If a system is highly delocalized, a band model can be applied, somewhat similarly to what happens in inorganic crystals. A more localized system, on the other hand, relies on the hopping of polarons, which are quasi-particles resultant from the polarization of, in this case, the organic matter by the charge carrier. Typically, the first model is more relevant for organic molecular crystals, where the delocalization is high. This usually results in higher mobilities than for a system reliant on hopping. In either case, these values are low compared to inorganic materials. In fact, one of the main drawbacks of low carrier mobility in organic materials is it can lead to a build-up of charge at the interfaces (specially the metal-organic ones), creating an electrical field that opposes the externally applied one [3]. Moreover, a low mobility requires the use of very thin layers, which, depending on the material, can be difficult to achieve in a controlled and reproducible manner [3].

One strategy to address these drawbacks is the electrical doping of the organic layers. This allows to increase the charge carrier concentration, leading to an increase in the conductivity [4]. Moreover, the width of the space charge region at the interfaces can be reduced by doping, leading to smaller energy barriers [4]. Additional advantages of doping include the ability to improve charge balance (by the use of appropriate dopants), as well as the ability to use thicker layers (which may be important for production related reasons) [1].

Hole doping typically requires that the LUMO of the dopant is close or below the HOMO of the HTL material [1]. The reverse is true for electron doping, where the dopant's HOMO should be close or above the ETL material's LUMO. Of course, this should take into account that for organic molecular crystals HOMO and LUMO aren't discrete levels with fixed energies as in individual, isolated molecules. Note, however, that so far it is not totally clear whether complete charge transfer occurs [1]. A good example of hole doping (p-type doping) is the increase in conductivity of vanadyl-phthalocyanine (VOPc) by the introduction of a small amount of tetrafluoro-tetra-cyano-chinodimethane (F4-TCNQ) [19]. As for electron organic dopants, these are harder to find, due to the requirement that they possess a low ionization energy (shallow HOMO). This property makes such materials unstable with respect to oxidation [4]. Nonetheless, some options exist, such as alkali metals (mostly Li and Cs), with a disadvantage of the ease with which atomic dopants migrate towards the EML [1].

As for the transport materials themselves, N,N'-Bis(3-methylphenyl)-N,N'-diphenylbenzidine (TPD), N,N-bis-(1-naphthyl)-N,N'-diphenyl-1,1'-biphenyl-4,4'-diamine (NPB), 1-(3-methylphenyl)-1,2,3,4-tetrahydroquinoline-6-carboxyaldehyde-1,19-diphenylhydrazone (MTCD) and 4,48-bis(Ncarbazolyl)biphenyl (CBP) are commonly used as HTLs, while Alq_3, 2-(4-biphenyl)-5-(4-tert-butylphenyl)-1,3,4-oxadiazole (butyl-PBD), 1,3,5-tris(2-N-phenylbenzimidazolyl) benzene (TPBi) and 1,3-Bis[(p-tert-butyl)phenyl-1,3,4-oxadiazoyl]benzene (OXD7) can be employed as ETLs [3].

Both HTL and ETL often play two other important roles: confining the excitons in the EML and blocking electrons and holes, respectively. The first goal is achieved by the use of materials with higher triplet energy (triplets are the lowest energy level excitons, as will be explored later) [4]. For the second goal, electrical doping of the charge transport layers can once again have a beneficial effect [1]. However, the solution often adopted is to include additional blocking layers.

1.4.1.4 Blocking layers

Besides having the characteristics mentioned above, the blocking layers should present low barriers to the majority carrier injection [3], as with any other interface in the OLED structure. Some of the materials often employed as blocking layers are usually very hard to dope. As such, they tend to present low conductivities, which requires them to be very thin in order to not have any unwanted effects on the majority charge carrier transport [1].

Some examples of charge carrier blocking materials include Bathocuproine (BCP) for hole blocking and PEDOT:PSS for electron blocking (this one in particular exhibits high electrical conductivity) [3]. In terms of exciton blocking, 4,4',4''-tri(N-carbazolyl)triphenylamine (TCTA) is common in phosphorescent blue OLEDs, at the HTL/EML interface [1].

1.4.1.5 Emission layer

The EML is where the charge carriers combine to form excitons, which are the sources of the emitted photons, through radiative recombination. Several types of excitons can be distinguished based on the separation between the electron and the hole. The most common ones, in the case of organic materials, are the Frenkel and the Charge-Transfer excitons, with the two charges being on the same molecule or on adjacent ones, respectively [1].

For excitons, much like for two-electron systems, the possible combinations of the spins of the interacting carriers lead to the formation of distinct states: singlet and triplet, with the latter

being triple degenerate (hence the name). The close proximity of the opposing charge carriers leads to a considerable overlap between their wavefunctions, which in turn leads to a separation of these states' energies, with the triplet states having a lower one [4]. The recombination occurs when the electrons relax from the excited singlet or triplet state to the ground singlet state [3]. When a singlet decays to the ground state, the light emission process is referred to as fluorescence, with it being a relatively fast process. The decay of a triplet is known as phosphorescence, being a much slower process.

Depending on the way the excitons decay, several working principles of OLEDs are possible (**Figure 1.4.3**) [7]. A fluorescent OLED relies on the radiative decay from the singlet states only, which occurs in fluorescent molecules. Since only 25% of the excited states are singlets, the internal efficiency of the conversion of an electron-hole pair into a photon is limited at this value, with the maximum external quantum efficiencies of the order of just 5%. Such OLEDs are usually designated as 1st generation ones. An improvement on this principle is the triplet-triplet fluorescent OLED, where two triplet states combine to form a singlet one which can then decay radiatively (this process is known as triplet-triplet annihilation, TTA, or triplet fusion) [4]. This allows for internal conversion efficiencies of up to 62.5%. A third strategy (2nd generation OLEDs) relies on the introduction of heavy metal ions, such as Ir, Re, Ru or Pt, into the EML. These are phosphorescent OLEDs, due to the fact that the strong spin-orbit coupling of the metal ions allows an intersystem crossing (ISC) from excited singlets to excited triplets and accelerates the radiative decay (phosphorescence) of the latter [7]. Here, internal conversion efficiencies of up to 100% are possible, in principle, although for larger driving currents this value becomes lower (due to an accumulation of triplet excitons that start interacting with each other, leading to a quenching effect) [4]. Lastly, thermally activated delayed fluorescent (TADF) emission is based on the reduction of the overlap between the electron and hole wavefunctions, with a spatial separation of the HOMO and LUMO orbitals, leading to a smaller energetic separation between the singlet and triplet states due to the minimization of the exchange energy integral *J* [7]. This allows to re-populate the excited singlet state from the excited triple one, at room temperature, through reverse intersystem crossing (RISC), with a consequent delayed fluorescence emission. In these so-called 3rd generation OLEDs, a theoretical internal conversion efficiency of up to 100% is also possible, with a maximum theoretical external quantum efficiency near 52%. Although similar to the 2nd generation OLEDs, TADF emitters provide the advantage of being pure organic emitters without any expensive metal atom inside an organic coordination sphere.

Nowadays, the EMLs, instead of consisting entirely of an electroluminescent material where the recombination occurs, possess a structure where the host material transfers its excitons to the emitting dopant (guest) [1]. This model is based on the fact that efficient organic emitters (2nd and 3rd generation) easily exhibit quenching when employed in an active layer on their own. The exciton transfer can occur by different processes. The Förster process is mediated by dipole-dipole interactions, which can be seen as the decay of the donor and the excitation of the acceptor [4]. This type of energy transfer is relatively long-range and can occur between states of different spin multiplicity. The Dexter mechanism is a short-range one, relying on the overlap of the donor and acceptor wavefunctions [4]. It is essentially a direct transfer of the electrons between the HOMO and LUMO of the donor and the acceptor. The Dexter process must conserve the total spin multiplicity, allowing singlet-singlet and triplet-triplet transfers, with the former being less likely to occur than the singlet-singlet Förster transfer. The TTA process described previously is also an example of Dexter energy transfer. It is worth pointing

out that both processes require a considerable overlap between the emission spectra of the different materials [4].

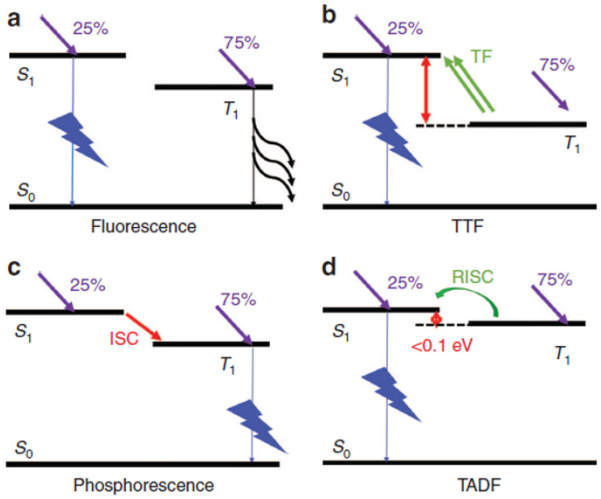

Figure 1.4.3. The different emission mechanisms of OLEDs. TF – triplet fusion; TTF – triplet-triplet fluorescence; ISC – intersystem crossing; RISC – reverse intersystem crossing; TADF – thermally activated delayed fluorescence. Adapted from [7].

As the excitons travel inside the host material, mostly Förster singlet-singlet and Dexter triplet-triplet transfers occur [4]. This knowledge is particularly relevant for TADF OLEDs, where the former mechanism should be dominant in the host-to-dopant transition energy transfer to promote fluorescent emission from the singlet states of the dopant, with nearly 100% photon generation efficiency [4]. This is achieved by separating donors and acceptors through appropriate molecular design and doping.

As a final note, the host:guest model also has the advantage of a relatively simple way to modulate the electrical charge transport properties and recombination.

Some common EML formulations consist of wide-bandgap hosts, such as p-bis(triphenylsilylyl) (UGH2), with bis(2,4-difluorophenylpyridinato)-tetrakis(1-pyrazolyl)borate iridium(III) (Fir6) as a blue phosphorescent emitter [1]. Other phosphorescent emitters include bis[2-(2-pyridinyl-N)phenyl-C](2,4-pentanedionato-O^2,O^4)iridium(III) ($Ir(ppy)_2(acac)$) and bis(2-methyldibenzo[f,h]quinoxaline) (acetylacetonate) iridium(III) ($Ir(MDQ)_2(acac)$), as green and red, respectively [4]. Phosphine oxides, like 3,6-bis(diphenylphosphoryl)-9-ethylcarbazole (PO10), can also be used as hosts with good electron transport properties, with iridium(III) bis[(4,6-difluorophenyl)-pyridinato-N,C2'] picolinate (FIrpic) as a guest [1]. Structures using rare-earth (RE) complexes dispersed in a host material are also possible, with the host populating the excited states of the RE, as in the case of the $Eu(TTA)_3bipy$ complex in a poly(N-vinylcarbazole) (PVK) host (which is a non-conjugated polymer) [3].

1.4.1.6 Light outcoupling

Once the charge carriers are converted into photons in the EML, it is still necessary to extract these photons from the OLED for them to be considered as useful light. This is a non-trivial task. In fact, it is the main limitation of the device efficiency, with almost 70% of the generated light being lost inside the device itself [20]. This is mainly due to the internal reflections of light at the different interfaces, leading to the so-called waveguided modes (**Figure 1.4.4**). Moreover, the generated light can be coupled to the plasmon modes of the metallic cathode, due to

plasmonic oscillations at its surface [1]. Only the so-called external modes, which represent the light extracted from the OLED device, are of practical interest. As such, most efforts on improving the light outcoupling are focused either on the suppression of the non-external modes, or on their conversion to the external ones [1].

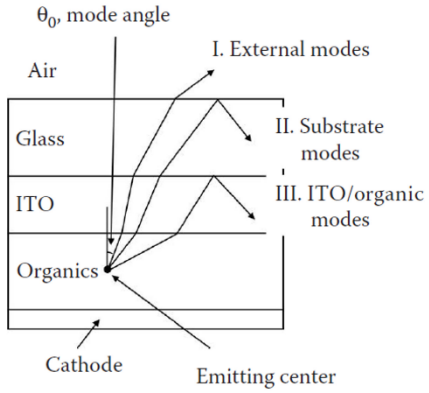

Figure 1.4.4. Illustration of the different total internal reflections resulting in light that is not outcoupled from the device. Adapted from [1].

Several solutions exist for the extraction of the light internally reflected at the substrate/air interface (with the most common substrate being glass). In fact, it is a relatively easily addressable problem, in the sense that one can alter the substrate without perturbing the OLED itself. A number of approaches rely on the patterning of the backside of the substrate, with solutions ranging from small lens patterning on the surface of the substrate to large hemispherical macroextractors [20]. The backside of the substrate can be patterned randomly so that the incidence angle at the interface varies with each internal reflection until it is such that allows the light to exit. Films with scattering centres can also be employed, following a similar strategy of randomly varying the direction in which the light reaches the interface [1].

The modes confined inside the OLED itself are usually due to internal reflections at the TCM/substrate interface. These can be eliminated by the use of a substrate with a high refractive index, such as polyethylene naphthalate (PEN) [20]. A drawback of this approach is the relatively higher cost of such substrates. Moreover, such substrates may not be suitable for blue emission or applications where the mechanical flexibility of the devices is important [1]. Some internal structures, placed between the OLED and the substrate, have also been reported, including low refractive index grids to direct the light out from the OLED [20], while the organic layers themselves can be used to scatter the light out, as in the case of NET-61 (developed by NOVALED) that is inserted into the ETL [21].

The surface plasmon polariton (SPP) modes are arguably the most difficult to address, while contributing to around 30%−40% of the total light loss due to outcoupling issues [1]. Among the proposed strategies to overcome this hurdle, cathodes with random roughness (or "buckling") have shown some promise, by inducing some degree of Bragg scattering of the SPP modes [1]. Alternatively, by "sandwiching" the metallic cathode between dielectric materials with a relative permittivity that is higher than the negative real part of that of the metal, the SPP modes can be supressed (although this route also needs further experimental exploration) [1].

Interestingly, graphene can also have an effect on light outcoupling from an OLED. S.-Y. Kim et al. have shown by theoretical calculations that the light outcoupling efficiency of graphene-

based OLEDs should be similar to the ones with a 150 nm thick ITO electrode [22]. Moreover, the authors show that, when using waveguided modes light extraction approaches, graphene-based OLEDs show higher ultimate outcoupling efficiencies than ITO-based ones.

1.4.1.7 Encapsulation

Some final remarks regarding encapsulation should be made to wrap up this basic overview of the OLED structure. OLED encapsulation is very critical, due to the extreme sensitivity of organic materials to oxygen and moisture [1]. Organic devices working in ambient conditions have been shown to degrade a lot faster than equivalent devices operating in vacuum [23]. M. Schaer et al. have shown that oxygen diffuses into the OLED, through pinhole defects formed by dust particles present during device fabrication, leading to the formation of dark spots at the metallic cathode/organic layers interface, due to oxidation of the metal and Alq_3 material (when oxidised under an applied bias) [24]. The situation is even worse in the presence of water vapour, as it diffuses into the device and gives origin to the formation of H_2 bubbles, the bursting of which leads to the creation of additional defects through which more water molecules can enter. The end result is the delamination of the cathode around these defects, leading to dark spots where electrons are not injected into the OLED. The authors conclude that water is three orders of magnitude more destructive for an OLED than pure oxygen.

Encapsulations with metal covers or glass caps are the most common approaches (**Figure 1.4.5**) [1]. The covers are typically treated thermally or by UV irradiation before being placed on OLEDs, in order to remove moisture. A desiccant (usually a Ba, Ca or Sr oxide) is placed in the cover [1], which is then glued to the OLED substrate by an epoxy adhesive. The latter is the most vulnerable element for oxygen and moisture permeation into the device.

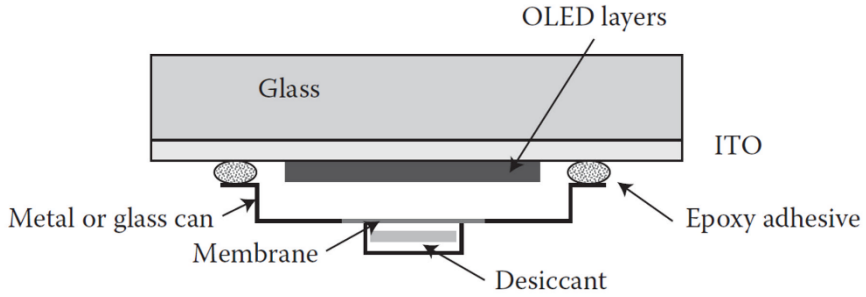

Figure 1.4.5. Typical OLED encapsulation method with a metal or glass cap (here referred to as can). Adapted from [1].

Alternatively, thin-film barriers have shown great promise in OLED encapsulation [23]. These films can be deposited by CVD and atomic or molecular layer deposition (ALD or MLD). SiN_x and Al_2O_3, as well as hybrids such as Al_2O_3/ZrO_2 and Al_2O_3/TiO_2 are some of the materials employed in thin-film barriers. Multilayer polymer/inorganic encapsulation films, such as the proprietary Barix coating, have also seen considerable success in commercial OLED applications [1]. Recently, OLEDs encapsulated on both sides using a hybrid of inorganic nanolaminates with parylene-C were developed [25]. Parylene-C is a widely used polymeric coating, particularly in the biomedical field, but suffers from high moisture permeability to be an efficient encapsulant on its own. This is addressed by the nanolaminate, in this case consisting of alternating layers of Al_2O_3 and ZrO_2 deposited by ALD. The OLEDs employing this encapsulation strategy were shown to be stable for more than 70 days in air and for over 2 weeks in deionized water and phosphate buffer saline. Additionally, the encapsulation films were robust enough for the OLEDs to be completely free-standing, showing great flexibility even at bending radii as

small as 1.5 mm. In the wider context of OLED encapsulation, graphene can also play an important role, as its impermeability to gases and liquids makes it a very good candidate as an OLED encapsulant [26,27].

1.4.2 Figures of merit for OLEDs

Before moving onto an overview of some recent trends in OLED research, some commonly used figures of merit have to be defined (**Table 1.4.1**) [3].

Table 1.4.1. Figures of merit commonly used to characterize the performance of OLEDs.

Figure of merit	Mathematical expression	Units
External Quantum Efficiency	$EQE = \eta_{EQE} = \frac{N_{\text{Photons}}}{N_{\text{electrons}}} = \frac{q}{hcI}\int_0^\infty P_{\text{OLED}}(\lambda)\,\lambda\,d\lambda$	-
Wall-Plug power efficiency	$\eta_{WP} = \frac{\int_0^\infty P_{\text{OLED}}(\lambda)\,d\lambda}{IV}$	-
Luminance	$L = \frac{l_0}{S}$	cd m^{-2}
Total luminous flux	$\Phi_{\text{Total}} = 638\int_0^\infty y(\lambda)\,P_{\text{OLED}}(\lambda)\,d\lambda = \pi l_0$	lm
Luminous efficiency (or current efficiency), assuming Lambertian emission	$CE = \eta_l = \frac{L}{J} = \frac{l_0}{I}$	cd A^{-1}
Luminous power efficiency (or, simply, power efficiency)	$PE = \eta_{lp} = \frac{\Phi_{\text{Total}}}{IV} = \frac{\pi}{V}\eta_l$	lm W^{-1}

P_{OLED} = optical power spectrum, l_0 = luminous intensity perpendicular to the emitting surface, S = area of the device, y(λ) = photoptic response function, J = current density, I = applied current, V = applied voltage, q = charge of the electron, h = Planck's constant, and c = speed of light.

As an important issue to consider, the measured external efficiency of an OLED depends on the product of three individual factors: the photoluminescence quantum yield of the emitter (PLQY), the electrical balance between electrons and holes and the light extraction efficiency.

Also worth mentioning is that in the case of the substrates and the electrodes in OLEDs, surface roughness can be a very important parameter. This is due to the fact that typically OLEDs are very thin devices, so a rough substrate or bottom electrode can result in localized thinning of the device, increasing the leakage current or even causing a short circuit. Here, the relevant metric is the root mean square (rms) surface roughness (*Rq*), which for OLEDs should ideally be of the order of few nm or less.

1.4.3 Graphene-based Transparent Conducting Materials (TCMs) and OLED applications

1.4.3.1 Graphene-based Transparent Conducting Materials

1.4.3.1.1 Doping

When looking into the use of graphene as a TCM for OLEDs, one should be aware of the strategies typically employed to dope it.

The two main approaches are substitutional doping, where dopant atoms are inserted into graphene's lattice, replacing some of the carbon ones, and charge-transfer doping, where the dopant in close proximity with graphene induces a transfer of electrons, either to or from graphene [28]. The doping may also be induced electrostatically, by the dipole moment of the dopant [29].

In what concerns substitutional doping, one of the first reports was presented by L. S. Panchakarla et al., who used graphene formed during arc discharge between carbon electrodes in hydrogen atmosphere [30]. Boron doping was achieved by adding diborane (B_2H_6) gas to the atmosphere, or by using boron-stuffed graphite electrodes. Similarly, nitrogen doping was undertaken in the presence of pyridine or ammonia. Another instance of nitrogen doping was reported by J. O. Hwang et al., who doped rGO by treating it with hydrazine (N_2H_4) vapour, followed by a thermal treatment in H_2 and NH_3 [31]. Sheet resistance of 300 Ω sq^{-1} was achieved.

In one of the first examples of substitutional doping of CVD graphene, D. Wei and colleagues introduced nitrogen atoms into graphene's lattice by adding NH_3 to the growth atmosphere [32]. Also for the case of CVD graphene, boron doping was achieved by H. Wang et al. by using phenylboronic acid ($C_6H_7BO_2$), sublimated upstream inside the CVD chamber as the sole precursor, providing both C and B atoms for the growth [33]. It is worth pointing out that substitutional doping disrupts the ideal sp^2 lattice of graphene, which may impact negatively its electronic properties [34]. In fact, most of the substitutional doping works covered here use the appearance of defect-induced D and D' bands in graphene's Raman spectra to confirm its successful doping.

Regarding charge-transfer doping, small inorganic molecules are commonly employed in the literature. Nitric acid (HNO_3) has been used by several authors. S. Bae et al. have identified this compound as an effective p-type dopant for CVD graphene, and were able to reduce the latter's sheet resistance down to ~30 Ω sq^{-1} after just 5 minutes of exposure to this compound [35]. A disadvantage of doping with nitric acid is that it is volatile, and thus unstable, as brought to attention by A. Kasry and colleagues [36]. The authors performed multiple consecutive transfers of CVD graphene, either doping each transferred layer or only the last one. The achieved sheet resistance values (down to ~90 Ω sq^{-1}) were comparable between these two cases, leading to the conclusion that either the dopant intercalates easily between the layers, or the volatility of HNO_3 leads to the evaporation of the dopant before the next layer is transferred.

More specifically in the context of OLED development, T.-H. Han et al. functionalized their CVD graphene anodes with HNO_3 or $AuCl_3$ [37]. A four-layer graphene anode doped with $AuCl_3$ had a sheet resistance of ~30 Ω sq^{-1}, lower than for HNO_3. The doping also had a beneficial effect on the work function, increasing it to values as high as 5.077 eV for $AuCl_3$-doped four-layer graphene. However, the current efficiency of the resulting OLEDs with $AuCl_3$ was lower in comparison to nitric acid doping. This was explained by the formation of gold clusters on graphene as $AuCl_3$ gets reduced. This nanoparticle formation is undesirable, as it lowers the transmittance and may cause local thinning in OLEDs, potentially leading to short circuits in the devices [28]. K. K. Kim et al. observed the same Au particle formation (10–100 nm in size) when doping CVD graphene with $AuCl_3$, using nitromethane (CH_3NO_2) as a solvent [38]. At 87% transmittance, sheet resistances as low as 150 Ω sq^{-1} were achieved. The authors also monitor the

stability of this doping, having observed an increase in R_S of up to 11% after 20 days (for doping with 10 mM of $AuCl_3$). This increase is even higher for lower concentration doping, possibly because nitromethane itself may be doping graphene. But, it being a volatile molecule, this doping effect may be reduced with time. To address the issue of environmental stability, F. Güneş et al. performed a layer-by-layer doping of CVD graphene transferred onto a PET substrate, in a process very similar to the one of K. K. Kim et al. (**Figure 1.4.6a**) [39]. The layer-by-layer doping was shown to be more stable than the topmost-layer doping, with R_S as low as 54 Ω sq^{-1} having been achieved, at 85% transmittance, and with this value increasing by less than 25% after 21 days (while the topmost-layer doped sample's R_S increased by more than 40% in the same period of time). Water can also be used as a solvent for $AuCl_3$ doping [40]. Other metal chlorides that can be used as p-dopants are $IrCl_3$, $MoCl_3$, $OsCl_3$, $PdCl_3$, and $RhCl_3$, as reported by K. C. Kwon et al. [41]. The authors exposed HNO_3 doped CVD graphene to these compounds and observed that the lowest R_S values were obtained for $AuCl_3$ and $PdCl_3$ (500 Ω sq^{-1} and 520 Ω sq^{-1}, respectively, from the original 750 Ω sq^{-1} of nitric acid doped graphene and 1100 Ω sq^{-1} of pristine graphene). Moreover, these dopants led to an increase of the work function to as high as 5.14 eV for doping with 20 mM of $RhCl_3$. However, a reduction in transmittance after each of these doping experiments was observed, due to the formation of metal particles on graphene's surface.

Metal oxides, such as WO_3, V_2O_5, and MoO_3 can also be used for p-type doping of CVD graphene (**Figure 1.4.6b**) [42–45]. This is achieved by the deposition by thermal evaporation, for example, of a very thin (>10 nm) layer of these materials on top of graphene. Here, besides reducing graphene's sheet resistance to <300 Ω sq^{-1} (in the case of WO_3) or even ~30 Ω sq^{-1} (for MoO_3 on four-layer graphene), the oxide layer has the additional benefit of acting as a protective mask for graphene patterning by O_2 plasma. This type of doping has been shown to be more effective, in terms of the measured Fermi level shift, than the one with HNO_3, for example, with OLEDs based on doped graphene TCMs having been demonstrated [43]. These devices showed slightly better performance than ITO-based ones, achieving power efficiencies of 60 lm W^{-1} at 1000 cd m^{-2}. More recently, the deposition of Re_2O_7 over epitaxial graphene was also shown to be a promising doping approach, resulting in an increase of the work function from 4.50 eV to 4.95 eV [46].

Graphene can also be p-doped by adsorption and intercalation of Br_2 and I_2, through its exposure to the halogen vapours [47]. NO_2 is another molecule capable of extracting electrons from graphene when adsorbed on its surface [48,49]. But perhaps one of the first reports of p-type doping of graphene was presented by W. Chen et al. [50]. The authors evaporated tetrafluorotetracyanoquinodimethane (F4-TCNQ) to dope graphene grown on SiC. An increase in work function was observed, from 4.0 eV to as high as 5.5 eV for a 1 nm thick layer of F4-TCNQ. Despite the effectiveness of this compound in doping graphene (**Figure 1.4.6c**), a further theoretical study raised concerns regarding its effect on graphene's carrier mobility, which may reduce due to additional Coulomb scattering induced by F4-TCNQ [51]. This mobility reduction was later observed experimentally [52]. A somewhat similar compound, tetracyanoquinodimethane (TCNQ), has also been used to dope graphene, with the additional benefit of resulting in low surface roughness (**Figure 1.4.6d**) [53]. Layer-by-layer doping of four-layer graphene resulted in a reduction of R_S from ~850 Ω sq^{-1} to ~140 Ω sq^{-1}, while the work function increased from 5.0 eV to 5.2 eV, according to the authors. Interestingly, the measured carrier mobility of the doped sample increased relative to pristine graphene.

Compounds such as bis(trifluoromethanesulfonyl)amide ($[CF_3SO_2]_2NH$, TFSA, **Figure 1.4.6e**) [54,55], as well as trifluoromethanesulfonic acid (CF_3SO_3H, TFMS, **Figure 1.4.6f**) [56], have also been used to p-dope CVD graphene (using nitromethane as a solvent for both dopants). The former resulted in a decrease of R_S from 425 Ω to 129 Ω, and in an increase of the work function by 0.5–0.7 eV, despite a slight reduction in charge carrier mobility, while the latter, performed on a four-layer CVD sample prepared by stacked transfers, led to a decrease of R_S from 212.7±7.2 Ω sq^{-1} to 63.3±2.5 Ω sq^{-1}, while increasing the work function to 5.23 eV. TFMS doping was also shown to be very stable due to this molecule's non-planar configuration, higher binding energy with graphene, more hydrophobic nature, and excellent chemical stability.

Impressive results have also been obtained by hole doping with triethyloxonium hexachlorantimonate (OA) [57]. The doping reduced the sheet resistance of graphene from ~1 kΩ sq^{-1} to <200 Ω sq^{-1} and increased its work function to ~5.1 eV. It should be noted, however, that in a recent work proposing another dopant, tetrakis(penta-fluorophenyl)boric acid (HTB), its performance was compared with OA, TFSA, $AuCl_3$ and HNO_3 [58]. The authors found that OA and TFSA were less stable than the other ones, with HTB's effect remaining for at least 8 weeks. The sheet resistance decrease observed for this dopant was from 657 to 96 Ω sq^{-1} for single-crystal graphene, accompanied by a work function increase from 4.6 to 5.3 eV.

Over the last several years the group of G. V. Bianco has been optimizing p-type doping of CVD graphene with thionyl chloride ($SOCl_2$) for different applications [59–62]. Typically, the graphene is placed in a dry chamber alongside 1 mL of liquid $SOCl_2$, at 105 °C for 60 min, and this process can be repeated after each additional graphene layer is transferred on top of the previously doped one. This is a covalent doping approach, with the introduction of covalently bonded chlorine atoms at graphene defect sites with hydroxyl and carboxyl functionalities. Initial works reported sheet resistances of ~25 Ω sq^{-1} at transmittances above 85% for 5-layer graphene. More recently, the doping process was improved by the addition of pyridine, to aid in the introduction of sulphur (as well as SO and SO_2 groups) at grain boundaries and carbon vacancies [62]. Ultimately, this allowed to achieve a sheet resistance of 18 Ω sq^{-1} at T=87% for 6-layer doped graphene.

Other p-type graphene dopants reported in the literature include 2,3-dichloro-5,6-dicyanobenzoquinone (DDQ) [63], aromatic molecules (**Figure 1.4.6g**) such as 9,10-dibromoan-thracene (An-Br) and tetrasodium 1,3,6,8-pyrenetetrasulfonicacidand (TPA) [64], and gold [65].

As for n-type charge-transfer dopants, these come with an additional requirement of having to be stable with respect to oxygen (as they are strong electron donors) [66]. The organic compound (4-(1,3-dimethyl-2,3-dihydro-1H-benzoimidazol-2-yl)phenyl)dimethylamine (N-DMBI), having been used as n-type dopant in organic field-effect transistors [67], was employed by W. Xu et al. to dope CVD graphene [68]. This compound can be activated by thermal annealing after it is deposited on graphene, which causes it to release a hydrogen atom and to become a radical. A reduction of ~0.2 eV in the work function after doping was confirmed by the authors using Kelvin probe force microscopy, as well as by UPS.

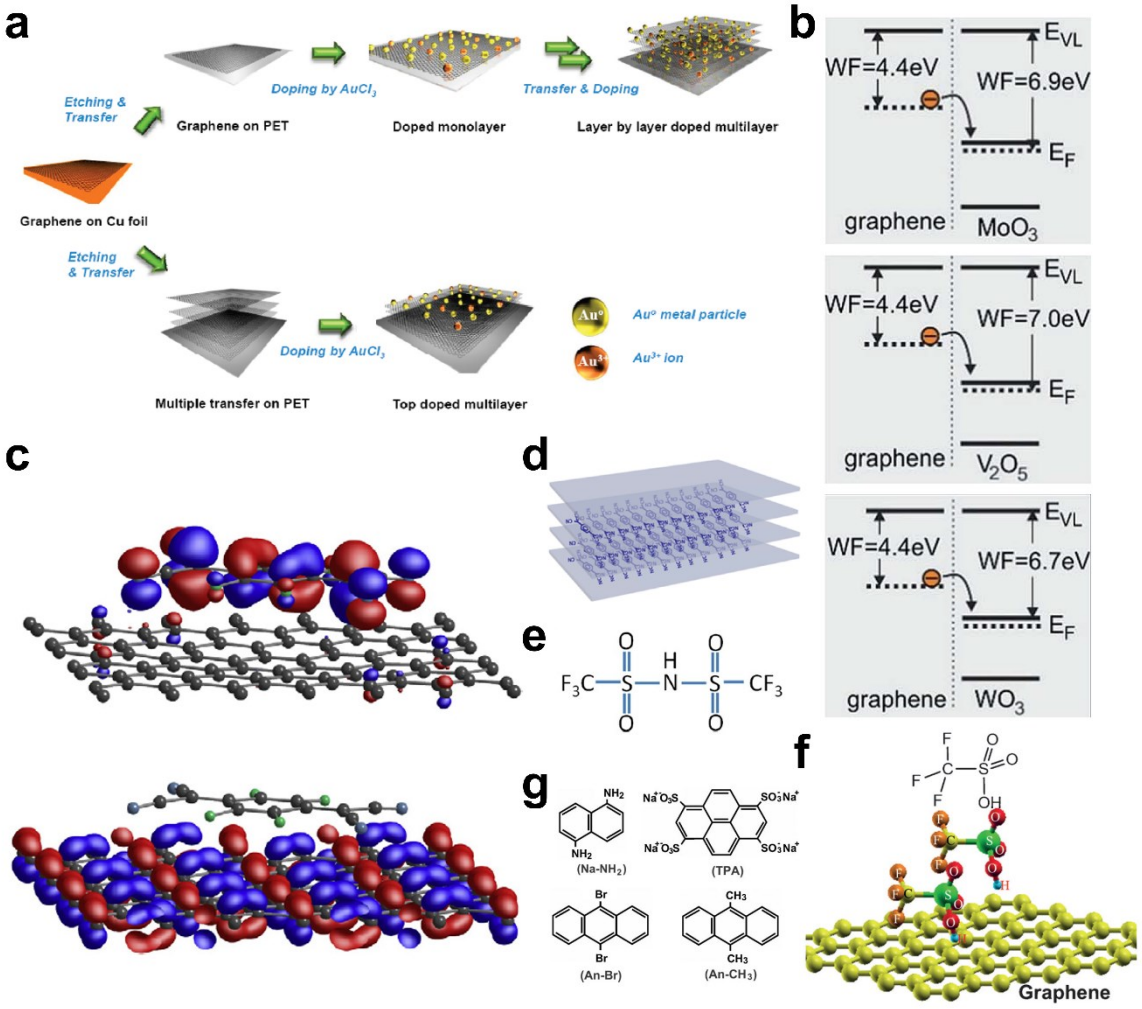

Figure 1.4.6. (a) Illustration of graphene doping with $AuCl_3$, both layer-by-layer and topmost layer only. The formation of gold particle is also illustrated. Adapted from ref. [39]. **(b)** Illustration of the doping effect by metal oxides, with the relevant energy levels. Adapted from ref. [45]. **(c)** Wavefunctions of the HOMO (top) and LUMO (bottom) levels of the graphene/F4-TCNQ system. The fact that the LUMO is localized on graphene while the HOMO level is on F4-TCNQ indicates electron transfer from the former to the latter. Adapted from ref. [51]. **(d)** Illustration of layer-by-layer doping of graphene with TCNQ. Adapted from ref. [53]. **(e)** Chemical structure of TFSA. Adapted from ref. [54]. **(f)** Chemical structure of TFMS and its interaction with graphene. Adapted from ref. [56]. **(g)** Chemical structures of several aromatic molecules capable of doping graphene. Adapted from ref. [64].

Decamethylcobaltocene (DMC) has also been used for electron doping of CVD graphene [69]. The work function of the doped samples reached values as low as 3.53 eV. Another n-type dopant, cesium carbonate (Cs_2CO_3), was thermally evaporated on single-layer CVD graphene by S. Sanders et al. [70]. The sheet resistance went from ~1300 Ω sq^{-1} to ~250 Ω sq^{-1}. Moreover, the stability of this doping was ensured by co-evaporating Cs_2CO_3 and Bphen, a commonly used organic for the ETL. An OLED with a cathode based on this doping approach reached a current efficiency of 40 cd A^{-1}, higher than that of an equivalent ITO-based device (which had a current efficiency of 37 cd A^{-1}). In an earlier example of doping with Cs_2CO_3, by direct contact with the dopant solution, a sheet resistance as low as 270 Ω sq^{-1} (four individually doped graphene layers stacked on top of each other) was achieved [71]. In the same work, CsF doping led to R_S=118 Ω sq^{-1} for a four-layer graphene sample (each layer individually doped). Among aromatic molecules, 1,5-naphthalenediamine (Na-NH_2) and 9,10-dimethylanthracene (An-CH_3)

can also play the role of n-dopants [64]. Another interesting approach to dope graphene is by forming an NH_2 self-assembled monolayer on a Si/SiO_2 substrate onto which the pristine graphene is later transferred [52].

I.-Y. Lee et al. doped CVD-grown graphene by simply dipping the latter into a hydrazine monohydrate solution (N_2H_4-H_2O) [72]. Interestingly, the electron mobility increased after doping. However, the doping effect seemed to get lower after exposure to air for 8 days, as well as after a 40 s thermal annealing at 90 °C.

Some oxides can also have an n-type doping effect on graphene. P.-H. Ho and colleagues doped CVD graphene with sol-gel synthesized titanium suboxide TiO_x [73]. The work function of graphene decreased from ~4.68 eV to ~4.33 eV for films transferred onto a Si/SiO_2 substrate spin coated with TiO_x. Moreover, the n-doping effect was observed to be stronger with amorphous TiO_x than with crystalline TiO_2. The authors explain this based on density functional theory calculations that show that, unlike in TiO_2, the oxygen deficiency of TiO_x allows for substantial transfer of electrons from Ti atoms to graphene, even though oxygen atoms have the opposite effect. By doping both sides of graphene, the stability of the doping effect was improved. Zinc oxide (ZnO) was also shown to be capable of n-doping graphene [74]. CVD-grown graphene was also doped with $AgNO_3$, achieving R_S=202 Ω sq^{-1} at 96% transmittance [75]. A disadvantage of this process is the formation, after doping, of Ag particles on graphene's surface, due to the use of sodium citrate in the doping process.

Y. Kim et al. studied graphene vapour-phase doping by ethylene amines, namely ethylene diamine (EDA), diethylene triamine (DETA), and triethylene tetramine (TETA) [76]. The same group later compared several other ethylene amines as CVD graphene dopants, namely triethylenetetramine (TETA), tetraethylenepentamine (TEPA), pentaethylenehexamine (PEHA), and poly(ethyleneimine) (PEI) [77]. The doping effect was stronger for compounds with a higher amount of amine groups (PEHA > TEPA > TETA), although it was the lowest for PEI. The sheet resistance reduction follows the same trend, with PEHA doping resulting in R_S=385.0±43.4 Ω sq^{-1} (while pristine graphene's sheet resistance had a value of 1520.0±67.6 Ω sq^{-1}). The doping was shown to be stable even after a 20 min long thermal treatment at 90 °C. However, the charge carrier mobility was observed to become lower with increased doping.

R. K. Castro and colleagues used a polymeric blend of ethylene-propylene-diene monomer (EPDM) and polyaniline (PAni) as supporting material for graphene transfer [78]. Here, the presence of PAni also contributed with doping, reducing graphene's R_S from ~2400 Ω sq^{-1} to ~1700 Ω sq^{-1}. As such, the polymeric blend didn't have to be removed, having been directly incorporated in an organic device (organic photovoltaic cell).

Recently, n-type doping with Na^- was reported [79]. Graphene on SiO_2 was immersed, for 30 min, into a solution of [K(15-crown-5)2]Na, and then rinsed with THF, methanol, and isopropyl alcohol, followed by blow-drying with N_2 gas. The authors did not measure the sheet resistance, but observed indications of doping by Raman spectroscopy and by the shift of the charge neutrality point towards negative potentials in the GFET transfer curves.

To summarize, a wide range of approaches to dope graphene is available. Among these, the main issue that remains is the stability of the doping. For OLED applications, the most promising strategies are those that allow to stably reduce the sheet resistance and control the

work function while maintaining high transparency and low surface roughness of the films. Unfortunately, so far, no strategy has emerged as a clear candidate to address all these points.

1.4.3.1.2 Hybrid graphene-based TCMs

When talking about graphene-based TCMs, it is important to consider the integration of graphene with other materials, particularly those that themselves are promising for such applications.

Several authors have reported hybrid TCMs based on graphene and CNTs (**Figure 1.4.7a,b**) [80–85]. C. Li et al. transferred a CVD-grown CNT film onto a CVD-grown graphene film [84]. Etching away the copper catalyst used for graphene synthesis, a TCM with sheet resistance of 735 Ω sq^{-1} at 90% transmittance was obtained. Alternatively, graphene/CNT hybrids can be formed from suspensions, as reported by P. J. King and colleagues [83]. Here, graphene was obtained by sonication of graphite in a sodium cholate solution and subsequent centrifugation of the resulting dispersion. After blending this suspension with a CNT dispersion, a thin film could be formed by vacuum filtration. This film, after being treated with nitric acid to reduce contact resistance between the different components of the hybrid, had a sheet resistance of 100 Ω sq^{-1} at 80% transmittance. In another example, a hybrid TCM, dubbed "rebar graphene" (**Figure 1.4.7b**), was synthesized by growing graphene on copper coated with dodecyl-functionalized CNTs, without the use of any carbon precursor [82]. This hybrid was measured to have a sheet resistance of ~600 Ω sq^{-1} at ~95.8% transmittance. In another report, few-layer CVD graphene doped with 1-Pyrenebutyric acid N-hydroxysuccinimide ester (PBASE) and transferred onto horizontally aligned CNTs was successfully employed to build a phosphorescent OLED, reaching CE=14.7 cd A^{-1} and η_{lp}=9.21 lm W^{-1} [85].

As mentioned previously, metals, particularly metallic grids and meshes, are also a viable TCM for flexible applications. As such, a considerable body of work has been devoted to the combination of such materials with graphene, in order to overcome the individual drawbacks of each of these components. These efforts can be rather straightforward, like directly transferring a CVD graphene film onto a silver nanowire (AgNW) TCM, resulting in a hybrid with R_S=34.4±1.5 Ω sq^{-1} at 92.8% transmittance (**Figure 1.4.7c**) [86], or onto other metals, such as copper, gold or aluminium (**Figure 1.4.7d**), reaching sheet resistances of 20±4 Ω sq^{-1} at 91% transmittance (in the case of gold), for example [87]. Alternatively, more elaborate approaches are possible, such as growing graphene, by, for example, plasma-enhanced CVD (PECVD), directly on top of copper nanowires (**Figure 1.4.7e**) [88]. Here, the role of graphene is to protect the copper nanowires from oxidation by exposure to air. Moreover, in a similar work, it was shown that graphene coating improves the transport properties in copper nanowires, due to the passivation of the latter's surface states [89]. Another approach explored in this context is a graphene/AgNW/graphene sandwich structure formed by conventional transfer of graphene onto the desired substrate, AgNW deposition by spin coating, and a second conventional graphene transfer, resulting in R_S=19.9±1.2 Ω sq^{-1} at 88.9% [90].

Hybrids based on graphene and conducting polymers are also possible. H. Chang et al., for example, dispersed rGO into PEDOT:PSS [91]. The resulting TCM had a sheet resistance of 80 Ω sq^{-1} at 79% transmittance, and was successfully used as anode in a flexible OLED (Hybrid TCM (~150 nm)/PEDOT:PSS (50 nm)/TPD (60 nm)/Alq_3 (60 nm)/LiF (1 nm)/Al (100 nm)) that reached a current efficiency of 3.9 cd A^{-1}. Graphene exfoliated electrochemically can also be blended with PEDOT:PSS for hybrid TCMs [92]. Alternatively, PEDOT:PSS can be polymerized in situ in the presence of rGO dispersed in PSS (**Figure 1.4.7f**) [93].

Integration of graphene with different oxide materials is also highly attractive for TCM applications. For example, a sandwich structure composed of TiO_2/graphene/WO_3 was shown to be capable of increasing light outcoupling in OLEDs [94]. Attempts to combine graphene with ITO have also been reported, such as the work of J. Liu et al., who transferred a CVD-grown graphene film onto ITO [95]. The authors observed an improvement of the stability of ITO's electronic properties under bending by the addition of graphene, while maintaining a relatively low sheet resistance (78.34 Ω sq^{-1}), making this hybrid material suitable as a flexible TCM. Alternatively, ITO nanoparticles have been deposited on top of CVD-grown graphene, by dipping the latter into a solution of the former and by thermally annealing the resulting hybrid after its transfer onto the desired substrate (**Figure 1.4.7g**) [96]. This material had a lower sheet resistance (522.21 Ω sq^{-1} at 85% transmittance) than pristine graphene (727.43 Ω sq^{-1}), due to electron doping induced by the nanoparticles.

Interestingly, despite the fact that graphene oxide is not, by itself, a good candidate for TCM applications, its integration with graphene can be quite promising, as shown by S. Jia et al. [97]. The authors subjected a CVD graphene sample formed by successive stacked transfers to a mild ozone treatment, in order to oxidize the topmost layer (**Figure 1.4.7h**). The resulting flexible electrode had a sheet resistance of 230 Ω sq^{-1} and a work function of 5.0 eV, possibly due to the doping effect of oxidized graphene on the underlying layers. The oxidized layer, thanks to its hydrophilicity and abundance of functional groups that can act as anchoring sites, also allows for a more uniform deposition of, for example, MoO_3, a commonly used HIL in OLEDs. A green flexible OLED using this hybrid TCM as anode, and a structure of anode/MoO_3 (3 nm)/TAPC (60 nm)/$Ir(ppy)_2(acac)$:TCTA (8 nm)/$Ir(ppy)_2(acac)$:Bphen (8 nm)/Bphen (60 nm)/Li (0.5)/Al (130 nm), achieved a current efficiency of 82.0 cd A^{-1} and a power efficiency of 98.2 lm W^{-1}, higher than for pristine graphene- or ITO-based devices.

Lastly, it is worth pointing out that even more complex hybrids are possible by the combination of more than two different classes of materials. F. Li et al., for example, reported a flexible multilayer TCM composed by Ag and Al-doped zinc oxide (AZO) sputtered onto CVD graphene, which was used as an anode in a flexible OLED [98]. In another work, a TiO_x sol-gel solution was spin coated onto single-layer CVD graphene, followed by UV-ozone treatment and spin coating of PEDOT:PSS (and further thermal annealing) [99]. The TiO_x coating led to n-type doping, lowering the sheet resistance of graphene (from 628 Ω sq^{-1} to 228 Ω sq^{-1}), but also its work function. Consequent PEDOT:PSS coating counter-acts the work function decrease (increasing it to 5.12 eV), while reducing R_S even more, to 86 Ω sq^{-1} at 94.1% transmittance.

1.4.3.2 Graphene as encapsulant

As mentioned previously, graphene can also play an important role as an encapsulant material for OLEDs. Some reports of the use of this material in other organic electronic devices can already be found in the literature, such as the work of H.-K. Seo et al., for example, who built a flexible polymer LED (PLED) using a PDMS/6-layer graphene/PET encapsulating film [100]. The authors observed a greatly increased operational lifetime of such devices, relative to the equivalent ones without encapsulation or with a PDMS/PET protective layer only. Interestingly, a 10 nm thick film of rGO has also shown potential as a protective barrier for organic materials [101]. For OLEDs, a graphene-based barrier, formed by CVD growth followed by atomic layer deposition of AlO_x and a second CVD growth on the Cu/Graphene/AlO_x stack, was also successfully employed to improve the devices' stability [102].

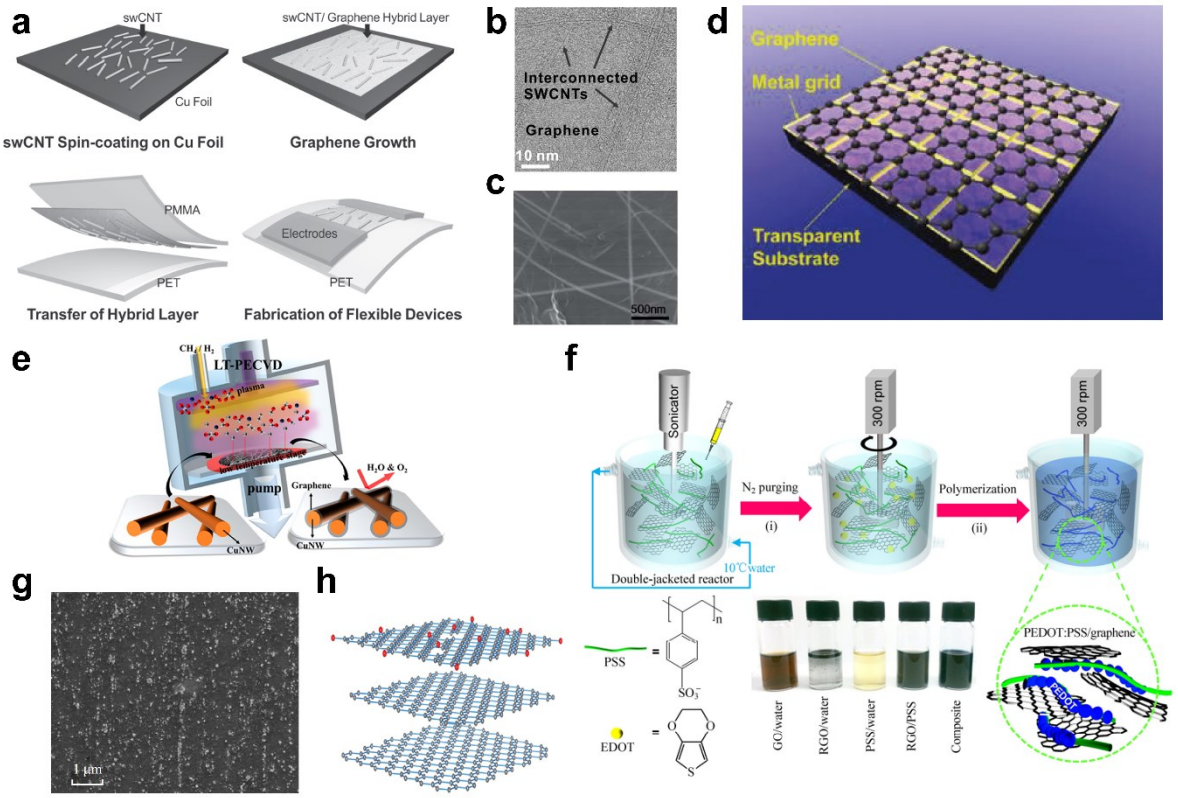

Figure 1.4.7. (a) Illustration of the fabrication process of a CNT/graphene hybrid TCM. Adapted from ref. [81]. **(b)** Bright field (BF) STEM image of "rebar graphene", a CNT/graphene hybrid. Adapted from ref. [82]. **(c)** SEM image of a AgNW/graphene hybrid. Adapted from ref. [86]. **(d)** Illustration of a metal grid/graphene hybrid TCM. Adapted from ref. [87]. **(e)** Illustration of the synthesis of CuNW/graphene core-shell nanostructure by plasma enhanced CVD. Adapted from ref. [88]. **(f)** Illustration of the synthesis of PEDOT:PSS/graphene composites. Adapted from ref. [93]. **(g)** SEM image of ITO nanoparticles on top of graphene. Adapted from ref. [96]. **(h)** Illustration of a TCM fabricated by oxidizing the topmost layer of a multilayer CVD graphene stack. Adapted from ref. [97].

An additional advantage of graphene for encapsulation is that it can simultaneously play the role of an active layer as an electrode. This has already been demonstrated for other types of organic electronic devices, such as the one built by Z. Liu et al., who showed that a package-free organic solar cell using a multilayer CVD graphene electrode was stable in air due to the latter's inability to permeate between graphene layers [27].

1.4.3.3 OLED applications of graphene

One of the first reports of an OLED using a graphene-based electrode was presented, in 2009, by J. Wu et al. [103]. The authors used graphene oxide reduced by vacuum annealing at 1100 °C for 3h. The structure of the OLED was rGO/PEDOT:PSS/NPD/Alq_3/LiF/Al, and its performance was comparable to an equivalent device using an ITO anode. Reduced graphene oxide was also used in a composite anode, by mixing it with a PEDOT:PSS solution [91]. The composite was then spin coated onto flexible PET substrates. Layers of PEDOT:PSS (50 nm), TPD (60 nm), Alq_3 (60 nm), LiF (1 nm), and Al (100 nm) were deposited on top of this anode to complete the flexible OLED. This device achieved a current efficiency of 3.9 cd A^{-1} at 10 V, higher than that of an equivalent ITO-based OLED (CE_{ITO}=1.7 cd A^{-1}). D. W. Lee et al. showed that rGO can also form transparent electrodes through layer-by-layer stacking [104]. This was achieved by functionalizing the negatively charged GO sheets with NH_3^+ groups (**Figure 1.4.8a**). Both types of GOs were then reduced, maintaining their charges so that, after deposition, the alternating

layers interact electrostatically. The resulting electrodes showed R_S values of 8.6 kΩ sq^{-1} and 32 kΩ sq^{-1} at 86% and 91% transmittance, respectively. Despite these poor values, the authors built an OLED based on these electrodes (rGO/PEDOT:PSS/poly(2-methoxy-5-(20-ethylhexyloxy)-1,4-phenylene vinylene) (MEH-PPV)/Ba/Al), reaching a rather low current efficiency of 0.10 cd A^{-1}. A similar work was published in 2014, where electrodes composed of alternating layers of GO (which was later reduced to rGO by a thermal annealing at 1000 °C) functionalized with N,N,Ntrimethyl-1-dodecanaminium bromide (CTAB) and sodium dodecylbenzene sulfonate (SDBS) were used in an OLED that reached a current efficiency of 4.5 cd A^{-1} [105].

T. Sun et al. employed multilayer CVD graphene in an OLED with the structure Al (60 nm)/glass/multilayer graphene/V_2O_5 (5 nm)/NPB (40 nm)/CBP:Ir(ppy)$_2$(acac) (10 wt %, 40 nm)/Bphen (25 nm)/Bphen:Cs_2CO_3 (mass rate 1:1, 15 nm)/Sm (15 nm)/Au (15 nm) [106]. The authors note that the V_2O_5 layer acts as a buffer for better hole injection and to inhibit current leakage. However, it should be pointed out that this oxide is also known to be able to dope graphene with holes [45]. The device built by T. Sun and colleagues reached a current efficiency of 0.75 cd A^{-1} at 226.3 cd m^{-2} of luminance, and a power efficiency of 0.38 lm W^{-1} at 66.9 cd m^{-2}, both rather modest values (considering that a 2nd generation emitter was employed), justified by the roughness of the graphene anode and the lack of p-doping (at least as far as the authors were aware). In 2012, a very similar work was reported by H. Meng et al., where the authors used bilayer graphene as an anode in an OLED with the structure graphene/V_2O_5 (5 nm)/NPB (60 nm)/Alq_3 (45 nm)/Bphen:Cs_2CO_3 (15 nm)/Sm (15 nm)/Au (15 nm) [107]. The bilayer graphene has a sheet resistance of 754.2 Ω sq^{-1} without any intentional doping, and the light emitting device had a current efficiency of 1.18 cd A^{-1} at 10 V and a power efficiency of 0.41 lm W^{-1} at 8 V, close to the values of an equivalent ITO-based device.

Far better results with CVD graphene were obtained by T.-H. Han et al., who reported a flexible OLED using graphene as an anode (on a PET substrate) [37]. The authors overcame the issue of graphene's low work function by using a gradient HIL ("GraHIL"), consisting of PEDOT:PSS with tetrafluoroethylene-perfluoro-3,6-dioxa-4-methyl-7-octenesulphonic acid copolymer. This resulted in a self-organised layer with a work function gradient, thus facilitating the hole injection from the graphene anode (**Figure 1.4.8b**). Additionally, the graphene was doped with HNO_3 or $AuCl_3$ to increase its conductivity. The authors went on to make several flexible OLEDs, including a green phosphorescent device and a white fluorescent one, using the anode and HIL described above, and compared them with equivalent ITO-based OLEDs. For graphene-based ones, η_{lp} of 102.7 lm W^{-1} and a current efficiency 98.1 cd A^{-1} were observed for the green-emitting phosphorescent flexible device, outperforming the ITO-based ones in both cases.

A blue phosphorescent OLED using a multilayer CVD graphene anode has also been reported [108]. The pristine graphene films had a sheet resistance of 289 Ω sq^{-1}. These films were then treated with O_2 plasma in order to improve hole-injection, possibly by increasing graphene's work function (despite an increase in R_S up to 552 Ω sq^{-1}). OLEDs with a structure of O_2 plasma treated graphene (2–3 nm)/TAPC (30 nm)/1,4,5,8,9,11-hexaazatriphenylene hexacarbonitrile (HAT-CN) (10 nm)/TAPC (30 nm)/HAT-CN(10 nm)/TAPC (30 nm)/4,4',4''-tri(N-carbazolyl) triphenylamine:iridium(III)bis[(4,6-difluorophenyl)-pyridinato-N,C2']picolinate (TCTA:FIrpic) (5 nm)/2,6-bis[3'-(N-carbazole)phenyl]pyridine:iridium(III) bis[(4,6-difluorophenyl)-pyridinato-N,C2']picolinate (DCzPPy:FIrpic) (5 nm)/1,3-bis(3,5-dipyrid-3-yl-phenyl)benzene (BmPyPB) (40 nm)/LiF (1 nm)/Al (100 nm) showed a power efficiency of 24.1 lm W^{-1}, higher than with a pristine graphene anode (η_{lp}=14.5 lm W^{-1}). However, the untreated graphene-

based OLED had a slightly higher EQE of 15.6%. The authors used a similar approach to build blue fluorescent OLEDs [109].

In the context of CVD graphene, several works have been devoted to the optimization of the graphene transfer process from the catalyst on which it is grown to the substrate on which the OLED will be built. This aspect is important because the most commonly used transfer process utilizes PMMA as a supporting polymer, which leaves residues on graphene's surface. These residues increase surface roughness [110], lead to charge carrier scattering [111], and cause unintentional doping [29]. D.-Y. Wang et al. avoided the use of a supporting material by electrostatically charging the target substrates, which resulted in the attraction of graphene, along with the metal catalyst, to the substrate [111]. The catalyst was then etched away in an iron nitrate solution. This clean transfer technique resulted in higher carrier mobility and better charge neutrality of graphene. Residue-free transfer was also achieved by the introduction, by evaporation, of an organic small molecular buffer (2-(diphenylphosphory) spirofluorene (SPPO1)) between graphene and PMMA (**Figure 1.4.8c**) [110]. The resulting flexible OLEDs (graphene/MoO_3 (20 nm)/NPB:MoO_3 (80 nm)/TAPC (10 nm)/CBP:$Ir(ppy)_2acac$ (15 nm)/TPBi (65 nm)/Liq (2 nm)/Al (150 nm)) achieved CE=11.44 cd A^{-1} and η_{lp}=2.24 lm W^{-1}. In another approach, electrostatic force was used for the graphene transfer, without employing any organic supports or adhesives [111]. This allowed to form TCMs by four-layer stacked transfers and HNO_3 doping (reaching R_S=50 Ω sq^{-1}), which were then used in OLEDs (graphene/PEDOT:PSS (50 nm)/NPB (50 nm)/Alq_3 (60 nm)/LiF (1 nm)/Al (100 nm)) that had a current efficiency of 3.3 cd A^{-1}. Z. Zhang and colleagues built a green OLED using CVD graphene films transferred with rosin as a supporting material [112]. Rosin has low adsorption energy on graphene, and is easily soluble in acetone, leaving virtually no residues and a very smooth graphene surface (**Figure 1.4.8d**). A graphene-based electrode was then prepared by stacking three graphene layers and by exposing one side to ozone treatment for better work function alignment. The flexible OLED device (graphene-based anode/MoO_3 (5 nm)/TAPC (60 nm)/$Ir(ppy)_2(acac)$:TCTA (8 nm)/$Ir(ppy)_2(acac)$:Bphen (8 nm)/Bphen (60 nm)/Li (0.5 nm)/Al (30 nm)) reached a current efficiency of 89.7 cd A^{-1} and a power efficiency of 102.6 lm W^{-1}, while, more importantly, being more stable than an equivalent device using PMMA-transferred graphene, with the latter showing burn-out at high driving voltages due to the higher roughness of the anode and the consequent current leakage. Rosin was also used by L.-P. Ma et al., who built a flexible OLED on PET using HTB-doped graphene [57]. With this anode having a roughness of ~1-2 nm (root mean square), the resulting devices reached a current efficiency of 111.4 cd A^{-1}, PE=124.9 lm W^{-1} and EQE=29.7%. A fluoropolymer (CYTOP) was also used instead of PMMA, resulting in graphene films with lower R_S and higher work function, which enabled green OLEDs with better performance (CE=7.91 cd A^{-1}) than the equivalent ITO-based devices [113]. H. Meng et al. avoided the transfer altogether by including the copper CVD growth catalyst into a top-emission OLED structure (Cu/graphene/V_2O_5 (5nm)/NPB (60 nm)/Alq_3:C545T (30 nm)/Alq_3 (15 nm)/Bphen:Cs_2CO_3 (15 nm)/Sm (15 nm)/Au (15 nm)) [114]. The copper sheet acted as a back reflector and lowered the sheet resistance of the anode to as low as R_S=0.0039 Ω sq^{-1}, with the OLED reaching CE=6.1 cd A^{-1} and η_{lp}=7.6 lm W^{-1}, better than the equivalent devices with only graphene or ITO. In another approach, a poly(9,9-di-n-octylfluorene-alt-(1,4-phenylene-((4-sec-butylphenyl)imino)-1,4-phenylene) (TFB) organic layer doped with F4-TCNQ was spin coated onto CVD graphene, followed by another layer of PMMA (**Figure 1.4.8e**) [115]. After transfer onto the desired substrate, the PMMA film was removed in acetone, leaving the organic film, which acted as a HIL in a green OLED (graphene/TFB:F4-TCNQ (40 nm)/TAPC (40 nm)/mCP: $Ir(ppy)_3$ (30 nm)/TmPyPB (50

nm)/LiF (0.5 nm)/Al (100 nm)). The latter had a *CE* of 74.5 cd A^{-1} and a *PE* of 26.6 lm W^{-1}, with *EQE* being 20.7%. As an example of a hybrid anode, Z. Zhang et al. transferred 5-layer CVD graphene onto PET without any polymeric support, by simply etching away the Cu film and scooping out the graphene with the PET substrate, followed by the deposition of PEDOT:PSS to complete the hybrid electrode [116]. This was then used to fabricate a flexible OLED which achieved *CE*=76 cd A^{-1} and *PE*=61 lm W^{-1}.

Excellent current efficiencies (>240 cd A^{-1} for a flexible green OLED and >120 cd A^{-1} for a white one, with light-outcoupling structures) were obtained by N. Li et al., using single layer graphene p-doped with a triethyloxonium hexachloroantimonate (OA)/dichloroethene solution (**Figure 1.4.8f**) [57]. Another good result was the one of an OLED based on MoO_3-doped graphene, which reached a current efficiency of 55 cd A^{-1} at 1000 cd m^{-2} [42]. Alternatively, V_2O_5 doping of CVD graphene allowed to build an OLED with a power efficiency of 80 lm W^{-1} at 2000 cd m^{-2} [45]. Another impressive result was achieved by T.-H. Han et al., who built a flexible green phosphorescent OLED using four-layer TFMS-doped graphene [56]. This device showed a current efficiency of 104.1 cd A^{-1} and a power efficiency of 80.7 lm W^{-1}. More recently, L. Liu et al. reported OLEDs with *CE*=129.3 cd A^{-1}, *PE*=77.6 lm W^{-1} and *EQE*=36.5% using single-layer CVD-grown graphene doped with phosphomolybdic acid ($H_3PMo_{12}O_{40}$, abbreviated as PMA) [117]. The doping is performed by spin coating a solution of PMA in acetonitrile, followed by baking at 140 °C for 15 min. Averaging the results coming from 30 samples, including different substrates, the sheet resistance of graphene decreases from 771 to 220 Ω sq^{-1} (stable for at least 30 days), while also lowering the surface roughness. The doping mechanism is explained by the extraction of electrons by Mo, and an increase in the work function from 4.53 to 4.93 eV was measured.

Focusing on light outcoupling, J. Lee et al. used a high-index TiO_2 layer between a multilayer, HNO_3-doped graphene anode and the substrate [118]. This, along with the previously mentioned GraHIL layer, allowed to achieve *EQE* as high as 40.8% (on a glass substrate), further enhanced to 64.7% using a hemispherical lens for a green emitting OLED.

S. Chen et al. achieved, in a white OLED, *CE*=95.9 cd A^{-1}, *PE*=39.3 lm W^{-1} and *EQE*=29.2%, further increased to *CE*=326.5 cd A^{-1}, *PE*=128.2 lm W^{-1} and *EQE*=99.5% at 5270 cd m^{-2} with a high-index half-ball lens for better light extraction [119]. This was enabled by coating single-layer graphene, treated with UV O_3, with a PSS layer, followed by PEDOT:PSS and PEDOT:PSS doped with tetra-fluoroethylene-perfluoro-3,6-dioxa-4-methyl-7-octenesulfonic acid copolymer (PFI, as in GraHIL). The introduction of PSS on graphene results in a vacuum level bending, which reduced the hole injection barrier. Using the same approach, the authors also obtained *CE*=201.9 cd A^{-1}, *PE*=76.1 lm W^{-1} and *EQE*=45.2% in a blue OLED (*CE*=73.8 cd A^{-1}, *PE*=26.9 lm W^{-1} and *EQE*=16.5% without a half-ball lens).

In the context of the recent progress made in the field of CVD growth directly on insulating substrates, single-layer graphene was deposited on sapphire and doped with HNO_3 [120]. This resulted in a reduction of the sheet resistance from 2290 to 450 Ω sq^{-1}, allowing to use this transparent electrode as an anode in OLEDs that performed as well as equivalent ones made using ITO.

Also worth mentioning is a tandem flexible device using four-layer graphene doped with HNO_3 [121]. The doping brought the sheet resistance of the four-layer film down to 58.3±3.8 Ω sq^{-1} (with PET as a substrate), while the tandem structure, formed by vertically stacking two electroluminescence units with a charge generation layer in between (**Figure 1.4.8g**), led to an

increase in device efficiency. The latter was necessary because the single electroluminescence unit OLED, despite reaching *CE*=120.8 cd A^{-1} on glass (*EQE*=32.7%), had a considerable efficiency roll-off at higher luminance, possibly due to charge imbalance. The tandem device, on a flexible PET substrate, reached a current efficiency of 205.9 cd A^{-1} and an *EQE* of 45.2%, with low efficiency roll-off, a value that was further increased using a hemispherical lens for better light outcoupling (*CE*=395.0 cd A^{-1} and *EQE*=86.5%).

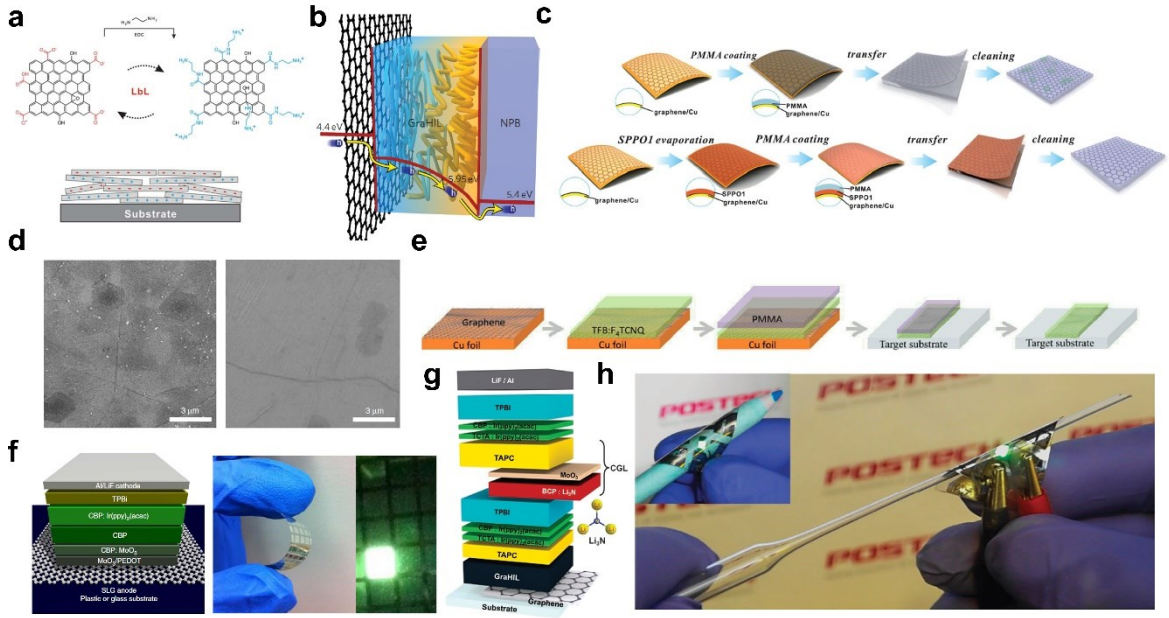

Figure 1.4.8. (a) Illustration of the layer-by-layer deposition process of rGO. On the left, rGO terminated with COO^- groups. On the right, with NH_3^+ groups. Adapted from ref. [104]. **(b)** Schematic representation of the effect of GraHIL on the hole injection barrier from graphene. Adapted from ref. [37]. **(c)** Comparison between a conventional (top) and a clean transfer technique using a buffer layer (bottom). Adapted from ref. [110]. **(d)** SEM images of graphene samples transferred using PMMA (left) and rosin (right) as support layers. Adapted from ref. [112]. **(e)** The use of a HIL as a buffer for graphene transfer. Adapted from ref. [115]. **(f)** Structure of a graphene-based, flexible phosphorescent OLED (left) and the respective photograph (right). Adapted from ref. [57]. **(g)** Structure (left) and photograph (right) of a flexible tandem OLED using graphene as an anode. Adapted from ref. [121].

Finally, while there are no reports of OLEDs on paper or cellulose substrates employing graphene as an electrode, it is important in the context of this work to mention some examples of such devices using other transparent conductors. The group of M. Cremona explored different types of composites of bacterial cellulose (BC) with polymeric and inorganic components as substrates for OLEDs. Namely, composites of BC with polystyrene [122], polyurethane [123] and an organic–inorganic sol composed of nanoparticulate boehmite (Boe) and epoxy modified siloxane (glycidoxypropyltrimethoxysilane, GPTS) [124]. Benefitting from high optical transparency and low surface roughness, these composites were used to fabricate OLEDs with ITO anodes, after SiO_2 deposition on the substrates. Cellulose films coated with PEDOT:PSS PH1000 have also been used to fabricate OLEDs, with the cellulose films obtained by dissolving cellulose powder in N-Methylmorpholine-N-oxide (with antioxidant propyl gallate and water) and coating a glass plate with this solution [125]. After soaking in water, the film was then sandwiched between two glass plates and dried at 40 °C for 12 h, resulting in a transparent film. J. Tao et al. prepared hybrid polymer substrates using cellulose nanofibrils (CNFs) and polyarylate to be used in flexible OLEDs [126]. With the substrates having a transmittance of 85% and a root mean square roughness of 2.97 nm, further reduced after the deposition of ITO, OLEDs were able to be made on them, reaching *CE*=5.65 cd A^{-1} and *EQE*=1.68%.

Some of the most prominent examples of OLEDs employing graphene electrodes are presented in **Table 1.4.2**, summarizing their structures, transfer and doping strategies and performance.

---------- // ----------

Organic light emitting diodes are fascinating devices with a substantial presence in people's everyday lives. Flexible OLEDs are a particularly sought-after implementation of this technology, and this, along with the rising costs of indium tin oxide, has motivated increasing efforts to find suitable alternatives to this transparent conductor. Graphene is one of the main candidates for this role, but several hurdles still need to be overcome. Specifically, the search for a stable and effective doping approach is still underway. Additionally, the need for the graphene to be transferred is another bottleneck for its widespread implementation, not just because of the increased complexity that it brings, but also due to the introduction of defects and impurities. In this context, direct synthesis of graphene on transparent substrates is highly desirable, a research field which is still in its infancy, but which has already provided some very encouraging results.

Table 1.4.2. Comparison of different OLEDs reported in the literature employing graphene electrodes.

Ref.	OLED Structure	Colour	Flex.?	Graphene type*/transfer support	Doping	Current efficiency (light outcoup. approach)	Power efficiency
[121]	Gr/Gra-HIL/TAPC/$Ir(ppy)_2(acac)$:TCTA/$Ir(ppy)_2(acac)$:CBP/TPBi/LiF/Al	Green	Yes	4L CVD/PMMA	HNO_3	120.8 cd A^{-1}	-
	Gr/Gra-HIL/TAPC/$Ir(ppy)_2(acac)$:TCTA/$Ir(ppy)_2(acac)$:CBP/TPBi/BCP:Li_3N/MoO_3/TAPC/$Ir(ppy)_2(acac)$:TCTA/$Ir(ppy)_2(acac)$:CBP/TPBi/LiF/Al					205.9 cd A^{-1} 395.0 cd A^{-1} (hemisph. lens)	-
[119]	Gr/PSS/PEDOT:PSS/Gra-HIL/TAPC/mCP:FIrpic:PO-01/TmPyPb/LiF/Al	White	No	1L CVD/PMMA	-	95.9 cd A^{-1} 326.5 cd A^{-1} (hemisph. lens)	39.3 lm W^{-1} 128.2 lm W^{-1} @ 5270 cd m^{-2} (hemisph. lens)
	Gr/PSS/PEDOT:PSS/GraHIL/TAPC/mCP:FIrpic/TmPyPb/LiF/Al	Blue				73.8 cd A^{-1} @ 866 cd m^{-2} 201.9 cd A^{-1} @ 1494 cd m^{-2} (hemisph. lens)	26.9 lm W^{-1} @ 97 cd m^{-2} 76.1 lm W^{-1} @ 896 cd m^{-2} (hemisph. lens)
[118]	Gr/PEDOT:PSS/MoO_3/CBP/CBP:B3PYMPM:$Ir(ppy)_2(acac)$/LiF/Al	Green	Yes	Multi-layer/PMMA	HNO_3	-	155.8 lm W^{-1} (TiO_2 layer below anode)
	Gr/Gra-HIL/TAPC/TCTA:$Ir(ppy)_2(acac)$/CBP $Ir(ppy)_2(acac)$/TPBi/LiF/Al		No	4L CVD/PMMA		168.4 cd A^{-1} (TiO_2 layer below anode) 257.0 cd A^{-1} (TiO_2+hemisph. lens)	160.3 lm W^{-1} (TiO_2 layer below anode) 250.4 lm W^{-1} (TiO_2+hemisph. lens)

Ref.	OLED Structure	Colour	Flex.?	Graphene type*/transfer support	Doping	Current efficiency (light outcoup. approach)	Power efficiency
[118]	Gr/GraHIL/TAPC/TCTA:Ir(ppy)$_2$(acac)/CBP Ir(ppy)$_2$(acac)/TPBi/BCP:Li/MoO$_3$/TAPC/ TCTA: Ir(ppy)$_2$(acac)/CBP Ir(ppy)$_2$(acac)/TPBi/LiF/Al	Green	No			~275 cd A^{-1}** (TiO_2 layer below anode) ~450 cd A^{-1}** (TiO_2+hemisph. lens)	120.8 lm W^{-1} (TiO_2 layer below anode) 183.5 lm W^{-1} (TiO_2+hemisph. lens)
[57]	Gr/PEDOT:PSS/MoO$_3$/CBP:MoO$_3$/CBP/CBP:Ir(ppy)$_2$(acac)/TPBi/LiF/Al	Green	Yes	1L CVD/PMMA	OA	250 cd A^{-1} @ 10000 cd m^{-2} (light outcoup.) 80 cd A^{-1} @ 3000 cd m^{-2} (no light outc.)	160 lm W^{-1} @ 3000 cd m^{-2} (light outcoup.)
	Gr/PEDOT:PSS/MoO$_3$/CBP:MoO$_3$/CBP/ CBP:Ir(ppy)$_2$(acac):Ir(MDQ)$_2$(acac)/ CBP:Ir(ppy)$_2$(acac)/CBP:FIrpic/TPBi/LiF/Al	White			OA	-	90 lm W^{-1} 1000 cd m^{-2} (light outcoup.)
[56]	Gr/DNTPD/TAPC/TCTA:Ir(ppy)$_2$(acac)/CBP:Ir(ppy)$_2$(acac)/TPBi/LiF/Al	Green	Yes	4L CVD/PMMA	TFMS	104.1 cd A^{-1}***	80.7 lm W^{-1}***
[37]	Gr/GraHIL/TAPC/TCTA:Ir(ppy)$_3$/CBP:Ir(ppy)$_3$/TPBi/LiF/Al	Green	Yes	4L CVD/PMMA (on the first layer only)	HNO_3	98.1 cd A^{-1}	102.7 lm W^{-1}
	Gr/GraHIL/NPB/Bebq$_2$:C545T/Bebq$_2$/Liq/Al					30.2 cd A^{-1}	37.2 lm W^{-1}
					$AuCl_3$	27.4 cd A^{-1}	28.1 lm W^{-1}
	Gr/GraHIL/NPB/NPB:TBADN:rubrene/NPB:TBADN:DPAVBi/TBADN:DPAVBi/Bebq$_2$/BaF_2/Al	White			HNO_3	16.3 cd A^{-1}	-

Ref.	OLED Structure	Colour	Flex.?	Graphene type*/transfer support	Doping	Current efficiency (light outcoup. approach)	Power efficiency
[112]	Gr-GO hybrid/MoO_3/TAPC/Ir(ppy)$_2$(acac):TCTA/Ir(ppy)$_2$(acac):Bphen/Bphen/Li/Al	Green	Yes	2L CVD+Oxidized 1L CVD /Rosin	-	89.7 cd A^{-1}	102.6 lm W^{-1}
[97]	Gr-GO hybrid/MoO_3/TAPC/Ir(ppy)$_2$(acac):TCTA/Ir(ppy)$_2$(acac):Bphen/Bphen/Li/Al	Green	Yes	2L CVD+Oxidized 1L CVD/PMMA	-	82.0 cd A^{-1}	98.2 lm W^{-1}
	Gr-GO hybrid/MoO_3/TAPC/Ir(MDQ)$_2$(acac)/Bphen/Li/Al	Red				~45 cd A^{-1}****	~50 lm W^{-1}****
	Gr-GO hybrid/MoO_3/TAPC/FIrpic:TCTA:26DCZ/Bphen/Li/Al	Blue				~37 cd A^{-1}****	~33 lm W^{-1}****
	Gr-GO hybrid/MoO_3/TAPC/ bis(2-phenylbenzothiazolato)(acetylacetonate)iridium(III):4P-NPB/4P-NPB/Bphen/Li/Al	White				36.7 cd A^{-1}	41.8 lm W^{-1}
[115]	Gr/TFB:F4-TCNQ/TAPC/mCP:Ir(ppy)$_3$/TmPyPB/LiF/Al	Green	No	1L CVD/TFB:F4-TCNQ+PMMA	-	74.5 cd A^{-1}	26.6 lm W^{-1}
[42]	Gr/MoO_3/MoO_3:CBP/CBP/Ir(ppy)$_3$:CBP/TPBi:Ir(ppy)$_3$/TPBi/LiF/Al	Green	No	1L CVD/PMMA	-	55 cd A^{-1} @ 1000 cd m^{-2}	-
[108]	Gr/TAPC/HAT-CN/TAPC/HAT-CN/TAPC/TCTA:FIrpic/DCzPPy:FRipic/BmPyPB/LiF/Al	Blue	No	5-8L CVD/PMMA or Thermal Release Tape	O_2 plasma treatment	-	24.1 lm W^{-1}

Ref.	OLED Structure	Colour	Flex.?	Graphene type*/transfer support	Doping	Current efficiency (light outcoup. approach)	Power efficiency
[127]	Gr/MoO_3/PEDOT:PSS/MoO_3/NPB/Mcp:Ir(ppy)$_3$/TPBi/Ca/Ag	Green	No	2L CVD/S1805G photoresist	-	33 cd A^{-1}	17.59 lm W^{-1}
			Yes	2L CVD/S1805G photoresist		31.4 cd A^{-1}	-
[110]	Gr/MoO_3/NPB:MoO_3/TAPC/Ir(ppy)$_2$(acac):CBP/TPBi/Liq/Al	Green	Yes	1L CVD/SPPO1+PMMA	-	11.44 cd A^{-1}	2.24 lm W^{-1}
[113]	Gr/NPB:WO_3/Alq_3:C545T/Alq_3/LiF/Al	Green	No	3L CVD/CYTOP	Doping by CYTOP	7.91 cd A^{-1}	-
[105]	rGO/Al4083/NPB/Alq_3/Liq/Al	Green	No	Layer-by-layer deposited rGO/-	-	4.5 cd A^{-1}	-
[45]	Gr/V_2O_5/CBP:MoO_3/CBP/Ir(ppy)$_2$(acac):CBP/TPBi/Liq/Al	Green	No	1L CVD/PMMA	-	-	80 lm W^{-1} @ 2000 cd m^{-2}
[57]	Gr/MoO_3/TAPC/Bepp2:Ir(ppy)$_2$/Bepp2/Bphen/LiF/Al	Green	Yes	1L CVD/Rosin	HTB	111 cd A^{-1}	124.9 lm W^{-1}
[120]	Gr/NPB/Alq_3/LiF/Al	Green	No	1L MOCVD/-	HNO_3	-	-
[117]	Gr/PEDOT:PSS/TAPC/mCP:Ir(ppy)$_3$/TmPyPB/LiF/Al	Green	No	1L/PMMA	PMA	129.3 cd A^{-1}	77.6 lm W^{-1}

* L refers to the number of graphene layers.
** Approximate maximum values extracted by visual inspection of the presented *CE* charts.
*** Despite a flexible OLED having been demonstrated, the reported figures of merit do not correspond to a device built on a flexible substrate.
**** Approximate maximum values extracted by visual inspection of the presented *CE* and *PE* charts.

1.4.4 References

[1] D.J. Gaspar, E. Polikarpov, OLED fundamentals: materials, devices, and processing of organic light-emitting diodes, CRC Press, **2018**.

[2] P.S. Vincett, W.A. Barlow, R.A. Hann, G.G. Roberts, "Electrical conduction and low voltage blue electroluminescence in vacuum-deposited organic films," *Thin Solid Films*, 94, 171–183, **1982**. https://doi.org/10.1016/0040-6090(82)90509-0.

[3] L. Pereira, Organic Light Emitting Diodes: the Use of Rare Earth and Transition Metals, Pan Stanford Publishing, Boca Raton, FL, USA, **2012**. https://www.crcpress.com/Organic-Light-Emitting-Diodes-The-Use-of-Rare-Earth-and-Transition-Metals/Pereira/p/book/9789814267298 (accessed January 12, 2019).

[4] Y.L. Chang, Efficient organic light-emitting diodes (OLEDs), **2015**. https://doi.org/10.1201/b18760.

[5] C.W. Tang, S.A. VanSlyke, "Organic electroluminescent diodes," *Appl. Phys. Lett.*, 51, 913–915, **1987**. https://doi.org/10.1063/1.98799.

[6] M. Schott, "Introduction to the Physics of Organic Electroluminescence," *Comptes Rendus l'Academie Des Sci. Ser. IV, Phys. Astrophys.*, 1, 381–402, **2000**. https://doi.org/10.1016/S1296-2147(00)00138-4.

[7] H.-W. Chen, J.-H. Lee, B.-Y. Lin, S. Chen, S.-T. Wu, "Liquid crystal display and organic light-emitting diode display: present status and future perspectives," *Light Sci. Appl.*, 7, 17168, **2018**. https://doi.org/10.1038/lsa.2017.168.

[8] T. Minami, "Transparent conducting oxide semiconductors for transparent electrodes," *Semicond. Sci. Technol.*, 20, **2005**. https://doi.org/10.1088/0268-1242/20/4/004.

[9] S.T. Lee, Z.Q. Gao, L.S. Hung, "Metal diffusion from electrodes in organic light-emitting diodes," *Appl. Phys. Lett.*, 75, 1404–1406, **1999**. https://doi.org/10.1063/1.124708.

[10] A. Kumar, C. Zhou, "The race to replace tin-doped indium oxide: Which material will win?," *ACS Nano*, 4, 11–14, **2010**. https://doi.org/10.1021/nn901903b.

[11] R.P. Xu, Y.Q. Li, J.X. Tang, "Recent advances in flexible organic light-emitting diodes," *J. Mater. Chem. C*, 4, 9116–9142, **2016**. https://doi.org/10.1039/c6tc03230c.

[12] N. Kim, H. Kang, J.H. Lee, S. Kee, S.H. Lee, K. Lee, "Highly conductive all-plastic electrodes fabricated using a novel chemically controlled transfer-printing method," *Adv. Mater.*, 27, 2317–2323, **2015**. https://doi.org/10.1002/adma.201500078.

[13] K. Kawano, R. Pacios, D. Poplavskyy, J. Nelson, D.D.C. Bradley, J.R. Durrant, "Degradation of organic solar cells due to air exposure," *Sol. Energy Mater. Sol. Cells*, 90, 3520–3530, **2006**. https://doi.org/10.1016/j.solmat.2006.06.041.

[14] D.S.H. and A.M.H. and R.L. and L.H. and B.M. and C.C. and S. Risser, "High conductivity transparent carbon nanotube films deposited from superacid," *Nanotechnology*, 22, 75201, **2011**. http://stacks.iop.org/0957-4484/22/i=7/a=075201.

[15] Y.S. Woo, "Transparent conductive electrodes based on graphene-related materials," *Micromachines*, 10, 24–28, **2018**. https://doi.org/10.3390/mi10010013.

[16] N. Yang, D. Yang, L. Chen, D. Liu, M. Cai, X. Fan, "Design and adjustment of the graphene work function via size, modification, defects, and doping: a first-principle theory study," *Nanoscale Res. Lett.*, 12, **2017**. https://doi.org/10.1186/s11671-017-2375-3.

[17] C. Tengstedt, W. Osikowicz, W.R. Salaneck, I.D. Parker, C.H. Hsu, M. Fahlman, "Fermi-level pinning at conjugated polymer interfaces," *Appl. Phys. Lett.*, 88, 1–3, **2006**. https://doi.org/10.1063/1.2168515.

[18] H. Vázquez, Y.J. Dappe, J. Ortega, F. Flores, "A unified model for metal/organic interfaces: IDIS, 'pillow' effect and molecular permanent dipoles," *Appl. Surf. Sci.*, 254, 378–382, **2007**. https://doi.org/10.1016/j.apsusc.2007.07.047.

[19] J. Blochwitz, M. Pfeiffer, T. Fritz, K. Leo, "Low voltage organic light emitting diodes featuring doped phthalocyanine as hole transport material," *Appl. Phys. Lett.*, 73, 729–731, **1998**. https://doi.org/10.1063/1.121982.

[20] M.C. Gather, S. Reineke, "Recent advances in light outcoupling from white organic light-emitting diodes," *J. Photonics Energy*, 5, 057607, **2015**. https://doi.org/10.1117/1.JPE.5.057607.

[21] F. Löser, "Improvement of device efficiency in PIN-OLEDs by controlling the charge carrier balance and intrinsic outcoupling methods," *J. Photonics Energy*, 2, 021207, **2012**. https://doi.org/10.1117/1.JPE.2.021207.

[22] S.Y. Kim, J.J. Kim, "Outcoupling efficiency of organic light emitting diodes employing graphene as the anode," *Org. Electron. Physics, Mater. Appl.*, 13, 1081–1085, **2012**. https://doi.org/10.1016/j.orgel.2012.02.018.

[23] D. Yu, Y.-Q. Yang, Z. Chen, Y. Tao, Y.-F. Liu, "Recent progress on thin-film encapsulation technologies for organic electronic devices," *Opt. Commun.*, 362, 43–49, **2016**. https://doi.org/10.1016/J.OPTCOM.2015.08.021.

[24] M. Schaer, F. Nüesch, D. Berner, W. Leo, L. Zuppiroli, "Water vapor and oxygen degradation mechanisms in organic light emitting diodes," *Adv. Funtional Mater.*, 11, 116–121, **2001**. https://doi.org/10.1002/1616-3028(200104)11:2<116::AID-ADFM116>3.0.CO;2-B.

[25] C. Keum, C. Murawski, E. Archer, S. Kwon, A. Mischok, M.C. Gather, "A substrateless, flexible, and water-resistant organic light-emitting diode," *Nat. Commun.*, 11, 6250, **2020**. https://doi.org/10.1038/s41467-020-20016-3.

[26] S. Chen, L. Brown, M. Levendorf, W. Cai, S.-Y. Ju, J. Edgeworth, X. Li, C.W. Magnuson, A. Velamakanni, R.D. Piner, J. Kang, J. Park, R.S. Ruoff, "Oxidation Resistance of Graphene-Coated Cu and Cu/Ni Alloy," *ACS Nano*, 5, 1321–1327, **2011**. https://doi.org/10.1021/nn103028d.

[27] Z. Liu, J. Li, F. Yan, "Package-free flexible organic solar cells with graphene top electrodes," *Adv. Mater.*, 25, 4296–4301, **2013**. https://doi.org/10.1002/adma.201205337.

[28] T.-H. Han, H. Kim, S.-J. Kwon, T.-W. Lee, "Graphene-based flexible electronic devices," *Mater. Sci. Eng. R Reports*, 118, 1–43, **2017**. https://doi.org/https://doi.org/10.1016/j.mser.2017.05.001.

[29] W.H. Lee, J.W. Suk, J. Lee, Y. Hao, J. Park, J.W. Yang, H.-W. Ha, S. Murali, H. Chou, D. Akinwande, K.S. Kim, R.S. Ruoff, "Simultaneous Transfer and Doping of CVD-Grown Graphene by Fluoropolymer for Transparent Conductive Films on Plastic," *ACS Nano*, 6, 1284–1290, **2012**. https://doi.org/10.1021/nn203998j.

[30] L.S. Panchakarla, K.S. Subrahmanyam, S.K. Saha, A. Govindaraj, H.R. Krishnamurthy, U. V. Waghmare, C.N.R. Rao, "Synthesis, structure, and properties of boron- and nitrogen-doped graphene," *Adv. Mater.*, 21, 4726–4730, **2009**. https://doi.org/10.1002/adma.200901285.

[31] J.O. Hwang, J.S. Park, D.S. Choi, J.Y. Kim, S.H. Lee, K.E. Lee, Y.H. Kim, M.H. Song, S. Yoo, S.O. Kim, "Workfunction-tunable, N-doped reduced graphene transparent electrodes for high-performance polymer light-emitting diodes," *ACS Nano*, 6, 159–167, **2012**. https://doi.org/10.1021/nn203176u.

[32] D. Wei, Y. Liu, Y. Wang, H. Zhang, L. Huang, G. Yu, "Synthesis of N-Doped Graphene by Chemical Vapor Deposition and Its Electrical Properties," *Nano Lett.*, 9, 1752–1758, **2009**. https://doi.org/10.1021/nl803279t.

[33] H. Wang, Y. Zhou, D. Wu, L. Liao, S. Zhao, H. Peng, Z. Liu, "Synthesis of boron-doped graphene monolayers using the sole solid feedstock by chemical vapor deposition," *Small*, 9, 1316–1320, **2013**. https://doi.org/10.1002/smll.201203021.

[34] R. Lv, Q. Li, A.R. Botello-Méndez, T. Hayashi, B. Wang, A. Berkdemir, Q. Hao, A.L. Eléas, R. Cruz-Silva, H.R. Gutiérrez, Y.A. Kim, H. Muramatsu, J. Zhu, M. Endo, H. Terrones, J.C. Charlier, M. Pan, M. Terrones, "Nitrogen-doped graphene: Beyond single substitution and enhanced molecular sensing," *Sci. Rep.*, 2, 1–8, **2012**. https://doi.org/10.1038/srep00586.

[35] S. Bae, H. Kim, Y. Lee, X. Xu, J.-S. Park, Y. Zheng, J. Balakrishnan, T. Lei, H. Ri Kim, Y. Il Song, Y.-J. Kim, K.S. Kim, B. Ozyilmaz, J.-H. Ahn, B.H. Hong, S. Iijima, B. Özyilmaz, J.-H. Ahn, B.H. Hong, S. Iijima, "Roll-to-roll production of 30-inch graphene films for transparent electrodes," *Nat Nano*, 5, 574–578, **2010**. https://doi.org/10.1038/nnano.2010.132.

[36] A. Kasry, M.A. Kuroda, G.J. Martyna, G.S. Tulevski, A.A. Bol, "Chemical doping of large-area stacked graphene films for use as transparent, conducting electrodes," *ACS Nano*, 4, 3839–3844, **2010**. https://doi.org/10.1021/nn100508g.

[37] T.H. Han, Y. Lee, M.R. Choi, S.H. Woo, S.H. Bae, B.H. Hong, J.H. Ahn, T.W. Lee, "Extremely efficient flexible organic light-emitting diodes with modified graphene anode," *Nat. Photonics*, 6, 105–110, **2012**. https://doi.org/10.1038/nphoton.2011.318.

[38] K.K. Kim, A. Reina, Y. Shi, H. Park, L.J. Li, Y.H. Lee, J. Kong, "Enhancing the conductivity of transparent graphene films via doping," *Nanotechnology*, 21, **2010**. https://doi.org/10.1088/0957-4484/21/28/285205.

[39] F. Güneş, H.-J. Shin, C. Biswas, G.H. Han, E.S. Kim, S.J. Chae, J.-Y. Choi, Y.H. Lee, "Layer-by-Layer Doping of Few-Layer Graphene Film," *ACS Nano*, 4, 4595–4600, **2010**. https://doi.org/10.1021/nn1008808.

[40] Y. Shi, K.K. Kim, A. Reina, M. Hofmann, L.-J. Li, J. Kong, "Work Function Engineering of Graphene Electrode via Chemical Doping," *ACS Nano*, 4, 2689–2694, **2010**. https://doi.org/10.1021/nn1005478.

[41] K.C. Kwon, K.S. Choi, S.Y. Kim, "Increased work function in few-layer graphene sheets via metal chloride Doping," *Adv. Funct. Mater.*, 22, 4724–4731, **2012**. https://doi.org/10.1002/adfm.201200997.

[42] J. Meyer, P.R. Kidambi, B.C. Bayer, C. Weijtens, A. Kuhn, A. Centeno, A. Pesquera, A. Zurutuza, J. Robertson, S. Hofmann, "Metal oxide induced charge transfer doping and band alignment of graphene electrodes for efficient organic light emitting diodes.," *Sci. Rep.*, 4, 5380, **2014**. https://doi.org/10.1038/srep05380.

[43] P.R. Kidambi, C. Weijtens, J. Robertson, S. Hofmann, J. Meyer, "Multifunctional oxides for integrated manufacturing of efficient graphene electrodes for organic electronics," *Appl. Phys. Lett.*, 106, 1–6, **2015**. https://doi.org/10.1063/1.4908292.

[44] H. Park, P.R. Brown, V. Bulović, J. Kong, "Graphene As Transparent Conducting Electrodes in Organic Photovoltaics: Studies in Graphene Morphology, Hole Transporting Layers, and Counter Electrodes," *Nano Lett.*, 12, 133–140, **2012**. https://doi.org/10.1021/nl2029859.

[45] A. Kuruvila, P.R. Kidambi, J. Kling, J.B. Wagner, J. Robertson, S. Hofmann, J. Meyer, "Organic light emitting diodes with environmentally and thermally stable doped graphene electrodes," *J. Mater. Chem. C*, 2, 6940–6945, **2014**. https://doi.org/10.1039/c4tc01224k.

[46] P. Krukowski, D.A. Kowalczyk, M. Piskorski, P. Dabrowski, M. Rogala, P. Caban, P. Ciepielewski, J. Jung, J.M. Baranowski, J. Ulanski, Z. Klusek, "Work Function Tunability of Graphene with Thermally Evaporated Rhenium Heptoxide for Transparent Electrode Applications," *Adv. Eng. Mater.*, 22, 1900955, **2020**. https://doi.org/10.1002/adem.201900955.

[47] N. Jung, N. Kim, S. Jockusch, N.J. Turro, P. Kim, L. Brus, "Charge transfer chemical doping of few layer graphenes: Charge distribution and band gap formation," *Nano Lett.*, 9, 4133–4137, **2009**. https://doi.org/10.1021/nl902362q.

[48] A.C. Crowther, A. Ghassaei, N. Jung, L.E. Brus, "Strong charge-transfer doping of 1 to 10 layer graphene by NO2," *ACS Nano*, 6, 1865–1875, **2012**. https://doi.org/10.1021/nn300252a.

[49] T.O. Wehling, K.S. Novoselov, S. V. Morozov, E.E. Vdovin, M.I. Katsnelson, A.K. Geim, A.I. Lichtenstein, "Molecular doping of graphene," *Nano Lett.*, 8, 173–177, **2008**. https://doi.org/10.1021/nl072364w.

[50] W. Chen, S. Chen, C.Q. Dong, Y.G. Xing, A.T.S. Wee, "Surface transfer p-type doping of epitaxial graphene," *J. Am. Chem. Soc.*, 129, 10418–10422, **2007**. https://doi.org/10.1021/ja071658g.

[51] H. Pinto, R. Jones, J.P. Goss, P.R. Briddon, "P-type doping of graphene with F4-TCNQ," *J. Phys. Condens. Matter*, 21, 3–6, **2009**. https://doi.org/10.1088/0953-8984/21/40/402001.

[52] J. Park, S.B. Jo, Y.J. Yu, Y. Kim, J.W. Yang, W.H. Lee, H.H. Kim, B.H. Hong, P. Kim, K. Cho, K.S. Kim, "Single-gate bandgap opening of bilayer graphene by dual molecular doping," *Adv. Mater.*, 24, 407–411, **2012**. https://doi.org/10.1002/adma.201103411.

[53] C.-L. Hsu, C.-T. Lin, J.-H. Huang, C.-W. Chu, K.-H. Wei, L.-J. Li, "Layer-by-Layer Graphene/TCNQ Stacked Films as Conducting Anodes for Organic Solar Cells," *ACS Nano*, 6, 5031–5039, **2012**. https://doi.org/10.1021/nn301721q.

[54] S. Tongay, K. Berke, M. Lemaitre, Z. Nasrollahi, D.B. Tanner, A.F. Hebard, B.R. Appleton, "Stable hole doping of graphene for low electrical resistance and high optical transparency," *Nanotechnology*, 22, **2011**. https://doi.org/10.1088/0957-4484/22/42/425701.

[55] D. Kim, D. Lee, Y. Lee, D.Y. Jeon, "Work-function engineering of graphene anode by bis(trifluoromethanesulfonyl)amide doping for efficient polymer light-emitting diodes," *Adv. Funct. Mater.*, 23, 5049–5055, **2013**. https://doi.org/10.1002/adfm201301386.

[56] T.H. Han, S.J. Kwon, N. Li, H.K. Seo, W. Xu, K.S. Kim, T.W. Lee, "Versatile p-type chemical doping to achieve ideal flexible graphene electrodes," *Angew. Chemie - Int. Ed.*, 55, 6197–6201, **2016**. https://doi.org/10.1002/anie.201600414.

[57] N. Li, S. Oida, G.S. Tulevski, S.J. Han, J.B. Hannon, D.K. Sadana, T.C. Chen, "Efficient and bright organic light-emitting diodes on single-layer graphene electrodes," *Nat. Commun.*, 4, 1–7, **2013**. https://doi.org/10.1038/ncomms3294.

[58] L.-P. Ma, Z. Wu, L. Yin, D. Zhang, S. Dong, Q. Zhang, M.-L. Chen, W. Ma, Z. Zhang, J. Du, D.-M. Sun, K. Liu, X. Duan, D. Ma, H.-M. Cheng, W. Ren, "Pushing the conductance and transparency limit of monolayer graphene electrodes for flexible organic light-emitting diodes," *Proc. Natl. Acad. Sci.*, 117, 25991–25998, **2020**. https://doi.org/10.1073/pnas.1922521117.

[59] M. Grande, G.V. Bianco, M.A. Vincenti, D. de Ceglia, P. Capezzuto, M. Scalora, A. D'Orazio, G. Bruno, "Optically Transparent Microwave Polarizer Based On Quasi-Metallic Graphene," *Sci. Rep.*, 5, 17083, **2015**. https://doi.org/10.1038/srep17083.

[60] L. La Notte, E. Villari, A.L. Palma, A. Sacchetti, M. Michela Giangregorio, G. Bruno, A. Di Carlo, G.V. Bianco, A. Reale, "Laser-patterned functionalized CVD-graphene as highly transparent conductive electrodes for polymer solar cells," *Nanoscale*, 9, 62–69, **2017**. https://doi.org/10.1039/C6NR06156G.

[61] M. Grande, G.V. Bianco, F.M. Perna, V. Capriati, P. Capezzuto, M. Scalora, G. Bruno, A. D'Orazio, "Reconfigurable and optically transparent microwave absorbers based on deep eutectic solvent-gated graphene," *Sci. Rep.*, 9, 5463, **2019**. https://doi.org/10.1038/s41598-019-41806-w.

[62] G.V. Bianco, A. Sacchetti, A. Milella, M. Grande, A. D'Orazio, P. Capezzuto, G. Bruno, "Extraordinary low sheet resistance of CVD graphene by thionyl chloride chemical doping," *Carbon*, 170, 75–84, **2020**. https://doi.org/10.1016/j.carbon.2020.07.038.

[63] H.J. Shin, W.M. Choi, D. Choi, G.H. Han, S.M. Yoon, H.K. Park, S.W. Kim, Y.W. Jin, S.Y. Lee, J.M. Kim, J.Y. Choi, Y.H. Lee, "Control of electronic structure of graphene by various dopants and their effects on a nanogenerator," *J. Am. Chem. Soc.*, 132, 15603–15609, **2010**. https://doi.org/10.1021/ja105140e.

[64] X. Dong, D. Fu, W. Fang, Y. Shi, P. Chen, L.-J. Li, "Doping Single-Layer Graphene with Aromatic Molecules," *Small*, 5, 1422–1426, **2009**. https://doi.org/10.1002/smll.200801711.

[65] I. Gierz, C. Riedl, U. Starke, C.R. Ast, K. Kern, "Atomic Hole Doping of Graphene," *Nano Lett.*, 8, 4603–4607, **2008**. https://doi.org/10.1021/nl802996s.

[66] K. Walzer, B. Maennig, M. Pfeiffer, K. Leo, "Highly Efficient Organic Devices Based on Electrically Doped Transport Layers," *Chem. Rev.*, 107, 1233–1271, **2007**. https://doi.org/10.1021/cr050156n.

[67] P. Wei, J.H. Oh, G. Dong, Z. Bao, "Use of a 1 H -benzoimidazole derivative as an n -type dopant and to enable air-stable solution-processed n -channel organic thin-film transistors," *J. Am. Chem. Soc.*, 132, 8852–8853, **2010**. https://doi.org/10.1021/ja103173m.

[68] W. Xu, T.S. Lim, H.K. Seo, S.Y. Min, H. Cho, M.H. Park, Y.H. Kim, T.W. Lee, "N-doped graphene field-effect transistors with enhanced electron mobility and air-stability," *Small*, 10, 1999–2005, **2014**. https://doi.org/10.1002/smll.201303768.

[69] W. Xu Dr, L. Wang, Y. Liu, S. Thomas, H.K. Seo, K.I. Kim, K.S. Kim, T.W. Lee, "Controllable n-type doping on CVD-grown single- And double-layer graphene mixture," *Adv. Mater.*, 27, 1619–1623, **2015**. https://doi.org/10.1002/adma.201405353.

[70] S. Sanders, A. Cabrero-Vilatela, P.R. Kidambi, J.A. Alexander-Webber, C. Weijtens, P. Braeuninger-Weimer, A.I. Aria, M.M. Qasim, T.D. Wilkinson, J. Robertson, S. Hofmann, J. Meyer, "Engineering high charge transfer n-doping of graphene electrodes and its application to organic electronics," *Nanoscale*, 7, 13135–13142, **2015**. https://doi.org/10.1039/c5nr03246f.

[71] J.H. Chang, W.H. Lin, P.C. Wang, J.I. Taur, T.A. Ku, W.T. Chen, S.J. Yan, C.I. Wu, "Solution-processed transparent blue organic light-emitting diodes with graphene as the top cathode," *Sci. Rep.*, 5, 1–6, **2015**. https://doi.org/10.1038/srep09693.

[72] I.Y. Lee, H.Y. Park, J.H. Park, J. Lee, W.S. Jung, H.Y. Yu, S.W. Kim, G.H. Kim, J.H. Park, "Hydrazine-based n-type doping process to modulate Dirac point of graphene and its application to complementary inverter," *Org. Electron. Physics, Mater. Appl.*, 14, 1586–1590, **2013**. https://doi.org/10.1016/j.orgel.2013.03.022.

[73] P.-H. Ho, Y.-C. Yeh, D.-Y. Wang, S.-S. Li, H.-A. Chen, Y.-H. Chung, C.-C. Lin, W.-H. Wang, C.-W. Chen, "Self-Encapsulated Doping of n-Type Graphene Transistors with Extended Air Stability," *ACS Nano*, 6, 6215–6221, **2012**. https://doi.org/10.1021/nn301639j.

[74] H. Kim, J. Byun, S.-H. Bae, T. Ahmed, J.-X. Zhu, S.-J. Kwon, Y. Lee, S.-Y. Min, C. Wolf, H.-K. Seo, J.-H. Ahn, T.-W. Lee, "On-Fabrication Solid-State N-Doping of Graphene by an Electron-Transporting Metal Oxide Layer for Efficient Inverted Organic Solar Cells," *Adv. Energy Mater.*, 6, 1600172, **2016**. https://doi.org/10.1002/aenm.201600172.

[75] D.H. Shin, K.W. Lee, J.S. Lee, J.H. Kim, S. Kim, S.H. Choi, "Enhancement of the effectiveness of graphene as a transparent conductive electrode by AgNO3 doping," *Nanotechnology*, 25, **2014**. https://doi.org/10.1088/0957-4484/25/12/125701.

[76] Y. Kim, J. Ryu, M. Park, E.S. Kim, J.M. Yoo, J. Park, J.H. Kang, B.H. Hong, "Vapor-Phase Molecular Doping of Transparent Electrodes," *ACS Nano*, 8, 868–874, **2014**. https://doi.org/10.1021/nn405596j.

[77] I. Jo, Y. Kim, J. Moon, S. Park, J.S. Moon, W.B. Park, J.S. Lee, B.H. Hong, "Stable n-type

doping of graphene via high-molecular-weight ethylene amines," *Phys. Chem. Chem. Phys.*, 17, 29492–29495, **2015**. https://doi.org/10.1039/c5cp03196f.

[78] R.K. de Castro, J.R. Araujo, R. Valaski, L.O.O. Costa, B.S. Archanjo, B. Fragneaud, M. Cremona, C.A. Achete, "New transfer method of CVD-grown graphene using a flexible, transparent and conductive polyaniline-rubber thin film for organic electronic applications," *Chem. Eng. J.*, 273, 509–518, **2015**. https://doi.org/10.1016/j.cej.2015.03.092.

[79] S. Park, Y.-T. Kim, H. Min, S.M. Moon, S. Lee, C.Y. Lee, "Alkalide-Assisted Direct Electron Injection for the Noninvasive n-Type Doping of Graphene," *ACS Appl. Mater. Interfaces*, 13, 1270–1276, **2021**. https://doi.org/10.1021/acsami.0c19153.

[80] I.N. Kholmanov, C.W. Magnuson, R. Piner, J.Y. Kim, A.E. Aliev, C. Tan, T.Y. Kim, A.A. Zakhidov, G. Sberveglieri, R.H. Baughman, R.S. Ruoff, "Optical, electrical, and electromechanical properties of hybrid graphene/carbon nanotube films," *Adv. Mater.*, 27, 3053–3059, **2015**. https://doi.org/10.1002/adma.201500785.

[81] S.H. Kim, W. Song, M.W. Jung, M.A. Kang, K. Kim, S.J. Chang, S.S. Lee, J. Lim, J. Hwang, S. Myung, K.S. An, "Carbon nanotube and graphene hybrid thin film for transparent electrodes and field effect transistors," *Adv. Mater.*, 26, 4247–4252, **2014**. https://doi.org/10.1002/adma.201400463.

[82] Z. Yan, Z. Peng, G. Casillas, J. Lin, C. Xiang, H. Zhou, Y. Yang, G. Ruan, A.R.O. Raji, E.L.G. Samuel, R.H. Hauge, M.J. Yacaman, J.M. Tour, "Rebar graphene," *ACS Nano*, 8, 5061–5068, **2014**. https://doi.org/10.1021/nn501132n.

[83] J.N. Coleman, P.J. King, U. Khan, M. Lotya, S. De, "Improvement of Transparent Conducting Nanotube Films by Addition of Small Quantities of Graphene," *ACS Nano*, 4, 4238–4246, **2010**.

[84] C. Li, Z. Li, H. Zhu, K. Wang, J. Wei, X. Li, P. Sun, H. Zhang, D. Wu, "Graphene Nano-'patches' on a Carbon Nanotube Network for Highly Transparent/Conductive Thin Film Applications," *J. Phys. Chem. C*, 114, 14008–14012, **2010**. https://doi.org/10.1021/jp1041487.

[85] Y. Liu, E. Jung, Y. Wang, Y. Zheng, E.J. Park, S.M. Cho, K.P. Loh, "Quasi-freestanding graphene-on-single walled carbon nanotube electrode for applications in organic light-emitting diode," *Small*, 10, 944–949, **2014**. https://doi.org/10.1002/smll.201301829.

[86] D. Lee, H. Lee, Y. Ahn, Y. Jeong, D.Y. Lee, Y. Lee, "Highly stable and flexible silver nanowire-graphene hybrid transparent conducting electrodes for emerging optoelectronic devices," *Nanoscale*, 5, 7750–7755, **2013**. https://doi.org/10.1039/c3nr02320f.

[87] R. Design, H.G. Films, H.T. Electrodes, "Rational Design of Hybrid Graphene Films for High-Performance," *ACS Nano*, 5, 6472–6479, **2011**.

[88] Y. Ahn, Y. Jeong, D. Lee, Y. Lee, "Copper nanowire-graphene core-shell nanostructure for highly stable transparent conducting electrodes.," *ACS Nano*, 9, 3125–33, **2015**. https://doi.org/10.1021/acsnano.5b00053.

[89] R. Mehta, S. Chugh, Z. Chen, "Enhanced electrical and thermal conduction in graphene-

encapsulated copper nanowires," *Nano Lett.*, 15, 2024–2030, **2015**. https://doi.org/10.1021/nl504889t.

[90] D. Lee, H. Lee, Y. Ahn, Y. Lee, "High-performance flexible transparent conductive film based on graphene/AgNW/graphene sandwich structure," *Carbon*, 81, 439–446, **2015**. https://doi.org/10.1016/j.carbon.2014.09.076.

[91] H. Chang, G. Wang, A. Yang, X. Tao, X. Liu, Y. Shen, Z. Zheng, "A transparent, flexible, low-temperature, and solution-processible graphene composite electrode," *Adv. Funct. Mater.*, 20, 2893–2902, **2010**. https://doi.org/10.1002/adfm.201000900.

[92] Z. Liu, K. Parvez, R. Li, R. Dong, X. Feng, K. Müllen, "Transparent conductive electrodes from graphene/PEDOT:PSS hybrid inks for ultrathin organic photodetectors," *Adv. Mater.*, 27, 669–675, **2015**. https://doi.org/10.1002/adma.201403826.

[93] D. Yoo, J. Kim, J.H. Kim, "Direct synthesis of highly conductive poly(3,4-ethylenedioxythiophene):poly(4-styrenesulfonate) (PEDOT:PSS)/graphene composites and their applications in energy harvesting systems," *Nano Res.*, 7, 717–730, **2014**. https://doi.org/10.1007/s12274-014-0433-z.

[94] S. Kim, K.C. Kwon, J.Y. Park, H.W. Cho, I. Lee, S.Y. Kim, J.L. Lee, "Challenge beyond Graphene: Metal Oxide/Graphene/Metal Oxide Electrodes for Optoelectronic Devices," *ACS Appl. Mater. Interfaces*, 8, 12932–12939, **2016**. https://doi.org/10.1021/acsami.5b12443.

[95] J. Liu, Y. Yi, Y. Zhou, H. Cai, "Highly Stretchable and Flexible Graphene/ITO Hybrid Transparent Electrode," *Nanoscale Res. Lett.*, 11, 1–7, **2016**. https://doi.org/10.1186/s11671-016-1323-y.

[96] B.W.N.H. Hemasiri, J.K. Kim, J.M. Lee, "Synthesis and Characterization of Graphene/ITO Nanoparticle Hybrid Transparent Conducting Electrode," *Nano-Micro Lett.*, 10, 1–12, **2018**. https://doi.org/10.1007/s40820-017-0174-0.

[97] S. Jia, H.D. Sun, J.H. Du, Z.K. Zhang, D.D. Zhang, L.P. Ma, J.S. Chen, D.G. Ma, H.M. Cheng, W.C. Ren, "Graphene oxide/graphene vertical heterostructure electrodes for highly efficient and flexible organic light emitting diodes," *Nanoscale*, 8, 10714–10723, **2016**. https://doi.org/10.1039/c6nr01649a.

[98] F. Li, Z. Lin, B. Zhang, Y. Zhang, C. Wu, T. Guo, "Fabrication of flexible conductive graphene/Ag/Al-doped zinc oxide multilayer films for application in flexible organic light-emitting diodes," *Org. Electron. Physics, Mater. Appl.*, 14, 2139–2143, **2013**. https://doi.org/10.1016/j.orgel.2013.05.023.

[99] X.Z. Zhu, Y.Y. Han, Y. Liu, K.Q. Ruan, M.F. Xu, Z.K. Wang, J.S. Jie, L.S. Liao, "The application of single-layer graphene modified with solution-processed TiO x and PEDOT:PSS as a transparent conductive anode in organic light-emitting diodes," *Org. Electron. Physics, Mater. Appl.*, 14, 3348–3354, **2013**. https://doi.org/10.1016/j.orgel.2013.10.003.

[100] H.K. Seo, M.H. Park, Y.H. Kim, S.J. Kwon, S.H. Jeong, T.W. Lee, "Laminated Graphene Films for Flexible Transparent Thin Film Encapsulation," *ACS Appl. Mater. Interfaces*, 8, 14725–14731, **2016**. https://doi.org/10.1021/acsami.6b01639.

[101] H. Yamaguchi, J. Granstrom, W. Nie, H. Sojoudi, T. Fujita, D. Voiry, M. Chen, G. Gupta, A.D.

Mohite, S. Graham, M. Chhowalla, "Reduced graphene oxide thin films as ultrabarriers for organic electronics," *Adv. Energy Mater.*, 4, 1–6, **2014**. https://doi.org/10.1002/aenm.201300986.

[102] A.A. Sagade, A.I. Aria, S. Edge, P. Melgari, B. Gieseking, B.C. Bayer, J.C. Meyer, D. Bird, P. Brewer, S. Hofmann, "Graphene-based nanolaminates as ultra-high permeation barriers," *Npj 2D Mater. Appl.*, 1, 35, **2017**. https://doi.org/10.1038/s41699-017-0037-z.

[103] J. Wu, M. Agrawal, H.A. Becerril, Z. Bao, Z. Liu, Y. Chen, P. Peumans, "Organic Light-Emitting Diodes on Solution-Processed Graphene Transparent Electrodes," *ACS Nano*, 4, 43–48, **2010**. https://doi.org/10.1021/nn900728d.

[104] D.W. Lee, T.K. Hong, D. Kang, J. Lee, M. Heo, J.Y. Kim, B.S. Kim, H.S. Shin, "Highly controllable transparent and conducting thin films using layer-by-layer assembly of oppositely charged reduced graphene oxides," *J. Mater. Chem.*, 21, 3438–3442, **2011**. https://doi.org/10.1039/c0jm02270e.

[105] X. Wu, S. Li, Y. Zhao, Y. Tang, J. Liu, X. Guo, D. Wu, G. He, "Using a layer-by-layer assembly method to fabricate a uniform and conductive nitrogen-doped graphene anode for indium-tin oxide-free organic light-emitting diodes," *ACS Appl. Mater. Interfaces*, 6, 15753–15759, **2014**. https://doi.org/10.1021/am502629b.

[106] T. Sun, Z.L. Wang, Z.J. Shi, G.Z. Ran, W.J. Xu, Z.Y. Wang, Y.Z. Li, L. Dai, G.G. Qin, "Multilayered graphene used as anode of organic light emitting devices," *Appl. Phys. Lett.*, 96, 4–7, **2010**. https://doi.org/10.1063/1.3373855.

[107] H. Meng, Y. Dai, Y. Ye, J.X. Luo, Z.J. Shi, L. Dai, G.G. Qin, "Bilayer graphene anode for small molecular organic electroluminescence," *J. Phys. D. Appl. Phys.*, 45, **2012**. https://doi.org/10.1088/0022-3727/45/24/245103.

[108] J. Hwang, H. Kyw Choi, J. Moon, T. Yong Kim, J.W. Shin, C. Woong Joo, J.H. Han, D.H. Cho, J. Woo Huh, S.Y. Choi, J.I. Lee, H. Yong Chu, "Multilayered graphene anode for blue phosphorescent organic light emitting diodes," *Appl. Phys. Lett.*, 100, **2012**. https://doi.org/10.1063/1.3697639.

[109] J. Hwang, H.K. Choi, J. Moon, J.W. Shin, C.W. Joo, J.H. Han, D.H. Cho, J.W. Huh, S.Y. Choi, J.I. Lee, H.Y. Chu, "Blue fluorescent organic light emitting diodes with multilayered graphene anode," *Mater. Res. Bull.*, 47, 2796–2799, **2012**. https://doi.org/10.1016/j.materresbull.2012.04.087.

[110] Y. Han, L. Zhang, X. Zhang, K. Ruan, L. Cui, Y. Wang, L. Liao, Z. Wang, J. Jie, "Clean surface transfer of graphene films via an effective sandwich method for organic light-emitting diode applications," *J. Mater. Chem. C*, 2, 201–207, **2014**. https://doi.org/10.1039/c3tc31722f.

[111] D.Y. Wang, I.S. Huang, P.H. Ho, S.S. Li, Y.C. Yeh, D.W. Wang, W.L. Chen, Y.Y. Lee, Y.M. Chang, C.C. Chen, C. Te Liang, C.W. Chen, "Clean-lifting transfer of large-area residual-free graphene films," *Adv. Mater.*, 25, 4521–4526, **2013**. https://doi.org/10.1002/adma.201301152.

[112] Z. Zhang, J. Du, D. Zhang, H. Sun, L. Yin, L. Ma, J. Chen, D. Ma, H.-M. Cheng, W. Ren, "Rosin-enabled ultraclean and damage-free transfer of graphene for large-area flexible organic

light-emitting diodes," *Nat. Commun.*, 8, 14560, **2017**. https://doi.org/10.1038/ncomms14560.

[113] K.C. Kwon, S. Kim, C. Kim, J.-L. Lee, S.Y. Kim, "Fluoropolymer-assisted graphene electrode for organic light-emitting diodes," *Org. Electron.*, 15, 3154–3161, **2014**. https://doi.org/10.1016/j.orgel.2014.08.041.

[114] H. Meng, J. Luo, W. Wang, Z. Shi, Q. Niu, L. Dai, G. Qin, "Top-emission organic light-emitting diode with a novel copper/graphene composite anode," *Adv. Funct. Mater.*, 23, 3324–3328, **2013**. https://doi.org/10.1002/adfm.201203283.

[115] L. Liu, W. Shang, C. Han, Q. Zhang, Y. Yao, X. Ma, M. Wang, H. Yu, Y. Duan, J. Sun, S. Chen, W. Huang, "Two-In-One Method for Graphene Transfer: Simplified Fabrication Process for Organic Light-Emitting Diodes," *ACS Appl. Mater. Interfaces*, 10, 7289–7295, **2018**. https://doi.org/10.1021/acsami.7b19039.

[116] Z. Zhang, L. Xia, L. Liu, Y. Chen, Z. Wang, W. Wang, D. Ma, Z. Liu, "Ultra-smooth and robust graphene-based hybrid anode for high-performance flexible organic light-emitting diodes," *J. Mater. Chem. C*, 9, 2106–2114, **2021**. https://doi.org/10.1039/D0TC05213B.

[117] L. Liu, R. Dong, D. Ye, Y. Lu, P. Xia, L. Deng, Y. Duan, K. Cao, S. Chen, "Phosphomolybdic Acid-Modified Monolayer Graphene Anode for Efficient Organic and Perovskite Light-Emitting Diodes," *ACS Appl. Mater. Interfaces*, 13, 12268–12277, **2021**. https://doi.org/10.1021/acsami.0c22456.

[118] J. Lee, T.H. Han, M.H. Park, D.Y. Jung, J. Seo, H.K. Seo, H. Cho, E. Kim, J. Chung, S.Y. Choi, T.S. Kim, T.W. Lee, S. Yoo, "Synergetic electrode architecture for efficient graphene-based flexible organic light-emitting diodes," *Nat. Commun.*, 7, 1–9, **2016**. https://doi.org/10.1038/ncomms11791.

[119] S. Chen, Q. Zhang, W. Shang, L. Liu, H. Yu, S. Zhang, L. Deng, M. Wang, M. Wang, X. Li, B. Mi, W. Huang, "Interfacial engineering of graphene for highly efficient blue and white organic light-emitting devices," *Sci. Rep.*, 8, 1–9, **2018**. https://doi.org/10.1038/s41598-018-26464-8.

[120] Z. Weng, S.C. Dixon, L.Y. Lee, C.J. Humphreys, I. Guiney, O. Fenwick, W.P. Gillin, "Wafer-Scale Graphene Anodes Replace Indium Tin Oxide in Organic Light-Emitting Diodes," *Adv. Opt. Mater.*, 2101675, **2021**. https://doi.org/10.1002/adom.202101675.

[121] T.-H. Han, M. Park, S. Kwon, S. Bae, H. Seo, H. Cho, J. Ahn, T. Lee, "Approaching ultimate flexible organic light-emitting diodes using a graphene anode," *Nat. Publ. Gr.*, 8, e303-8, **2016**. https://doi.org/10.1038/am.2016.108.

[122] A.V.S. Cebrian, R.S. Carvalho, A.R.J. Barreto, F.E. Maturi, H.S. Barud, R.R. Silva, C. Legnani, M. Cremona, S.J.L. Ribeiro, "Development of Conformable Substrates for OLEDs Using Highly Transparent Bacterial Cellulose Modified with Recycled Polystyrene," *Adv. Sustain. Syst.*, 6, 2000258, **2022**. https://doi.org/10.1002/adsu.202000258.

[123] E.R.P. Pinto, H.S. Barud, R.R. Silva, M. Palmieri, W.L. Polito, V.L. Calil, M. Cremona, S.J.L. Ribeiro, Y. Messaddeq, "Transparent composites prepared from bacterial cellulose and castor oil based polyurethane as substrates for flexible OLEDs," *J. Mater. Chem. C*, 3, 11581–11588, **2015**. https://doi.org/10.1039/C5TC02359A.

[124] C. Legnani, H.S. Barud, J.M.A. Caiut, V.L. Calil, I.O. Maciel, W.G. Quirino, S.J.L. Ribeiro, M. Cremona, "Transparent bacterial cellulose nanocomposites used as substrate for organic light-emitting diodes," *J. Mater. Sci. Mater. Electron.*, 30, 16718–16723, **2019**. https://doi.org/10.1007/s10854-019-00979-w.

[125] Q. Zheng, H. Li, Y. Zheng, Y. Li, X. Liu, S. Nie, X. Ouyang, L. Chen, Y. Ni, "Cellulose-based flexible organic light-emitting diodes with enhanced stability and external quantum efficiency," *J. Mater. Chem. C*, 9, 4496–4504, **2021**. https://doi.org/10.1039/D1TC00019E.

[126] J. Tao, R. Wang, H. Yu, L. Chen, D. Fang, Y. Tian, J. Xie, D. Jia, H. Liu, J. Wang, F. Tang, L. Song, H. Li, "Highly Transparent, Highly Thermally Stable Nanocellulose/Polymer Hybrid Substrates for Flexible OLED Devices," *ACS Appl. Mater. Interfaces*, 12, 9701–9709, **2020**. https://doi.org/10.1021/acsami.0c01048.

[127] Y. Chen, N. Zhang, Y.-F. Li, Y.-G. Bi, Y.-Y. Yue, J. Feng, H.-B. Sun, "Microscale-Patterned Graphene Electrodes for Organic Light-Emitting Devices by a Simple Patterning Strategy," *Adv. Opt. Mater.*, 6, 1701348, **2018**. https://doi.org/10.1002/adom.201701348.

Chapter 2

Conversion of paper into graphene for sensors

The possibility to easily synthesize laser-induced graphene (LIG) from cellulose paper opens the door to a wide range of low-cost, flexible and biodegradable sensors. This chapter presents four reports emerging from the present work, which take advantage of this material, dubbed paper-LIG, for the development of different types of sensors.

Section 2.1 *describes the synthesis of paper-LIG using a CO_2 laser, exploring different process parameters. The obtained material is then shown to be sensitive to strain and bending, displaying, its potential for low-cost and disposable mechanical sensors. This work is adapted from the article published in "ACS Applied Materials & Interfaces", under the reference "Laser-Induced Graphene from Paper for Mechanical Sensing,"* ACS Appl. Mater. Interfaces*, 13(8), 10210-10221, 2021 (https://doi.org/10.1021/acsami.0c20270).*

Section 2.2 *presents a report on the synthesis of paper-LIG with an ultraviolet (UV) laser and its response to varying relative humidity and temperature. The mechanisms of this response are also discussed here. This work was published in "Advanced Materials Technologies", under the reference "Laser-Induced Graphene from Paper by Ultraviolet Irradiation: Humidity and Temperature Sensors,"* Adv. Mater. Technol.*, 7, 2101311, 2022 (https://doi.org/10.1002/admt.202101311).*

Section 2.3 *examines the possibility of the synthesis of paper-LIG using a single irradiation step, uncovering the underlying mechanisms. Moreover, the formation of LIG from paper containing activated charcoal and from xylan, an abundant and often underutilized biopolymer, is also explored. In the latter case, the resulting material is demonstrated to have great potential for temperature sensing. This work was published in "Diamond and Related Materials", under the reference "Conversion of paper and xylan into laser-induced graphene for environmentally friendly sensors,"* Diam. Relat. Mater.*, 108855, 2022 (https://doi.org/10.1016/j.diamond.2022.108855).*

Section 2.4 *gives an account of the use of paper-LIG as an electrode for non-enzymatic electrochemical sensors, capable of detecting and quantifying uric acid in phosphate buffer saline, synthetic urine and human samples. This work was published in "Carbon", under the reference "Laser-induced graphene from paper for non-enzymatic uric acid electrochemical sensing in urine,"* Carbon*, 197, 253-263, 2022 (https://doi.org/10.1016/j.carbon.2022.06.013).*

2.1 Laser-induced graphene from paper for mechanical sensing

Bohdan Kulyk[1], Beatriz F.R. Silva[1], Alexandre F. Carvalho[1], Sara Silvestre[2], António J.S. Fernandes[1], Rodrigo Martins[2], Elvira Fortunato[2], Florinda M. Costa[1]

1 – i3N, Department of Physics, University of Aveiro, Campus Universitário de Santiago, 3810-193 Aveiro, Portugal.

2 – i3N/CENIMAT, Department of Materials Science and CEMOP/UNINOVA, NOVA School of Science and Technology, NOVA University Lisbon, Campus de Caparica, 2829-516 Caparica, Portugal.

Abstract:

The ability to synthesize laser-induced graphene (LIG) on cellulosic materials such as paper opens the door to a wide range of potential applications, from consumer electronics to biomonitoring. In this work, strain and bending sensors fabricated by irradiation of regular filter paper with a CO_2 laser are presented. A systematic study of the influence of the different process parameters on the conversion of cellulose fibres into LIG is undertaken, by analysing the resulting morphology, structure, conductivity, and surface chemistry. The obtained material is characterized by porous electrically conductive weblike structures with sheet resistances reaching as low as 32 Ω sq^{-1}. The functionality of both strain (gauge factor of ≈42) and bending sensors is demonstrated for different sensing configurations, emphasizing the versatility and potential of this material for low-cost, sustainable, and environmentally friendly mechanical sensing.

2.1.1 Introduction

Graphene has attracted significant attention since its discovery in 2004 [1], revealing itself as a promising candidate in a vast number of potential applications [2]. Among these, the field of physical parameter sensing is a particularly active area of research, motivated by the prominence of the "Internet of Things" (IoT) concept, which relies on the need for continuous data acquisition. To this end, and particularly in situations where low-cost or even discardable technologies are needed, simple and inexpensive sensing solutions are desirable. Thanks to the recent developments in graphene production and transfer research [3–8], not only does this material satisfy these requirements, but it also provides new opportunities in terms of the devices which can be developed, owing to its unique properties. In particular, the flexibility of graphene opens the door to its application in wearable sensing [9,10], from consumer electronics to healthcare and biomedical monitoring [11–14].

Many examples of the use of graphene-based materials for the sensing of different physical parameters exist, such as the ones where graphene oxide was dispersed or incorporated into a substrate and then subsequently reduced to form conductive coatings, with a change in the resistance in response to different mechanical stimuli [15–17]. The use of dispersions of graphene flakes embedded or coated onto a substrate has also been reported in several works [11,18]. Typically, in these approaches, the resistance of the material changes due to variations in the electrical contact between the individual graphene flakes. Graphene synthesized by chemical vapor deposition, a technique which allows to grow large optically transparent single-layer graphene films with excellent charge carrier properties [19], has also been used in strain sensors [20,21], relying on its intrinsic piezoresistive effect.

More recently, the ability to quickly synthesize graphene by converting polyimide into a graphene foam, through laser irradiation, has led to a whole new range of sensors relying on what is now known as laser-induced graphene (LIG) [3]. With demonstrated applications in both physical and chemical sensing [4,6,7,22,23], this approach benefits from fast and scalable graphene fabrication directly on a flexible substrate, also presenting a direct response to some forms of physical stimuli, which relies on the resulting changes in size of the LIG foam pores and the electrical contact between their walls [24].

Not long after the first report of LIG formation from polyimide by Tour and co-workers [3], the same group showed that LIG can be formed by multiple lasing of a wide range of carbon-based materials, including, wood, paper, etc. [25]. The latter is particularly attractive for the field of physical sensing, on account of being a low-cost, biodegradable material with well-established industrial fabrication processes [26]. Compared to polyimide, paper also has a potential advantage for wearable devices directly applied to the user's skin, since it is a more breathable material thanks to its permeable nature. These characteristics, coupled to the ability to form LIG patterns directly on paper, allow us to easily make inexpensive environmentally friendly sensors [27–29]. Still, to date, and to the best of our knowledge, only a handful of reports about LIG formation on cellulose-based substrates have been published [25,30–36].

In this work, we provide a systematic study of LIG formation by CO_2 laser irradiation on filter paper. In particular, we have explored the influence of several synthesis parameters, such as laser power, scan speed and substrate distance to focus on the resulting material, in terms of its morphology, electrical conductivity, Raman signature and chemical composition. Furthermore, we demonstrate the applicability of paper-LIG for physical sensing, by fabricating and characterizing strain and bending sensors. These devices have demonstrated stable real-time

response to the applied physical parameters, reinforcing graphene's potential for low-cost and environmentally friendly sensing devices.

2.1.2 Results and discussion

Unlike in the case of LIG formation directly from polyimide, the transformation of cellulose into LIG requires the treatment (by spray coating, for example) of the paper with a fire retardant, to prevent the volatilization of the cellulose building blocks [25]. Accordingly, throughout this work, the irradiation of untreated filter paper by a CO_2 laser beam did not result in the formation of an electrically conductive material under any set of conditions. Without fire retardant, the exposed area appeared to undergo gradual ablation, accompanied by the appearance of a brown coloration. Moreover, Tour's group has reported that two irradiation steps are needed for the formation of paper-LIG: the first one out of focus, to turn the cellulose into char, and the second one in (or close to) focus, to convert the char into LIG [25]. Here, a preliminary study was undertaken, exposing 6×6 mm^2 areas of filter paper to a CO_2 laser beam scanned continuously along parallel lines with a set distance between them. A single irradiation step in focus (with a scan speed of 30 mm s^{-1}) resulted in localized damage which led to a gridlike pattern of pinhole defects (**Figure 2.1.1a**). On the other hand, irradiation out of focus (7 mm below the focal plane of the laser) led to the transformation of the cellulose fibres into an electrically insulating black material (**Figure 2.1.1b**) with the characteristic Raman signature of amorphous carbon (**Figure 2.1.1c**). A second out-of-focus irradiation (using the same conditions as the first one) did not result in any changes neither in conductivity nor in the Raman spectra. However, when the second irradiation step was performed in focus, the obtained material (**Figure 2.1.1d,e**) exhibited Raman spectra characteristic of LIG (**Figure 2.1.1f**) and a sheet resistance as low as R_S=71.6 Ω sq^{-1}.

A better understanding of the transformation process can be obtained from secondary electron scanning electron microscopy (SE-SEM) images. **Figure 2.1.1g-i** shows the filter paper before and after the formation of LIG, respectively. Originally, paper presents a densely packed structure of interwoven fibres (**Figure 2.1.1g**). The fibres seem to be compressed, having a ribbon-like appearance with widths as large as ≈50 μm. After the formation of LIG, however, the space between the fibres increases, resulting in a more open structure (**Figure 2.1.1h**). The fibres themselves appear to become slightly thinner and more cylindrical in shape. Moreover, upon inspection at higher magnifications, the development of porosity inside the irradiated fibres can be seen, with the appearance of thin-walled blisters which can open to expose the interior of the fibres (**Figure 2.1.1i**). This porosity formation is reminiscent of the well-known process of phosphoric acid activation of cellulosic material (paper, wood, etc.) to obtain, by means of thermal treatment, activated carbon. In such processes, an initial contraction due to bond cleavage induced by the phosphoric acid (although cellulose appears to be more resistant to this cleavage than, for example, lignin or hemicellulose), is followed by the porosity development enabled by the formation of cross-links through phosphate linkages [37–39]. The latter are also important in blocking the transformation of cellulose into volatile levoglucosan. A similar process would explain the role of the phosphate-based fire retardant treatment employed here in preventing the ablation of cellulose under laser irradiation [37].

The need for two irradiation steps greatly increases the number of process variables that can be controlled. This way, a systematic study exploring selected variables, such as irradiation power, scan speed, and the substrate distance to focus in the two irradiation steps, was performed. General trends in terms of their impact on the resulting material can be identified, as discussed below. For the characterization of this impact we have, once again, employed Raman

spectroscopy and sheet resistance measurements. While the former provides local information about the degree of graphitization and presence of defects in the sp^2 lattice over a small scale, the latter gives an overall idea of the crystalline quality and structural morphology of the LIG. The characterization is also complemented by visual inspection, through optical photographs and secondary electron scanning electron microscopy (SE-SEM).

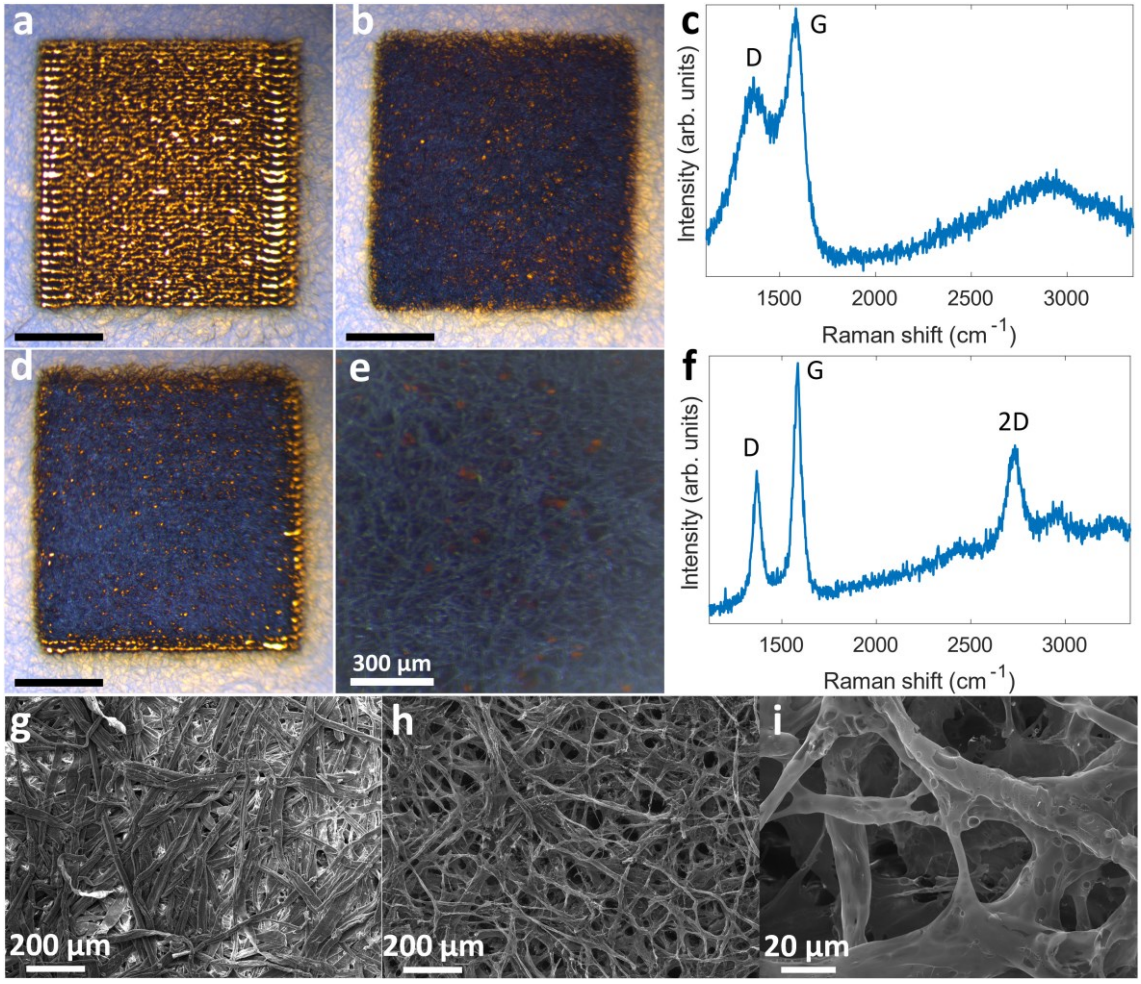

Figure 2.1.1. Optical photographs of filter paper irradiated by the laser **(a)** at the focal plane and **(b)** 7 mm below the focal plane. **(c)** Representative Raman spectrum of the sample in (b). **(d)** Optical photograph of filter paper irradiated by the laser twice, first at 7 mm below the focal plane and the second time in focus. **(e)** Magnified view of the sample in (d). **(f)** Representative Raman spectrum of the sample in (d) and (e). Secondary electron scanning electron microscopy (SE-SEM) image of filter paper treated with the fire retardant **(g)** before and **(h)** after the formation of LIG. **(i)** Magnified view of the structure of paper-LIG. The scale bars in (a), (b), and (d) correspond to 2 mm.

To establish the impact of the irradiation power on the resulting material, this parameter was systematically studied, while being fixed for the two irradiation steps. **Figure 2.1.2a** presents photographs of the 6×6 mm^2 samples of filter paper irradiated with increasing laser power. As can be seen, at ≈1.1 W of irradiation power, the samples are considerably damaged, with visible tearing and a general tendency to crumble easily. The increased damage to the transformed cellulose fibres under higher laser powers is also evident in the SE-SEM images (**Figure 2.1.2b-d**), where they appear to progressively open up from the inside, with partial detachment of thin flaky sheets from the surface of the fibres while the inside becomes increasingly porous. As for sheet resistance measurements, the average values taken from several equivalent samples for each irradiation power indicate that the ones with the lowest sheet

resistances are obtained for irradiation powers above 650 mW (**Figure 2.1.2e**). Note that these measurements were not performed on the samples synthesized at ≈1.1 W of irradiation power, due to their extensive damage and the way they tear and crumble when in contact with the contacts of the measurement setup. Interestingly, nearly all of the samples present at least one Raman spectrum characteristic of LIG or graphitized material, characterized by the presence of a symmetrical 2D band, such as the one in **Figure 2.1.2f**, corresponding to a sample formed with ≈800 mW of power. The LIG spectra, however, become more common as the irradiation power is increased, pointing toward a correlation between this parameter and the graphitization of the charred fibres.

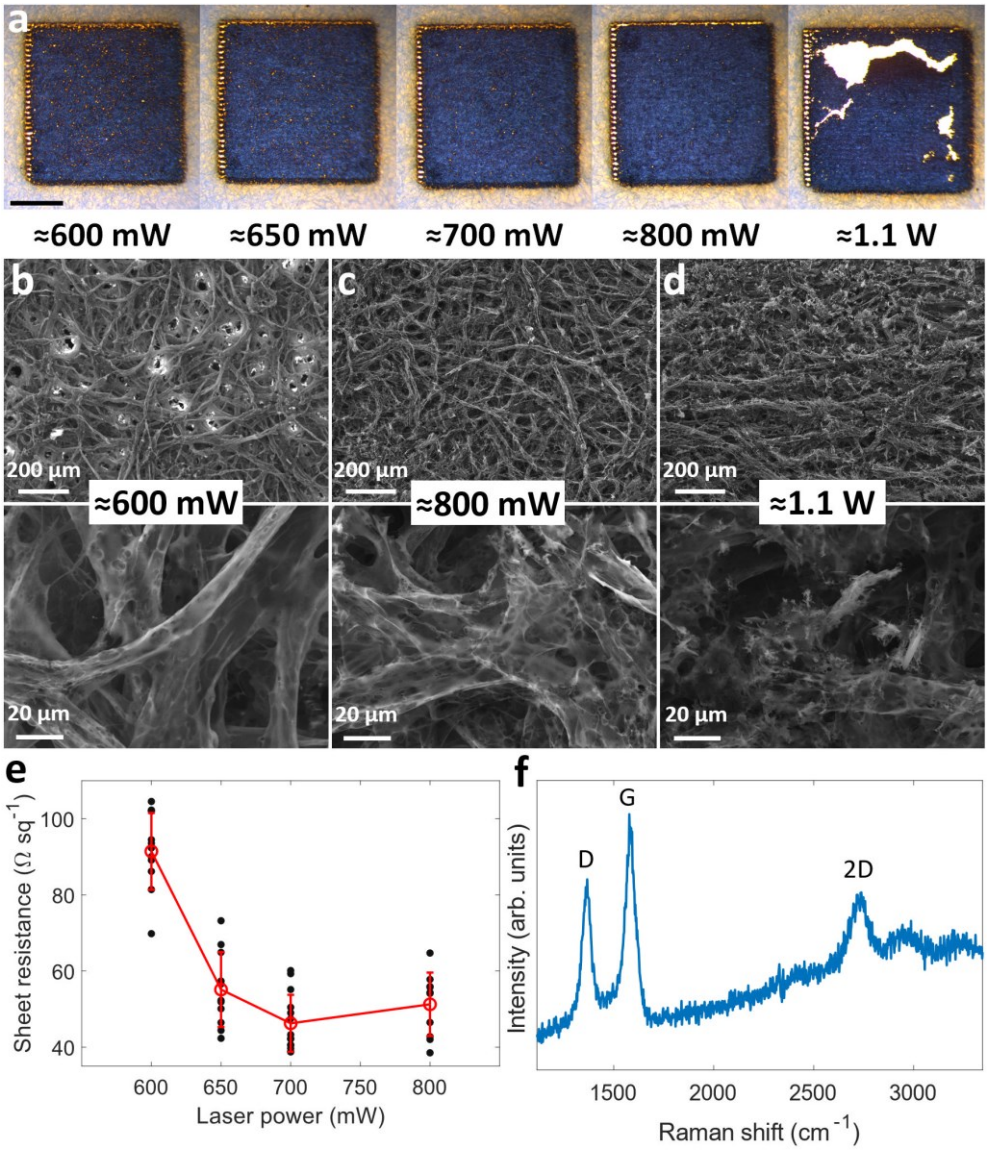

Figure 2.1.2. (a) Optical photographs of the samples formed under different laser powers. The scale bar corresponds to 2 mm. **(b)** SE-SEM images of the samples formed under ≈600 mW, **(c)** ≈800 mW, and **(d)** ≈1.1 W of laser power, at two different magnifications. **(e)** Sheet resistance values of the samples formed under different laser powers (black filled circles), along with the average values for each laser power (red open circles). The red line is a guide to the eye, and the error bars correspond to the standard deviation. **(f)** Representative Raman spectrum of the samples formed under 800 mW of laser power.

Taking into account these observations, it appears that higher irradiation powers lead to a more complete conversion of the char material formed after the first irradiation step into LIG. The incomplete transformation may occur due to the inhomogeneous nature of the paper, with different orientations of the fibres, their overlap, and the varying contact between them, leading to different local exposures to the laser beam. Higher irradiation powers help ensure that there is enough energy for the conversion of as many charred cellulose fibres into LIG as possible. According to this description, this is also what leads to lower average sheet resistance values for higher irradiation powers, as there is more electrically conductive LIG in the samples. However, increased power also leads to physical damage, as indicated by the presence of tearing, and, eventually, crumbling. As such, it appears that the power should be as high as possible, but only up to the limit where the samples begin to lose their mechanical integrity, maintaining a compromise between high power and mechanical integrity.

The impact of the laser scanning speed was also evaluated. Using laser powers of both ≈700 and ≈800 mW, scanning speeds from 20 to 70 mm s^{-1} were tested (maintaining the same scanning speed for the two irradiation steps). At 20 mm s^{-1}, both sets of samples (one for each irradiation power) were too damaged, while in the case of the samples formed at ≈700 mW, scan speeds of 60 and 70 mm s^{-1} resulted in a brown-coloured material (**Figure 2.1.3a**). The latter is similar to the appearance of laser-processed paper when no fire retardant is used, indicative of poor conversion of cellulose into char. The sheet resistances for the rest of the explored scan speeds are shown in **Figure 2.1.3b**, with the lowest ones observed for scan speeds of 30 and 40 mm s^{-1}. It is also noteworthy that the conductivity of the resulting material drops quickly as the scan speed is increased, revealing the importance of this parameter. In fact, for scan speeds of 60 and 70 mm s^{-1} at ≈700 mW of laser power, the sheet resistance was too high to be reliably measured under the same measurement conditions as the rest of the samples. Low scan speeds result in more energy being delivered at each location on the paper. Thus, the trend appears to be similar to what has been seen for different irradiation powers: low scan speeds ensure that there is enough energy for the conversion of more charred cellulose fibres into conductive LIG. Moreover, and also similarly to the dependence on irradiation power, there appears to be a limit above which the energy imparted on the paper begins to damage its charred fibres significantly. The damage is not as extensive for scan speeds which result in more conductive samples, such as the one synthesized with ≈700 mW of laser power and with a scan speed of 30 mm s^{-1}, which shows a weblike structure of porous fibres without too much damage (**Figure 2.1.3c**).

The influence of the substrate's distance to focus was also assessed. For the first irradiation step, the sample position was varied between 5 and 17 mm below the focal plane, using ≈800 mW of nominal laser power and a scan speed of 30 mm s^{-1}. The second irradiation step was performed at the focal point, maintaining the rest of the process parameters equal to the first irradiation. The photographs of the resultant samples are shown in **Figure 2.1.4a**, demonstrating very few visible defects for most of the samples, except for the ones where the first irradiation was performed closest (5 mm) and farthest (17 mm) from the focal plane. As for the samples' microstructure (**Figure 2.1.4b-d**), it appears that the closer the first irradiation step is performed to the focal plane, the more damage of the fibres occurs after both steps are completed. On the other hand, when the first irradiation is performed too far below the focal plane, there seems to be less transformation of the cellulose fibres, as indicated by the presence of only a relatively small number of blister-like closed pores. The sheet resistance measurements, averaged over several equivalent samples for each distance below focus at the first irradiation step, are shown in **Figure 2.1.4e**. The general trend seems to be that there is a

slight improvement in the conductivity of the samples as their distance to focus is increased during the first irradiation step, most likely due to better overlap between adjacent scan lines provided by the more out of focus beam, resulting in a more uniform charring. However, above a certain limit, the sheet resistance increases considerably, accompanied by visibly inconsistent transformation of the irradiated paper into black char during the first irradiation step. This points toward an energy per unit area barrier for the initial transformation to occur, a threshold that cannot be surpassed consistently once the beam is too out of focus and the delivered energy begins to be too spread out over the increasing spot size area. This also explains the increased dispersion in the obtained sheet resistance values for the same synthesis parameters. The best Raman spectra are also obtained for the samples possessing the lowest sheet resistances (the ones where, for the first irradiation step, the sample was 11 mm below the focal plane), characterized by a comparatively low I_D/I_G intensity ratio of ≈0.5 (**Figure 2.1.4f**).

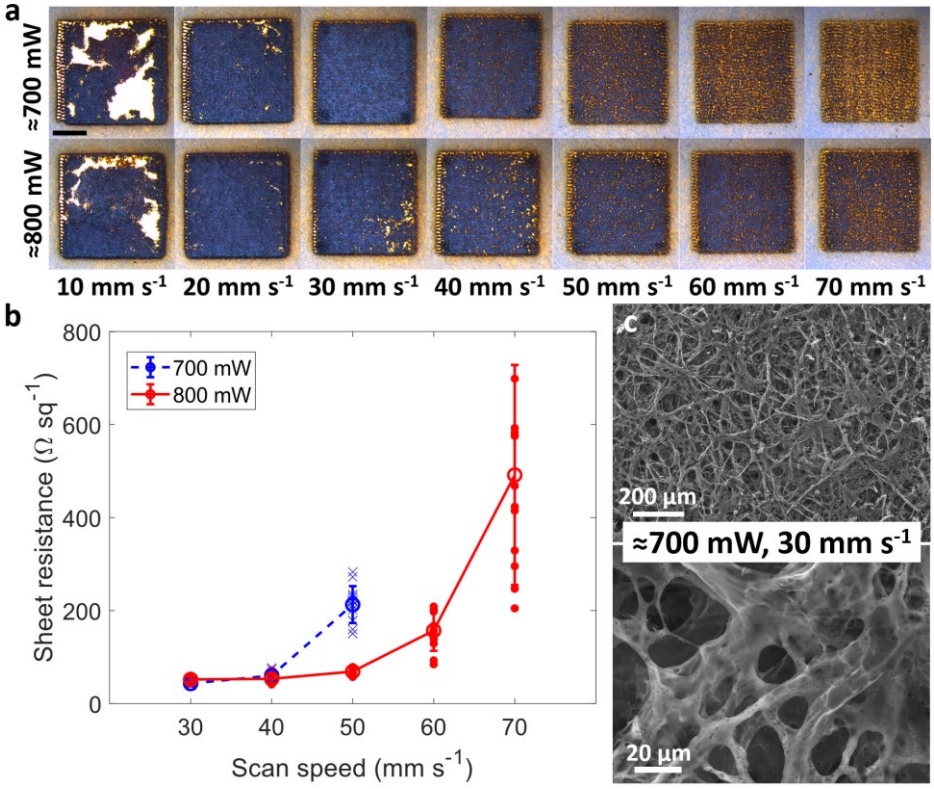

Figure 2.1.3. (a) Optical photographs of the samples formed under different scan speeds, for laser powers of ≈700 and ≈800 mW. The scale bar corresponds to 2 mm. **(b)** Sheet resistance values of the samples formed under different scan speeds, for laser powers of ≈700 and ≈800 mW (blue crosses and red filled circles, respectively), along with the average values for each laser scan speed and laser power (open circles). The blue and red lines are a guide to the eye, and the error bars correspond to the standard deviation. **(c)** SE-SEM images of a sample formed under 30 mm s^{-1}, at a laser power of ≈700 mW, at two different magnifications.

Fixing the paper substrate 11 mm below the focal plane for the first irradiation step and varying its distance to focus during the second one between 1 and 4 mm below the focal plane, several sets of samples were synthesized, maintaining the irradiation power at ≈800 mW and the scan speed at 30 mm s^{-1}. All of the resulting samples show good morphological integrity with few visible defects (**Figure 2.1.5a**). The structure of the fibres is also retained for all samples (**Figure 2.1.5b,c**), with a higher degree of porosity in the sample irradiated at 1 mm below the focal plane (**Figure 2.1.5b**). The lowest sheet resistance values were obtained for substrate

positions where the sample was closest to being in focus (1 mm below the focal plane), reaching as low as 32 Ω sq^{-1}, as shown in **Figure 2.1.5d**. The corresponding Raman spectra are, in general, characteristic of LIG, with I_D/I_G<1 (**Figure 2.1.5e**). Thus, it seems that, similarly to the dependence on irradiation power and scan speed, a high local energy delivery is desirable for the conversion of char into LIG during the second irradiation step, something which can be achieved with a focused or nearly focused laser beam.

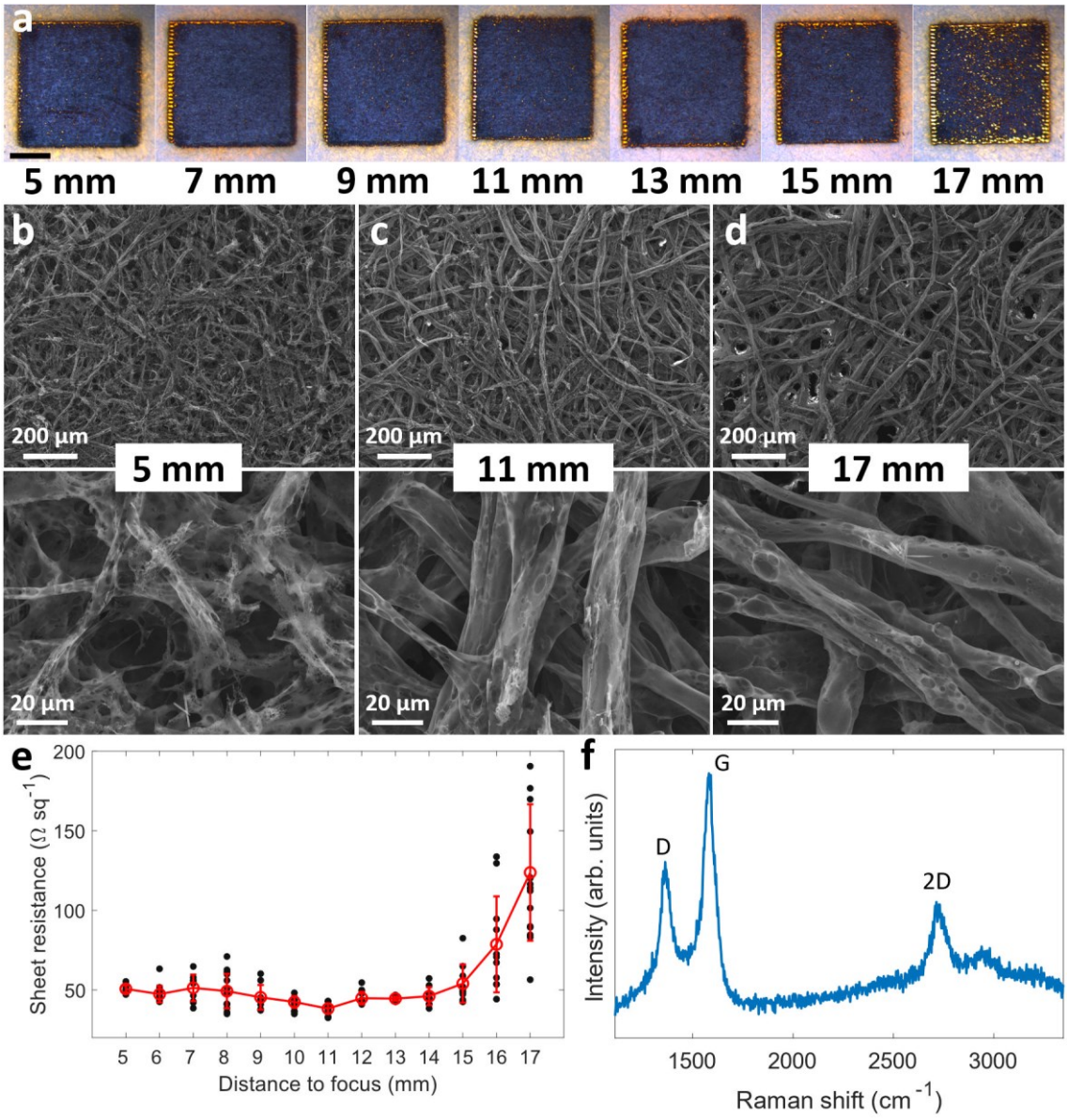

Figure 2.1.4. (a) Optical photographs of the samples formed at different distances to focus during the first irradiation step. The scale bar corresponds to 2 mm. **(b)** SE-SEM images of the samples formed at 5 mm, **(c)** 11 mm, and **(d)** 17 mm below the focal plane during the first irradiation step, at two different magnifications. **(e)** Sheet resistance values of the samples formed at different distances to focus during the first irradiation step (black filled circles), along with the average values for each distance (red open circles). The red line is a guide to the eye, and the error bars correspond to the standard deviation. **(f)** Representative Raman spectrum of the samples formed at 11 mm below the focal plane during the first irradiation step.

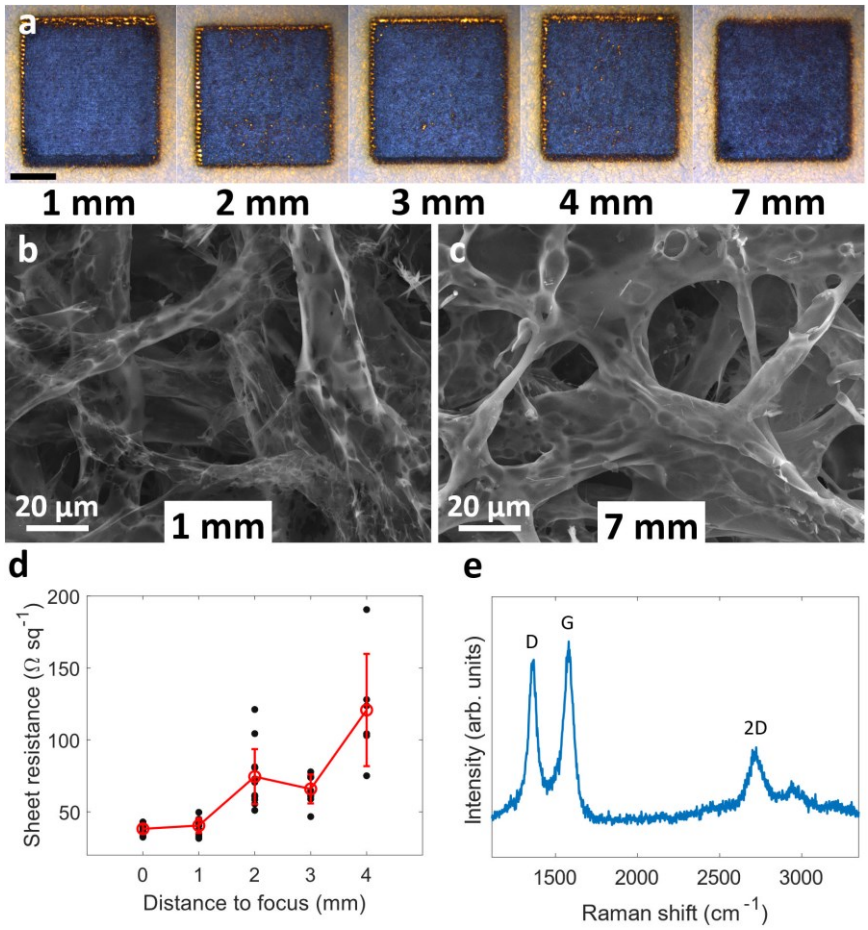

Figure 2.1.5. (a) Optical photographs of the samples formed at different distances to focus during the second irradiation step. The scale bar corresponds to 2 mm. **(b)** SE-SEM images of the samples formed at 1 mm and **(c)** 7 mm below the focal plane during the second irradiation step. **(d)** Sheet resistance values of the samples formed at different distances to focus during the second irradiation step (black filled circles), along with the average values for each distance (red open circles). The red line is a guide to the eye, and the error bars correspond to the standard deviation. **(e)** Representative Raman spectrum of the samples formed at 1 mm below the focal plane during the second irradiation step.

The chemical composition of the paper-LIG sample synthesized with the first and second irradiation steps performed at 11 and 1 mm below the focal plane, with an output power of ≈800 mW, a scan speed of 30 mm s^{-1} and a line separation of 0.1 mm, was assessed by X-ray photoelectron spectroscopy (XPS). The survey spectrum of paper-LIG (**Figure 2.1.6a**, bottom) indicates the presence of C and O, as well as P, N, Na, and Ca. The presence of C and O is to be expected from LIG itself (with the oxygen pointing toward oxidation due to the synthesis being performed in air). Some unconverted cellulose may also account for both C and O. The presence of P, N, Na, and Ca is, most likely, due to the fire retardant, with P and N being expected from a phosphate-based fire retardant [40]. These elements were also detected in the energy-dispersive spectrometry (EDS) analysis of the fire retardant used in this work (**Figure S2.1.1**, **Section 2.1.6**). Most of them can also be seen in the survey spectrum of paper treated with the fire retardant (**Figure 2.1.6a**, top).

Looking at the high-resolution spectrum of the C 1s peak (**Figure 2.1.6b**), a deconvolution into five peaks can be performed: C=C (sp^2) at 284.7 eV, C–C (sp^3) at 285.6 eV, C–O at 286.6 eV, O–C–O at 288.1 eV, O–C=O at 289.3 eV, and π–π* satellite at 290.4 eV [41–43]. The large area

of the sp^2 peak relative to the sp^3 one is in accordance with the graphitization that occurs during the conversion of the charred cellulose fibres into LIG, although one should bear in mind that there is often more than one possible deconvolution into sp^2 and sp^3 carbon peaks. Also noteworthy is the prominent C–O peak, which can originate from the oxidized LIG or even unconverted cellulose fibres. By comparison, the high-resolution C 1s XPS spectrum of filter paper coated with the fire retardant (prior to laser irradiation) features a prominent C–O peak at 286.7 eV that is more intense than the peak corresponding to the carbon-carbon bonds (285.0 eV), in agreement with the literature [42]. The relative decrease of the C–O peak's integrated area after laser irradiation, compared to the peaks corresponding to the bonds between carbon atoms, confirms the charring and graphitization of cellulose fibres.

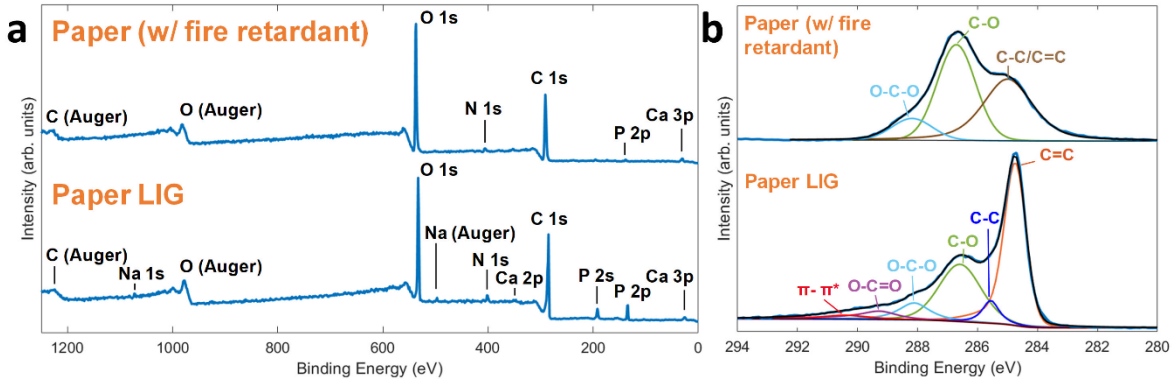

Figure 2.1.6. (a) Survey XPS spectra of the filter paper (treated with the fire retardant) before (top) and after (bottom) the formation of LIG. **(b)** Deconvoluted C 1s XPS spectra of the filter paper (treated with the fire retardant) before (top) and after (bottom) the formation of LIG.

Next, paper-LIG was used to fabricate strain sensors. To this end, a zigzag conductive path typical of strain gauges was adopted. This path could be directly patterned on paper by taking advantage of the automated x-y control of the laser position. However, such an approach has several disadvantages. Namely, the path of the laser head can affect the resulting material, due to variations in the time it takes between passes at adjacent locations on the substrate (as illustrated in **Figure S2.1.2**, **Section 2.1.6**), which can affect the local heat dissipation and, consequently, temperature. This issue can be exacerbated in situations where out-of-focus irradiation is employed, if the diameter of the affected area becomes larger than the distance between adjacent scan lines, with some overlapping occurring. The power stability of the laser can also be affected, due to its intermittent turning on and off as it passes over the different regions of the paper. Moreover, if several irradiation steps at different distances to focus are employed, as in the present work, any slight misalignment between these steps can have a significant effect on the strain gauge, due to the narrowness of the conductive path. As such, here we produced a brass mask for exposing only the regions of the paper substrate that need to be converted into LIG to form the conductive path of the strain gauge (**Figure 2.1.7a**). The laser, set to 1 W, was scanned over the mask at 30 mm s^{-1}, outlining a 15×23 mm^2 rectangle, with the first and second scans performed at 5 and 1 mm below the focal plane, respectively, a set of parameters chosen on account of the larger irradiation area compared to the squares synthesized previously for the electrical characterization.

The obtained strain gauges (**Figure 2.1.7b,c**) were characterized by monitoring the changes in resistance of the conductive path as linear elongation was cyclically applied to the sensors. By observing the values of resistance with each cycle (**Figure 2.1.7d**), also represented in **Figure 2.1.7e** as resistance variation (ΔR) divided by the resistance at the start of the

measurement (R) as a function of strain (ratio between the change in length, ΔL, and the initial length, L), an increase of the relative resistance change with the applied strain can be seen. Moreover, by extending the strain to 1.67% (0.5 mm), two response ranges can be seen: one from 0 to 0.5% and the other from 0.5 to 1% (**Figure 2.1.7f**). The latter presents a linear dependence on the applied strain ($r^2 \approx 0.992$ and 0.981 for the first and last measured cycles, respectively), with gauge factors corresponding to 41.9 and 31.7 for the first and last cycles. The presence of two distinct response ranges can arise from the interplay between the intrinsic piezoresistive response of the conductive LIG fibres and the changes in the separation between them, with each effect dominating at different ranges. Above 1% of strain, the resistance change saturates, possibly corresponding to a range where a large number of fibres are already separated so that any further increase in strain (up to a certain point) does not result in a change in the resistance. It is also noteworthy that a small inverse response mode, where the resistance change has an opposite sign to the strain variation, can be seen in this sensor (particularly in **Figure 2.1.7e**). A strain gauge of a different geometry and slightly different synthesis conditions also presents two response modes (**Figure S2.1.3**, **Section 2.1.6**), as does a sensor of the same geometry but synthesized under different conditions (1.4 W and a scan speed of 40 mm s^{-1}), for which the inverse response mode is the most significant one (**Figure S2.1.4**, **Section 2.1.6**). This mode can be explained by an initial tightening of the network formed by the processed cellulose fibres, increasing the electrical contact between them [44,45]. As the strain is increased, other effects, such as the intrinsic piezoresistive response of the conductive LIG fibres and the changes in the separation between them, come into play, resulting in the increase of the resistance with the strain. Overall, the response of the sensor is reversible, but some hysteresis can still be seen. The stability of the strain sensors was also tested by performing a measurement for over 17 h of continuous cycling. Although some drift toward higher resistance values was observed, as well as an increase in noise in the latter cycles, the sensor remained responsive for the total duration of the measurement (**Figure 2.1.7g**). Also noteworthy are the response times of the paper-LIG strain sensors, showing values of 63.4 and 62.3 ms for the rise and fall times, respectively (**Figure S2.1.5**, **Section 2.1.6**).

The effects of the applied tension on the microstructure of paper-LIG were further examined by acquiring SE-SEM images of the strain sensor under tension and by comparing them to images from the same regions at a lesser level of strain. To this end, the sample was secured at one end to a fixed frame and at the other end to a mobile base, capable of being pulled away from the frame with a screw (**Figure S2.1.6**, **Section 2.1.6**). When the separation between the base and the fixed frame was increased by ≈100 μm (**Figure S2.1.7**, **Section 2.1.6**), several changes inside the LIG could be identified by SEM. Namely, some cracks and breaks in the fibrelike structures that compose this material can be identified after the increase in the applied tension (**Figure 2.1.8a-d**). It is likely that these cracks and breaks are at the origin of the response of the sensors. As strain is applied to the sensor for the first time (during a preconditioning cycle, for example), rearrangement and settlement of the internal structure occur through breaking of the paper-LIG fibres. Then, once the measurement begins, the disconnection of the broken parts of the fibres leads to the change in the resistance of the sensors, and when a considerable number of broken fibres are separated far enough, they no longer contribute to changes in the resistance, leading to saturation behaviour like the one seen in **Figure 2.1.7f**. It is also likely that further breaks can occur during the subsequent cycles, which may be responsible for the gradual resistance drift toward higher values seen in the long-duration measurement (**Figure 2.1.7g**). Other factors, like small dimensional variations at the pore scale due to the applied tension, the intrinsic piezoresistive response of the LIG

fibres or the separation of the unbroken fibres can also contribute to the overall response of the sensors. While we were not able to observe any dimensional variations using SEM and the experimental approach described above (**Figure 2.1.8e,f**), it is possible that the locations selected for observation, being close to the surface rather than deeper in the sample, were not the ones experiencing the most tensile force, resulting in negligible dimensional variation.

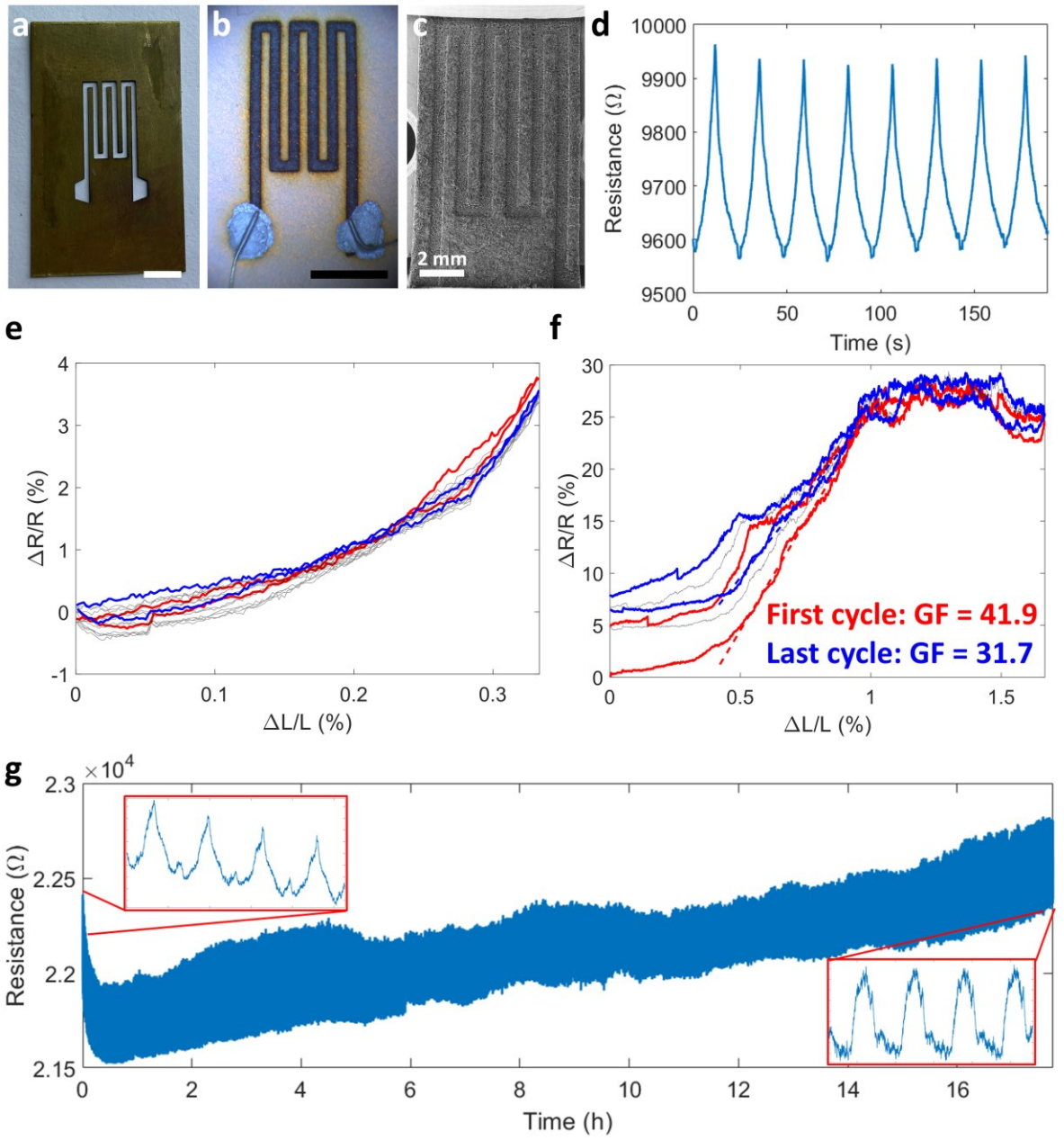

Figure 2.1.7. (a) Optical photograph of the brass mask used for the fabrication of the strain sensor. **(b)** Optical photograph of the paper-LIG strain sensor showing the silver paste electrical contacts. The scale bars in (a) and (b) correspond to 5 mm. **(c)** SE-SEM image of the paper-LIG strain sensor. **(d)** Resistance of the LIG conductive path as a function of time during the cyclic application of up to 0.33% of strain. **(e)** Relative resistance variation of the LIG conductive path as a function of strain, in the range up to 0.33% and **(f)** up to 1.67% of strain. The red and blue dashed lines are linear fits to the elongation phases of the first and last cycles, respectively, in the range between 0.5% and 1% of strain. The corresponding gauge factor values are also indicated. **(g)** Long-time measurement showing the continuous operation of the strain sensor for over 17 h in the range up to 0.33%, with the insets highlighting the sensor's response at the beginning and at the end of the measurement.

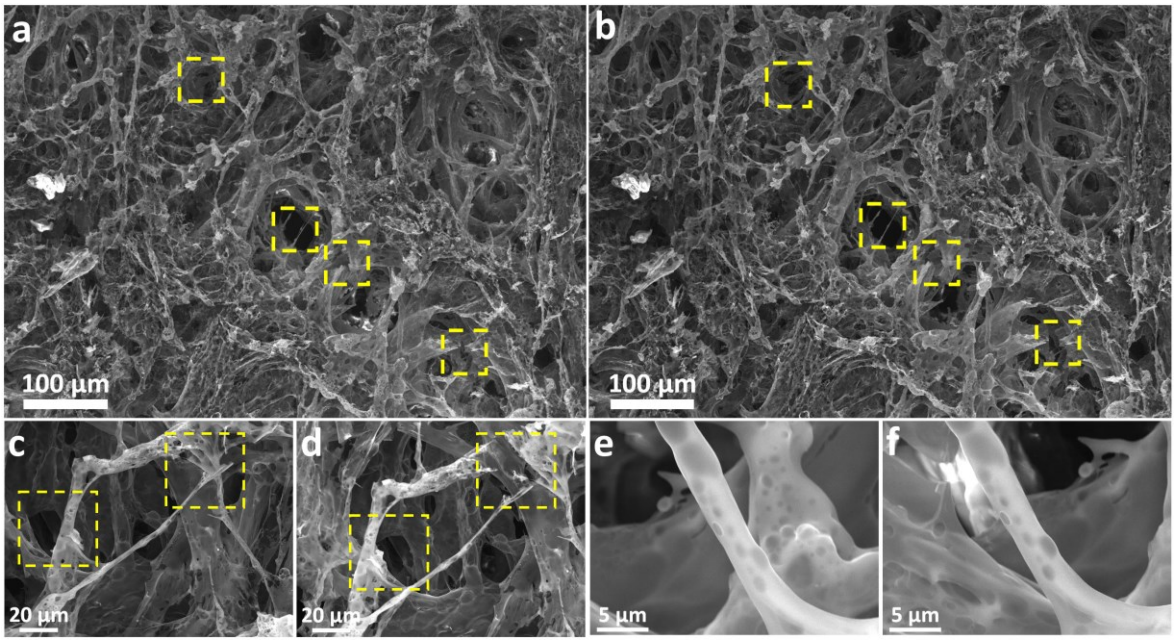

Figure 2.1.8. SE-SEM images of the paper-LIG strain sensor microstructure **(a)** before and **(b)** after the increase in applied tension. The dashed yellow squares highlight some of the structural changes that the material suffered. SE-SEM image of a region of paper-LIG where cracking and breaking of the fibrelike structures can be seen, **(c)** before and **(d)** after the increase in applied tension. The dashed yellow squares highlight some of the structural changes that the material suffered. SE-SEM image of a small paper-LIG fibre **(e)** before and **(f)** after the increase in applied tension, showing no significant change in the pores' dimensions.

The bending sensing capability of the paper-LIG produced in this work was also evaluated. Using the same design and LIG formation conditions as for the strain sensors, the bending sensors were fixed, with double-sided tape, to the underside of a flexible plastic support, and subjected to cyclic bending in a three-point bending setup (**Figure 2.1.9a**, inset). This setup allows us to calculate the bend radius at each point of the test and to monitor the corresponding relative resistance change, which can be expressed as a function of 1/radius (**Figure 2.1.9a**). The results show a clear response of the sensor, with the resistance increasing as the bending radius decreases (more bending), and with the response being nearly identical in each cycle (**Figure 2.1.9b,c**). The increase in resistance can be interpreted according to the same explanation as the one given for the strain sensors, as the bending results in an in-plane strain along the surface of the sensor. This in turn leads to the disconnection of the paper-LIG fibres (some of which become broken during the preconditioning cycle), which then originates a change in the resistance of the sensors. Moreover, the sensor remained responsive for more than 21 h of continuous measurement, although some drift toward higher resistance values was observed (**Figure 2.1.9d**). This, in addition to the increased noise seen in the latter cycles, points toward some structural degradation of the paper-LIG, most likely through breaks and cracks like the ones seen in **Figure 2.1.8**. Still, the relative increase in resistance in each cycle remained similar throughout the entire measurement, showing that the sensor remains fully functional for long measurement periods. In addition, the response times of this paper-LIG bending sensor showed values of 67.0 and 27.4 ms for the rise and fall times, respectively (**Figure S2.1.8**, **Section 2.1.6**). It is also worth pointing out that a bending sensor with different design and synthesis conditions was also evaluated under the same measurement setup and has shown a clear

response with only a small amount of drift and little hysteresis throughout more than 2 h of continuous measurement (**Figure S2.1.9**, **Section 2.1.6**).

Finally, the bending sensor was tested in a different configuration, where the paper with the LIG conductive path acted as a cantilever, which was cyclically bent with a vertically displaced actuator (**Figure 2.1.9e**, inset). The corresponding bending angle varied between ≈0 and ≈40°. The relative resistance change was not as large as in the previous measurement setup (**Figure 2.1.9e**). However, the response profile was very similar (**Figure 2.1.9f,g**), indicating that the paper-LIG sensors are capable of measuring bending in different configurations, making them promising for different application contexts.

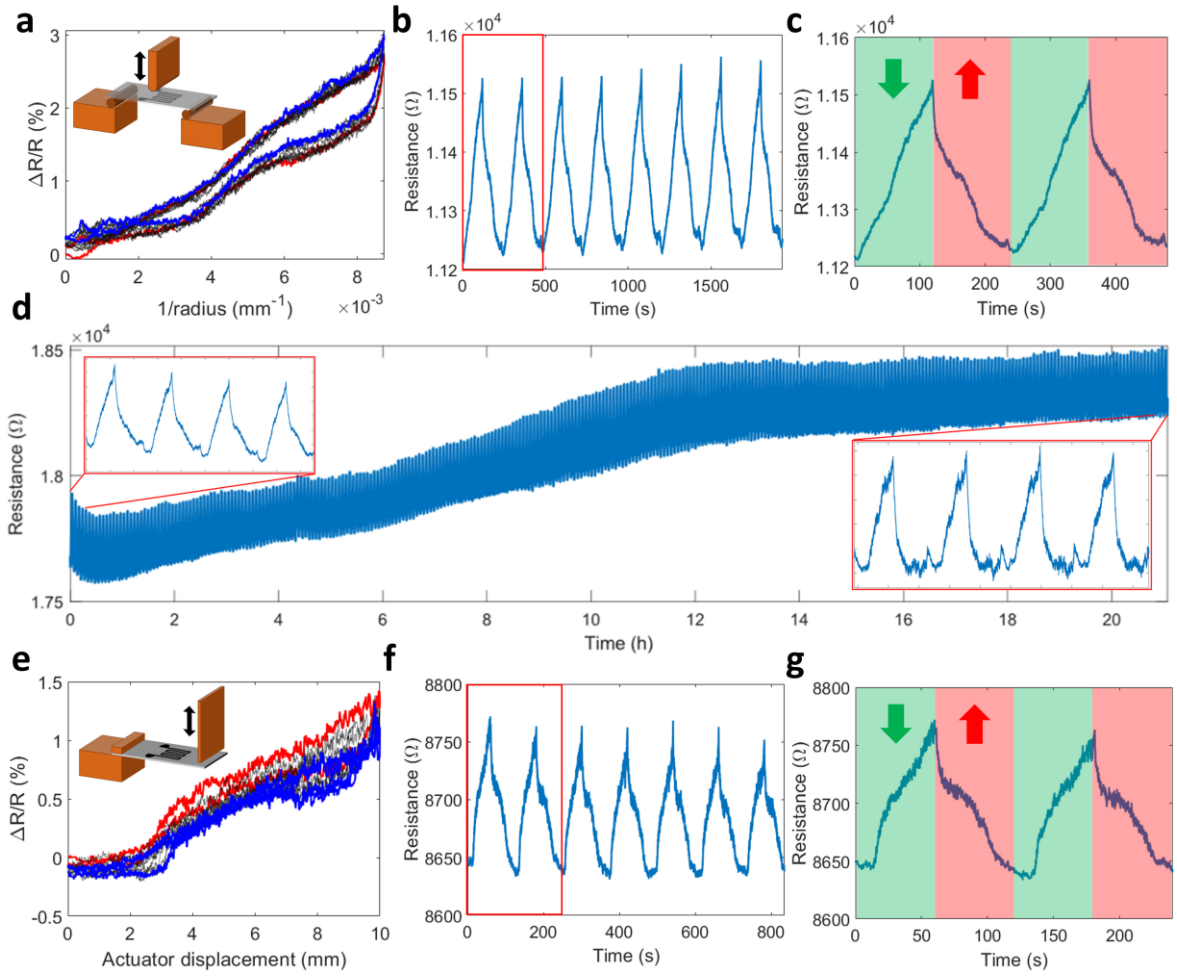

Figure 2.1.9. (a) Relative resistance variation of the LIG conductive path as a function of the inverse of the bend radius in the three-point bending setup (illustrated in the inset). The red and blue traces correspond to the first and last cycles of the measurement, respectively. **(b)** Resistance of the LIG conductive path as a function of time during cyclic bending in the three-point bending setup. **(c)** More detailed view of the first two cycles (highlighted in (b)). **(d)** Long-time measurement showing the continuous operation of the bending sensor in the three-point bending setup for over 21 h, with the insets highlighting the sensor's response at the beginning and end of the measurement. **(e)** Relative resistance variation of the LIG conductive path as a function of the displacement of the actuator in the cantilever setup. The red and blue traces correspond to the first and last cycles of the measurement, respectively. **(f)** Resistance of the LIG conductive path as a function of time during the cyclic bending in the cantilever setup. **(g)** More detailed view of the first two cycles (highlighted in (c)).

2.1.3 Conclusions

Formation of LIG on filter paper has been systematically studied in this work. The effect of different processing parameters, such as laser power, scan speed, and distance to focus, has been explored, pointing toward the need for as high irradiation powers as possible, up to the limit where the resulting material begins to suffer structural damage in the form of tearing and crumbling. The obtained material presents porous weblike structures with good electrical conductivity, with sheet resistances reaching as low as 32 Ω sq^{-1}. The paper-LIG was then employed, for the first time, in real-time strain and bending sensing, showing a clear and stable response of its electrical resistance to the applied stimuli for different measurement configurations. For the strain sensors, gauge factors as high as 41.9 were obtained, while the bending sensors were responsive for more than 21 h of continuous measurement. These results open the doors toward further development of paper-LIG electronic devices for low-cost, environmentally conscious applications.

2.1.4 Materials and methods

2.1.4.1 LIG formation

Cellulose filter paper (290 μm of thickness, 80 g m^{-2}, hardened, 0.02% ash content), by Prat Dumas, was sprayed with ≈130 mL of a commercial phosphate-based fire retardant (Anti-Flame by BBT), prior to irradiation by an M500 CO_2 (10.6 μm) continuous-wave 50 W laser engraver, by Redsail. The latter was operated in a line scan swing mode, with the line separation set at 0.1 mm. Other parameters varied throughout this work were laser power, laser beam scan speed, and sample distance to focus. We also note that, while it was not one of the studied parameters, the application of larger quantities of fire retardant, even going as far as soaking the paper in it, did not appear to have a significant effect on the resulting material. In a typical paper-LIG synthesis experiment, the paper was fixed at 11 mm below the focal plane for the first irradiation step and at or close (1 mm below) to the focal plane for the second one, with the output power set to ≈800 mW, the scan speed at 30 mm s^{-1} and an irradiated area of 6×6 mm^2 for both steps.

2.1.4.2 Material characterization

Optical photographs of the samples were acquired with a UI-3880CP-C-HQ R2 CMOS 6.41 MP camera, by IDS, through a stereo microscope, using simultaneously front and back lighting. Secondary electron SEM images were acquired using a Vega 3 SBH system, by TESCAN, with an acceleration voltage of 15 kV and a working distance of 15 mm. Raman spectroscopy was performed using a Jobin Yvon HR800 Raman system, by Horiba, and a He-Cd 441.6 nm laser, with a ×50 lens (NA=0.5), by Olympus. A neutral density filter OD=0.6 was used to attenuate the laser power to prevent any potential thermally induced chemical modification of the samples. Sheet resistance measurements were performed by the van der Pauw method, using a Keysight B2902A dual-channel source meter unit. Measurements for several equivalent samples were made. XPS spectra were acquired in an Ultra High Vacuum (UHV) system with a base pressure of 2×10^{-10} mbar, located at TEMA, University of Aveiro. The system is equipped with a hemispherical electron energy analyzer (SPECS Phoibos 150), a delay-line detector, and a monochromatic Al Kα (1486.74 eV) X-ray source. High-resolution spectra were recorded at a normal emission takeoff angle and with a pass energy of 20 eV, which provides an overall instrumental peak broadening of 0.5 eV. The XPS spectrum of paper was corrected by taking the C–C peak as reference (285.0 eV). All of the fittings were performed using the XPS Peak software.

2.1.4.3 Mechanical sensor fabrication and testing

The paper-LIG mechanical sensors were made by scanning the laser following a rectangular shape over a brass mask placed over the paper, to allow selective irradiation of the regions of interest, defining a zigzag conductive path and two contact pads. A power of 1 W and a scan speed of 30 mm s^{-1} were used. Silver paste was used to connect tin-coated 20 awg copper wires to the contact pads of the sensors. To test the response of the sensors to tensile stress and bending, a Shimadzu Autograph AGS-5kND was used, operating cyclically at a speed of 0.5 mm min^{-1} for the strain sensors, 2 mm min^{-1} for the three-point bending setup, and 10 mm min^{-1} for the cantilever bending setup. The first cycle of any measurement (not shown) was considered to be a preconditioning one, a cycle where the internal structure of the sensors was able to rearrange and settle into a more stable configuration. In the case of bending sensing, two different setups were employed. In the first one, the paper-LIG sensors were fixed, with double-sided tape, to a flexible plastic support and subjected to cyclical bending in a three-point bending test, allowing us to calculate the bend radius according to **Equation 2.1.1**:

$$radius = \frac{C^2 + 4\Delta L^2}{8\Delta L} \tag{2.1.1}$$

where ΔL is the applied strain and C is the distance between the two points on which the plastic support rests, fixed in this work at 60 mm. In the second setup, the paper-LIG sensors acted as cantilevers subjected to bending by a vertically translated actuator. The resistance of the sensors (along the conductive path) in response to the different mechanical stimuli was measured by a Keysight B2902A source meter unit, applying a constant voltage of 0.5 V.

Acknowledgements

This work was developed within the scope of the projects i3N, UIDB/50025/2020, and UIDP/50025/2020, financed by national funds through the FCT I.P. B.K., A.F.C., and S.S. acknowledge the Ph.D. grants SFRH/BD/141525/2018, DAEPHYS-FCT PD/BD/114063/2015, and SFRH/BD/149751/2019, respectively. E.F. acknowledges the ERC AdG grant 787410 from the project DIGISMART. The authors gratefully acknowledge P. Claro for sharing useful information on the conversion of paper into LIG, as well as G. Otero for the XPS characterization.

2.1.5 References

[1] K.S. Novoselov, A.K. Geim, S. V. Morozov, D. Jiang, Y. Zhang, S. V. Dubonos, I. V. Grigorieva, A.A. Firsov, "Electric field effect in atomically thin carbon films," *Science*, 306, 666–669, **2004**. https://doi.org/10.1126/science.1102896.

[2] A.C. Ferrari, F. Bonaccorso, V.I. Fal'ko, K.S. Novoselov, S. Roche, P. Bøggild, S. Borini, F.H.L. Koppens, V. Palermo, N.M. Pugno, J.A. Garrido, R. Sordan, A. Bianco, L. Ballerini, M. Prato, E. Lidorikis, J. Kivioja, C. Marinelli, T. Ryhänen, A.F. Morpurgo, J.N. Coleman, V. Nicolosi, L. Colombo, A. Fert, M. Garcia-Hernandez, A. Bachtold, G.F. Schneider, F. Guinea, C. Dekker, M. Barbone, Z.Z. Sun, C. Galiotis, A.N. Grigorenko, G. Konstantatos, A. Kis, M.I. Katsnelson, L.M.K. Vandersypen, A. Loiseau, V. Morandi, D. Neumaier, E. Treossi, V. Pellegrini, M. Polini, A. Tredicucci, G.M. Williams, B. Hee Hong, J.-H. Ahn, J. Min Kim, H. Zirath, B.J. van Wees, H. van der Zant, L. Occhipinti, A. Di Matteo, I.A. Kinloch, T. Seyller, E. Quesnel, X.L. Feng, K.B.K. Teo, N.L. Rupesinghe, P.J. Hakonen, S.R.T. Neil, Q. Tannock, T. Löfwander, J.M. Kinaret, "Science and technology roadmap for graphene, related two-dimensional crystals, and hybrid systems," *Nanoscale*, 7, 4598–4810, **2015**. https://doi.org/10.1039/C4NR01600A.

[3] J. Lin, Z. Peng, Y. Liu, F. Ruiz-Zepeda, R. Ye, E.L.G.G. Samuel, M.J. Yacaman, B.I. Yakobson, J.M. Tour, "Laser-induced porous graphene films from commercial polymers," *Nat. Commun.*, 5, 1–8, **2014**. https://doi.org/10.1038/ncomms6714.

[4] A.F. Carvalho, A.J.S. Fernandes, C. Leitão, J. Deuermeier, A.C. Marques, R. Martins, E. Fortunato, F.M. Costa, "Laser-Induced Graphene Strain Sensors Produced by Ultraviolet Irradiation of Polyimide," *Adv. Funct. Mater.*, 28, 1–8, **2018**. https://doi.org/10.1002/adfm.201805271.

[5] D.X. Luong, K. V. Bets, W.A. Algozeeb, M.G. Stanford, C. Kittrell, W. Chen, R. V. Salvatierra, M. Ren, E.A. McHugh, P.A. Advincula, Z. Wang, M. Bhatt, H. Guo, V. Mancevski, R. Shahsavari, B.I. Yakobson, J.M. Tour, "Gram-scale bottom-up flash graphene synthesis," *Nature*, 577, 647–651, **2020**. https://doi.org/10.1038/s41586-020-1938-0.

[6] A.C. Marques, A.R. Cardoso, R. Martins, M.G.F. Sales, E. Fortunato, "Laser-Induced Graphene-Based Platforms for Dual Biorecognition of Molecules," *ACS Appl. Nano Mater.*, 3, 2795–2803, **2020**. https://doi.org/10.1021/acsanm.0c00117.

[7] A.F. Carvalho, A.J.S. Fernandes, R. Martins, E. Fortunato, F.M. Costa, "Laser-Induced Graphene Piezoresistive Sensors Synthesized Directly on Cork Insoles for Gait Analysis," *Adv. Mater. Technol.*, 5, 2000630, **2020**. https://doi.org/10.1002/admt.202000630.

[8] A.F. Carvalho, A.J.S. Fernandes, M. Ben Hassine, P. Ferreira, E. Fortunato, F.M. Costa, "Millimeter-sized few-layer suspended graphene membranes," *Appl. Mater. Today*, 21, 100879, **2020**. https://doi.org/10.1016/j.apmt.2020.100879.

[9] H. Jang, Y.J. Park, X. Chen, T. Das, M.S. Kim, J.H. Ahn, "Graphene-Based Flexible and Stretchable Electronics," *Adv. Mater.*, 28, 4184–4202, **2016**. https://doi.org/10.1002/adma.201504245.

[10] H. Kim, J.-H. Ahn, "Graphene for flexible and wearable device applications," *Carbon*, 120, 244–257, **2017**. https://doi.org/10.1016/j.carbon.2017.05.041.

[11] C.S. Boland, U. Khan, C. Backes, A. O'Neill, J. McCauley, S. Duane, R. Shanker, Y. Liu, I. Jurewicz, A.B. Dalton, J.N. Coleman, "Sensitive, high-strain, high-rate bodily motion sensors based on graphene-rubber composites," *ACS Nano*, 8, 8819–8830, **2014**. https://doi.org/10.1021/nn503454h.

[12] P. Sahatiya, S. Badhulika, "Wireless, Smart, Human Motion Monitoring Using Solution Processed Fabrication of Graphene–MoS2 Transistors on Paper," *Adv. Electron. Mater.*, 4, 1–9, **2018**. https://doi.org/10.1002/aelm.201700388.

[13] A.R. Cardoso, A.C. Marques, L. Santos, A.F. Carvalho, F.M. Costa, R. Martins, M.G.F. Sales, E. Fortunato, "Molecularly-imprinted chloramphenicol sensor with laser-induced graphene electrodes," *Biosens. Bioelectron.*, 124–125, 167–175, **2019**. https://doi.org/10.1016/j.bios.2018.10.015.

[14] J. Rodrigues, J. Zanoni, G. Gaspar, A.J.S. Fernandes, A.F. Carvalho, N.F. Santos, T. Monteiro, F.M. Costa, "ZnO decorated laser-induced graphene produced by direct laser scribing," *Nanoscale Adv.*, 1, 3252–3268, **2019**. https://doi.org/10.1039/c8na00391b.

[15] H. Tian, Y. Shu, Y.L. Cui, W.T. Mi, Y. Yang, D. Xie, T.L. Ren, "Scalable fabrication of high-performance and flexible graphene strain sensors," *Nanoscale*, 6, 699–705, **2014**.

https://doi.org/10.1039/c3nr04521h.

[16] Y. Cheng, R. Wang, J. Sun, L. Gao, "A Stretchable and Highly Sensitive Graphene-Based Fiber for Sensing Tensile Strain, Bending, and Torsion," *Adv. Mater.*, 27, 7365–7371, **2015**. https://doi.org/10.1002/adma.201503558.

[17] R. Mao, W. Yao, A. Qadir, W. Chen, W. Gao, Y. Xu, H. Hu, "3-D graphene aerogel sphere-based flexible sensors for healthcare applications," *Sensors Actuators, A Phys.*, 312, 112144, **2020**. https://doi.org/10.1016/j.sna.2020.112144.

[18] P. Liu, J. Liu, X. Zhu, C. Wu, Y. Liu, W. Pan, J. Zhao, X. Guo, C. Liu, Y. Huang, A. Song, "A highly adhesive flexible strain sensor based on ultra-violet adhesive filled by graphene and carbon black for wearable monitoring," *Compos. Sci. Technol.*, 182, 107771, **2019**. https://doi.org/10.1016/j.compscitech.2019.107771.

[19] B. Kulyk, A.F. Carvalho, A.J.S. Fernandes, F.M. Costa, "Millimeter sized graphene domains through in situ oxidation/reduction treatment of the copper substrate," *Carbon*, 169, 403–415, **2020**. https://doi.org/10.1016/j.carbon.2020.08.002.

[20] S.H. Bae, Y. Lee, B.K. Sharma, H.J. Lee, J.H. Kim, J.H. Ahn, "Graphene-based transparent strain sensor," *Carbon*, 51, 236–242, **2013**. https://doi.org/10.1016/j.carbon.2012.08.048.

[21] S. Chun, Y. Choi, W. Park, "All-graphene strain sensor on soft substrate," *Carbon*, 116, 753–759, **2017**. https://doi.org/10.1016/j.carbon.2017.02.058.

[22] A. Kaidarova, M.A. Khan, M. Marengo, L. Swanepoel, A. Przybysz, C. Muller, A. Fahlman, U. Buttner, N.R. Geraldi, R.P. Wilson, C.M. Duarte, J. Kosel, "Wearable multifunctional printed graphene sensors," *Npj Flex. Electron.*, 3, 1–10, **2019**. https://doi.org/10.1038/s41528-019-0061-5.

[23] J. An, T.S.D. Le, Y. Huang, Z. Zhan, Y. Li, L. Zheng, W. Huang, G. Sun, Y.J. Kim, "All-Graphene-Based Highly Flexible Noncontact Electronic Skin," *ACS Appl. Mater. Interfaces*, 9, 44593–44601, **2017**. https://doi.org/10.1021/acsami.7b13701.

[24] R. Ye, D.K. James, J.M. Tour, "Laser-Induced Graphene: From Discovery to Translation," *Adv. Mater.*, 31, 1–15, **2019**. https://doi.org/10.1002/adma.201803621.

[25] Y. Chyan, R. Ye, Y. Li, S.P. Singh, C.J. Arnusch, J.M. Tour, "Laser-Induced Graphene by Multiple Lasing: Toward Electronics on Cloth, Paper, and Food," *ACS Nano*, 12, 2176–2183, **2018**. https://doi.org/10.1021/acsnano.7b08539.

[26] M. Jian, Y. Zhang, Z. Liu, "Natural Biopolymers for Flexible Sensing and Energy Devices," *Chinese J. Polym. Sci.*, 38, 459–490, **2020**. https://doi.org/10.1007/s10118-020-2379-9.

[27] Y. Li, Y.A. Samad, T. Taha, G. Cai, S.Y. Fu, K. Liao, "Highly Flexible Strain Sensor from Tissue Paper for Wearable Electronics," *ACS Sustain. Chem. Eng.*, 4, 4288–4295, **2016**. https://doi.org/10.1021/acssuschemeng.6b00783.

[28] G.W. Huang, N. Li, H.M. Xiao, Q.P. Feng, S.Y. Fu, "A paper-based touch sensor with an embedded micro-probe array fabricated by double-sided laser printing," *Nanoscale*, 9, 9598–9605, **2017**. https://doi.org/10.1039/c7nr02469j.

[29] C. Casiraghi, M. Macucci, K. Parvez, R. Worsley, Y. Shin, F. Bronte, C. Borri, M. Paggi, G.

Fiori, "Inkjet printed 2D-crystal based strain gauges on paper," *Carbon*, 129, 462–467, **2018**. https://doi.org/10.1016/j.carbon.2017.12.030.

[30] X. Zang, C. Shen, Y. Chu, B. Li, M. Wei, J. Zhong, M. Sanghadasa, L. Lin, "Laser-Induced Molybdenum Carbide-Graphene Composites for 3D Foldable Paper Electronics," *Adv. Mater.*, 30, 1800062, **2018**. https://doi.org/10.1002/adma.201800062.

[31] Y. Yao, X. Duan, M. Niu, J. Luo, R. Wang, T. Liu, "One-step process for direct laser writing carbonization of NH4H2PO4 treated cellulose paper and its use for facile fabrication of multifunctional force sensors with corrugated structures," *Cellulose*, 26, 7423–7435, **2019**. https://doi.org/10.1007/s10570-019-02617-4.

[32] S. Lee, S. Jeon, "Laser-Induced Graphitization of Cellulose Nanofiber Substrates under Ambient Conditions," *ACS Sustain. Chem. Eng.*, 7, 2270–2275, **2019**. https://doi.org/10.1021/acssuschemeng.8b04955.

[33] W.R. de Araujo, C.M.R. Frasson, W.A. Ameku, J.R. Silva, L. Angnes, T.R.L.C. Paixão, "Single-Step Reagentless Laser Scribing Fabrication of Electrochemical Paper-Based Analytical Devices," *Angew. Chemie - Int. Ed.*, 56, 15113–15117, **2017**. https://doi.org/10.1002/anie.201708527.

[34] S. Lee, H. Jang, H. Lee, D. Yoon, S. Jeon, "Direct Fabrication of a Moisture-Driven Power Generator by Laser-Induced Graphitization with a Gradual Defocusing Method," *ACS Appl. Mater. Interfaces*, 11, 26970–26975, **2019**. https://doi.org/10.1021/acsami.9b08056.

[35] Y. Chyan, J. Cohen, W. Wang, C. Zhang, J.M. Tour, "Graphene Art," *ACS Appl. Nano Mater.*, 2, 3007–3011, **2019**. https://doi.org/10.1021/acsanm.9b00391.

[36] P. Zhao, G. Bhattacharya, S.J. Fishlock, J.G.M. Guy, A. Kumar, C. Tsonos, Z. Yu, S. Raj, J.A. McLaughlin, J. Luo, N. Soin, "Replacing the metal electrodes in triboelectric nanogenerators: High-performance laser-induced graphene electrodes," *Nano Energy*, 75, 104958, **2020**. https://doi.org/10.1016/j.nanoen.2020.104958.

[37] M. Jagtoyen, F. Derbyshire, "Activated carbons from yellow poplar and white oak by H3PO4 activation," *Carbon*, 36, 1085–1097, **1998**. https://doi.org/https://doi.org/10.1016/S0008-6223(98)00082-7.

[38] M.S. Solum, R.J. Pugmire, M. Jagtoyen, F. Derbyshire, "Evolution of carbon structure in chemically activated wood," *Carbon*, 33, 1247–1254, **1995**. https://doi.org/https://doi.org/10.1016/0008-6223(95)00067-N.

[39] Y. Guo, D.A. Rockstraw, "Physical and chemical properties of carbons synthesized from xylan, cellulose, and Kraft lignin by H3PO4 activation," *Carbon*, 44, 1464–1475, **2006**. https://doi.org/10.1016/j.carbon.2005.12.002.

[40] I. van der Veen, J. de Boer, "Phosphorus flame retardants: Properties, production, environmental occurrence, toxicity and analysis," *Chemosphere*, 88, 1119–1153, **2012**. https://doi.org/10.1016/j.chemosphere.2012.03.067.

[41] R. Ye, Y. Chyan, J. Zhang, Y. Li, X. Han, C. Kittrell, J.M. Tour, "Laser-Induced Graphene Formation on Wood," *Adv. Mater.*, 29, 1–7, **2017**. https://doi.org/10.1002/adma.201702211.

[42] L. Johansson, J.M. Campbell, O.J. Rojas, "Cellulose as the in situ reference for organic XPS. Why? Because it works," *Surf. Interface Anal.*, **2020**. https://doi.org/10.1002/sia.6759.

[43] J. Zhang, Y. Xu, Z. Liu, W. Yang, J. Liu, "A highly conductive porous graphene electrode prepared via in situ reduction of graphene oxide using Cu nanoparticles for the fabrication of high performance supercapacitors," *RSC Adv.*, 5, 54275–54282, **2015**. https://doi.org/10.1039/C5RA07857A.

[44] J.J. Park, W.J. Hyun, S.C. Mun, Y.T. Park, O.O. Park, "Highly Stretchable and Wearable Graphene Strain Sensors with Controllable Sensitivity for Human Motion Monitoring," *ACS Appl. Mater. Interfaces*, 7, 6317–6324, **2015**. https://doi.org/10.1021/acsami.5b00695.

[45] D. Du, P. Li, J. Ouyang, "Graphene coated nonwoven fabrics as wearable sensors," *J. Mater. Chem. C*, 4, 3224–3230, **2016**. https://doi.org/10.1039/c6tc00350h.

2.1.6 Supporting information

2.1.6.1 Chemical composition of the fire retardant

The elemental composition of the fire retardant employed in this work was evaluated by energy dispersive X-ray spectroscopy (EDS), by spraying the fire retardant over an aluminium sample holder and analysing the solid residue left after it dried. The presence of P, O, Na and N was identified (**Figure S2.1.1**).

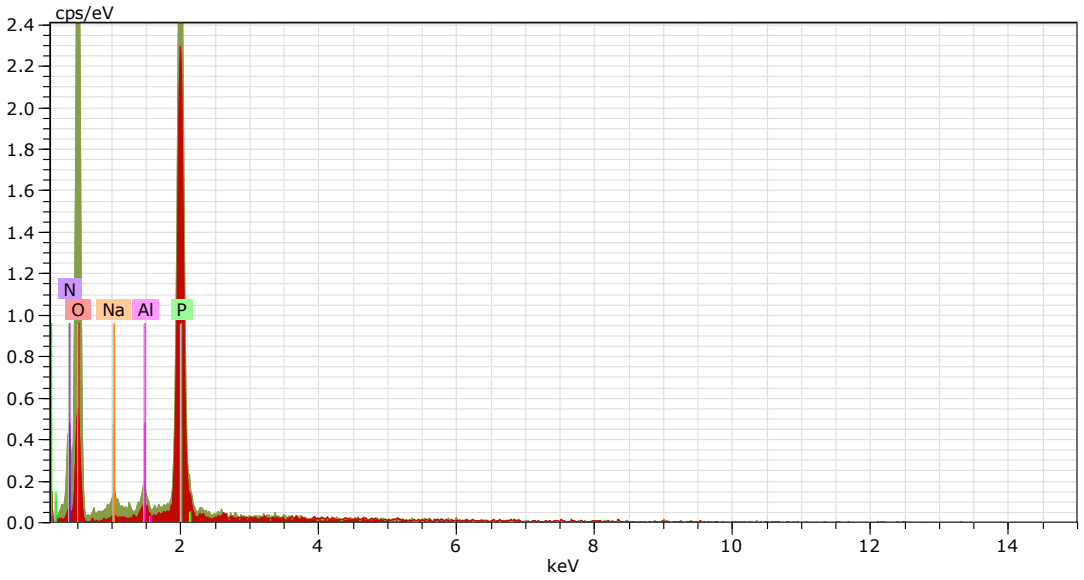

Figure S2.1.1. Two overlaid EDS spectra of the fire retardant, from two distinct locations on the dried-up residue.

2.1.6.2 Differences in the path of the laser head

During the laser marking of complex shapes, the control algorithm leads to differences in the total time it takes to complete each line of the desired shape. **Figure S2.1.2** illustrates this effect, taking the shape of the conductive path used in this work as an example. In the contact pad region, the laser scans each line in a time interval of t_1, while in the rest of the shape each line takes a shorter amount of time, t_2, to complete. As such, the laser irradiates adjacent locations of the substrate along the y axis with varying intervals of time, potentially resulting in

non-uniformities due to differences in temperature between the two regions (as in the contact pads there is more time for heat dissipation to occur, in this example).

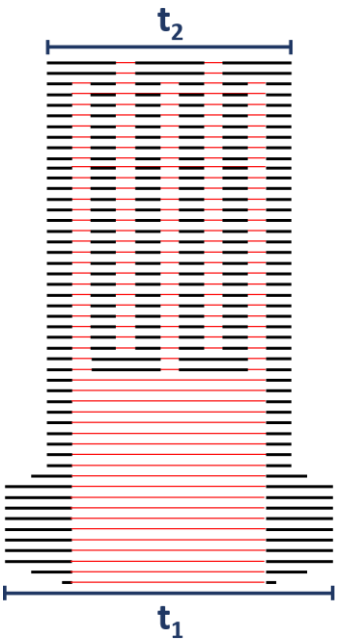

Figure S2.1.2. Illustration of the differences in the time it takes the laser head to scan each line of the desired shape. The red lines correspond to sections where the laser is turned off while it scans across the shape.

2.1.6.3 Additional strain sensor tests

As an alternative to the sensors described in the main text, a sensor with a smaller design and different synthesis conditions was also tested (**Figure S2.1.3a-c**). The laser was set to 1.2 W and was scanned over the brass mask at 30 mm s^{-1}, outlining an 8×15 mm^2 rectangle, with the first and second scans performed at 11 mm and 1 mm below the focal plane, respectively. These strain gauges were also characterized by monitoring the changes in resistance along the conductive path as linear elongation was cyclically applied to the sensors (**Figure S2.1.3d-f**). Here, two response modes can be seen. The first one, corresponding to small elongations, shows a reduction in resistance as the elongation increases. In the second mode, as the increase of elongation continues over a certain limit, the resistance begins to increase, displaying an approximately linear behaviour. The first cycle can be fitted to a straight line ($r^2 \approx 0.989$) in the elongation range between 0.2% and 0.42%, allowing to obtain a gauge factor value of 11.8, while for the last measured cycle a linear fit in the same range ($r^2 \approx 0.978$) gives a gauge factor of 9.6, which shows a slight decrease in performance after an increased number of cycles. As discussed in the main text, the presence of the inverse response mode (where the resistance reduces with strain) can be explained by an initial tightening of the network formed by the processed cellulose fibres, increasing the electrical contact between them.

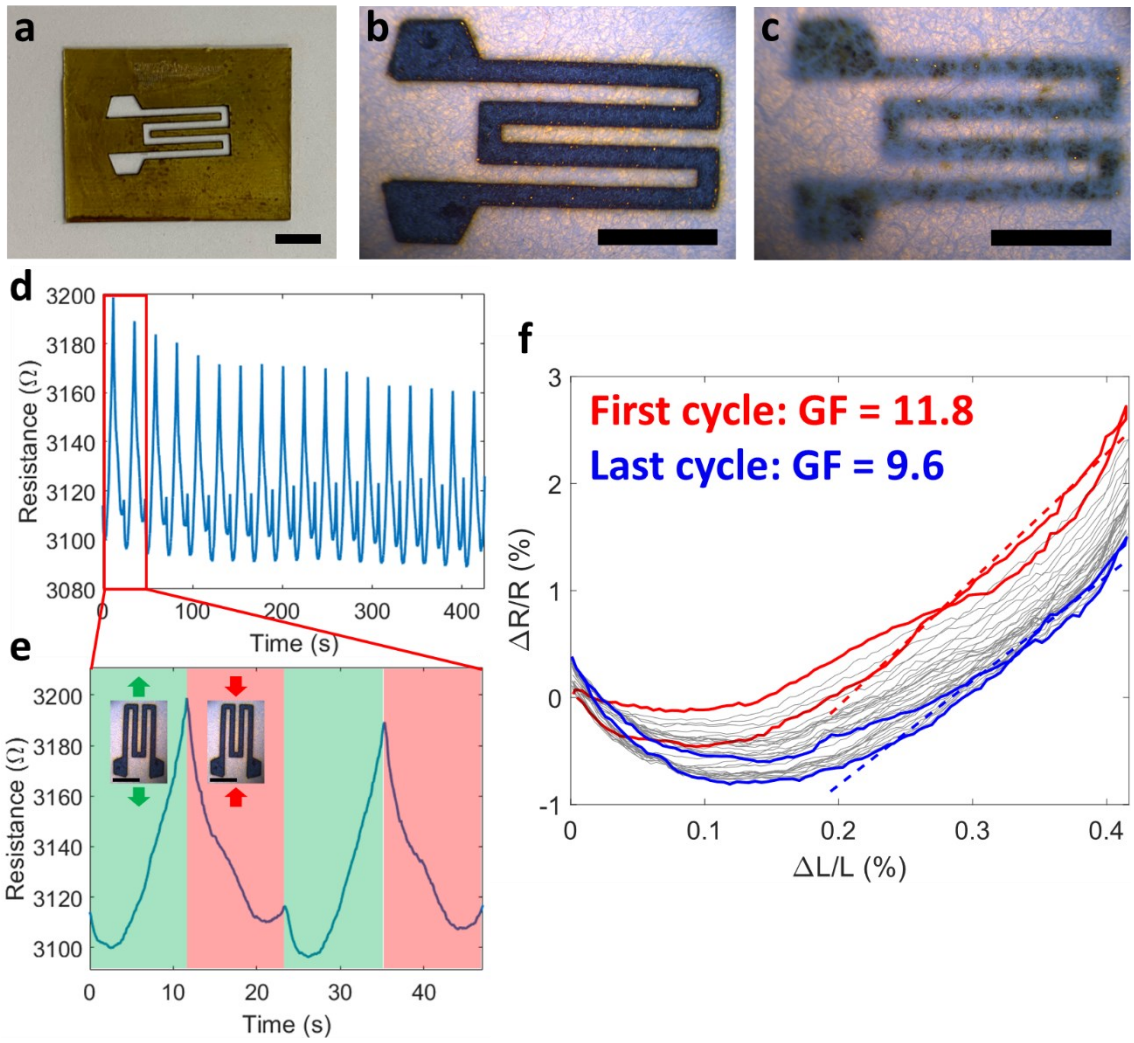

Figure S2.1.3. (a) Optical photograph of the brass mask used for the fabrication of the smaller design strain sensor. **(b)** Optical photograph of the paper-LIG strain sensor with the smaller design, as seen from the front and **(c)** the back side of the filter paper. The scale bars in (a), (b) and (c) correspond to 4 mm. **(d)** Resistance of the LIG conductive path as a function of time during the cyclic application of strain, along with **(e)** a more detailed view of the first two cycles (highlighted in (a)). **(f)** Relative resistance variation as a function of strain. The red and blue traces correspond to the first and last cycles of the measurement, respectively. The red and blue dashed lines are linear fits to the elongation phases of the first and last cycles, respectively, in the range between 0.2% and 0.42% of strain. The corresponding gauge factor values are also indicated.

A strain gauge of the same geometry as the one described in the main text but synthesized under different conditions (1.4 W and a scan speed of 40 mm s^{-1}) also possesses both response modes, with the inverse one being the most significant one (**Figure S2.1.4**). This indicates that the presence of this response mode also depends on the synthesis conditions and the resulting material and not just on the strain gauge geometry and size.

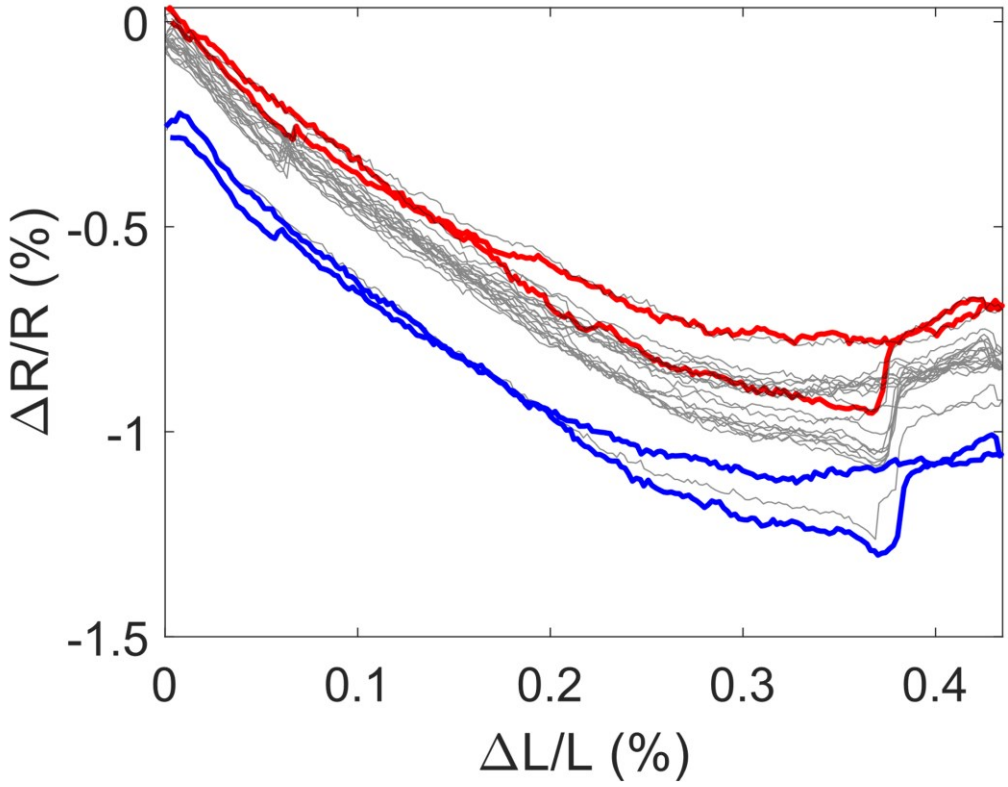

Figure S2.1.4. Relative resistance variation as a function of strain, in the range up to 0.42% of strain, for the larger design paper-LIG conductive path formed under 1.4 W of laser power and a scan speed of 40 mm s^{-1}. The red and blue traces correspond to the first and last cycles of the measurement, respectively.

The strain gauges were also evaluated in terms of their response time. To this end, a sensor was fixed at one end and coupled to a piezoelectric actuator at the other. A square wave pulse was applied to the actuator, with a frequency of 5 Hz, resulting in a periodic displacement of 60 µm. The response of the sensor, mounted in a voltage divider, was measured by evaluating the output voltage. The results (**Figure S2.1.5**) show a clear periodic response to the actuation of the piezoelectric device. The rise and fall response times, defined as the time necessary to reach 90% of the stable signal after the sensor is stretched and relaxed, respectively, were determined to be 63.4 ms for the rise time and 62.3 ms for the fall time.

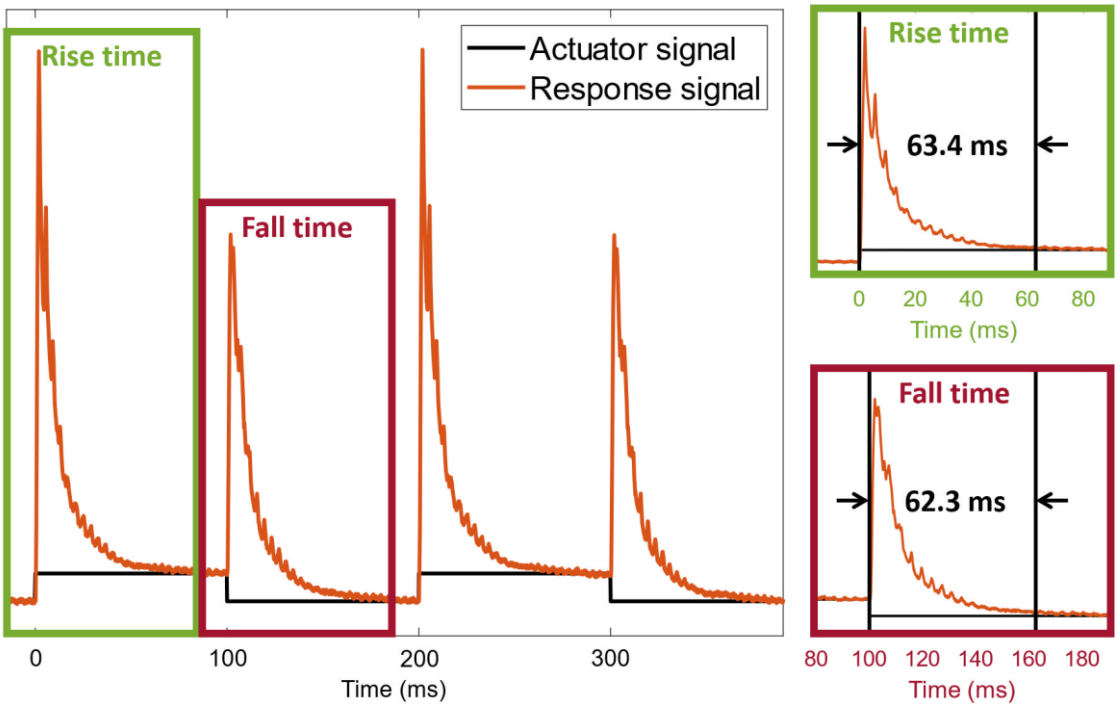

Figure S2.1.5. Normalized response of the paper-LIG strain gauge to a 5 Hz periodic strain, allowing to determine the rise and fall response times.

2.1.6.4 Study of the effects of the applied tension on the microstructure of paper-LIG

As discussed in the main text, to evaluate the effects of the tension applied to the paper-LIG strain sensors, a scanning electron microscopy study was performed. A photograph of the experimental setup for this study is shown in **Figure S2.1.6**. The sample was secured at one end to a fixed frame and at the other end to a mobile base, capable of being pulled away from the frame with a screw. The approximate elongation of the sensor was determined by measuring the change in the separation between the mobile base and the fixed frame (**Figure S2.1.7**).

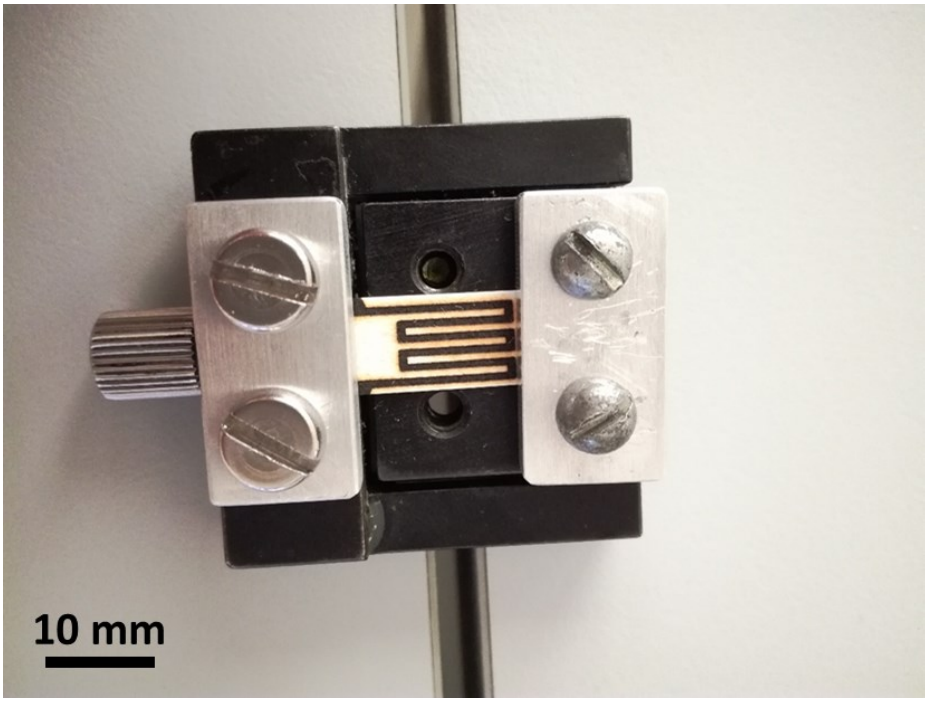

Figure S2.1.6. Experimental setup for the study of the effect of the applied tension on the microstructure of paper-LIG. The clamp on the left is attached to a fixed frame, while the one on the right is attached to a mobile base. The leftmost screw allows to move the base relative to the frame, resulting in the application of tension on the paper-LIG sensor.

Figure S2.1.7. Measurement of the separation between the mobile platform and the fixed base used to examine the effect of the applied tension on the microstructure of paper-LIG.

2.1.6.5 Additional bending sensor tests

The bending sensors were also evaluated in terms of their response time. To this end, a sensor fixed to the underside of a flexible plastic support with double sided tape was bent against two vertical supports by a piezoelectric actuator. A square wave pulse was applied to the actuator, with a frequency of 5 Hz, resulting in a periodic displacement of 90 µm at the tip of actuator. The response of the sensor, mounted in a voltage divider, was measured by evaluating the output voltage. The results (**Figure S2.1.8**) show a clear periodic response to the actuation of the piezoelectric device. The rise and fall response times, defined as the time necessary to reach 90% of the stable signal after the sensor is stretched and relaxed, respectively, were determined to be 67.0 ms for the rise time and 27.4 ms for the fall time.

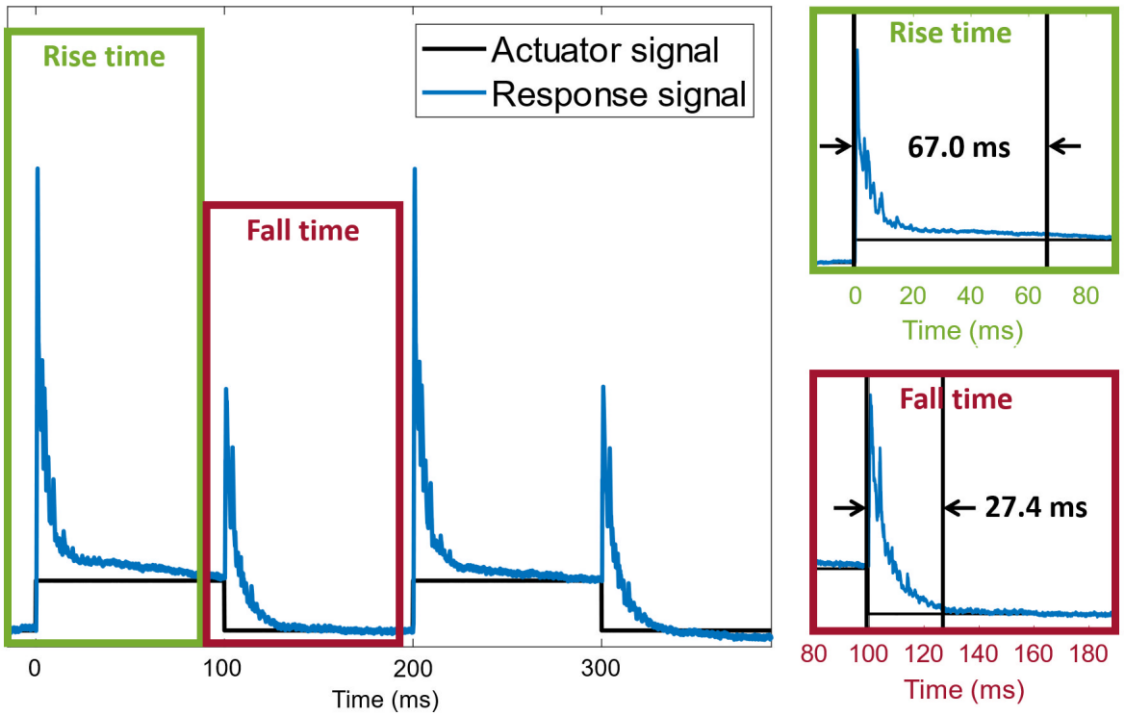

Figure S2.1.8. Normalized response of the paper-LIG bending sensor (in a three-point bending setup) to a 5 Hz periodic bending, allowing to determine the rise and fall response times.

The bending sensing capability of the paper-LIG produced in this work has also been evaluated with a smaller design and different synthesis conditions. The laser was set to 1.2 W and was scanned over the brass mask at 30 mm s^{-1}, outlining an 8×15 mm^2 rectangle, with the first and second scans performed at 11 mm and 1 mm below the focal plane, respectively. Similarly to the sensors described in the main text, this bending sensor was fixed, with double sided tape, to the underside of a flexible plastic support and subjected to cyclic bending in a three-point bending setup (**Figure S2.1.9a**). The results show the sensor responding, with the resistance increasing as the bending radius decreases (more bending), with only a small amount of drift and little hysteresis throughout more than 2 hours of continuous measurement (**Figure S2.1.9c,d**).

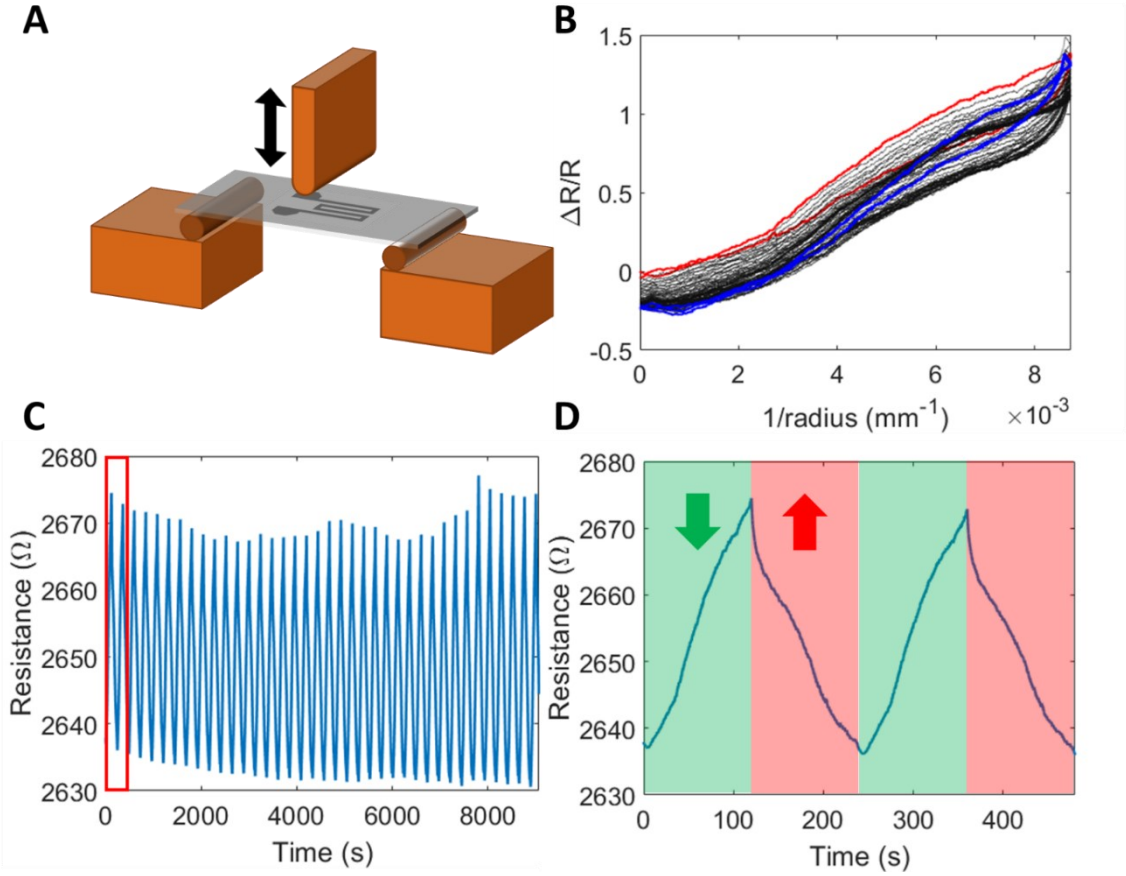

Figure S2.1.9. **(a)** Schematic representation of the three-point bending setup for bending sensor testing. **(b)** Relative resistance variation as a function of the inverse of the bend radius. The red and blue traces correspond to the first and last cycles of the measurement, respectively. **(c)** Resistance of the LIG conductive path as a function of time during the cyclic bending, along with **(d)** a more detailed view of the first two cycles (highlighted in (c)).

2.1.6.6 Cross-section analysis

The thickness of the paper-LIG was evaluated by scanning electron microscopy, looking at the irradiated paper in cross-section (**Figure S2.1.10**).

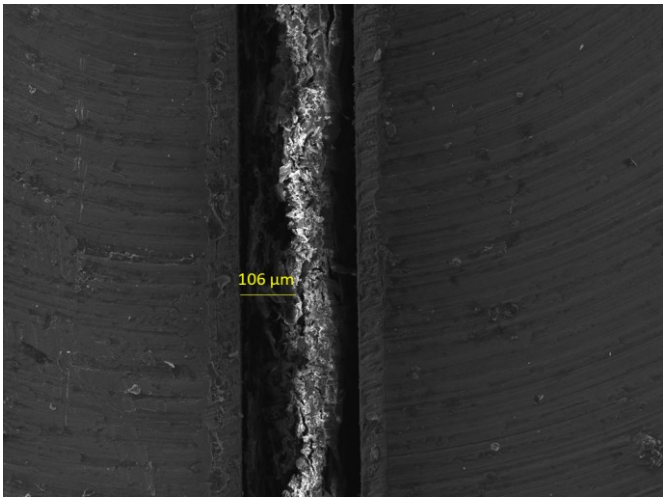

Figure S2.1.10. Cross-section SE-SEM image of paper-LIG. The brighter region corresponds to the unconverted paper.

2.2 Laser-induced graphene from paper by ultraviolet irradiation: humidity and temperature sensors

Bohdan Kulyk[1,2], Beatriz F.R. Silva[1,3], Alexandre F. Carvalho[1,3], Paula Barbosa[3], Ana V. Girão[4], Jonas Deuermeier[2], António J.S. Fernandes[1], Filipe M.L. Figueiredo[1,3], Elvira Fortunato[2], Florinda M. Costa[1]

1 – i3N, Department of Physics, University of Aveiro, Campus Universitário de Santiago, 3810-193 Aveiro, Portugal.

2 – i3N/CENIMAT, Department of Materials Science and CEMOP/UNINOVA, NOVA School of Science and Technology, NOVA University Lisbon, Campus de Caparica, 2829-516 Caparica, Portugal.

3 – CICECO – Aveiro Institute of Materials, Department of Physics, University of Aveiro, Campus Universitário de Santiago, 3810-193 Aveiro, Portugal.

4 – CICECO – Aveiro Institute of Materials, Department of Materials and Ceramic Engineering, University of Aveiro, Campus Universitário de Santiago, 3810-193 Aveiro, Portugal.

Abstract:

Laser-induced graphene (LIG) produced by irradiation of paper (paper-LIG) holds substantial promise for flexible devices. This article presents paper-LIG humidity and temperature sensors fabricated by single-step irradiation of common filter paper with a pulsed UV laser (355 nm). The influence of the process parameters on the conversion of cellulose fibres into LIG is discussed based on the resulting morphology, structure, conductivity, and chemical composition, revealing a distinct barrier to transformation and a propagation behaviour not seen under CO_2 laser irradiation. The obtained material is constituted by a porous, electrically conductive network of fibres. The paper-LIG relative humidity (RH) and temperature sensors with sensitivities of up to 1.3×10^{-3}% RH^{-1} and -2.8×10^{-3} $°C^{-1}$, respectively, are examined in terms of their linearity, reproducibility, and response time. A detailed discussion on the response mechanism is presented in the context of literature, pointing towards the absorption of water molecules in the interlayer spacing of graphene as the main reason for the increase in resistance with RH. Additionally, a contribution from variable range hopping along the *ab* plane of graphene at high RH is suggested. These results demonstrate the potential of paper-LIG for low-cost, sustainable, and environmentally friendly sensing.

2.2.1 Introduction

Since its discovery in 2004 [1], graphene has been attracting vast amounts of interest from the scientific community [2]. This interest is motivated by the unique combination of outstanding properties which characterize graphene, such as the excellent electrical transport properties [3,4], large specific surface area [5], and flexibility [6], among many others. Besides providing a fertile ground for fundamental research, these characteristics pave the way towards a host of potential applications. One particular field where graphene can play a big role is low-cost sensing [7], specifically in the context of wearable devices [8]. Propelled by recent advances in graphene production research [9–12], this material can be used for the qualitative and quantitative detection of a wide range of stimuli, from chemical ones such as different contaminants [12,13] to physical ones such as strain and bending [14,15].

Humidity is an important parameter which can have an influence on an extensive variety of processes, including industrial operations, agricultural activity, and medical procedures [16]. Moreover, it has an impact on the general sense of comfort. Graphene and graphene-related materials have also made their claim to fame in the field of humidity sensing, with several examples of the use of pristine graphene [17,18], graphene oxide [19–21], and reduced graphene oxide (rGO) [22–24] available in the literature.

Another member of the graphene family that has been employed in humidity sensing is laser-induced graphene (LIG) [16,25–27]. Consisting of a foam-like material with multi-layered graphene pore walls, LIG can be formed by laser irradiation of a range of different polymers [10] and other materials [28]. More recently, it was shown that LIG can also be obtained by multiple lasing of wood, cork, and paper [15,29,30]. The latter is hugely important in its own right, not only for the role it has been playing throughout the history of humanity, but also for the growing field of paper electronics [31,32]. Being a low-cost, flexible, biodegradable material, while also having well-established industrial fabrication processes, paper has been employed in a wide range of electronic devices, from transistors to sensors [33–35]. Thus, laser-induced graphene formed from paper, also referred to as paper-LIG, is a powerful combination of two versatile materials that provides new possibilities for the facile and direct integration of electronic circuits and components into any paper-based object, contributing to the growing field of paper electronics [32]. So far, the use of this material, which presents a distinct morphology compared to LIG obtained from more commonly used precursors such as polyimide, has only been described in a limited number of reports [29,36–42].

In this work, we demonstrate the applicability of paper-LIG for humidity and temperature sensing. To this end, the formation of paper-LIG by single-step irradiation of cellulose paper with a pulsed 355 nm UV laser, a wavelength known to favour photochemical rather than photothermal effects and to allow a shallower penetration depth, is explored. A study of the relevant process variables, namely Q-switching frequency of the pulsed laser and the scanning speed of the beam, is undertaken, allowing us to identify trends in their influence on the resulting material and to establish relationships between structure, morphology, and electrical conductivity. Several unique peculiarities of the LIG formation process with UV laser, not observed in the case of the synthesis with the commonly employed infrared irradiation, are highlighted. Lastly, the humidity and temperature sensing capabilities of paper-LIG are explored and discussed in the context of the variable range hopping electrical conductivity model, pointing towards the response of the sensors being dominated by water intercalation in the interlayer spacing, with an additional contribution from hopping along the *ab* plane of graphene, which is favoured by the increase of humidity. The obtained sensitivity, response time, and

reproducibility highlight the potential of graphene and paper-based devices for low-cost, environmentally friendly applications, which, together with other previously reported sensing capabilities of this material, are another step towards fully integrated multisensing devices.

2.2.2 Results and discussion

2.2.2.1 Synthesis and characterization of paper-LIG by UV laser irradiation

The initial approach to the synthesis of paper-LIG by UV laser irradiation consisted in scanning the laser beam linearly across a 6×6 mm^2 area, at the focal plane. Interestingly, no visible transformation of the filter paper was observed during the initial stages of the scan (**Figure 2.2.1a**). Instead, the transformation began at a single point further into the square (highlighted in **Figure 2.2.1a**) and then appeared to expand from there with each additional scan line, forming a triangular shape (the scanning was performed along the horizontal direction, evolving from bottom to top). Additionally, even in the regions where transformation did occur, the obtained material is brown and nonconductive. Similar results were seen for laser scans performed with the filter paper out of focus, from 1 to 4 mm above the focal plane. At 5 mm, a black conductive material was obtained. At this distance to focus, during the laser scan, the incidence spot of the beam emitted a bright white light indicative of the formation of a localized plasma. This is similar to what can be seen in the formation of LIG on polyimide, for both CO_2 and UV lasers [43,44], indicating that the used parameters (including distance to focus) are close to those appropriate for LIG synthesis. However, the lack of immediate transformation at the start of the laser scan, only initiating from random spots further into the irradiated area, is still observed (**Figure S2.2.1**, **Section 2.2.6**).

It appears that a large energy barrier exists for the filter paper to be affected by the incident UV laser beam. Once this barrier is overcome at some point along the beam path, the altered cellulose fibres begin to absorb the incident energy more easily. This appears to lower the transformation energy barrier around the affected spot, as subsequent passes of the laser beam near this spot result in easier transformation. This effect is extended with each scanned line, resulting in the formation of a triangular shape, the tip of which is the location of the initial transformation. Note that there can be more than one spot where the energy barrier for the transformation is overcome, each one giving rise to a triangular shape, as seen in **Figure 2.2.1a**. Additionally, by performing the synthesis at different scanning speeds, one can see that the slope of the sides of these triangular shapes changes monotonously with the scanning speed (**Figure 2.2.1b**). This points toward a propagation effect, where the transformation at each point affects an increasingly larger area around it the longer the laser beam stays in that area. The larger this affected area is, the wider the transformed segment of the next scan line can be (**Figure 2.2.1c**), as the barrier for the transformation is lower in the affected area than in the unmodified regions of the paper. Overall, once the transformation begins at a certain location, it can spread from there to the surrounding regions.

As for the physical phenomena at the origin of this barrier behaviour, these might reside in the absorbance of cellulose in the UV spectral range. We have observed that, by slightly darkening (with a pencil, for example) a specific spot of the area to be irradiated, the initial transformation can be forced to happen at that point, as depicted in **Figure 2.2.1d**, where one (sample on the left) and three (sample on the right) dots were marked with a pencil, leading to the transformation of the paper starting at these points. Still, this approach, on its own, is not enough to

guarantee that the entire irradiated area undergoes transformation, as triangular shapes are still formed. It should be noted that we did not observe such barrier and triangular propagation behaviour under CO_2 laser irradiation, and, to the best of our knowledge, there are no reports of similar effects in the literature. Moreover, filter paper without fire retardant treatment shows a similar resistance to transformation under UV irradiation.

To overcome the issues associated with the behaviour discussed above, so that arbitrary paper-LIG shapes can be formed, we have marked the initial corner of the area to be irradiated with a small pencil dot. Next, we scanned the contour of the shape to be formed with a slow scanning speed, so that the initial transformation at the pencil mark could be carried on along the contour. This way, each line of the subsequent scan of the desired shape starts at the already transformed contour, thus having a much lower transformation barrier. In the case of a 6×6 mm² square, this approach leads to a uniformly black, electrically conductive material, with a sheet resistance of 132 Ω sq^{-1} and Raman spectra representative of LIG (**Figure 2.2.1d,e**).

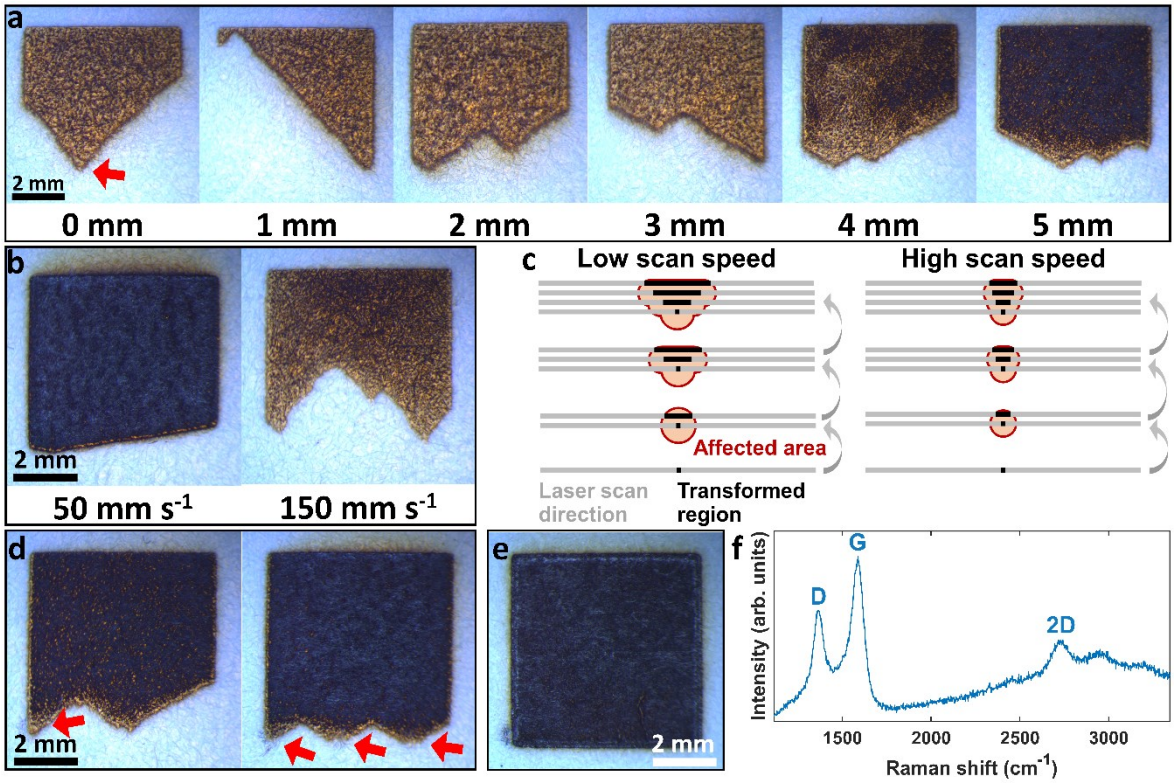

Figure 2.2.1. (a) Photographs of samples formed by laser irradiation at distances to focus ranging from 0 mm to 5 mm. The red arrow highlights the location where the transformation of paper begins. **(b)** Optical photographs of samples formed at 5 mm above the focal plane and with two different scanning speeds. **(c)** Schematic illustration of the explanation proposed for the formation of the triangular shapes seen in (a) and (b) and how their shape is affected by the scanning speed. **(d)** Optical photographs showing a forced transformation of the irradiated paper at points darkened with one (sample on the left) and three (sample on the right) pencil dots (highlighted by red arrows). **(e)** Optical photograph of a 6×6 mm² sample produced by marking the corner of the area to be irradiated with a pencil, scanning the contour with a slow scanning speed and then irradiating the whole area. **(f)** Raman spectrum of the sample in (e).

The effect of other parameters, such as Q-switching frequency and scanning speed, was assessed by systematic variation of their values, within the range of 40-80 kHz (corresponding to average laser powers of ≈380–150 mW) and of 20-140 mm s^{-1}, respectively (maintaining

the distance to focus at 5 mm). Sets of several samples were synthesized for each parameter combination, accounting for any potential lack of reproducibility. **Figure 2.2.2a** shows optical photographs of samples representative of the different parameter combinations. For low values of Q-switching frequency (corresponding to higher power and larger energy per pulse) and scanning speed, the obtained material is too brittle, cracking and breaking easily. On the other hand, at higher values of Q-switching frequency, the irradiated paper does not fully convert into a black material. **Figure 2.2.2b** shows the dependence of the sheet resistance values with the scanning speed, for different values of Q-switching frequency (for some parameter combinations no sheet resistance values were obtained, either due to the corresponding samples being non-conductive or due to a significant lack of structural integrity). The most conductive samples were obtained with low Q-switching frequency (40 and 50 kHz) and scanning speed in the range of 80 to 100 mm s^{-1}. Further insights into the crystalline structure of the obtained material can be acquired through Raman spectroscopy (**Figure 2.2.2c**). Focusing on the samples irradiated at a scanning speed of 80 mm s^{-1}, higher Q-switching frequency leads to amorphous carbon, characterized by broad D and G peaks as the only significant spectral features. For lower Q-switching frequency, on the other hand, these peaks become sharper, akin to what can be seen for high temperature treated microcrystalline cellulose as it becomes carbonized [45]. Lastly, at 50 and 40 kHz, a symmetrical 2D peak emerges, which is a hallmark of the linear dispersion found in graphene [46], with the overall spectra being similar to what has been previously reported for LIG [10,14]. The ratio of the areas of the D and G peaks allows us to determine the crystalline size along the in-plane direction (L_a) [47], giving values of 13 nm.

These results indicate that there is a specific range of parameters that lead to a better transformation of the irradiated cellulose into LIG. As Q-switching frequency and scanning speed affect the energy deposited by the laser beam per unit of irradiated area, it appears that the formation of LIG from paper is dependent on providing sufficient energy to the irradiated cellulose fibres, up to a point where the transformation begins to compromise their structural integrity, which eventually leads to cracking and breaking. The energy provided by the laser irradiation needs to be enough to ensure sufficient transformation of cellulose to amorphous carbon, as well as to promote the graphitization of the latter.

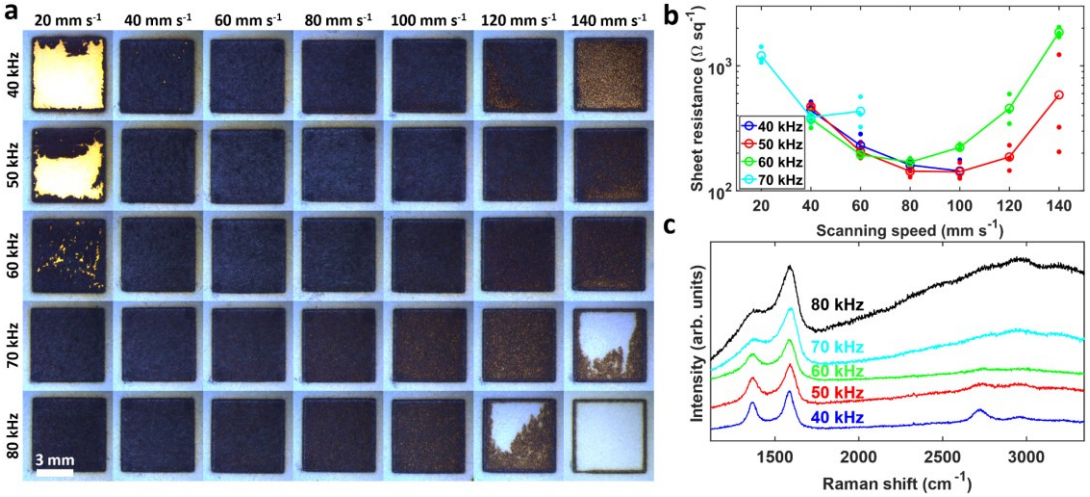

Figure 2.2.2. (a) Optical photographs of 6×6 mm^2 samples produced with different Q-switching frequencies and scanning speeds. **(b)** Sheet resistance of the conductive samples made using variable Q-switching frequency and scanning speed. The solid circles correspond to individual samples while the open ones are the corresponding average values. The lines are guides to the eye. **(c)** Raman spectra representative of samples produced with five different Q-switching frequencies, at a scanning speed of 80 mm s^{-1} (central column of (a)).

Secondary electron scanning electron microscopy (SE-SEM) images of some of the samples were acquired, to better understand the morphology and the internal structure of the produced material (**Figure 2.2.3**, with a cross-section image in **Figure S2.2.2**, **Section 2.2.6**). For all the analysed scanning speed and Q-switching frequency combinations, a clear fibrous structure can be seen. The fibres appear to be packed more tightly, closely resembling the non-irradiated paper, at faster scanning speed, which can be explained by the fact that a higher value for this parameter corresponds to less power being delivered per unit of irradiated area (thus better preserving the original structure of the paper). Additionally, the irradiated fibres seem to undergo a porosity formation process. For higher scanning speed, the pores are relatively small, with some appearing to be closed, like blisters, while for lower scanning speed they are larger and open. Overall, this leads to the conclusion that the transformation of cellulose into LIG follows a sequence where blisters are formed, grow, and eventually open as their walls become thinner and thinner. The more energy is delivered to the cellulose fibres, the further they undergo this process, which also leads to the breaking of some of the fibres. This porosity formation has also been observed in paper-LIG formation with CO_2 laser irradiation [48], and is reminiscent of what happens in phosphoric acid activation of cellulosic material (paper, wood, etc.) to obtain, through a thermal treatment, activated carbon. In this activation process, the bond cleavage induced by the phosphoric acid leads to an initial contraction of the material, followed by porosity development enabled by the formation of crosslinks through phosphate linkages [49–51]. These linkages also play an important role in blocking the transformation of cellulose into volatile levoglucosan, hinting towards a similar process preventing the ablation of cellulose under laser irradiation thanks to the phosphate-based fire retardant treatment employed here [49].

It is also relevant to note that the mechanical and structural integrity of the obtained paper-LIG is good. Compared to LIG from other materials, such as polyimide for example, which can be easily damaged under physical contact, paper-LIG tends to have a more cohesive internal structure, most likely due to the flexibility of the intertwined cellulose fibres of the precursor paper. Even under strain or bending the electrical properties of this material (and, accordingly, its sensing performance) are not affected significantly, as shown previously [48].

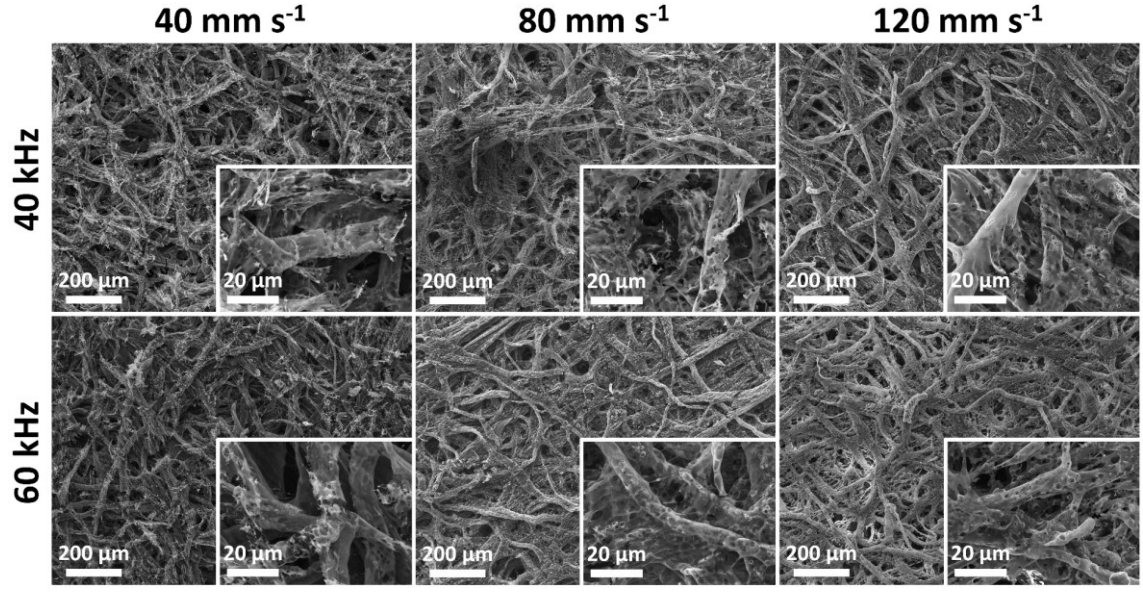

Figure 2.2.3. SE-SEM images of samples produced with variable Q-switching frequency and scanning speed.

Additional characterization was performed by transmission electron microscopy (TEM), using a sample synthesized with a Q-switching frequency of 40 kHz and a scanning speed of 80 mm s^{-1}. The obtained images (**Figure 2.2.4**) show a dense distribution of graphene structures with 5–6 layers, on average, appearing as curved and bent flakes. The interlayer distances correspond to 0.35 nm, slightly larger than the 0.34 nm interlayer spacing of LIG obtained from polyimide [10]. The lateral dimensions of these structures along the in-plane direction were measured to be 5 to 10 nm, on average, corroborating the previously discussed crystalline size estimation from the ratios of the integrated areas of the D and G peaks of the Raman spectra. Generally, the material between the flakes does not seem to present a well-defined crystalline structure, pointing towards a disordered phase.

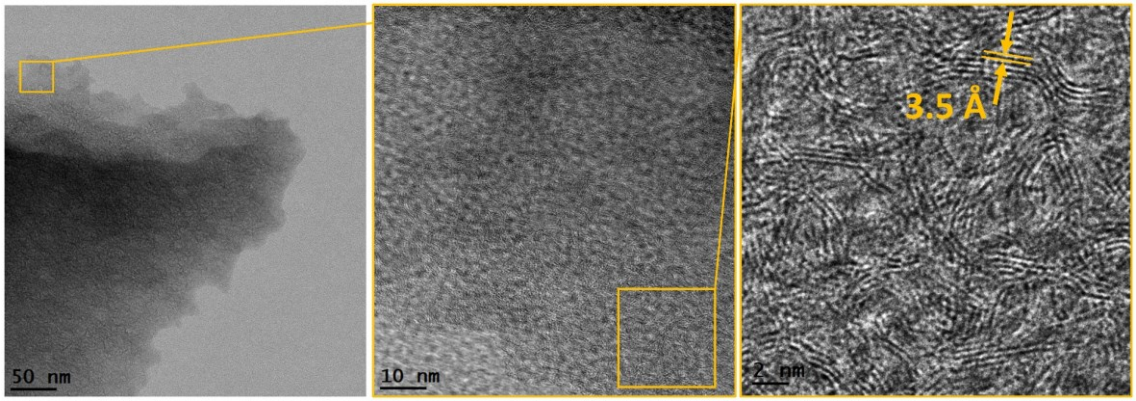

Figure 2.2.4. TEM images of a sample produced using a Q-switching frequency of 40 kHz and a scanning speed of 80 mm s^{-1}. In the rightmost panel of the image, the yellow lines highlight the individual layers of the graphene flakes, with an interlayer distance of 0.35 nm.

The chemical composition of the produced material, namely for a Q-switching frequency of 40 kHz and scanning speed of 80 mm s^{-1}, was assessed by X-ray photoelectron spectroscopy (XPS) and compared to the paper prior to irradiation. The survey spectrum **(Figure 2.2.5a**) reveals the presence of C and O, as well as N and P. The first two are to be expected in paper, as the constituents of cellulose, and also in LIG, with the oxygen potentially pointing towards a partial oxidation of the laser-induced graphene (due to synthesis in air) or to unconverted cellulose. As for N and P, these most likely come from the fire retardant used to treat the paper prior to irradiation, being present in the commonly used phosphate-based fire retardants.

Focusing on the high-resolution spectrum of the C1s peak of paper-LIG, it can be deconvoluted into seven peaks: three C–C components (low, primary, and high, with the primary being an asymmetrical one), at 283.80, 284.37, and 284.92 eV, respectively, C–O at 286.14 eV, C=O at 287.41 eV, COO at 288.90, and π–π* satellite at 291.76 eV, consistent with the components found in C1s XPS spectra of cellulose chars (**Figure 2.2.5b**) [52]. The primary C–C component is typically assigned to aromatic C–C/C–H bonds, while the other two peaks have been attributed to different defective carbon structures, and, in the case of the one at ≈285 eV, to sp^3 carbons. The presence of the C–C/C–H component is consistent with the graphitization that is expected to occur in the formation of LIG under laser irradiation. There is also a prominent C–O component, as well as components corresponding to other oxygen-containing functional groups. These can be justified by a partial oxidation of the laser-induced graphene or by the presence of some unconverted cellulose. Nonetheless, these components are considerably less pronounced than in the case of paper coated with the fire retardant prior to irradiation, once again showing the conversion of cellulose into graphitic carbon (**Figure 2.2.5b**). Also

supporting this idea are the D-parameters obtained from the differentiated C KLL Auger features (**Figure S2.2.3**, **Section 2.2.6**). While in the case of paper this parameter has a value of 12.7 eV, typical of sp^3-rich carbon, in paper-LIG the D-parameter is 15.2 eV, closer to the values seen for sp^2-rich carbons [53].

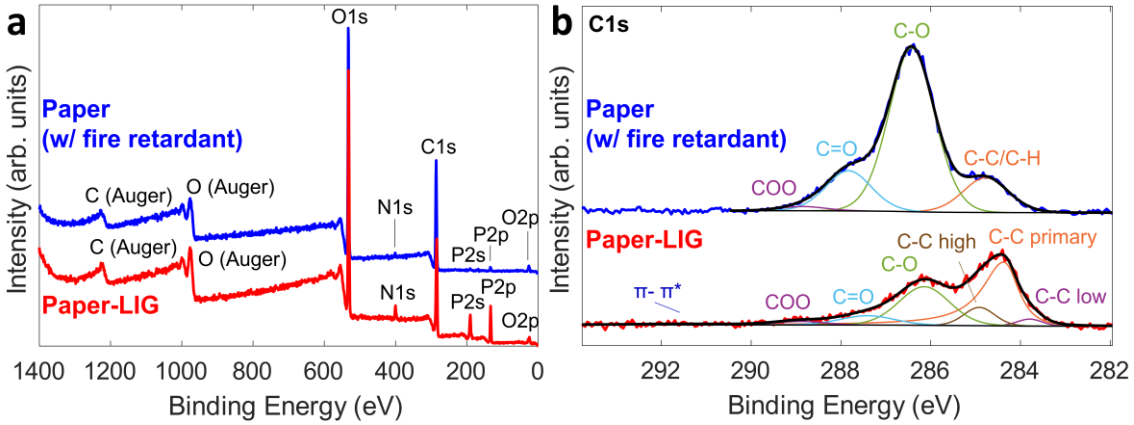

Figure 2.2.5. (a) XPS overview comparing fire retardant treated paper and paper-LIG. **(b)** High-resolution XPS spectra of the C1s peaks of the same samples, with the respective deconvolutions.

2.2.2.2 Paper-LIG humidity and temperature sensors

The apparent porous and fibrous nature of the paper-LIG, coupled with its electrical conductivity, make it attractive for application in humidity sensing. Thus, we have fabricated simple, flexible, low-cost, and environmentally friendly devices, consisting of 6×20 mm^2 paper-LIG conductive paths produced using a Q-switching frequency of 40 kHz and a scanning speed of 80 mm s^{-1} (**Figure 2.2.6a**). To test their sensitivity to humidity, these devices were placed inside a climatic chamber at 20 °C, where the humidity was varied in steps of 10% of relative humidity (RH), from 10% to 90%, with additional steps at 95% and 98% RH, and then descending again step by step to 10%. Each step lasted ≈1 h.

Figure 2.2.6b shows the response of the electrical resistance (blue trace) to variable relative humidity conditions in the chamber (orange trace). The resistance increases in response to the rise of the relative humidity. Overall, there is a clear stepwise response to each humidity condition, apart from RH values above 60% in the descending portion of the measurement. This difficulty in resolving the individual steps corresponding to the RH values in this range seems to be originated by the gradual drift of the resistance towards lower values, the slope of which is more pronounced at higher relative humidity. It should also be noted that the resistance values corresponding to each RH value in the descending part of the measurement are slightly higher than the corresponding ones in the ascending part. A slower water desorption can explain this effect, as in this case water would be partially retained in the sensor after exposure to high humidity, resulting in larger resistance values than when arriving at the same RH value from a less humid condition. Another interesting feature is the occurrence of spikes in the resistance values each time the relative humidity is lowered. This can be explained by a small temperature decrease (with a subsequent return to equilibrium) of the sensor due to the endothermic nature of the water desorption process, as is discussed further below [54].

To evaluate the linearity of the fabricated sensor, the last ≈5 min of each humidity stage were considered, and the corresponding resistance values were plotted against the relative humidity. By performing a linear regression (**Figure 2.2.6c**), it can be seen that the sensor displays a

fairly linear response, with coefficients of determination (r^2) of 0.988 and 0.981 for the ascending and descending parts of the experiment, respectively. The linearization also allows us to quantify the sensitivity of the sensor, by looking at the relative change in the resistance per RH percentage unit, giving values of 1.3×10^{-3}% RH^{-1} and 1.0×10^{-3}% RH^{-1} (uncertainties of $\approx10^{-5}$% RH^{-1} or smaller) for the ascending and descending humidity ranges, respectively (considering the resistance at 50% RH in the ascending portion of the measurement as the reference value). Both the coefficient of determination and the sensitivity values underline a slightly worse performance of the sensor in the regime where the relative humidity decreases, as has been pointed out in relation to **Figure 2.2.6b**.

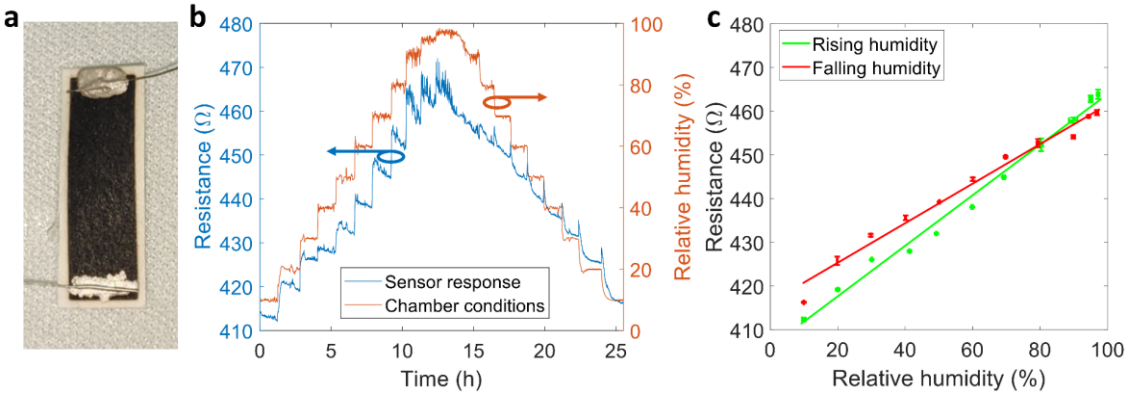

Figure 2.2.6. (a) Photograph of a paper-LIG humidity sensor (the paper-LIG area is 6×20 mm^2). **(b)** Resistance of the paper-LIG humidity sensor (blue trace) in response to different relative humidity conditions as measured by the climatic chamber's capacitive sensor (orange trace). **(c)** Electrical resistance of the paper-LIG sensor as a function of the reference relative humidity, measured in the last ≈5 min of each relative humidity stage of the experiment shown in (b) (green trace for increasing RH, red trace for decreasing RH). The error bars correspond to the standard deviation with respect to the mean values.

The response time of the paper-LIG humidity sensor was also evaluated. To achieve this, the sensor was placed above a saturated aqueous solution of potassium acetate, in a volumetric flask, and then subjected to a discontinuous change in humidity by quickly moving it to another flask containing a saturated aqueous solution of potassium chloride. The solutions ensure equilibrium RH values (at ≈20 °C) of 23% and 85%, respectively. The sensor was moved between the two flasks several times, to obtain both the rise (response to an increase in RH) and fall (response to a decrease in RH) times, defined as the time to reach 90% of the steady-state response. The obtained rise time was 95 s, while the fall time reached 637 s (**Figure 2.2.7**). This gives credence to the previously presented idea that water desorption takes a longer time than sorption in paper-LIG, something which is also commonly seen in other humidity sensors [19,23].

Additional tests were performed to examine stability and reproducibility of the paper-LIG humidity sensor. To this end, the relative humidity conditions were cyclically alternated between 20%, 50%, and 80% RH, at a fixed temperature, with each condition lasting between one to several hours (**Figure S2.2.4**, **Section 2.2.6**). The observed behaviour is similar to the one seen in **Figure 2.2.6b**, particularly in the first cycle, where for each RH value the resistance was higher in the decreasing humidity portion of the measurement compared to the increasing one. However, the response profile stabilized in the following cycles, yielding approximately the same resistances independently of the previous RH value, indicating that a preconditioning step at high humidity can reduce the hysteresis of the sensor. The gradual drift towards lower resistance values at each RH stage can also be seen here. However, it is worth pointing out that

this drift is fairly slow, with the resistance lowering by only ≈0.35% per hour. The stability of the paper-LIG sensors with respect to temperature was also evaluated, with the measurements presented in **Figure 2.2.6b** having been repeated for temperatures of 30, 40, and 50 °C, going back to 20 °C for the last cycle. The results show that the overall profile of the sensor response to each relative humidity value remains the same at each temperature, with the resistance showing a descending trend as the temperature is increased (**Figure S2.2.5**, **Section 2.2.6**).

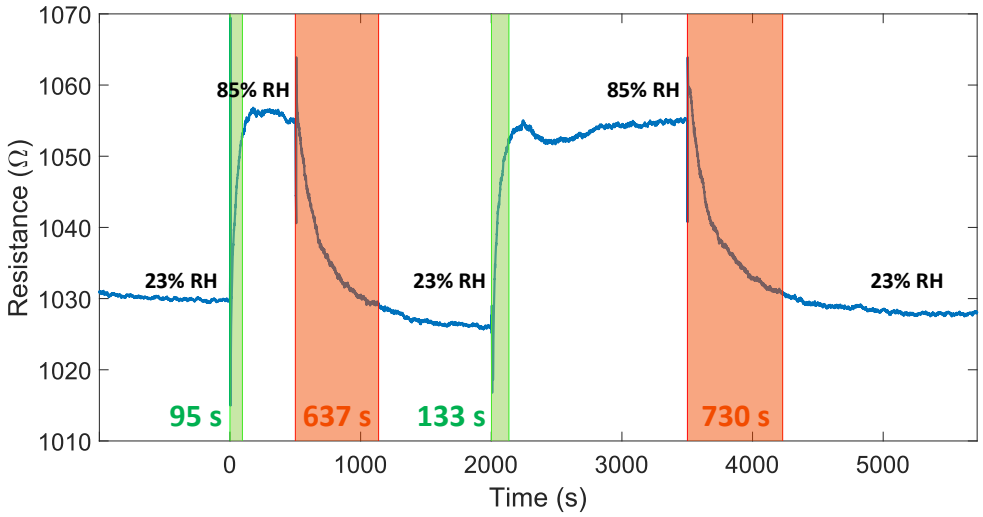

Figure 2.2.7. Response time of the paper-LIG humidity sensor to step-like increase (in green) and decrease (in red) of relative humidity, from 23% to 85% RH and vice-versa.

As to what concerns the response mechanism of this type of humidity sensor employing graphene and graphene-based materials, it is important to begin by noting the contradictory reports found in the literature. For instance, the resistance has been observed to decrease with relative humidity in some sensors featuring bilayer graphene [17], a graphene/polypyrrole composite [55], and rGO [23], among others. To explain such a decrease several authors resort to the idea of ionic conduction through adsorbed water, which increases as more H_2O molecules adsorb on the surface of the sensing material [17,55]. The decrease in resistance with relative humidity has also been ascribed to doping effects by the adsorbed water molecules [18,56]. The increase of the resistance of graphene-type materials in response to increasing relative humidity has also been reported [57]. This is explained by considering water as an electron donor dopant to graphene, which often presents p-type doping, thus reducing the charge carrier density in graphene and its conductivity. Others have suggested the intercalation of water between the graphene layers, with an effect on the overlap areas of adjacent graphene or graphene-based sheets, which also increases the overall electrical resistance [24]. The underlying reasons for such conflicting reports have been addressed by Popov et al., who fabricated CVD graphene sensors with different morphologies (different thicknesses on different substrates) and observed both an increase and a decrease of the resistance, as well as a mixed non-monotonous behaviour, depending on the morphology of the synthesized material [58]. Their explanation relies on the competition between two distinct mechanisms, one related to water adsorption at grain boundary defects and another at edge defects in multilayer regions.

In the present work, we observe a strictly increasing resistance in response to the rise of relative humidity. The fact that our sensors are paper based could potentially point towards the

swelling of the cellulose (or partially transformed cellulose) fibres as the culprit behind the resistance increase with the relative humidity. This has indeed been proposed in some works involving conductive carbon based materials on paper [59,60]. More specifically, the idea is that the swelling of the hygroscopic cellulose fibres due to humidity, which is known to be as large as 20% in the thickness direction in paper made from chemical pulp [61], leads to an increased separation between the conductive carbon based elements, thus disturbing the percolative network. However, given that other humidity sensors which had no presence of paper or cellulose of any kind, such as the one described by Zaharie-Butucel et al. [24], show a response very similar to ours, we are led to believe that another mechanism may be at play. Among those described above, doping effects and intercalation of water between the basal planes of graphene crystallites seem like the most promising ones. Further discussion on this subject is presented below in the context of the effect of temperature on the resistance/humidity dependence.

In order to better evaluate the paper-LIG sensor response to temperature, they were subjected to a stepwise increase and decrease in temperature between 10 and 60 °C (in steps of 10 °C), for three distinct RH values (20%, 50%, and 80%). **Figure 2.2.8a** shows a clear response to each temperature, with the resistance following the same trend as in **Figure S2.2.5**, **Section 2.2.6** (decrease in resistance as the temperature rises). The sensor behaviour was particularly stable and reproducible at 20% RH, with only a small degree of drifting towards lower resistance values at each temperature stage, and with the resistances being approximately the same at the same temperature in the ascending and descending portions of the test. This can be seen clearly in **Figure 2.2.8b**, where the data corresponding to the last 5 min of each temperature stage was used to perform linear regression, with the continuous lines corresponding to the ascending temperature parts of the measurement and the dashed lines corresponding to the descending ones. Overall, the sensor shows good linearity, with coefficients of determination close to or above 0.99. The highest sensitivity is obtained at 50% RH, in the rising temperature part, giving a value of -2.8×10^{-3} °C^{-1}, while attaining -2.4×10^{-3} °C^{-1} (uncertainties of $\approx10^{-5}$ °C^{-1} or below) at both 20% and 80% RH (considering the resistances at 20 °C in the ascending portion of the measurement at each RH stage as the corresponding reference values). The sensitivity is always slightly smaller for the descending temperature part, being -2.2×10^{-3} °C^{-1} at 20% and 50% RH and -2.0×10^{-3} °C^{-1} at 80% RH.

We also note that this dependence on temperature sheds light on the resistance spikes each time the relative humidity is lowered, seen in **Figure 2.2.6b** and **Figure S2.2.5** (**Section 2.2.6**). As mentioned before, the desorption of water is an endothermic process and as such can lower the sensor temperature for a short period of time when the relative humidity is lowered. The spikes have an amplitude of up to 5 Ω, which, given the sensitivity in response to temperature, would correspond to a temperature decrease of ≈5 °C. These temperature dependence tests allow us to gain further insight into the response mechanism of these sensors. One started by testing the hypothesis of a possible contribution of proton transport by representing the data according to the Arrhenius law $\sigma=\sigma_0\exp(-E_a/kT)$, where σ_0 is a pre-exponential factor, k is the Boltzmann constant and E_a is the activation energy. **Figure S2.2.6** (**Section 2.2.6**) shows that the data can indeed follow the Arrhenius dependence, but the obtained activation energy values are close to 40 meV, which is considerably lower than the activation enthalpy reported for proton conductivity on various kinds of materials [62], namely rGO [63]. Any significant contribution of ionic transport to the electrical conductivity of the paper-LIG should thus be ruled out.

As discussed previously, paper-LIG appears to consist of small (5–10 nm) few-layer graphene domains surrounded by disordered material. The electrical conduction in such systems lends itself nicely to description by the 2D Mott variable range hopping (2D Mott VRH) model, which was previously applied to discuss the electrical conductivity in chemically and thermally reduced graphene oxides [64,65] and graphene-based composites [66,67]. This model can describe the electrical conduction in disordered materials where there is a considerable density of overlapping localized states near the Fermi level. In such a case, the electrical conductivity σ assumes the following form (**Equation 2.2.1**):

$$\sigma(T) = \sigma_0 \exp\left(-\frac{B}{T^{1/3}}\right) \tag{2.2.1}$$

where σ_0 is the pre-exponential factor and B is the hopping parameter dependent on the density of states near the Fermi level $N(E_F)$ and on the electronic wavefunction localization length. Here, one assumes that the electrical transport occurs trough the hopping of the carriers between the pristine graphene domains along the *ab* plane. **Figure 2.2.8c** shows the data in terms of ln(1/resistance) versus $T^{-1/3}$, with the resulting parameters of the fittings to **Equation 2.2.1** listed in **Table 2.2.1**. The magnitude of these B estimates is in line with literature data for composites containing graphene nanoplatelets in a dielectric ceramic matrix [66,67], or for rGO monolayers (≈20.5 $K^{1/3}$) [64].

It can be seen that the estimate for the hopping parameter B (close to 14 $K^{1/3}$) in the low humidity test conditions (20% and 50% RH) and within the entire temperature range (10–60 °C) is roughly constant. This indicates that, overall, the density of states near the Fermi level does not change significantly, rendering any doping effects by the adsorbed water molecules unlikely to be the main response mechanism of these sensors. One may invoke the absorption of water molecules in the interlayer spacing to explain the increase of the resistance with increasing humidity, at least for the lower relative humidity, because the data collected at 80% RH suggests that other contributions may be at play, especially at higher temperatures. Indeed, the data collected above 40 °C denotes a distinct lowering of B down to values of the order of 9 $K^{1/3}$, potentially pointing towards the presence of another mechanism active in this temperature range. Assuming that the density of states near the Fermi level does not change, this suggests that water may be actively contributing to facilitate hopping along the *ab* planes by increasing the overlap of the electronic localization wavefunctions of the pure graphene domains. However, if this would be the dominating effect, one would expect a decrease of the resistance with increasing humidity, which is not the case. To explain both observations—the increase of the electrical resistance and the decrease of the hopping parameter with increasing humidity—one may consider the existence of two electric transport paths in series within the material: one ascribed to the hopping along the *ab* plane of the graphene, which is favoured by the increase of humidity and has a weaker temperature dependence, and another which tends to dominate the overall resistance in the selected test conditions, resulting from the resistance offered by the graphene domain interfaces and/or along the direction perpendicular to the *ab* plane, where water is known to diffuse into the increasing interlayer spacing. The latter may also introduce additional kinetic limitations that could account for the significant transient effects observed at RH higher than ≈70% (**Figure 2.2.6b**).

Further detailed studies of the effect of the temperature and humidity on the resistance of paper-LIG materials prepared with a different microstructure, namely the graphene domain size, could provide the desired insight into the underlying transport mechanisms. This will allow further optimization of the already extremely attractive sensing properties of these materials.

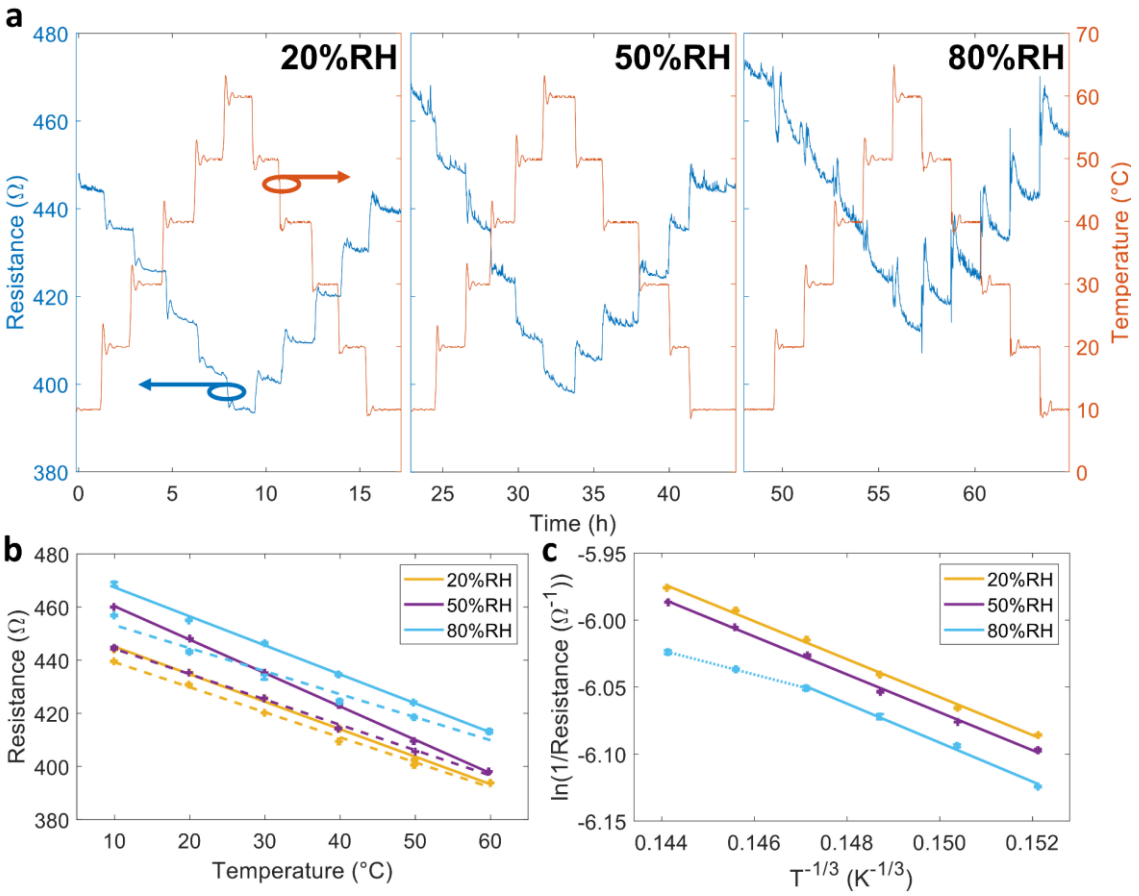

Figure 2.2.8. (a) Resistance of the paper-LIG humidity sensor (blue trace) in response to different temperature conditions as measured by the temperature sensor of the climatic chamber (orange trace), for 20%, 50%, and 80% RH. **(b)** Linear regression of the resistance values of the paper-LIG sensor in the last ≈5 min of each temperature stage as a function of the corresponding temperature, in the ascending (solid lines) and descending (dashed lines) parts of the experiment shown in (a). The error bars correspond to the standard deviation with respect to the mean values. **(c)** Natural logarithm of the inverse of the resistance plotted according to the 2D Mott variable range hopping (2D Mott VRH) model. We have considered the parts of the measurement where the temperature was decreasing, to account for the drift towards lower resistance values at each relative humidity. The dotted line portion is a linear fitting, highlighting a weaker temperature dependence (smaller hopping parameter) in the range above 40 °C for 80% RH. The error bars correspond to the standard deviation.

2.2.3 Conclusions

In this work, laser-induced graphene was obtained by single-step irradiation of filter paper with a pulsed UV laser (355 nm). Some peculiarities of the synthesis process were revealed, such as the lack of immediate transformation of the irradiated cellulose fibres and a transformation propagation behaviour, where the affected area increases with each subsequent scanning line. Overall, the obtained paper-LIG consists of porous fibres composed of 5–10 nm few-layer graphene flakes and shows good electrical conductivity (as low as 125 Ω sq^{-1}). This material was employed for humidity and temperature sensing, with the sensors showing excellent linearity and sensitivities of 1.3×10^{-3}% RH^{-1} and -2.8×10^{-3} $°C^{-1}$, respectively. Lastly, the response mechanisms of these sensors were discussed, particularly in the context of 2D Mott variable range hopping model, pointing towards the absorption of water molecules in the interlayer spacing of graphene as the main reason for the increase in resistance with RH, together

with an additional contribution from variable range hopping along the *ab* plane of graphene at high RH. These results demonstrate the potential of paper-LIG for low-cost and environmentally friendly sensing applications.

Table 2.2.1. Fitting parameters of the 2D Mott VRH model applied to the temperature dependence data collected under variable relative humidity.

	Hopping parameter, *B* [$K^{1/3}$]	**Intercept**	**Coefficient of determination, r^2**
20% RH	14.1459 ± 0.0286	−3.9342 ± 0.0042	0.9972
50% RH	14.1468 ± 0.0242	−3.9469 ± 0.0036	0.9978
80% RH (up to 40 °C)	14.5542 ± 0.0575	−3.9084 ± 0.0086	0.9927
80% RH (above 40 °C)	9.0219 ± 0.0519	−4.7234 ± 0.0076	0.9884

2.2.4 Materials and methods

2.2.4.1 LIG formation

Cellulose filter paper (290 μm of thickness, 80 g m^{-2}, hardened, 0.02% ash content, by Prat Dumas) was sprayed with a commercial phosphate-based fire retardant (AntiFlame by BBT), prior to irradiation by a 3 W 355 nm diode-pumped Nd:YVO_4 pulsed laser (by Inngu Laser), scanned linearly with the line separation set at 0.01 mm using an F-Theta lens (*f*=160 mm). The parameters varied throughout this work were distance to focus (above the focal plane), Q-switching frequency, and scanning speed.

2.2.4.2 Materials characterization

Optical photographs of the samples were acquired with a UI-3880CP-C-HQ R2 CMOS 6.41 MP camera (by IDS) through a stereo microscope, using simultaneously front and back lighting. Secondary electron SEM images were acquired using a Vega 3 SBH system (by TESCAN), with an acceleration voltage of 15 kV and a working distance of 15 mm. Raman spectroscopy was performed using a Jobin Yvon HR800 Raman system (by Horiba) and a He-Cd 441.6 nm laser (by Kimmon), with a ×50 lens (NA=0.5, by Olympus). Each spectrum is the average of five consecutive 20 s acquisitions. A neutral density filter (OD=1) was used to attenuate the laser power in order to prevent any potential thermally induced chemical modification of the samples. Sheet resistance measurements were performed by the van der Pauw method, using a Keysight B2902A dual-channel source meter unit. Measurements for several equivalent samples were made. XPS spectra were acquired in an Axis Supra Spectrometer by Kratos Analytical using monochromatized Al Ka radiation. The pass energy was 160 eV for survey scans and 5 eV for detailed scans. The XPS spectrum of paper was corrected by taking the C−C/C−H peak as reference (284.8 eV). All the fittings were performed with CasaXPS Version 2.3.19PR1.0. High-resolution transmission electron microscopy (HR-TEM) was performed employing a Field Emission Microscope Jeol JEM-2200FS, operated in imaging mode, at 200 kV. The samples were prepared by gently scraping the LIG from the underlying paper and dispersing the obtained material in isopropyl alcohol. A drop of this dispersion was placed onto a holey carbon film

copper grid and left to evaporate in air. The acquired images were processed using ImageJ and Digital Micrograph version 3.42.3055.0 (Gatan Inc.) software.

2.2.4.3 Humidity and temperature sensor fabrication and testing

The paper-LIG humidity sensors were made by scanning the 355 nm laser over the fire retardant treated filter paper following a rectangular shape over a 6×20 mm^2 area. A Q-switching frequency of 40 kHz and a scanning speed of 80 mm s^{-1} were used. The sensors were rinsed with 150 mL of deionized (DI) water to remove any residues from the fire retardant. This washing protocol was established on the basis of an increase in the conductivity of the effluent DI water, most likely due to salts contained in the fire retardant used to treat the paper. This conductivity drops to negligible values after the washing procedure is completed. Silver paste (Electrodag 1415) was used to connect tin coated 20 awg copper wires to the opposite edges of the rectangular sensors, and the surrounding unprocessed paper was cut away.

The response of the sensors to various relative humidity conditions at different temperatures was tested in an Angelantoni ACS 110 climatic chamber equipped with a Rotronic capacitive humidity probe and a Pt100 Class A thermal probe. The humidity was varied in steps of 10% RH, from 10% to 90% RH, with additional steps at 95% and 98% RH, and back to 10% RH. Each step lasted for ≈1 h, and the whole cycle was repeated for 20, 30, 40, and 50 °C, going back to 20 °C for the last cycle. For temperature response tests, the temperature inside the chamber was varied from 10 to 60 °C and back to 10 °C, in 10 °C steps. This was done at three fixed RH values: 20%, 50%, and 80%. The resistance of the sensors was measured by the Keysight B2902A source meter unit, applying a constant voltage of 0.5 V (to avoid any potential electrolysis of water at high relative humidity) and measuring the current across the sensor at a sampling rate of 5 Hz.

Stability and reproducibility measurements were performed in the same climatic chamber, by cyclically alternating the conditions between 20%, 50%, and 80% RH at a fixed temperature, with each condition lasting from 1 to 8 h.

The response time was measured at room temperature (≈20 °C) by quickly moving a sensor from one large volumetric flask containing a saturated aqueous solution of CH_3CO_2K (corresponding to 23% RH) to another one containing a saturated aqueous solution of KCl (corresponding to 85% RH), while monitoring the resistance of the sensor with the Keysight B2902A source meter unit. The time to reach 90% of the steady-state response was considered as the response time.

Acknowledgements

This work was developed within the scope of project i3N, UIDB/50025/2020 and UIDP/50025/2020, and project CICECO-Aveiro Institute of Materials, UIDB/50011/2020 and UIDP/50011/2020, financed by national funds through the Portuguese Foundation for Science and Technology/MCTES (FCT I.P.). B.K. and A.F.C. acknowledge the PhD grants SFRH/BD/141525/2018 and DAEPHYS-FCT PD/BD/114063/2015, respectively, both financed by FCT I.P. E.F. acknowledges the European Research Council AdG grant 787410 from the project DIGISMART. The research contracts of P.B. and A.V.G. are funded by national funds (OE), through FCT I.P., in the scope of the framework contract foreseen in the numbers 4, 5, and 6 of article 23, of the Decree-Law 57/2016, of August 29, changed by Law 57/2017, of July 19.

2.2.5 References

[1] K.S. Novoselov, A.K. Geim, S. V. Morozov, D. Jiang, Y. Zhang, S. V. Dubonos, I. V. Grigorieva, A.A. Firsov, "Electric field effect in atomically thin carbon films," *Science*, 306, 666–669, **2004**. https://doi.org/10.1126/science.1102896.

[2] A.C. Ferrari, F. Bonaccorso, V.I. Fal'ko, K.S. Novoselov, S. Roche, P. Bøggild, S. Borini, F.H.L. Koppens, V. Palermo, N.M. Pugno, J.A. Garrido, R. Sordan, A. Bianco, L. Ballerini, M. Prato, E. Lidorikis, J. Kivioja, C. Marinelli, T. Ryhänen, A.F. Morpurgo, J.N. Coleman, V. Nicolosi, L. Colombo, A. Fert, M. Garcia-Hernandez, A. Bachtold, G.F. Schneider, F. Guinea, C. Dekker, M. Barbone, Z.Z. Sun, C. Galiotis, A.N. Grigorenko, G. Konstantatos, A. Kis, M.I. Katsnelson, L.M.K. Vandersypen, A. Loiseau, V. Morandi, D. Neumaier, E. Treossi, V. Pellegrini, M. Polini, A. Tredicucci, G.M. Williams, B. Hee Hong, J.-H. Ahn, J. Min Kim, H. Zirath, B.J. van Wees, H. van der Zant, L. Occhipinti, A. Di Matteo, I.A. Kinloch, T. Seyller, E. Quesnel, X.L. Feng, K.B.K. Teo, N.L. Rupesinghe, P.J. Hakonen, S.R.T. Neil, Q. Tannock, T. Löfwander, J.M. Kinaret, "Science and technology roadmap for graphene, related two-dimensional crystals, and hybrid systems," *Nanoscale*, 7, 4598–4810, **2015**. https://doi.org/10.1039/C4NR01600A.

[3] K.I.I. Bolotin, K.J.J. Sikes, Z. Jiang, M. Klima, G. Fudenberg, J. Hone, P. Kim, H.L.L. Stormer, "Ultrahigh electron mobility in suspended graphene," *Solid State Commun.*, 146, 351–355, **2008**. https://doi.org/10.1016/j.ssc.2008.02.024.

[4] C. Stampfer, F. Haupt, T. Taniguchi, M. Schmitz, L. Banszerus, K. Watanabe, M. Oellers, J. Dauber, S. Engels, B. Beschoten, "Ultrahigh-mobility graphene devices from chemical vapor deposition on reusable copper," *Sci. Adv.*, 1, e1500222, **2015**. https://doi.org/10.1126/sciadv.1500222.

[5] M.D. Stoller, S. Park, Y. Zhu, J. An, R.S. Ruoff, "Graphene-Based Ultracapacitors," *Nano Lett.*, 8, 3498–3502, **2008**. https://doi.org/10.1021/nl802558y.

[6] K.S.K.S. Kim, Y. Zhao, H. Jang, S.Y. Lee, J.M. Kim, K.S.K.S. Kim, J.-H.H. Ahn, P. Kim, J.-Y.Y. Choi, B.H. Hong, "Large-scale pattern growth of graphene films for stretchable transparent electrodes," *Nature*, 457, 706–710, **2009**. https://doi.org/10.1038/nature07719.

[7] A.F. Carvalho, B. Kulyk, A.J.S. Fernandes, E. Fortunato, F.M. Costa, "A Review on the Applications of Graphene in Mechanical Transduction," *Adv. Mater.*, 2101326, **2021**. https://doi.org/10.1002/adma.202101326.

[8] H. Kim, J.-H. Ahn, "Graphene for flexible and wearable device applications," *Carbon*, 120, 244–257, **2017**. https://doi.org/10.1016/j.carbon.2017.05.041.

[9] B. Kulyk, A.F. Carvalho, A.J.S. Fernandes, F.M. Costa, "Millimeter sized graphene domains through in situ oxidation/reduction treatment of the copper substrate," *Carbon*, 169, 403–415, **2020**. https://doi.org/10.1016/j.carbon.2020.08.002.

[10] J. Lin, Z. Peng, Y. Liu, F. Ruiz-Zepeda, R. Ye, E.L.G.G. Samuel, M.J. Yacaman, B.I. Yakobson, J.M. Tour, "Laser-induced porous graphene films from commercial polymers," *Nat. Commun.*, 5, 1–8, **2014**. https://doi.org/10.1038/ncomms6714.

[11] D.X. Luong, K. V. Bets, W.A. Algozeeb, M.G. Stanford, C. Kittrell, W. Chen, R. V. Salvatierra, M. Ren, E.A. McHugh, P.A. Advincula, Z. Wang, M. Bhatt, H. Guo, V. Mancevski, R. Shahsavari, B.I. Yakobson, J.M. Tour, "Gram-scale bottom-up flash graphene synthesis," *Nature*, 577, 647–651, **2020**. https://doi.org/10.1038/s41586-020-1938-0.

[12] A.C. Marques, A.R. Cardoso, R. Martins, M.G.F. Sales, E. Fortunato, "Laser-Induced Graphene-Based Platforms for Dual Biorecognition of Molecules," *ACS Appl. Nano Mater.*, 3, 2795–2803, **2020**. https://doi.org/10.1021/acsanm.0c00117.

[13] A.R. Cardoso, A.C. Marques, L. Santos, A.F. Carvalho, F.M. Costa, R. Martins, M.G.F. Sales, E. Fortunato, "Molecularly-imprinted chloramphenicol sensor with laser-induced graphene electrodes," *Biosens. Bioelectron.*, 124–125, 167–175, **2019**. https://doi.org/10.1016/j.bios.2018.10.015.

[14] A.F. Carvalho, A.J.S. Fernandes, C. Leitão, J. Deuermeier, A.C. Marques, R. Martins, E. Fortunato, F.M. Costa, "Laser-Induced Graphene Strain Sensors Produced by Ultraviolet Irradiation of Polyimide," *Adv. Funct. Mater.*, 28, 1–8, **2018**. https://doi.org/10.1002/adfm.201805271.

[15] A.F. Carvalho, A.J.S. Fernandes, R. Martins, E. Fortunato, F.M. Costa, "Laser-Induced Graphene Piezoresistive Sensors Synthesized Directly on Cork Insoles for Gait Analysis," *Adv. Mater. Technol.*, 5, 2000630, **2020**. https://doi.org/10.1002/admt.202000630.

[16] C. Lv, C. Hu, J. Luo, S. Liu, Y. Qiao, Z. Zhang, J. Song, Y. Shi, J. Cai, A. Watanabe, "Recent Advances in Graphene-Based Humidity Sensors," *Nanomaterials*, 9, 422, **2019**. https://doi.org/10.3390/nano9030422.

[17] M. Chen, C. Hsu, T. Hsueh, "Fabrication of Humidity Sensor Based on Bilayer Graphene," *IEEE Electron Device Lett.*, 35, 590–592, **2014**. https://doi.org/10.1109/LED.2014.2310741.

[18] A.D. Smith, K. Elgammal, F. Niklaus, A. Delin, A.C. Fischer, S. Vaziri, F. Forsberg, M. Råsander, H. Hugosson, L. Bergqvist, S. Schröder, S. Kataria, M. Östling, M.C. Lemme, "Resistive graphene humidity sensors with rapid and direct electrical readout," *Nanoscale*, 7, 19099–19109, **2015**. https://doi.org/10.1039/C5NR06038A.

[19] S. Borini, R. White, D. Wei, M. Astley, S. Haque, E. Spigone, N. Harris, J. Kivioja, T. Ryhänen, "Ultrafast graphene oxide humidity sensors," *ACS Nano*, 7, 11166–11173, **2013**. https://doi.org/10.1021/nn404889b.

[20] H. Bi, K. Yin, X. Xie, J. Ji, S. Wan, L. Sun, M. Terrones, M.S. Dresselhaus, "Ultrahigh humidity sensitivity of graphene oxide," *Sci. Rep.*, 3, 1–7, **2013**. https://doi.org/10.1038/srep02714.

[21] D.-T. Phan, G.-S. Chung, "Effects of rapid thermal annealing on humidity sensor based on graphene oxide thin films," *Sensors Actuators B Chem.*, 220, 1050–1055, **2015**. https://doi.org/10.1016/j.snb.2015.06.055.

[22] D. Zhang, J. Tong, B. Xia, "Humidity-sensing properties of chemically reduced graphene

oxide/polymer nanocomposite film sensor based on layer-by-layer nano self-assembly," *Sensors Actuators, B Chem.*, 197, 66–72, **2014**. https://doi.org/10.1016/j.snb.2014.02.078.

[23] L. Guo, H.B. Jiang, R.Q. Shao, Y.L. Zhang, S.Y. Xie, J.N. Wang, X. Bin Li, F. Jiang, Q.D. Chen, T. Zhang, H.B. Sun, "Two-beam-laser interference mediated reduction, patterning and nanostructuring of graphene oxide for the production of a flexible humidity sensing device," *Carbon*, 50, 1667–1673, **2012**. https://doi.org/10.1016/j.carbon.2011.12.011.

[24] D. Zaharie-Butucel, L. Digianantonio, C. Leordean, L. Ressier, S. Astilean, C. Farcau, "Flexible transparent sensors from reduced graphene oxide micro-stripes fabricated by convective self-assembly," *Carbon*, 113, 361–370, **2017**. https://doi.org/10.1016/j.carbon.2016.11.013.

[25] M.G. Stanford, C. Zhang, J.D. Fowlkes, A. Hoffman, I.N. Ivanov, P.D. Rack, J.M. Tour, "High-Resolution Laser-Induced Graphene. Flexible Electronics beyond the Visible Limit," *ACS Appl. Mater. Interfaces*, 12, 10902–10907, **2020**. https://doi.org/10.1021/acsami.0c01377.

[26] K.K. Adhikari, C. Wang, T. Qiang, Q. Wu, "Polyimide-derived laser-induced porous graphene-incorporated microwave resonator for high-performance humidity sensing," *Appl. Phys. Express*, 12, 106501, **2019**. https://doi.org/10.7567/1882-0786/ab3c7a.

[27] J.-U. Lee, Y.-W. Ma, S.-Y. Jeong, B.-S. Shin, "Direct Fabrication of Ultra-Sensitive Humidity Sensor Based on Hair-Like Laser-Induced Graphene Patterns," *Micromachines*, 11, 476, **2020**. https://doi.org/10.3390/mi11050476.

[28] C. Zhang, Y. Xie, C. Zhang, J. Lin, "Upgrading coal to multifunctional graphene-based materials by direct laser scribing," *Carbon*, 153, 585–591, **2019**. https://doi.org/10.1016/j.carbon.2019.07.070.

[29] Y. Chyan, R. Ye, Y. Li, S.P. Singh, C.J. Arnusch, J.M. Tour, "Laser-Induced Graphene by Multiple Lasing: Toward Electronics on Cloth, Paper, and Food," *ACS Nano*, 12, 2176–2183, **2018**. https://doi.org/10.1021/acsnano.7b08539.

[30] R. Ye, Y. Chyan, J. Zhang, Y. Li, X. Han, C. Kittrell, J.M. Tour, "Laser-Induced Graphene Formation on Wood," *Adv. Mater.*, 29, 1–7, **2017**. https://doi.org/10.1002/adma.201702211.

[31] D. Ha, Z. Fang, N.B. Zhitenev, "Paper in Electronic and Optoelectronic Devices," *Adv. Electron. Mater.*, 4, 1700593, **2018**. https://doi.org/10.1002/aelm.201700593.

[32] R. Martins, I. Ferreira, E. Fortunato, "Electronics with and on paper," *Phys. Status Solidi - Rapid Res. Lett.*, 5, 332–335, **2011**. https://doi.org/10.1002/pssr.201105247.

[33] E. Fortunato, N. Correia, P. Barquinha, L. Pereira, G. Goncalves, R. Martins, "High-performance flexible hybrid field-effect transistors based on cellulose fiber paper," *IEEE Electron Device Lett.*, 29, 988–990, **2008**. https://doi.org/10.1109/LED.2008.2001549.

[34] R. Martins, P. Barquinha, L. Pereira, N. Correia, G. Goṇalves, I. Ferreira, E. Fortunato, "Write-erase and read paper memory transistor," *Appl. Phys. Lett.*, 93, 2006–2009, **2008**. https://doi.org/10.1063/1.3030873.

[35] M.N. Costa, B. Veigas, J.M. Jacob, D.S. Santos, J. Gomes, P. V. Baptista, R. Martins, J. Inácio, E. Fortunato, "A low cost, safe, disposable, rapid and self-sustainable paper-based platform for diagnostic testing: lab-on-paper," *Nanotechnology*, 25, **2014**. https://doi.org/10.1088/0957-4484/25/9/094006.

[36] X. Zang, C. Shen, Y. Chu, B. Li, M. Wei, J. Zhong, M. Sanghadasa, L. Lin, "Laser-Induced Molybdenum Carbide-Graphene Composites for 3D Foldable Paper Electronics," *Adv. Mater.*, 30, 1800062, **2018**. https://doi.org/10.1002/adma.201800062.

[37] Y. Yao, X. Duan, M. Niu, J. Luo, R. Wang, T. Liu, "One-step process for direct laser writing carbonization of NH4H2PO4 treated cellulose paper and its use for facile fabrication of multifunctional force sensors with corrugated structures," *Cellulose*, 26, 7423–7435, **2019**. https://doi.org/10.1007/s10570-019-02617-4.

[38] S. Lee, S. Jeon, "Laser-Induced Graphitization of Cellulose Nanofiber Substrates under Ambient Conditions," *ACS Sustain. Chem. Eng.*, 7, 2270–2275, **2019**. https://doi.org/10.1021/acssuschemeng.8b04955.

[39] W.R. de Araujo, C.M.R. Frasson, W.A. Ameku, J.R. Silva, L. Angnes, T.R.L.C. Paixão, "Single-Step Reagentless Laser Scribing Fabrication of Electrochemical Paper-Based Analytical Devices," *Angew. Chemie - Int. Ed.*, 56, 15113–15117, **2017**. https://doi.org/10.1002/anie.201708527.

[40] S. Lee, H. Jang, H. Lee, D. Yoon, S. Jeon, "Direct Fabrication of a Moisture-Driven Power Generator by Laser-Induced Graphitization with a Gradual Defocusing Method," *ACS Appl. Mater. Interfaces*, 11, 26970–26975, **2019**. https://doi.org/10.1021/acsami.9b08056.

[41] Y. Chyan, J. Cohen, W. Wang, C. Zhang, J.M. Tour, "Graphene Art," *ACS Appl. Nano Mater.*, 2, 3007–3011, **2019**. https://doi.org/10.1021/acsanm.9b00391.

[42] P. Zhao, G. Bhattacharya, S.J. Fishlock, J.G.M. Guy, A. Kumar, C. Tsonos, Z. Yu, S. Raj, J.A. McLaughlin, J. Luo, N. Soin, "Replacing the metal electrodes in triboelectric nanogenerators: High-performance laser-induced graphene electrodes," *Nano Energy*, 75, 104958, **2020**. https://doi.org/10.1016/j.nanoen.2020.104958.

[43] Z. Wan, N.-T. Nguyen, Y. Gao, Q. Li, "Laser induced graphene for biosensors," *Sustain. Mater. Technol.*, 25, e00205, **2020**. https://doi.org/10.1016/j.susmat.2020.e00205.

[44] J.-U. Lee, Y.-W. Ma, S.-Y. Jeong, B.-S. Shin, "Fabrication of UV Laser-Induced Porous Graphene Patterns with Nanospheres and Their Optical and Electrical Characteristics," *Materials (Basel).*, 13, 3930, **2020**. https://doi.org/10.3390/ma13183930.

[45] Y. Rhim, D. Zhang, D.H. Fairbrother, K.A. Wepasnick, K.J. Livi, R.J. Bodnar, D.C. Nagle, "Changes in electrical and microstructural properties of microcrystalline cellulose as

function of carbonization temperature," *Carbon*, 48, 1012–1024, **2010**. https://doi.org/10.1016/j.carbon.2009.11.020.

[46] A.C. Ferrari, "Raman spectroscopy of graphene and graphite: Disorder, electron-phonon coupling, doping and nonadiabatic effects," *Solid State Commun.*, 143, 47–57, **2007**. https://doi.org/10.1016/j.ssc.2007.03.052.

[47] L.G. Cançado, K. Takai, T. Enoki, M. Endo, Y.A. Kim, H. Mizusaki, A. Jorio, L.N. Coelho, R. Magalhães-Paniago, M.A. Pimenta, "General equation for the determination of the crystallite size La of nanographite by Raman spectroscopy," *Appl. Phys. Lett.*, 88, 163106, **2006**. https://doi.org/10.1063/1.2196057.

[48] B. Kulyk, B.F.R. Silva, A.F. Carvalho, S. Silvestre, A.J.S. Fernandes, R. Martins, E. Fortunato, F.M. Costa, "Laser-Induced Graphene from Paper for Mechanical Sensing," *ACS Appl. Mater. Interfaces*, 13, 10210–10221, **2021**. https://doi.org/10.1021/acsami.0c20270.

[49] M. Jagtoyen, F. Derbyshire, "Activated carbons from yellow poplar and white oak by H3PO4 activation," *Carbon*, 36, 1085–1097, **1998**. https://doi.org/https://doi.org/10.1016/S0008-6223(98)00082-7.

[50] M.S. Solum, R.J. Pugmire, M. Jagtoyen, F. Derbyshire, "Evolution of carbon structure in chemically activated wood," *Carbon*, 33, 1247–1254, **1995**. https://doi.org/https://doi.org/10.1016/0008-6223(95)00067-N.

[51] Y. Guo, D.A. Rockstraw, "Physical and chemical properties of carbons synthesized from xylan, cellulose, and Kraft lignin by H3PO4 activation," *Carbon*, 44, 1464–1475, **2006**. https://doi.org/10.1016/j.carbon.2005.12.002.

[52] M. Smith, L. Scudiero, J. Espinal, J.-S. McEwen, M. Garcia-Perez, "Improving the deconvolution and interpretation of XPS spectra from chars by ab initio calculations," *Carbon*, 110, 155–171, **2016**. https://doi.org/10.1016/j.carbon.2016.09.012.

[53] B. Lesiak, L. Kövér, J. Tóth, J. Zemek, P. Jiricek, A. Kromka, N. Rangam, "C sp2/sp3 hybridisations in carbon nanomaterials – XPS and (X)AES study," *Appl. Surf. Sci.*, 452, 223–231, **2018**. https://doi.org/10.1016/j.apsusc.2018.04.269.

[54] S. Sapieha, M. Inoue, P. Lepoutre, "Conductivity and water sorption in paper," *J. Appl. Polym. Sci.*, 30, 1257–1266, **1985**. https://doi.org/10.1002/app.1985.070300329.

[55] W.-D. Lin, H.-M. Chang, R.-J. Wu, "Applied novel sensing material graphene/polypyrrole for humidity sensor," *Sensors Actuators B Chem.*, 181, 326–331, **2013**. https://doi.org/10.1016/j.snb.2013.02.017.

[56] T.O. Wehling, M.I. Katsnelson, A.I. Lichtenstein, "Adsorbates on graphene: Impurity states and electron scattering," *Chem. Phys. Lett.*, 476, 125–134, **2009**. https://doi.org/10.1016/j.cplett.2009.06.005.

[57] M. Khalifa, G. Wuzella, H. Lammer, A.R. Mahendran, "Smart paper from graphene coated cellulose for high-performance humidity and piezoresistive force sensor," *Synth. Met.*,

266, 116420, **2020**. https://doi.org/10.1016/j.synthmet.2020.116420.

[58] V.I. Popov, D. V Nikolaev, V.B. Timofeev, S.A. Smagulova, I. V Antonova, "Graphene-based humidity sensors: the origin of alternating resistance change," *Nanotechnology*, 28, 355501, **2017**. https://doi.org/10.1088/1361-6528/aa7b6e.

[59] Y. Chen, P. Pötschke, J. Pionteck, B. Voit, H. Qi, "Smart cellulose/graphene composites fabricated by: In situ chemical reduction of graphene oxide for multiple sensing applications," *J. Mater. Chem. A*, 6, 7777–7785, **2018**. https://doi.org/10.1039/c8ta00618k.

[60] P. Zhu, Y. Liu, Z. Fang, Y. Kuang, Y. Zhang, C. Peng, G. Chen, "Flexible and Highly Sensitive Humidity Sensor Based on Cellulose Nanofibers and Carbon Nanotube Composite Film," *Langmuir*, 35, 4834–4842, **2019**. https://doi.org/10.1021/acs.langmuir.8b04259.

[61] D. Tobjörk, R. Österbacka, "Paper Electronics," *Adv. Mater.*, 23, 1935–1961, **2011**. https://doi.org/10.1002/adma.201004692.

[62] K.-D. Kreuer, "Proton Conductivity: Materials and Applications," *Chem. Mater.*, 8, 610–641, **1996**. https://doi.org/10.1021/cm950192a.

[63] G.-C. Ri, J.-S. Kim, C.-J. Yu, "Role of Water Molecules in Enhancing the Proton Conductivity on Reduced Graphene Oxide under High Humidity," *Phys. Rev. Appl.*, 10, 034018, **2018**. https://doi.org/10.1103/PhysRevApplied.10.034018.

[64] M. Park, S.J. Hong, K.H. Kim, H. Kang, M. Lee, D.H. Jeong, Y.W. Park, B.H. Kim, "Electrical and thermoelectric transport by variable range hopping in reduced graphene oxide," *Appl. Phys. Lett.*, 111, **2017**. https://doi.org/10.1063/1.4987021.

[65] A.B. Kaiser, G.N. Cristina, R.S. Sundaram, M. Burghard, K. Kern, "Electrical conduction mechanism in chemically derived graphene monolayers," *Nano Lett.*, 9, 1787–1792, **2009**. https://doi.org/10.1021/nl803698b.

[66] C. Ramirez, F.M. Figueiredo, P. Miranzo, P. Poza, M.I. Osendi, "Graphene nanoplatelet/silicon nitride composites with high electrical conductivity," *Carbon*, 50, 3607–3615, **2012**. https://doi.org/10.1016/j.carbon.2012.03.031.

[67] B. Román-Manso, E. Domingues, F.M. Figueiredo, M. Belmonte, P. Miranzo, "Enhanced electrical conductivity of silicon carbide ceramics by addition of graphene nanoplatelets," *J. Eur. Ceram. Soc.*, 35, 2723–2731, **2015**. https://doi.org/10.1016/j.jeurceramsoc.2015.03.044.

2.2.6 Supporting information

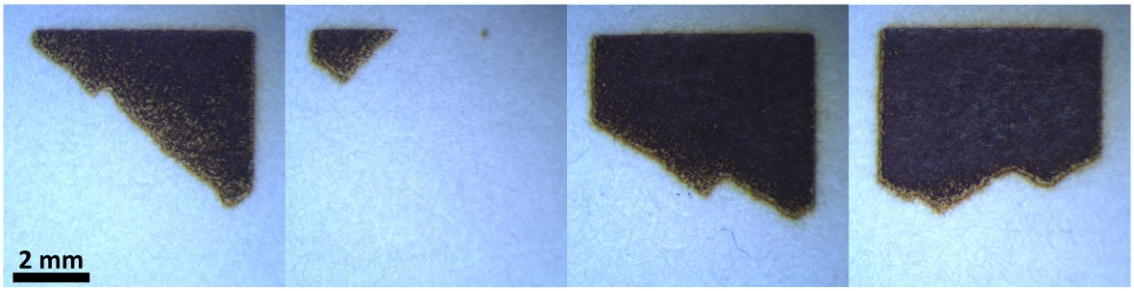

Figure S2.2.1. Four distinct samples showing how the transformation of cellulose begins at random locations inside the irradiated area, with each such location giving rise to a widening triangular shape as subsequent lines are scanned by the laser (the scanning direction is bottom to top).

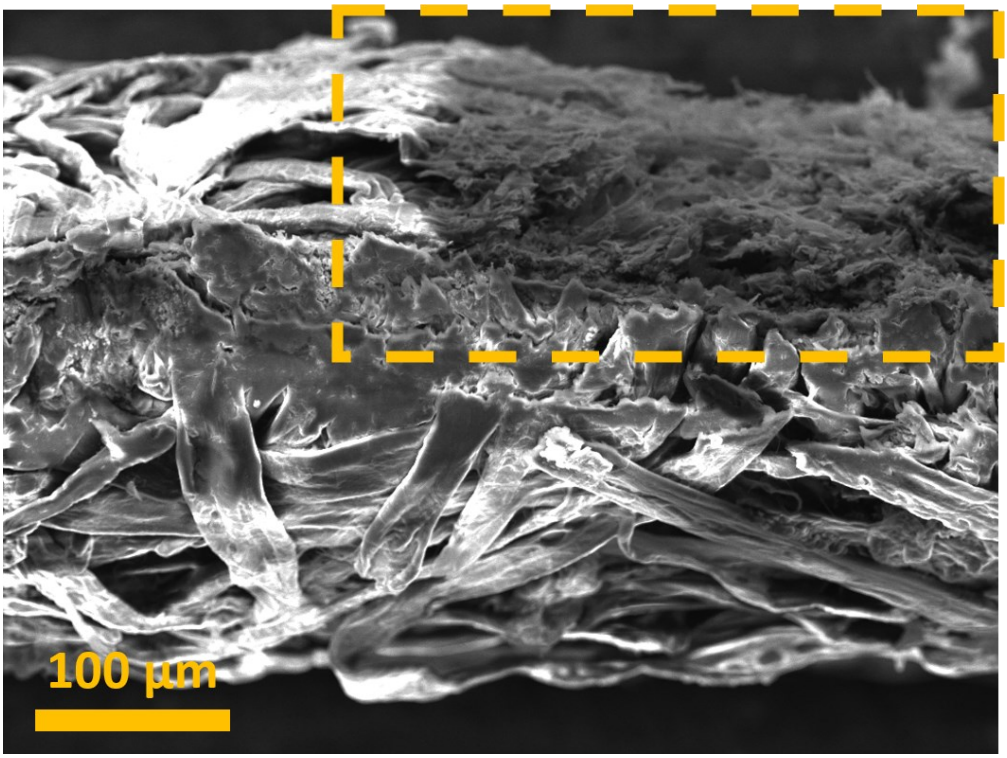

Figure S2.2.2. Secondary electron scanning electron microscopy (SE-SEM) cross-section image of the edge of a paper-LIG sample (highlighted by the dashed rectangle).

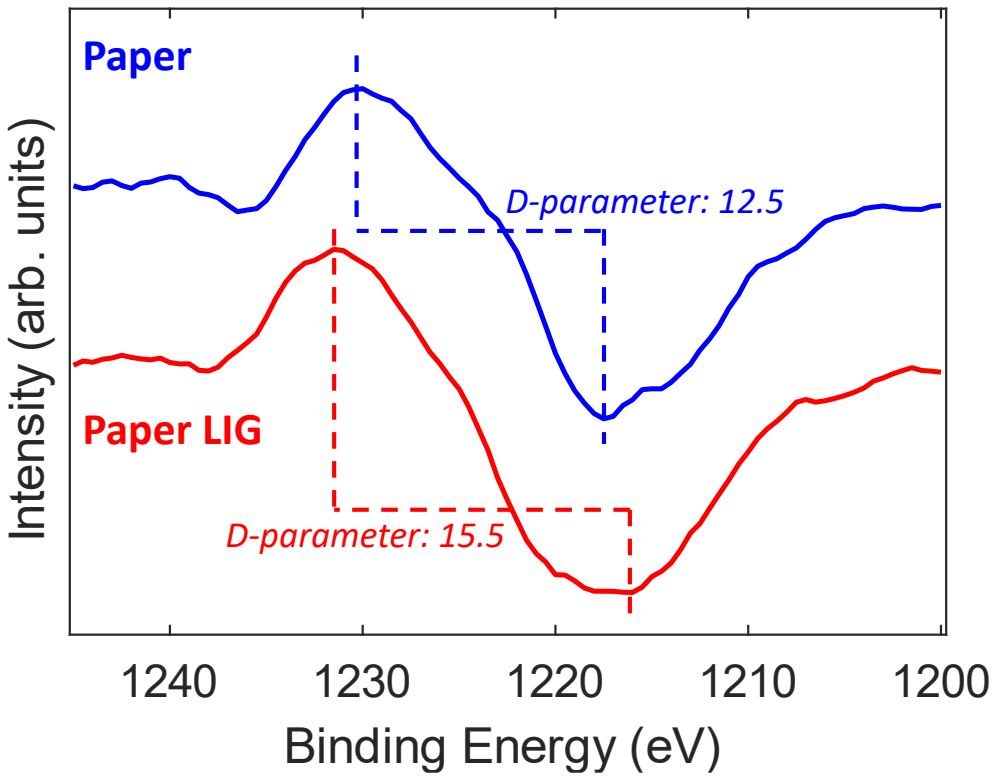

Figure S2.2.3. Differentiated C KLL Auger features for paper and paper-LIG, with the corresponding D-parameters.

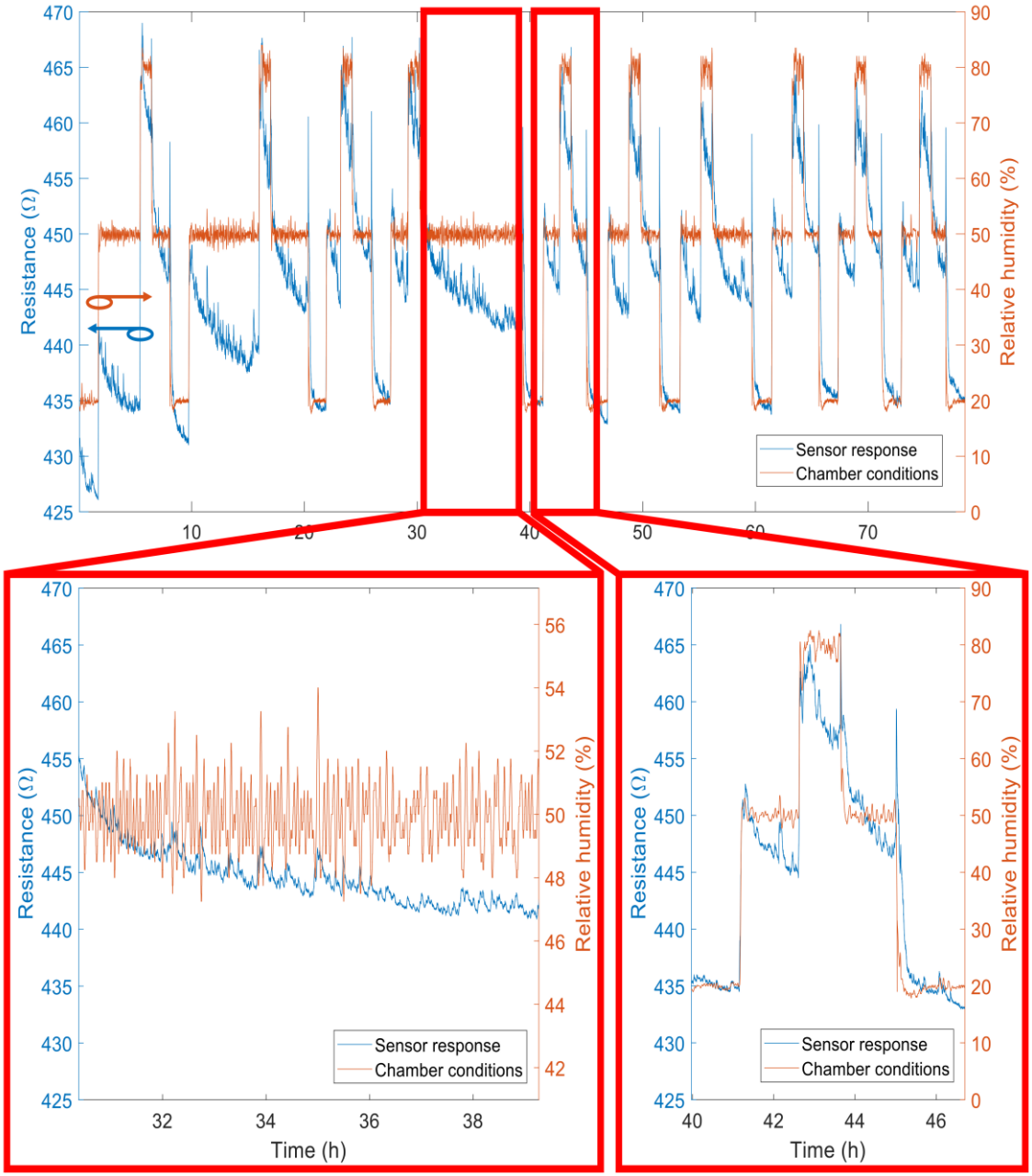

Figure S2.2.4. Resistance of the paper-LIG humidity sensor (blue trace) in response to different relative humidity conditions as measured by the climatic chamber capacitive sensor (orange trace), with relative humidity conditions cyclically alternated between 20%, 50% and 80% RH, at a fixed temperature. The panel on the lower left of the figure shows an amplified view of the gradual drift towards lower resistance values at a fixed relative humidity, while the panel on the lower right gives a better view at one of the cycles, highlighting how the resistance trace of the paper-LIG sensor closely reproduces the smallest variations in the relative humidity conditions inside the chamber (as measured by the chamber's capacitive sensor).

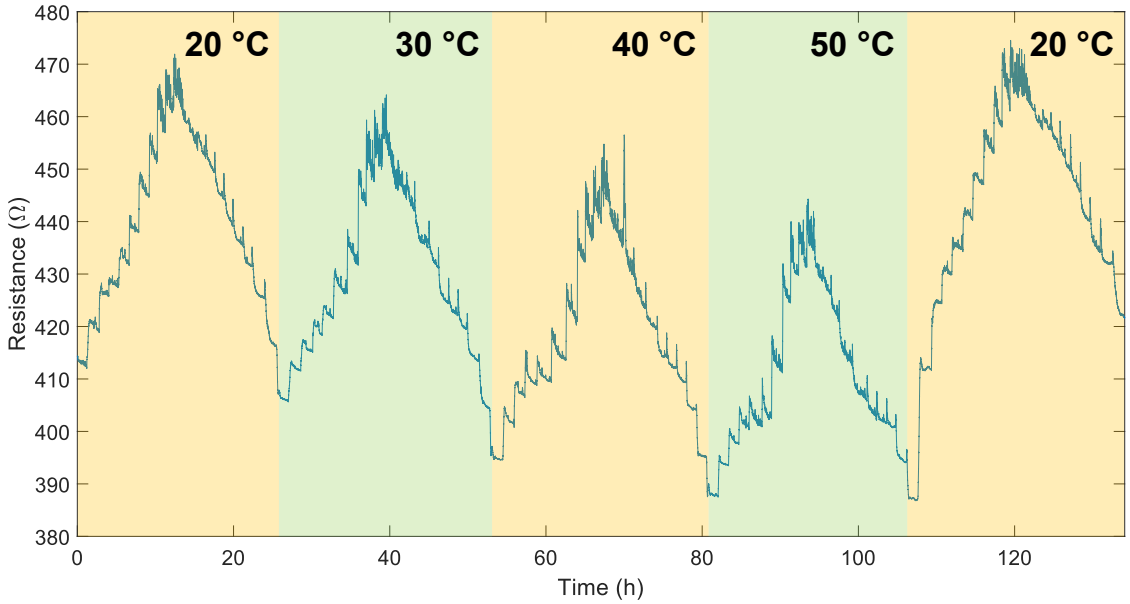

Figure S2.2.5. Resistance of the paper-LIG humidity sensor in response to different relative humidity conditions for temperatures of 20 °C, 30 °C, 40 °C, 50 °C and 20 °C again, revealing the performance of the sensor at different temperatures.

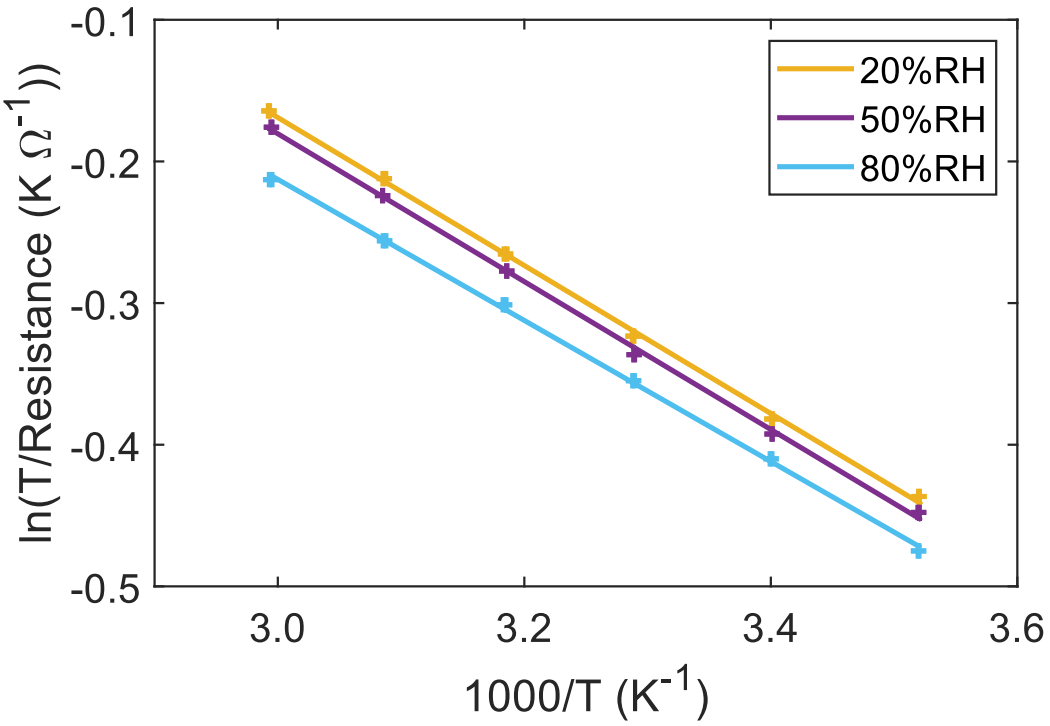

Figure S2.2.6. Response of the paper-LIG sensor plotted in Arrhenius coordinates.

2.3 Conversion of paper and xylan into laser-induced graphene for environmentally friendly sensors

Bohdan Kulyk[1,2], Marina Matos[3], Beatriz F.R. Silva[1,4], Alexandre F. Carvalho[1,4], António J.S. Fernandes[1], Dmitry V. Evtuguin[3], Elvira Fortunato[2], Florinda M. Costa[1]

1 – i3N, Department of Physics, University of Aveiro, Campus Universitário de Santiago, 3810-193 Aveiro, Portugal.

2 – i3N/CENIMAT, Department of Materials Science and CEMOP/UNINOVA, NOVA School of Science and Technology, NOVA University Lisbon, Campus de Caparica, 2829-516 Caparica, Portugal.

3 – CICECO – Aveiro Institute of Materials, Department of Chemistry, University of Aveiro, 3810-193 Aveiro, Portugal.

4 – CICECO – Aveiro Institute of Materials, Department of Physics, University of Aveiro, 3810-193 Aveiro, Portugal.

Abstract:

Laser-induced graphene (LIG) is a foam-like porous material consisting of few-layer graphene obtained by laser irradiation of a wide range of carbon-containing substrates. Among these, the ability to synthesize LIG from paper and other cellulose-related materials is particularly exciting, as it opens the door to a wide assortment of potential applications in the form of low-cost, flexible, and biodegradable devices. Here, the synthesis of this material, dubbed paper-LIG, on different types of filter papers and xylan biopolymer is discussed. In particular, we report the formation of paper-LIG by single-step irradiation, providing an improvement over the conventional multiple lasing approach and giving an explanation of the conditions that allow this simplified synthesis. All the relevant process parameters are covered, assessing their effect on the resulting electrical properties, structure, and morphology. Additionally, we demonstrate the application of LIG obtained from xylan, an abundant and often underutilized biopolymer, for temperature sensing. These results provide a better understanding of the conditions required for the synthesis of highly conductive LIG from paper and related materials, paving the way for its application, with reduced cost and low environmental impact, in fields ranging from biomonitoring to consumer electronics.

2.3.1 Introduction

The emergence of graphene in 2004 as a novel material with outstanding properties [1] has captivated the attention of not just the scientific community, but of the world at large. Motivated by the promise of scientific discovery and ground-breaking applications, this interest spurred an ever-growing body of work [2]. Remarkably, the world of graphene turned out to be even richer than perhaps initially expected, with a wide range of different types of graphene-based materials. From chemical vapor deposited large area single-layer graphene films with extremely high charge carrier mobilities [3] and large crystal sizes [4], to the easily processable liquid-phase exfoliated few-layer graphene flakes [5,6], each class of graphene-based materials shows unique properties which make them ideally suited for their respective fields of application.

One of the most recent additions to the graphene family is laser-induced graphene (LIG) [7]. The first report concerning its synthesis was given in 2014, by the group of James M. Tour, describing porous 3D-structures composed of few-layer graphene, obtained by CO_2 laser (10.6 μm) irradiation of flexible commercial polymers such as polyimide [8]. This ability to easily pattern conductive paths onto flexible insulating substrates motivated great interest, spurred by the demonstration of applications in sensing [9,10], actuation [11] and energy storage [8], among others. Since then, the formation of LIG has been achieved using laser radiation with different wavelengths [9,10], as well as using other materials as precursors, such as wood [12], cork [10] and paper [13,14]. Among these, paper is a particularly attractive one, being extremely versatile, cheap, lightweight and biodegradable. After the initial report of the use of paper for the synthesis of laser-induced graphene in 2018, this material, also referred to as paper-LIG, has already shown potential in several different fields [15–21]. Still, having been recently discovered, there are many unanswered questions about the synthesis process of paper-LIG.

In this work, we attempt to shed light on some of these questions. Namely, we systematically explore the formation of paper-LIG from activated charcoal filter paper. Secondly, we report the synthesis of this material from common filter paper using a single irradiation step, not only improving on the conventional multiple lasing process, but also providing an explanation of the mechanisms and conditions which allow it. Lastly, we show, for the first time (to the best of our knowledge), the formation of laser-induced graphene from xylan, an abundant, environmentally friendly biopolymer, demonstrating its proof-of-concept application in temperature sensing. These results further the understanding of the laser-induced graphene formation process from paper and related materials, widening the array of precursor substrates and resulting materials, as well as encouraging their future applications.

2.3.2 Results and discussion

2.3.2.1 Paper-LIG from activated charcoal filter paper

Commonly, the formation of laser-induced graphene from paper requires two irradiation steps. The first one converts the cellulose of the paper into aromatic char. To this end, the paper usually must be treated beforehand with a fire-retardant compound, in order to prevent the volatilization of the cellulose [13]. We note that irradiation under inert atmosphere is a viable alternative to the use of fire-retardants, as has been reported for the synthesis of LIG from wood [12]. However, this requires a more complicated setup. Moreover, one must consider the active role of the phosphate-based fire retardant in the synthesis process, as the phosphate groups

promote the dehydration of cellulose, preventing its decomposition into levoglucosan and further volatilization, as has also been reported previously [16]. Then, the second laser irradiation step leads to the graphitization of the aromatic char into a graphene-based material. As such, it becomes appealing to explore the formation of laser-induced graphene from papers already containing amorphous carbon components, with filter paper containing activated charcoal presenting itself as an example of such precursors.

In a typical laser-induced graphene synthesis experiment, the laser beam is scanned over the precursor paper along straight lines filling up the area to be irradiated. Here, the varied parameters were irradiation power, scan speed and separation between the scan lines (the position of the sample relative to the laser head was fixed at 9 mm below focus for the first step, while the second one was performed in focus). **Figure 2.3.1** shows secondary electron scanning electron microscopy (SE-SEM) images of the samples obtained at different irradiation powers and scan speeds, at 100 μm line separation. For lower irradiation power one can see that the fibres retain more of their original shape and structure than for higher power. The porosity appears to increase with the irradiation power, with more voids in the fibres irradiated at higher power. Lower scan speed also seems to lead to greater porosity inside the fibres, which can be explained by the fact that a lower scan speed implies that the laser beam remains for a longer period of time at each point along the scanned lines, delivering more energy at each such point. This is consistent with what has been reported for common filter paper [14], with greater porosity signalling a more extensive transformation of the cellulose fibres into laser-induced graphene. However, it can also be seen that as the porosity development becomes more extensive there is greater damage to the fibres, as each fibre loses its structural integrity. This is reflected in the sheet resistance measurements of the obtained samples (**Figure 2.3.2a**). Here, one can see a trend where, for irradiation power of 700 mW and 800 mW, lower scan speed results in more conductive samples, up to the point where the scan speed becomes too low and the energy delivered at each point along the scanned region becomes too large, leading to the damage of the top layers of the transformed paper. Interestingly, however, for an even further irradiation power increase this tendency is inverted for scan speeds lower than 40 mm s^{-1}, with the sheet resistance being lower for slower scan speed. This can be explained by the irradiation power being high enough to allow a fast removal of the top layers of the laser-induced graphene with enough time remaining for the graphitization of the remaining ones (but not enough for them to suffer extensive damage and be removed as well). Additionally, **Figure 2.3.2a** shows that, in general, smaller line separations result in less conductive samples, potentially due to the increased damage suffered by the irradiated material on account of the larger overlap between the scan lines. Finally, in what concerns the crystalline quality of the obtained material, Raman spectroscopy of the most conductive samples presents the typical spectra of laser-induced graphene, characterized by a sharp and narrow G peak and a symmetrical 2D peak, with the respective intensity ratio, I_{2D}/I_G, of ~0.5 (**Figure 2.3.2b**, bottom). As for the D peak, while it indicates the presence of disorder, it is common in LIG [8]. We also note that the less conductive samples predominantly show spectra representative of amorphous carbon (**Figure 2.3.b**, top), indicating that the reason behind their high sheet resistance is incomplete graphitization. In the case of samples formed at 800 mW and low scan speed, this provides further support to the idea that there is a removal of the upper layers of the irradiated paper, revealing poorly transformed material underneath.

Overall, it appears that the presence of activated charcoal does not provide substantial advantage to the process of formation of laser-induced graphene from paper. However, one has to consider the role of the other additives present in this type of paper, with energy dispersive

X-ray spectra (EDS) of the paper revealing the presence of elements such as Mg, Si, Ca and Fe. These can be attributed to inorganic fillers, which are additives commonly used in the papermaking process [22]. Thus, we argue that these additives cover the underlying fibres from the incident laser radiation, which leads to incomplete graphitization in these regions and, consequently, low conductivity, with even the most conductive samples presenting sheet resistances nearly five times larger than those obtained with hardened ashless filter paper without any additives [14]. Still, the high quality of the synthesized material, as indicated by the Raman spectra of the most conductive samples, show that activated charcoal filter paper can function as a LIG precursor.

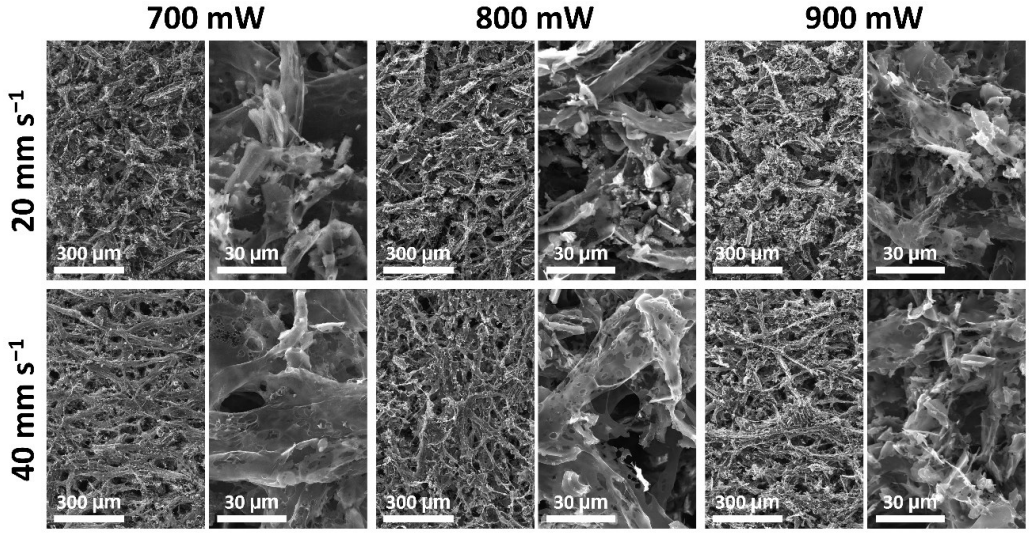

Figure 2.3.1. SE-SEM images of laser-induced graphene formed on activated charcoal filter paper, for different irradiation powers and scan speeds, at 0.1 mm scan line separation.

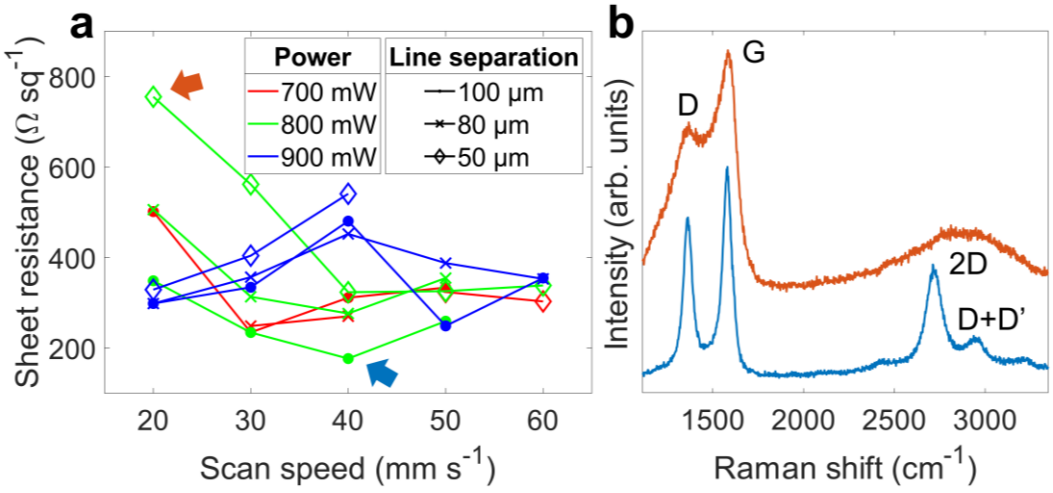

Figure 2.3.2. (a) Sheet resistance of paper-LIG samples synthesized on activated charcoal filter paper at different irradiation powers, scan line separations and scan speeds. **(b)** Raman spectra of the most (top) and least (bottom) resistive samples (identified in (a) by coloured arrows).

2.3.2.2 Paper-LIG with a single irradiation

The formation of laser-induced graphene on materials such as paper is a two-step process, where the first irradiation, performed with the sample out of focus, converts the cellulose into char, and the second one, done in focus, graphitizes this char into laser-induced graphene.

However, any future commercial application of this material could benefit if it were possible to obtain it using just a single irradiation step. This would reduce the synthesis time, which would represent a significant productivity gain, particularly for scaled up production.

Figure 2.3.3a shows a photograph of a sample obtained by scanning the laser beam once over fire-retardant treated filter paper. Extensive damage of the paper can be seen, with the yellow backlight revealing perforations along the lines scanned by the laser. However, as the separation between the scan lines is reduced, this damage becomes less extensive, with fewer perforations visible (**Figure 2.3.3b-d**). The sample obtained with a line separation of 30 μm is fairly continuous, with only a few through holes visible, while SE-SEM cross-section images reveal an ~85 μm layer of transformed fibres (**Figure 2.3.3e**). Moreover, the sample shows a blacker coloration indicative of a more complete transformation of the irradiated cellulose, which is confirmed by Raman spectroscopy, indicating that paper-LIG was obtained (**Figure 2.3.3f**).

These observations can be explained as follows. When the laser beam is scanned over the paper, due to the Gaussian intensity profile of the beam, the central part of the scanned line is ablated due to the high peak fluence of the focused laser (**Figure 2.3.3g**). However, in the periphery of the scanned line, where the fluence is lower, the irradiated paper gets charred without ablation. This charred material is more resistant to laser damage, so when the next adjacent line is scanned by the beam, if the lines are sufficiently close to ensure the overlapping of the irradiated regions, the beam will pass over the char formed by the previous scan, and it will get graphitized into laser-induced graphene without getting ablated (as seen in **Figure 2.3.3d**). If, however, the line separation is too large, each new one will pass over non-charred paper, which will get ablated due to its lower resistance to damage, resulting in perforations seen in **Figure 2.3.3a-c**. This also explains the presence of an extensive cut at the top of the sample in **Figure 2.3.3d**, as the first line necessarily passes over non-charred paper, resulting in ablation along this line. In our experimental setup the laser beam diameter at focus was determined to be 140 μm, so to ensure that each subsequent scanning line passes inside the area irradiated by the previous one, the line separation must be below 70 μm. This is why already at 50 μm one begins to see some black coloured material reminiscent of LIG. Still, one has to take into account that the charring at the edges of the affected area is not as extensive as near the centre of the scanned line, so a further decrease in line separation, down to 30 μm, is necessary for the subsequent lines to pass over sufficiently charred cellulose, as confirmed by **Figure 2.3.3d**.

The general observation that smaller line separations result in less perforated samples is confirmed by SE-SEM images of samples obtained with different irradiation powers and distance between lines (**Figure 2.3.4**). Separations of 80 μm and 50 μm lead to ablation along the scanned lines, which gets more pronounced at higher irradiation powers. With a line separation of 30 μm, however, even at 900 mW the sample shows no through holes. Moreover, with large line separations the remaining material appears to be poorly transformed, showing limited porosity development and thicker fibre walls. On the contrary, a line separation of 30 μm yields a thin, porous, veil-like material characteristic of paper-LIG, even at irradiation powers as low as 700 mW. This feature is in accordance with the above proposed explanation, as with larger line separations the charred paper does not undergo a second irradiation by the subsequent scan of the laser beam passing over the next line.

Figure 2.3.5a shows photographs of samples obtained using different irradiation powers and scan speeds. While increasing the irradiation power results in fewer through holes, in agreement with the discussion above, a combination of high power and low scan speed can lead to the crumbling of the resulting material. This is similar to what was observed for activated

charcoal filter paper, where excessive energy delivery originates the loss of the structural integrity of the fibres, and has also been reported for paper-LIG formed using two irradiation steps [14].

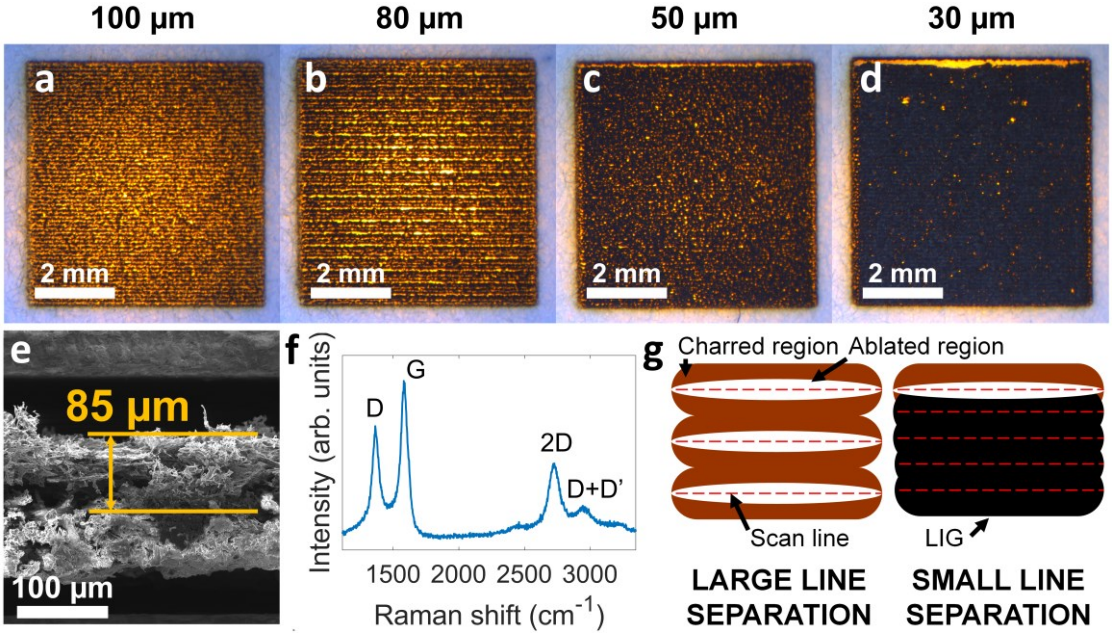

Figure 2.3.3. (a-d) Photographs of samples obtained after single scan irradiation (in focus) of filter paper, at scan line separations of 100 µm, 80 µm, 50 µm and 30 µm, respectively. **(e)** SE-SEM cross-section image and **(f)** representative Raman spectrum of the paper-LIG sample in (d). **(g)** Illustration of how a reduced scan line separation allows to obtain paper-LIG with a single scan. Each time the laser beam passes over the regions charred when scanning the previous line, these regions convert into paper-LIG without ablation.

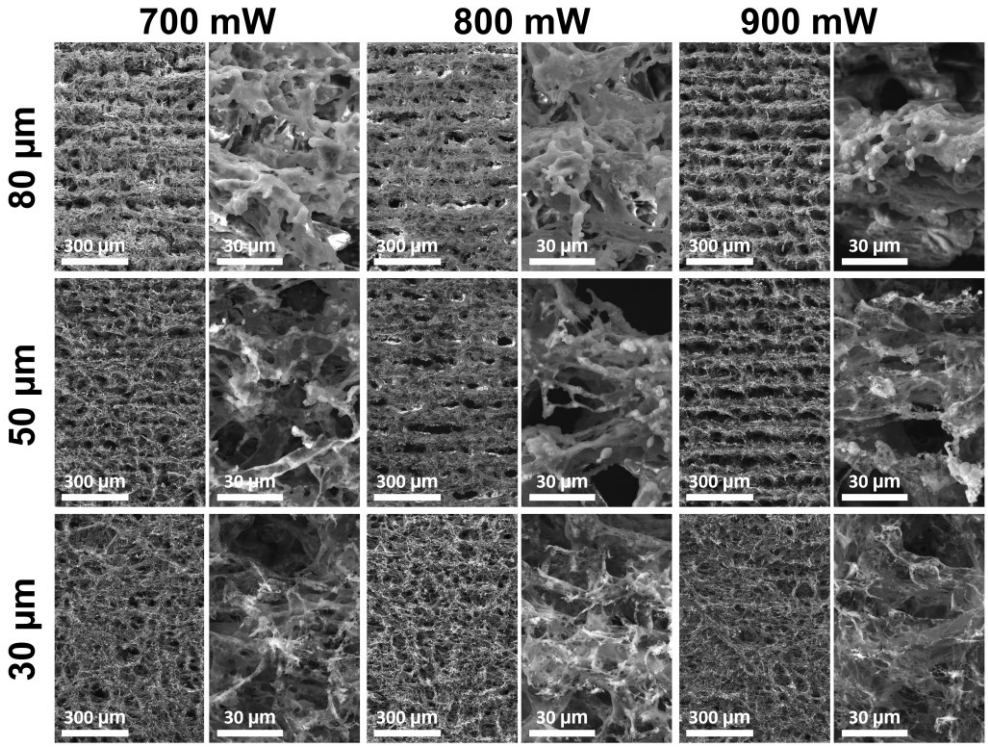

Figure 2.3.4. SE-SEM images of paper-LIG formed on filter paper, for different irradiation powers and scan line separation, at a scan speed of 40 mm s^{-1}.

The sheet resistance measurements, presented in **Figure 2.3.5b**, reflect the ideas discussed in this section. In general, smaller line separation and higher irradiation energy gives more conductive samples. Moreover, there is a trend where lower scan speeds result in smaller sheet resistances, up to the point where the energy delivered to the irradiated substrate becomes too large and the samples lose their structural integrity by cracking and crumbling. In these cases, even though the obtained material might be highly conductive, no sheet resistance values can be obtained.

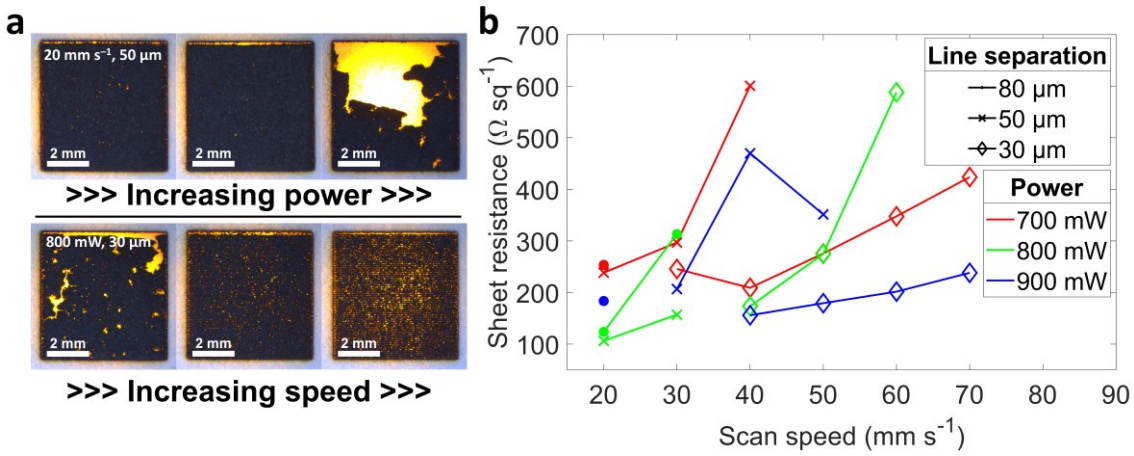

Figure 2.3.5. (a) Photographs of samples obtained after single scan irradiation (in focus) of filter paper, at irradiation powers of 700 mW, 800 mW and 900 mW (top) and scan speeds of 30 mm s^{-1}, 40 mm s^{-1} and 50 mm s^{-1} (bottom). **(b)** Sheet resistance of paper-LIG samples synthesized with single scan irradiation (in focus) of filter paper, at different irradiation powers, scan line separations and scan speeds.

On balance, paper-LIG can be obtained after a single irradiation step in focus, as long as the separation between the scan lines is small enough to ensure overlap. In this case, the two irradiation steps are essentially replicated by the repeated irradiation of the same regions by adjacent scan lines. Higher irradiation energies and lower scan speeds lead to more conductive samples, up to a limit where the samples begin to crack and crumble due to the loss of the structural integrity of the fibres as they become thinner and more porous. Compared to the conventional approach involving two irradiation steps, the paper-LIG obtained here presents a slightly more fragile appearance with a bit more damage to the fibres [14]. This is also reflected in a somewhat larger sheet resistance than the one reported for double-irradiated paper-LIG. However, the obtained material is still very conductive, while benefitting from a faster synthesis process. This is particularly important when exploring the low-cost and environmentally friendly applications enabled by paper-LIG, with the efficiency of the synthesis process being as important as the material itself.

2.3.2.3 Paper-LIG from xylan and its application in temperature sensing

Beside cellulose, there are other abundant structural biopolymers present in plants which are often underutilized. With vast amounts of biomass residues/subproducts generated by agriculture every year, there is a growing interest in its valorisation. The most abundant components of plant-based biomass, beside cellulose, are lignin and hemicellulose, with xylan being the most common type of the latter in vascular plants [23]. Throughout the last several decades xylan has been proposed for several application fields, with potential in wound dressings, coatings or as a pharmaceutical auxiliary, for example [24]. As such, it becomes appealing to explore

xylan as a precursor for LIG synthesis, which we undertake by irradiating carboxymethyl xylan films prepared by the solvent casting method. Two irradiation steps were employed, with the film being fixed at 9 mm below focus during the first one and in focus during the second one. The laser power was set to ~1 W, the scan speed was 30 mm s^{-1} and the line separation was 0.1 mm. **Figure 2.3.6a** shows a photograph of the material obtained after irradiation. While some through holes can be observed, overall it presents the dark colour characteristic of laser-induced graphene. Raman spectroscopy allows to confirm it as LIG (**Figure 2.3.6b**). The observed transformation of carboxymethyl xylan into laser-induced graphene is further illustrated by the porosity development revealed in SE-SEM images, although some heterogeneity can be observed (**Figure 2.3.6c**). This porosity is typical of laser-induced graphene obtained from both commercial polymers [8] and cellulose paper [14]. Compared to the latter, however, xylan-derived LIG presents a denser structure. The lack of long, porous fibres such as those in paper-LIG can be explained by the non-fibrous morphology of the carboxymethyl xylan precursor. Additionally, the thickness of the LIG layer was measured at ~80 μm (**Figure 2.3.6d**). This is slightly thinner that what has been observed for paper-LIG (~100 μm) [14], probably due to the denser nature of the xylan film, which should result in a shallower penetration depth of the laser beam during synthesis. The sheet resistance of the LIG obtained from carboxymethyl xylan was measured at 186 Ω sq^{-1}.

These results provide a solid basis for the application of laser-induced graphene obtained from xylan in devices such as sensors. To better demonstrate this, we develop a simple, low-cost and environmentally friendly temperature sensor employing this material. For this purpose, a 6×12 mm^2 conductive path was obtained by laser irradiation of the modified xylan film (an output power of ~1.5 W was used). Then, the resistance along this path was measured in response to different temperatures (controlled by a Peltier element), in the range of 20 °C to 45 °C. **Figure 2.3.6e** shows real-time monitoring of the sensor's response to two sweeps where the temperature was varied several times between 20 °C and 45 °C in steps of 5 °C. Additionally, the temperature was repeatedly set at either 30 °C or 35 °C to evaluate the reproducibility and stability of the measured resistances at each temperature. Lastly, sweeps between 30 °C and 35 °C in 1 °C steps were performed. A magnified view of these steps can be seen in **Figure 2.3.6f**, demonstrating the sensor's ability to reproducibly resolve temperature changes of 1 °C. Overall, the response is stable and reproducible, and the resistance values stabilize quickly at each temperature.

Interestingly, the resistance decreases with temperature. The negative temperature coefficient is consistent with the trend previously reported for both laser-induced graphene from polyimide [25,26] and for reduced graphene oxide (rGO) [27,28]. In the case of the latter, it has been ascribed to the increase of the number of charge carriers with temperature, as well as to hopping and tunneling between adjacent rGO sheets, with the increase in temperature allowing to overcome potential barriers. A similar explanation has been recently given for the temperature response of glass-like carbon obtained by laser irradiation of polyimide [29]. Likewise, recently the concept of temperature dependent hopping (more specifically variable range hopping) has been employed to describe the electronic conduction mechanism (and, correspondingly, its temperature dependence) in paper-LIG formed under UV laser [30].

In **Figure 2.3.6g**, the resistance values measured during the four sweeps in the range between 45 °C and 20 °C in steps of 5 °C were used to determine the calibration curve of the sensor (the values corresponding to the last 30 s at each temperature were used). The response is confirmed to be linear (coefficient of determination, r^2, of 0.998) and the sensitivity has a value

of −1.29 Ω °C^{-1}, demonstrating the potential of this material for sensing applications. For example, taking into consideration the prospective application of xylan as an effective barrier coating for packaging papers [31], this could open new opportunities for sensing solutions in food packing materials.

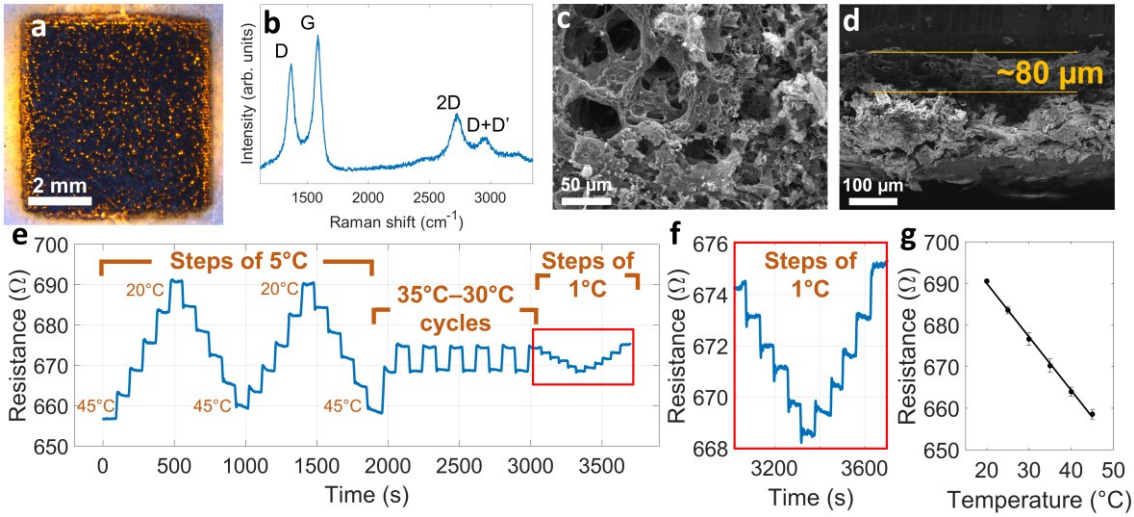

Figure 2.3.6. (a) Photograph of the sample obtained by laser irradiation of the carboxymethyl xylan film. **(b)** Raman spectrum of the sample in (a), showing the characteristic signature of laser-induced graphene. **(c)** SE-SEM image of LIG obtained from modified xylan. **(d)** Cross-section SE-SEM image of LIG obtained from xylan, showing the thickness of the LIG. **(e)** Real-time measurements of the resistance along the conductive path formed by laser irradiation of the carboxymethyl xylan film in response to different temperatures. Showcased are sweeps where the temperature was varied several times between 20 °C and 45 °C in steps of 5 °C, repeating cycles between 30 °C and 35 °C, as well as sweeps between 30 °C and 35 °C in 1 °C steps. **(f)** Amplified view of the sweeps between 30 °C and 35 °C (highlighted in (e) by a red frame), showing the sensor's ability to reproducibly resolve temperature changes of 1 °C. **(g)** Calibration curve of the temperature sensor employing LIG obtained from modified xylan, showing good linearity (r^2=0.998).

2.3.3 Conclusions

In this work, we presented a systematic study of the formation of paper-LIG, a versatile porous 3D graphene material obtained by laser irradiation of paper, on activated charcoal filter paper. Moreover, we reported the synthesis of paper-LIG with a single irradiation step, improving upon the conventional multiple lasing approach. These results are accompanied by a description of the conditions and mechanisms that allow this simplified synthesis, where the scan line separation must be reduced to ensure the overlap of adjacent beam paths. Lastly, we show that laser-induced graphene can be obtained by irradiation of fire retardant treated xylan film, which is an abundant, environmentally friendly biopolymer. The obtained material is then employed as a proof-of-concept temperature sensor, showing a sensitivity of −1.29 Ω °C^{-1}. Overall, this work contributes to a better understanding of the laser-induced graphene synthesis process, complementing the array of precursor substrates and resulting materials in this field. This encourages future applications in flexible, conductive, and environmentally friendly devices.

2.3.4 Materials and methods

2.3.4.1 Laser-induced graphene synthesis from filter paper

Cellulose filter paper with activated charcoal by Prat Dumas (500 µm of thickness, 160 g m^{-2}) and hardened ashless cellulose filter paper by Cytiva (Whatman grade 40, 95 g m^{-2}, 210 µm of

thickness, ≤0.007% ash content) were sprayed with a commercial phosphate-based fire retardant (Anti-Flame by BBT), prior to irradiation by a K40 CO_2 (10.6 μm) continuous wave 40 W laser engraver, by Liaocheng Julong CO. Ltd. The latter was operated in a unidirectional line scan mode. The parameters varied throughout this work were laser power, beam scan speed and distance (separation) between scan lines. The laser powers used throughout this work were 700 mW, 800 mW and 900 mW, corresponding to power densities of 45.5 W mm^{-2}, 51.9 W mm^{-2} and 58.4 W mm^{-2} in focus, and 4.8 W mm^{-2}, 5.5 W mm^{-2} and 6.2 W mm^{-2} at 9 mm below focus, respectively (nominal focal length of the lens is 50.8 mm). For the synthesis of LIG from activated charcoal filter paper, two irradiation steps were employed. In the first one the paper was placed 9 mm below focus, while in the second one it was irradiated in focus. For the study of paper-LIG formation with a single irradiation step, the filter paper was fixed at the focal plane. In all instances the irradiated area was 6×6 mm^2.

2.3.4.2 Xylan film preparation and laser-induced graphene synthesis

Xylan was isolated from Eucalyptus globulus bleached kraft pulp by extraction with 10% NaOH according to previously described procedure [32]. Carboxymethyl xylan synthesis was carried out according to the method developed by Petzold et al. [33]. Xylan was dissolved in NaOH aqueous solution (5 M), and vigorously stirred at 30 °C for 30 min. After that, sodium chloroacetate (SCA) was added to the mixture and the temperature was raised up to 65 °C for 60 min. Carboxymethyl xylan was then neutralised by the addition of sulfuric acid until pH ~7, and further dialysed in a tubing, benzoylated with molecular weight cut-off 2000 Da, to remove salts. Subsequently, the dialysed carboxymethyl xylan was freeze-dried. The synthesis procedure was performed with the molar ratio of 1:2:4 for xyl:SCA:NaOH.

Carboxymethyl xylan films were prepared by the solvent casting approach. Specifically, carboxymethyl xylan (1 g) was dissolved in distilled water (2%, 50 mL) under magnetic stirring for 3 h. The solution was then deposited into a square Teflon mould (7 cm^2) and the films were cast, at 45 °C for 96 h at relative humidity of 50%. For the synthesis of LIG, the obtained films were then sprayed with a commercial phosphate-based fire retardant (Anti-Flame by BBT), fixing the 50-70 micrometres-thick films onto filter paper to provide support. Two irradiation steps were employed, at 9 mm below focus and in focus, with 1 W of irradiation power, 30 mm s^{-1} of scan speed and a line separation of 0.1 mm.

2.3.4.3 Material characterization

Optical photographs of the samples were acquired with a UI-3880CPC-HQ R2 CMOS 6.41 MP camera, by IDS, through a stereo microscope, using both front and back lighting. Secondary and backscattered electron scanning electron microscopy (SE-SEM and BSE-SEM) images were acquired using Vega 3 SBH system, by TESCAN, with an acceleration voltage of 15 kV and a working distance of 15 mm. Raman spectroscopy was performed using a Jobin Yvon HR800 Raman system, by Horiba, and a He-Cd 441.6 nm laser, with a ×50 lens (NA=0.5), by Olympus. A neutral density filter OD=1 was used to attenuate the laser power to prevent any potential thermally induced modification of the samples. Sheet resistance measurements were performed by the van der Pauw method, using a Keysight B2902A dual-channel source meter unit.

2.3.4.4 Preparation and testing of the xylan film temperature sensor

A temperature sensor employing LIG obtained from modified xylan was prepared by irradiating a 6×12 mm^2 area of the xylan film fixed onto filter paper, using 1.5 W of power, 30 mm s^{-1} as the scan speed and a line separation of 0.1 mm. Silver paste was used to connect tin-coated 20 awg copper wires at each end of the sensor. To test the response to temperature, the sensor was placed over a TECD2S Peltier element, controlled by a MTDEVAL1 board by ThorLabs. The temperature was varied in 5 °C steps over a 20 °C to 45 °C range, while the resistance of the LIG sensor (along the conductive path) was measured by a Keysight B2902A source meter unit, applying a constant voltage of 0.05 V. Each temperature value was held for ~90 s and the resistance values of the last 30 s of each stage were averaged to obtain the response of the sensor at that temperature. Additional real-time measurements were performed by repeatedly alternating the temperature between 30 °C and 35 °C, as well as by varying it in steps of 1 °C in the range between 30 °C and 35 °C.

Acknowledgements

This work was developed within the scope of the project i3N (LA/P/0037/202, UIDB/50025/2020, and UIDP/50025/2020), financed by national funds through the (Portuguese Science and Technology Foundation/MCTES (FCT I.P.)). This work was also financially supported by the CICECO – Aveiro Institute of Materials, within the scope of the projects UIDB/50011/2020 and UIDP/50011/2020, financed by national funds through the (Portuguese Science and Technology Foundation/MCTES (FCT I.P.)). B. Kulyk acknowledges the Ph.D. grant SFRH/BD/141525/2018 by FCT I.P. E. Fortunato acknowledges the European Research Council AdG grant 787410 from the project DIGISMART.

2.3.5 References

[1] K.S. Novoselov, A.K. Geim, S. V. Morozov, D. Jiang, Y. Zhang, S. V. Dubonos, I. V. Grigorieva, A.A. Firsov, "Electric field effect in atomically thin carbon films," *Science*, 306, 666–669, **2004**. https://doi.org/10.1126/science.1102896.

[2] A.C. Ferrari, F. Bonaccorso, V.I. Fal'ko, K.S. Novoselov, S. Roche, P. Bøggild, S. Borini, F.H.L. Koppens, V. Palermo, N.M. Pugno, J.A. Garrido, R. Sordan, A. Bianco, L. Ballerini, M. Prato, E. Lidorikis, J. Kivioja, C. Marinelli, T. Ryhänen, A.F. Morpurgo, J.N. Coleman, V. Nicolosi, L. Colombo, A. Fert, M. Garcia-Hernandez, A. Bachtold, G.F. Schneider, F. Guinea, C. Dekker, M. Barbone, Z.Z. Sun, C. Galiotis, A.N. Grigorenko, G. Konstantatos, A. Kis, M.I. Katsnelson, L.M.K. Vandersypen, A. Loiseau, V. Morandi, D. Neumaier, E. Treossi, V. Pellegrini, M. Polini, A. Tredicucci, G.M. Williams, B. Hee Hong, J.-H. Ahn, J. Min Kim, H. Zirath, B.J. van Wees, H. van der Zant, L. Occhipinti, A. Di Matteo, I.A. Kinloch, T. Seyller, E. Quesnel, X.L. Feng, K.B.K. Teo, N.L. Rupesinghe, P.J. Hakonen, S.R.T. Neil, Q. Tannock, T. Löfwander, J.M. Kinaret, "Science and technology roadmap for graphene, related two-dimensional crystals, and hybrid systems," *Nanoscale*, 7, 4598–4810, **2015**. https://doi.org/10.1039/C4NR01600A.

[3] L. Banszerus, M. Schmitz, S. Engels, M. Goldsche, K. Watanabe, T. Taniguchi, B. Beschoten, C. Stampfer, "Ballistic Transport Exceeding 28 μm in CVD Grown Graphene," *Nano Lett.*, 16, 1387–1391, **2016**. https://doi.org/10.1021/acs.nanolett.5b04840.

[4] B. Kulyk, A.F. Carvalho, A.J.S. Fernandes, F.M. Costa, "Millimeter sized graphene domains

through in situ oxidation/reduction treatment of the copper substrate," *Carbon*, 169, 403–415, **2020**. https://doi.org/10.1016/j.carbon.2020.08.002.

[5] Z. Li, R.J. Young, C. Backes, W. Zhao, X. Zhang, A.A. Zhukov, E. Tillotson, A.P. Conlan, F. Ding, S.J. Haigh, K.S. Novoselov, J.N. Coleman, "Mechanisms of Liquid-Phase Exfoliation for the Production of Graphene," *ACS Nano*, 14, 10976–10985, **2020**. https://doi.org/10.1021/acsnano.0c03916.

[6] B. Kulyk, M.A. Freitas, N.F. Santos, F. Mohseni, A.F. Carvalho, K. Yasakau, A.J.S. Fernandes, A. Bernardes, B. Figueiredo, R. Silva, J. Tedim, F.M. Costa, "A critical review on the production and application of graphene and graphene-based materials in anti-corrosion coatings," *Crit. Rev. Solid State Mater. Sci.*, 0, 1–48, **2021**. https://doi.org/10.1080/10408436.2021.1886046.

[7] R. Ye, D.K. James, J.M. Tour, "Laser-Induced Graphene: From Discovery to Translation," *Adv. Mater.*, 31, 1–15, **2019**. https://doi.org/10.1002/adma.201803621.

[8] J. Lin, Z. Peng, Y. Liu, F. Ruiz-Zepeda, R. Ye, E.L.G.G. Samuel, M.J. Yacaman, B.I. Yakobson, J.M. Tour, "Laser-induced porous graphene films from commercial polymers," *Nat. Commun.*, 5, 1–8, **2014**. https://doi.org/10.1038/ncomms6714.

[9] A.F. Carvalho, A.J.S. Fernandes, C. Leitão, J. Deuermeier, A.C. Marques, R. Martins, E. Fortunato, F.M. Costa, "Laser-Induced Graphene Strain Sensors Produced by Ultraviolet Irradiation of Polyimide," *Adv. Funct. Mater.*, 28, 1–8, **2018**. https://doi.org/10.1002/adfm.201805271.

[10] A.F. Carvalho, A.J.S. Fernandes, R. Martins, E. Fortunato, F.M. Costa, "Laser-Induced Graphene Piezoresistive Sensors Synthesized Directly on Cork Insoles for Gait Analysis," *Adv. Mater. Technol.*, 5, 2000630, **2020**. https://doi.org/10.1002/admt.202000630.

[11] A.F. Carvalho, B. Kulyk, A.J.S. Fernandes, E. Fortunato, F.M. Costa, "A Review on the Applications of Graphene in Mechanical Transduction," *Adv. Mater.*, 2101326, **2021**. https://doi.org/10.1002/adma.202101326.

[12] R. Ye, Y. Chyan, J. Zhang, Y. Li, X. Han, C. Kittrell, J.M. Tour, "Laser-Induced Graphene Formation on Wood," *Adv. Mater.*, 29, 1–7, **2017**. https://doi.org/10.1002/adma.201702211.

[13] Y. Chyan, R. Ye, Y. Li, S.P. Singh, C.J. Arnusch, J.M. Tour, "Laser-Induced Graphene by Multiple Lasing: Toward Electronics on Cloth, Paper, and Food," *ACS Nano*, 12, 2176–2183, **2018**. https://doi.org/10.1021/acsnano.7b08539.

[14] B. Kulyk, B.F.R. Silva, A.F. Carvalho, S. Silvestre, A.J.S. Fernandes, R. Martins, E. Fortunato, F.M. Costa, "Laser-Induced Graphene from Paper for Mechanical Sensing," *ACS Appl. Mater. Interfaces*, 13, 10210–10221, **2021**. https://doi.org/10.1021/acsami.0c20270.

[15] X. Zang, C. Shen, Y. Chu, B. Li, M. Wei, J. Zhong, M. Sanghadasa, L. Lin, "Laser-Induced Molybdenum Carbide-Graphene Composites for 3D Foldable Paper Electronics," *Adv. Mater.*, 30, 1800062, **2018**. https://doi.org/10.1002/adma.201800062.

[16] Y. Yao, X. Duan, M. Niu, J. Luo, R. Wang, T. Liu, "One-step process for direct laser writing carbonization of NH4H2PO4 treated cellulose paper and its use for facile fabrication of multifunctional force sensors with corrugated structures," *Cellulose*, 26, 7423–7435,

2019. https://doi.org/10.1007/s10570-019-02617-4.

[17] S. Lee, S. Jeon, "Laser-Induced Graphitization of Cellulose Nanofiber Substrates under Ambient Conditions," *ACS Sustain. Chem. Eng.*, 7, 2270–2275, **2019**. https://doi.org/10.1021/acssuschemeng.8b04955.

[18] W.R. de Araujo, C.M.R. Frasson, W.A. Ameku, J.R. Silva, L. Angnes, T.R.L.C. Paixão, "Single-Step Reagentless Laser Scribing Fabrication of Electrochemical Paper-Based Analytical Devices," *Angew. Chemie - Int. Ed.*, 56, 15113–15117, **2017**. https://doi.org/10.1002/anie.201708527.

[19] S. Lee, H. Jang, H. Lee, D. Yoon, S. Jeon, "Direct Fabrication of a Moisture-Driven Power Generator by Laser-Induced Graphitization with a Gradual Defocusing Method," *ACS Appl. Mater. Interfaces*, 11, 26970–26975, **2019**. https://doi.org/10.1021/acsami.9b08056.

[20] Y. Chyan, J. Cohen, W. Wang, C. Zhang, J.M. Tour, "Graphene Art," *ACS Appl. Nano Mater.*, 2, 3007–3011, **2019**. https://doi.org/10.1021/acsanm.9b00391.

[21] P. Zhao, G. Bhattacharya, S.J. Fishlock, J.G.M. Guy, A. Kumar, C. Tsonos, Z. Yu, S. Raj, J.A. McLaughlin, J. Luo, N. Soin, "Replacing the metal electrodes in triboelectric nanogenerators: High-performance laser-induced graphene electrodes," *Nano Energy*, 75, 104958, **2020**. https://doi.org/10.1016/j.nanoen.2020.104958.

[22] J.L. Velho, Mineral fillers for paper: why, what, how, TECNICELPA Technical books, **2003**.

[23] A. Ebringerová, "Structural Diversity and Application Potential of Hemicelluloses," *Macromol. Symp.*, 232, 1–12, **2005**. https://doi.org/10.1002/masy.200551401.

[24] R. Deutschmann, R.F.H. Dekker, "From plant biomass to bio-based chemicals: Latest developments in xylan research," *Biotechnol. Adv.*, 30, 1627–1640, **2012**. https://doi.org/10.1016/j.biotechadv.2012.07.001.

[25] M.G. Stanford, K. Yang, Y. Chyan, C. Kittrell, J.M. Tour, "Laser-Induced Graphene for Flexible and Embeddable Gas Sensors," *ACS Nano*, 13, 3474–3482, **2019**. https://doi.org/10.1021/acsnano.8b09622.

[26] M.R. Bobinger, F.J. Romero, A. Salinas-Castillo, M. Becherer, P. Lugli, D.P. Morales, N. Rodríguez, A. Rivadeneyra, "Flexible and robust laser-induced graphene heaters photothermally scribed on bare polyimide substrates," *Carbon*, 144, 116–126, **2019**. https://doi.org/10.1016/j.carbon.2018.12.010.

[27] R. Han, L. Wang, X. Tang, J. Qian, J. Yu, X. Chen, Y. Huang, "Facile fabrication of rGO/LIG-based temperature sensor with high sensitivity," *Mater. Lett.*, 304, 130637, **2021**. https://doi.org/10.1016/j.matlet.2021.130637.

[28] L. Dan, A.L. Elias, "Flexible and Stretchable Temperature Sensors Fabricated Using Solution-Processable Conductive Polymer Composites," *Adv. Healthc. Mater.*, 9, 2000380, **2020**. https://doi.org/10.1002/adhm.202000380.

[29] S. Gandla, M. Naqi, M. Lee, J.J. Lee, Y. Won, P. Pujar, J. Kim, S. Lee, S. Kim, "Highly Linear and Stable Flexible Temperature Sensors Based on Laser-Induced Carbonization of

Polyimide Substrates for Personal Mobile Monitoring," *Adv. Mater. Technol.*, 5, 2000014, **2020**. https://doi.org/10.1002/admt.202000014.

[30] B. Kulyk, B.F.R. Silva, A.F. Carvalho, P. Barbosa, A. V. Girão, J. Deuermeier, A.J.S. Fernandes, F.M.L. Figueiredo, E. Fortunato, F.M. Costa, "Laser-Induced Graphene from Paper by Ultraviolet Irradiation: Humidity and Temperature Sensors," *Adv. Mater. Technol.*, 2101311, 2101311, **2022**. https://doi.org/10.1002/admt.202101311.

[31] A. Ramos, S. Sousa, D. V. Evtuguin, J.A.F. Gamelas, "Functionalized xylans in the production of xylan-coated paper laminates," *React. Funct. Polym.*, 117, 89–96, **2017**. https://doi.org/10.1016/j.reactfunctpolym.2017.06.006.

[32] T.M.P. Gomes, A.P. Mendes De Sousa, Y.I. Belenkiy, D. V. Evtuguin, "Xylan accessibility of bleached eucalypt pulp in alkaline solutions," *Holzforschung*, 74, 141–148, **2020**. https://doi.org/10.1515/hf-2019-0023.

[33] K. Petzold, K. Schwikal, W. Günther, T. Heinze, "Carboxymethyl Xylan - Control of Properties by Synthesis," *Macromol. Symp.*, 232, 27–36, **2005**. https://doi.org/10.1002/masy.200551404.

2.4 Laser-induced graphene from paper for non-enzymatic uric acid electrochemical sensing in urine

Bohdan Kulyk[1,2], Sónia O. Pereira[1], António J.S. Fernandes[1], Elvira Fortunato[2], Florinda M. Costa[1], Nuno F. Santos[1]

1 – i3N, Department of Physics, University of Aveiro, Campus Universitário de Santiago, 3810-193 Aveiro, Portugal.

2 – i3N/CENIMAT, Department of Materials Science and CEMOP/UNINOVA, NOVA School of Science and Technology, NOVA University Lisbon, Campus de Caparica, 2829-516 Caparica, Portugal.

Abstract:

Laser-induced graphene from paper (paper-LIG) was applied in non-enzymatic electrochemical sensing of uric acid (UA) in human urine. Paper-LIG was formed by CO_2 laser modification of paper into a 3D graphene arrangement. Kinetic analysis of paper-LIG electrodes returned effective heterogeneous electron transfer standard rate constants of 1.4×10^{-3} cm s^{-1} and 7.8×10^{-4} cm s^{-1} for $[Ru(NH_3)_6]^{2+/3+}$ and $[Fe(CN)_6]^{4-/3-}$ redox probes, respectively. These electrodes were able to detect and quantify uric acid in PBS within the 10–300 μM range at pH between 5.6 and 7.4. At pH 7.4, a linear response (r^2=0.999) from 10 to 250 μM was achieved, with a limit of detection of 3.97 μM and a sensitivity of 0.363 μA cm^{-2} μM^{-1}. Paper-LIG electrodes denoted adequate selectivity in synthetic urine as well as in ascorbic acid (AA) and dopamine (DA)-containing electrolytes. Determination of urinary UA content in human samples returned a concentration of c.a. 1.8–1.9 mM, within the range for healthy individuals. Recoveries of samples spiked with 50 and 100 μM UA were 100.6% and 95.4%, respectively, with satisfactory reproducibility and stability. These cheap, lightweight, flexible, and eco-friendly paper-LIG biosensors for non-enzymatic quantification of UA in human urine pave the way to widespread application in the detection of other important biomarkers.

2.4.1 Introduction

The unique combination of outstanding properties of graphene, a two-dimensional sheet of carbon atoms first isolated in 2004 [1], has spurred a considerable body of work aimed at realizing the substantial promise it holds in a vast number of fields [2]. Among these, the advancements in its potential biomedical applications are particularly encouraging, encompassing topics such as drug delivery [3,4], tissue engineering [5], and biosensors [6]. In the latter, and particularly in the context of electrochemical sensing, graphene and graphene-based materials are excellent candidates on account of their electrocatalytic activity and electrochemical performance [7,8]. With heterogeneous electron transfer (HET) rates rivalling or even exceeding those of other commonly employed materials such as glassy carbon [9], graphite [10] and carbon nanotubes [9], while aided by its high specific surface area and chemical stability, graphene has a bright future as an electrochemical transducer [11].

Adding to an already rich tapestry of graphene-based materials, in 2014 it was shown that irradiation of flexible commercial polymers such as polyimide with an infrared (CO_2) laser can produce a porous, conductive graphene foam [12]. This material was dubbed laser-induced graphene (LIG), and the ability to easily pattern conductive paths and electrodes onto flexible substrates opened the door to its use in actuators [13], sensors [14–19], and energy storage devices [12], among other applications. Currently, LIG can be formed using different laser wavelengths [14,19], and on different carbon-containing substrates, including nature-derived materials such as wood [20], cork [21], xylan [22], and paper (the latter referred to as paper-LIG) [23].

Paper is a remarkable material in its own right. Being cheap, lightweight, and flexible, it finds many uses in the daily lives of people throughout the world [24]. In addition to that, paper is recyclable and biodegradable, features which are worth noting as humanity faces considerable challenges concerning the management of natural resources and the preservation of the environment [25].

These attributes make paper particularly well suited for application in low-cost point-of-care biomedical devices [26]. This has been best exploited in lateral flow tests [27], and currently there is a growing interest concerning paper-based microfluidic assay devices (μPADs) [28], taking advantage of paper's water absorption capacity and wicking ability. Being cheap and disposable, these devices seek to facilitate the access to affordable and fast on-site diagnostics and healthcare. Graphene-based materials have also been employed in paper-based analytical devices [29–33]. However, as most of the examples of paper-supported graphene biosensors require a specific step for the application of the graphene-based material onto the paper, none of them can boast the ease of fabrication characteristic of paper-LIG, where the paper itself is converted into the electrochemically active graphene material. Even comparing to the previously reported biosensors employing polyimide derived LIG (PI-LIG), the abundance and availability of paper at a substantially lower cost presents a considerable advantage from the production point of view. Recognizing these benefits relative to LIG obtained from synthetic polymers, recently paper-LIG started getting attention in the detection of analytes such as ascorbic and caffeic acids [34], and more recently in enzymatic amperometric biosensors for glucose detection [35], but so far sensing in real biological samples has not been demonstrated using this material.

In this work, we employ laser-induced graphene obtained from common filter paper as an electrode for the non-enzymatic electrochemical detection and quantification of uric acid (UA).

Uric acid is the main product of purine metabolism, constituting a clinically relevant compound, since abnormal levels of UA are associated to diseases such as hyperuricemia, gout, inflammatory arthritis, and chronic renal disease. In conjunction with other biomarkers, UA concentration levels are also useful for the screening and monitoring of some cardiovascular diseases and diabetes-related complications [36,37]. The sensing capabilities of these paper-LIG electrodes are demonstrated both in artificial and real human urine samples. Both the synthesis of paper-LIG and the electrochemical measurements are facile and fast, while the sensors themselves are low-cost and disposable, encouraging real-life applications in affordable, environmentally friendly biosensing.

2.4.2 Results and discussion

2.4.2.1 Synthesis and characterization of paper-LIG

Cellulose paper was used for the synthesis of laser-induced graphene. While non-enzymatic uric acid sensors based on PI-LIG have been reported previously, cellulose paper presents considerable advantages as the precursor substrate, from both the production and the application standpoints. Specifically, paper is substantially cheaper and more widely available than the commercial polymers used for LIG synthesis. Moreover, paper is recyclable and biodegradable. These attributes make paper-LIG biosensors extremely attractive for low-cost, single-use, point-of-care analytical applications, particularly in low-income areas. For the synthesis, illustrated in **Figure 2.4.1a**, the cellulose paper is treated with an environmentally friendly fire retardant to prevent its breakdown into volatile compounds [23]. Then, the paper is irradiated twice with a 10.6 μm laser, first out of focus and then in focus. The first irradiation promotes the conversion of cellulose into char, while the second one graphitizes it into laser-induced graphene [15]. The resulting material presents Raman spectra characteristic of LIG, with well defined, symmetrical D, G and 2D peaks (**Figure 2.4.1b**) [12]. The magnitude of the I_D/I_G intensity ratio is closely related to structural disorder in the sp^2 carbon lattice, scaling with the concentration of defects [38]. Paper-LIG displays an I_D/I_G ratio close to 1 for 442 nm excitation wavelength, which outlines a relatively high concentration of defects. Provided that it does not compromise the electrical conductivity, this is desirable for electrochemical sensing, since defects in carbon nanostructures, such as edge plane defects, are known to play an important role in electron transfer due to enhanced local density-of-states [39,40]. A further inspection of these flexible paper-LIG electrodes, depicted in **Figure 2.4.1c** after the encapsulation with insulating varnish, allows to compare the morphology of paper before (**Figure 2.4.1d,e**) and after (**Figure 2.4.1f-h**) its transformation into LIG, as revealed by secondary electron scanning electron microscopy (SE-SEM). Here, it can be seen that the irradiated cellulose fibres become porous, forming web-like structures. Similar porosity formation is known to occur in phosphoric acid activation of cellulosic material (paper, wood, etc.) to obtain activated carbon, where cross-links are formed through phosphate linkages [41,42], which is relevant here due to the use of the phosphate based fire retardant. This porosity, which can be associated with a larger surface area, can be particularly beneficial for biosensing applications.

Additional information about the transformation of paper into paper-LIG can be obtained from XPS analysis. **Figure 2.4.1i** shows overview spectra of fire retardant treated paper and the resulting paper-LIG (both after being washed with DI water). While the paper substrate shows the presence of only C and O, characteristic of cellulose, after laser irradiation one finds additional chemical elements, namely P, N and Na. This is due to some retention of the phosphate-based fire retardant in the paper-LIG, most likely inside the porous structure that is formed. As

for the C 1s peak (**Figure 2.4.1j**), in the case of paper the most prominent components are due to C–O and C=O bonds, at 286.46 eV and 287.91 eV, respectively, accompanied by less intense components at 284.80 eV and 289.32 eV, assigned to C–C/C–H and O–C=O bonds [43]. For paper-LIG, on the other hand, the main feature is the asymmetrical component at 284.36 eV, corresponding to sp^2-hybridized carbon, while the components corresponding to carbons bonded with oxygen [44] are far less prominent than in non-irradiated paper. The relative atomic concentration of C–O bonds, for example, decreases from 69.69% to 8.92% after laser irradiation. This points toward the release of oxygen under laser irradiation, accompanied by the reorganization of the carbon atoms to form graphitic domains (although some oxygen remains, either due to some unconverted cellulose or due to partial oxidation of the paper-LIG). The predominantly sp^2 nature of paper-LIG is further confirmed by the D-values obtained from the differentiated C KLL Auger features (**Figure 2.4.1k**), being equal to 10 for non-irradiated paper and 18 for paper-LIG, the latter being much closer to the values seen for sp^2-rich carbons [45]. The loss of oxygen content is also confirmed by the lowering of its atomic percentage from 41.99% in paper to 17.24% in paper-LIG. The paper-LIG is also confirmed to be conductive, possessing sheet resistances of 40–50 $\Omega\ sq^{-1}$, in line with previous reports concerning paper-LIG [15]. This conductivity, coupled with the apparent porosity of paper-LIG and its defect-rich structure, make it potentially attractive as an electrochemically active material with electrocatalytic properties.

The paper-LIG electrodes were subjected to electrochemical impedance spectroscopy measurements to gain insights into the underlying electrochemical mechanisms of the porous graphene arrangement. Two different equivalent circuits were used to model the cell as schematically shown in **Figure 2.4.2**. The first one, the modified Randles (MR) circuit, is commonly employed to model electrochemical response of planar electrodes and is composed of (i) an equivalent series resistance, R_S, which gathers all uncompensated resistances including contact and paper-LIG bulk resistance, (ii) a resistance R modelling possible capacitance self-discharge effects, and (iii) a constant phase element (CPE) Q, which models non-ideal capacitive behaviour due to surface roughness effects. This model does not consider the porosity of the electrode material, but rather the existence of a continuous front electrode surface. On the other hand, the second one is a transmission line model as described by Bisquert [46,47], known as Bisquert open (BTO). In the BTO, only phenomena occurring at the inner pore walls are taken into account, and the base electrode region is considered inactive. R_{EL} represents the pore resistance to electrolyte diffusion and ζ the reactions occurring at the inner pore surface, constituted by a parallel combination of a resistor and a CPE. Pore depth is represented by L and dashed circuit lines represent the stepwise repetition of the $R_{EL}||\zeta$ block along the pore. Detailed information on transmission line models and simplifications/assumptions of the Bisquert open model can be found in the related original works [46,47].

It is clear from the high-frequency portion of the Bode and Nyquist plots that the electrochemical cell is characterized by relatively low internal resistances R_S, demonstrating the conductive nature of paper-LIG, in agreement with the Van der Pauw measurements that returned a sheet resistance of 40–50 $\Omega\ sq^{-1}$. On the other hand, the MR circuit shows a poor agreement with the impedance spectrum at all frequency ranges as seen in the Bode plots of **Figure 2.4.2b** and in the Nyquist plots of **Figure 2.4.2c**. It fails to describe the incremental increase of |Z| with decreasing frequency down to 1 Hz as well as the particular evolution of the phase at higher frequencies (**Figure 2.4.2b**). It also fails to explain the response in the complex plane at higher frequencies, where a straight line with approximately a unitary slope is observed (inset of **Figure 2.4.2c**). These features arise from porosity effects, which are contemplated by the BTO

model, which in turn denotes excellent agreement with the data at all frequencies, both in the Bode and Nyquist plots. Hence, it is clear that porosity plays a role in the electrochemical response of paper-LIG electrodes, similarly to the observed for PI-LIG [48] using the same electrolyte. Note that **Figure 2.4.2a** shows a schematic representation of paper-LIG porosity as an inter-fibre arrangement, but in fact the intra-fibre porosity should actually be the porosity governing the observed impedimetric response, so that **Figure 2.4.2a** is to be interpreted regarding schematization purposes only. **Table S2.4.1** and **Table S2.4.2** in **Section 2.4.7** compile the fitting results of the MR and BTO models, respectively.

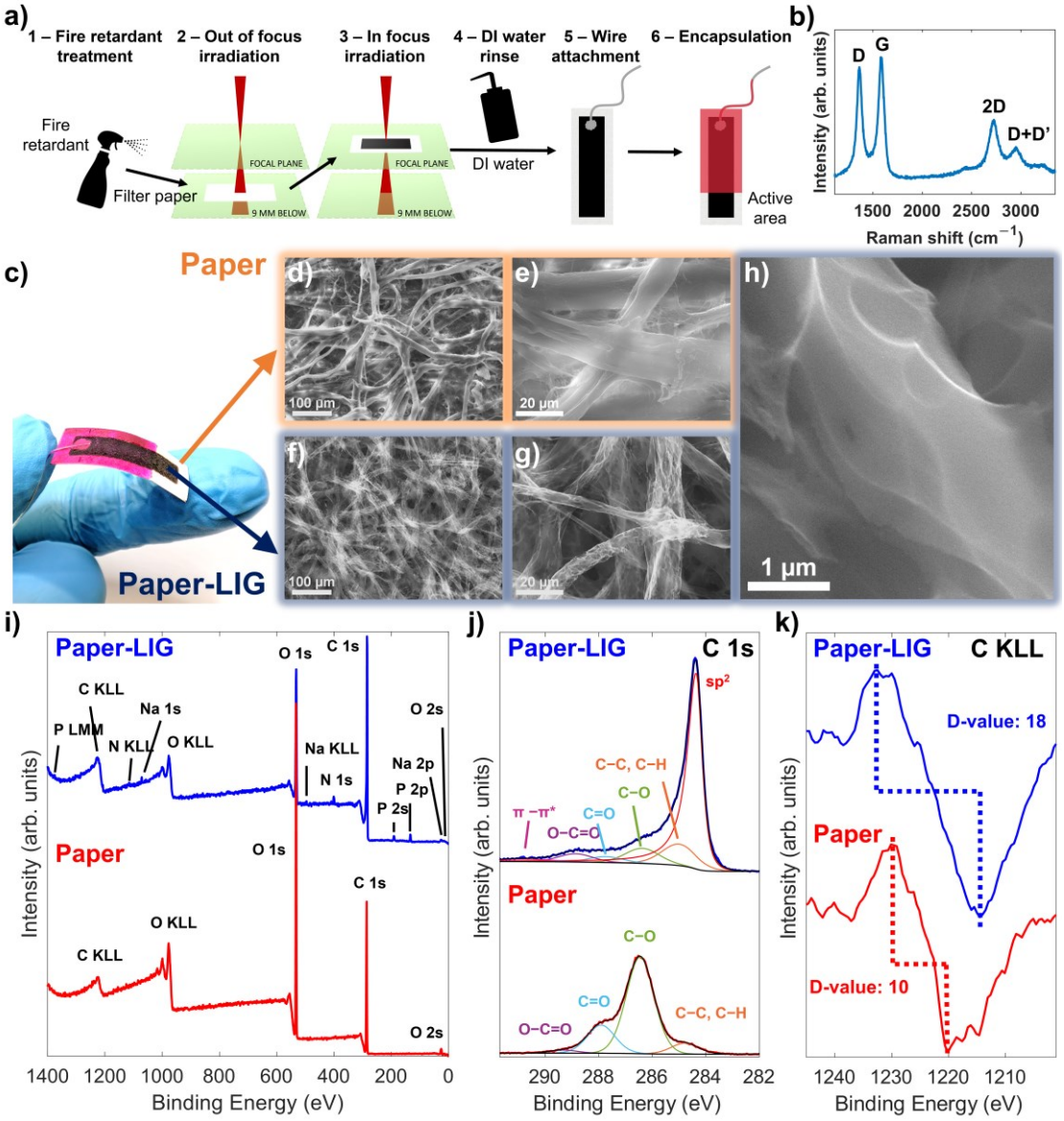

Figure 2.4.1. (a) Schematic illustration of the preparation of the paper-LIG electrodes. **(b)** Representative Raman spectrum of paper-LIG. **(c)** Photograph of a paper-LIG sensing unit. SEM micrographs of the **(d,e)** unmodified paper and **(f,g)** laser irradiated paper. **(h)** SEM micrograph showing a magnified view of the paper-LIG structure, evidencing its thin "veil-like" appearance. **(i)** Overview XPS spectra comparing paper and paper-LIG. **(j)** High-resolution XPS spectra of the C 1s peak of the paper and paper-LIG, with the identification of the respective components. **(k)** Differentiated C KLL Auger features of paper and paper-LIG, with the corresponding D-values.

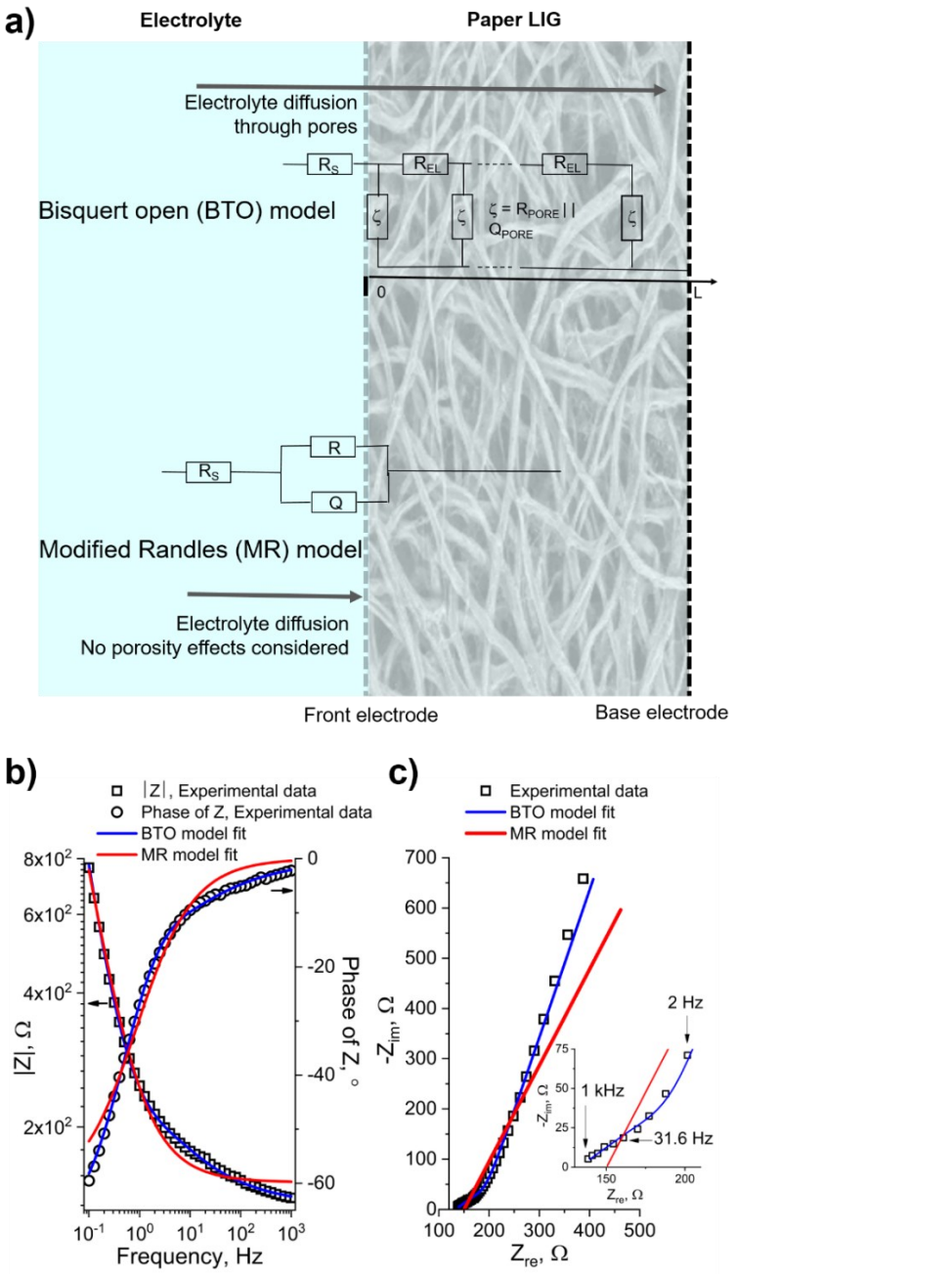

Figure 2.4.2. (a) Schematic representation of the paper-LIG-electrolyte interface and the two equivalent circuit models employed to describe the impedimetric response, which is shown via the **(b)** Bode and **(c)** Nyquist plots. Note that the number of points in the data of the inset in (c) has been reduced for clarity's sake. The electrolyte is 3.5 M KCl aqueous solution.

The electron transfer capabilities of the paper-LIG electrodes were assessed via cyclic voltammetry analysis employing reversible, well-behaved redox pairs, $[Ru(NH_3)_6]^{2+/3+}$ and $[Fe(CN)_6]^{4-/3-}$. The usage of different redox pairs to characterize the electrochemical response is desirable, allowing probing different potential window regions, distinct charge states and reaction mechanisms at the electrode surface. The outer-sphere $[Ru(NH_3)_6]^{2+/3+}$ redox system is regarded as a standard probe for heterogeneous electron transfer (HET) analysis, permitting a general comparison among different electrodes whilst minimizing surface chemistry effects on HET, which can be exacerbated employing inner-sphere redox pairs, such as $[Fe(CN)_6]^{4-/3-}$.

Figure 2.4.3a shows the cyclic voltammograms of 5 mM $[Ru(NH_3)_6]^{2+/3+}$ in PBS (pH 7.4) at varying scan rate (ν).

The voltammograms denote well-defined anodic and cathodic waves, with peak-to-peak separation (ΔE_p) falling within 120−335 mV and a half wave potential of −200 mV vs SCE. Peak currents of both cathodic and anodic branches increase linearly with the square root of the scan rate with similar slopes (**Figure 2.4.3b**), indicating that the redox reaction is limited by semi-infinite planar-diffusion of $[Ru(NH_3)_6]^{2+/3+}$ species. The log(I)-log(ν) plot of **Figure 2.4.3b** denotes superimposed linearity for the anodic and cathodic branches with slopes of about 0.4. Whilst close to the theoretical value of 0.5 for a purely semi-infinite diffusion process, the observed deviations point to the presence of a competing mechanism to electron transfer. Such deviations are observed often for several electrode materials and in the present case it is most likely due to the thin layer effect [49], where small portions of electrolyte are trapped within the immediate surroundings of the electrode surface, thus influencing the process of diffusion of electroactive species. This is prone to occur in porous and intricate morphologies such as the present paper-LIG and is in accordance with the need to consider a transmission line model to properly describe the electrode's impedimetric response. Nevertheless, the present analysis indicates that the redox reaction proceeds in a quasi-reversible regime suitable for HET kinetic analysis employing the Nicholson method (**Figure 2.4.3c**). The calculated effective HET standard rate constant, k^0_{eff}, is about 1.4×10^{-3} cm s^{-1}, which is nearly one order of magnitude lower than that calculated in similar experimental conditions for LIG on polyimide [16], yet comparable to several types of graphene-based electrodes reported in the literature [39,50,51].

Regarding the inner-sphere $[Fe(CN)_6]^{4-/3-}$ redox pair, the voltammograms also denote well-defined anodic and cathodic waves with half wave potential of 186 mV (**Figure S2.4.2a**, **Section 2.4.7**). The log(I)-log(ν) slopes are about 0.44 and peak currents also scale linearly with the square root of the scan rate, yet at different cathodic/anodic slopes, as seen in **Figure S2.4.2b**, **Section 2.4.7**. This indicates a higher irreversibility degree of the redox reaction. Compared to $[Ru(NH_3)_6]^{2+/3+}$, the k^0_{eff} for $[Fe(CN)_6]^{4-/3-}$ is therefore lower, 7.8×10^{-4} cm s^{-1} (**Figure S2.4.2c**, **Section 2.4.7**), a value slightly higher than the one obtained from independently conducted measurements concerning a paper-LIG enzymatic glucose sensor [35]. This is an order of magnitude lower compared to LIG on polyimide [16] for the same redox probe in similar experimental conditions, but still comparable to other graphene-based electrodes in the literature [39,52].

All around, these results underline the appropriate structural arrangement as well as electrical and electron transfer capabilities of paper-LIG, suitable for electroanalytical purposes, further encouraging the study of non-enzymatic detection of clinically relevant analytes via direct electrooxidation/reduction, such as the case of uric acid as presented in the following sections.

2.4.2.2 Quantification of uric acid in PBS

The uric acid electrochemical oxidation on paper-LIG electrodes was evaluated employing different PBS formulations yielding different pH values, specifically pH 7.4, 6.6 and 5.6 at a constant ionic strength, up to a concentration of UA of 300 μM, close to the solubility limit of UA in water (~350 μM) [53]. Actually, in urine, UA is found at much higher concentrations, as this complex matrix contains for instance proteins and other compounds aiding to achieve a higher solubility [54,55]. Moreover, temperature, ionic strength, and pH also play an important role in the solubility of UA [53]. Uric acid is a diprotic acid that, above its acid dissociation constant

(pK_{a1}=5.4 and pK_{a2}=9.8), appears in the form of urate ions [56], see the chemical structure in **Figure S2.4.3a** (**Section 2.4.7**).

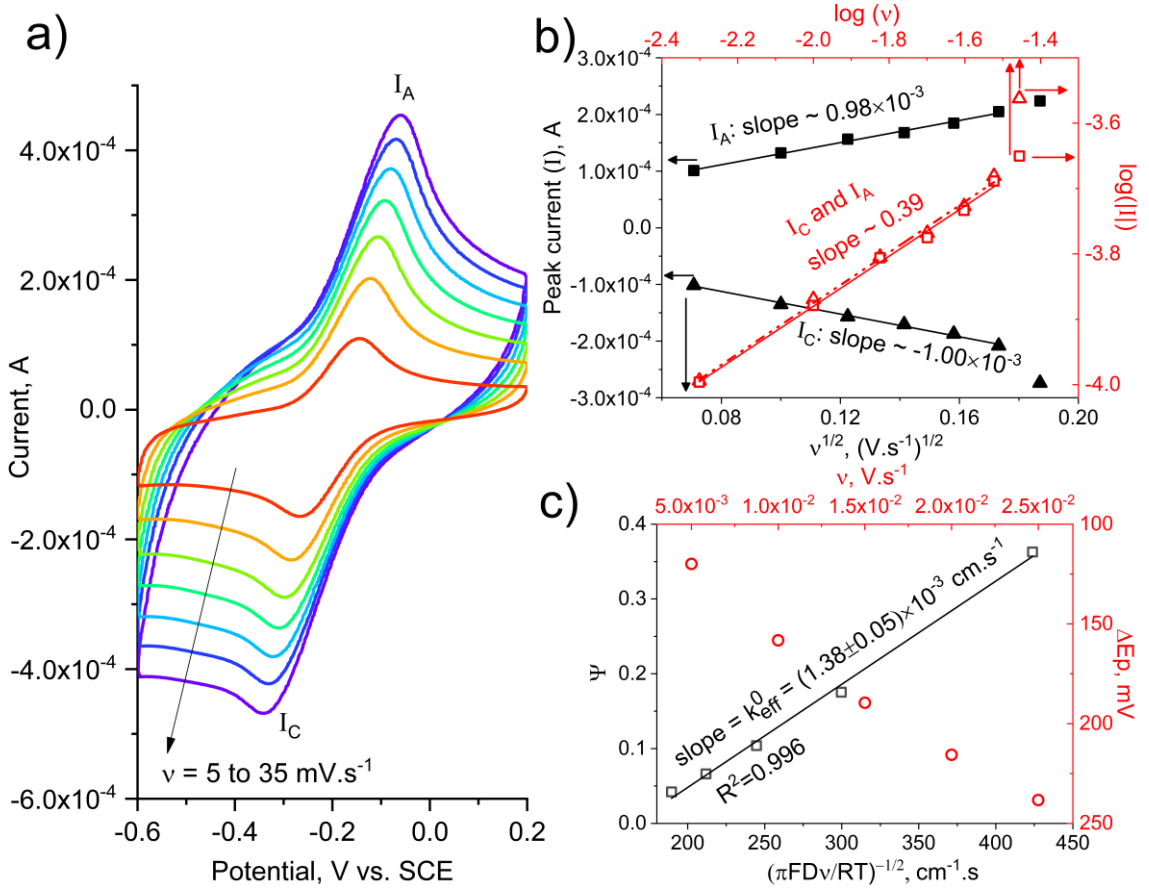

Figure 2.4.3. (a) Cyclic voltammograms at varying scan rate (from red to purple: 5, 10, 15, 20, 25, 30 and 35 mV s^{-1}) of paper-LIG electrode in PBS (pH 7.4) containing 5 mM $[Ru(NH_3)_6]^{3+}$. **(b)** Anodic and cathodic peak current versus square root of scan rate (black squares and triangles, respectively) after capacitive current subtraction, and the corresponding linear regressions (solid black lines). Logarithmic correlation plot between peak current and scan rate for the cathodic (red triangles) and anodic (red squares) branches, along with the corresponding linear regressions (dashed and solid red lines, respectively). **(c)** HET kinetic analysis within the scan rate range of 5–25 mV s^{-1}, showing ΔE_p (red circles) and kinetic parameter Ψ (black squares) obtained via **Equation (1)**, along with the linear regression (solid black line) for estimation of effective HET standard rate constant, k^0_{eff}, via **Equation (2)**.

Figure 2.4.4a shows the DPV oxidation waves assignable to uric acid electrochemical oxidation into a diimide quininoid by transferring 2 protons and 2 electrons (see **Figure S2.4.3b**, **Section 2.4.7**). The diimide quininoid is very unstable and undergoes subsequent reactions, which follow different pathways dependent of the pH below or above the pK_a, forming for instance allantoin [57,58]. For pH 7.4 and 6.6, the DPV peaks are sharp and well-defined, whereas for pH 5.6 (close to the pK_{a1}) they tend to widen. The deformed peak shape at pH 5.6 could therefore evidence the contribution of other redox processes downstream of UA oxidation, such as the presence of intermediary subproducts of the redox reaction at pH≤pK_{a1} that have electroactivity near or superimposed to the UA [58]. A strong linear correlation (r^2=0.999) between peak current density and UA concentration exists at pH 7.4 up to 250 µM, whilst linearity is progressively lost with decreasing pH for values close to pK_{a1} (**Figure 2.4.4b**), even though peak current densities and sensitivity increase with decreasing pH, as observed elsewhere [59,60]. The peak potential shifts linearly with the pH within the 5.6 to 7.4 range at a rate of −75 mV pH^{-1} for 50 µM UA (see **Figure S2.4.4**, **Section 2.4.7**). A similar behaviour was found

by Liu et al. [61], where a slope of −73 mV pH^{-1}, in a pH range from 4 to 8, was obtained for a wide range of UA concentrations (5–600 µM). The observed linear behaviour indicates that the same reaction regime, the UA oxidation into diimide quininoid, is ruling in this pH range.

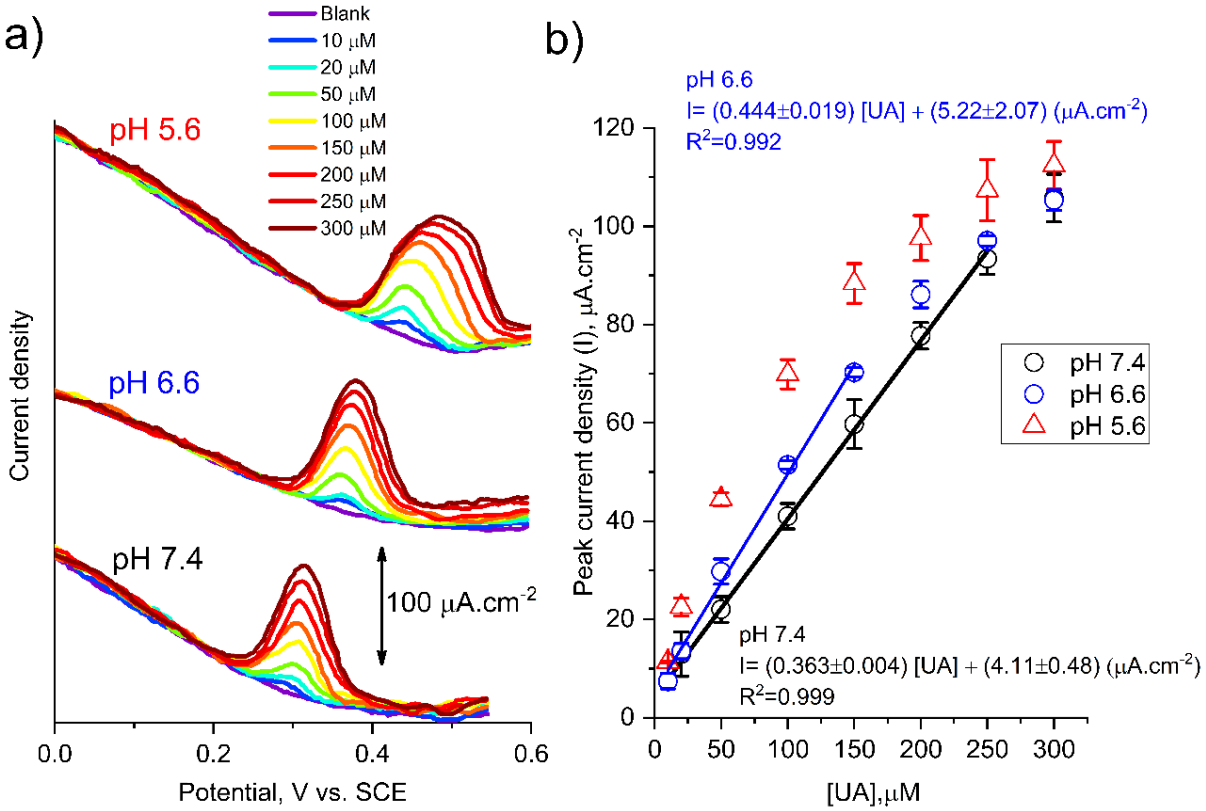

Figure 2.4.4. (a) DPV response of paper-LIG electrodes in UA-containing PBS at different pH values. Measurements at each pH are grouped and shifted in intensity for clarity. **(b)** Corresponding peak current density versus concentration of UA and linear calibration curves, where applicable. Error bars are standard deviations from independent quadruplicate measurements.

The limit of detection (LOD) for pH 7.4 is 3.97 µM, calculated via the calibration curve using the $3\sigma/S$ criterion, where σ is the standard deviation of the y-intercept of the analytical curve and S is the sensitivity equalling the slope of the analytical curve [62]. The LOD obtained for these non-enzymatic sensing units based on paper-LIG is higher compared to some enzymatic biosensors presented in the literature, including paper-based sensors, where LOD as low as 0.06 µM [63] and 0.008 µM [64] have been reported. It is also slightly higher compared to non-enzymatic LIG sensors scribed on polyimide and modified with Pt nanoparticles (0.22 µM) [65]. Nevertheless, one should keep in mind that extremely low LOD is not mandatory regarding UA detection and quantification in human urine, given the reference values usually under consideration, above 1 mM [66,67]. Indeed, the paper-LIG electrodes provide a linear range within 10–250 µM UA, which constitutes a wide and useable range suitable for analysis of dilute urine samples. For instance, using a 1:20 dilution, this means that UA quantification is possible in the range of about 200 µM to 5 mM, which covers the 1 mM–4.4 mM range taken as reference values encountered in real, non-diluted human urine [66]. Moreover, these simple, environmentally friendly and inexpensive sensing units provide a sensitivity of 0.363 µA cm^{-2} $µM^{-1}$ at pH 7.4, which surpasses that of some enzymatic UA sensors reported in the literature that are much more complex and costly to produce [63,68]. Compared to PI-LIG UA sensors, for which electron transfer kinetics are found to be impressive [16], sensitivities are one order of

magnitude lower, 5.4 μA cm^{-2} μM^{-1} for PI-LIG [65], yet within a much narrower UA concentration range up to 20 μM and for which no measurements in biological fluids were demonstrated. **Table 2.4.1** gathers several reports on non-enzymatic UA sensors based on LIG, for comparison purposes.

Table 2.4.1. Comparison of figures of merit determined for LIG-based biosensors for non-enzymatic detection of uric acid.

Electrode	Linear Range(s), μM	Sensitivity, μA μM^{-1} cm^{-2}	LOD (μM)	Detection technique	Selectivity tests	Tested in real samples?	[Ref]
Paper-LIG	10-250	0.363	3.97	DPV	AA, DA, synthetic urine	Human urine	This work
PI-LIG	~0-20	5.4	-	DPV	-	No	[65]
PI-LIG/Pt NPs	~0-60	8.29	0.22	DPV	AA, DA	No	[65]
PI-LIG on ITO	5 -100	3.1	5.0 (measured)	DPV	AA, DA	No	[69]
PI-LIG	3 - 40	3.50	0.74	DPV	Glucose, tyrosine, urea, DA, AA	Human sweat	[70]
PI-LIG/ PBSE/Pt NPs	5-480	0.157	0.018	Amperometry	AA, lactic acid, acetaminophen	No	[71]
PI-LIG/ Chitosan/ Au NPs	1-30; 30-100	1.65; 0.48 (μA μM^{-1})	0.33	DPV	AA, DA, Glucose, lactate	Human blood serum	[72]

*DA-dopamine, AA-ascorbic acid, NPs – nanoparticles, ITO – indium tin oxide, PBSE – succinimide ester.

Reproducibility among sensing units is found to be highly dependent on the UA concentration. Relative standard deviations of the signal from quadruplicates diminish with increasing UA concentration, being above 20% for 10 and 20 μM UA and below 11% for 50 μM UA and above, for both pH 7.4 and pH 6.6, and always below 8% for pH 5.6. Moreover, the electroanalytical performance has shown no dependence on long-term storage up to one year, the response of the sensing units varying within the mentioned standard deviation values with no observable correlation with storage time.

2.4.2.3 Selectivity tests – ascorbic acid, dopamine and synthetic urine

Ascorbic acid (AA), also known as vitamin C, is a major interfering agent in clinical analysis, including urinalysis. Studies employing commercially available dipstick tests unambiguously show that the presence of AA in the urine samples severely interferes with bilirubin, nitrite, haemoglobin and glucose detection, causing false negative results [73,74]. Moreover, ascorbic acid is an electroactive compound that often interferes in electroanalytical measurements, especially with analytes for which the formal redox potential is close to that of AA, which is the case of dopamine [16,65], and of UA to a lesser extent. Ascorbic acid in urine can reach relevant

levels depending on the amounts of vitamin C ingestion, mostly when ingested as supplementation [73,74]. The selectivity test against AA of the paper-LIG UA sensors in PBS (pH 7.4) is presented in **Figure 2.4.5a**.

Ascorbic acid exists as a monovalent anion at physiological pH of 7.4 denominated by ascorbate [75], which can be electrochemically oxidized into dehydroascorbate (DHA) by the loss of two electrons and one proton [75]. This reaction occurs at about 0 V vs SCE. At lower AA concentrations, the signal from this reaction is low in intensity and rather broad. In fact, it is known that AA presents lower adsorption strength on graphene-based surfaces compared to UA, namely on LIG, resulting in much lower oxidation currents for similar concentrations [16,65,76]. Both, AA and UA, at physiological pH (pI 4.2 and 5.4, respectively) are found in their anionic form favouring electrostatic repulsion with the LIG surface, namely due to carboxyl groups present on LIG structure as confirmed by XPS (**Figure 2.4.1j**). Still, the fact that UA possesses some degree of aromaticity in its molecular structure, whereas AA does not, favours UA adsorption onto sp^2-rich carbon surfaces, such as paper-LIG (see Raman spectra and XPS in **Figure 2.4.1**).

The UA oxidation signal is unperturbed up to 100 μM AA, with the peak current densities falling within the range as determined for 50 μM UA in PBS (pH 7.4) as shown in **Figure 2.4.5c**. At 500 μM AA and above, the AA oxidation peak at 0 V becomes more defined, several additional anodic waves appear downstream of AA oxidation and the UA oxidation currents increase beyond the expected range. At 10 mM AA, the signal from UA is heavily masked by such reactions, the nature of which is complex and beyond the scope of the present paper. These results indicate relevant interference from AA activity at 500 μM AA and above (**Figure 2.4.5c**). Moreover, after measurements at high AA concentrations and after thorough stirring and washing in DI water, AA and/or DHA-related anodic peaks still appear in the DPV in pure PBS electrolyte, indicating that electrode fouling by AA and related oxidation products has occurred. Hence, the paper-LIG UA sensors suffer from interference and fouling in AA containing electrolyte solutions, yet only at abnormally high AA concentrations. Considering a 1:20 urine dilution as employed in the next section whilst measuring real human urine samples, this would correspond to a concentration of roughly 10 mM AA. Such values did not occur in the human urine collected from volunteers after ingestion of several doses of Vitamin C -containing juices [74], but do occur in the case of Vitamin C supplementation, yet at relatively low probabilities and only at high ingestion doses, above 500 mg [74]. Although out of the scope of this work, it is of note that the use of acetate buffers (pH 4) is reported elsewhere to suppress or minimize the interference of high concentrations of AA in UA detection when employing glassy carbon electrodes [59], which can be a useful strategy for paper-LIG electrodes in such situations.

In addition to AA, dopamine (DA) also constitutes a potential interferent in UA quantification due to its easy electrooxidation and formal electrode potential close to that of UA [16]. DA belongs to the family of catecholamines, constituting a neurotransmitter in several pathways in the central nervous system, with special activity in the kidneys. Normal DA levels in human urine can reach 2–3 μM in 24 h urine tests [77,78], but can be substantially increased in case of some physiological conditions and diseases, such as specific tumours [78]. As seen in **Figure S2.4.5** (**Section 2.4.7**), paper-LIG electrodes are able to separate DA and UA signals by ~150 mV and the quantification of UA is immune to abnormally high DA levels (up to 20 μM), despite some overlapping of DA and UA oxidation waves at higher DA concentrations. This is two orders of magnitude higher than the maximum (normal) levels of DA when considering 1:10 and 1:20 human urine dilutions as employed in this work.

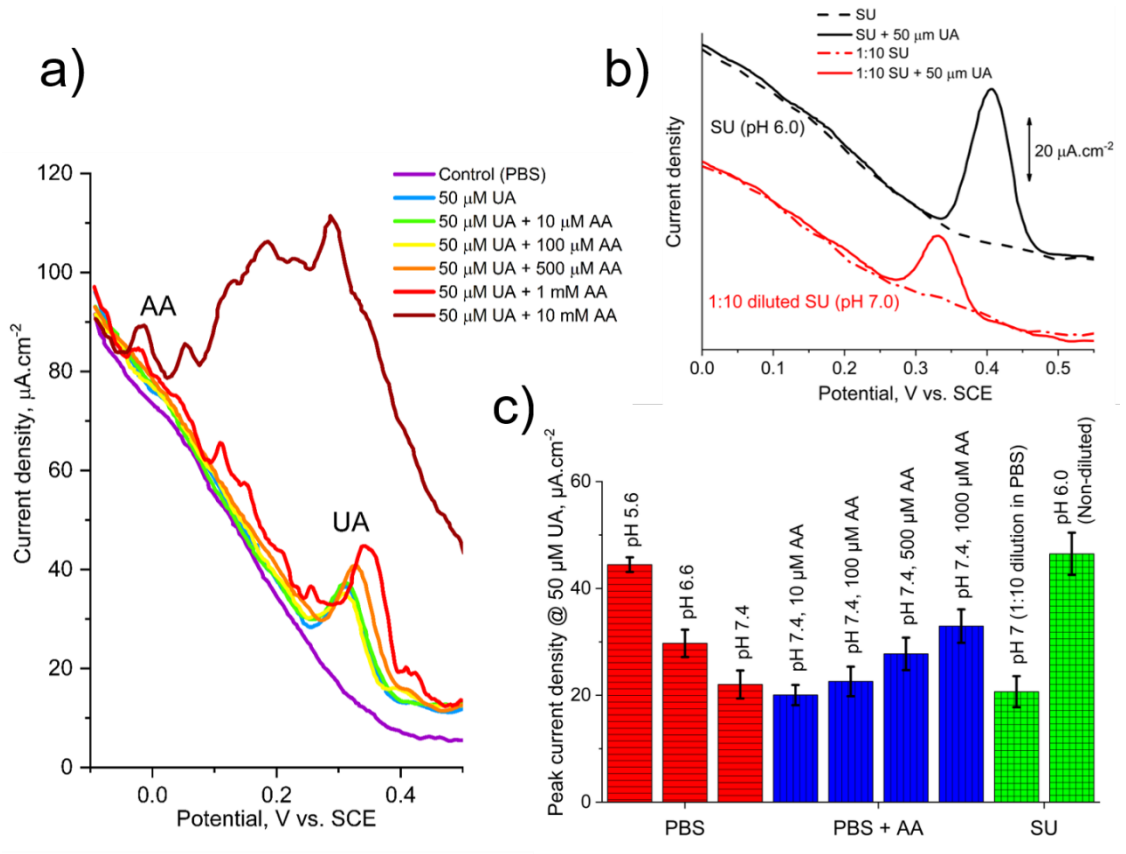

Figure 2.4.5. DPV scans at 50 µM UA concentration: **(a)** in PBS (pH 7.4) plus varying concentrations of AA, and **(b)** in non-diluted and 1:10 diluted synthetic urine (SU). In (b), DPV scans are grouped and shifted in intensity for clarity. **(c)** UA (50 µM) oxidation peak current densities for the previous measurements. Results for PBS at varying pH (see also **Figure 2.4.4**) are also shown for comparison. Error bars are standard deviations from independent quadruplicate measurements.

Selectivity tests were also conducted in synthetic urine (SU) samples, the composition of which is detailed in the experimental section. As seen in **Figure 2.4.5b**, despite the complex formulation of possible interferents in UA detection, none of the constituents of SU induces any measurable faradaic activity in the potential range of interest and hence no direct interference occurs, even if measuring non-dilute samples. Peak potentials closely follow a linear trend with pH at a −75 mV pH^{-1} slope for a UA concentration of 50 µM, as seen in **Figure S2.4.4** (**Section 2.4.7**). This is in line with the observed for measurements in PBS at varying pH, confirming that reaction mechanisms and kinetics are unaltered by the compounds present in SU.

2.4.2.4 Determination of uric acid in real human urine samples

Figure 2.4.6a shows the DPVs of a paper-LIG electrode in 1:10 and 1:20 dilutions of real human urine in PBS (pH 7.4). Uric acid recoveries were tested in 1:20 diluted urine by spiking 50 and 100 µM of uric acid followed by stirring for 5 min, and the corresponding DPVs are also shown. **Table 2.4.2** gathers and details all the measurements and the retrieved values of UA content in urine samples. Firstly, no signs of interfering electroactive species are discernible near the UA oxidation peak. Secondly, the electrochemically inactive species present in urine, such as proteins, have not affected the analytical performance of the electrodes (**Figure 2.4.6b**) taking the calibration curve in PBS pH 7.4 as reference. Indeed, regarding the 1:20 diluted urine, the results point to a concentration of about 1.83 mM of UA in the non-diluted urine, which is

consistent with the expected for urine from healthy individuals, within the ~1–4.4 mM range [66]. Furthermore, the value often taken as reference for 24 h urine tests is about 1 mM [67], yet it is to note that in this work the samples correspond to first morning urine, which tends to concentrate UA.

The average UA recoveries for spiked samples of 1:20 diluted urine are very close to 100%, demonstrating the accuracy of the paper-LIG sensing units and of the measuring methods. A dilution of 1:10 urine was also measured for comparison purposes. Results indicate a concentration of 1.94 mM of UA in non-diluted urine samples, about 106% of that found via the 1:20 diluted urine. This discrepancy is within the standard deviation of the measurements. It is notable that the pH was seen to drop from 7.3 for 1:20 diluted urine to about 7.0–7.1 for 1:10 diluted urine, causing a shift of the oxidation peak towards more positive potentials (red curve in **Figure 2.4.6a**). This is in agreement with measurements in synthetic urine where a 1:10 dilution, pH 7.0, yielded statistically similar current densities compared to those in PBS (pH 7.4).

Reproducibility among different paper-LIG electrodes for measurement of real human urine is satisfactory, always below 11% relative standard deviation (n=4), increasing with UA content.

Despite the inherent suitableness of paper-LIG to be employed as disposable sensing units due to their low cost and environmental friendliness, these electrodes are in fact reusable. Indeed, a blank baseline without any faradaic activity from UA can be easily recovered for every electrode after washing with DI water, after employing either PBS or 1:20 diluted urine in PBS (**Figure S2.4.6a**, **Section 2.4.7**). Moreover, the original UA oxidation signal could be recovered after washing with DI water (**Figure S2.4.6b**, **Section 2.4.7**). This denotes a good stability and repeatability of the paper-LIG electrodes and shows that no severe electrode fouling has occurred. However, the DI water-washing step is necessary, given a small but relevant current intensity from oxidation of adsorbed UA obtained when measuring in pure PBS solution the unwashed electrodes that had previously been subjected to measurements in UA-containing electrolyte solutions.

2.4.3 Conclusions

Paper-LIG constitutes a suitable material for uric acid (UA) quantification in human urine. The porous graphene network formed after CO_2 laser irradiation of paper exhibits adequate electron transfer capabilities, characterized by effective heterogeneous electron transfer standard rate constants of 1.4×10^{-3} cm s^{-1} and 7.8×10^{-4} cm s^{-1} for $[Ru(NH_3)_6]^{2+/3+}$ and $[Fe(CN)_6]^{4-/3-}$ redox probes, respectively. Quantification of UA is immune to physiologically relevant concentrations of dopamine and to several interferents present in synthetic urine formulations. Ascorbic acid (AA) is shown to interfere but only at concentrations of 500 μM and above. Since the determination of UA in real human urine was performed employing 1:20 dilutions in PBS, interference with AA only starts at urinary concentrations of about 10 mM, which seldom occurs and specifically in cases of heavy vitamin C supplementation. Determination of UA in real human urine returned a concentration of c. a. 1.8–1.9 mM and recoveries from spiked samples were about 100.6% and 95.4% for 50 and 100 μM spiked UA concentrations, respectively. These results demonstrate that non-enzymatic uric acid detection is possible using considerably cheaper and more widely available materials than the previously reported commercial polymer derived LIG biosensors. With satisfactory reproducibility and repeatability upon long term storage at ambient conditions, and allowing both reusability and disposable applications,

these paper-LIG sensors are a smart solution for biosensing within the contemporary paradigm focused on materials and processing sustainability.

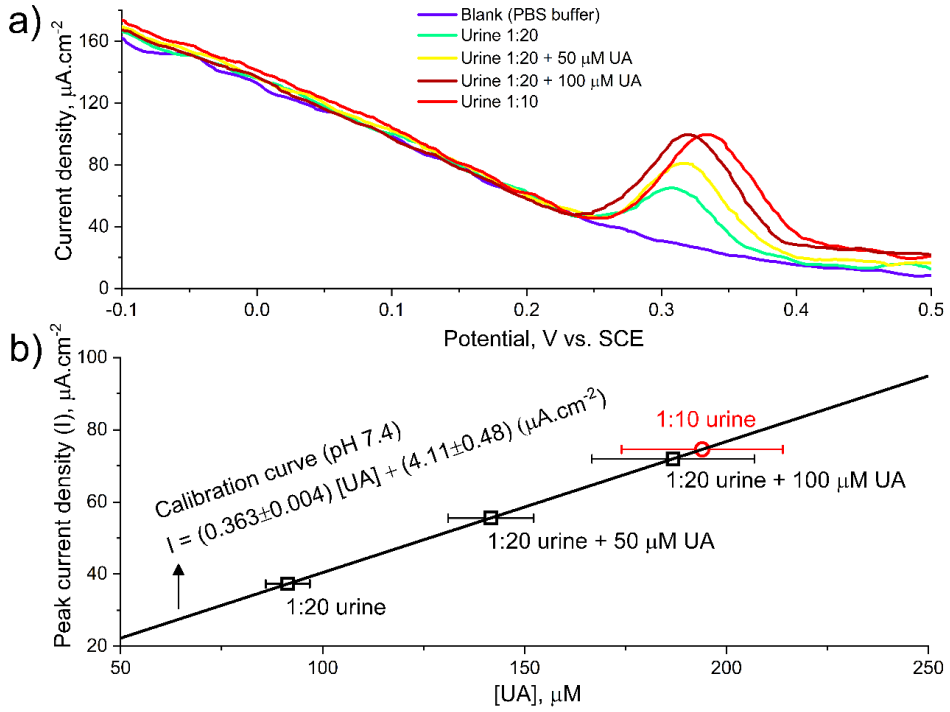

Figure 2.4.6. (a) DPV scans of paper-LIG electrode in diluted urine and spiked urine samples. **(b)** Determination of UA content using the calibration curve in PBS (pH 7.4). Horizontal error bars are standard deviations from quadruplicate measurements.

Table 2.4.2. Determination of uric acid in diluted urine and spiked urine samples. Standard deviations from quadruplicate measurements are also shown.

Trial	Spiked UA concentration (μM)	Average UA content retrieved from calibration plot (μM)	Standard deviation (μM, %)	Average recovery (%)
1:20 urine	0	91.39	5.48, 5.94	-
1:20 urine + 50 μM UA	50	141.68	10.59, 7.47	100.58
1:20 urine + 100 μM UA	100	186.78	20.12, 10.77	95.39
1:10 urine	0	193.97	19.99, 10.30	-

2.4.4 Materials and methods

2.4.4.1 Reagents and electrolyte solutions

Whatman grade 40 hardened ashless cellulose filter paper (95 g m^{-2}, 210 μm of thickness, ≤0.007% ash content) was obtained from Cytiva. A commercial phosphate based Anti-Flame fire retardant was purchased from BBT. Electrodag 1415 silver paste and Lacomit varnish G371 were acquired from Agar Scientific.

Hexaaminеruthenium(III) chloride ($[Ru(NH_3)_6]Cl_3$, >98%), sodium sulphate (Na_2SO_4, ACS reagent, ≥99.0% anhydrous, powder), sodium citrate tribasic dihydrate ($Na_3C_6H_5O_7{\cdot}2H_2O$, ACS reagent, ≥99.0%), creatinine ($C_4H_7N_3O$, anhydrous, ≥98%), urea (CH_4N_2O, ReagentPlus®, ≥99.5%, pellets), potassium chloride (KCl, SigmaUltra Minimum 99.0%), sodium chloride (NaCl, ACS reagent, ≥99.0%), ammonium chloride (NH_4Cl, ACS reagent, ≥ 99.5%), potassium oxalate monohydrate ($K_2C_2O_4{\cdot}H_2O$, ACS reagent, 99%), magnesium sulphate heptahydrate ($MgSO_4{\cdot}7H_2O$, ReagentPlus®, ≥99.0%), sodium phosphate monobasic monohydrate ($NaH_2PO_4{\cdot}H_2O$, ACS reagent, ≥98%), and sodium phosphate dibasic heptahydrate ($Na_2HPO_4{\cdot}7H_2O$, ≥99.99% trace metals basis) were purchased from Sigma-Aldrich. Potassium hexacyanoferrate(II) trihydrate ($K_4[Fe(CN)_6]\cdot 3H_2O$, AGR) was supplied by Labkem. Uric acid ($C_5H_4N_4O_3$, 99%), dopamine hydrochloride (>99%) and ascorbic acid (>99.7%) were obtained from Alfa Aesar. Calcium chloride ($CaCl_2$, anhydrous granules) was acquired from Supelco, Merck. Deionized (DI) water was obtained from a MilliQ water purification system, with a resistivity of 18.2 MΩ cm. All reagents were used as received.

Phosphate buffer saline (PBS) solution at pH 7.4 was prepared using tablets from Fisher Bioreagents, 1 tablet per 200 mL providing a solution with 0.137 M NaCl, 0.027 M KCl and 10 mM of phosphate buffer. The phosphate buffer saline solutions, with pH 6.6 and 5.6, were prepared keeping constant the phosphate buffer concentration in 10 mM and the ionic strength (0.137 M NaCl and 0.027 M KCl). Ratios of 6:4 mM and 9.5:0.5 mM of NaH_2PO_4:Na_2HPO_4 were used to prepare the pH 6.6 and 5.6, respectively. The pH of each solution was confirmed using a pH meter form Hanna Instruments.

Synthetic Urine (SU) was prepared a day prior to its use, as described in Ref. [67]. Briefly, the compounds that composed the urine were weighted and added in the following order to 1 L of deionized (DI) water, at 37 °C under stirring: 1.700 g Na_2SO_4, 0.720 g sodium citrate, 0.881 g creatinine, 15 g urea, 2.308 g KCl, 1.756 g NaCl, 0.185 g $CaCl_2$, 1.266 g NH_4Cl, 0.035 g potassium oxalate, 1.082 g $MgSO_4{\cdot}7H_2O$, 2.912 g $NaH_2PO_4{\cdot}H_2O$ and 0.831 g $Na_2HPO_4{\cdot}7H_2O$. After overnight stirring at 37 °C, a pH value of 6.0 was measured with the pH meter. Uric acid was not added in this formulation of SU, as it is the compound under analysis throughout this work.

Real human urine sample was voluntarily provided by one of the co-authors, a healthy male aged between 30 and 40 years (being fully aware and consenting of all the implications of the present study, in accordance with all the ethical requirements). The volunteer collected the first morning urine sample after fasting for at least 8 h and the urine was immediately stored at 4 °C and measured within 2 h from collection, with no requirement for long-term sample storage and having been properly disposed of immediately after the measurement. In accordance with the literature [67], first morning and fasting urine samples do not have contaminants from the food consumed by the person, and thus represent the urine composition due to metabolism only.

2.4.4.2 Paper-LIG electrode fabrication

The cellulose filter paper was sprayed with the fire retardant and left to dry in air. It was then irradiated by a K40 CO_2 (10.6 μm) continuous wave 40 W laser engraver, by Liaocheng Julong CO. Ltd., operated in a unidirectional line scan mode, at 800–900 mW of power, 30 mm s^{-1} of scan speed, and with a line separation of 0.1 mm. Two irradiation steps were employed, the first one at 9 mm below focus and the second one at focus. A rectangular area of 20×5 mm^2 was irradiated for each electrode, transforming the paper into paper-LIG, and later cut out with a 2.5 mm margin on each side of this area. It should be noted that care must be taken during the LIG production regarding possible laser power fluctuations and unintentional defocusing of the laser beam. For this reason, laser power was closely monitored between the irradiation steps. Moreover, some cracks can appear during paper-LIG production due to power fluctuations, and preliminary quality check and electrode selection procedure is necessary. All these factors can severely affect the paper-LIG electroanalytical performance and thus the reproducibility of the sensors.

The electrodes were then rinsed with 150 mL of DI water to wash off the excess fire retardant and left to dry overnight in air. Next, a 20 awg tin-coated copper wire was attached at the end of the irradiated area, using silver paste. Finally, non-conductive and electrochemically inactive Lacomit varnish was used to encapsulate the electrode (on both sides of the paper) and the contact wire, leaving exposed a ~5×5 mm^2 area of paper-LIG to act as the active area.

2.4.4.3 Morphological and structural analysis

Secondary electron scanning electron microscopy (SE-SEM and BSE-SEM) images were acquired using a Vega 3 SBH system, by TESCAN, with an acceleration voltage of 15 kV and a working distance of 15 mm. Raman spectroscopy was performed using a Jobin Yvon HR800 Raman system, by Horiba, and a He-Cd 441.6 nm laser, by Kimmon, with a ×50 lens (NA=0.5), by Olympus. A neutral density filter OD=1 was used to attenuate the laser power to prevent any potential thermally induced chemical modification of the samples. Sheet resistance measurements were performed by the van der Pauw method, using a Keysight B2902A dual-channel source meter unit. XPS spectra were acquired in an Axis Supra Spectrometer by Kratos Analytical using monochromatized Al Ka radiation at an X-ray power of 225 W. The pass energy was 80 eV for survey scans and 5 eV for detailed scans. The XPS spectrum of paper was corrected by taking the C–C/C–H peak as reference (284.8 eV). All the fittings were performed with CasaXPS Version 2.3.19PR1.0. The samples were washed with DI water before the measurements.

2.4.4.4 Electrochemical methods and apparatus

A Versastat3 (Princeton Applied Research) was used for all the electrochemical measurements. A homemade 3D-printed electrochemical cell was employed in the three-electrode configuration, where paper-LIG was the working electrode (WE), a standard Calomel electrode (SCE) was the reference electrode (RE), placed at a distance from the WE of twice the diameter of the SCE tip, and a Pt wire was the counter electrode (CE). The measurements were performed at high electrolyte volume to electrode area ratio conditions (25 mm^2 WE area in 35 mL electrolyte solution). In order to stabilize the electrodes, ten potential cycles between −1 and 1 V vs SCE at a scan rate of 100 mV s^{-1}, starting and stopping at the open circuit potential, were performed in PBS electrolyte prior to any measurements (**Figure S2.4.1**, **Section 2.4.7**). The EIS measurements were performed employing a sinusoidal 5 mV perturbation at the open circuit potential (223 mV vs SCE), within the 1 kHz to 0.1 Hz range.

The Nicholson method was employed to estimate the effective heterogeneous electron transfer standard rate constant of paper-LIG electrode k^0_{eff}, using both reversible outer-sphere ($[Ru(NH_3)_6]^{3+}$) and inner-sphere ($[FeCN_6]^{4-}$) redox probes. Briefly, a collection of values for a kinetic parameter Ψ was retrieved via the scan rate (ν)-dependent cyclic voltammograms through **Equation 2.4.1**:

$$\Psi = \frac{-0.6288 + 0.0021\Delta E_{\text{p}}}{1 - 0.017\Delta E_{\text{p}}} \tag{2.4.1}$$

where ΔE_{p} is the separation of the anodic and cathodic peak potentials for each scan rate. If the electrode reaction proceeds in a quasi-reversible regime, i.e. for ΔE_{p} up to about 250 mV, and assuming (i) a similar diffusion coefficient D for the oxidized and reduced forms in aqueous solution (9.10×10^{-6} cm^2 s^{-1} and 6.67×10^{-6} cm^2 s^{-1} for $[Ru(NH_3)_6]^{3+/2+}$ and $[Fe(CN)_6]^{4-/3-}$, respectively), and (ii) symmetrical redox kinetics of the redox couple (charge transfer coefficient of 0.5), one can infer k^0_{eff} (cm s^{-1}) by **Equation 2.4.2**:

$$\Psi = \frac{k^0_{\text{eff}}}{\left(\frac{n\pi FD\nu}{RT}\right)^{\frac{1}{2}}} \tag{2.2.1}$$

where n=1 is the number of electrons involved in the $[Ru(NH_3)_6]^{2+/3+}$ and $[Fe(CN)_6]^{4-/3-}$ redox reaction, F is the Faraday constant (96485.33 C mol^{-1}), R the universal gas constant (8.314 J mol^{-1} K^{-1}) and T the absolute temperature (K). The electrolyte solution was thoroughly bubbled with N_2 for 60 min and kept under N_2 blanket during these measurements, as to eliminate the interfering contribution from the oxygen reduction reaction occurring at about −0.5 V vs SCE. Voltammograms for HET estimations were acquired from faster to slower scan rates.

Differential pulse voltammetry (DPV) was employed for UA sensing tests via oxidation signal. The DPV parameters were chosen based on previous optimization for the paper-LIG electrodes: pulse height was 45 mV, pulse width 0.03 s, step height 3 mV and step width 0.3 s, yielding a scan rate of 10 mV s^{-1}. All measurements were performed in quadruplicate with increasing concentration of UA. The electrodes were washed with DI water in between each measurement in UA-containing samples to remove adsorbed reactants/products at the electrode's surface.

Acknowledgements

This work was developed within the scope of project i3N (LA/P/0037/2020, UIDB/50025/2020 and UIDP/50025/2020), financed by national funds through the Portuguese Foundation for Science and Technology/MCTES (FCT I.P.). B. Kulyk acknowledges the PhD grant SFRH/BD/141525/2018 from FCT I.P. N. F. Santos thanks i3N for the BPD Grant BPD/UI96/5177/2020. S. O. Pereira thanks i3N for the BPD Grant BPD/UI96/5808/2017. The financial support by National Funds through FCT I.P. under the NANOBIOSENSE project PTDC/NAN-MAT/28755/2017 (POCI-01-0145-FEDER-028755) is gratefully acknowledged. E. Fortunato acknowledges the ERC AdG grant 787410 from the project DIGISMART. The authors also thank Jonas Deuermeier for the XPS measurements.

2.4.5 References

[1] K.S. Novoselov, A.K. Geim, S. V. Morozov, D. Jiang, Y. Zhang, S. V. Dubonos, I. V. Grigorieva,

A.A. Firsov, "Electric field effect in atomically thin carbon films," *Science*, 306, 666–669, **2004**. https://doi.org/10.1126/science.1102896.

[2] A.C. Ferrari, F. Bonaccorso, V.I. Fal'ko, K.S. Novoselov, S. Roche, P. Bøggild, S. Borini, F.H.L. Koppens, V. Palermo, N.M. Pugno, J.A. Garrido, R. Sordan, A. Bianco, L. Ballerini, M. Prato, E. Lidorikis, J. Kivioja, C. Marinelli, T. Ryhänen, A.F. Morpurgo, J.N. Coleman, V. Nicolosi, L. Colombo, A. Fert, M. Garcia-Hernandez, A. Bachtold, G.F. Schneider, F. Guinea, C. Dekker, M. Barbone, Z.Z. Sun, C. Galiotis, A.N. Grigorenko, G. Konstantatos, A. Kis, M.I. Katsnelson, L.M.K. Vandersypen, A. Loiseau, V. Morandi, D. Neumaier, E. Treossi, V. Pellegrini, M. Polini, A. Tredicucci, G.M. Williams, B. Hee Hong, J.-H. Ahn, J. Min Kim, H. Zirath, B.J. van Wees, H. van der Zant, L. Occhipinti, A. Di Matteo, I.A. Kinloch, T. Seyller, E. Quesnel, X.L. Feng, K.B.K. Teo, N.L. Rupesinghe, P.J. Hakonen, S.R.T. Neil, Q. Tannock, T. Löfwander, J.M. Kinaret, "Science and technology roadmap for graphene, related two-dimensional crystals, and hybrid systems," *Nanoscale*, 7, 4598–4810, **2015**. https://doi.org/10.1039/C4NR01600A.

[3] D. Iannazzo, A. Pistone, M. Salamò, S. Galvagno, R. Romeo, S. V. Giofré, C. Branca, G. Visalli, A. Di Pietro, "Graphene quantum dots for cancer targeted drug delivery," *Int. J. Pharm.*, 518, 185–192, **2017**. https://doi.org/10.1016/j.ijpharm.2016.12.060.

[4] K. Yang, L. Feng, Z. Liu, "Stimuli responsive drug delivery systems based on nano-graphene for cancer therapy," *Adv. Drug Deliv. Rev.*, 105, 228–241, **2016**. https://doi.org/10.1016/j.addr.2016.05.015.

[5] S. Kumar, K. Chatterjee, "Comprehensive Review on the Use of Graphene-Based Substrates for Regenerative Medicine and Biomedical Devices," *ACS Appl. Mater. Interfaces*, 8, 26431–26457, **2016**. https://doi.org/10.1021/acsami.6b09801.

[6] P. Bollella, G. Fusco, C. Tortolini, G. Sanzò, G. Favero, L. Gorton, R. Antiochia, "Beyond graphene: Electrochemical sensors and biosensors for biomarkers detection," *Biosens. Bioelectron.*, 89, 152–166, **2015**. https://doi.org/10.1016/j.bios.2016.03.068.

[7] M. Pumera, "Graphene in biosensing," *Mater. Today*, 14, 308–315, **2011**. https://doi.org/10.1016/S1369-7021(11)70160-2.

[8] M. Coroş, S. Pruneanu, R.-I.S. Staden, "Review—Recent Progress in the Graphene-Based Electrochemical Sensors and Biosensors," *J. Electrochem. Soc.*, 167, 037528, **2019**. https://doi.org/10.1149/2.0282003JES.

[9] H.L. Poh, M. Pumera, "Nanoporous carbon materials for electrochemical sensing," *Chem. - An Asian J.*, 7, 412–416, **2012**. https://doi.org/10.1002/asia.201100681.

[10] S.C.S. Lai, A.N. Patel, K. McKelvey, P.R. Unwin, "Definitive evidence for fast electron transfer at pristine basal plane graphite from high-resolution electrochemical imaging," *Angew. Chemie - Int. Ed.*, 51, 5405–5408, **2012**. https://doi.org/10.1002/anie.201200564.

[11] S.K. Krishnan, E. Singh, P. Singh, M. Meyyappan, H.S. Nalwa, "A review on graphene-based nanocomposites for electrochemical and fluorescent biosensors," *RSC Adv.*, 9, 8778–8881, **2019**. https://doi.org/10.1039/C8RA09577A.

[12] J. Lin, Z. Peng, Y. Liu, F. Ruiz-Zepeda, R. Ye, E.L.G.G. Samuel, M.J. Yacaman, B.I. Yakobson, J.M. Tour, "Laser-induced porous graphene films from commercial polymers," *Nat.*

Commun., 5, 1–8, **2014**. https://doi.org/10.1038/ncomms6714.

[13] A.F. Carvalho, B. Kulyk, A.J.S. Fernandes, E. Fortunato, F.M. Costa, "A Review on the Applications of Graphene in Mechanical Transduction," *Adv. Mater.*, 2101326, **2021**. https://doi.org/10.1002/adma.202101326.

[14] A.F. Carvalho, A.J.S. Fernandes, C. Leitão, J. Deuermeier, A.C. Marques, R. Martins, E. Fortunato, F.M. Costa, "Laser-Induced Graphene Strain Sensors Produced by Ultraviolet Irradiation of Polyimide," *Adv. Funct. Mater.*, 28, 1–8, **2018**. https://doi.org/10.1002/adfm.201805271.

[15] B. Kulyk, B.F.R. Silva, A.F. Carvalho, S. Silvestre, A.J.S. Fernandes, R. Martins, E. Fortunato, F.M. Costa, "Laser-Induced Graphene from Paper for Mechanical Sensing," *ACS Appl. Mater. Interfaces*, 13, 10210–10221, **2021**. https://doi.org/10.1021/acsami.0c20270.

[16] N.F. Santos, S.O. Pereira, A. Moreira, A. V Girão, A.F. Carvalho, A.J.S. Fernandes, F.M. Costa, "IR and UV Laser-Induced Graphene: Application as Dopamine Electrochemical Sensors," *Adv. Mater. Technol.*, 6, 2100007, **2021**. https://doi.org/10.1002/admt.202100007.

[17] A.R. Cardoso, A.C. Marques, L. Santos, A.F. Carvalho, F.M. Costa, R. Martins, M.G.F. Sales, E. Fortunato, "Molecularly-imprinted chloramphenicol sensor with laser-induced graphene electrodes," *Biosens. Bioelectron.*, 124–125, 167–175, **2019**. https://doi.org/10.1016/j.bios.2018.10.015.

[18] S.O. Pereira, N.F. Santos, A.F. Carvalho, A.J.S. Fernandes, F.M. Costa, "Electrochemical Response of Glucose Oxidase Adsorbed on Laser-Induced Graphene," *Nanomaterials*, 11, 1893, **2021**. https://doi.org/10.3390/nano11081893.

[19] B. Kulyk, B.F.R. Silva, A.F. Carvalho, P. Barbosa, A. V. Girão, J. Deuermeier, A.J.S. Fernandes, F.M.L. Figueiredo, E. Fortunato, F.M. Costa, "Laser-Induced Graphene from Paper by Ultraviolet Irradiation: Humidity and Temperature Sensors," *Adv. Mater. Technol.*, 2101311, 2101311, **2022**. https://doi.org/10.1002/admt.202101311.

[20] R. Ye, Y. Chyan, J. Zhang, Y. Li, X. Han, C. Kittrell, J.M. Tour, "Laser-Induced Graphene Formation on Wood," *Adv. Mater.*, 29, 1–7, **2017**. https://doi.org/10.1002/adma.201702211.

[21] A.F. Carvalho, A.J.S. Fernandes, R. Martins, E. Fortunato, F.M. Costa, "Laser-Induced Graphene Piezoresistive Sensors Synthesized Directly on Cork Insoles for Gait Analysis," *Adv. Mater. Technol.*, 5, 2000630, **2020**. https://doi.org/10.1002/admt.202000630.

[22] B. Kulyk, M. Matos, B.F.R. Silva, A.F. Carvalho, A.J.S. Fernandes, D. V. Evtuguin, E. Fortunato, F.M. Costa, "Conversion of paper and xylan into laser-induced graphene for environmentally friendly sensors," *Diam. Relat. Mater.*, 123, 108855, **2022**. https://doi.org/10.1016/j.diamond.2022.108855.

[23] Y. Chyan, R. Ye, Y. Li, S.P. Singh, C.J. Arnusch, J.M. Tour, "Laser-Induced Graphene by Multiple Lasing: Toward Electronics on Cloth, Paper, and Food," *ACS Nano*, 12, 2176–2183, **2018**. https://doi.org/10.1021/acsnano.7b08539.

[24] D. Ha, Z. Fang, N.B. Zhitenev, "Paper in Electronic and Optoelectronic Devices," *Adv. Electron. Mater.*, 4, 1700593, **2018**. https://doi.org/10.1002/aelm.201700593.

[25] Danish, R. Ulucak, S.U.-D. Khan, "Determinants of the ecological footprint: Role of renewable energy, natural resources, and urbanization," *Sustain. Cities Soc.*, 54, 101996, **2020**. https://doi.org/10.1016/j.scs.2019.101996.

[26] A.W. Martinez, S.T. Phillips, M.J. Butte, G.M. Whitesides, "Patterned paper as a platform for inexpensive, low-volume, portable bioassays," *Angew. Chemie - Int. Ed.*, 46, 1318–1320, **2007**. https://doi.org/10.1002/anie.200603817.

[27] M. Sajid, A.-N. Kawde, M. Daud, "Designs, formats and applications of lateral flow assay: A literature review," *J. Saudi Chem. Soc.*, 19, 689–705, **2015**. https://doi.org/10.1016/j.jscs.2014.09.001.

[28] E. Carrilho, A.W. Martinez, S.T. Phillips, G.M. Whitesides, "Diagnostics for the Developing World: Microfluidic Paper-Based Analytical Devices," *Anal. Chem.*, 82, 3–10, **2010**. https://doi.org/10.1021/ac9013989.

[29] C. Karuwan, A. Wisitsoraat, P. Chaisuwan, D. Nacapricha, A. Tuantranont, "Screen-printed graphene-based electrochemical sensors for a microfluidic device," *Anal. Methods*, 9, 3689–3695, **2017**. https://doi.org/10.1039/c7ay00379j.

[30] Y. Fan, S. Shi, J. Ma, Y. Guo, "A paper-based electrochemical immunosensor with reduced graphene oxide/thionine/gold nanoparticles nanocomposites modification for the detection of cancer antigen 125," *Biosens. Bioelectron.*, 135, 1–7, **2019**. https://doi.org/10.1016/j.bios.2019.03.063.

[31] M. Alafeef, K. Dighe, P. Moitra, D. Pan, "Rapid, Ultrasensitive, and Quantitative Detection of SARS-CoV-2 Using Antisense Oligonucleotides Directed Electrochemical Biosensor Chip," *ACS Nano*, 14, 17028–17045, **2020**. https://doi.org/10.1021/acsnano.0c06392.

[32] M.A. Ehsan, S.A. Khan, A. Rehman, "Screen-Printed Graphene/Carbon Electrodes on Paper Substrates as Impedance Sensors for Detection of Coronavirus in Nasopharyngeal Fluid Samples," *Diagnostics*, 11, 1030, **2021**. https://doi.org/10.3390/diagnostics11061030.

[33] J.G. Giuliani, T.E. Benavidez, G.M. Duran, E. Vinogradova, A. Rios, C.D. Garcia, "Development and characterization of carbon based electrodes from pyrolyzed paper for biosensing applications," *J. Electroanal. Chem.*, 765, 8–15, **2016**. https://doi.org/10.1016/j.jelechem.2015.07.055.

[34] W.R. de Araujo, C.M.R. Frasson, W.A. Ameku, J.R. Silva, L. Angnes, T.R.L.C. Paixão, "Single-Step Reagentless Laser Scribing Fabrication of Electrochemical Paper-Based Analytical Devices," *Angew. Chemie - Int. Ed.*, 56, 15113–15117, **2017**. https://doi.org/10.1002/anie.201708527.

[35] T. Pinheiro, S. Silvestre, J. Coelho, A.C. Marques, R. Martins, M.G.F. Sales, E. Fortunato, "Laser-Induced Graphene on Paper toward Efficient Fabrication of Flexible, Planar Electrodes for Electrochemical Sensing," *Adv. Mater. Interfaces*, 2101502, 2101502, **2021**. https://doi.org/10.1002/admi.202101502.

[36] Q. Wang, X. Wen, J. Kong, "Recent Progress on Uric Acid Detection: A Review," *Crit. Rev. Anal. Chem.*, 50, 359–375, **2020**. https://doi.org/10.1080/10408347.2019.1637711.

[37] R. El Ridi, H. Tallima, "Physiological functions and pathogenic potential of uric acid: A

review," *J. Adv. Res.*, 8, 487–493, **2017**. https://doi.org/10.1016/j.jare.2017.03.003.

[38] A.C. Ferrari, "Raman spectroscopy of graphene and graphite: Disorder, electron-phonon coupling, doping and nonadiabatic effects," *Solid State Commun.*, 143, 47–57, **2007**. https://doi.org/10.1016/j.ssc.2007.03.052.

[39] M. Velický, M.A. Bissett, P.S. Toth, H. V. Patten, S.D. Worrall, A.N.J. Rodgers, E.W. Hill, I.A. Kinloch, K.S. Novoselov, T. Georgiou, L. Britnell, R.A.W. Dryfe, "Electron transfer kinetics on natural crystals of MoS2 and graphite," *Phys. Chem. Chem. Phys.*, 17, 17844–17853, **2015**. https://doi.org/10.1039/c5cp02490k.

[40] D.A.C. Brownson, C.E. Banks, The Handbook of Graphene Electrochemistry, **2014**. https://doi.org/10.1007/978-1-4471-6428-9.

[41] Y. Guo, D.A. Rockstraw, "Physical and chemical properties of carbons synthesized from xylan, cellulose, and Kraft lignin by H3PO4 activation," *Carbon*, 44, 1464–1475, **2006**. https://doi.org/10.1016/j.carbon.2005.12.002.

[42] M. Jagtoyen, F. Derbyshire, "Activated carbons from yellow poplar and white oak by H3PO4 activation," *Carbon*, 36, 1085–1097, **1998**. https://doi.org/https://doi.org/10.1016/S0008-6223(98)00082-7.

[43] L. Johansson, J.M. Campbell, O.J. Rojas, "Cellulose as the in situ reference for organic XPS. Why? Because it works," *Surf. Interface Anal.*, **2020**. https://doi.org/10.1002/sia.6759.

[44] M. Smith, L. Scudiero, J. Espinal, J.-S. McEwen, M. Garcia-Perez, "Improving the deconvolution and interpretation of XPS spectra from chars by ab initio calculations," *Carbon*, 110, 155–171, **2016**. https://doi.org/10.1016/j.carbon.2016.09.012.

[45] B. Lesiak, L. Kövér, J. Tóth, J. Zemek, P. Jiricek, A. Kromka, N. Rangam, "C sp2/sp3 hybridisations in carbon nanomaterials – XPS and (X)AES study," *Appl. Surf. Sci.*, 452, 223–231, **2018**. https://doi.org/10.1016/j.apsusc.2018.04.269.

[46] J. Bisquert, "Influence of the boundaries in the impedance of porous film electrodes," *Phys. Chem. Chem. Phys.*, 2, 4185–4192, **2000**. https://doi.org/10.1039/b001708f.

[47] J. Bisquert, "Theory of the Impedance of Electron Diffusion and Recombination in a Thin Layer," *J. Phys. Chem. B*, 106, 325–333, **2002**. https://doi.org/10.1021/jp011941g.

[48] N.F. Santos, J. Rodrigues, S.O. Pereira, A.J.S. Fernandes, T. Monteiro, F.M. Costa, "Electrochemical and photoluminescence response of laser-induced graphene/electrodeposited ZnO composites," *Sci. Reports 2021 111*, 11, 1–15, **2021**. https://doi.org/10.1038/s41598-021-96305-8.

[49] I. Streeter, G.G. Wildgoose, L. Shao, R.G. Compton, "Cyclic voltammetry on electrode surfaces covered with porous layers: An analysis of electron transfer kinetics at single-walled carbon nanotube modified electrodes," *Sensors Actuators, B Chem.*, 133, 462–466, **2008**. https://doi.org/10.1016/j.snb.2008.03.015.

[50] D.A.C. Brownson, P.J. Kelly, C.E. Banks, "In situ electrochemical characterisation of graphene and various carbon-based electrode materials: An internal standard approach," *RSC Adv.*, 5, 37281–37286, **2015**. https://doi.org/10.1039/c5ra03049h.

[51] D.A.C. Brownson, S.A. Varey, F. Hussain, S.J. Haigh, C.E. Banks, "Electrochemical

properties of CVD grown pristine graphene: Monolayer- vs. quasi-graphene," *Nanoscale*, 6, 1607–1621, **2014**. https://doi.org/10.1039/c3nr05643k.

[52] L. Tang, Y. Wang, Y. Li, H. Feng, J. Lu, J. Li, "Preparation, structure, and electrochemical properties of reduced graphene sheet films," *Adv. Funct. Mater.*, 19, 2782–2789, **2009**. https://doi.org/10.1002/adfm.200900377.

[53] W.R. Wilcox, A. Khalaf, A. Weinberger, I. Kippen, J.R. Klinenberg, "Solubility of uric acid and monosodium urate," *Med. Biol. Eng. 1972 104*, 10, 522–531, **1972**. https://doi.org/10.1007/BF02474201.

[54] I. Kippen, J.R. Klinenberg, A. Weinberger, W.R. Wilcox, "Factors affecting urate solubility in vitro.," *Ann. Rheum. Dis.*, 33, 313–317, **1974**. https://doi.org/10.1136/ARD.33.4.313.

[55] H. Iwata, S. Nishio, M. Yokoyama, A. Matsumoto, M. Takeuchi, "Solubility of uric acid and supersaturation of monosodium urate: Why is uric acid so highly soluble in urine?," *J. Urol.*, 142, 1095–1098, **1989**. https://doi.org/10.1016/S0022-5347(17)39003-1.

[56] D.P. Chong, "Theoretical Study of Uric Acid and its Ions in Aqueous Solution," *J. Theor. Comput. Sci.*, 1, **2016**. https://doi.org/10.4172/2376-130X.1000104.

[57] D. Lakshmi, M.J. Whitcombe, F. Davis, P.S. Sharma, B.B. Prasad, "Electrochemical Detection of Uric Acid in Mixed and Clinical Samples: A Review," *Electroanalysis*, 23, 305–320, **2011**. https://doi.org/10.1002/ELAN.201000525.

[58] R.N. Goyal, A. Brajter-Toth, G. Dryhurst, "Futher insights into the electrochemical oxidation of uric acid," *J. Electroanal. Chem. Interfacial Electrochem.*, 131, 181–202, **1982**. https://doi.org/10.1016/0022-0728(82)87070-8.

[59] S.A. John, "Simultaneous determination of uric acid and ascorbic acid using glassy carbon electrodes in acetate buffer solution," *J. Electroanal. Chem.*, 579, 249–256, **2005**. https://doi.org/10.1016/J.JELECHEM.2005.02.012.

[60] T. Yao, Y. Taniguchi, T. Wasa, S. Musha, "Anodic Voltammetry and Its Analytical Application to the Detection and Simultaneous Determination of Hypoxanthine, Xanthine, and Uric Acid," *Bull. Chem. Soc. Jpn.*, 51, 2937–2941, **1978**. https://doi.org/10.1246/bcsj.51.2937.

[61] J. Liu, W. Lu, L. Zhang, J. Yang, Z.P. Yao, Y. He, Y. Li, "Integrated hand-held electrochemical sensor for multicomponent detection in urine," *Biosens. Bioelectron.*, 193, 113534, **2021**. https://doi.org/10.1016/J.BIOS.2021.113534.

[62] A. Shrivastava, V. Gupta, "Methods for the determination of limit of detection and limit of quantitation of the analytical methods," *Chronicles Young Sci.*, 2, 21, **2011**. https://doi.org/10.4103/2229-5186.79345.

[63] Q. Yan, N. Zhi, L. Yang, G. Xu, Q. Feng, Q. Zhang, S. Sun, "A highly sensitive uric acid electrochemical biosensor based on a nano-cube cuprous oxide/ferrocene/uricase modified glassy carbon electrode," *Sci. Rep.*, 10, **2020**. https://doi.org/10.1038/S41598-020-67394-8.

[64] F.H. Cincotto, E.L. Fava, F.C. Moraes, O. Fatibello-Filho, R.C. Faria, "A new disposable microfluidic electrochemical paper-based device for the simultaneous determination of

clinical biomarkers," *Talanta*, 195, 62–68, **2019**. https://doi.org/10.1016/j.talanta.2018.11.022.

[65] P. Nayak, N. Kurra, C. Xia, H.N. Alshareef, "Highly Efficient Laser Scribed Graphene Electrodes for On-Chip Electrochemical Sensing Applications," *Adv. Electron. Mater.*, 2, **2016**. https://doi.org/10.1002/aelm.201600185.

[66] L.A. Pachla, D.L. Reynolds, P.T. Kissinger, "Analytical methods for determining ascorbic acid in biological samples, food products, and pharmaceuticals.," *J. Assoc. Off. Anal. Chem.*, 68, 1–12, **1985**.

[67] N. Sarigul, F. Korkmaz, İ. Kurultak, "A New Artificial Urine Protocol to Better Imitate Human Urine," *Sci. Reports 2019 91*, 9, 1–11, **2019**. https://doi.org/10.1038/s41598-019-56693-4.

[68] S. Verma, J. Choudhary, K.P. Singh, P. Chandra, S.P. Singh, "Uricase grafted nanoconducting matrix based electrochemical biosensor for ultrafast uric acid detection in human serum samples," *Int. J. Biol. Macromol.*, 130, 333–341, **2019**. https://doi.org/10.1016/j.ijbiomac.2019.02.121.

[69] Q. Hong, L. Yang, L. Ge, Z. Liu, F. Li, "Direct-laser-writing of three-dimensional porous graphene frameworks on indium-tin oxide for sensitive electrochemical biosensing," *Analyst*, 143, 3327–3334, **2018**. https://doi.org/10.1039/C8AN00888D.

[70] Y. Yang, Y. Song, X. Bo, J. Min, O.S. Pak, L. Zhu, M. Wang, J. Tu, A. Kogan, H. Zhang, T.K. Hsiai, Z. Li, W. Gao, "A laser-engraved wearable sensor for sensitive detection of uric acid and tyrosine in sweat," *Nat. Biotechnol.*, 38, 217–224, **2020**. https://doi.org/10.1038/s41587-019-0321-x.

[71] M. Faruk Hossain, G. Slaughter, "Flexible electrochemical uric acid and glucose biosensor," *Bioelectrochemistry*, 141, 107870, **2021**. https://doi.org/10.1016/J.BIOELECHEM.2021.107870.

[72] K. Samoson, A. Soleh, K. Saisahas, K. Promsuwan, J. Saichanapan, P. Kanatharana, P. Thavarungkul, K.H. Chang, A.F. Lim Abdullah, K. Tayayuth, W. Limbut, "Facile fabrication of a flexible laser induced gold nanoparticle/chitosan/ porous graphene electrode for uric acid detection," *Talanta*, 243, 123319, **2022**. https://doi.org/10.1016/J.TALANTA.2022.123319.

[73] A. Unic, N. Nikolac Gabaj, M. Miler, J. Culej, A. Lisac, A. Horvat, N. Vrkic, "Ascorbic acid—A black hole of urine chemistry screening," *J. Clin. Lab. Anal.*, 32, **2018**. https://doi.org/10.1002/JCLA.22390.

[74] M.L. Brigden, D. Edgell, M. McPherson, A. Leadbeater, G. Hoag, "High incidence of significant urinary ascorbic acid concentrations in a west coast population--implications for routine urinalysis.," *Clin. Chem.*, 38, 426–431, **1992**.

[75] G. V. Rebec, "From Interferant Anion to Neuromodulator: Ascorbate Oxidizes its Way to Respectability," *Electrochem. Methods Neurosci.*, **2007**.

[76] F. Gao, X. Cai, X. Wang, C. Gao, S. Liu, F. Gao, Q. Wang, "Highly sensitive and selective detection of dopamine in the presence of ascorbic acid at graphene oxide modified electrode," *Sensors Actuators, B Chem.*, 186, 380–387, **2013**.

https://doi.org/10.1016/j.snb.2013.06.020.

[77] Y.C. Kudva, A.M. Sawka, W.F. Young, "The Laboratory Diagnosis of Adrenal Pheochromocytoma: The Mayo Clinic Experience," *J. Clin. Endocrinol. Metab.*, 88, 4533–4539, **2003**. https://doi.org/10.1210/JC.2003-030720.

[78] J.W. Yi, E.M. Oh, K.E. Lee, J.Y. Choi, D.H. Koo, K.J. Kim, K.C. Jung, S.Y. Kim, Y.K. Youn, "An exclusively dopamine secreting paraganglioma in the retroperitoneum: a first clinical case in Korea," *J. Korean Surg. Soc.*, 82, 389–393, **2012**. https://doi.org/10.4174/JKSS.2012.82.6.389.

2.4.6 Supporting information

2.4.6.1 Cyclic voltammetry

Figure S2.4.1 shows some of the cycles of cyclic voltammetry of a paper-LIG electrode in PBS (pH 7.4) electrolyte performed prior to any electrochemical characterization or UA detection measurements. The voltammogram shows the progressive stabilization of electrode response, with superimposed 9th and 10th cycles. The same occurs for PBS with pH 5.6 and pH 6.6 (not shown).

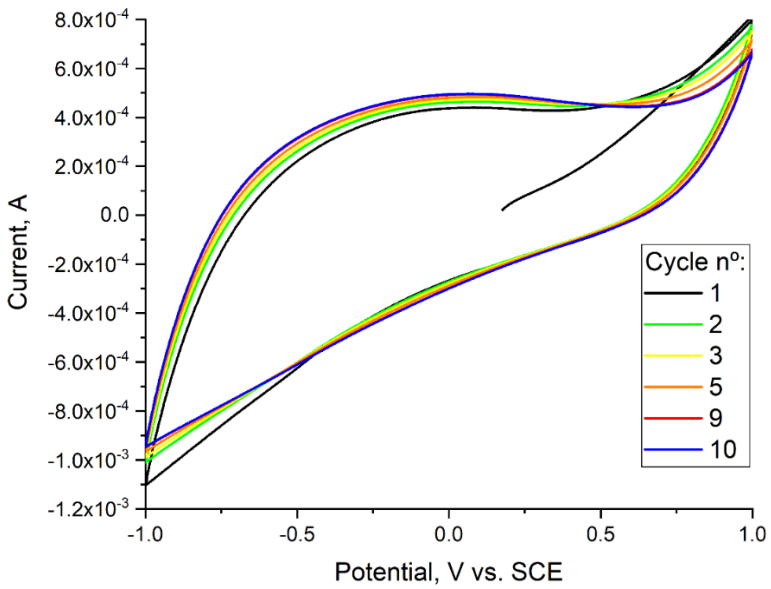

Figure S2.4.1. Cyclic voltammograms between −1 to 1 V vs SCE at a scan rate of 100 mV s^{-1}, starting and stopping at the open circuit potential, performed in PBS (pH 7.4).

Figure S2.4.2a shows the cyclic voltammetry analysis of $[Fe(CN)_6]^{4-/3-}$ electrochemistry at varying scan rate (v). The log(I)-log(v) slopes are about 0.44 and peak currents scale linearly with the square root of the scan rate (**Figure S2.4.2b**), indicating that redox reaction proceeds in a quasi-reversible regime suitable for HET kinetic analysis employing the Nicholson method (**Figure S2.4.2c**). Briefly, a collection of values for a kinetic parameter Ψ was retrieved via the scan rate (v)-dependent cyclic voltammograms through **Equation S2.4.1**:

$$\Psi = \frac{-0.6288 + 0.0021\Delta E_{\mathrm{p}}}{1 - 0.017\Delta E_{\mathrm{p}}} \qquad \text{(S2.4.1)}$$

where ΔE_p is the separation of the anodic and cathodic peak potentials for each scan rate. If the electrode reaction proceeds in a quasi-reversible regime, i.e. for ΔE_p up to about 250 mV, and assuming (i) a similar diffusion coefficient D for the oxidized and reduced forms in aqueous solution (6.67×10^{-6} cm^2 s^{-1} for $[Fe(CN)_6]^{4-/3-}$), and (ii) symmetrical redox kinetics of the redox couple (charge transfer coefficient of 0.5), one can infer k^0_{eff} (cm s^{-1}) by **Equation S2.4.2**:

$$\Psi = \frac{k^0_{eff}}{\left(\frac{n\pi FDv}{RT}\right)^{\frac{1}{2}}} \qquad \text{(S2.4.2)}$$

where n=1 is the number of electrons involved in $[Fe(CN)_6]^{4-/3-}$ redox reaction, F is the Faraday constant (96485.33 C mol^{-1}), R the universal gas constant (8.314 J mol^{-1} K^{-1}) and T the absolute temperature (K). The calculated heterogeneous electron transfer effective standard rate constants, k^0_{eff}, is 7.8×10^{-4} cm s^{-1} (**Figure S2.4.1c**).

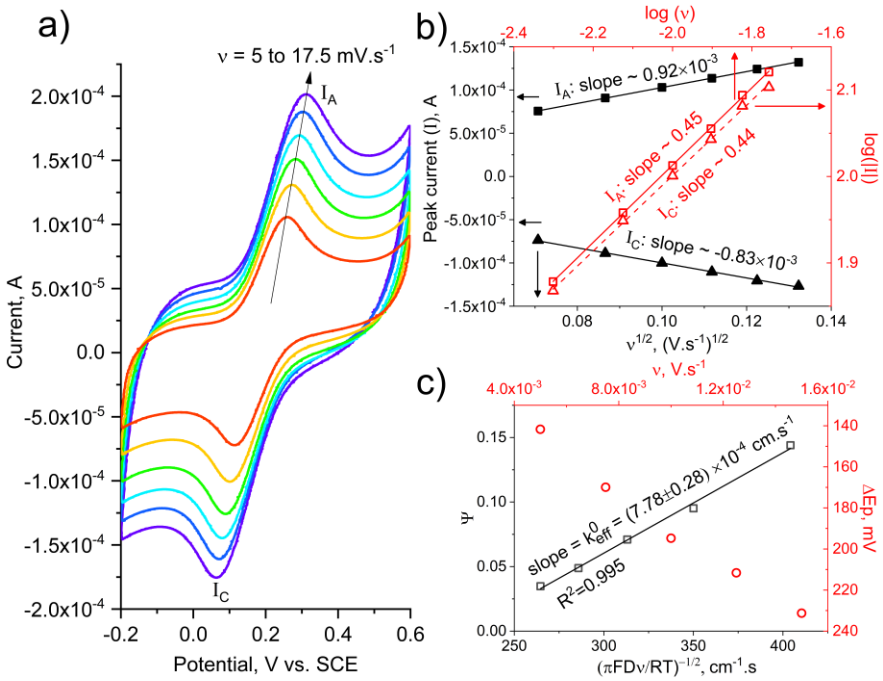

Figure S2.4.2. (a) Cyclic voltammograms at varying scan rate of paper-LIG electrode in PBS (pH 7.4) plus 5 mM $[Fe(CN)_6]^{4-}$. **(b)** Anodic and cathodic peak current versus square root of scan rate (black rectangles and triangles, respectively) after capacitive current subtraction, and correspondent linear regressions (solid black lines). Logarithmic correlation plot between peak current and scan rate for the cathodic (red triangles) and anodic (red squares) branches, along with the corresponding linear regressions (dashed and solid red lines, respectively). **(c)** HET kinetic analysis within the scan rate range of 5 to 15 mV s^{-1}, showing ΔE_p (red circles) and kinetic parameter Ψ (black squares) obtained via **Equation S2.4.1**, along with the linear regression (solid black line) for estimation of HET standard rate constant, k^0_{eff}, via **Equation S2.4.2**.

2.4.6.2 Electrochemical impedance spectroscopy

Table S2.4.1 and **Table S2.4.2** compile the fitting results of the modified Randels (MR) and Bisquert open (BTO) [S1], [S2] models, respectively. The squared sum of weighted residuals (χ^2) used to evaluate the goodness of fitting is also shown. Note that the values of R and R_{PORE} in **Table S2.4.1** and **Table S2.4.2**, respectively, tend to infinite and errors are larger than resistance values, which is expected. This is because no faradaic currents are expected in the absence of electroactive species in the electrolyte (3.5 M KCl), and other resistive phenomena

such as capacitance self-discharge are usually very large in magnitude and its signature is only discernible at very low frequencies.

Note also that the impedance of the CPE elements employed in the models, Z_Q, is given by **Equation S2.4.3**:

$$Z_Q = \frac{1}{P_0(iw)^a} \quad \text{(S2.4.3)}$$

Where P_0 is the CPE pre-exponential factor, a is the CPE exponent, i is the imaginary unit and w is the angular frequency.

Table S2.4.1. EIS spectrum fitting results employing the modified Randles (MR) model.

R_S (Ω)	R (Ω)	P_0* ($s^a\,\Omega^{-1}$)	a*	χ^2
150.2 ± 1.0	$1.4\times10^{27} \pm 1\times10^{38}$	$2.05\times10^{-3} \pm 3.86\times10^{-4}$	0.693 ± 0.011	4.67×10^{-3}

*see **Equation S2.4.3**.

Table S2.4.2. EIS spectrum fitting results employing the Bisquert open (BTO) model.

R_S (Ω)	R_{EL} (Ω)	R_{PORE} (Ω)	$P_{0,PORE}$* ($s^a\,\Omega^{-1}$)	a_{PORE}*	χ^2
132.6 ± 2.0	157.2 ± 67.7	$1.78\times10^{9} \pm 2.68\times10^{20}$	$2.08\times10^{3} \pm 2.49\times10^{-4}$	0.792 ± 0.061	1.27×10^{-4}

*see **Equation S2.4.3**.

2.4.6.3 Chemical structure of uric acid and its electrochemical oxidation

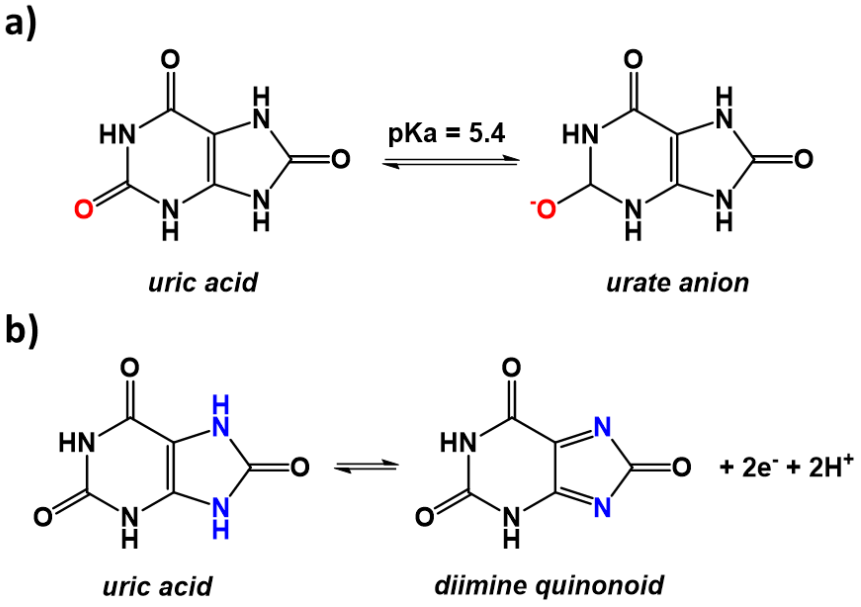

Figure S2.4.3. Chemical structure of uric acid **(a)** below and above the pK_{a1}; and **(b)** electrochemical oxidation reaction.

2.4.6.4 Dependence of the formal redox potential on the pH

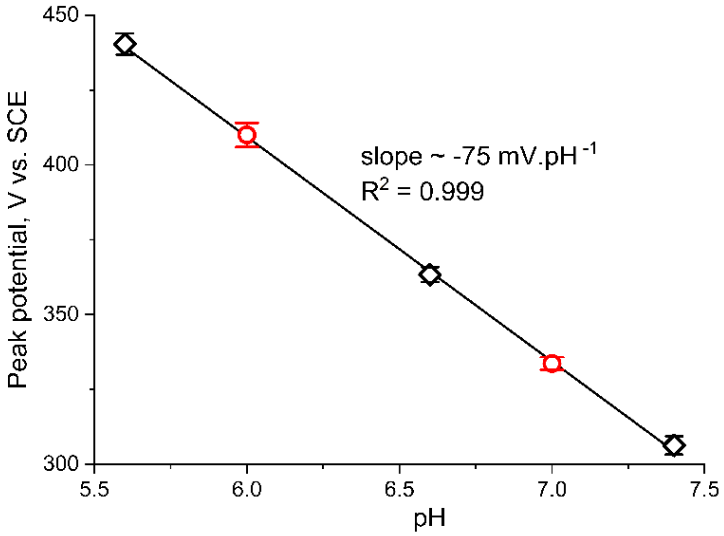

Figure S2.4.4. Dependence of the UA oxidation potential on the pH of the electrolyte solution, measured for a concentration of UA of 50 µM. Black diamonds are measurements in PBS and red circles are measurements in synthetic urine (pH 6.0) and 1:10 synthetic urine dilution in PBS (pH 7.0).

2.4.6.5 Selectivity tests – dopamine

In addition to the measurements in ascorbic acid-containing electrolyte and in synthetic urine formulations presented in the main manuscript, the possible interference of dopamine (DA) in UA quantification was also assessed (**Figure S2.4.5**). Despite some overlapping of DA and UA oxidation waves at higher DA concentrations, UA quantification is not affected by the oxidation process of DA nor by its by-products up to 20 µM DA (**Figure S2.4.5b**).

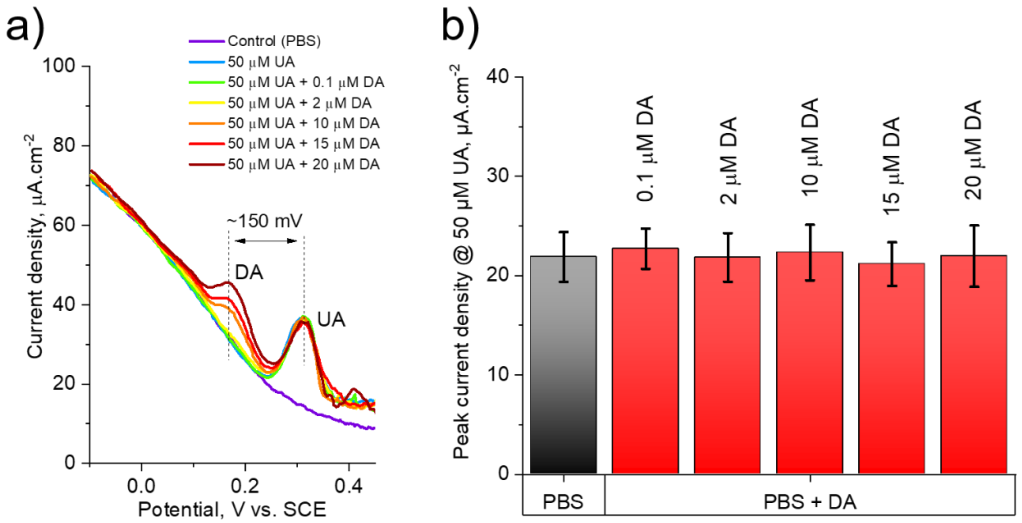

Figure S2.4.5. (a) DPV scans at 50 µM UA concentration in PBS (pH 7.4) plus varying concentrations of dopamine (DA). **(b)** UA oxidation peak current densities for the previous measurements. Error bars are standard deviations from independent quadruplicate measurements.

2.4.6.6 Reusability of paper-LIG sensors

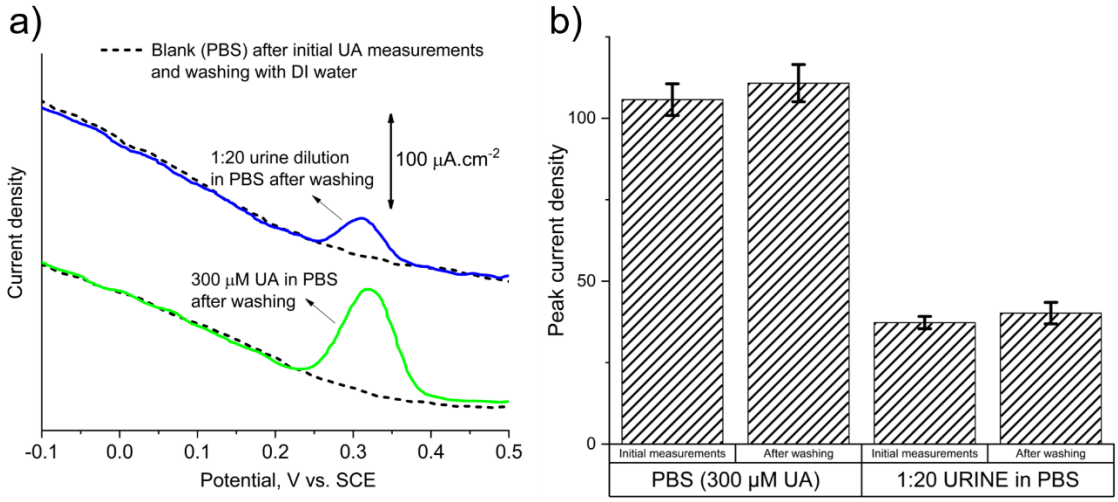

Figure S2.4.6. Reusability assessment of paper-LIG electrodes. **(a)** Blank DPV scans in PBS after initial measurements of UA and posterior washing with DI water (dashed black lines) and posterior re-measurement of UA (solid lines) in 1:20 diluted urine (blue) and PBS (green). Measurements are grouped and shifted in intensity for clarity. **(b)** Comparison of peak current densities from UA oxidation before and after electrode washing step. Error bars are standard deviations from independent quadruplicate measurements.

2.4.6.7 Supporting references

[S1] J. Bisquert, "Theory of the Impedance of Electron Diffusion and Recombination in a Thin Layer," *J. Phys. Chem. B*, 106, 2,325–333, **2002**. https://doi.org/10.1021/jp011941g.

[S2] J. Bisquert, "Influence of the boundaries in the impedance of porous film electrodes," *Phys. Chem. Chem. Phys.*, 2, 18, 4185–4192, **2000**. https://doi.org/10.1039/B001708F.

[S3] Y. C. Kudva, A. M. Sawka, and W. F. Young, "The Laboratory Diagnosis of Adrenal Pheochromocytoma: The Mayo Clinic Experience," *J. Clin. Endocrinol. Metab.*, 88, 10, 4533–4539, **2003**. https://doi.org/10.1210/jc.2003-030720.

[S4] J. W. Yi *et al.*, "An exclusively dopamine secreting paraganglioma in the retroperitoneum: a first clinical case in Korea," *J. Korean Surg. Soc.*, 82, 6, 389–393, **2012**. https://doi.org/10.4174/jkss.2012.82.6.389.

Chapter 3

CVD graphene for paper-based OLEDs

Graphene is a great candidate for the role of transparent conducting material, particularly for OLEDs envisaging applications in devices such as flexible displays. This chapter provides an account of the development of single-layer CVD graphene films for and their use in OLEDs on cellulose substrates.

Section 3.1 *introduces an in situ oxidation/reduction treatment of the copper substrate for CVD growth of single-layer graphene, resulting in millimetre-sized domains with low nucleation density and improved electrical transport properties. This work is adapted from the article published in "Carbon", under the reference "Millimetre sized graphene domains through in situ oxidation/reduction treatment of the copper substrate,"* Carbon*, 169, 403-415, 2020 (https://doi.org/10.1016/j.carbon.2020.08.002).*

Section 3.2 *presents the first report on the application of CVD graphene films as transparent anodes in flexible OLEDs on cellulose substrates. This work is a manuscript in preparation for publication.*

3.1 Millimetre sized graphene domains through in situ oxidation/reduction treatment of the copper substrate

Bohdan Kulyk, Alexandre F. Carvalho, António J.S. Fernandes, Florinda M. Costa

1 – i3N, Department of Physics, University of Aveiro, Campus Universitário de Santiago, 3810-193 Aveiro, Portugal.

Abstract:

In chemical vapor deposition of graphene, low nucleation density and large domain sizes are desirable. In the particular case of growth on copper, throughout recent years, several works have reported the oxidation of the substrate through various means, which leads to a reduced nucleation density. In this work, an in situ oxidation and reduction treatment is explored, establishing its connection with the removal of carbon impurities from the copper bulk, as well as clarifying the role of these impurities as graphene nucleation sites. The extent of the contribution of these impurities to the growth of graphene is inferred by experiments using carbon-13 methane feed. The effect of the oxidation and reduction treatment on the substrate's surface roughness is also addressed. Lastly, the synthesis recipe based on this treatment is supplemented with a growth stage splitting, an increased argon flowrate and a short etching stage, resulting in millimetre sized hexagonal graphene domains (diameters 2–3 mm) with improved electrical transport properties. Thus, the deposition process presented here stands out on account of its streamlined nature, which makes it an attractive candidate for industrial scale-up.

3.1.1 Introduction

Chemical vapor deposition (CVD) has shown to be capable of high-quality graphene and graphene-based materials' synthesis with potential for mass production [1–6]. Cu substrates are commonly used in graphene CVD, acting as a catalyst for the carbon-containing gas precursor breakdown. Moreover, unlike other transition metal catalysts, Cu shows a very low carbon solubility, which, in principle, should lead to self-limiting growth of single-layer graphene (SLG).

Throughout the years, a lot of effort has been directed towards understanding the growth mechanisms of CVD graphene [7–10]. The substrate itself has been shown to have a large impact on graphene growth, with its surface roughness, purity, structural defects and crystal orientation affecting the nucleation density of graphene [11–14]. This density is a particularly important aspect of the growth process, since the grain boundaries formed as the individual graphene domains coalesce have a negative impact on electronic transport properties [15,16]. As such, a low nucleation density and correspondingly large single crystal domains are typically desirable.

Several approaches towards low nucleation density, often used together, have been described in the literature, particularly in what concerns the substrate. Electrochemical polishing has been widely used to lower its surface roughness [11,17]. Heat treatments and long high-temperature annealings have also been employed to smooth the substrate surface [18,19]. Alternatively, another proposed strategy has been the controlled copper recrystallization into Cu(111) [20,21], as well as growth on resolidified melted copper [22]. Different substrate configurations and morphologies have also been identified as a means towards a lower graphene nucleation density [23–27]. The fine-tuning of the precursor gas mixture composition [28], as well as localized gas supply [29], are among other reported strategies.

Numerous works aiming to achieve a lower nucleation density have relied in some way on oxygen. Some initial reports suggested that the presence of oxygen in or at the surface of the copper used as substrates leads to a lower nucleation density [30–32]. As such, several processes based on the oxidation of the copper substrate prior to graphene growth have been proposed [13,31,33–37]. Magnuson et al., for example, observed a lower nucleation density for graphene grown on copper foils pre-oxidized ex situ at up to 300 °C, with subsequent thermal decomposition (in vacuum) of the oxide [31]. J. Pang and colleagues, on the other hand, pre-oxidized their substrates in situ, by introducing air into the growth chamber at 1025 °C prior to reduction back to metallic copper in H_2 atmosphere and subsequent introduction of methane for graphene synthesis [34], having also employed a similar approach for CVD graphene synthesis from organic solvent molecules adsorbed on copper [38]. Similarly, G. Eres et al. oxidized the copper substrates in air, at temperatures up to 500 °C, followed by a 3 h long reduction in H_2 at 1040 °C [35]. According to these works, the improvement in the nucleation density is explained by the removal of surface contaminants during the reduction of copper oxide. In fact, the presence of impurities has been shown to play an important role in controlling the nucleation density of graphene domains [12,39]. These contaminants may be difficult to avoid, as even copper foils with the highest nominal purity present contaminants such as C, O, Ca, Na and Si on their surface [40]. Carbon impurities are particularly relevant here, as these may act as a precursor for graphene nucleation and growth [41].

Later, new reports emerged indicating that the carbonaceous contaminants may in fact come from the bulk of the copper foils. J. Kraus et al. employed a mild oxidation strategy, using O_2 diluted in Ar in order to avoid the formation of copper oxide and the accompanying Cu surface

restructuring [42]. The authors postulate that the oxygen atoms remove the carbon present inside the copper foils, possibly introduced during the cold rolling process by which the foils are manufactured. Further evidence supporting this possibility was presented by P. Braeuninger-Weimer and colleagues, who, using time-of-flight secondary ion mass spectrometry (ToFSIMS), showed a relative carbon enrichment in the copper foils along the rolling striations from the manufacturing process [43]. This carbon content is highest at the surface, decreasing as the depth increases. The authors also state that other commonly used pre-treatment processes, such as electropolishing or acid etching, decrease the nucleation density of graphene by removing the carbon-containing copper layers, once again underlining the large influence of these contaminations. B. Huet et al., having annealed their substrates in the presence of oxygen, also conclude that the lower nucleation density results from the oxidative carbon removal not only from the surface, but also from the bulk of the foils [44].

A number of alternative explanations of oxygen's role has also been given in the literature. Y. Hao and colleagues proposed that oxygen may passivate the active sites on the substrate's surface, which would otherwise act as preferential nucleation sites due to the accumulation of hydrocarbon species [45]. Alternatively, several authors observed that a superficial oxidation favours copper recrystallization, either into Cu(100) [46] or Cu(111) [47], which, in turn, promotes fast graphene domain growth and a lower nucleation density. A change in the surface roughness of the substrate was also proposed as a reason for lower nucleation density [48].

One should also be aware that the discussion of oxygen's (and, in particular, copper oxide's) role gets further complicated when considering a number of works which do not subject the substrate to a reducing atmosphere prior to the graphene growth step. This includes synthesis after hydrogen-free annealing, where the substrate's surface at the start of the growth step is, in fact, copper oxide and not metallic copper [24,49–51].

In this work, an in situ substrate oxidation/reduction procedure is proposed, without requiring any additional copper pre-treatments or complex substrate configurations. The impact of this procedure is clarified, showing its ability to remove carbon-based impurities which otherwise segregate to the surface from the bulk of the substrate. The proposed procedure, along with an optimization of the growth parameters, is shown to allow the growth of millimetre sized graphene domains.

3.1.2 Results and discussion

3.1.2.1 Influence of carbon impurities

Figure 3.1.1a,b shows optical microscopy and SE-SEM images of a graphene sample grown on a conventionally treated copper substrate, a process which consists of subjecting the substrate to a 25 °C/min ramp from 940 °C to 1080 °C (with the pressure increasing from 0.3 mbar to 276 mbar), followed by a 10 min annealing at 1080 °C, both under H_2 and Ar flow, prior to the introduction of CH_4 for the growth itself. These conditions result in small (<5 μm in diameter) domains, aligned along the striations induced by the rolling process used to produce the thin copper sheets (25 μm-thickness) used here as substrates. At the centre of the domains one can see blot-like regions, which, as indicated by Raman spectra (**Figure 3.1.1c**), consist of a graphitic carbon phase, which can be identified by the characteristic D and G bands of sp^2-hybridized carbon materials. These are fairly broad, but not enough to label this phase as amorphous carbon. The same graphitic carbon can also be seen in the form of large irregularly shaped patches, as highlighted in **Figure 3.1.1b**. As for the graphene itself, Raman spectroscopy shows

the characteristic 2D and G peaks, with a large intensity ratio between them (I_{2D}/I_G=~2) and a small D band (**Figure 3.1.1c**) [52]. Interestingly, the transfer of these samples onto insulating substrates (Si with 300 nm of SiO_2) results in tearing at the centre of the graphene domains, as evidenced by both optical microscopy (**Figure 3.1.1d**) and Raman mapping of the G peak intensity (**Figure 3.1.1e**), with no signs of the graphitic carbon phase seen prior to the transfer at the centre of the domains (**Figure 3.1.1f**) except for the occasional presence of a peak at ~1600 cm^{-1}. This phase, however, continues present on the sample's surface in the form of the previously described irregularly shaped patches.

By comparison, graphene grown on electropolished copper substrates shows a reduced nucleation density, as well as larger (<50 μm in diameter) hexagonally shaped domains (**Figure 3.1.1g**). Moreover, there does not appear to be a preferential alignment of these domains along the rolling striations of the substrate. The reduced nucleation density and larger graphene domains are in line with what is often observed for CVD graphene deposited on electropolished copper [39].

As for the samples grown on copper subjected to the oxidation/reduction treatment (without a prior electropolishing step), which consists of a 10 min pre-annealing at 940 °C, exposure of the substrate to air at 940 °C for 5 min, and a 20 min annealing in hydrogen (a process which is compared to the conventional one in **Figure 3.1.1h**), these present even larger (~50 μm in diameter) sparsely distributed hexagonal domains (**Figure 3.1.1i**). The edges of these domains are not perfectly straight, with the graphene appearing to grow faster towards the vertices of the domains, which is consistent with the behaviour described in the literature for growth in the presence of oxygen [45,53]. Moreover, the underlying copper substrate can also affect the domains' edges, as seen on the highly terraced copper grains often visible after the oxidation/reduction treatment employed here, which can be identified by a characteristic wavy pattern in SEM images, for example (**Figure 3.1.1j**). Wrinkling and tearing of the graphene sometimes also occurs, most likely due to the mismatch of coefficient of thermal expansion with the copper substrate (also seen in **Figure 3.1.1j**) [54]. At the centres of the domains one can identify secondary layers, also with six-fold symmetry, occasionally presenting a silicon-containing particle in the middle. Such particles are often seen on CVD grown graphene, forming through the interaction of the copper vapor with the quartz tube where the deposition takes place [55]. The graphene grown on oxidation/reduction treated substrates displays Raman spectra characteristic of single-layer graphene (**Figure 3.1.1k**) [52], without the graphitic carbon phase seen on the conventionally grown samples, neither in, nor outside the hexagonal domains.

To clarify the origin of the graphitic phase present on the conventionally grown samples, Raman spectra of the copper substrate's surface after different annealing treatments preceding the graphene growth stage were acquired. A standard annealing, performed for different times at 1080 °C (after a temperature ramp from 940 °C, at a rate of 25 °C/min) in a hydrogen atmosphere (190 sccm H_2/190 sccm Ar), results in the appearance of an incomplete coating over the substrate's surface, which highlights the rolling striations of the copper (**Figure 3.1.2a-c**). The regions not covered by this coating are more or less circular, increasing in size for larger annealing times, with the coating disappearing entirely after 1 h of annealing. The Raman spectra taken from this coating are indicative of a graphitic carbon phase (blue trace in **Figure 3.1.2d**), similar to the one found on the graphene samples grown on the conventionally treated substrates, as described above. Given that a 10 min annealing in these same conditions directly precedes the growth stage in the recipes used in this work, it is possible that this coating may act as an additional carbon source for graphene growth. Even if long annealing times are

employed, some exogenous carbon may remain, as even for 1 h long annealings the samples present some dark spots with similar Raman signatures (**Figure 3.1.2e,f**).

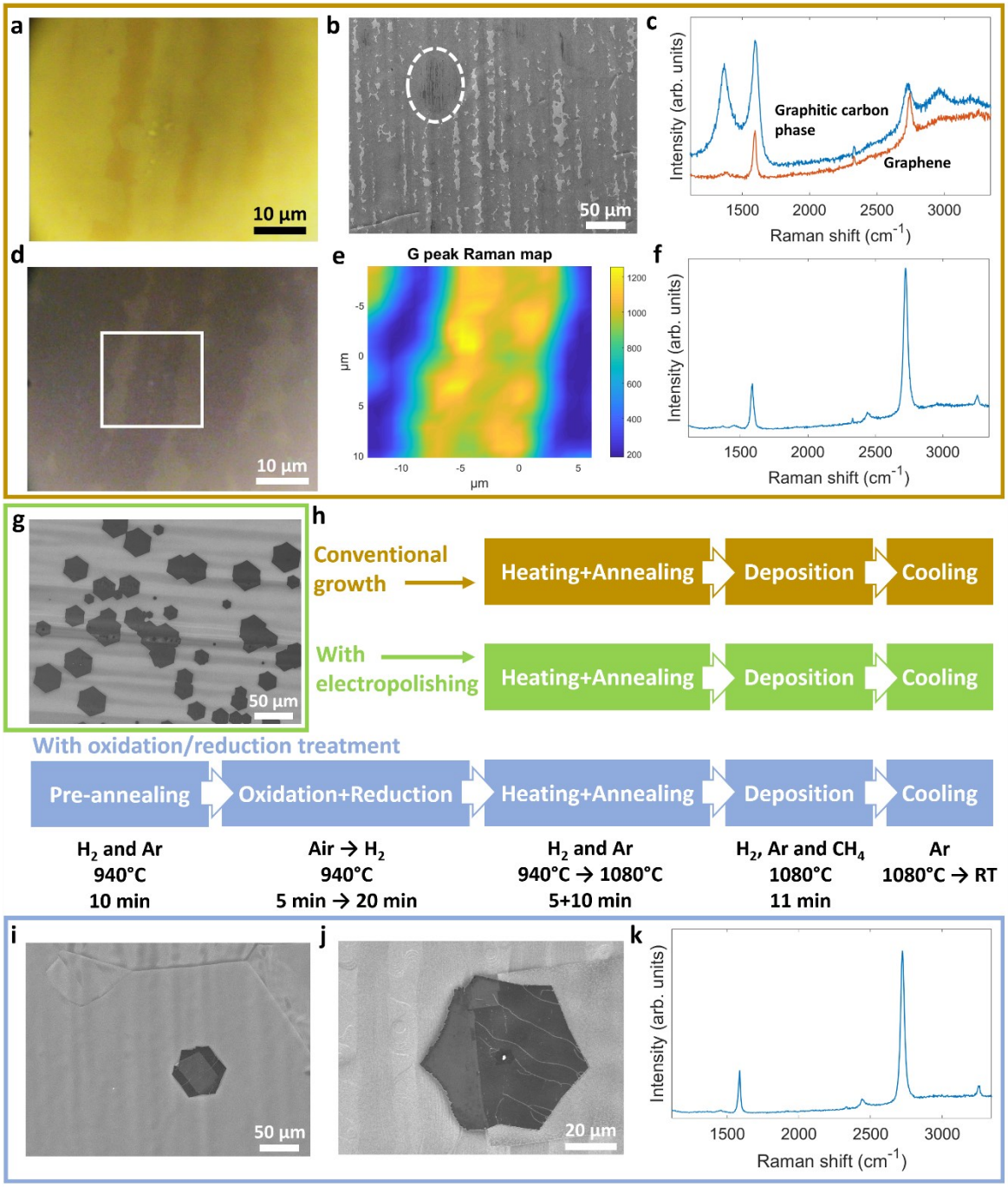

Figure 3.1.1. (a) Optical microscopy and **(b)** SE-SEM images of graphene grown on conventionally treated copper. The dashed line ellipse highlights an irregularly shaped graphitic carbon patch. **(c)** Raman spectra of the graphitic carbon phase seen at the centre of graphene domains and in the irregularly shaped graphitic carbon patches, as well as of the graphene itself. **(d)** Optical microscopy image of conventionally grown graphene transferred onto a Si/SiO_2 substrate. **(e)** Raman map of the G peak intensity over the area highlighted in (d). **(f)** Raman spectrum of transferred graphene. **(g)** SE-SEM image of graphene grown on electropolished copper. **(h)** Schematic comparison of the synthesis processes on the conventionally and oxidation/reduction treated substrates. **(i)** and **(j)** SE-SEM images of graphene domains grown on oxidation/reduction treated substrates. **(k)** Representative Raman spectrum of the same sample (after transfer onto Si/SiO_2).

No signs of carbon material can be observed after the oxidation/reduction treatment (green trace in **Figure 3.1.2d**), even after repeating the same annealing procedure as in the conventionally treated samples (blue trace in **Figure 3.1.2d**). The latter result excludes any possibility of the carbon composing the graphitic phase coming from the surrounding environment, either from the reactor walls or from any possible carbon-containing contaminations in the hydrogen or argon gas feedstocks. As such, the only remaining possibility for the origin of the carbon phase seen in the conventionally prepared samples is the copper substrate itself. Specifically, and since the "clean" copper substrate, that is, the as-purchased one (after washing with acetone and isopropanol, a cleaning procedure employed for all substrates used in this work prior to their loading into the CVD reactor), also shows no signs of any carbon material on its surface (red trace in **Figure 3.1.2d**), the carbon must originate from the bulk of the copper. This is in agreement with other works previously reported in the literature, in which the presence of amorphous carbon in commercial copper substrates has been identified [42,43]. ToF-SIMS studies, for example, have shown that this carbon phase is concentrated along the rolling striations typically found in commercial copper sheets. This points towards a link between this carbon material and the blot-like regions and irregularly shaped patches found in the conventionally grown graphene described above.

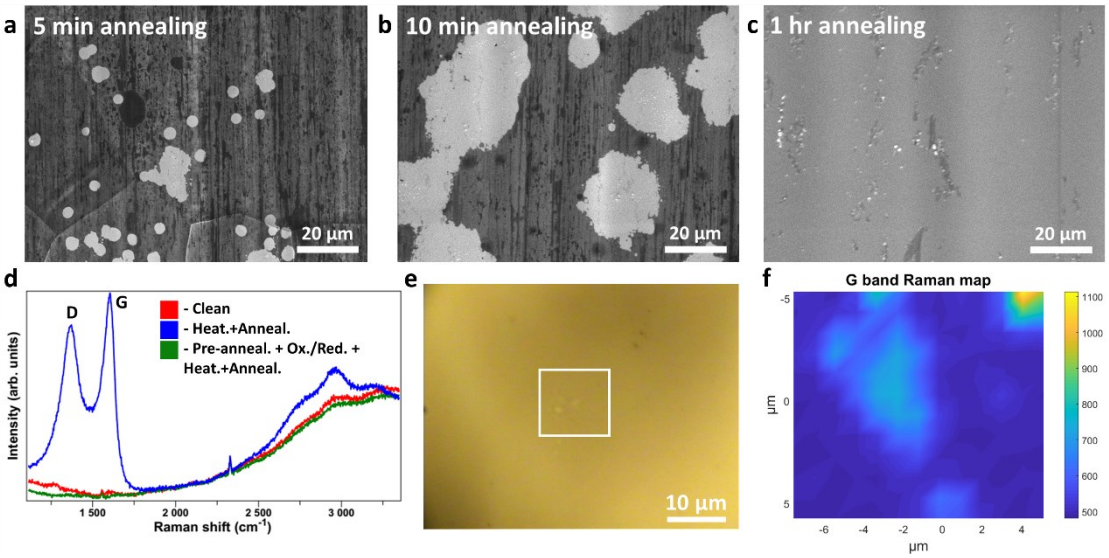

Figure 3.1.2. (a), (b) and **(c)** SE-SEM images of the copper substrate for different pre-growth annealing times in a hydrogen atmosphere. **(d)** Raman spectra of the copper substrate after different pre-growth treatments. **(e)** Optical microscopy image of the copper substrate after a 1 h high temperature annealing in a hydrogen atmosphere. **(f)** Raman map of the G band intensity over the area highlighted in (e).

In order to understand the influence of this graphitic phase on the deposition of graphene, growth on both conventionally and oxidation/reduction treated substrates was repeated using isotopically purified methane containing ^{13}C atoms as the gaseous precursor (in both cases no ^{12}C source was introduced into the chamber and care was taken to grow the sample by the conventional method after the one treated by oxidation/reduction). This way, using Raman spectroscopy, one can probe the presence of any additional source of carbon that may be involved in the graphene growth alongside the carbon from the supplied methane. The presence of ^{13}C in the material is known to result in a redshift of the Raman spectral position for the graphene peaks, given by **Equation 3.1.1**:

$$\omega = \omega_{12}\sqrt{\frac{m_{12}}{n_{12}m_{12} + n_{13}m_{13}}} \tag{3.1.1}$$

where ω_{12} is the Raman spectral position (or Raman shift) corresponding to the respective Raman peak in graphene formed exclusively by ^{12}C atoms, m_{12}=12.000000 and m_{13}=13.003355 are the atomic masses of the two carbon isotopes, and n_{12} and n_{13} are their atomic fractions in the analysed sample [56]. Taking the G peak as an example, in the case of ^{12}C graphene, its spectral position corresponds to ~1580 cm^{-1}. As such, the same peak in isotopically pure ^{13}C graphene is expected to appear at ~1518 cm^{-1}. One should be aware, however, that other factors can cause shifts in the spectral positions of graphene's peaks, such as mechanical strain, doping, interactions with charge impurities in the substrate, etc. [57–62]. For example, we routinely obtain G peaks at spectral positions of up to ~1590 cm^{-1} for ^{12}C graphene transferred onto Si/SiO_2 substrates, which would correspond to a spectral position of ~1527 cm^{-1} for ^{13}C graphene.

Starting with the conventionally grown graphene (optical microscopy image in **Figure 3.1.3a**), the Raman spectra on copper allow to identify three types of regions. The blot-like formations at the centres of the nearly hexagonal domains present D, G and 2D peaks with spectral positions of ~1318 cm^{-1}, ~1530 cm^{-1} and ~2610 cm^{-1}, respectively (with the latter two marked by blue dashed lines in **Figure 3.1.3b**), as well as D and G bands corresponding to the graphitic carbon phase composed of ^{12}C, with spectral positions of ~1380 cm^{-1} and ~1600 cm^{-1} (marked by a red dashed line in **Figure 3.1.3b**). The Raman spectra taken at the periphery of the blot-like regions (around centres of domains), on the other hand, show two distinct sets of G and 2D peaks with varying intensities and Raman spectral positions. Lastly, towards the edges of the domains, one finds spectra with only the G and 2D peaks at ~1530 cm^{-1} and ~2610 cm^{-1}, respectively (with an occasional D peak at ~1318 cm^{-1}).

Since the Raman spectral positions of the graphene spectra acquired on copper often present considerable inhomogeneities due to localized strains and stresses, as well as due to the formation of an underlying copper oxide layer, resulting in variability in the spectral positions of the Raman peaks [63,64], the conventionally grown sample was transferred onto Si/SiO_2 substrates (**Figure 3.1.3c**). The transfer allows to relax the mechanical stresses in the graphene films, facilitating the identification of the spectral positions of the Raman features. Interestingly, after performing a mapping acquisition over a 20×20 μm^2 area on the transferred sample, it appeared to only have spectra with the G and 2D peaks at ~1527 cm^{-1} and at ~2620 cm^{-1}, respectively, which can be attributed to isotopically pure ^{13}C graphene, with no signs of any additional graphene peaks observed in the as-grown sample. The disappearance of the latter can be explained considering that, during transfer, the graphitic phase at the centre of the graphene domains is mostly left behind on the substrate (note also the central regions of the graphene domains mapped in **Figure 3.1.3d**, where the intensity of the graphene signal in the spectra is lower, possibly due to holes where the graphene directly attached to the graphitic phase got ripped out during the transfer). Thus, no peaks at ~1380 cm^{-1} and ~1600 cm^{-1} are found after this procedure. As for the regions with two distinct sets of G and 2D peaks that were seen on copper, these are consistent with what one would see for bilayer graphene where each of the layers contains different atomic fractions of ^{13}C [65,66]. Consequently, it is possible that one of these layers is connected more closely to the graphitic phase, also ending up being left behind during the transfer process. It is, however, important to point out that for longer growth times, namely 13 min, 15 min, and 20 min, no regions with two distinct sets of graphene peaks

were found. Moreover, the average spectral position of the G peak does not vary for different times, remaining close to what is expected of pure ^{13}C graphene (**Figure 3.1.3e**).

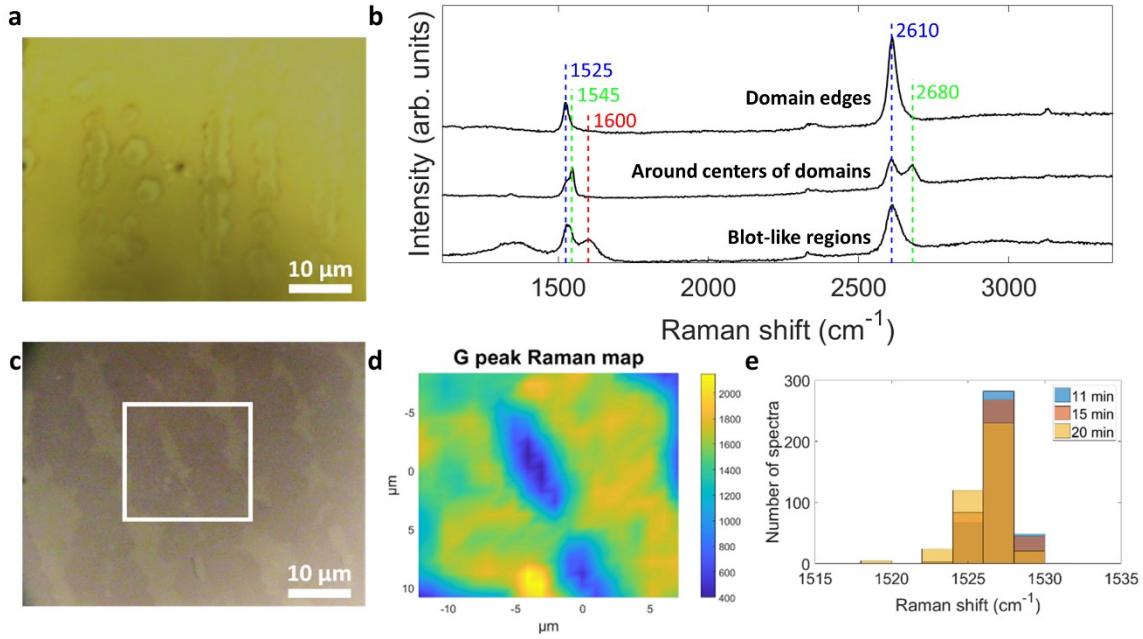

Figure 3.1.3. (a) Optical microscopy image of graphene grown on a conventionally treated substrate using ^{13}C methane as precursor. **(b)** Raman spectra taken at different points of the sample shown in (a). The spectra have been offset for clarity. **(c)** Optical microscopy image of transferred conventionally grown graphene with ^{13}C methane as precursor. **(d)** Raman map of the G peak intensity over the area highlighted in (c). **(e)** Histogram of the spectral position distribution of the G Raman peak for ~400 spectra acquired from conventionally grown samples with different growth times (after transfer).

The isotopically pure ^{13}C nature of the obtained graphene indicates that the graphitic phase seen on the copper's surface (both along the rolling striations and as part of the carbonaceous coating seen after annealing) does not provide carbon atoms for the growth of graphene. At first glance, one can postulate that by the time the graphene nucleation begins, most of the carbonaceous coating has been etched away by hydrogen and only the more stable graphitic material remains. To probe this hypothesis, the growth recipe was changed by increasing the methane flowrate for the nucleation to begin sooner, with a considerable amount of carbonaceous coating still remaining on the copper's surface. Still, no sign of ^{12}C graphene was found, neither before, nor after the transfer onto the Si/SiO_2 substrate (**Figure 3.1.4**).

As for the oxidation/reduction treated sample, it shows no discernible ^{12}C signal, neither before, nor after the transfer process, presenting only the characteristic Raman spectra of ^{13}C graphene (**Figure 3.1.5**).

The results presented so far allow to formulate a description of the conventional deposition process. Firstly, a high temperature annealing in hydrogen brings the amorphous carbon from the bulk of the copper substrate to its surface, along the rolling striations. There it becomes more graphitic throughout the process, as indicated by the narrowing of its Raman peaks, forming the blot-like regions. When the methane precursor is introduced into the reactor, it starts to decompose catalytically at the exposed copper surface, followed by the diffusion of the graphene forming species. The latter, once they reach the graphitic material along the

rolling striations, begin to nucleate, as indicated by the fact that the graphene domains are centred predominantly at the blot-like regions along the striations.

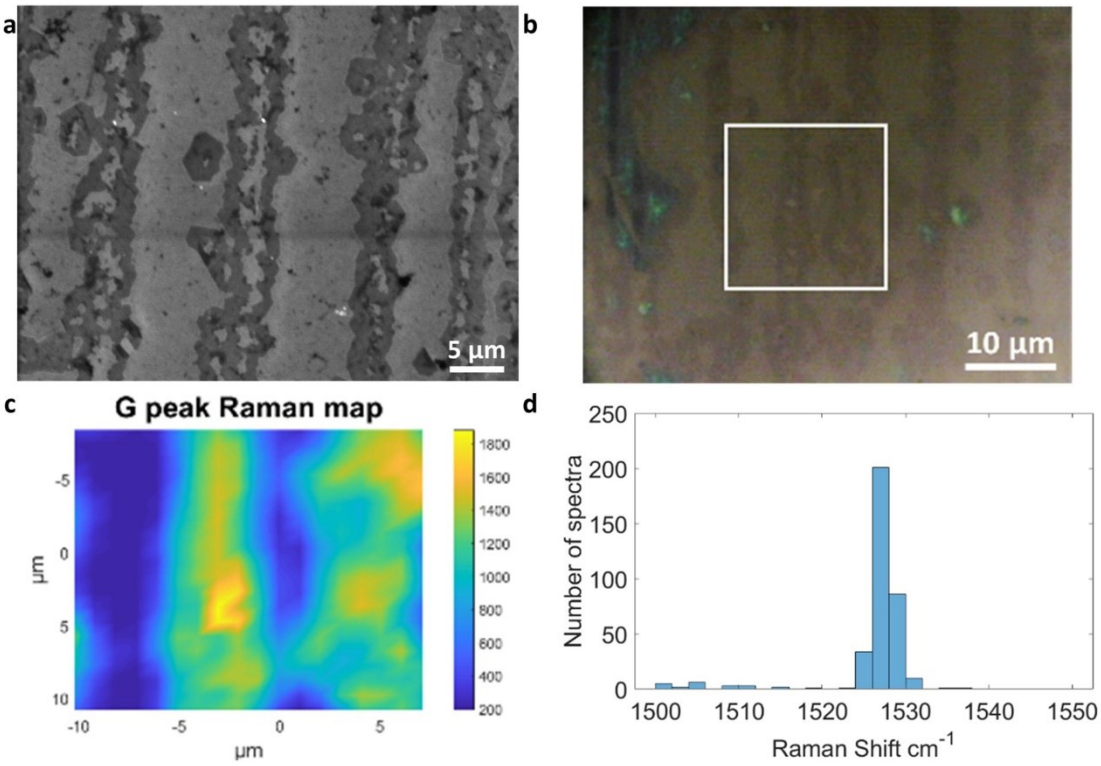

Figure 3.1.4. (a) SE-SEM and **(b)** optical microscopy images of transferred graphene grown on a conventionally treated substrate with an increased ^{13}C methane flowrate. **(c)** Raman map of the G peak intensity over the region highlighted in (b). **(d)** Histogram of the spectral position distribution of the G Raman peak for ~400 spectra acquired from the same sample.

More interestingly, the graphitic phase does not appear to be acting as a major source of carbon for graphene formation, as one could be inclined to think due to the fact that the conventional growth results in far greater surface coverage by graphene than for the growth on the oxidation/reduction treated substrates. Instead, it is only at the periphery of the blot-like regions that one observes what appears to be two distinct types of graphene, although none of which corresponds to purely ^{12}C composed graphene as the Raman spectral positions of their peaks do not correspond to the typical ones for the latter. For longer growth times only ^{13}C graphene is found. This points towards the conclusion that even though the graphitic phase is susceptible to hydrogen etching (as one can see by the gradual disappearance of the carbonaceous coating in **Figure 3.1.2**), the released carbon species do not contribute significantly to the growth of graphene compared to the contribution of the carbon species from the methane precursor. Still, the presence of the graphitic carbon phase appears to promote graphene nucleation, resulting in higher domain density.

3.1.2.2 Influence of the substrate's surface roughness

It is also important to address any possible changes to the substrate surface due to the oxidation/reduction treatment, specifically, how it can affect the substrate's roughness. The latter

has been pointed out as an important parameter in the control of the growth process of graphene on copper [11], as well as its transfer [67].

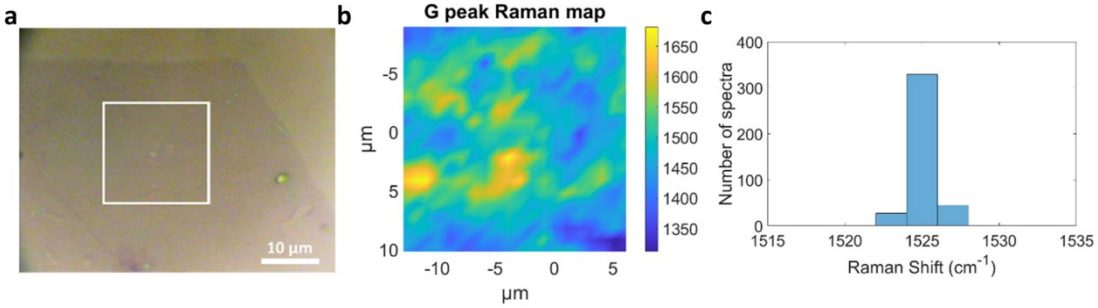

Figure 3.1.5. (a) Optical microscopy image of transferred graphene grown on oxidation/reduction treated substrate with ^{13}C methane as precursor. **(b)** Raman map of the G peak intensity over the region highlighted in (a). **(c)** Histogram of the spectral position distribution of the G Raman peak for ~400 spectra acquired from the same sample.

Here, the surface roughness of as-purchased ("clean", after washing with acetone and isopropanol), conventionally treated (temperature ramp followed by a 10 min annealing at 1080 °C in a hydrogen and argon atmosphere), and oxidation/reduction treated copper foils were compared, based on the root mean square height values obtained from optical profilometry measurements (**Table 3.1.1**). The oxidation/reduction treatment results in a slight increase in the surface roughness relative to the as-purchased copper, from ~0.5 µm to ~0.6 µm, while a conventional annealing leads to a surface roughness of ~0.4 µm. As such, one can conclude that, despite a higher surface roughness of the substrate, a significantly lower nucleation density can be obtained. This once again points towards the carbon coming from the bulk of the substrate as having the biggest impact on the nucleation density of the resulting graphene.

Table 3.1.1. Surface roughness in terms of RMS height for different substrate pre-treatments

Substrate	Pre-growth treatment (after washing)	RMS height
As-purchased ("clean") Cu	-	~0.5 µm
Conventionally treated Cu	25 °C/min ramp from 940 °C to 1080 °C + 10 min annealing at 1080 °C	~0.4 µm
Oxidation/Reduction treated Cu	10 min annealing at 940 °C + 5 min oxidation in air + 20 min H_2 reduction (50 sccm) + 25 °C/min ramp from 940 °C to 1080 °C + 10 min annealing at 1080 °C	~0.6 µm

3.1.2.3 Influence of methane flowrate

In general, one can summarize a CVD graphene growth process as being composed by the following steps: (i) adsorption/desorption of carbohydrate precursors on the substrate's surface, (ii) decomposition of the precursors, (iii) migration of the carbon-containing species along the surface, and either (iv-a) aggregation of the carbon-containing species to nucleate graphene, or (iv-b) attachment/detachment (the latter most likely due to etching by hydrogen [28,68]) of the carbon-containing species to/from an existing graphene domain [8]. Step (iv-a) is often described in terms of carbon supersaturation, which has to be reached for the nuclei to form [69]. As such, methane flowrate (and, consequently, its partial pressure in the chamber, as well as the CH_4/H_2 ratio) has a direct effect on the nucleation density, where higher carbon supply

results in higher nucleation density as well as accelerated growth rate [35,70,71]. Thus, one should expect that the nucleation density of the graphene grown on the oxidation/reduction treated substrates should decrease by lowering the methane flowrate, albeit at the cost of longer growth times for equivalent domain sizes.

Figure 3.1.6a-c show SEM images of graphene on copper grown under three different methane flowrates (0.15, 0.10 and 0.05 sccm), with a fixed growth time (15 min). The density of the formed graphene domains becomes lower as the methane flowrate is lowered, reaching as low as ~0.01 mm^{-2}. Their size diminishes as well. However, by increasing the growth time (up to 45 min, in this case), domain sizes similar to those obtained for the sample grown under 0.15 sccm methane flow are recovered, while maintaining a lower nucleation density of ~0.91 mm^{-2} (**Figure 3.1.6d**). A further increase in growth time allows to achieve even bigger domains (**Figure 3.1.6e,f**).

Thus, by lowering the methane flowrate, growth (albeit at a slower rate) can be sustained while inhibiting additional nucleation, to some extent.

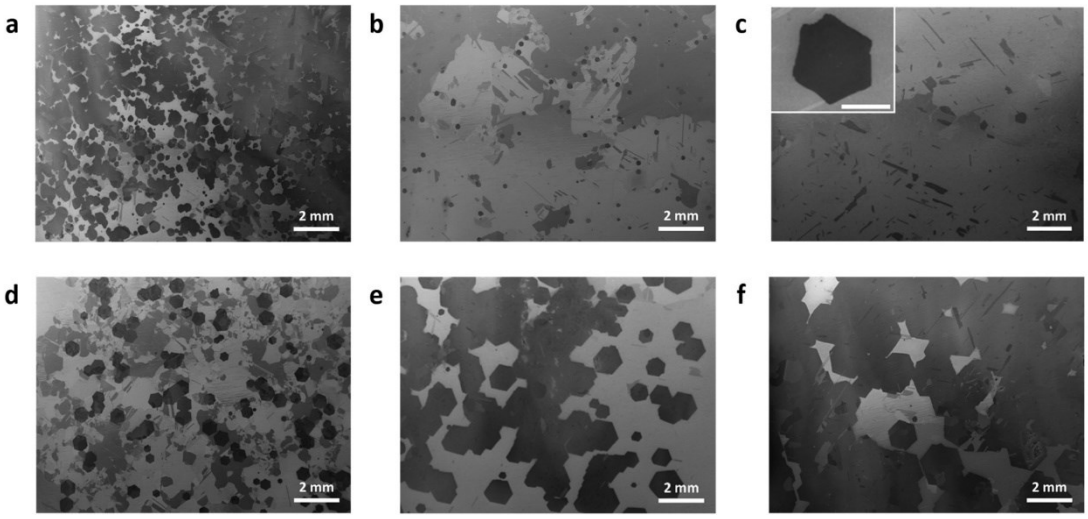

Figure 3.1.6. SE-SEM images of graphene grown on oxidation/reduction treated copper under **(a)** 0.15 sccm, **(b)** 0.10 sccm and **(c)** 0.05 sccm of methane flowrate (with the inset of the latter showing an amplified image of a graphene domain, the scale bar corresponding to 10 μm), for 15 min, as well as for growth times of **(d)** 45 min, **(e)** 70 min and **(f)** 90 min under 0.05 sccm of methane.

3.1.2.4 Growth stage splitting

As mentioned previously, the nucleation of graphene requires carbon supersaturation, resulting in an initial accumulation of carbon-containing species on the copper's surface [69]. Once nucleation begins, the carbon-containing species present at the substrate's surface begin to be consumed by the newly formed domains, thus lowering their concentration. Eventually, an equilibrium is reached, where the carbon species' surface density remains constant and growth is maintained. When considering this description, one should also keep in mind that the supersaturation requirement, as well as the rate at which it is fulfilled, can vary depending on the specific location on the substrate. This explains why different nucleation events can occur at different times, as has been shown by in situ SEM monitoring of the growth process [72], as well as why nucleation can occur preferentially at certain spots (the so-called active sites). The above provided explanation thus suggests that, by lowering the carbon precursor supply after

an initial stage where the first nucleations are formed, one can hinder supersaturation at other locations, thus limiting further nucleation events.

As such, building on the previously described recipe, the growth stage was split into two, where in the second one the methane flowrate was halved relatively to the first one (from 0.10 sccm to 0.05 sccm). The effect of this growth stage splitting can be seen in **Figure 3.1.7a**. Compared to the sample grown for 70 min at 0.05 sccm of CH_4, the one where the initial 10 min of growth were performed at 0.10 sccm of CH_4 flow shows a considerably lower domain density (~0.45 mm^{-2}). This is in accordance to the description of the nucleation process provided above, as well as to some previous reports in the literature, where the growth of newly formed nucleations results in the consumption of carbon-containing species, quickly leading to desaturation and inhibition of further nucleation events [69,72]. In other words, the existence of sufficiently stable domains formed during the first 10 min may be inhibiting the formation of new ones, with carbon attaching preferentially to the edges of the existing domains instead of nucleating new ones. The resulting domain density is thus lower under the growth stage splitting mode, despite the total amount of supplied precursor exceeding that of the sample grown at a constant CH_4 flowrate of 0.05 sccm for the same amount of time.

It is also possible to observe some secondary layers inside the graphene domains, seen as dark patches. These are undesirable in single-layer graphene growth. However, as only a handful of such patches can be seen per graphene domain, their overall surface coverage is quite low, which is a good step towards strictly single-layer large area graphene films.

3.1.2.5 Influence of argon flowrate

The effect of argon flowrate was also probed, by doubling it (from 200 sccm to 400 sccm) in the second part of the growth stage. The resulting sample shows a higher surface coverage by graphene, in part due to an increased nucleation density of ~1.05 mm^{-2} (**Figure 3.1.7b**). However, the uncoalesced domains appear to achieve larger sizes than in the sample grown under constant argon flowrate. The larger domain sizes point towards increased growth rate, which is appealing in order to avoid exceedingly large growth times. This result is in agreement with other works reporting that the Ar feedstock contains trace amounts of oxygen [33,51]. The latter is believed to increase the growth rate of graphene by lowering the carbon edge-attachment energy barrier [45,53].

3.1.2.6 Nucleation-etching-growth stages

Attention should also be paid to the role played by hydrogen in the CVD process, particularly during the growth stage. With this gas being an etching agent during synthesis, small domains, due to their high perimeter to area ratio, are particularly vulnerable to its action [28]. Thus, in principle, it should be possible to take advantage of this by introducing a short period with no methane supply during the growth stage, as has been done for graphene-diamond hybrids synthesized by microwave plasma CVD, for example [6]. This should result in "natural selection" growth, where only the biggest domains "survive" the hydrogen etching. This way, the number of domains remaining after the first part of the growth stage can be reduced even further before the second part, in which growth of existing domains is promoted, begins. Consequently, the final domain density should be reduced. In fact, a similar approach has been explored previously on Pt substrates, allowing to achieve graphene domains with diameters as large as 3 mm by periodically cutting off the methane supply to promote the etching of the smaller, newly formed domains that appear during the growth process [73].

Figure 3.1.7c shows the sample grown in conditions where the methane supply was cut off for 1 min during the growth stage. The domain density becomes lower (~0.52 mm^{-2}) as a result of this short etching stage. Moreover, the graphene domains appear to be more regular than in the case of the sample grown simply under the growth stage splitting (**Figure 3.1.7a**), while also displaying a more homogeneous size distribution compared to the sample under the growth stage splitting and increased argon flowrate (**Figure 3.1.7b**).

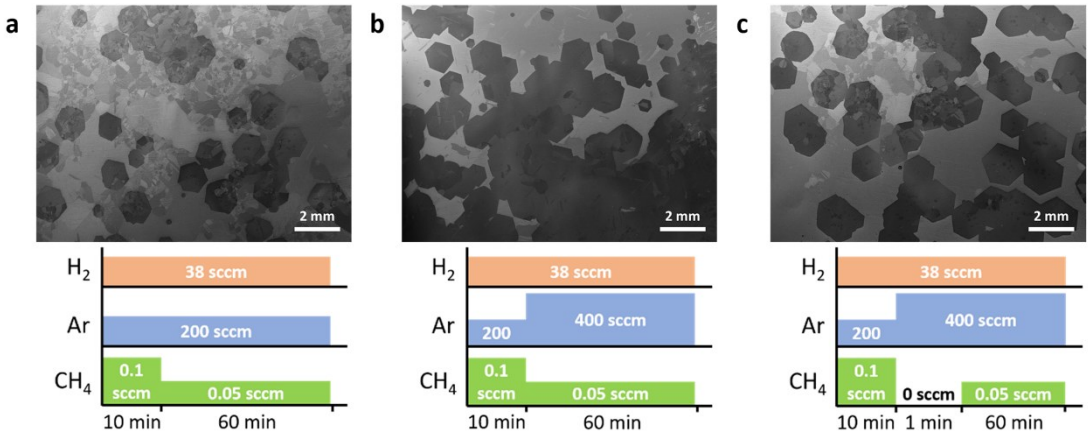

Figure 3.1.7. SE-SEM images of graphene grown on oxidation/reduction treated copper with **(a)** growth stage splitting, **(b)** increased argon flowrate and **(c)** a short stage without methane supply, along with the corresponding gas flow profiles.

3.1.2.7 Characterization of millimetre sized graphene domains

To confirm the thickness of the graphene obtained on oxidation/reduction treated substrates after the recipe optimization outlined above, the sample was transferred onto a Si/SiO_2 substrate (**Figure 3.1.8a**) and atomic force microscopy (AFM) measurements were performed. **Figure 3.1.8b** shows an AFM height image of a graphene domain, as well as a height profile corresponding to a line across the edge of this domain. The height difference is equal to ~1.5 nm. This value is higher than the thickness typically attributed to single-layer graphene, however the interaction strength with the substrate can have a large effect on the measured thickness [74], with values as large as 1.8 nm having been reported in the literature for single-layer CVD graphene on Si/SiO_2 [75]. Moreover, the Raman spectra of these graphene domains (**Figure 3.1.8c**) are characteristic of single-layer graphene, presenting a high intensity ratio of the 2D and G peaks (I_{2D}/I_G=4.8) and a full-width at half-maximum (FWHM) of the 2D peak of ~29 cm^{-1}, values which are in agreement with what is commonly reported for high-quality SLG transferred onto SiO_2 [76].

In order to characterize the electrical properties of the millimetre sized SLG domains obtained on oxidation/reduction treated substrates after the recipe optimization outlined above, as well as with a growth time increase up to 2 h, the graphene was transferred onto microfabricated backgated FET devices (**Figure 3.1.8d**), resulting in graphene field-effect transistors (GFETs). The obtained dependence of I_{DS} on V_{GS} results in the characteristic V-shaped transfer curves of graphene, revealing its linear dispersion relation and ambipolar electric field effect (**Figure 3.1.8e**). The slope of the linear portions of the transfer curve allows to obtain the charge carrier mobility, resulting in a rather modest value of ~1980.5 $cm^2\ V^{-1}\ s^{-1}$ for holes and ~1026.8 $cm^2\ V^{-1}\ s^{-1}$ for electrons, at room conditions. One should, however, be aware that measurements performed on GFET devices are highly sensitive to the environment, with adsorption of air and water molecules on the graphene's surface resulting in significantly lower

charge carrier mobility values than those obtained on GFET devices measured in vacuum [77]. Moreover, the transfer process itself exposes the graphene to contaminants such as polymer residues [78]. The latter fact is known to result in a p-type doping, which is, in fact, seen in the present work, identifiable by the shift of the charge neutrality point towards positive gate voltages (~0.7 V). In fact, the results obtained in this work surpass the ones obtained for a commercial CVD graphene sample transferred and measured under the same conditions, on the same FET devices, which presented mobilities of 517.6 $cm^2\ V^{-1}\ s^{-1}$ for holes and 399.7 $cm^2\ V^{-1}\ s^{-1}$ for electrons, at most. Moreover, the charge carrier mobilities obtained for millimetre sized SLG domains are 3–4 times higher than those for the graphene grown on conventionally treated substrates, which had mobilities of 485.0 $cm^2\ V^{-1}\ s^{-1}$ for holes and 354.8 $cm^2\ V^{-1}\ s^{-1}$ for electrons, at most. This points towards a significantly higher quality of the graphene grown on the oxidation/reduction treated substrates.

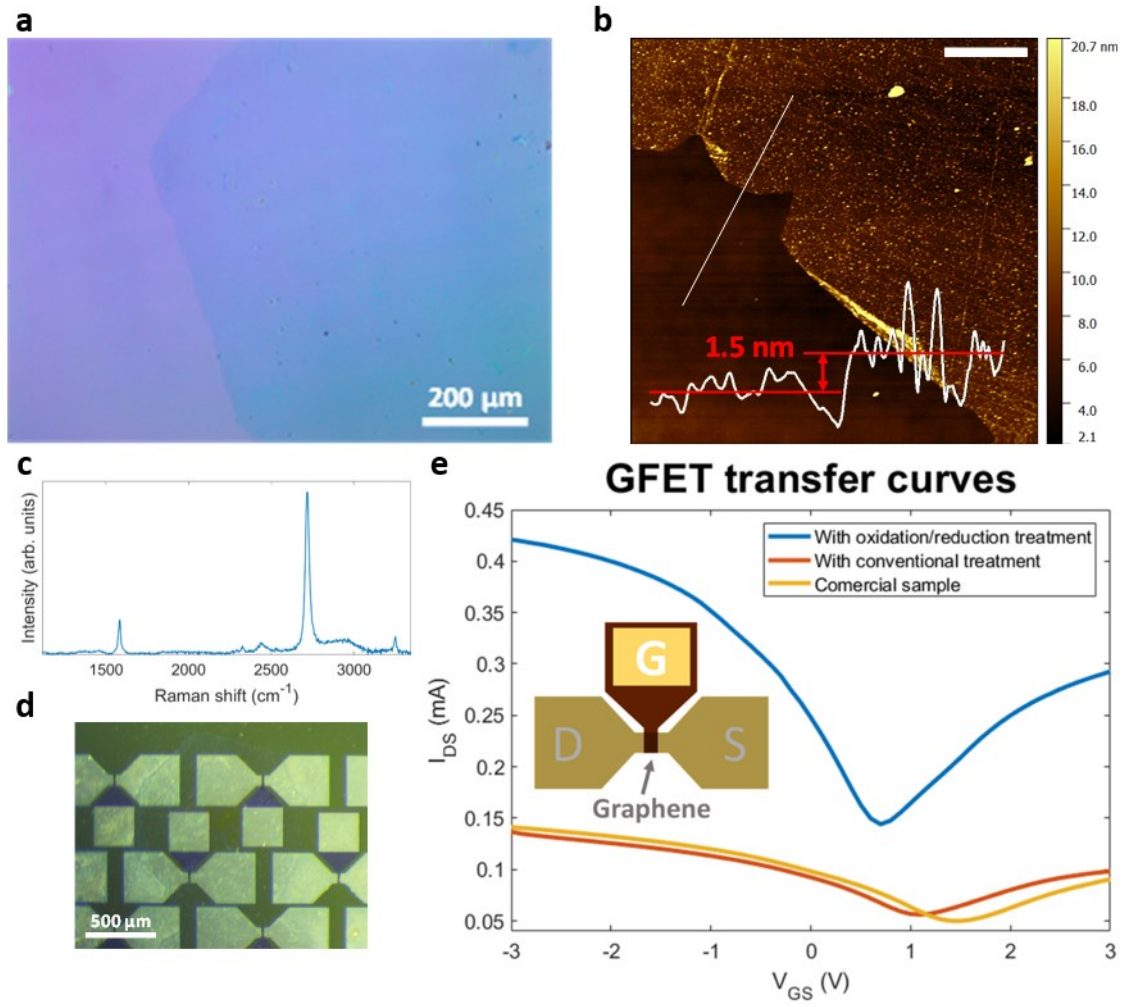

Figure 3.1.8. (a) Optical image of a graphene domain on Si/SiO_2. **(b)** AFM height image of a millimetre-sized graphene domain on Si/SiO_2, with a height profile along the white line. The scale bar corresponds to 2 mm. **(c)** Raman spectrum of a millimetre-sized graphene domain on Si/SiO_2 (a baseline has been removed). **(d)** Optical image of a graphene domain on the microfabricated FET devices prior to the patterning of graphene. **(e)** Transfer curves of GFET devices using the millimetre sized graphene domains obtained on oxidation/reduction treated copper after the growth recipe optimization outlined in this work, as well as for the conventionally grown graphene and a commercial sample. The inset shows a schematic representation of the GFET device, with S, D and G representing the source, drain and gate electrodes, respectively.

3.1.3 Conclusions

An in situ treatment of the copper substrate for CVD graphene growth, based on high-temperature oxidation in air followed by reduction in hydrogen, has been developed. This treatment is shown to result in a considerably lower nucleation density compared to the conventional high temperature annealing in hydrogen-rich atmosphere (either with or without a prior electropolishing of the substrate), with the latter shown to produce patches of carbonaceous impurities on the substrate's surface. This carbonaceous phase does not appear to constitute a direct source of carbon for graphene growth, as shown by graphene depositions performed with ^{13}C methane as a precursor. The oxidation/reduction treatment removes this carbonaceous phase, allowing, after optimization of the deposition parameters, the growth of millimetre sized hexagonal graphene domains with improved electrical transport properties. This work clarifies the role of carbon impurities in the copper substrates and presents a streamlined deposition process capable of dealing with these impurities in situ and having the potential for industrial production upscale.

3.1.4 Materials and methods

3.1.4.1 Substrate preparation

For substrate preparation and cleaning, a 25 μm-thick copper foil (>99.99%, MTI) was cut into ~2×4 cm^2 sheets and washed in acetone and isopropanol (15 min ultrasonication in each of the solvents), with each sheet constituting a single substrate. This procedure was applied before the conventional and oxidation/reduction growth approaches.

The conventional pre-growth substrate treatment consisted of loading the substrate into a homemade thermal chemical vapor deposition reactor, pre-heated to a temperature of 940 °C. The air was pumped out of the reactor, achieving a base pressure of ~0.3 mbar (note that the temperature reported here is 10 °C lower than the measured one, as the latter is obtained using a pair of thermocouples outside the quartz tube; the offset was determined by the copper's melting temperature). The substrate was then subjected to a 25 °C/min temperature ramp from 940 °C to 1080 °C, under 190 sccm of H_2 and 190 sccm of Ar, followed by a 10 min annealing at 1080 °C in the same atmosphere. The pressure during these two steps was allowed to rise to 276 mbar and was then maintained at this value.

For electropolishing pre-growth substrate treatment, the copper substrate was placed in phosphoric acid (>85 wt% in H_2O, Sigma-Aldrich) and a 1.5 V potential was applied to it against a copper counter electrode for 20 min [11]. The substrate was then washed in DI water.

For the oxidation/reduction pre-growth substrate treatment, the substrate was placed inside the reactor, pre-heated to a temperature of 940 °C, and subjected to a 10 min annealing, under 190 sccm of H_2 and 190 sccm of Ar, at 276 mbar. Afterwards, the chamber was pumped down to ~0.13 mbar and ~200 sccm of air was introduced, for 5 min. Next, the system was pumped down once again to ~0.15 mbar and 50 sccm of H_2 were introduced, for 20 min. The gas was then pumped out and Ar was used to fill up the chamber to atmospheric pressure. The conventional pre-growth substrate treatment described above was then performed.

3.1.4.2 Graphene growth

For the growth of graphene, immediately after either of the substrate treatments described above, CH_4 was introduced into the chamber, alongside 38 sccm of H_2 and 200 sccm of Ar. The

flowrate of CH_4 was 0.10 sccm for the non-optimized growth, with deposition times varying between 11 and 20 min. For the optimized growth recipe, a CH_4 flowrate of 0.10 was maintained for 10 min, followed by 1 min without any CH_4 supply (but maintaining the same flowrates of H_2 and Ar), and finally 60 min of 0.05 sccm of CH_4, with an increased flowrate of 400 sccm of Ar throughout these last 60 min. The sample was then rapidly pulled out towards the cold end of the reactor and all the gases were pumped out, followed by the pressurization of the chamber to atmospheric pressure with Ar.

3.1.4.3 Graphene transfer

The transfer of graphene for further processing and characterization was done according to the commonly employed electrochemical bubbling process, using PMMA (poly(methyl methacrylate), average molecular weight 550 000, Alfa Aesar, 4.5 wt% in anisole) as a supporting polymer.

3.1.4.4 Graphene characterization

The backgated field effect transistors were microfabricated on Si substrates with a 200 nm SiO_2 layer. Each device had a 50 nm TiWN gate electrode, while a 30 nm Al_2O_3 layer (both materials deposited using a Singulus Timaris multi-target sputtering system) acted as the gate dielectric, defining a 25 µm long and 75 µm wide channel. The source and drain contacts were formed by Au (90 nm) with a Cr adhesion layer (3 nm), deposited in a Kenosystec multi-target sputtering system. The graphene to be characterized was then transferred onto these transistors as described above and patterned mechanically using a sharp micro positioner tip. All the other patterning steps were performed using a Nordiko 7500 broad beam ion milling system with secondary ion mass spectroscopy end point detection, while the photoresist deposition, exposure and etching were done in a Karl SUSS Gamma Cluster track-stepper, with a 500 nm spin-coated layer of cured AZ 1505 positive photoresist and with a Heidelberg DWL 2000 direct write laser system for exposure.

Secondary electron scanning electron microscopy (SE-SEM) images were acquired using a Vega 3 SBH system by TESCAN, with an acceleration voltage of 5 kV and a working distance of 15 mm. Raman spectroscopy was performed using a Jobin Yvon HR800 Raman system, by Horiba, and a He-Cd 441.6 nm laser by Kimmon. An S neox non-contact optical profiler from Sensofar Metrology, operated in confocal mode, was used for optical profilometry. Atomic force microscopy (AFM) analysis was performed in tapping mode, using a Nanoscope IIIa Veeco controller by Bruker, a Super-SharpSilicon probe with 2 nm tip radius by Nanosensors, and the WSXM 5.0 software [79]. A Keysight B2902A dual-channel source meter unit was used to test the field-effect mobility, with one channel providing a constant V_{DS} of 0.1 V and the other a variable V_{GS}, between −3 V and 3 V in 0.1 V steps. The field-effect mobility of the charge carriers was calculated according to **Equation 3.1.2**:

$$\mu^{e,h} = \frac{L g_m^{e,h}}{W C_g V_{DS}} \tag{3.1.2}$$

where L and W are the length and width of the graphene conducting channel, C_g is the gate capacitance given by $C_g=\varepsilon_r\varepsilon_0/d_{ox}$, with d_{ox} being the thickness of the gate dielectric and ε_r and ε_0 being the relative and vacuum electric permittivities, respectively [80]. The parameter $g_m^{e,h}$ is the transconductance given, for each type of charge carriers, by the slope of the corresponding linear part of the transfer curve.

Acknowledgements

This work was financially supported by FEDER funds through the COMPETE 2020 Programme and National Funds through FCT – Portuguese Foundation for Science and Technology under projects Ultragraf-M-ERA-NET2/0003/2016, UIDB/50025/2020, UIDP/50025/2020. Bohdan Kulyk thanks FCT for the PhD grant SFRH/BD/141525/2018. Alexandre Carvalho thanks FCT for the PhD grant DAEPHYSeFCT PD/BD/114063/2015. The authors gratefully acknowledge Professor Pedro Alpuim and International Iberian Nanotechnology Laboratory for FET device fabrication, as well as Eduardo Silva, PhD, for the optical profilometry characterization and Violeta Girão, PhD, for the AFM characterization.

3.1.5 References

[1] X. Li, W. Cai, J. An, S. Kim, J. Nah, D. Yang, R. Piner, A. Velamakanni, I. Jung, E. Tutuc, S.K. Banerjee, L. Colombo, R.S. Ruoff, "Large area synthesis of high quality and uniform graphene films on copper foils," *Science*, 324, 1312–1314, **2009**. https://doi.org/10.1126/science.1171245.

[2] S. Bae, H. Kim, Y. Lee, X. Xu, J.-S. Park, Y. Zheng, J. Balakrishnan, T. Lei, H. Ri Kim, Y. Il Song, Y.-J. Kim, K.S. Kim, B. Ozyilmaz, J.-H. Ahn, B.H. Hong, S. Iijima, B. Özyilmaz, J.-H. Ahn, B.H. Hong, S. Iijima, "Roll-to-roll production of 30-inch graphene films for transparent electrodes," *Nat Nano*, 5, 574–578, **2010**. https://doi.org/10.1038/nnano.2010.132.

[3] T. Kobayashi, M. Bando, N. Kimura, K. Shimizu, K. Kadono, N. Umezu, K. Miyahara, S. Hayazaki, S. Nagai, Y. Mizuguchi, Y. Murakami, D. Hobara, "Production of a 100-m-long high-quality graphene transparent conductive film by roll-to-roll chemical vapor deposition and transfer process," *Appl. Phys. Lett.*, 102, 23112, **2013**. https://doi.org/10.1063/1.4776707.

[4] B. Deng, Z. Liu, H. Peng, "Toward Mass Production of CVD Graphene Films," *Adv. Mater.*, 31, 1800996, **2019**. https://doi.org/10.1002/adma.201800996.

[5] A.F. Carvalho, T. Holz, N.F. Santos, M.C. Ferro, M.A. Martins, A.J.S. Fernandes, R.F. Silva, F.M. Costa, "Simultaneous CVD synthesis of graphene-diamond hybrid films," *Carbon*, 98, 99–105, **2016**. https://doi.org/10.1016/j.carbon.2015.10.095.

[6] N.F. Santos, U. Zubets, A.F. Carvalho, A.J.S. Fernandes, L. Pereira, F.M. Costa, "Tuning the field emission of graphene-diamond hybrids by pulsed methane flow CVD," *Carbon*, 122, 726–736, **2017**. https://doi.org/10.1016/j.carbon.2017.07.024.

[7] Y.I. Zhang, L. Zhang, C. Zhou, "Review of chemical vapor deposition of graphene and related applications," *Acc. Chem. Res.*, 46, 2329–2339, **2013**. https://doi.org/10.1021/ar300203n.

[8] R. Muñoz, C. Gómez-Aleixandre, "Review of CVD synthesis of graphene," *Chem. Vap. Depos.*, 19, 297–322, **2013**. https://doi.org/10.1002/cvde.201300051.

[9] M.R. Habib, T. Liang, X. Yu, X. Pi, Y. Liu, M. Xu, V. Georgakilas, J.N. Tiwari, K.C. Kemp, J.A. Perman, A.B. Bourlinos, K.S. Kim, R. Zboril, "A review of theoretical study of graphene chemical vapor deposition synthesis on metals: Nucleation, growth, and the role of hydrogen and oxygen," *Reports Prog. Phys.*, 81, 5464–5519, **2018**. https://doi.org/10.1088/1361-6633/aa9bbf.

[10] J. Pang, A. Bachmatiuk, I. Ibrahim, L. Fu, D. Placha, G.S. Martynkova, B. Trzebicka, T. Gemming, J. Eckert, M.H. Rümmeli, "CVD growth of 1D and 2D sp2 carbon nanomaterials," *J. Mater. Sci.*, 51, 640–667, **2016**. https://doi.org/10.1007/s10853-015-9440-z.

[11] Z. Luo, Y. Lu, D.W. Singer, M.E. Berck, L.A. Somers, B.R. Goldsmith, A.T.C. Johnson, "Effect of substrate roughness and feedstock concentration on growth of wafer-scale graphene at atmospheric pressure," *Chem. Mater.*, 23, 1441–1447, **2011**. https://doi.org/10.1021/cm1028854.

[12] S.M. Kim, A. Hsu, Y.-H. Lee, M. Dresselhaus, T. Palacios, K.K. Kim, J. Kong, "The effect of copper pre-cleaning on graphene synthesis," *Nanotechnology*, 24, 365602, **2013**. https://doi.org/10.1088/0957-4484/24/36/365602.

[13] X. Ge, Y. Zhang, Z. Chen, Y. Liang, S. Hu, Y. Sui, G. Yu, S. Peng, Z. Jin, X. Liu, "Effects of carbon-based impurities on graphene growth," *Phys. Chem. Chem. Phys.*, 20, 15419–15423, **2018**. https://doi.org/10.1039/C8CP00944A.

[14] G.H. Han, F. Güneş, J.J. Bae, E.S. Kim, S.J. Chae, H.-J. Shin, J.-Y. Choi, D. Pribat, Y.H. Lee, "Influence of Copper Morphology in Forming Nucleation Seeds for Graphene Growth," *Nano Lett.*, 11, 4144–4148, **2011**. https://doi.org/10.1021/nl201980p.

[15] O. V. Yazyev, S.G. Louie, "Electronic transport in polycrystalline graphene," *Nat. Mater.*, 9, 806–809, **2010**. https://doi.org/10.1038/nmat2830.

[16] D. Perera, J. Rohrer, "Structure sensitivity of electronic transport across graphene grain boundaries," *Phys. Rev. B*, 98, 155432, **2018**. https://doi.org/10.1103/PhysRevB.98.155432.

[17] M.H. Griep, E. Sandoz-Rosado, T.M. Tumlin, E. Wetzel, "Enhanced Graphene Mechanical Properties through Ultrasmooth Copper Growth Substrates," *Nano Lett.*, 16, 1657–1662, **2016**. https://doi.org/10.1021/acs.nanolett.5b04531.

[18] L. Meng, Q. Sun, J. Wang, F. Ding, "Molecular Dynamics Simulation of Chemical Vapor Deposition Graphene Growth on Ni (111) Surface," *J. Phys. Chem. C*, 116, 6097–6102, **2012**. https://doi.org/10.1021/jp212149c.

[19] S.-Y. Cho, M. Kim, M.-S. Kim, M.-H. Lee, K.-B. Kim, "Effect of Cu surface treatment in graphene growth by chemical vapor deposition," *Mater. Lett.*, 236, 403–407, **2019**. https://doi.org/10.1016/j.matlet.2018.10.134.

[20] X. Xu, Z. Zhang, J. Dong, D. Yi, J. Niu, M. Wu, L. Lin, R. Yin, M. Li, J. Zhou, S. Wang, J. Sun, X. Duan, P. Gao, Y. Jiang, X. Wu, H. Peng, R.S. Ruoff, Z. Liu, D. Yu, E. Wang, F. Ding, K. Liu, "Ultrafast epitaxial growth of metre-sized single-crystal graphene on industrial Cu foil," *Sci. Bull.*, 62, 1074–1080, **2017**. https://doi.org/https://doi.org/10.1016/j.scib.2017.07.005.

[21] V.L. Nguyen, B.G. Shin, D.L. Duong, S.T. Kim, D. Perello, Y.J. Lim, Q.H. Yuan, F. Ding, H.Y. Jeong, H.S. Shin, S.M. Lee, S.H. Chae, Q.A. Vu, S.H. Lee, Y.H. Lee, "Seamless Stitching of Graphene Domains on Polished Copper (111) Foil," *Adv. Mater.*, 27, 1376–1382, **2015**. https://doi.org/10.1002/adma.201404541.

[22] Y.A. Wu, Y. Fan, S. Speller, G.L. Creeth, J.T. Sadowski, K. He, A.W. Robertson, C.S. Allen, J.H. Warner, "Large Single Crystals of Graphene on Melted Copper Using Chemical Vapor

Deposition," *ACS Nano*, 6, 5010–5017, **2012**. https://doi.org/10.1021/nn3016629.

[23] X. Li, C.W. Magnuson, A. Venugopal, R.M. Tromp, J.B. Hannon, E.M. Vogel, L. Colombo, R.S. Ruoff, "Large-area graphene single crystals grown by low-pressure chemical vapor deposition of methane on copper," *J. Am. Chem. Soc.*, 133, 2816–2819, **2011**. https://doi.org/10.1021/ja109793s.

[24] V. Miseikis, D. Convertino, N. Mishra, M. Gemmi, T. Mashoff, S. Heun, N. Haghighian, F. Bisio, M. Canepa, V. Piazza, C. Coletti, "Rapid CVD growth of millimetre-sized single crystal graphene using a cold-wall reactor," *2D Mater.*, 2, 014006, **2015**. https://doi.org/10.1088/2053-1583/2/1/014006.

[25] H.D. Phan, J. Jung, Y. Kim, V.N. Huynh, C. Lee, "Large-area single-crystal graphene grown on a recrystallized Cu(111) surface by using a hole-pocket method," *Nanoscale*, 8, 13781–13789, **2016**. https://doi.org/10.1039/C6NR04416F.

[26] J. Pang, R.G. Mendes, P.S. Wrobel, M.D. Wlodarski, H.Q. Ta, L. Zhao, L. Giebeler, B. Trzebicka, T. Gemming, L. Fu, Z. Liu, J. Eckert, A. Bachmatiuk, M.H. Rümmeli, "Self-Terminating Confinement Approach for Large-Area Uniform Monolayer Graphene Directly over Si/SiOx by Chemical Vapor Deposition," *ACS Nano*, 11, 1946–1956, **2017**. https://doi.org/10.1021/acsnano.6b08069.

[27] M.H. Rümmeli, S. Gorantla, A. Bachmatiuk, J. Phieler, N. Geißler, I. Ibrahim, J. Pang, J. Eckert, "On the Role of Vapor Trapping for Chemical Vapor Deposition (CVD) Grown Graphene over Copper," *Chem. Mater.*, 25, 4861–4866, **2013**. https://doi.org/10.1021/cm401669k.

[28] I. Vlassiouk, M. Regmi, P. Fulvio, S. Dai, P. Datskos, G. Eres, S. Smirnov, "Role of Hydrogen in Chemical Vapor Deposition Growth of Large Single-Crystal Graphene," *ACS Nano*, 5, 6069–6076, **2011**. https://doi.org/10.1021/nn201978y.

[29] I. V. Vlassiouk, Y. Stehle, P.R. Pudasaini, R.R. Unocic, P.D. Rack, A.P. Baddorf, I.N. Ivanov, N. V. Lavrik, F. List, N. Gupta, K. V. Bets, B.I. Yakobson, S.N. Smirnov, "Evolutionary selection growth of two-dimensional materials on polycrystalline substrates," *Nat. Mater.*, 17, 318–322, **2018**. https://doi.org/10.1038/s41563-018-0019-3.

[30] Y. Hao, M.S. Bharathi, L. Wang, Y. Liu, H. Chen, S. Nie, X. Wang, H. Chou, C. Tan, B. Fallahazad, H. Ramanarayan, C.W. Magnuson, E. Tutuc, B.I. Yakobson, K.F. McCarty, Y.-W. Zhang, P. Kim, J. Hone, L. Colombo, R.S. Ruoff, "The Role of Surface Oxygen in the Growth of Large Single-Crystal Graphene on Copper," *Science*, 342, 720–723, **2013**. https://doi.org/10.1126/science.1243879.

[31] C.W. Magnuson, X. Kong, H. Ji, C. Tan, H. Li, R. Piner, C.A. Ventrice, R.S. Ruoff, "Copper oxide as a 'self-cleaning' substrate for graphene growth," *J. Mater. Res.*, 29, 403–409, **2014**. https://doi.org/DOI: 10.1557/jmr.2013.388.

[32] Z.R. Robinson, E.W. Ong, T.R. Mowll, P. Tyagi, D.K. Gaskill, H. Geisler, Ventrice Carl A., "Influence of Chemisorbed Oxygen on the Growth of Graphene on Cu(100) by Chemical Vapor Deposition," *J. Phys. Chem. C*, 117, 23919–23927, **2013**. https://doi.org/10.1021/jp410142r.

[33] B. Huet, J. Raskin, "Role of the Cu substrate in the growth of ultra-flat crack-free highly-crystalline single-layer graphene," *Nanoscale*, 10, 21898–21909, **2018**.

https://doi.org/10.1039/c8nr06817h.

[34] J. Pang, A. Bachmatiuk, L. Fu, C. Yan, M. Zeng, J. Wang, B. Trzebicka, T. Gemming, J. Eckert, M.H. Rummeli, "Oxidation as a Means to Remove Surface Contaminants on Cu Foil Prior to Graphene Growth by Chemical Vapor Deposition," *J. Phys. Chem. C*, 119, 13363–13368, **2015**. https://doi.org/10.1021/acs.jpcc.5b03911.

[35] G. Eres, M. Regmi, C.M. Rouleau, J. Chen, I.N. Ivanov, A.A. Puretzky, D.B. Geohegan, "Cooperative Island Growth of Large-Area Single-Crystal Graphene on Copper Using Chemical Vapor Deposition," *ACS Nano*, 8, 5657–5669, **2014**. https://doi.org/10.1021/nn500209d.

[36] X. Chen, P. Zhao, R. Xiang, S. Kim, J. Cha, S. Chiashi, S. Maruyama, "Chemical vapor deposition growth of 5 mm hexagonal single-crystal graphene from ethanol," *Carbon*, 94, 810–815, **2015**. https://doi.org/10.1016/j.carbon.2015.07.045.

[37] M.-C. Chuang, W.-Y. Woon, "Nucleation and growth dynamics of graphene on oxygen exposed copper substrate," *Carbon*, 103, 384–390, **2016**. https://doi.org/10.1016/j.carbon.2016.03.049.

[38] J. Pang, A. Bachmatiuk, L. Fu, R.G. Mendes, M. Libera, D. Placha, G.S. Martynková, B. Trzebicka, T. Gemming, J. Eckert, M.H. Rümmeli, "Direct synthesis of graphene from adsorbed organic solvent molecules over copper," *RSC Adv.*, 5, 60884–60891, **2015**. https://doi.org/10.1039/c5ra09405d.

[39] I. Vlassiouk, P. Fulvio, H. Meyer, N. Lavrik, S. Dai, P. Datskos, S. Smirnov, "Large scale atmospheric pressure chemical vapor deposition of graphene," *Carbon*, 54, 58–67, **2013**. https://doi.org/10.1016/j.carbon.2012.11.003.

[40] A.T. Murdock, C.D. van Engers, J. Britton, V. Babenko, S.S. Meysami, H. Bishop, A. Crossley, A.A. Koos, N. Grobert, "Targeted removal of copper foil surface impurities for improved synthesis of CVD graphene," *Carbon*, 122, 207–216, **2017**. https://doi.org/10.1016/j.carbon.2017.06.075.

[41] M.H. Khaksaran, I.I. Kaya, "Spontaneous Nucleation and Growth of Graphene Flakes on Copper Foil in the Absence of External Carbon Precursor in Chemical Vapor Deposition," *ACS Omega*, 3, 12575–12583, **2018**. https://doi.org/10.1021/acsomega.8b01652.

[42] J. Kraus, M. Böbel, S. Günther, "Suppressing graphene nucleation during CVD on polycrystalline Cu by controlling the carbon content of the support foils," *Carbon*, 96, 153–165, **2016**. https://doi.org/10.1016/J.CARBON.2015.09.048.

[43] P. Braeuninger-Weimer, B. Brennan, A.J. Pollard, S. Hofmann, "Understanding and Controlling Cu-Catalyzed Graphene Nucleation: The Role of Impurities, Roughness, and Oxygen Scavenging," *Chem. Mater.*, 28, 8905–8915, **2016**. https://doi.org/10.1021/acs.chemmater.6b03241.

[44] B. Huet, J.P. Raskin, "Role of Cu foil in-situ annealing in controlling the size and thickness of CVD graphene domains," *Carbon*, 129, 270–280, **2018**. https://doi.org/10.1016/j.carbon.2017.12.043.

[45] Y. Hao, M.S. Bharathi, L. Wang, Y. Liu, H. Chen, S. Nie, X. Wang, H. Chou, C. Tan, B. Fallahazad, H. Ramanarayan, C.W. Magnuson, E. Tutuc, B.I. Yakobson, K.F. McCarty, Y.-

W. Zhang, P. Kim, J. Hone, L. Colombo, R.S. Ruoff, "The Role of Surface Oxygen in the Growth of Large Single-Crystal Graphene on Copper," *Science*, 342, 720–723, **2013**. https://doi.org/10.1126/science.1243879.

[46] H. Wang, X. Xu, J. Li, L. Lin, L. Sun, X. Sun, S. Zhao, C. Tan, C. Chen, W. Dang, H. Ren, J. Zhang, B. Deng, A.L. Koh, L. Liao, N. Kang, Y. Chen, H. Xu, F. Ding, K. Liu, H. Peng, Z. Liu, "Surface Monocrystallization of Copper Foil for Fast Growth of Large Single-Crystal Graphene under Free Molecular Flow," *Adv. Mater.*, 28, 8968–8974, **2016**. https://doi.org/10.1002/adma.201603579.

[47] N. Reckinger, X. Tang, F. Joucken, L. Lajaunie, R. Arenal, E. Dubois, B. Hackens, L. Henrard, J.-F. Colomer, "Oxidation-assisted graphene heteroepitaxy on copper foil," *Nanoscale*, 8, 18751–18759, **2016**. https://doi.org/10.1039/C6NR02936A.

[48] Y.-P. Hsieh, Y.-H. Chu, H.-G. Tsai, M. Hofmann, "Reducing the graphene grain density in three steps," *Nanotechnology*, 27, 105602, **2016**. https://doi.org/10.1088/0957-4484/27/10/105602.

[49] D. Ding, P. Solís-Fernández, R.M. Yunus, H. Hibino, H. Ago, "Behavior and role of superficial oxygen in Cu for the growth of large single-crystalline graphene," *Appl. Surf. Sci.*, 408, 142–149, **2017**. https://doi.org/https://doi.org/10.1016/j.apsusc.2017.02.250.

[50] Y.C. Shin, J. Kong, "Hydrogen-excluded graphene synthesis via atmospheric pressure chemical vapor deposition," *Carbon*, 59, 439–447, **2013**. https://doi.org/10.1016/j.carbon.2013.03.037.

[51] L. Gan, Z. Luo, "Turning off hydrogen to realize seeded growth of subcentimeter single-crystal graphene grains on copper," *ACS Nano*, 7, 9480–9488, **2013**. https://doi.org/10.1021/nn404393b.

[52] A.C. Ferrari, D.M. Basko, "Raman spectroscopy as a versatile tool for studying the properties of graphene," *Nat. Publ. Gr.*, 8, 235–246, **2013**. https://doi.org/10.1038/nnano.2013.46.

[53] B.M. Srinivasan, Y. Hao, R. Hariharaputran, S. Rywkin, J.C. Hone, L. Colombo, R.S. Ruoff, Y.W. Zhang, "Oxygen-Promoted Chemical Vapor Deposition of Graphene on Copper: A Combined Modeling and Experimental Study," *ACS Nano*, 12, 9372–9380, **2018**. https://doi.org/10.1021/acsnano.8b04460.

[54] Y. Zhang, T. Gao, Y. Gao, S. Xie, Q. Ji, K. Yan, H. Peng, Z. Liu, "Defect-like structures of graphene on copper foils for strain relief investigated by high-resolution scanning tunneling microscopy," *ACS Nano*, 5, 4014–4022, **2011**. https://doi.org/10.1021/nn200573v.

[55] S. Al-Kamiyani, T. Mohiuddin, "Improved control in elimination of white impurities on graphene by chemical vapor deposition (CVD)," *AIP Adv.*, 8, 125325, **2018**. https://doi.org/10.1063/1.5051693.

[56] X. Li, W. Cai, L. Colombo, R.S. Ruoff, "Evolution of graphene growth on Ni and Cu by carbon isotope labeling," *Nano Lett.*, 9, 4268–4272, **2009**. https://doi.org/10.1021/nl902515k.

[57] C. Neumann, S. Reichardt, P. Venezuela, M. Drögeler, L. Banszerus, M. Schmitz, K. Watanabe, T. Taniguchi, F. Mauri, B. Beschoten, S. V. Rotkin, C. Stampfer, "Raman spectroscopy as probe of nanometre-scale strain variations in graphene," *Nat. Commun.*, 6, 1–7, **2015**. https://doi.org/10.1038/ncomms9429.

[58] P. Klar, C. Casiraghi, "Raman spectroscopy of graphene in different dielectric solvents," *Phys. Status Solidi Curr. Top. Solid State Phys.*, 7, 2735–2738, **2010**. https://doi.org/10.1002/pssc.200983817.

[59] C. Casiraghi, S. Pisana, K.S. Novoselov, A.K. Geim, A.C. Ferrari, "Raman fingerprint of charged impurities in graphene," *Appl. Phys. Lett.*, 91, 1–4, **2007**. https://doi.org/10.1063/1.2818692.

[60] S. Berciaud, S. Ryu, L.E. Brus, T.F. Heinz, "Probing the lntrinsic properties of exfoliated graphene: Raman spectroscopy of free-standing monolayers," *Nano Lett.*, 9, 346–352, **2009**. https://doi.org/10.1021/nl8031444.

[61] N.S. Mueller, S. Heeg, M.P. Alvarez, P. Kusch, S. Wasserroth, N. Clark, F. Schedin, J. Parthenios, K. Papagelis, C. Galiotis, M. Kalbáč, A. Vijayaraghavan, U. Huebner, R. Gorbachev, O. Frank, S. Reich, "Evaluating arbitrary strain configurations and doping in graphene with Raman spectroscopy," *2D Mater.*, 5, **2018**. https://doi.org/10.1088/2053-1583/aa90b3.

[62] T.M.G. Mohiuddin, A. Lombardo, R.R. Nair, A. Bonetti, G. Savini, R. Jalil, N. Bonini, D.M. Basko, C. Galiotis, N. Marzari, K.S. Novoselov, A.K. Geim, A.C. Ferrari, "Uniaxial strain in graphene by Raman spectroscopy: G peak splitting, Grüneisen parameters, and sample orientation," *Phys. Rev. B - Condens. Matter Mater. Phys.*, 79, 1–8, **2009**. https://doi.org/10.1103/PhysRevB.79.205433.

[63] X. Yin, Y. Li, F. Ke, C. Lin, H. Zhao, L. Gan, Z. Luo, R. Zhao, T.F. Heinz, Z. Hu, "Evolution of the Raman spectrum of graphene grown on copper upon oxidation of the substrate," *Nano Res.*, 7, 1613–1622, **2014**. https://doi.org/10.1007/s12274-014-0521-0.

[64] U. Lee, Y. Han, S. Lee, J.S. Kim, Y.H. Lee, U.J. Kim, H. Son, "Time Evolution Studies on Strain and Doping of Graphene Grown on a Copper Substrate Using Raman Spectroscopy," *ACS Nano*, **2020**. https://doi.org/10.1021/acsnano.9b08205.

[65] M. Kalbac, H. Farhat, J. Kong, P. Janda, L. Kavan, M.S. Dresselhaus, "Raman spectroscopy and in situ raman spectroelectrochemistry of bilayer 12C/13C graphene," *Nano Lett.*, 11, 1957–1963, **2011**. https://doi.org/10.1021/nl2001956.

[66] O. Frank, L. Kavan, M. Kalbac, "Carbon isotope labelling in graphene research," *Nanoscale*, 6, 6363–6370, **2014**. https://doi.org/10.1039/c4nr01257g.

[67] B. Huet, J.P. Raskin, D.W. Snyder, J.M. Redwing, "Fundamental limitations in transferred CVD graphene caused by Cu catalyst surface morphology," *Carbon*, 163, 95–104, **2020**. https://doi.org/10.1016/j.carbon.2020.02.074.

[68] Y. Zhang, Z. Li, P. Kim, L. Zhang, C. Zhou, "Anisotropic Hydrogen Etching of Chemical Vapor Deposited Graphene," *ACS Nano*, 6, 126–132, **2012**. https://doi.org/10.1021/nn202996r.

[69] H. Kim, C. Mattevi, M.R. Calvo, J.C. Oberg, L. Artiglia, S. Agnoli, C.F. Hirjibehedin, M.

Chhowalla, E. Saiz, "Activation energy paths for graphene nucleation and growth on Cu," *ACS Nano*, 6, 3614–3623, **2012**. https://doi.org/10.1021/nn3008965.

[70] W. Zhang, P. Wu, Z. Li, J. Yang, "First-Principles Thermodynamics of Graphene Growth on Cu Surfaces," *J. Phys. Chem. C*, 115, 17782–17787, **2011**. https://doi.org/10.1021/jp2006827.

[71] L. Colombo, X. Li, B. Han, C. Magnuson, W. Cai, Y. Zhu, R.S. Ruoff, Growth Kinetics and Defects of CVD Graphene on Cu, in: **2010**: pp. 109–114. https://doi.org/10.1149/1.3367942.

[72] Z.-J. Wang, G. Weinberg, Q. Zhang, T. Lunkenbein, A. Klein-Hoffmann, M. Kurnatowska, M. Plodinec, Q. Li, L. Chi, R. Schloegl, M. Willinger, W.E.T. Al, "Direct Observation of Graphene Growth and Associated Copper Substrate Dynamics by in Situ Scanning Electron Microscopy," *ACS Nano*, 9, 1506–1519, **2015**.

[73] T. Ma, W. Ren, Z. Liu, L. Huang, L.-P. Ma, X. Ma, Z. Zhang, L. Peng, H. Cheng, "Repeated Growth–Etching–Regrowth for Large-Area Defect-Free Single-Crystal Graphene by Chemical Vapor Deposition," *ACS Nano*, 8, 12806–12813, **2014**. https://doi.org/10.1021/nn506041t.

[74] C.J. Shearer, A.D. Slattery, A.J. Stapleton, J.G. Shapter, C.T. Gibson, "Accurate thickness measurement of graphene," *Nanotechnology*, 27, 125704, **2016**. https://doi.org/10.1088/0957-4484/27/12/125704.

[75] W. Jung, J. Park, T. Yoon, T.-S. Kim, S. Kim, C.-S. Han, "Prevention of Water Permeation by Strong Adhesion Between Graphene and SiO 2 Substrate," *Small*, 10, 1704–1711, **2014**. https://doi.org/10.1002/smll.201302729.

[76] C. Stampfer, F. Haupt, T. Taniguchi, M. Schmitz, L. Banszerus, K. Watanabe, M. Oellers, J. Dauber, S. Engels, B. Beschoten, "Ultrahigh-mobility graphene devices from chemical vapor deposition on reusable copper," *Sci. Adv.*, 1, e1500222, **2015**. https://doi.org/10.1126/sciadv.1500222.

[77] B. Chen, H. Huang, X. Ma, L. Huang, Z. Zhang, L.-M. Peng, "How good can CVD-grown monolayer graphene be?," *Nanoscale*, 6, 15255–15261, **2014**. https://doi.org/10.1039/C4NR05664G.

[78] G. Borin Barin, Y. Song, I. de Fátima Gimenez, A.G. Souza Filho, L.S. Barreto, J. Kong, "Optimized graphene transfer: Influence of polymethylmethacrylate (PMMA) layer concentration and baking time on graphene final performance," *Carbon*, 84, 82–90, **2015**. https://doi.org/10.1016/j.carbon.2014.11.040.

[79] I. Horcas, R. Fernández, J.M. Gómez-Rodríguez, J. Colchero, J. Gómez-Herrero, A.M. Baro, "WSXM: A software for scanning probe microscopy and a tool for nanotechnology," *Rev. Sci. Instrum.*, 78, 013705, **2007**. https://doi.org/10.1063/1.2432410.

[80] F. Schwierz, "Graphene transistors," *Nat. Nanotechnol.*, 5, 487–496, **2010**. https://doi.org/10.1038/nnano.2010.89.

3.2 Graphene electrodes for flexible cellulose-supported OLEDs

Bohdan Kulyk[1,2], José C. Germino[1], Diana Gaspar[2,3], António J.S. Fernandes[1], Jonas Deuermeier[2], Alexandre F. Carvalho[1], António F. da Cunha[1], Luís M.N. Pereira[2,3], Luiz Pereira[1], Florinda M. Costa[1]

1 – i3N, Department of Physics, University of Aveiro, Campus Universitário de Santiago, 3810-193 Aveiro, Portugal.

2 – i3N/CENIMAT, Department of Materials Science and CEMOP/UNINOVA, NOVA School of Science and Technology, NOVA University Lisbon, Campus de Caparica, 2829-516 Caparica, Portugal.

3 – AlmaScience, Campus da Caparica, 2829-516 Caparica, Portugal.

Abstract:

Graphene shows great potential as a transparent conducting material (TCM) for organic light emitting diodes (OLEDs), particularly in what concerns flexible devices. In this context, a lot of attention has been dedicated to the optimization of the graphene electrodes, to improve their electrical conductivity while maintaining high optical transparency. Moreover, for the development of flexible and sustainable devices, the choice of an appropriate substrate is a critical task. Here, we describe, for the first time, the development of OLEDs employing chemical vapour deposition (CVD) graphene anodes on cellulose nanocrystal (CNC) membranes and cellulose rolling papers. These transparent biodegradable materials provide a more environmentally conscious alternative to the conventional synthetic polymers commonly used as flexible OLED substrates. By stacking multiple graphene layers on these cellulose-based substrates, followed by the evaporation of MoO_3, we improve the electrical conductivity of graphene, allowing us to fabricate third generation solution processed OLEDs, with external quantum efficiencies (EQE) of up to 0.34% and maximum brightness reaching ~400 cd m^{-2}. This proof-of-concept demonstration paves the way for novel environmentally friendly flexible OLEDs, realizing the synergic potential of both graphene and cellulose-based materials.

3.2.1 Introduction

One of the opportunities offered by Organic Light Emitting Diodes (OLEDs) concerns flexible displays, highlighted, for example, by the recent emergence of foldable and bendable smartphones [1,2]. This requires two particularly important elements: a flexible substrate and compatible electrodes. Concerning the substrate, synthetic polymers such as polyethylene terephthalate (PET) are the most commonly used ones, but their non-biodegradable nature goes against the ongoing efforts to lessen the environmental impact of the e-waste produced by the disposal of consumer electronics [3].

Cellulose substrates are a possible sustainable alternative, since it is an abundant natural biopolymer, cellulose is at the basis of paper, a cheap, versatile material which continues to find new applications, ranging from transistors [4,5] to physical [6–8] and biochemical [9,10] sensors. Importantly, paper and many other cellulose-based materials are biodegradable, avoiding the environmental issues typically associated with the final stages of a product's lifecycle. Despite these attractive qualities, only a handful of reports on OLEDs supported exclusively by cellulose exist, none of which use graphene electrodes [11–13].

The other element of great importance for flexible OLEDs is the transparent conductive material (TCM) which allows the light to extracted from the device [14]. Any such material must combine good electrical conductivity with high optical transparency, with the added requirement of being able to withstand deformations such as bending without losing its performance. The most commonly used TCM, indium-doped tin oxide (ITO), tends to come short of this requirement due to its brittleness [15]. Moreover, ITO is facing growing problems regarding its high cost and dwindling natural reserves [15]. One of the most promising candidates to assume ITO's role as the preferred TCM in OLEDs and other devices is graphene [16,17]. Presenting a unique combination of excellent electronic properties, high optical transparency across the entire visible range and remarkable mechanical characteristics, the use of graphene as a TCM enables to tackle known issues in this field, while simultaneously opening the door to entirely new concepts. In addition, despite the electrical conductivity of single-layer graphene tending to be considerably higher than that of ITO, there are many examples in the literature of high-performing OLEDs with graphene electrodes where a number of different strategies, such as charge transfer doping and multiple layer stacking, have been employed to overcome graphene's shortcomings [18–24].

In this work we present a proof-of-concept demonstration of flexible OLEDs employing a graphene anode on two different cellulose-based substrates: transparent regenerated cellulose rolling paper and nanocrystalline cellulose (CNC) membranes. We focus on the development of the graphene anode, describing its synthesis by chemical vapour deposition (CVD) and transfer to achieve multiple stacked graphene layers. We also cover the doping of this transparent anode. Finally, we showcase OLEDs both on quartz and cellulose-based substrates, highlighting the challenges in the transition to the latter, along with the techniques employed to overcome these challenges.

3.2.2 Results and Discussion

3.2.2.1 CVD graphene transparent electrodes

Before considering any application of CVD graphene it is important to achieve good control over its synthesis. Here, characteristics such as number of layers, nucleation density and uniformity are the most important ones, as they have a direct influence on graphene's properties.

In a previous work we demonstrated that the nucleation density and the presence of secondary layers (adlayers) depend, among other variables, on the carbon impurities present in the copper substrate [25]. To overcome this, an in-situ oxidation/reduction treatment of the substrate was performed prior to the regular CVD process, by allowing air inside the reaction chamber at high temperature, followed by a reduction in H_2 atmosphere. This, aided by other tweaks to the growth recipe (**Figure 3.2.1a**), resulted in the formation of millimetre-sized, sparsely distributed hexagonal graphene domains with improved charge carrier mobility. For this work, this growth recipe was adapted in order to achieve complete coverage of the substrate by promoting the coalescence of the individual graphene domains, at the expense of a slightly higher nucleation density (and, consequently, higher density of grain boundaries). The Raman spectra (with a representative one, this time on a fused silica substrate, in **Figure 3.2.1b**) reveal additional information about the obtained material. The sharp and narrow G and 2D peaks, with a high intensity ratio of $I_{2D}/I_G \approx 2$, are typical of single-layer graphene (SLG). Moreover, the absence of the D peak (typically at 1370 cm^{-1} for 442 nm excitation wavelength) is indicative of the absence of defects in its crystalline structure. As for the microscopic morphology of this material, secondary electron scanning electron microscopy (SE-SEM) images (**Figure 3.2.1c)** reveal a mostly uniform film with some wrinkles, which are typical in CVD grown graphene [26]. Some small white features can also be observed, attributed to silicates, which are known to occur during CVD of graphene due to the silica contamination from the quartz walls of CVD reactors [27,28]. Occasionally, some secondary layers can also be seen across the samples, due to their darker contrast relative to the underlying film. These usually assume either a flower-like shape (**Figure 3.2.1d**), referencing the six-fold symmetry of the graphene domains, or a more dendritic form, with further adlayers in the middle (**Figure 3.2.1e**). Importantly, these secondary layers are sporadic, as can be seen at low magnifications (**Figure S3.2.1**, **Section 3.2.6**).

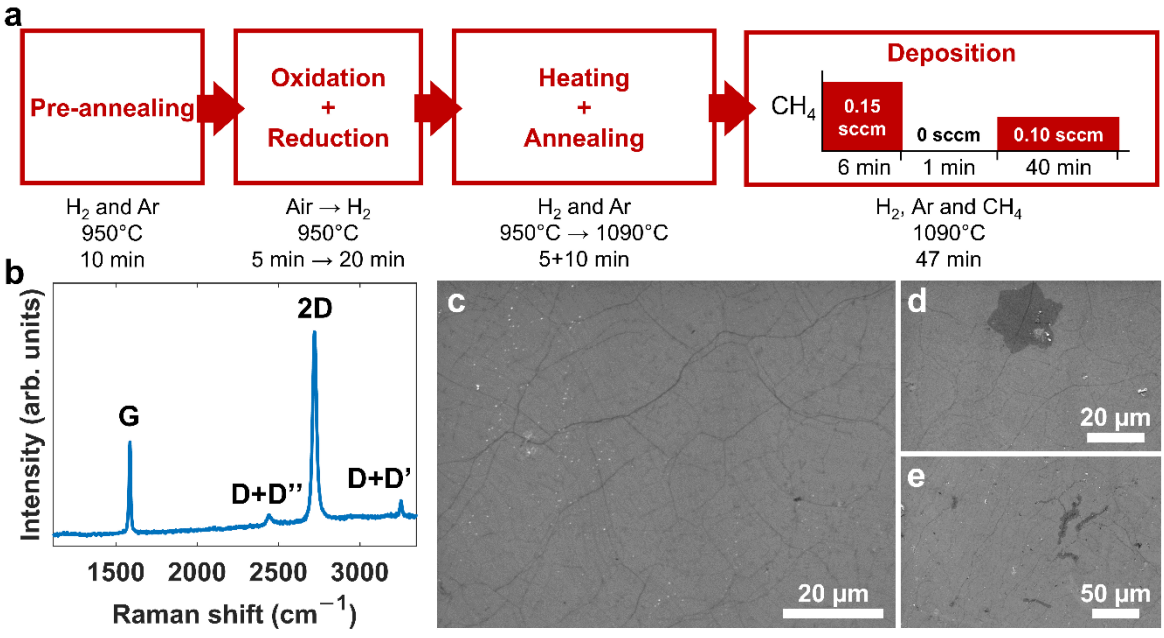

Figure 3.2.1. (a) Schematic representation of the CVD process to synthesize single-layer graphene (SLG) films. **(b)** Representative Raman spectrum of the obtained SLG film. **(c)** SE-SEM image of the SLG film. **(d)** and **(e)** SE-SEM images of the secondary layers occasionally seen on the SLG films.

A good transparent conductive material should combine low electrical resistance with high optical transparency. In the case of one of the most used TCMs, ITO, the sheet resistance is typically ~10 Ω sq^{-1}, while its transmittance at 550 nm (the typically employed reference wavelength, roughly corresponding to the region of highest sensitivity of the human eye to visible light) is around 90% [17]. Single-layer CVD graphene typically presents a much larger sheet resistance (500-1000 Ω sq^{-1}), but benefits from higher optical transparency, showing a mostly flat absorption of ~2.3% in the visible part of the spectrum [29]. As such, a commonly employed strategy to produce CVD graphene-based transparent electrodes capable of competing with ITO is to stack, by successive transfers, multiple graphene layers (usually 3 or 4) on top of each other. Additionally, in many cases the graphene must be doped, typically by charge transfer approaches [18,30–35]. This is done not only to further reduce the sheet resistance of this TCM, but also, in the case of OLED applications, to change the work function of graphene and thus ensure better charge injection into the device, through a more favourable energy level alignment.

Here, we performed the stacking of three graphene layers by two different strategies, followed by thermal evaporation of MoO_3, which is known to induce p-type doping in graphene [36,37]. In the first transfer approach (the "layering" transfer), each graphene layer is transferred onto the target substrate in succession, after the PMMA support layer from the previous transfer is removed (**Figure 3.2.2a**). The second approach (the "stack" transfer) consists in transferring the graphene layers onto a copper substrate where another graphene film was grown and then, once a three-layer stack is complete, transferring it to the target substrate (**Figure 3.2.2b**). This strategy has the advantage of requiring only one PMMA support layer throughout the entire process, reducing the transfer time and avoiding the trapping of PMMA residues between the graphene layers.

The effect of each additional layer, transferred by the "layering" approach, on the optical transmittance of the resulting graphene TCM is shown in **Figure 3.2.2c** (blue lines). As can be seen, the overall transparency decreases with each additional layer (**Figure 3.2.2d**). Additionally, a transmittance spectrum corresponding to a three-layer sample obtained by the "stack" transfer is presented (yellow line in **Figure 3.2.2c**), and, interestingly, its transparency is slightly lower than for the three-layer sample obtained by the "layering" approach. This can be explained by a higher density of holes and tears in the "layering" films, as in this case we expect more impurities to be trapped between the layers, compromising the structural integrity of the films. Finally, after the evaporation of 15 nm of MoO_3 on top of a three-layer sample obtained by the "stack" transfer approach, there is a very small decrease in the transmittance (dashed yellow line in **Figure 3.2.2c**). Importantly, its value is 92.7% at 550 nm, which is above the typical requirement of 90% for TCMs, and no new features can be seen in the spectrum (**Figure 3.2.2d**).

Figure 3.2.2e shows the evolution of the sheet resistance of various equivalent samples for different numbers of layers (both transfer approaches are included), as well as after the evaporation of a 15 nm thick layer of MoO_3 on top of the three-layer graphene "stack" films. While there is a fairly large spread of sheet resistance (R_S) values, a clear trend can be seen as the average R_S decreases from 713 to 375 Ω sq^{-1}. Furthermore, the doping effect of the evaporated MoO_3 layer can be confirmed, as R_S decreases from 375 to 288 Ω sq^{-1} after the evaporation. This agrees well with previous reports of MoO_3 evaporation on top of graphene, as due to the large difference between the work functions of these two materials, the Fermi level alignment occurs by charge transfer, which dopes the graphene [37].

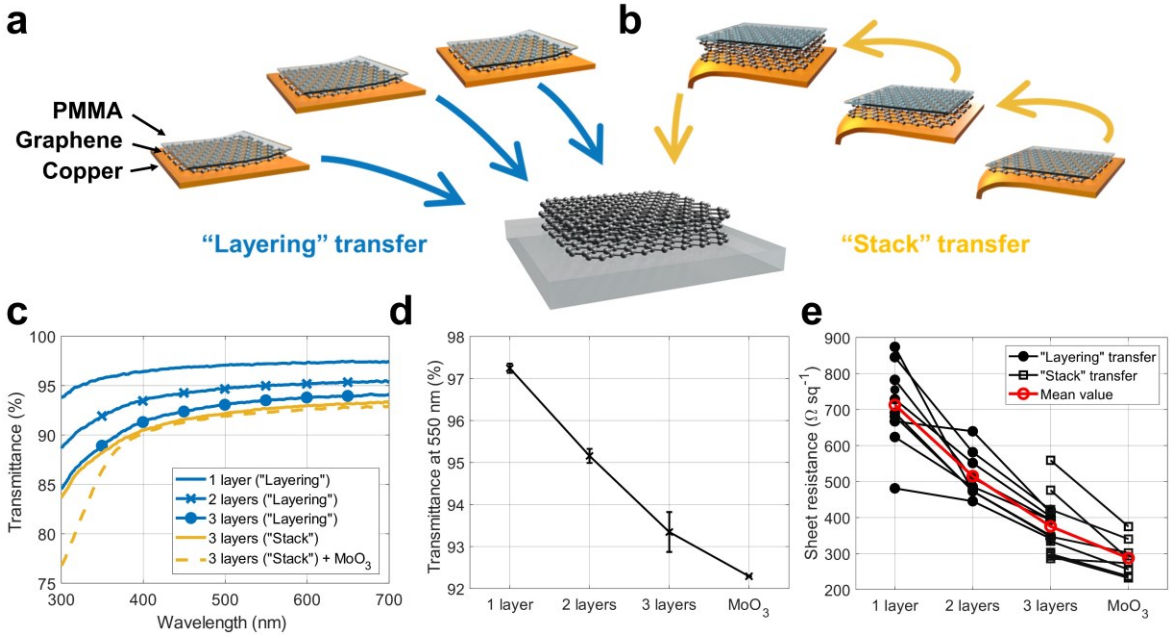

Figure 3.2.2. (a) Schematic representation of the "layering" transfer approach, where each graphene layer is transferred onto the target substrate, and **(b)** the "stack" transfer, where each additional layer of graphene is "picked up" from its catalytic Cu substrate by the previous layers and then, once complete, the entire multilayer stack is transferred to the target substrate. **(c)** Optical transmittance spectra of single, double and three-layer graphene (by both transfer approaches), and of three-layer graphene after evaporation of 15 nm of MoO_3. **(d)** The evolution of the optical transmittance at 550 nm with each additional graphene layer and after MoO_3 evaporation (15 nm). The error bars represent the standard deviation for several equivalent samples. **(e)** Sheet resistance of samples with different number of graphene layers, as well as after evaporation of 15 nm of MoO_3.

3.2.2.2 Thermally activated delayed fluorescence OLEDs on quartz

Next, we employed the graphene films obtained by "stack" transfer, as this approach is faster and results in fewer PMMA residues, and MoO_3 doping as anodes in thermally activated delayed fluorescence (TADF) OLEDs on quartz substrates. The effect of varying thickness of MoO_3 (10, 15, 20 and 30 nm) on the performance of the devices was evaluated. The chosen emitter was the yellow-orange TADF 2-[4 (diphenylamino)phenyl]-10,10-dioxide-9H-thioxanthen-9-one (TXO-TPA) in a solution-processable host mixture of poly(N-vinylcarbazole) and 1,3-bis(N-carbazolyl)benzene (PVK:mCP). This enables a device structure with reduced complexity (**Figure 3.2.3a**) as the chosen host can efficiently transfer the electrical charge to the emitter (guest), while also allowing (due to the mixed effect of both PVK and mCP) a better balance of electron and hole mobilities. The emissive layer (EML) was spin coated on top of the thermally evaporated MoO_3, followed by further evaporation of 40 nm of 2,2',2''-(1,3,5-Benzinetriyl)-tris(1-phenyl-1-H-benzimidazole) (TPBi) electron transport layer (ETL), with an electron mobility in the range of $3.3–8\times10^{-5}$ cm^2 V^{-1} s^{-1} [38]. The device was completed by an anode consisting of thermally evaporated LiF (1 nm) and Al (100 nm). The entire structure of the OLED can be summarized as quartz/graphene (3 layers)/MoO_3 (different thicknesses)/PVK:mCP:TXO-TPA (~50 nm)/TPBi (40 nm)/LiF (1 nm)/Al (100 nm). As such, the OLEDs have only two organic layers.

Figure 3.2.3b shows the current density and luminescence of the OLEDs as a function of voltage (a photograph of one of these devices can be seen in **Figure S3.2.2**, **Section 3.2.6**). As can be seen**,** all the devices show a turn-on voltage of 3 V, except for the one with 10 nm of MoO_3

(3.5 V). This indicates that the increase in the thickness of MoO_3 does not significantly increase the energy barrier for the injection of holes, meaning that the energy band alignment (and, consequently, the graphene doping) does not change with the thickness of MoO_3 (withing the range explored here). Moreover, this turn-on voltage is slightly lower than the ones reported previously for devices employing ITO/PEDOT:PSS anodes [39]. As the work function of MoO_3 is usually larger compared to PEDOT:PSS [40], the energy barrier for hole injection into HOMO level of the host:guest matrix, is slightly lower in our devices, justifying the lower turn-on voltage. As for the brightness, the device with 15 nm of MoO_3 achieves the highest value (900 cd m^{-2}), which is fairly stable over a wide range of voltages. The current density, however, increases steadily, ultimately resulting in an external quantum efficiency (EQE) that drops progressively (as a function of brightness) from the maximum value of 1.22% at 4 V (**Figure 3.2.3c**). This data is not surprising in OLEDs employing TXO-TPA emitter and can be related to some possible TTA (triplet-triplet annihilation), as previously indicated [39]. Larger thicknesses of MoO_3 achieve higher EQE of around 3%, but their brightness curves show oscillations. This might be caused by the morphology of the oxide layer, with an increase in the density of defects for larger thicknesses. In order to understand the impact of MoO_3 thickness on the charge carrier transport in quartz-supported OLEDs, we can make an analysis under the space-charge-limited current (SCLC) model in the J-V data (**Figure 3.2.3d**), according to the Child's law [41]:

$$J_{\mathrm{SCLC}} = \frac{9}{8}\varepsilon_r \varepsilon_0 \mu_{\mathrm{SCLC}} \frac{V^2}{L^3} \tag{3.2.1}$$

where J_{SCLC} is the current density at the space-charge domain, ε_r the relative dielectric constant of the emissive layer, ε_0 the free-space permittivity, μ_{SCLC} the electrical mobility under SCLC conditions, L the organic layer thickness (~90 nm) and V the applied voltage. The SCLC physical model can be applied after the devices undergo the trap-filling process ($J \propto V^n$ with n>2), where electronic energy levels acting as traps for electrical charges become completely filled. It is well known that the Child's law can be applied to obtain the charge-carrier mobility when only one type of charge-carrier drifts along the device (electron- or hole-only device) [42]. However, an estimate of the global electrical mobility could be achieved by applying this law in an OLED, despite its bipolar electrical nature [43]. In this sense, electrical mobility is ruled by the minority charge-carriers in the device bulk, that, in our case, will be the electrons, following the known data about the different organic materials employed in the device [44]. The electrical mobility for each OLED decreases with increasing MoO_3 thickness, following the sequence: $\mu_{(10\ \mathrm{nm})}=3.76\times10^{-6} > \mu_{(15\ \mathrm{nm})}=3.44\times10^{-6} > \mu_{(20\ \mathrm{nm})}=2.64\times10^{-6} > \mu_{(30\ \mathrm{nm})}=2.41\times10^{-6}$ $cm^2\ V^{-1}\ s^{-1}$. Looking at these electrical mobility values and correlating with the performance of the OLEDs (**Figure 3.2.3**), we chose the MoO_3 thickness of 15 nm for the flexible cellulose-supported OLEDs that are discussed further below.

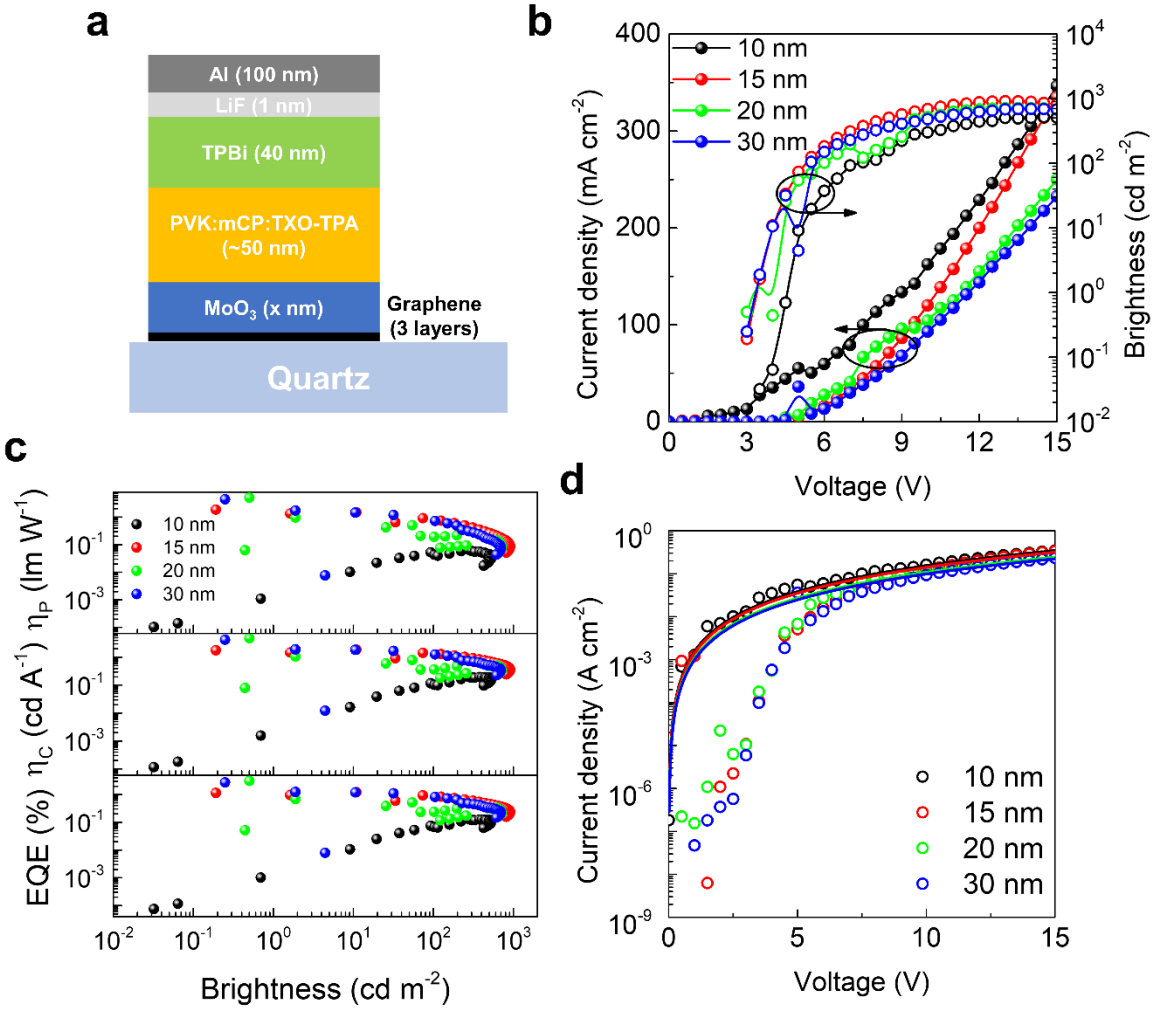

Figure 3.2.3. (a) Schematic representation of the OLED structure on quartz substrates. Different thicknesses of MoO_3 were explored (x=10, 15, 20 and 30 nm). **(b)** Current density and brightness of the OLEDs with different thicknesses of MoO_3, as a function of applied voltage. **(c)** Current (η_C), power (η_P) and external quantum efficiencies of OLEDs with different thicknesses of MoO_3, as a function of brightness. **(d)** Current density versus voltage of OLEDs with different thicknesses of MoO_3, fitted to the space charge current limit (SCLC) model.

3.2.2.3 Cellulose-based substrates for OLEDs

For the flexible OLEDs we explored two cellulose-based substrates: cellulose nanocrystal (CNC) membranes and commercial transparent cigarette rolling papers. Besides being naturally derived and biodegradable, both substrates possess additional advantages that make them well suited as supporting materials for environmentally friendly OLEDs. The CNC membranes, thanks to the nanometric size and packing of the cellulose crystals, allow to obtain very low surface roughness (nanometre range), while conventional paper presents values in the micrometre range [45]. Moreover, under the proper drying conditions, CNC substrates are able to self-organize in chiral structures that may present very interesting optical properties, such as structural colour, a photonic bandgap, and, due to intrinsic left-handedness of such structures, the capability of interacting selectively with left and right circular polarized light. This, however, is dependent on the phase used, and thus requires phase separation of the CNC aqueous suspension before the preparation of the membranes. The CNC substrates used here were produced with a mixture of anisotropic and isotropic phases. As for the rolling papers, these

are made from cellophane and glycerine, not only possessing relatively high smoothness, but also being extremely transparent and flexible. **Figure 3.2.4a** shows transmittance spectra of CNC and rolling paper used in this work (where it should be noted that both substrates have similar thicknesses, with CNC in the range of 15–25 μm and rolling paper at ~18 μm). The CNC membrane has decreased transmittance at ~550 nm. This is due to the photonic bandgap of this material [46,47]. The rolling paper, on the other hand, shows a good transmittance over the entire visible wavelength range. Additionally, to confirm that the surface morphology of these cellulose-based substrates is suitable for OLED applications, we performed atomic force microscopy measurements (**Figure 3.2.4b,c**). The CNC membrane had a root mean square (rms) surface roughness of ~13 nm, while for the rolling paper the value was ~15 nm. In the case of the rolling paper, one can see a sort of granular morphology, with small particles on the surface which may originate from either the manufacturing process or from environmental contaminations (they are not, however, visible by scanning electron microscopy, **Figure S3.2.3**, **Section 3.2.6**). These may be detrimental, as they can cause short-circuits between the anode and the cathode. Nonetheless, both materials show a surface roughness low enough for OLED applications.

To reduce the exposure of these substrates to water, which can result in uneven swelling (or, in the case of CNC, complete breakdown of the membrane), we modified the typical wet transfer process of graphene (**Figure 3.2.4d**). The "stack" approach was taken as the starting point, as it has the advantage of introducing the substrate only at the very end of the process. After the electrochemical delamination of the three-layer graphene, previously cut in the shape of a narrow conductive track (~2–3 mm wide), the graphene+PMMA film is scooped out with a polytetrafluoroethylene (PTFE) plate. Immediately after, the target substrate (either CNC or rolling paper) is briefly wet in water and placed on top of the PTFE plate, covering the graphene. The entire assembly is then left to dry in air, in ambient conditions. Finally, once dried, cellulose-based substrate is removed from the PTFE, with the graphene+PMMA sticking to the substrate (as the adhesion of graphene to PTFE is very low). This results in a substrate+PMMA+graphene stack, which can then move on to the MoO_3 deposition stage.

3.2.2.4 Flexible OLEDs on cellulose-based substrates

The flexible OLEDs were fabricated with the following structure: cellulose substrate/PMMA/graphene (3 layers)/MoO_3 (15 nm)/PVK:mCP:TXO-TPA (~50 nm)/TPBi (40 nm)/Ca (10 nm)/Al (100 nm), where Ca was employed instead of LiF, as the latter may form a non-continuous layer, leading to a non-planar LiF surface (**Figure 3.2.5a**). OLEDs made on both types of substrates (designated as CNC-OLED and RP-OLED, for CNC and rolling paper substrates, respectively) show visible light emission under applied voltage, as seen in **Figure 3.2.5b** for RP-OLED, which continues to operate even under fairly extreme bending and twisting. In contrast, the CNC-OLED (**Figure S3.2.4**, **Section 3.2.6**), while allowing some degree of flexibility, is far more brittle. **Figure 3.2.5c** shows representative electroluminescence spectra of the obtained OLEDs. In both cases, the maximum of electroluminescence spectra is near 560 nm, characteristic of TXO-TPA, with a small band at ~400 nm, corresponding to the PVK host. The latter is particularly common when the energy (electrical carriers) transfer from the host to the guest is not achieved completely [45]. **Figure 3.2.5d** shows the current density and brightness of CNC-OLED and RP-OLED as a function of voltage. Similarly to the devices on quartz, the turn-on voltage is around 3 V, indicating that the energy levels are still well aligned independent of the substrate. The maximum brightness of RP-OLED, at ~400 cd m^{-2}, is four times larger than that of CNC-OLED (~100 cd m^{-2}). Moreover, the current density of RP-OLED

is also larger than for CNC-OLED at the same brightness. As such, the maximum current and power efficiencies are higher for RP-OLED, at 0.4 cd A^{-1} and 0.3 lm W^{-1}, respectively (versus 0.2 cd A^{-1} and 0.2 lm W^{-1} for CNC-OLED), as seen in **Figure 3.2.5e**. The EQE is also higher for RP-OLED, with a value of 0.34% (versus 0.17% for CNC-OLED). We also note the earlier onset of efficiency roll-off for CNC-OLED (**Figure 3.2.5f**).

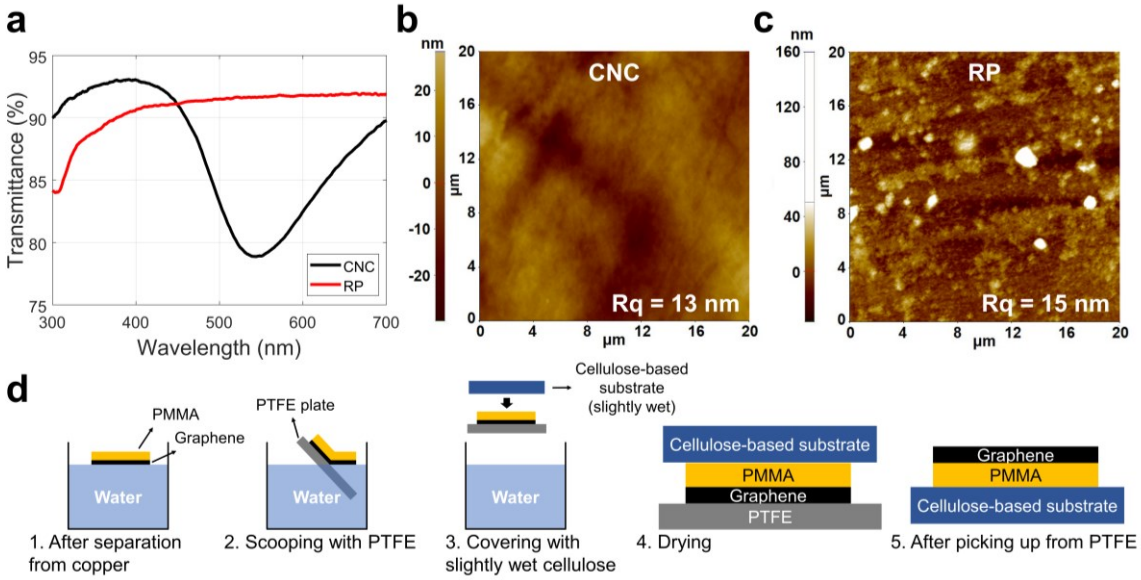

Figure 3.2.4. (a) Transmittance spectra of the CNC and RP substrates. **(b)** AFM images of CNC and **(c)** RP substrates, with the root mean square roughness values. **(d)** Schematic representation of the modified transfer of graphene onto cellulose-based substrates.

We begin the analysis of these devices by exploring the charge-carrier transport features in shallow- and deep-trap SCLC behaviour, as well as after the trap-filling process (Child's law) (**Figure 3.2.5g**). Charge-carrier mobility from Child's model suffers a direct impact of densities of trap defects (N_t) and free-carriers (n_0), during the trap-filling process (Mott-Gurney model) [48]. Taking into account this characteristic, **Equation 3.2.1** can be rewritten in terms of the effective mobility (μ_{eff}):

$$J_{SCLC} = \frac{9}{8}\varepsilon_r\varepsilon_0\mu_{eff}\frac{V^2}{L^3} \tag{3.2.2}$$

where $\mu_{eff}=\theta_0\mu_{SCLC}$, and θ_0 is the density of trap defects parameter, which is the ratio of the density of free-carriers and the total density of charge carriers:

$$\theta_0 = \frac{n_0}{n_0 + N_t} \tag{3.2.3}$$

In this context, the obtained effective electrical mobilities for RP and CNC-OLEDs are 3.14×10^{-9} and 3.85×10^{-9} $cm^2\ V^{-1}\ s^{-1}$, respectively. It should be noted that, in the whole device, we are calculating the electrical mobility of the slowest electrical carrier (that, in almost all of the organic materials employed in these OLEDs, is the electron). On the other hand, electrical mobilities after the trap-filling process (under Child's law domain) have values about 10^3 times higher than the ones under shallow-trap SCLC conditions, with μ_{SCLC}(RP)$=5.11\times10^{-6}$ $cm^2\ V^{-1}\ s^{-1}$ and μ_{SCLC}(CNC)$=4.16\times10^{-6}$ $cm^2\ V^{-1}\ s^{-1}$. Thus, the density of trap defects parameters (θ_0) for RP and CNC are 6.14×10^{-4} and 9.25×10^{-4}, respectively. Applying Mark-Helfrich's equation [49], in the deep-trap filling behaviour (between shallow-trap and Child's law domain) to calculate the

average energy of trap-states (E_t) for each OLED, we obtain E_t(RP)=280 meV and E_t(CNC)=252 meV. These values are similar and typical of shallow defects.

The voltage where the Mott-Gurney regime transitions into the Mark-Helfrich domain, designated as the trap-filling limit voltage (V_{TFL}), allows to obtain the total density of trap defects (N_t) by combining the equations corresponding to these two domains:

$$V_{\mathrm{TFL}} = \frac{qN_tL^2}{2\varepsilon_r\varepsilon_0} \tag{3.2.4}$$

where q is the elementary electrical charge. Both OLEDs exhibit almost the same values of N_t, 1.00×10^{17} and 1.02×10^{17} cm^{-3} for RP-OLED and CNC-OLED, respectively. This is not surprising, as the device structure and fabrication process are similar. When we combine **Equation 3.2.3** with **Equation 3.2.4** and calculate the total density of free charge-carriers for both RP-OLED and CNC-OLED, it is possible to observe that the main difference between each device charge-carrier transport and recombination is related to their n_0 values: 6.17×10^{13} and 9.46×10^{13} cm^{-3}, respectively. As the trap densities are almost equal, and the density of free charge carriers is actually higher for CNC-OLED compared to RP-OLED, we can speculate that one of the reasons behind the worse performance of CNC-OLED might be that the electrical charge carrier densities injected at the anode are different for the two substrates. This could be due to the different densities of interfacial defects at the anode layer, induced by morphological differences in the substrates.

At the same time, one cannot disregard the effect of the optical outcoupling, which, considering the transmittance spectra of both substrates (**Figure 3.2.4a**), could be expected to be better in RP-OLEDs compared to CNC-OLEDs. However, there might be a possible underestimation of the brightness due to the photonic bandgap reflection in the CNC, which can result in a deviation from the Lambertian emission profile. If the photons reflected in this substrate are emitted at an angle away from the normal direction (used for brightness measurement in this work), the total measured brightness will be underestimated. In this hypothesis, the CNC-OLED figures of merit would be slightly better than the ones that we obtain here. On the other hand, if there is total internal reflection, photon loss is expected, justifying the lower performance of CNC-OLED.

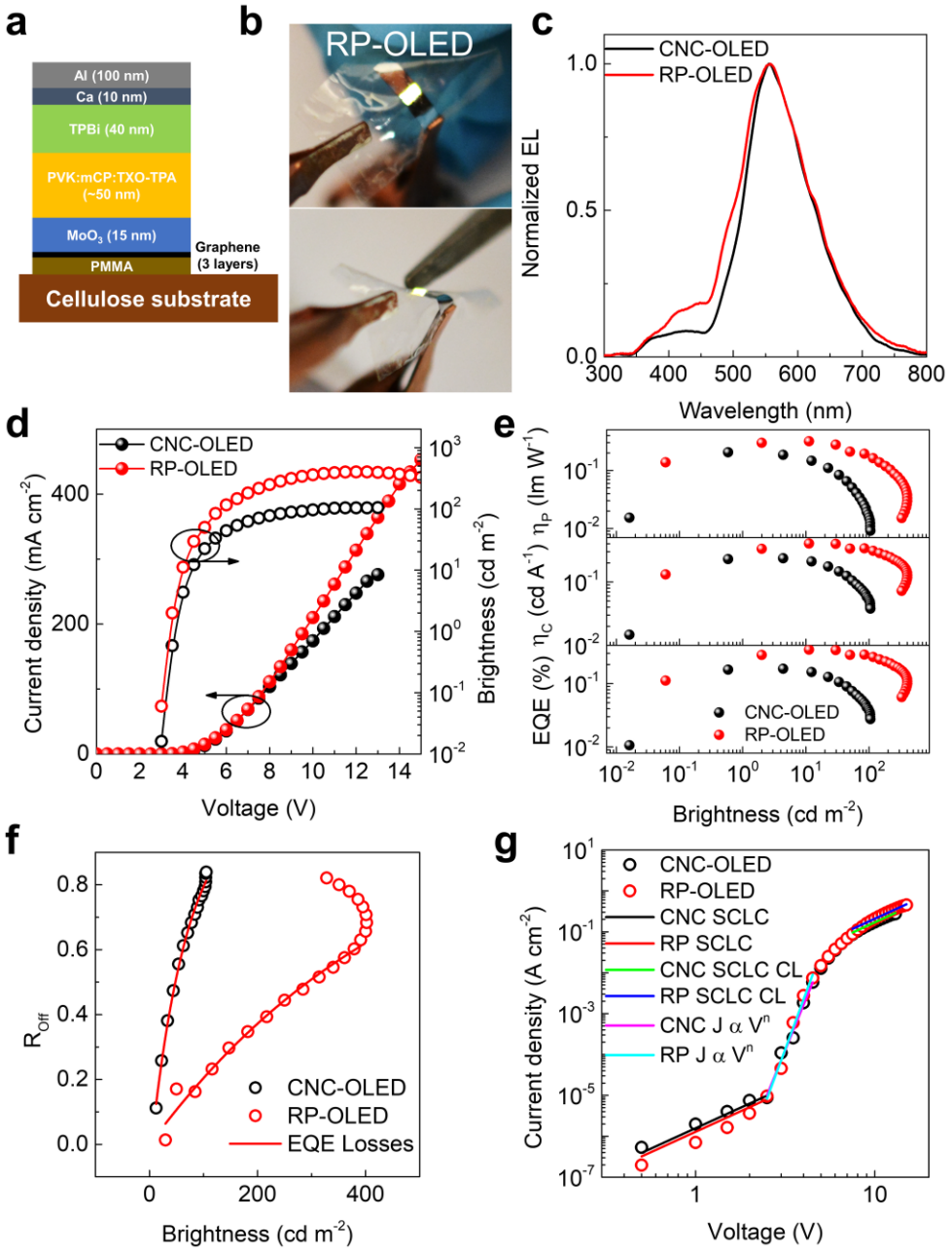

Figure 3.2.5. (a) Schematic representation of the OLED structure on the cellulose-based substrates. **(b)** Photographs of RP-OLED emitting light, even under considerable bending. **(c)** Electroluminescence spectra of CNC-OLED and RP-OLED. **(d)** Current density and brightness of the OLEDs on cellulose-based substrate, as a function of applied voltage. **(e)** Current (η_C), power (η_P) and external quantum efficiencies of the cellulose-supported OLEDs and **(f)** their efficiency roll-off, as a function of brightness. **(g)** Current density versus voltage of CNC-OLED and RP-OLED, fitted to the SCLC model, where CL corresponds to the Child's law regime and $J \propto V^n$ to the Mark-Helfrich domain, with the Mott-Gurney regime at low voltages.

3.2.3 Conclusions

We explored the use of CVD graphene in flexible OLEDs on cellulose nanocrystal membranes and transparent rolling papers. The graphene anodes, with a sheet resistance of 288 Ω sq^{-1}, were obtained using an optimized CVD recipe, multiple layer stacking and charge transfer doping by MoO_3. The effect of the MoO_3 thickness on the performance of solution processed TADF OLEDs was also investigated, with a film of 15 nm resulting in the best performing device in

terms of stability of maximum brightness. Finally, we applied these findings to fabricate cellulose-supported OLEDs, after appropriate adaptations of the graphene transfer process to these water-sensitive substrates. Despite the modest external quantum efficiencies, as well as low current and power efficiencies (0.34%, 0.4 cd A^{-1} and 0.3 lm W^{-1}, respectively, in the best case), these devices demonstrate for the first time the combined potential of graphene and cellulose-based substrates for flexible environmentally conscious applications.

3.2.4 Materials and Methods

3.2.4.1 Single-layer CVD graphene synthesis

Single-layer graphene was deposited, by chemical vapour deposition, on 25 μm-thick copper foil (>99.99%, MTI) cut into ~3×7 cm^2 sheets and washed in acetone and isopropanol (15 min ultrasonication in each of the solvents). Based on the previously reported CVD process [25], the substrate was placed inside the thermal CVD chamber (a quartz tube) and annealed at 950 °C for 10 min, under 190 sccm of H_2 and 190 sccm of Ar, at 276 mbar. Afterwards, the chamber was pumped down to ~0.13 mbar and ~200 sccm of air was introduced, for 5 min, while being continuously pumped out. Next, the system was pumped down once again and 50 sccm of H_2 were fed into the chamber, for 20 min, still under continuous pumping. The gas flow was then interrupted, and the system pressure allowed to drop to its lowest value. Afterwards, H_2 and Ar (both at 190 sccm) were introduced into the chamber, while the temperature was increased to 1090 °C, at a 25 °C/min rate (we note that the temperature was being measured by thermocouples just outside the quartz tube, presenting an offset relative to the actual temperature of the substrate; the 1090 °C growth temperature was chosen so that the copper substrate would be as close as possible to its melting point). This was followed by a 10 min annealing at 1090 °C in the same atmosphere, and the pressure during these two steps was allowed to rise to 276 mbar and then maintained at this value. Starting the growth phase, CH_4 was introduced into the chamber, alongside 38 sccm of H_2 and 200 sccm of Ar. The flowrate of CH_4 was 0.15 sccm for the first 6 min, then cut to 0 sccm for 1 min and finally 0.10 sccm for the last 40 min (see **Figure 3.2.1a**). At the end, the sample was rapidly pulled out towards the cold end of the reactor and all the gases were pumped out, followed by the pressurization of the chamber to atmospheric pressure with Ar.

3.2.4.2 CVD graphene transfer

The graphene was transferred by the well-established electrochemical bubbling approach, using poly(methyl methacrylate) (PMMA, average molecular weight 550 000, Alfa Aesar, 4.5 wt% in anisole) as a supporting polymer. Briefly, the PMMA was spin coated onto the as-grown graphene on copper, resulting in a ~300 nm thick film. Then, the sample was placed in an aqueous solution of NaCl (~6.5–7 mg mL^{-1}), and a voltage of −4 V was applied to it, leading to the formation of hydrogen bubbles at the Cu/graphene interface and allowing to separate them. The floating graphene+PMMA film was then passed through two DI water baths (~5 min each), to wash away any NaCl. The stacking of multiple graphene layers was performed by two different strategies. In the "layering" transfer, each graphene layer was scooped out of the last washing bath and transferred onto the target substrate, followed by the removal of the supporting PMMA layer. This was repeated multiple times, in succession, removing the PMMA after each individual transfer (see **Figure 3.2.2a**). In the "stack" transfer, the graphene layers were transferred onto a copper substrate with its own graphene film, "picking up" the latter and thus adding it to the stack. Then, after reaching the desired number of layers, the stack was

transferred onto the target substrate, concluding with the removal of the PMMA layer (see **Figure 3.2.2b**). Specifically in the case of flexible OLEDs, after separating the graphene stack from the last copper substrate, it was scooped out of the water using a PTFE plate. After placing the cellulose-based target substrate, briefly wetted in water, on top of this plate (covering the graphene+PMMA) and letting the entire assembly dry, the latter adhered to the target substrate.

3.2.4.3 Cellulose-based substrate preparation

The free-standing cellulose nanocrystal membranes were prepared from 2 wt% suspensions without phase separation of commercial Na neutralized spray-dried CNCs (provided by CelluForce©) in H_2O, by evaporation-assisted assembly at room temperature. To this end, these dispersions were further diluted (3 g of CNCs suspension in 5g of H_2O for each membrane) and poured into polystyrene Petri dishes (5 cm diameter), resulting in membranes which can be easily separated from the dish after evaporation, becoming completely free-standing. The resulting membranes presented a thickness of approximately 15-25 μm.

For the transparent regenerated cellulose cigarette rolling papers the brand "aLedinha", by aLeda, was used. The thickness of these papers was measured at ~18 μm.

3.2.4.4 OLED fabrication

The OLED structure was based on the host:guest concept, with a reduced number of organic layers. On top of the graphene anode, a thin (15 nm, with other thicknesses also explored in this work) layer of MoO_3 was deposited by thermal evaporation under high vacuum (10^{-5}–10^{-6} mbar), at relatively low evaporation rates (1 Å s^{-1}), in order to guarantee a uniform interface with graphene. The device active layer was deposited by spin coating (solution statically dispensed) at 2000 rpm for 30 seconds, after filtering the solution with a 0.1 μm polytetrafluoroethylene filter and drying in the glovebox at 80 °C for 30 min. For the active layer solution, a blend composed of [PVK:mCP] (0.7:0.3; 92 wt%):TXO-TPA (8 wt%), where the PVK (poly(Nvinylcarbazole)) and mCP (1,3-bis(N-carbazolyl)benzene) are the host constituents and the TXO-TPA (2-[4 (diphenylamino)phenyl]-10,10-dioxide-9H-thioxanthen-9-one) is the guest, a TADF (Thermally Activated Delayed Fluorescent) emitter. The materials were solubilized in chlorobenzene (10 mg mL^{-1}, for host and guest, independently) and then mixed in order to achieve the above-mentioned concentrations in the host:guest matrix. After the deposition of the active layer, the electron transport layer of TPBi (2,2',2''-(1,3,5-Benzinetriyl)-tris(1-phenyl-1-H-benzimidazole)) with a thickness of 40 nm was thermally evaporated in the same conditions of the molybdenum oxide. Finally, in the case of the rigid devices, a thin (1 nm) layer of LiF was evaporated, at an evaporation rate of 0.1 Å s^{-1}, followed by a thick (100 nm) layer of Al, evaporated at 2 Å s^{-1}. For the flexible devices, Ca was used instead of LiF (10 nm, thermally evaporated at 1 Å s^{-1}). Both LiF and Ca present a favourable match between the cathode work function and the TPBi LUMO level, while Al was used either to ensure electron injection by quantum tunnelling (in the former case), or to avoid the typically fast Ca oxidation (in the latter). The active areas of the devices were around 7–9 mm^2 for the rigid OLEDs and 2–4 mm^2 for the flexible ones.

3.2.4.5 Material and device characterization

Secondary electron scanning electron microscopy (SE–SEM) images were acquired using a Vega 3 SBH system by TESCAN, with an acceleration voltage of 5 kV and a working distance of 15 mm. Raman spectroscopy was performed using a Jobin Yvon HR800 Raman system, by Horiba, and a He–Cd 441.6 nm laser by Kimmon. Sheet resistance measurements were

performed by the van der Pauw method, using a Keysight B2902A dual-channel source meter unit and a computer-controlled multiplexer. Transmittance and reflectance spectra were acquired using a Shimadzu UV-3600 UV-Vis-NIR spectrophotometer. AFM measurements were performed with a PARK XE7 atomic force microscope, in non-contact mode, with a PPP-NCHR Standard Non-Contact Tapping Mode AFM probe. The probe had a standard beam shaped cantilever with a 30 nm thick reflex aluminium coating. The cantilever had a force constant of 42 N/m, length of 125 μm, width of 30 μm and thickness of 4 μm. The selected frequency for measurement was 304 kHz. The probe radius was <10 nm.

The current–voltage–luminance (J–V–L) characteristics were determined using a Keithley 2425 source meter unit and a Konica Minolta LS-100 Chromameter. For the electroluminescence spectra measurements, an Ocean Optics USB4000 spectrometer was used. The OLED efficiencies were calculated considering that the emission follows a Lambertian emitter.

Acknowledgements

This work was developed within the scope of project i3N (LA/P/0037/2020, UIDB/50025/2020 and UIDP/50025/2020), financed by national funds through the Portuguese Foundation for Science and Technology/MCTES (FCT I.P.). B. Kulyk acknowledges the PhD grant SFRH/BD/141525/2018 from FCT I.P. D. Gaspar, and L. Pereira would like to acknowledge FCT – Portuguese Foundation for Science and Technology under the project CELLECTIVE (PTDC/CTM-CTM/4653/2021). The authors also thank Maria João Sá Pereira for the AFM measurements. Helpful discussions with Prof. Caroline Murawski and with Jorge Moura are also gratefully acknowledged.

3.2.5 References

[1] S.-J. Zou, Y. Shen, F.-M. Xie, J.-D. Chen, Y.-Q. Li, J.-X. Tang, "Recent advances in organic light-emitting diodes: toward smart lighting and displays," *Mater. Chem. Front.*, 4, 788–820, **2020**. https://doi.org/10.1039/C9QM00716D.

[2] C. Keum, C. Murawski, E. Archer, S. Kwon, A. Mischok, M.C. Gather, "A substrateless, flexible, and water-resistant organic light-emitting diode," *Nat. Commun.*, 11, 6250, **2020**. https://doi.org/10.1038/s41467-020-20016-3.

[3] T. Wang, Y.-Z. Wang, L.-C. Jing, Q. Zhu, A.S. Ethiraj, W. Geng, Y. Tian, Z. Zhu, Z. Meng, H.-Z. Geng, "Novel biodegradable and ultra-flexible transparent conductive film for green light OLED devices," *Carbon*, 172, 379–389, **2021**. https://doi.org/10.1016/j.carbon.2020.10.027.

[4] E. Fortunato, N. Correia, P. Barquinha, L. Pereira, G. Goncalves, R. Martins, "High-performance flexible hybrid field-effect transistors based on cellulose fiber paper," *IEEE Electron Device Lett.*, 29, 988–990, **2008**. https://doi.org/10.1109/LED.2008.2001549.

[5] R. Martins, D. Gaspar, M.J. Mendes, L. Pereira, J. Martins, P. Bahubalindruni, P. Barquinha, E. Fortunato, "Papertronics: Multigate paper transistor for multifunction applications," *Appl. Mater. Today*, 12, 402–414, **2018**. https://doi.org/10.1016/j.apmt.2018.07.002.

[6] B. Kulyk, B.F.R. Silva, A.F. Carvalho, S. Silvestre, A.J.S. Fernandes, R. Martins, E. Fortunato, F.M. Costa, "Laser-Induced Graphene from Paper for Mechanical Sensing," *ACS Appl. Mater. Interfaces*, 13, 10210–10221, **2021**. https://doi.org/10.1021/acsami.0c20270.

[7] B. Kulyk, B.F.R. Silva, A.F. Carvalho, P. Barbosa, A. V. Girão, J. Deuermeier, A.J.S.

Fernandes, F.M.L. Figueiredo, E. Fortunato, F.M. Costa, "Laser-Induced Graphene from Paper by Ultraviolet Irradiation: Humidity and Temperature Sensors," *Adv. Mater. Technol.*, 2101311, 2101311, **2022**. https://doi.org/10.1002/admt.202101311.

[8] B. Kulyk, M. Matos, B.F.R. Silva, A.F. Carvalho, A.J.S. Fernandes, D. V. Evtuguin, E. Fortunato, F.M. Costa, "Conversion of paper and xylan into laser-induced graphene for environmentally friendly sensors," *Diam. Relat. Mater.*, 123, 108855, **2022**. https://doi.org/10.1016/j.diamond.2022.108855.

[9] B. Kulyk, S.O. Pereira, A.J.S. Fernandes, E. Fortunato, F.M. Costa, N.F. Santos, "Laser-induced graphene from paper for non-enzymatic uric acid electrochemical sensing in urine," *Carbon*, 197, 253–263, **2022**. https://doi.org/10.1016/j.carbon.2022.06.013.

[10] T. Pinheiro, S. Silvestre, J. Coelho, A.C. Marques, R. Martins, M.G.F. Sales, E. Fortunato, "Laser-Induced Graphene on Paper toward Efficient Fabrication of Flexible, Planar Electrodes for Electrochemical Sensing," *Adv. Mater. Interfaces*, 2101502, 2101502, **2021**. https://doi.org/10.1002/admi.202101502.

[11] S.H. Min, C.K. Kim, H.N. Lee, D.G. Moon, "An OLED using cellulose paper as a flexible substrate," *Mol. Cryst. Liq. Cryst.*, 563, 159–165, **2012**. https://doi.org/10.1080/15421406.2012.689153.

[12] Q. Zheng, H. Li, Y. Zheng, Y. Li, X. Liu, S. Nie, X. Ouyang, L. Chen, Y. Ni, "Cellulose-based flexible organic light-emitting diodes with enhanced stability and external quantum efficiency," *J. Mater. Chem. C*, 9, 4496–4504, **2021**. https://doi.org/10.1039/D1TC00019E.

[13] S. Purandare, E.F. Gomez, A.J. Steckl, "High brightness phosphorescent organic light emitting diodes on transparent and flexible cellulose films," *Nanotechnology*, 25, **2014**. https://doi.org/10.1088/0957-4484/25/9/094012.

[14] M. Morales-Masis, S. De Wolf, R. Woods-Robinson, J.W. Ager, C. Ballif, "Transparent Electrodes for Efficient Optoelectronics," *Adv. Electron. Mater.*, 3, 1600529, **2017**. https://doi.org/10.1002/aelm.201600529.

[15] A. Kumar, C. Zhou, "The race to replace tin-doped indium oxide: Which material will win?," *ACS Nano*, 4, 11–14, **2010**. https://doi.org/10.1021/nn901903b.

[16] Y. Chen, Y. Yue, S. Wang, N. Zhang, J. Feng, H. Sun, "Graphene as a Transparent and Conductive Electrode for Organic Optoelectronic Devices," *Adv. Electron. Mater.*, 5, 1900247, **2019**. https://doi.org/10.1002/aelm.201900247.

[17] A.E. Adetayo, T.N. Ahmed, A. Zakhidov, G.W. Beall, "Improvements of Organic Light-Emitting Diodes Using Graphene as an Emerging and Efficient Transparent Conducting Electrode Material," *Adv. Opt. Mater.*, 9, 2002102, **2021**. https://doi.org/10.1002/adom.202002102.

[18] L.-P. Ma, Z. Wu, L. Yin, D. Zhang, S. Dong, Q. Zhang, M.-L. Chen, W. Ma, Z. Zhang, J. Du, D.-M. Sun, K. Liu, X. Duan, D. Ma, H.-M. Cheng, W. Ren, "Pushing the conductance and transparency limit of monolayer graphene electrodes for flexible organic light-emitting diodes," *Proc. Natl. Acad. Sci.*, 117, 25991–25998, **2020**. https://doi.org/10.1073/pnas.1922521117.

[19] J.O. Hwang, J.S. Park, D.S. Choi, J.Y. Kim, S.H. Lee, K.E. Lee, Y.H. Kim, M.H. Song, S. Yoo, S.O. Kim, "Workfunction-tunable, N-doped reduced graphene transparent electrodes for high-performance polymer light-emitting diodes," *ACS Nano*, 6, 159–167, **2012**. https://doi.org/10.1021/nn203176u.

[20] J.-W. Shin, H. Cho, J. Lee, J. Moon, J.-H. Han, K. Kim, S. Cho, J.-I. Lee, B.-H. Kwon, D.-H. Cho, K.M. Lee, M. Suemitsu, N.S. Cho, "Overcoming the efficiency limit of organic light-emitting diodes using ultra-thin and transparent graphene electrodes," *Opt. Express*, 26, 617, **2018**. https://doi.org/10.1364/OE.26.000617.

[21] L. Liu, W. Shang, C. Han, Q. Zhang, Y. Yao, X. Ma, M. Wang, H. Yu, Y. Duan, J. Sun, S. Chen, W. Huang, "Two-In-One Method for Graphene Transfer: Simplified Fabrication Process for Organic Light-Emitting Diodes," *ACS Appl. Mater. Interfaces*, 10, 7289–7295, **2018**. https://doi.org/10.1021/acsami.7b19039.

[22] T.H. Han, Y. Lee, M.R. Choi, S.H. Woo, S.H. Bae, B.H. Hong, J.H. Ahn, T.W. Lee, "Extremely efficient flexible organic light-emitting diodes with modified graphene anode," *Nat. Photonics*, 6, 105–110, **2012**. https://doi.org/10.1038/nphoton.2011.318.

[23] Y. Han, L. Zhang, X. Zhang, K. Ruan, L. Cui, Y. Wang, L. Liao, Z. Wang, J. Jie, "Clean surface transfer of graphene films via an effective sandwich method for organic light-emitting diode applications," *J. Mater. Chem. C*, 2, 201–207, **2014**. https://doi.org/10.1039/c3tc31722f.

[24] T.-H. Han, M. Park, S. Kwon, S. Bae, H. Seo, H. Cho, J. Ahn, T. Lee, "Approaching ultimate flexible organic light-emitting diodes using a graphene anode," *Nat. Publ. Gr.*, 8, e303-8, **2016**. https://doi.org/10.1038/am.2016.108.

[25] B. Kulyk, A.F. Carvalho, A.J.S. Fernandes, F.M. Costa, "Millimeter sized graphene domains through in situ oxidation/reduction treatment of the copper substrate," *Carbon*, 169, 403–415, **2020**. https://doi.org/10.1016/j.carbon.2020.08.002.

[26] W.J. Zhu, T. Low, V. Perebeinos, a a Bol, Y. Zhu, H.G. Yan, J. Tersoff, P. Avouris, "Structure and Electronic Transport in Graphene Wrinkles," *Nano Lett.*, 12, 3431–3436, **2012**. https://doi.org/10.1021/nl300563h.

[27] S. Al-Kamiyani, T. Mohiuddin, "Improved control in elimination of white impurities on graphene by chemical vapor deposition (CVD)," *AIP Adv.*, 8, 125325, **2018**. https://doi.org/10.1063/1.5051693.

[28] Y. Çelik, W. Escoffier, M. Yang, E. Flahaut, E. Suvacı, "Relationship between heating atmosphere and copper foil impurities during graphene growth via low pressure chemical vapor deposition," *Carbon*, 109, 529–541, **2016**. https://doi.org/10.1016/j.carbon.2016.08.057.

[29] R.R. Nair, P. Blake, A.N. Grigorenko, K.S. Novoselov, T.J. Booth, T. Stauber, N.M.R. Peres, A.K. Geim, "Fine Structure Constant Defines Visual Transparency of Graphene," *Science*, 320, 1308–1308, **2008**. https://doi.org/10.1126/science.1156965.

[30] S.J. Kwon, T.H. Han, T.Y. Ko, N. Li, Y. Kim, D.J. Kim, S.H. Bae, Y. Yang, B.H. Hong, K.S. Kim, S. Ryu, T.W. Lee, "Extremely stable graphene electrodes doped with macromolecular acid," *Nat. Commun.*, 9, 1–9, **2018**. https://doi.org/10.1038/s41467-018-04385-4.

[31] I.-J. Park, T.I. Kim, T. Yoon, S. Kang, H. Cho, N.S. Cho, J.-I. Lee, T.-S. Kim, S.-Y. Choi, "Flexible and Transparent Graphene Electrode Architecture with Selective Defect Decoration for Organic Light-Emitting Diodes," *Adv. Funct. Mater.*, 28, 1704435, **2018**. https://doi.org/10.1002/adfm.201704435.

[32] G.V. Bianco, A. Sacchetti, A. Milella, M. Grande, A. D'Orazio, P. Capezzuto, G. Bruno, "Extraordinary low sheet resistance of CVD graphene by thionyl chloride chemical doping," *Carbon*, 170, 75–84, **2020**. https://doi.org/10.1016/j.carbon.2020.07.038.

[33] A.E. Mansour, M.M. Said, S. Dey, H. Hu, S. Zhang, R. Munir, Y. Zhang, K. Moudgil, S. Barlow, S.R. Marder, A. Amassian, "Facile Doping and Work-Function Modification of Few-Layer Graphene Using Molecular Oxidants and Reductants," *Adv. Funct. Mater.*, 27, **2017**. https://doi.org/10.1002/adfm.201602004.

[34] J.H. Heo, D.H. Shin, D.H. Song, D.H. Kim, S.J. Lee, S.H. Im, "Super-flexible bis(trifluoromethanesulfonyl)-amide doped graphene transparent conductive electrodes for photo-stable perovskite solar cells," *J. Mater. Chem. A*, 6, 8251–8258, **2018**. https://doi.org/10.1039/C8TA02672F.

[35] L. Liu, R. Dong, D. Ye, Y. Lu, P. Xia, L. Deng, Y. Duan, K. Cao, S. Chen, "Phosphomolybdic Acid-Modified Monolayer Graphene Anode for Efficient Organic and Perovskite Light-Emitting Diodes," *ACS Appl. Mater. Interfaces*, 13, 12268–12277, **2021**. https://doi.org/10.1021/acsami.0c22456.

[36] E. Cho, S. Cha, Y. Kim, C. Kim, "Transparent and flexible electrode composed of a graphene multilayer interlayer-doped with MoO3," *Org. Electron.*, 77, 105437, **2020**. https://doi.org/10.1016/j.orgel.2019.105437.

[37] J. Meyer, P.R. Kidambi, B.C. Bayer, C. Weijtens, A. Kuhn, A. Centeno, A. Pesquera, A. Zurutuza, J. Robertson, S. Hofmann, "Metal oxide induced charge transfer doping and band alignment of graphene electrodes for efficient organic light emitting diodes.," *Sci. Rep.*, 4, 5380, **2014**. https://doi.org/10.1038/srep05380.

[38] W.-Y. Hung, T.-H. Ke, Y.-T. Lin, C.-C. Wu, T.-H. Hung, T.-C. Chao, K.-T. Wong, C.-I. Wu, "Employing ambipolar oligofluorene as the charge-generation layer in time-of-flight mobility measurements of organic thin films," *Appl. Phys. Lett.*, 88, 064102, **2006**. https://doi.org/10.1063/1.2172708.

[39] M. Kumar, L. Pereira, "Towards Highly Efficient TADF Yellow-Red OLEDs Fabricated by Solution Deposition Methods: Critical Influence of the Active Layer Morphology," *Nanomaterials*, 10, 101, **2020**. https://doi.org/10.3390/nano10010101.

[40] M. Vasilopoulou, A.M. Douvas, D.G. Georgiadou, L.C. Palilis, S. Kennou, L. Sygellou, A. Soultati, I. Kostis, G. Papadimitropoulos, D. Davazoglou, P. Argitis, "The Influence of Hydrogenation and Oxygen Vacancies on Molybdenum Oxides Work Function and Gap States for Application in Organic Optoelectronics," *J. Am. Chem. Soc.*, 134, 16178–16187, **2012**. https://doi.org/10.1021/ja3026906.

[41] N.F. Mott, R.W. Gurney, Electronic Processes in Ionic Crystals, 2nd ed., Oxford University Press, London, UK, **1948**.

[42] M. Pope, C.E. Swenberg, Electronic Processes in Organic Crystals and Polymers, Oxford University Press, **1999**.

[43] J.C. Germino, L.G.T.A. Duarte, R.A. Mendes, M.M. Faleiros, A. de Morais, J.N. de Freitas, L. Pereira, T.D.Z. Atvars, "All-Solution Processed Single-Layer WOLEDs Using [Pt(salicylidenes)] as Guests in a PFO Matrix," *Nanomaterials*, 12, 2497, **2022**. https://doi.org/10.3390/nano12142497.

[44] M. Kumar, Highly Efficient Organic Light Emitting Diodes Based on Thermally Activated Delayed Fluorescent Materials, University of Aveiro, **2019**. http://hdl.handle.net/10773/29831.

[45] P. Grey, S.N. Fernandes, D. Gaspar, J. Deuermeier, R. Martins, E. Fortunato, M.H. Godinho, L. Pereira, "Ionically Modified Cellulose Nanocrystal Self-Assembled Films with a Mesoporous Twisted Superstructure: Polarizability and Application in Ion-Gated Transistors," *ACS Appl. Electron. Mater.*, 2, 426–436, **2020**. https://doi.org/10.1021/acsaelm.9b00652.

[46] P. Grey, Cellulose Nanocrystal Chiral Structures for Electronics and Photonics, NOVA University of Lisbon, **2021**. https://run.unl.pt/handle/10362/123021.

[47] M. V. Santos, A. Tercjak, J. Gutierrez, H.S. Barud, M. Napoli, M. Nalin, S.J.L. Ribeiro, "Optical sensor platform based on cellulose nanocrystals (CNC) – 4′-(hexyloxy)-4-biphenylcarbonitrile (HOBC) bi-phase nematic liquid crystal composite films," *Carbohydr. Polym.*, 168, 346–355, **2017**. https://doi.org/10.1016/j.carbpol.2017.03.078.

[48] L. Pereira, Organic Light Emitting Diodes: the Use of Rare Earth and Transition Metals, Pan Stanford Publishing, Boca Raton, FL, USA, **2012**. https://www.crcpress.com/Organic-Light-Emitting-Diodes-The-Use-of-Rare-Earth-and-Transition-Metals/Pereira/p/book/9789814267298 (accessed January 12, 2019).

[49] P. Zhang, Y.S. Ang, A.L. Garner, Á. Valfells, J.W. Luginsland, L.K. Ang, "Space–charge limited current in nanodiodes: Ballistic, collisional, and dynamical effects," *J. Appl. Phys.*, 129, 100902, **2021**. https://doi.org/10.1063/5.0042355.

3.2.6 Supporting Information

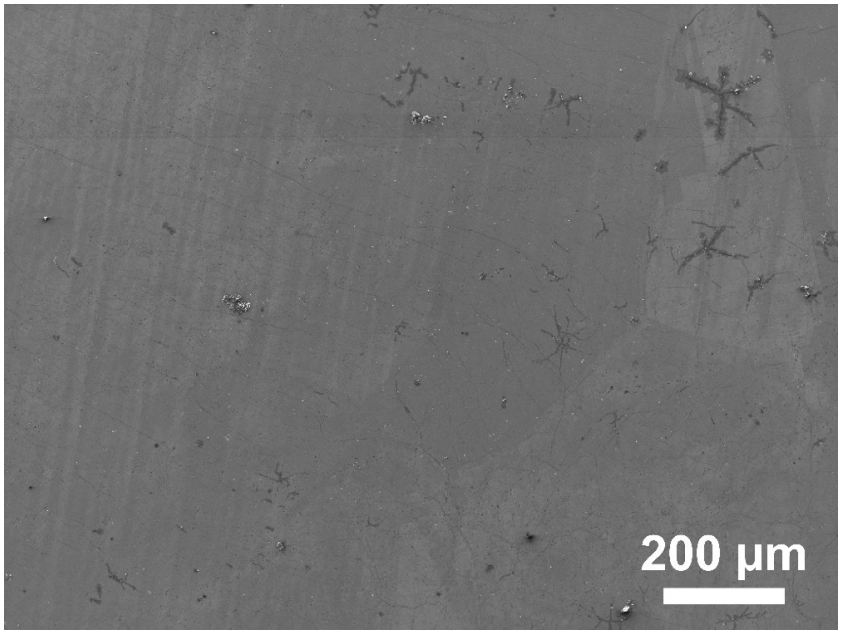

Figure S3.2.1. Low magnification SE-SEM image of the single-layer graphene film on the copper substrate.

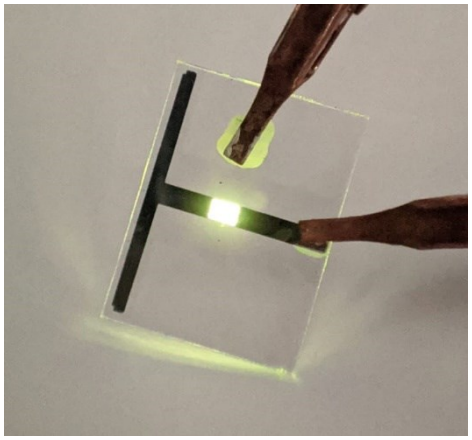

Figure S3.2.2. Photograph of the quartz-supported OLED.

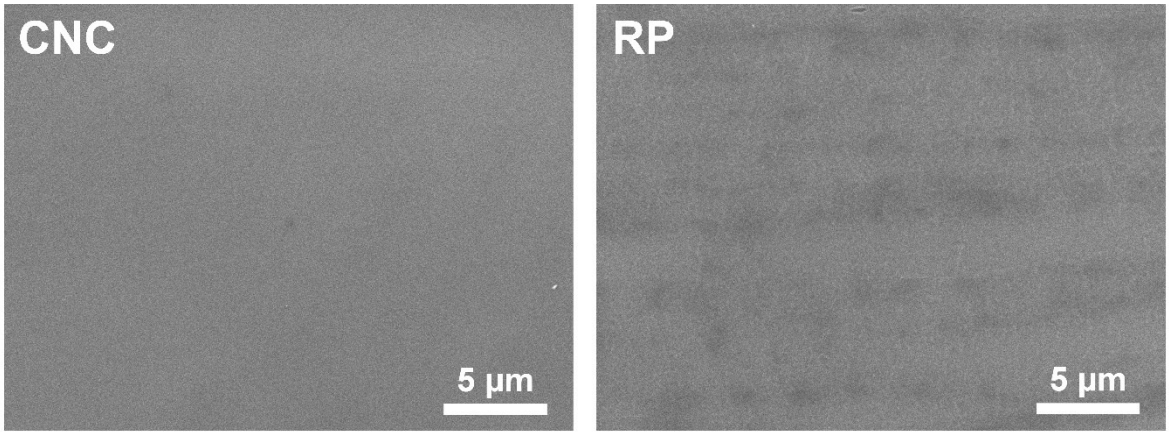

Figure S3.2.3. SE-SEM images of CNC and rolling paper.

Figure S3.2.4. Photograph of CNC-OLED.

Chapter 4

Conclusions and future perspectives

Bringing this thesis to a close, this chapter provides a summary of its main findings, along with some remarks on their significance, impact and future research.

Section 4.1 *lays out the results of this thesis, highlighting its implications for the field of flexible electronics.*

Section 4.2 *discusses the opportunities for further research provided by the reported findings.*

Section 4.3 *concludes this thesis by listing its outputs and how they were disseminated.*

4.1 Critical overview of the main findings

The main goal of this thesis was to explore the opportunities and challenges of combining graphene and paper as components of flexible electronic devices. Framing this objective as a question, is the combination of graphene with paper worth pursuing in the context of flexible devices?

Specifically in the case of sensors, the results presented in **Chapter 2** answer this question with a resounding "yes". If one seeks a functional material capable of transducing a wide range of physical and biochemical parameters, while also being biodegradable, easy to fabricate and inexpensive, paper-LIG should undoubtedly be one of the prime candidates for multiple applications. The piezoresistive response of this graphene material enables a straightforward application in the sensing of physical deformations, as shown in **Section 2.1**. The response to strain and bending was demonstrated, with a gauge factor of ~42. Another important aspect of this work was showing that good electrical conductivity can be achieved in paper-LIG synthesized with a CO_2 laser by making sure that the first irradiation step is performed far from the focal plane (but still ensuring a uniform charring), while the second one is undertaken in focus and with a high enough energy delivery (but below the damage threshold). As one of the first optimization studies of the synthesis of paper-LIG, this work was an important step in enabling future developments.

Further expanding the field of paper-LIG, the demonstration of the ability to synthesize it with an ultraviolet laser was another important contribution of this thesis, presented in **Section 2.2**. This proved to be non-trivial, as it became clear that the transformation of paper into LIG under UV irradiation occurs in a peculiar manner, with an apparent barrier in terms of the delivered energy for the transformation to take place. Nonetheless, a strategy to overcome this issue was proposed, and, by studying the response of the obtained paper-LIG to varying relative humidity and temperature, sensitivities of 1.3×10^{-3} $\%RH^{-1}$ and 2.8×10^{-3} $°C^{-1}$ were obtained, respectively. This gives another argument in support of the combined potential of graphene and paper in sensing.

Following up on these results, another important outcome of this thesis was presented in **Section 2.3**, showing that, using a CO_2 laser, paper-LIG could be formed in a single irradiation step, instead of the multiple lasing approach which was the standard synthesis technique for this type of laser. The importance of this finding resides in the simplification of the entire process, which can potentially result in significant time and cost savings when scaled up to an industrial level. Moreover, it was also shown that there is plenty of room for exploration in terms of the substrate choice, including not only cellulose-based ones like filter paper with activated-charcoal, but also extending to other abundant and often underutilized biopolymers like xylan. In the latter case, a noteworthy response to varying temperature was also showcased, capable of reliably resolving 1°C temperature variations, with a sensitivity of -1.29 Ω $°C^{-1}$.

The culmination of the extensive work performed on paper-LIG was the report concerning what is perhaps the most promising application field for this material: biosensing. Paper-LIG presents good electrical conductivity which enables it to take on the role of an electrode for the electrochemical detection of different analytes, something which had already been shown previously for polyimide-derived LIG, for example. In addition to that, the LIG obtained from paper is also hydrophilic. As such, it is expected to perform particularly well in aqueous solutions. As was shown in **Section 2.4**, paper-LIG electrodes were capable of reliable

quantification of uric acid in a real sample of human urine, showing remarkable selectivity, with a limit of detection of 3.97 μM and a sensitivity of 0.363 μA cm^{-2} μM^{-1} (at pH=7.4), while maintaining a linear response within the clinically relevant concentration range. More importantly, as paper is biodegradable and extremely affordable, this opens the door towards a vast spectrum of disposable analytical assays, further expanding point-of-care testing capabilities and enabling better access to diagnostic tools in regions where it may be limited. As such, the potential impact that this particular combination of graphene with paper, not just for uric acid quantification but also for other analytes, cannot be understated.

While these findings are already significant enough to confirm the vast potential of paper-based graphene devices, fulfilling one of the main objectives of this work, such devices are not limited to sensing functionalities only. The development of graphene-based OLEDs supported on paper is another possibility in this field, motivating their investigation in this thesis. The appeal of using graphene as an electrode in flexible OLEDs is well documented, as this application comes with the promise of taking full advantage of the unique combination of properties offered by graphene, enjoying the benefits of high optical transparency, good electrical conductivity and excellent mechanical characteristics. On the other hand, its combination with paper, in the context of OLEDs, is less intuitive, and therefore unexplored. One of the main issues is the surface roughness that must be as low as possible for these devices, which are at most just a few hundreds of nanometres thick. This is not a characteristic which can be typically attributed to common paper, but it can apply to some specific or engineered cellulose-based substrates. An important contribution of this thesis in this context is precisely the identification of transparent rolling paper and cellulose nanocrystal (CNC) membranes as two of such substrates. With surface roughness in the range of 15–25 nm, both materials were shown here to be viable supporting substrates for 3rd generation OLEDs with graphene anodes. This, however, was not without its challenges, since an improvement in the growth recipe of graphene had to be made, aiming at the reduction of the nucleation density and of the graphene adlayers. As discussed in **Section 3.1**, this was achieved thanks to an oxidation/reduction treatment of the copper substrate before the deposition of graphene, which ultimately allowed to obtain millimetre-sized graphene domains and continuous single-layer graphene films. Moreover, the properties of graphene had to be adapted to the intended application, particularly in what concerns its sheet resistance. Besides implying the stacking of multiple graphene layers, this required the exploration of various charge transfer doping approaches, with compounds such as triethyloxonium hexachloroantimonate and HNO_3 yielding unsatisfactory results (data not shown in this thesis). In the end, as covered in **Section 3.2**, thermal evaporation of MoO_3 proved to be the way to go, resulting in sheet resistances below 300 Ω sq^{-1}. Moreover, the transfer process of graphene had to be adapted to these cellulose substrates, given how their morphology and structural integrity tend to respond to contact with water, with the CNC membranes becoming particularly fragile when wet. Overall, while the final devices did not show outstanding performance, the work undertaken here was an important step in demonstrating the potential of graphene-based OLEDs supported on paper and other cellulose-based substrates, thus contributing to the main goal established for this thesis.

As a final remark, while the two categories of devices explored here (sensors and OLEDs) may seem too distinct, this is a natural consequence of the versatility of both paper and graphene. Thus, one can conclude by stating that this thesis makes a convincing case for graphene and paper as a powerful combination in the context of novel flexible devices, not just by giving clear

evidence supporting this proposition, but also by propelling the field forward with relevant results and contributions.

4.2 Future work

The results presented in this thesis leave plenty of room for future investigations, both in terms of questions that did not find a satisfactory answer in this work and in terms of entirely new ideas enabled by the reported findings. Some of these are listed below.

- Paper-LIG is sensitive to several different stimuli, such as mechanical deformation, temperature and humidity. As such, strategies to ensure the selectivity of this material should be investigated.
- Related to the previous point, more complex implementations such as lab-on-paper devices could be explored, integrating different types of sensors on the same substrate, in alignment with the concept of multisensing.
- For paper-LIG obtained by UV laser irradiation, further studies are needed to fully understand the transformation mechanisms.
- Following up on the report on temperature sensing using LIG obtained from xylan, many opportunities exist for the exploration of other types of sensors with this material.
- Having shown adequate performance in real samples, clinical trials appear as a natural continuation of the work on the paper-LIG uric acid biosensors.
- The investigation of the capabilities of paper-LIG electrodes for the electrochemical biosensing of other physiological and chemical parameters constitutes an interesting avenue of research.
- The great potential of paper-LIG notwithstanding, CVD graphene has shown great potential for bio and chemical sensing in GFET devices. The development of such devices on paper and other cellulose-based substrates is of great interest.
- For transparent electrode applications, other doping approaches, such as $AuCl_3$ doping, should be explored in greater detail. This also applies to the ones unsuccessfully used in this work (triethyloxonium hexachloroantimonate and HNO_3), as it is important to understand the origin of the issues presented by these compounds.
- In the context of OLEDs, studies on their encapsulation are of great importance, as this is an essential technological aspect for any potential application of these devices in commercial products. The issue becomes even more important when considering cellulose-based substrates which are permeable to water vapour.
- Microwave plasma chemical vapour deposition allows to synthesize multilayer graphene with very short growth times. Future work on transparent electrodes should explore this material.
- Other applications of graphene as a transparent electrode on paper should be considered. Graphene-based photovoltaic devices on paper substrates are one of the possibilities.

4.3 Thesis outputs and dissemination

The main findings of this thesis were disseminated by various means, including publishing in peer-reviewed journals, presentations at national and international conferences, coverage by news outlets and participation in science and technology dissemination events. Additionally, contributions were made to other works. A list of all these outputs is given below.

4.3.1 Publications included as thesis sections

B. Kulyk, A.F. Carvalho, A.J.S. Fernandes, F.M. Costa, "Millimetre sized graphene domains through in situ oxidation/reduction treatment of the copper substrate," *Carbon*, 169, 403-415, 2020. DOI: 10.1016/j.carbon.2020.08.002

B. Kulyk, B.F.R. Silva, A.F. Carvalho, S. Silvestre, A.J.S. Fernandes, R. Martins, E. Fortunato, F.M. Costa, "Laser-Induced Graphene from Paper for Mechanical Sensing," *ACS Appl. Mater. Interfaces*, 13, 8, 10210–10221, 2021. DOI: 10.1021/acsami.0c20270

B. Kulyk, B.F.R. Silva, A.F. Carvalho, P. Barbosa, A.V. Girão, J. Deuermeier, A.J.S. Fernandes, F.M. L. Figueiredo, E. Fortunato, F.M. Costa, "Laser-Induced Graphene from Paper by Ultraviolet Irradiation: Humidity and Temperature Sensors," *Adv. Mater. Technol.*, 7, 7, 2101311, 2022. DOI: 10.1002/admt.202101311

B. Kulyk, M. Matos, B.F.R. Silva, A.F. Carvalho, A.J.S. Fernandes, D.V. Evtuguin, E. Fortunato, F.M. Costa, "Conversion of paper and xylan into laser-induced graphene for environmentally friendly sensors," *Diam. Relat. Mater.*, 123, 108855, 2022. DOI: 10.1016/j.diamond.2022.108855

B. Kulyk, S.O. Pereira, A.J.S. Fernandes, E. Fortunato, F.M. Costa, N.F. Santos, "Laser-induced graphene from paper for non-enzymatic uric acid electrochemical sensing in urine," *Carbon*, 197, 253-263, 2022. DOI: 10.1016/j.carbon.2022.06.013

B. Kulyk, J.C. Germino, D. Gaspar, A.J.S. Fernandes, J. Deuermeier, A.F. Carvalho, A.F. da Cunha, L.M.N. Pereira, L. Pereira, F.M. Costa, "Graphene electrodes for flexible cellulose-supported OLEDs" (manuscript in preparation)

4.3.2 Other publications

B. Kulyk, A.M. Freitas, N.F. Santos, F. Mohseni, A.F. Carvalho, K. Yasakau, A.J.S. Fernandes, A. Bernardes, B. Figueiredo, R. Silva, J. Tedim, F.M. Costa, "A critical review on the production and application of graphene and graphene-based materials in anti-corrosion coatings," *Crit. Rev. Solid State Mater. Sci.*, 47, 309-355, 2022. DOI: 10.1080/10408436.2021.1886046

A.F. Carvalho, **B. Kulyk**, A.J.S. Fernandes, E. Fortunato, F.M. Costa, "A Review on the Applications of Graphene in Mechanical Transduction," *Adv. Mater.*, 34, 8, 2101326, 2022. DOI: 10.1002/adma.202101326

T.M. Ribeiro, T.E.C. Magalhães, **B. Kulyk**, A.F. Carvalho, A.J.S. Fernandes, F.M. Costa, H Crespo, "Measurement of ultrafast carrier dynamics in multilayer MPCVD graphene," *EPJ Web Conf.*, 266, 13028, 2022. DOI: 10.1051/epjconf/202226613028

B. Kulyk, A.F. Carvalho, N. Santos, A.J.S. Fernandes, F.M. Costa, "A short review on carbon-based nanomaterials and their hybrids," *Bol. Grupo Español Carbón*, 54, 44-54, dec. 2019,

https://www.gecarbon.org/boletines/articulos/BoletinGEC_054-art7.pdf (not peer-reviewed)

T. Gomes, M. Canhota, **B. Kulyk**, A. Carvalho, B. Jarrais, A.J. Fernandes, C. Freire, F. Costa, H. Crespo, "Ultrafast laser pulse characterization by THG d-scan using optically enhanced graphene coatings," arXiv:2206.01676 [physics.optics], 2022 (pre-print)

L. Martins, **B. Kulyk**, A. Theodosiou, A. Ioannou, N. Santos, C. Moreirinha, K. Kalli, F. Costa, S. Pereira, C. Marques, "Laser-induced graphene from commercial polyimide coated optical fibres for sensor development," *Opt. Laser Technol.*, 2022 (under review)

4.3.3 Oral presentations

B. Kulyk, L. Pereira, E. Fortunato, F.M. Costa, "Graphene on paper for flexible devices: sensors and OLEDs I," *Research Summit 2020*, Aveiro (Portugal), 24–26 June 2020

B. Kulyk, L. Pereira, E. Fortunato, F.M. Costa, "Graphene on paper for flexible devices: sensors and OLEDs II," *Research Summit 2021*, Aveiro (Portugal), 7–9 July 2021

B. Kulyk, A. Norinha, B.F.R. Silva, A.J.S. Fernandes, A.F. Carvalho, M. Matos, D. Evtuguin, F.M. Costa, "Synthesis of laser-induced graphene from papers and xylan film," *Advanced Nano Materials 2021*, Aveiro (Portugal), 23 July 2021

B. Kulyk, A.J.S. Fernandes, A.F.Carvalho, A.L. Patrício Silva, A.V. Girão, B.R. Figueiredo, R.P. Silva, V.E. Abrantes, A. Bernardes, T. Rocha-Santos, F.M. Costa, "Liquid-Phase Exfoliation of Graphene: Comparison of Laser-Induced Graphene and Graphite as Precursors," *European Graphene Forum 2021*, Milan (Italy), 20–22 October 2021

B. Kulyk, A.J.S. Fernandes, A.F. Carvalho, J.C. Germino, A.F. Cunha, L. Pereira, F.M. Costa, "CVD graphene transparent conductive electrodes for organic light emitting diodes (OLEDs)," *Nano 2022*, Seville (Spain), 6–10 June 2022

B. Kulyk, B.F.R. Silva, A.F. Carvalho, M. Matos, P. Barbosa, A.J.S. Fernandes, A.V. Girão, J. Deuermeier, S.O. Pereira, N.F. Santos, D.V. Evtuguin, F.M.L. Figueiredo, E. Fortunato, F.M. Costa, "Converting paper into laser-induced graphene for physical and biochemical sensors," *Graphene 2022*, Aachen (Germany), 5–8 June 2022

4.3.4 Contributions to other oral presentations

A.F. Carvalho, **B. Kulyk**, B.F.R. Silva, D. Santos, N.M. Ferreira, N.F. Santos, S.O. Pereira, J. Rodrigues, A.J.S. Fernandes, F. M. Costa, "Sensing Applications of Graphene, Transition Metal Oxides and Other Hybrid Materials," *PMI INNOV8*, Neuchâtel (Switzerland), September 2019.

A.F. Carvalho, **B. Kulyk**, A.J.S. Fernandes, E. Fortunato, F.M. Costa, "Towards large-scale freestanding few-layered graphene membranes and their application in acoustic transducers," *Graphene Week 2019*, Helsinki (Finland), 23–27 September 2019

A.F. Carvalho, N.M. Ferreira, **B. Kulyk**, N.F. Santos, A. Brinca, S.O. Pereira, M. Relvas, F. Rey-García, G. Gaspar, I. Azevedo, J. Rodrigues, T. Monteiro, A.J.S. Fernandes, F. M. Costa, "Tuning properties of materials by laser processing," *Materiais 2019*, Lisbon (Portugal), 14–17 April 2019

D.R. Pereira, C. Bouhafs, S.O. Pereira, C. Díaz-Guerra, M. Peres, A.J.S. Fernandes, **B. Kulyk**, F.M. Costa, M.R.P. Correia, E. Alves, S. Cardoso, P.P. Freitas, K. Lorenz, "Field effect transistors based

on α-MoO_3 exfoliated crystals and pseudo-layers," *45th WOCSDICE & 16th EXMATEC*, Ponta Delgada (Portugal), 3–6 May 2022

F. Costa, **B. Kulyk**, Nuno F. Santos, S.O. Pereira, A.J.S. Fernandes, A.F. Carvalho, "Laser-Induced Graphene for physical and electrochemical sensors," *RIVA 2022 – XII Iberian Vacuum and Applications Conference*, Braga (Portugal), 15–17 May 2022

A.F. Carvalho, **B. Kulyk**, A.J.S. Fernandes, E. Fortunato, F.M. Costa, "Laser-induced graphene on renewable substrates as a platform for integrated sensing," *Ciência 2022*, Lisbon (Portugal), 16–18 May 2022

A.F. Carvalho, **B. Kulyk**, N. Santos, S.O. Pereira, A. Moreira, A.J.S. Fernandes, F.M. Costa, "Laser-induced graphene: a platform for multisensing," *Nano 2022*, Seville (Spain), 6–10 June 2022

A.F. Carvalho, **B. Kulyk**, N.F. Santos, S.O. Pereira, A.J.S. Fernandes, F.M. Costa, "One-step approach for laser synthesis/patterning of graphene films with 3D networks for sensing," *ECCG7 – Seventh European Conference on Crystal Growth*, Paris (France), 25–27 July 2022

N.F. Santos, **B. Kulyk**, S.O. Pereira, A.F. Carvalho, A.J.S. Fernandes, F. Costa, "Laser-Induced Graphene on Polyimide and Paper Substrates for Low-Cost and Flexible Electrochemical Biosensors," *12th Ibero-American Congress on Sensors (IBERSENSOR2022)*, Aveiro (Portugal), 5–8 September 2022

4.3.5 Poster presentations

B. Kulyk, A.F. Carvalho, G. Gaspar, A. Norinha, A.J.S. Fernandes, F.M. Costa, "Reduction of secondary layer density by oxidative pre-treatment of the copper substrate in CVD graphene," *Graphene Study 2019*, Obergurgl (Austria), 3–8 February 2019

B. Kulyk, A.F. Carvalho, A. Norinha, G. Gaspar, A.J.S. Fernandes, F.M. Costa, "Reduction of secondary layer density by oxidative pre-treatment of the copper substrate in CVD graphene," *Materiais 2019*, Lisbon (Portugal), 14–17 April 2019

B. Kulyk, A.F. Carvalho, A.J.S. Fernandes, F.M. Costa, "Optimization of graphene growth parameters on in-situ oxidized and reduced copper," *Graphene Week 2019*, Helsinki (Finland), 23–27 September 2019

B. Kulyk, B.F.R. Silva, A.F. Carvalho, P. Barbosa, A.J.S. Fernandes, A.V. Girão, J. Deuermeier, F.M. L. Figueiredo, E. Fortunato, F. M. Costa, "Laser-induced graphene from paper: synthesis, characterization and sensing applications," *Graphene Week 2021*, online, 20–24 September 2021

B. Kulyk, B.F.R. Silva, A.F. Carvalho, M. Matos, P. Barbosa, A.J.S. Fernandes, A.V. Girão, J. Deuermeier, S.O. Pereira, N.F. Santos, D.V. Evtuguin, F.M.L. Figueiredo, E. Fortunato, F.M. Costa, "Transforming papers into graphene using lasers: applications in physical and biochemical sensors," *Ciência 2022*, Lisbon (Portugal), 16–18 May 2022

4.3.6 Contributions to other poster presentations

G. Gaspar, **B. Kulyk**, A.J.S. Fernandes, A.F. Carvalho, J. Deuermeier, E. Fortunato, R.F. Silva, F.M. Costa, "TCVD graphene growth on large-scale IR laser-textured copper substrates," *Materiais 2019*, Lisbon (Portugal), 14–17 April 2019

A.F. Carvalho, N.F. Santos, **B. Kulyk**, A. Norinha, G. Gaspar, A.V. Girão, F. Oliveira, R.F. Silva, A.J.S. Fernandes, B.R. Figueiredo, R.P. Silva, V.E. Abrantes, A. Bernardes, F.M. Costa, "Graphene obtained by mechanical exfoliation from natural and laser processed precursors," *IBERTRIVA 2019 – X Iberian Conference on Tribology / XI Iberian Vacuum Conference*, Seville (Spain), 2019

T.S. Gomes, M. Canhota, **B. Kulyk**, A.F. Carvalho, G. Gaspar, A.J.S. Fernandes, F.M. Costa, H. Crespo, "Broadband third-harmonic generation in multilayer graphene for the characterization of near single-cycle ultrashort light pulses," *Condensed Matter Physics National Conference 2019*, Porto (Portugal), 8–10 May 2019

T.S. Gomes, M. Canhota, H. Crespo, M. Miranda, C. Freire, B. Jarrais, **B. Kulyk**, F.M. Costa, A.J.S. Fernandes, A.F. Carvalho, "Broadband few cycle pulse characterization by third harmonic dispersion-scan in multilayer and optically improved functionalized graphene coatings," *Ultrafast Optics 2019*, Bol (Croatia), 6–11 October 2019

T.S. Gomes, M. Canhota, A.F. Carvalho, **B. Kulyk**, M. Miranda, B. Jarrais, A.J.S. Fernandes, C. Freire, F.M. Costa, H. Crespo, "Temporal measurement of few-cycle laser pulses by third-harmonic dispersion-scan with optically improved graphene coatings," *Graphene and 2DM Industrial Forum 2020*, online, 2020.

A.F. Carvalho, J. Marques, D. Gomes, **B. Kulyk**, A. J.S. Fernandes, F.M. Costa, "Laser induced graphene on wooden materials as a platform for smart furniture," *Nano 2022*, Seville (Spain), 6–10 June 2022

D. Pereira, C. Bouhafs, S. Pereira, C. Díaz-Guerra, M. Peres, A. Fernandes, **B. Kulyk**, F. Costa, M.R. Correia, E. Alves, "Incorporation of modified MoO_3 crystals and pseudo-layers into field effect transistors," 22nd International Conference on Ion Beam Modification of Materials, Lisbon (Portugal), 10–15 July 2022

D.R. Pereira, C. Bouhafs, S.O. Pereira, C. Díaz-Guerra, M. Peres, A.J.S. Fernandes, **B. Kulyk**, F.M. Costa, M.R.P. Correia, E. Alves, S. Cardoso, P.P. Freitas, K. Lorenz, "Field effect transistors on MoO_3 crystals and pseudo-layers: fabrication and characterization," *Física 2022*, Porto (Portugal), 7–10 September 2022

4.3.7 Dissemination in other media

"Papel deteta ácido úrico", *Jornal da Uma*, TVI, 9 October 2022 (news report, television broadcast)
https://tviplayer.iol.pt/programa/jornal-da-uma/53c6b2633004dc00624392e1/video/6342bbb50cf26256cd399f8f

"Papel deteta ácido úrico", *CNN Domingo*, CNN Portugal, 18:54:00 9 October 2022 (news report, television broadcast)

Cláudia Valente de Oliveira, "Investigadores de Aveiro criam papel para avaliar os níveis de ácido úrico em casa", *CNN Portugal*, 9 October 2022.
https://cnnportugal.iol.pt/videos/investigadores-de-aveiro-criam-papel-para-avaliar-os-niveis-de-acido-urico-em-casa/6342bbb50cf26256cd399f8f (news report, online)

"UA desenvolve sensor de papel para detetar ácido úrico na urina", *Diário de Aveiro*, 9 October 2022 (news report, daily journal)

Nuno de Noronha, "Equipa da UA desenvolve sensor de papel para detetar ácido úrico na urina", *Sapo Lifestyle*, 6 October 2022. https://lifestyle.sapo.pt/saude/noticias-saude/artigos/equipa-da-ua-desenvolve-sensor-de-papel-para-detetar-acido-urico-na-urina (article, online)

"Universidade de Aveiro cria sensor de papel e grafeno para testes de urina", *Saúde+*, 6 October 2022 (article, online)
https://saudemais.tv/noticia/41347-universidade-de-aveiro-cria-sensor-de-papel-e-grafeno-para-testes-de-urina

Laurie Winkless, "Paper-based graphene biosensor for urine testing", *Materials Today*, 11 July 2022 (article, online)
https://www.materialstoday.com/carbon/news/paperbased-graphene-biosensor-for-urine-testing/

A. F. Carvalho, **B. Kulyk**, A.J.S. Fernandes, F.M. Costa, "Bringing atom-thick materials to the millimeter scale," *research@UA* Vol. 11, 19 June 2021 (research highlights of the University of Aveiro)

N. F. Santos, **B. Kulyk**, S. O. Oliveira, A. F. Carvalho, A. J.S. Fernandes, F. M. Costa, "Laser-Induced Graphene: from physical sensing to electrochemical biosensors," *research@UA* Vol. 12, 5 September 2022 (research highlights of the University of Aveiro)

4.3.8 Public outreach

Demonstration of various innovative technological projects at "Aveiro Tech Week 2021": Laser-Induced Graphene (LIG); application of laser technology for cleaning and modification of surfaces; laser technology for the production of materials for energy transfer, conversion and storage. Largo do mercado Manuel Firmino, Aveiro, 10-16 October 2021

Demonstration of various projects and prototypes at "Noite Europeia dos Investigadores 2022": Laser processing: graphene sensors and surface engineering (Florinda Costa, António Fernandes, Alexandre Carvalho, Nuno Ferreira, Bohdan Kulyk, Nuno Santos, Sónia Pereira, Luís Pires, Alexandre Botas, Paulo Santos, Maria João Pereira, Ana Brinca e Rodrigo Santos). Fábrica Centro Ciência Viva de Aveiro, 30 September 2022

4.3.9 Awards

Best pitch award for the presentation "Graphene on paper for flexible devices: sensors and OLEDs" at *Research Summit 2021*, Aveiro, Portugal, 7-9 July 2021